VON KARMAN INSTITUTE FOR FLUID DYNAMICS

REVIEW OF THE VKI DOCTORAL RESEARCH

2015 - 2016

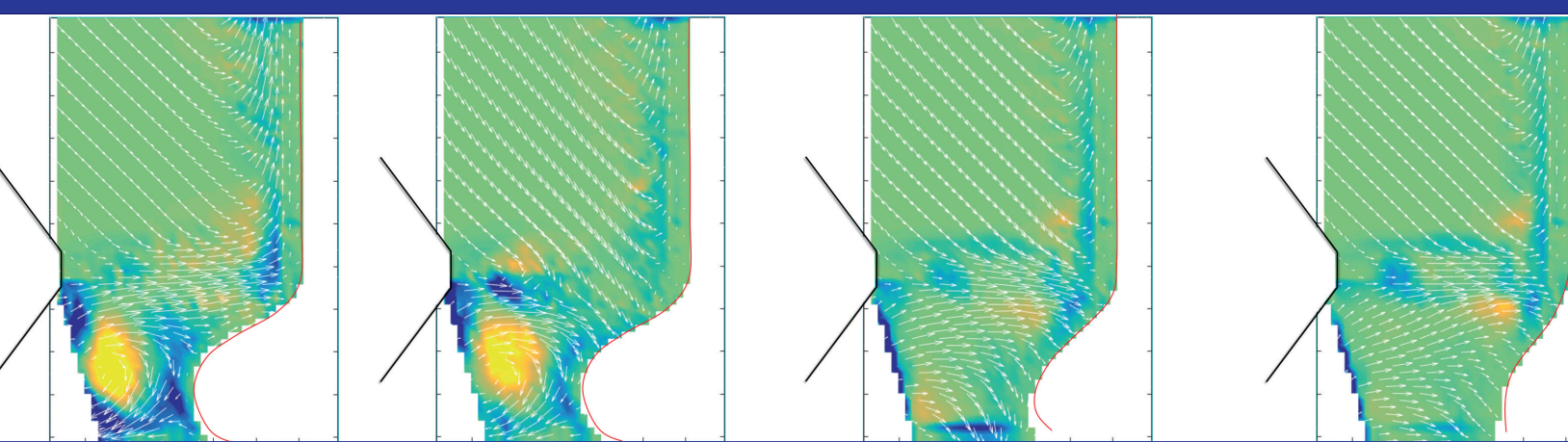

www.vki.ac.be

REVIEW OF THE VKI DOCTORAL RESEARCH

2015 - 2016



von Karman Institute for Fluid Dynamics

Covert art: Sequence of flow field snapshot and contour of the second invariant of the velocity field, for a plane turbulent jet impinging on a deformable, moving wall. The second invariant Q highlights recirculation dominated region (in yellow) over shear rate dominated regions (in blue) and potential flow like regions (in green). The flow field is obtained from Time-Resolved Particle Image Velocimetry (TR-PIV) and filtered via Proper Orthogonal Decomposition (POD). This decomposition allows for identifying the dominant modes in the velocity field, and to construct a lower dimensional approximation which captures coherent flow structure from the turbulent dataset.

©2016 by the von Karman Institute for Fluid Dynamics
Waterloosesteenweg 72, B-1640 Sint-Genesius-Rode
To order: https://www.vki.ac.be

ISBN 978-2-87516-108-6

D/2016/0238/675, T. Magin, Editor-in-Chief

The contents of this book are the property of the von Karman Institute for Fluid Dynamics. No part of this book may be reproduced or distributed in any form of by any means, or stored in a database or retrieval system, without the prior written permission from the Publisher.

PREFACE

The seventh symposium on the doctoral research of the von Karman Institute for Fluid Dynamics took place during the period March 1 to 3, 2016. The doctoral students have presented the progress of their research work carried out in the three departments: Aeronautics and Aerospace, Environmental and Applied Fluid Dynamics, Turbomachinery and Propulsion. The first year students have presented a poster on their research plans and some preliminary results, while the most advanced students have proposed a presentation followed by a session of questions.

This event was attended by the faculty of the von Karman Institute as well as by colleagues from universities and industrial partners. The Symposium was open to external attendees free of charge. In addition to the presentations of the PhD candidates, we had the pleasure to welcome three prominent keynote lecturers who have opened each day the Symposium:

- Prof. Christophe Brehm, Department of Aerospace and Mechanical Engineering, the University of Arizona, NASA Ames Research Center, NASA Advanced Supercomputing (NAS) Division, USA, "*A locally stabilized higher-order immersed boundary method and its application to NASA relevant flow problems*,"
- Prof. Alessandro Parente, Aero-Thermo-Mechanical Department, Université Libre de Bruxelles, *"Reduced-order modelling of turbulent combustion via Empirical Low-Dimensional Manifolds,"*
- Dr. John Coull, University of Cambridge, Whittle Laboratory, "*Understanding endwall losses in turbine cascades."*

A special IFAR virtual conference (International Forum for Aviation Research http://www.ifar.aero) was organized in collaboration with NASA. This virtual conference was broadcasted among the IFAR members and associated universities with interaction during the question session. Three PhD members were selected this year to present their work related to IFAR activities: Yakut Cansev Kucukosman, Daniel Guariglia and Giulia Dell'Era. Dr. Valerie Wiesner from NASA Glenn Research Center opened the IFAR session with a speech emphasizing the IFAR Young Researcher Network's opportunities for networking and engagement.

This year, the best presentation award has been attributed to Miguel Alfonso Mendez for his research on "*Oscillation of planar gas jet impinging on a deformable wall*." We would like to congratulate him on this achievement. The illustrated cover art of these proceedings is based on his research results.

This proceedings volume contains 44 papers which are divided into the following topics: "*Numerical Approach for Hypersonic and Plasma Flows*," "*Ablation*," "*Ground and Flight Experiments*," "*Multiphase Flows*," "*Development of Advanced CFD and Optimization*," "*Uncertainty Quantification*," "*Aero-Thermal Investigations in Turbomachinery*," "*Noise and Aeroacoustics*."

We would like to emphasize that this publication serves as a tool for communication and aims to enhance exchange between the doctoral candidates, the faculty and external attendees. The annual publication of their results in proceedings is of crucial importance to the VKI research providing a thorough review of the different activities within the three departments.
As such, the doctoral candidate students play a key role in strengthening the expertise in experimental research, computational methods, and physical modelling. In addition to basic research, works carried out at the von Karman Institute often leads to implementation of real life industrial applications critical to the fluid dynamics community.

Ana Isabel Del Val Benítez	Thierry Magin	Christelle Debeer	Jean Muylaert
Julien Clinckemaillie	Mario Rosaria Vetrano	Organizer	VKI Director
Phd Representatives	Professors	Editor	

The contribution of all VKI members who helped with this event is deeply acknowledged in particular the faculty, library and printing office staff.

TABLE OF CONTENTS

Editorial notes i

Table of contents iii

NUMERICAL APPROACH FOR HYPERSONIC AND PLASMA FLOWS

Alejandro ÁLVAREZ LAGUNA 3
Multi-fluid modeling of magnetic reconnection in astrophysical and laboratory plasmas

Gilles BAILET 15
Reentry platform for studying radiation, from payload design to performances

Federico BARISELLI (1st year PhD) 25
Development of an ablation model for rarefied flows with application to meteor entry

Georgios BELLAS CHATZIGEORGIS 27
Development of advanced gas surface interaction models for reusable materials

Aurélie BELLEMANS 37
SPARK: simplified plasma models based on reduced kinetics

Andrea CORTESI 45
Rebuilding freestream atmospheric conditions using surface pressure and heat flux data

Ana Isabel DEL VAL BENÍTEZ (1st year PhD) 55
Investigations on the reproduction of planetary re-entry flights in high enthalpy and plasma wind tunnels

Barros Bruno Ricardo DIAS 61
Simulation of the atmospheric entry of meteors with application to radio detection

Koen GROOT 73
Non-linear extensions of global flow stability theory

Fernando MIRÓ MIRÓ (1st year PhD) 83
Numerical investigation of hypersonic boundary-layer stability in the presence of ablation phenomena

Alan VILADEGUT 85
Assessment of gas-surface interaction modeling for lifting body re-entry flight design

GROUND AND FLIGHT EXPERIMENTS

Jorge FERNANDES LOPES DE SOUSA 97
Aerodynamic design methodology for supersonic internal passages

Zdenek ILICH (1st year PhD) 107
Experimental investigation of roughness induced transition phenomena at hypersonic Mach numbers

MULTIPHASE FLOWS

Elissavet BOUFIDI (1st year PhD) 115
The characterization of turbulence in high speed, compressible and complex industrial flows

Sophia BUCKINGHAM (1st year PhD) 121
Turbulent heat transfer of separated flows at low Prandlt number

Nicolas DE COCK 125
Splash plate nozzle design optimization

Claudia ESPOSITO (1st year PhD) 135
Experimental study of cavitating flow and fluid hammer in cryogenic conditions

Charline FOUCHIER (1st year PhD) 137
Scaled model of the pollutant dispersion after an explosion in a complex environment

Sara GONZÁLEZ RUIZ 139
Optical caustics produced by spheroidal droplets in the glory region:
experimental observations and numerical simulations

Miguel Alfonso MENDEZ 145
Oscillation of planar gas jet impinging on a deformable wall

Alessia SIMONINI 157
Cryogenic sloshing dynamics in partially filled cylinder subjected to horizontal sinusoidal excitations

Orkun TEMEL 167
Multiscale and multiphysical modeling of atmospheric boundary layer

Agustín VILLA ORTIZ 179
Turbulent heat transfer at different Prandtl number fluids in natural convection boundary
layer on a vertical plate

DEVELOPMENT OF ADVANCED CFD AND OPTIMIZATION

Hassanine Mohamed AISSA 195
Acceleration of turbomachinery steady simulations on GPU

Giacomo ALESSI (1st year PhD) 203
Adjoint surface optimization for internal and external aerodynamics applications by means of OpenFOAM

Christopher CHAHINE 205
Towards flutter analysis of composite aero-engine fan blades

Clara GARCÍA SÁNCHEZ 213
Quantifying inflow uncertainties for CFD simulations of dispersion in the atmospheric boundary layer

Aude LAHALLE 221
Experimentally and numerically driven optimization of a high performance instrumentation for
real engine testing

Lasse MÜLLER 231
Adjoint-based design optimization of a turbocharger radial turbine

Ismael SÀNCHEZ TORREGUITART (1st year PhD) 241
CAD based adjoint optimization of turbomachinery components using automatic differentiation

Marc SCHWALBACH (1st year PhD) 243
Adjoint optimization of turbomachinery components under mechanical constraints

Nikolaos STERGIANNIS 245
Full rotor CFD simulations of two wind turbines in a row using RANS

AERO-THERMAL INVESTIGATIONS IN TURBOMACHINERY

Bogdan Cezar CERNAT (1st year PhD) 257
Active tip leakage flow control in high pressure turbines

Julien CLINCKEMAILLIE 259
Analysis and consequences of the separation/transition mechanisms of the flow on a modern low-pressure gas turbine airfoil

Giulia DELL'ERA 269
Experimental characterization of unsteady flows in a high speed axial compressor

Cis DE MAESSCHALCK 279
Performance robustness of turbine squealer tip designs due to manufacturing and engine operation

Gian Luca GORI 291
Determination and modeling of the aero-thermal behavior of a cooling channel

Ignacio MAYO YAGUE 299
Flow field and heat transfer in a rotating cooling channel

Roberto TOMASSINI 311
Blade tip timing and blade tip clearance measurement system based on magnetoresistive sensors

Marco VIRGILIO (1st year PhD) 321
Advanced experimental aero-thermal investigations of wall-bounded swirling flows in three-dimensional ribbed tubes

NOISE AND AEROACOUSTICS

Gabriele GRASSO 325
Prediction of low-speed fan trailing-edge noise based on RANS and on scale resolved simulations

Daniel GUARIGLIA 339
Facility design and shock-cell noise investigation on a supersonic coaxial jet

Lionel HIRSCHBERG 351
SRM aeroacoustics

Yakut Cansev KUCUKOSMAN (1st year PhD) 357
Rotor noise extraction by in-duct modal decomposition technique

WHO'S WHO 365

NUMERICAL APPROACH FOR HYPERSONIC AND PLASMA FLOWS

Multi-fluid modeling of magnetic reconnection in astrophysical and laboratory plasmas

Alejandro Alvarez Laguna

von Karman Institute for fluid Dynamics, Aeronautics and Aerospace Department, alejandro.alvarez.laguna@vki.ac.be

Supervisor: Herman Deconinck

von Karman Institute for fluid Dynamics, Aeronautics and Aerospace Department, deconinck@vki.ac.be

University Supervisor: Stefaan Poedts

Professor, KU Leuven, Centrum voor mathematische Plasma-Astrofysica, stefaan.poedts@wis.kuleuven.be

Abstract

Improved models for characterizing magnetized partially ionized plasma are essential to understand the phenomena taking place in astrophysical and laboratory plasmas. Particularly, scenarios where dissipative processes and thermo-chemical inequilibrium play an important role are beyond the classical single-fluid Magnetohydrodynamics (MHD) representation. Multi-fluid models that consider each particle species as a separate fluid offer an alternative approach especially suitable for those conditions. In the present work, the magnetic reconnection taking place in the chromosphere is studied using a two-fluid model considering neutrals and charged species. The numerical method solving multi-fluid equations coupled to Maxwell's equations is presented in this work. Also, a finite volume method for solving the radiative transfer equation (RTE) is presented to be used in future studies of magnetic reconnection.

Keywords: Magnetohydrodynamics (MHD), Magnetic Fields, Plasmas, Magnetic Reconnection, Sun: Atmosphere, Radiative Transfer.

1. Introduction

Numerical study of plasma flows continues to be an important area of research in a number of fields ranging from astrophysics to engineering applications. The application of electromagnetic fields to control the dynamics of electrically conducting flows has a long tradition in the aerospace industry that uses different concepts for flight and propulsion including plasma actuators, plasma thrusters or MHD by-pass arrangements in scramjets. In the present work, we will focus in two areas of particular interest for the CFD community, solar physics and laboratory plasmas.

The activity of the Sun has a great impact in our technology and ultimately in today's modern society that strongly depends on communications and satellite operations. From a global socio-economic perspective, the most important manifestations of solar activity are the solar wind and solar eruptions, i.e. solar flares and coronal mass ejection (CMEs). The unsteady but continuous emission of particles at high speed and temperature from the Sun into the space can hinder human activity at different levels. Satellite operations can be seriously affected by plasma ejected during solar storms, producing important damages or the loss of some of them, like the Telstar 401 that was short cut in January 1997. More recently, in 2003, a solar storm caused disruptions in the airplane routes and the CME affected several communication satellites (two were total loss). Also, when the high energetic charged particles ejected from the Sun reach our atmosphere can produce the so-called Geo-magnetically Induced Currents (GICs) that cause hazards in oil pipelines and power grid outages. An example of the latter is the magnetic storm that burned a $36 million transformer in New Jersey and left 6 million people more than 10 hours without electrical

power in Quebec in winter conditions (March 1989). As a matter of fact, the cost of a severe space storm has been estimated to be trillions of dollars for the first year after the storm with recovery times of 4 to 10 years (an order of magnitude more than that of Hurricane Katrina) [1].

Different plasma models can be used depending on the characteristics studied phenomenon. The most universal description of plasma relies on the Boltzmann equation that, together with Maxwell's equations, describes the evolution of the distribution function for each plasma species. However, solving numerically Boltzmann equation is computationally too expensive since it involves seven dimensions, i.e., physical space, velocity phase and time. Because of this reason, usually, kinetic simulations are confined to limited domains.

The multi-fluid plasma description is obtained by taking moments of the Boltzmann equation for each species. This model is simpler since it averages over the velocity space of each plasma species. Therefore, the microscopic information of the individual particles contained in the Boltzmann equation is lost since only macroscopic quantities are considered by this model. The multi-fluid model considers each species in the plasma as a separate fluid, usually assuming that each fluid is in local thermodynamic equilibrium (LTE).

However, most of the models of magnetized plasmas are based on the magnetohydrodynamics (MHD) description. It is obtained by combining the multi-fluid equations and simplifying them (making certain assumptions on time and length scales). MHD models consider plasma behaving as one quasi-neutral conducting fluid, usually assuming LTE of all the species. Therefore, the model is sufficient to describe phenomena with characteristic lengths than are much larger than particles characteristic lengths, i.e., the mean free path of the collisions and the Larmor radius of the charged particles. Consequently, the MHD description neglects high frequency waves and other effects that are consequence of the particle interaction, such as, the Hall effect, ambipolar diffusion or diamagnetic effects. However, these effects are seen to play an important role in phenomena such as magnetic reconnection, where the width of the current sheet formed becomes comparable to the ion scales (i.e., the ion skin depth, ion gyroradius, ion-neutral collision mean free path) [5].

It is therefore necessary to improve the understanding and modeling of the phenomena taking place in the Sun for enhancing the tools used for the space weather forecasting and eventually reducing its risk on our technology. Magnetic reconnection is a process especially significant in space weather since it has been long considered as a mechanism for creating transient phenomena in magnetized plasma. It occurs when oppositely directed magnetic field lines in conducting plasma merge due to diffusive processes producing a change of topology. The rearrangement of magnetic field lines produces a change of the magnetic flux that due to the finite conductivity creates a current sheet. In addition, the reconnection process causes a conversion of magnetic energy into kinetic and thermal energy, heating up the flow and accelerating it up to very high speed in very small timescales.

There are a wide variety of astrophysical scenarios in which the magnetic reconnection plays an important role. It is considered to be a likely mechanism to heat the corona to a few million degrees, still one of the biggest mysteries in Heliophysics [2]. Also, in CMEs and solar flares it is considered as a triggering mechanism which is present during the onset and early stages of the ejection [3]. In the Earths magnetosphere it is said to produce the plasma outflow at the magnetotail that is driven by the Earths magnetic field into the atmosphere producing the aurorae borealis and the GICs [4].

Magnetic reconnection also occurs in nuclear fusion and laboratory plasmas producing instabilities such as sawtooth in tokamaks and relaxation processes in reverse field pinch and spheromak devices, causing degradation in energy and particle confinement. A recent experimental study [5] has shown that during reconnection taking place in laboratory plasmas, magnetic energy is transferred differently to ions than electrons. Also, it is shown the different dynamics of ions and electrons due to their different mass and electric charge. The latter is the so-called *two-fluid effects*.

In the present work, we will focus on studying the magnetic reconnection in the Sun chromosphere, following the work presented in [6]. Observational data [7] have unveiled that the magnetic reconnection is the driver mechanism for the chromospheric jets and the spicules. The former can have timescales of 200-1000 s and current sheet length scales up to 5 Mm, producing outflows of 10 km/s. On the other hand, the spicules are smaller but faster phenomena, that last 10-600 s in length scales up to 1 Mm causing outflows up to 20-150 km/s [6].

In the present work, we present a summary of the modeling of magnetic reconnection, focusing on the analytical models and explaining the possible benefits of multi-fluid modeling. The two-fluid partially

ionized reactive plasma model including neutrals and charge species is presented, as well as, the Maxwell's equations describing the evolution of the electromagnetic field. Also, the radiative transfer equation is presented, leaving the coupling with the fluid model for future developments. The numerical method including a finite volume method for solving Maxwell equations using hyperbolic divergence cleaning coupled to AUSM method for the fluids is explained hereafter. Additionally, the validation of the coupling on the Hartmann flow is presented. Furthermore, a finite volume method solving the RTE and its validation is shown in the present work. Finally, the results of a 2D reconnection under chromospheric conditions are presented with preliminary 3D results using the two-fluid model.

2. Modeling of the magnetic reconnection

Magnetic reconnection is a process that happens as a result of a diffusive mechanism that produces a decay in the electrical conductivity of the plasma. The frozen-in constrain that holds in ideal plasmas (with infinite conductivity) is broken in a small region of width δ and length L. In this region, the magnetic field lines reconnect producing a rate of magnetic flux that results in the formation of a current sheet. Thus, the non-dimensional magnetic reconnection rate is defined [8] as follows:

$$M = \frac{d\Phi/dt}{v_A B_i} \tag{1}$$

where Φ is the magnetic flux per unit length in the direction perpendicular to the plane containing the current sheet , v_A is the Alfven speed and B_i is the magnetic field evaluated upstream of the current sheet.

Therefore, it is obvious to realize that the classical ideal MHD equations that consider the conductivity to be infinite are not able to tackle the physics involved in the reconnection. Nevertheless, the resistive singlefluid theory has developed analytical models for 2D steady magnetic reconnection. The Sweet-Parker model [9] proposes a non-dimensional reconnection rate of the form:

$$M = R_m^{-1/2} \tag{2}$$

where

$$R_m = v_A L/\eta \tag{3}$$

is called the Lundquist number, and η is the resistivity.

However, the model is unable to explain the fast energy released by the solar flares or in chromospheric jets and spicules, providing reconnection rates several orders of magnitude smaller.

On the other hand, the Petschek model [10] predicts faster reconnections suggesting geometry different from the Sweet-Parker one, Eq. 4. However, the model assumes explicitly or tacitly that resistivity gives the configuration setup. Because of this controversial issue, the Petschek model has been gradually thrown back [11].

$$M = \frac{\pi}{8\ln(R_m)} \tag{4}$$

Therefore, it is necessary to consider alternative theories to model the reconnection. The multi-fluid models consider each particle species as a different fluid that interact among each other by means of collisions and chemical reactions, exchanging thus mass, momentum and energy in their interplay. Since the width of the diffusion region can be comparable to the ion scales [4], therefore, the multi-fluid description are considered to capture diffusive effects that are completely neglected by the single-fluid theory, as shown in experimental research [5].

In the literature, one can find several fluid closures accounting for the different behavior of the species of plasmas in presence of electromagnetic fields. Braginskii [12] derives a two-fluid formulation considering separate ions and electrons. In his seminal work, he proposes closures for the transport properties, accounting for the anisotropy introduced by the magnetic field. Similarly, Magin [13] proposes a multicomponent model separating heavy particles and electrons, treating the effect of the magnetic field on the transport properties. Most recently, Meier [14] has proposed a two-fluid model considering the charged particles and neutrals as separate fluids, considering both anisotropic effects in the plasma heat conduction due to the magnetic field and chemical reactions (ionization and recombination).

3. Governing Equations

3.1. Two-fluid plasma equations

The multi-fluid description used in the results shown hereafter is the model discussed in [14]. It is a two-fluid model that considers separately hydrogen neutrals and charged species, i.e. hydrogen ions and electrons. The full set of equations considered comprises mass, momentum and total energy conservation

for both fluids. The chemical reactions considered are electron impact ionization and radiative recombination. The excited states are not tracked, only an effective potential is assumed ϕ_{ion} for the ionization reaction. The plasma is assumed to be optically thin, so the radiation effects are completely lost from the system. Electrons are considered to be in thermal equilibrium with ions, allowing neutrals to be in non-LTE. Charge neutrality is assumed and the electrons inertia and viscosity is neglected. This simplification yields the following system:

$$\frac{\partial \rho_i}{\partial t} + \nabla \cdot (\rho_i \vec{v}_i) = m_i(\Gamma_i^{ion} + \Gamma_i^{rec}), \tag{5}$$

$$\frac{\partial \rho_n}{\partial t} + \nabla \cdot (\rho_n \vec{v}_n) = m_n(\Gamma_n^{ion} + \Gamma_n^{rec}), \tag{6}$$

$$\frac{\partial \rho_i \vec{v}_i}{\partial t} + \nabla \cdot (\rho_i \vec{v}_i \vec{v}_i + p_i \vec{\vec{\delta}} + p_e \vec{\vec{\delta}}) = -\nabla \cdot (\pi_i) + \vec{j} \times \vec{B} + \vec{R}_i^{in} + \Gamma_i^{ion} m_i \vec{v}_n - \Gamma_n^{rec} m_i \vec{v}_i, \tag{7}$$

$$\frac{\partial \rho_n \vec{v}_n}{\partial t} + \nabla \cdot (\rho_n \vec{v}_n \vec{v}_n + p_n \vec{\vec{\delta}}) = -\nabla \cdot (\pi_n) - \vec{R}_i^{in} - \Gamma_i^{ion} m_i \vec{v}_n + \Gamma_n^{rec} m_i \vec{v}_i, \tag{8}$$

$$\frac{\partial}{\partial t}\left(\varepsilon_i + \frac{p_e}{\gamma_e - 1}\right) + \nabla \cdot (\varepsilon_i \vec{v}_i + \frac{\gamma_e p_e}{\gamma_e - 1} \vec{v}_i + p_i \vec{v}_i) = -\nabla \cdot (\vec{v}_i \cdot \pi_i + \vec{q}_i + \vec{q}_e) + \vec{j} \cdot \vec{E} + \vec{v}_i \vec{R}_i^{in} + Q_i^{in} - \Gamma_n^{rec} \frac{1}{2} m_i v_i^2 - Q_n^{rec} + \Gamma_i^{ion} \left(\frac{1}{2} m_i v_n^2 - \phi_{ion}\right) + Q_i^{ion}, \tag{9}$$

$$\frac{\partial \varepsilon_n}{\partial t} + \nabla \cdot (\varepsilon_n \vec{v}_n + \vec{v}_n p_n) = -\nabla \cdot (\vec{v}_n \cdot \pi_n + \vec{q}_n) - \vec{v}_n \vec{R}_i^{in} + Q_n^{in} + \Gamma_n^{rec} \frac{1}{2} m_i v_i^2 + Q_n^{rec} - \Gamma_i^{ion} \frac{1}{2} m_i v_n^2 - Q_i^{ion} \tag{10}$$

Where the subindices i, e, n stand for ions, electrons and neutrals. The electrical current follows Ohm's law $\vec{E} + \vec{v}_i \times \vec{B} = \eta \vec{j}$ with the resistivity η assumed to be constant. The reaction rates Γ^{ion} and Γ^{rec} and the reaction energy production Q^{ion} and Q^{rec} are taken from [26] and [27]. The momentum and energy collisional terms $\vec{R}_\alpha^{\alpha\beta}$ and $Q_\alpha^{\alpha\beta}$ considered are discussed in [6]. Ions and neutrals viscosity stress tensor are assumed to be Newtonian, with constant viscosity. Neutrals heat conduction follows Fouriers law with constant thermal conductivity, whereas ions have anisotropic heat flux accounting for the effect of the magnetic field, described in [12]. The fluid are assumed to be perfect gases with $\gamma = 5/3$.

3.2. Maxwell's equations

The electromagnetic influence is tackled with the Maxwell equations:

$$\frac{\partial \vec{B}}{\partial t} + \nabla \times \vec{E} = 0 \tag{11}$$

$$\frac{\partial \vec{E}}{\partial t} - c^2 \nabla \times \vec{B} = -\frac{\vec{j}}{\epsilon_0} \tag{12}$$

$$\nabla \cdot \vec{B} = 0 \tag{13}$$

$$\nabla \cdot \vec{E} = \frac{\rho_c}{\epsilon_0} \tag{14}$$

where ρ_c is the charge density that is assumed to be zero.

3.3. Radiative transfer equation

In the results on the chromospheric magnetic reconnection shown hereafter, the radiative effects are neglected. However, in the solar atmosphere, particularly in the lower layers, i.e., photosphere and low-chromosphere, radiation is observed to play an important role [15]. The RTE in a non-scattering medium, neglecting the time derivative which is a lower order term, can be written:

$$\vec{\Omega} \cdot \nabla I_\nu = \kappa_\nu (S_\nu - I_\nu) \tag{15}$$

Where I_ν is the radiative intensity for the frequency ν, $\vec{\Omega}$ is the direction, κ_ν is the opacity of the medium and S_ν is the radiative source.

The radiative heat flux that should be included in the species energy equations 9 - 10 is calculated, as follows:

$$\vec{q}_{rad} = \int_\nu \int_\Omega I_\nu \vec{\Omega} \, d\Omega \, d\nu, \tag{16}$$

and the divergence of the flux:

$$\nabla \cdot \vec{q}_{rad} = \int_\nu \int_\Omega \kappa_\nu (S_\nu - I_\nu) \, d\Omega \, d\nu. \tag{17}$$

4. Numerical Modeling

4.1. Finite Volume Method

The results have been obtained using the FV solver for unstructured grids provided by the COOLFluiD platform [16]. The governing equations are written in conservative form, as follows:

$$\frac{d}{dt}\int_{\Omega_i}\mathbf{U}\,dV+\oint_{\partial\Omega_i}\mathbf{F^c}\cdot\mathbf{n}\,dS= \oint_{\partial\Omega_i}\mathbf{F^d}\cdot\mathbf{n}\,dS+\int_{\Omega_i}\mathbf{S}\,dV \tag{18}$$

The conservative form of Maxwell equations is found in [17]. The cell-centered FV discretization applies the integral conservation law to each cell, assuming the solution to be constant over the cell and storing the value at the centroid of it. In order to obtain second order accuracy in space, inverse-distance weighted least square reconstruction [18] is used. The multidimensional limiter of Venkatakhrisnan [19] is used to obtain oscillation free solutions. The discretization of the inviscid fluxes is explained hereafter.

4.2. Hyperbolic divergence cleaning for Maxwell equations

One of the biggest concerns in the development of a Maxwell solver is to satisfy the two divergence constrains Eq. 13 and Eq. 14 on the discrete level. The hyperbolic divergence cleaning method [21] is discussed to be an efficient way to enforce the constrains in Finite Volume solvers. Two Lagrange multipliers ϕ and ψ are added in Maxwell equations as follows:

$$\frac{\partial\vec{B}}{\partial t}+\nabla\times\vec{E}+\gamma^2\nabla\Psi=0 \tag{19}$$

$$\frac{\partial\vec{E}}{\partial t}-c^2\nabla\times\vec{B}+\chi^2c^2\nabla\Phi=-\frac{\vec{j}}{\epsilon_0} \tag{20}$$

$$\frac{\partial\Psi}{\partial t}+c^2\nabla\cdot\vec{B}=0 \tag{21}$$

$$\frac{\partial\Phi}{\partial t}+\nabla\cdot\vec{E}=\frac{\rho_c}{\epsilon_0} \tag{22}$$

Artificial waves are introduced at speeds γc and χc that remove the errors in the fulfillment of the constrains. Therefore, the two scalar parameters γ and χ should be chosen to be ≥ 1.

4.3. Steger-warming scheme for Maxwell equations

The Steger-Warming scheme [20] splits the flux at the interface into positive and negative components based on the eigenvalue structure of the system as follows:

$$\mathbf{F^c}=\mathbf{A}_+\mathbf{U}^L+\mathbf{A}_-\mathbf{U}^R \tag{23}$$

where

$$\mathbf{A}=\frac{\partial\mathbf{F^c}}{\partial\mathbf{U}}=\mathbf{A}_-+\mathbf{A}_+ \text{ and } \mathbf{A}_\pm=\mathbf{R}\Lambda_\pm\mathbf{R}^{-1} \tag{24}$$

where $\mathbf{R}$ is the matrix of right eigenvectors, $\Lambda_\pm$ the diagonal matrix of diagonal matrices with the positive and negative eigenvalues, $\mathbf{U}$ are the conservative variables.

As mentioned in [17], when the Maxwell equations are coupled to the fluid equations, the numerical dissipation is out of balance since some terms are proportional to the speed of light while other are proportional to the speed of the fluid. In the results presented in this work, we use a novel scaling of the numerical dissipation including the two divergence cleaning equations.

4.4. AUSM scheme for fluid equations

AUSM-family schemes [24] split the inviscid flux of each fluid at the cell interface into the convective part and the pressure flux as follows:

$$\mathbf{F^c}=\mathbf{F^{conv}}+\mathbf{P} \tag{25}$$

with

$$\mathbf{F^{conv}}=\dot{m}\mathbf{\Psi}^{L/R} \tag{26}$$

$\dot{m}$ is the numerical mass flux at the interface and $\mathbf{\Psi}^{L/R}$ is a vector with the variables convected. The superindex L/R denotes that the values are taken from the left or the right neighboring cell to the cell interface as follows:

$$\mathbf{\Psi}=\begin{cases}(1,\ u,\ v,\ w,\ h)_L & \text{if } \dot{m}>0\\ (1,\ u,\ v,\ w,\ h)_R & \text{if } \dot{m}<0\end{cases} \tag{27}$$

The methods to compute the numerical mass flux $\dot{m}$ and the pressure $\mathbf{P}$ at the cell interface are discussed in [24] and [25].

4.5. Implicit time stepping

The resulting set of equations is a very stiff system since it has characteristic speeds ranging from the speed of light to the speed of sound of the different fluids. In order to deal with the strong time step requirements, implicit time stepping is used. The second-order accurate three-point Backward Euler is used:

$$\frac{3}{2}\mathbf{U}^{n+1} - 2\mathbf{U}^{n} + \frac{1}{2}\mathbf{U}^{n-1} = \Delta t\, \mathbf{R}^{n+1} \qquad (28)$$

4.6. Validation of the coupling between Maxwell and fluid equations

4.6.1. Hartmann flow

The coupling of the Maxwell equations with the fluid equations is validated on the Hartmann flow [22]. In this verification, we consider only one conductive fluid. This study is used to analyze the complex coupling between the two systems, i.e., Maxwell and fluid equations, with so different characteristic speeds. The Hartmann flow considers a viscous, electrically conductive, fully developed flow between two parallel plates in the x-direction in presence of an imposed magnetic field in the y-direction ($B_{y_0} > 0$) and an imposed electric field in the direction perpendicular to the plane of the movement ($E_{z_0} < 0$). The electromagnetic field produces forces in the flow that change the velocity profile from the parabolic Poiseuille's one to a fuller profile. Also, the movement of the conductive flow produces a electric current that induces a magnetic field. The solution of the velocity and the magnetic field is compared to the analytical solution for a Hartmann number $\mathrm{Ha} = B_{y_0} L \sqrt{\frac{\sigma}{\mu}} = 10$ is compared in Fig. 1.

The performance of the divergence cleaning method is shown in Fig. 2. One can see that around 5 orders of magnitude of $\nabla \cdot \vec{B}$ are reduced setting $\chi = 1$.

4.6.2. Partially ionized two-fluid magnetic reconnection

In this section we present the results using the two-fluid, reactive collisional model presented in Section 3.1, Eqs. (5)-(10). In the literature, only a few examples of simulations reproducing self-consistent partially ionized reactive and collisional multi-fluid models can be found. From the numerical point of view, the main difference of such system of equations compared to ideal two-fluid plasma model [29]-[32] is the stiffness introduced by the source terms and the complexity of the diffusive terms that depend on the magnitude and direction of the magnetic field. In order to assess the numerical method explained in this work, we reproduce the results of a magnetic reconnection in a weakly ionized plasma comparing our results with those of [6].

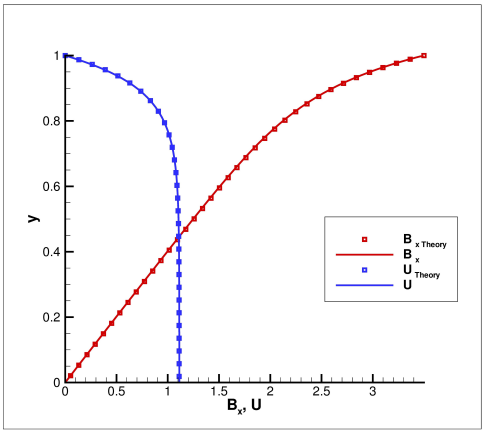

Figure 1: Comparison of non-dimensional velocity and magnetic field solution of Hartmann flow with analytical solution. Solution converged in 500 iterations on a 40×250 cells mesh.

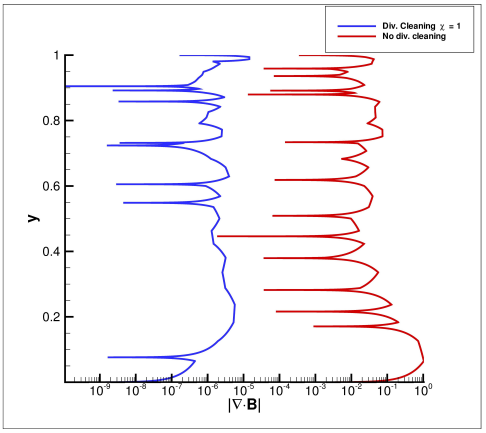

Figure 2: Non-dimensional $\nabla \cdot \vec{B}$ with and without divergence cleaning method

4.7. Parallel scalability of COOLFluiD Finite Volume Solver

We study the scalability of the cell-centered Finite Volume solver of COOLFluiD on an unstructured mesh using implicit time stepping. The parallel performance of the code is carried out using Pleiades supercomputer at NASA Ames Research Center. We test on a 14 M cell mesh up to 4096 processors. The parallel efficiency and speed-up, defined as, $S_p = 64 \frac{T_{64}}{T_p}$

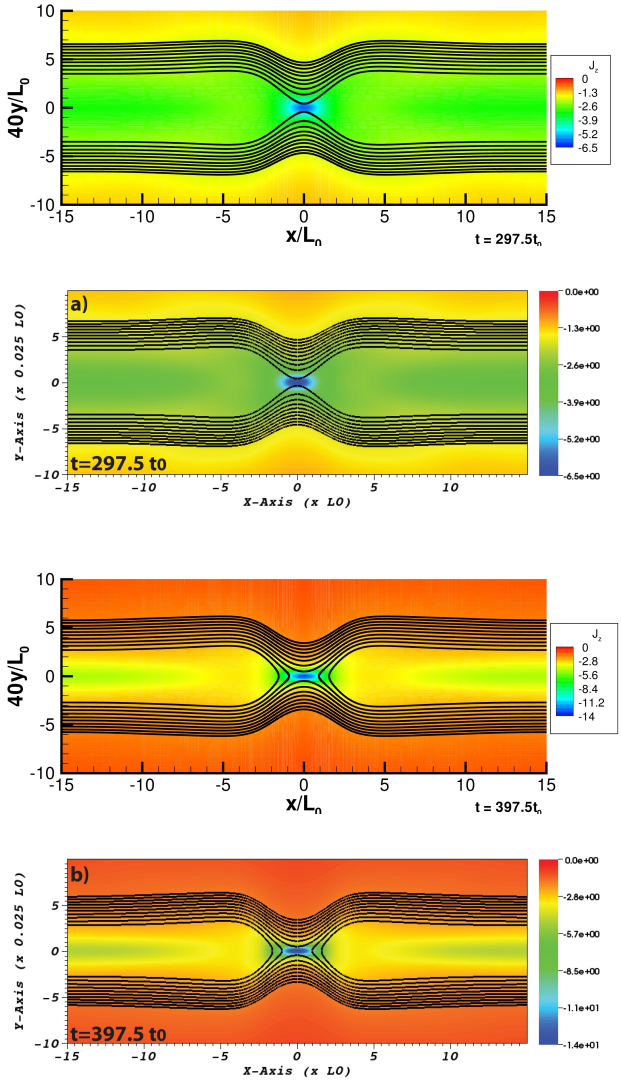

Figure 3: Evolution of the current sheet and magnetic field lines during the magnetic reconnection for different time steps: $297.5t_0$ (top) and $397.5t_0$ (bottom). The results obtained with the present numerical method (top) are compared with the results obtained in [6] (bottom).

and $E_p = \frac{S_p}{p}$ are presented in Figure 4. The result of the test show that almost a speed-up of $S_p = 0.9$ is achieved with 4096 processors. This can be achieved thanks to the parallel architecture of COOLFluiD and it can be considered a strong advantage for the 3D simulations that are presented hereafter.

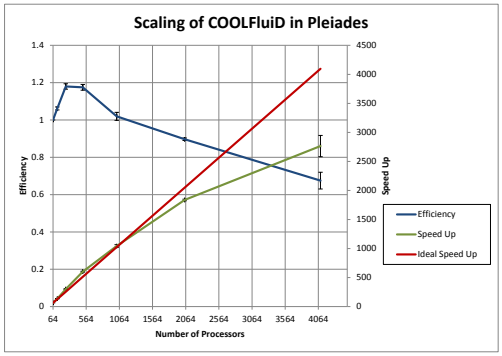

Figure 4: Parallel efficiency and speed-up of COOLFluiD cell-centered Finite Volume

4.8. *Improved finite volume method for the RTE*

The RTE, i.e, Eq. 15, can be also solved using the FV method. In the present work we use the improved method for unstructured grids explained in [23]. The method integrates Eq. 15 over the cell i, as follows:

$$\int_{\Omega_i} \vec{\Omega} \cdot \nabla I_\nu \, dV = \int_{\partial\Omega_i} I_\nu \vec{\Omega} \cdot d\vec{S} = \int_{\Omega_i} \kappa_\nu (S_\nu - I_\nu) \, dV. \tag{29}$$

The latter can be discretized as follows:

$$\sum_j I_{\nu,j}(\Omega)\vec{\Omega} \cdot \vec{n}_{ij} |\partial\Omega|_{ij} = \kappa_\nu (S_{\nu,i} - I_{\nu,i}(\Omega)) \, \Omega_i \tag{30}$$

where $S_{\nu,i}$ and $I_{\nu,i}$ are computed at the center of the cell i and $I_{\nu,j}$ at the center of the face $|\partial\Omega|_{ij}$.

The method explained in [23] approximates the value of $I_{\nu,j}$ at the interface solving the 1-d exact radiative solution for constant κ_ν and S_ν, as follows: considering a distance x along the direction $\vec{\Omega}$

$$I_\nu(x, \Omega) = I_\nu(0, \Omega) e^{-\kappa_\nu x} + (1 - e^{-\kappa_\nu x}) S_\nu \tag{31}$$

At the face where $\vec{\Omega} \cdot \vec{n}_{ij} < 0$, called in the following outgoing face, one can approximate the intensity using the previous solution. In the following expression, we use the superindex *out* for the value computed on an outgoing face and the superindex *in* for the value computed at the center of the incoming cell. Therefore,

$$I^{out}_{\nu,j}(\Omega) = \frac{\sum_{j,\vec{\Omega}\cdot\vec{n}_{ij}<0} I^{in}_{\nu,j}(\Omega)\vec{\Omega}\cdot\vec{n}_{ij}|\partial\Omega|_{ij}e^{-\kappa^{in}_{\nu,j}d}}{\sum_{j,\vec{\Omega}\cdot\vec{n}_{ij}<0}\vec{\Omega}\cdot\vec{n}_{ij}|\partial\Omega|_{ij}} + (1-e^{-\kappa^{in}_{\nu}d})S^{in}_{\nu,j} \quad (32)$$

One can see that the radiative intensity computed at the face center $|\partial\Omega|_{ij}$ is computed in terms of the values at the cell center of cell j and the propagation distance d that is approximated as $d = \left|\frac{\Omega_i}{\vec{\Omega}\cdot\vec{n}_{ij}|\partial\Omega|_{ij}}\right|$.

Using the approximation of the radiative transfer at the interface of the outgoing cells, assuming the source in the cell to be a piecewise-linear function, one can retrieve the radiative intensity at the center of cell i

$$I_{\nu,i}(\Omega) = \frac{\sum_{j,\vec{\Omega}\cdot\vec{n}_{ij}<0} I^{out}_{\nu,j}(\Omega)\vec{\Omega}\cdot\vec{n}_{ij}|\partial\Omega|_{ij}e^{-\frac{1}{2}\kappa^{in}_{\nu,j}d}}{\sum_{j,\vec{\Omega}\cdot\vec{n}_{ij}<0}\vec{\Omega}\cdot\vec{n}_{ij}|\partial\Omega|_{ij}} + \left(1-\frac{1-e^{-\frac{1}{2}\kappa_{\nu,i}d}}{\frac{1}{2}\kappa_{\nu,i}d}\right)S_{\nu,i} + \left(1-\frac{1-e^{-\frac{1}{2}\kappa^{in}_{\nu,j}d}}{\frac{1}{2}\kappa^{in}_{\nu,j}d}\right)S^{in}_{\nu,j} \quad (33)$$

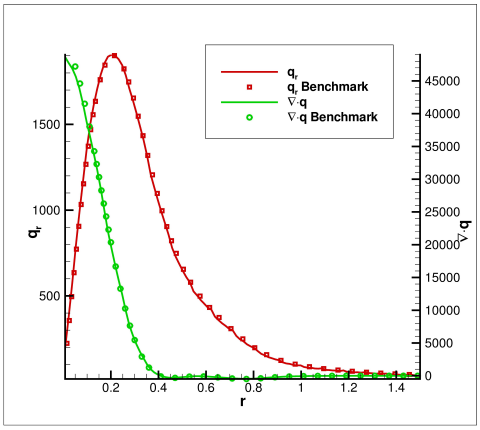

Figure 5: Verification of the RTE finite volume solver with a benchmark solution.

4.8.1. Validation of the RTE solver

We verify the method explained above studying the radiative transfer inside a sphere. We impose a Gaussian temperature profile in the radial direction. We test in a 84000 cells unstructured mesh with 60 mesh points in the radial direction and 20 in the azimuthal direction. For this study, we use the opacity table considering air composition and binning over 100 frequencies. The number of directions used for the azimuthal averaging is 24.

The solution of the heat flux over the radius and the radial heat flux vector compared to the benchmark shows great agreement as it is shown in Figure 5.

5. Results

The work carried out in this paper is aimed at studying, throughout numerical simulations, a phenomenon know as coronal heating. The distribution of the temperature in the sun atmosphere is still nowadays one of the biggest mysteries in solar physics: it rises from some thousands of Kelvin up to 2 million Kelvin in a very narrow layer called transition region situated around 2Mm above the Sun surface (the surface of the Sun is the layer where the plasma gets opaque). The sudden heating taking place in the transition region is responsible for the acceleration of the solar wind. There are two possible phenomena candidate for causing the coronal heating: magnetic reconnection and wave propagation. We will present a summary of the solutions studying both phenomena with the model presented in Sec. 3.1.

5.1. Propagation of slow magnetoacustic waves in the sun atmosphere

In the Fig. 6 , it is shown some snapshots of the results obtained in our work. At the bottom of the domain, on the Sun surface, the velocity of the plasma is excited. This perturbation travels along the sun atmosphere in form of slow magnetoacoustic waves. The lines of the plot represent the magnetic field corresponding to a magnetic flux that is anchored inside of the sun and expands towards the corona (the upper layer of the Sun, the one that can be seen with a telescope during an eclipse). These simulations propose an innovative formulation that has never been used before, considering partial ionization effects, interaction with the electromagnetic field and thermal and chemical non-equilibrium. We believe that the inclusion of these relevant physical phenomena will help to unveil the reasons of the coronal heating.

5.2. Magnetic reconnection with the effects of radiation in the sun atmosphere

We first study a 2D configuration of a Harris current sheet under chromospheric conditions corresponding for five different ionization degree levels, from 0.5% to 50%. Under these conditions, collisional effects,

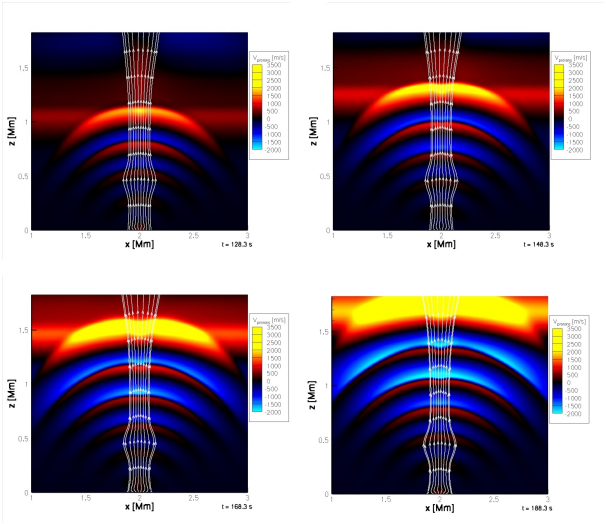

Figure 6: Evolution of slow magnetoacoustic waves in the sun low atmosphere. The plots represent different snapshots of the evolution of the vertical velocity of ions. The lines represent the magnetic field lines corresponding to a flux tube. The perturbation excited on the surface of the sun ravels along the atmosphere accelerating and forming shocks that heat up the plasma. The model used in these simulations allows for studying the effects of partial ionization and thermal and chemical non-equilibrium in the propagation of waves.

chemical reactions and radiation will play a different role in reconnection. We fix the non-dimensional values for all the cases. The characteristic values are:

$$n = 6.6 \times 10^{18} m^{-3}$$
$$T = 8750K$$
$$\Psi = \frac{n_{ions}}{n_{ions} + n_{neutrals}} = 0.5\%$$
$$B = 10^{-3} T.$$

The initial magnetic field topology is chosen to be a Harris sheet, with a small perturbation in order to force the reconnection to occur in the center of the domain. We study the impact of the radiation effect. The chromosphere is known to be optically thin and therefore, radiative cooling plays an important role in the dynamics of the chromosphere. In the present work we compare the results of the reconnection with different radiative models.

In Fig. 7, the reconnection for four different radiation levels is shown. It can be proven analytically that the presence of neutrals help to get thinner the reconnection layer and therefore to speed up the reconnection events. Because of it, as the ionization level increases, the current sheet gets wider and therefore the reconnection rate decreases, as shown in Fig. 8.

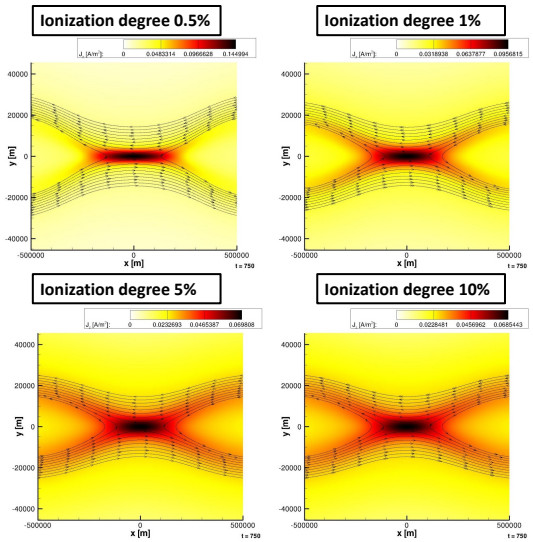

Figure 7: Snapshot of reconnection simulations for four different ionization levels: 0.5% (top left), 1% (top right), 5% (bottom left) and 10% (bottom right). The results are obtained without using any radiative cooling model.

.

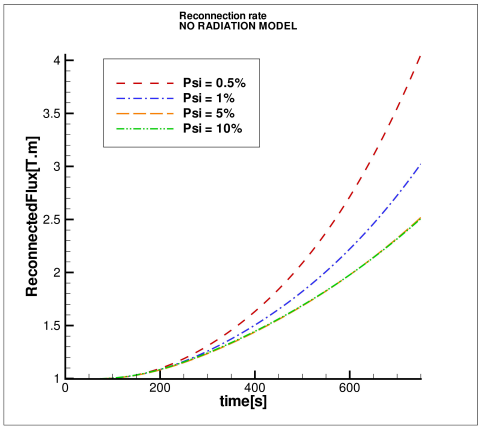

Figure 8: Reconnection rate for different ionization levels without using radiative model

.

When the radiative recombination heat losses are considered, one can see that the results are completely

different. As it can be seen it 9, when radiative losses are considered, the width of the current sheet decreases, producing an increase of the reconnection rate, as shown in 10.

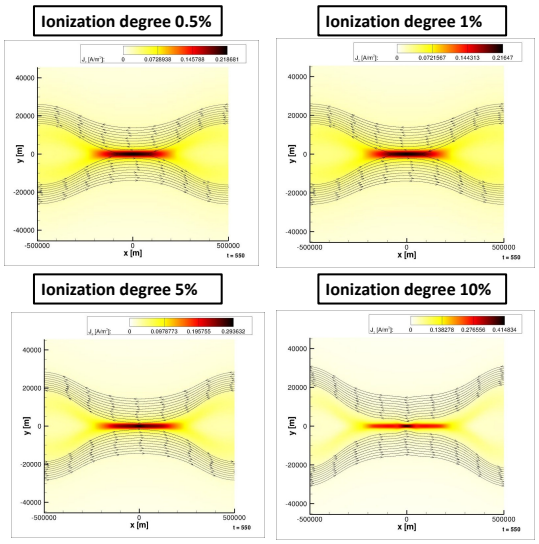

Figure 9: Snapshot of reconnection simulations for four different ionization levels: 0.5% (top left), 1% (top right), 5% (bottom left) and 10% (bottom right). The results are obtained using radiative cooling for the radiative recombination.

.

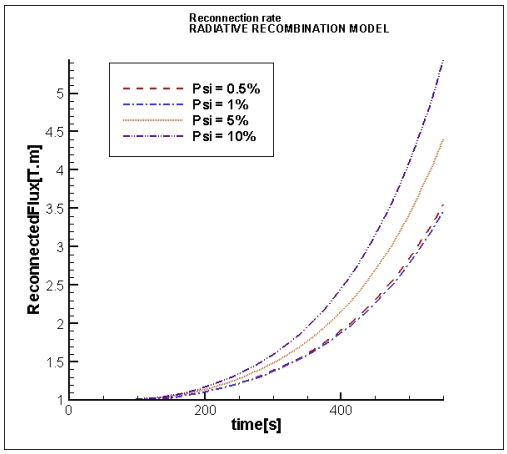

Figure 10: Reconnection rate for different ionization levels using radiative cooling for the radiative recombination.

.

A different radiative cooling model has been considered, accounting for the excited states of the hydrogen atom. As it can be seen it 11, the topology of the reconnection changes completely, producing an instability known as tearing mode. In this case, the reconnection rate is even greater, as shown in 12.

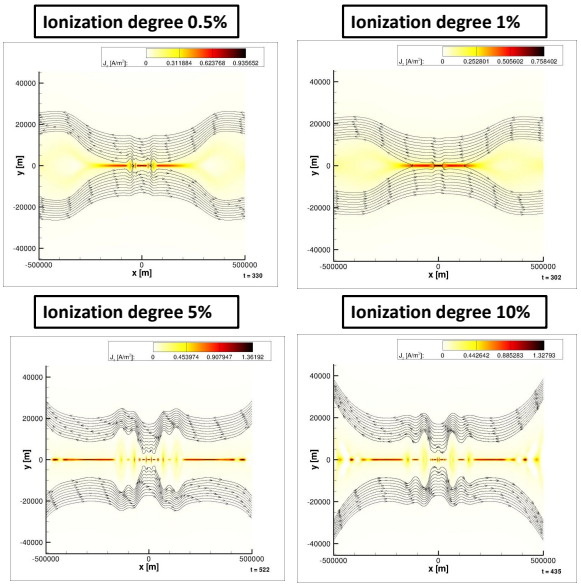

Figure 11: Snapshot of reconnection simulations for four different ionization levels: 0.5% (top left), 1% (top right), 5% (bottom left) and 10% (bottom right). The results are obtained using radiative cooling for the radiative recombination.

.

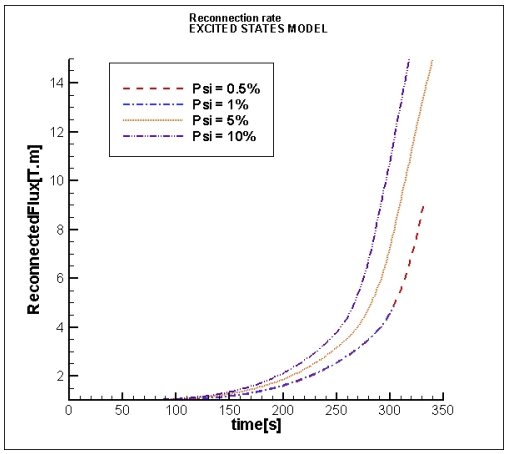

Figure 12: Reconnection rate for different ionization levels using radiative cooling for the radiative recombination.

.

6. Conclusions

The present PhD project is oriented towards the development of numerical tools and models of plasma for representing the magnetic reconnection process in astrophysical and laboratory plasmas. In the present work, we have highlighted the importance of magnetic reconnection process and the necessity of improving the modeling in order to represent this phenomenon more accurately. Multi-fluid models, that consider each species as different interpenetrating fluids, are able to represent microscopic and transport phenomena that is completely neglected in the single-fluid theory. In this work we have presented a two-fluid partially ionized reactive plasma model, especially suitable for the conditions in the Sun chromosphere. As well, we have presented the finite volume method for solving the two-fluid plasma model coupled to the full Maxwell equations using hyperbolic divergence cleaning. The coupling of the equations is validated on the Hartmann flow, showing perfect agreement with the analytical solution and showing the hyperbolic divergence cleaning method to be an efficient way of enforcing the divergence constrains. The parallel scalability of the finite volume solver implemented in COOLFluiD is tested in Pleiades, NASA's supercomputer, showing high efficiency up to 4096 processors. Also, the radiative transfer equation is solved using a finite volume method that improves its accuracy by performing linear-piecewise interpolation along the radiative direction. The verification of the RTE solver was presented showing great agreement with a benchmark solution. The coupling of the radiative effects in the reconnection will be carried out in future developments.

The magnetic reconnection in the chromosphere is simulated using a multi-fluid model considering two fluids, neutrals and charged particles. The results show the different dynamics of the species as well as the importance of the chemical reactions on the magnetic reconnection. Also, preliminary 3D results studying the same configuration are presented and will be extended in future works. The first stages of a magnetic reconnection in the chromosphere have been simulated using a multi-fluid model considering two fluids, neutrals and charged particles. These results can be considered as the first steps that will be continued during the PhD targeted towards the study of the magnetic reconnection with multi-fluid models.

Acknowledgments

This research is funded through a fellowship provided by IWT (agentschap voor Innovatie door Wetenschap en Technologie). We would also like to thank Dr. Nagi N. Mansour for the supervision of this work at NASA Ames Research Center and Dr. Andrea Lani, COOLFluiD architect and advisor of this work.

References

[1] Committee on the Societal and Economic Impacts of Severe Space Weather Events, *Severe Space Weather Events Understanding Societal and Economic Impacts: A Workshop Report*, The National Academies Press, 2008.

[2] J. Birn and E. Priest, *Reconnection of Magnetic Fields*, Cambridge University Press, 2007.

[3] F. Zuccarello, *Data analysis and mathematical modeling of the initiation of coronal mass ejections*, PhD thesis, KU Leuven, 2012.

[4] M. Yamada, R. Kulsrud, and H. Ji, *Magnetic Reconnection*, Reviews of Modern Physics vol.82, 2010.

[5] Yamada, M. et al. *Conversion of magnetic energy in the magnetic reconnection layer of a laboratory plasma.* Nature Communications 5:4774 doi: 10.1038/ncomms5774 (2014).

[6] J. E. Leake, V. Lukin, M. Linton and E. Meier, *Multi-fluid simulations of chromospheric magnetic reconnection*, ApJ. 760, 2012.

[7] K. Shibata et al., *Chromospheric Anemone Jets as Evidence of Ubiquitous Reconnection*, Science, Volume 318, Issue 5856, pp. 1591, 2008.

[8] K. Shibata and T. Magara, *Solar Flares: Magnetohydrodynamic Processes*, Living Rev. Solar Phys. 8, 2011.

[9] E. N. Parker, *Sweet's mechanism for merging magnetic fields in conducting fluids*, Geophysical research 62, No. 4, 509-520, 1957

[10] H. E. Petschek. *Magnetic Annihilation*. The Physics of Solar Flares, Proceedings of the AAS-NASA Symposium, October 1963

[11] D. Biskamp, *Magnetic Reconnection in Plasmas*, Cambridge University Press, 2005

[12] S. I. Braginskii, *Transport processes in a plasma*. Reviews of Plasma Physics, Volume 1., pp. 205 311. (1965)

[13] B. Graille , T. E. Magin , M. Massot, *Kinetic theory of plasmas. Translational Energy.* Mathematical Models and Methods in Applied Sciences, Vol. 19, 04 (2009) 527-599

[14] E. T. Meier, U. Shumlak, *A general nonlinear fluid model for reacting plasma-neutral mixtures.* Physics of Plasmas, Volume 19, Issue 7, pp. 072508-072508-11 (2012).

[15] M. Carlsson and J. Leenaarts, *Approximations for radiative cooling and heating in the solar chromosphere.* Astronomy & Astrophysics, Volume 539, March 2012.

[16] A. Lani, *An object Oriented and high perforrmance platform for aerothermodynamics simulations*, PhD Thesis, von Karman Institute for Fluid Dynamics, 2009

[17] R. W. MacCormack. *Numerical Simulation of Aerodynamic Flow Including Induced Magnetic and Electric Fields.* In 39th AIAA Plasmadynamics and Lasers Conference, Seattle, June 2008.

[18] T. Barth. Aspects of unstructured grids and finite volume solvers for the euler and navier-stokes equations. 25th Computational Fluid Dynamics Lecture Series. Von Karman Institute, March 1994.

[19] V. Venkatakrishnan. *Convergence to steady state solutions of the euler equations on unstructured grids with limiters.* Journal of Computational Physics, 118:120130, 1995.

[20] J. Steger, R. F. Warming, *Flux vector splitting for the inviscid gas dynamic equations with application to finite difference methods*, J. Comp. Phys., Vol. 40, No. 2, pp. 263-293, 1981

[21] C.-D. Munz., P. Ommes, R. Schneider. *A three-dimensional finite-volume solver for the Maxwell equations with divergence cleaning on unstructured meshes*. Computer Physics Communications130, 83-117, December,1999.

[22] M. Mitchner and C. H. Kruger, *Partially ionized gases*, Wiley series in plasma physics, 1973.

[23] A. Wray, *Improved Finite-Volume Method for Radiative Hydrodynamics.*, ICCFD7-1003, July 2012.

[24] M. S. Liou, *A sequel to AUSM, part II: AUSM+ -up for all speeds.* J. Comp. Phys., 214:137170, 2006.

[25] A. Alvarez Laguna, A. Lani, N. N. Mansour, A. Kosovichev, and S. Poedts, *A two-fluid computational model to study magnetic reconnection in reactive plasmas under chromospheric conditions*, WCCM XI-ECCM V-ECFD VI, Barcelona (2014).

[26] G. S. Voronov, *A practical fit formula for ionization rate coefficients of atoms and ions by electron impact*, Atomic data nad nuclear data tables 65, 1-35, 1997

[27] B. M. Smirnov, *Physics of Atoms and Ions*, Springer-Verlag New York, Inc., 2003

[28] Vernazza, J. E., Avrett, E. H., Loeser, R., *Structure of the solar chromosphere. III. Models of the EUV brightness components of the quiet Sun*, ApJS45, 635-725, 1981

[29] U. Shumlak and J. Loverich. Approximate riemann solver for the two-fluid plasma model. *J. Comput. Phys.*, 187(2):620–638, May 2003.

[30] A. Hakim, J. Loverich, and U. Shumlak. A high resolution wave propagation scheme for ideal two-fluid plasma equations. *J. Comput. Phys.*, 219(1):418–442, November 2006.

[31] J. Loverich and U. Shumlak. A discontinuous galerkin method for the full two-fluid plasma model. *Computer Physics Communications*, 169(1):251–255, July 2005.

[32] B. Srinivasan and U. Shumlak. Analytical and computational study of the ideal full two-fluid plasma model and asymptotic approximations for Hall-magnetohydrodynamics. *Physics of Plasmas*, 18(9):092113, September 2011.

Reentry platform for studying radiation, from payload design to performances

Gilles BAILET

Aeronautics and Aerospace Department, von Karman Institute for Fluid Dynamics, Belgium, bailet@vki.ac.be

Supervisor: Thierry E. Magin

Associate Professor, Aeronautics and Aerospace Department, von Karman Institute for Fluid Dynamics, Belgium, magin@vki.ac.be

University Supervisor: Christophe O. Laux

Professor, Laboratoire EM2C, CNRS, CentraleSuplec, Universit Paris-Saclay, France, Christophe.laux@centralesupelec.fr

Abstract

This paper presents the progress on a new type of emission spectrometry payload for a reentry vehicle, as part of the QB50 project led by the von Karman Institute for Fluid Dynamics (VKI). The key steps in the development of the payload from design perspective (choice of the wavelength range) to the specific calibration process are presented.

Keywords: Reentry, Emission Spectroscopy, Radiation, Ablation

1. Introduction

This paper presents the progress on a new type of emission spectrometry payload for a reentry vehicle, as part of the QB50 project led by the von Karman Institute for Fluid Dynamics (VKI). We first present an overview of the QARMAN (QubeSat for Atmospheric Research and Measurement on AblatioN) vehicle [1], a small/low cost reentry platform on which the emission spectrometer (ES) payload will be installed. Then, the following sections present the key steps in the development of the payload from design perspective (choice of the wavelength range) to the specific calibration process allowing maximal scientific return. In addition, a new experimental methodology is presented to quantify the emission/absorption components of the radiative heat flux in the presence of ablation products. Finally, the paper describes the expected outcomes of this new emission spectrometry payload for the atmospheric reentry community.

2. Mission overview

The QARMAN mission can be divided into 5 subphases, going from orbital deployment to atmospheric reentry. The flight scenario of QARMAN is summarised in Fig. 1.

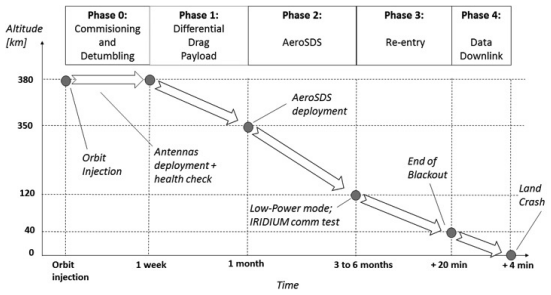

Figure 1: QARMAN Mission Timeline

These five main phases are described in detail in the following sections.

2.1. Phase 0: Commissioning and Detumbling Major

Right after deployment, at an altitude of approximately 400-380 km, the commissioning phase starts. The vital subsytems are booted and the UHF/VHF antennae are deployed after 30 minutes in order to establish the first ground contact. After powering up, the status of all the systems is automatically checked and the satellite is put into a safe mode waiting for first ground commands. Using magnetorquers, the satellite will be detumbled and stabilized from the initial

tumbling rates (expected to be below 10 deg/sec).

This phase is expected to last from a minimum of three days up to one week in the nominal scenario, after which QARMANs attitude should be known within 5 degrees of uncertainty. The z-axis of the satellite body frame (oxyz, see Fig. 3) will be aligned with the velocity direction with approximately 10 degrees pointing error accuracy, with the longitudinal axis aligned to the RAM direction (Z axis of the frame). This orientation can be considered the reference attitude for Phase 1, described bellow.

2.2. Phase 1: Differential Drag Payload

The first operational phase of QARMAN consists of the In-Orbit Demonstration of the so called differential drag maneuvers [2]. For an approximate duration of one month, the satellite attempts to chase a virtual target (or ideally a satellite) by controlling the surface exposed to the residual atmosphere. This is obtained by altering the CubeSat pitch angle (i.e. between the satellites longitudinal axis z and the direction of flight, X) thus controlling the atmospheric drag force. During this phase, the attitude control algorithm runs optimization calculations (ground-looped) to estimate the drag needed to perform an orbital change maneuver and it computes the corresponding pitch angle, actuated through the reaction wheel. During phase 1 the solar panels are kept in stowed configuration as shown in Fig. 2.

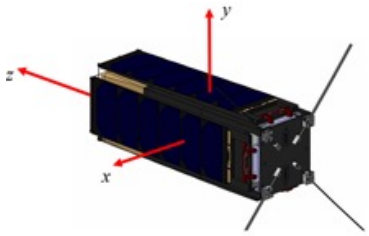

Figure 2: QARMAN in folded configuration

2.3. Phase 2: AeroSDS

At the end of phase 1 after 5 weeks of operations in orbit, the satellite will have naturally decayed down to an altitude of around 350 km. At this stage, the AeroSDS panels, consisting of the ceramic panels with integrated solar cells, will be deployed into a dart configuration with an angle of 15 degree with respect to the satellite longitudinal axis. The system will provide aerodynamic stabilization and an increased drag area, progressively reducing the satellite altitude faster compared to the stowed configuration. A picture of QARMAN in deployed configuration is shown in Fig. 3.

2.4. Phase 3: reentry

Phase 3 is the reentry, which can be considered the core part of the mission, where the major return for the science campaign and technology validation is expected. This is also the most critical part of the mission, as the satellite is subject to very high temperature and hypersonic velocities. Gas temperatures around the satellite are expected to exceed 10000 K (more than 50 % hotter than the Suns Photosphere), while the satellite flies through the upper atmosphere at a speed up to Mach 27.

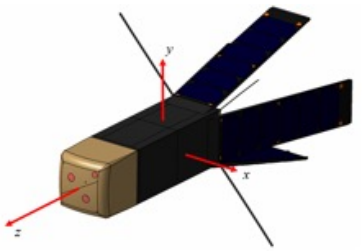

Figure 3: QARMAN in deployed configuration

To protect the electronics during the reentry, a thermal protection system is designed, based on high-tech insulation (e.g. Pyrogel, FiberFrax and ceramic walls) and special ablative material (P50 Cork).

2.5. Phase 4: data transmission

The cloud of free electrons surrounding the satellite during this phase will cause a communications black-out, where no data can be transmitted to mission control. The acquired data are stored on flash memory and the compressed data will be transmitted towards the Iridium constellation once the blackout has terminated, expected at an altitude of 45 km. The data budgets are calculated such that all data can be safely transmitted in the short time frame between the end of the black-out window and the satellites crash on ground.

3. State-of-the-art in emission spectroscopy instrumentation for reentry vehicles

Reentry represents a critical phase in many space missions designed to deliver payloads or crew to their final destination. For missions not dedicated to technology demonstration, the Thermal Protection System

(TPS) is just a mean to reach the goal of the mission. Nevertheless, its design is crucial because it is a single point failure system. A suitable TPS is essential to shield the vehicle from the harsh aerothermodynamic conditions of the reentry environment. Minimizing the weight and cost of the TPS by keeping the reliability objective of the subsystem is the continual challenge facing the scientific community. Several phenomena affect the design of TPS [3] with ablation and radiation as the two most important and critical among others (gas-surface interaction, transition) in case of ablative TPS. Ablation consists in the removal of material from the surface by erosion and sublimation triggered by endothermic reactions, hence protecting the rest of the vehicle by reducing the thermal constraint. The radiation phenomenon is an energy transfer from excited particles (mostly from the shock and the ablation products) in the form of an electromagnetic flux (i.e. radiative flux). Radiation within the shock layer will contribute to an increase of the aerothermal energy around the vehicle thus increasing the heat flux on the vehicle, which will constrain the design. In addition, radiation can contribute to a decrease of the surface temperature by dissipating energy but this property is mainly used at low heat fluxes (eg: thermal soak TPS tiles from space shuttle). Extensive research was mostly conducted with pre-eighties projects (Apollo, space shuttle). Massive efforts were then undertaken to characterize the phenomena of reentry and specifically TPS design-related issues. Several major projects can be identified such as the Flight Investigation of the FIRE-I&II missions [4] and several programs for risk reduction on the space shuttle [5]. Efforts in the following decades were sporadic but successful for some of them in the deeper understanding of the scientific background. Missions such as BSUV-I&II for bow shock ultraviolet experiments [6,7,8,9] gave a much improved understanding of flight data for numerical models and ground test facilities improvement.

Despite the success of the BSUV missions, the data cannot be extrapolated for reentry speeds above 5.3 km.s-1 where nonequilibrium chemistry becomes more important in the flow field. Regarding the understanding of the ablation process, most of the researches were done during the space reentry missions as secondary payloads [10]. This lack of risk reduction missions for research on thermal protection systems pushes to an excess of ground tests with high uncertainties as flight conditions are not fully duplicable on ground. This philosophy has resulted on a higher program cost and higher margins on the design ending up on a smaller mass budget available payload. In the case of Martian reentry, it even constrains the altitude of landing site thus potentially limiting the scientific return. More recently, efforts have been done in regard of flight data collection for the post space shuttle era and the sample return interest for the scientific community. The Japanese spacecraft Hayabusa [11] and the American Stardust [12] are two brilliant examples of sample return missions with the characteristic hypervelocity reentry (in these cases superior to 12km.s-1). In addition of their valuable asteroids sample payload, the two capsules were equipped with instrumentation. Important data have been retrieved from these missions and specifically on ablative TPS material response and on radiation from the bow shock and the vehicle itself (with spectrometer airborne, NASA's DC-8 airborne laboratory). The post space shuttle era has brought programs returning to capsule shaped reentry vehicles with Orion and Dragon (Space X) capsules. The Orion capsule [13] represents an ideal testbed for all reentry related phenomena and NASA has planned numerous test flights with a high density of instrumentation onboard. The results of MSL (Mars Science Laboratory) reentry permit to judge on the reliability and interest in the new TPS instrumentation tested during this Mars entry. In Europe, few programs have been developed for the study of ablation and radiation on reentry vehicles. An ongoing program named Experimental Reentry Testbed (EXPERT) is planning to conduct several experiments during a suborbital reentry (5 km.m-1 at 100 km of altitude). Unfortunately, the launch is not planned yet. One of the most important payloads of the mission is the ReEntry SPECTrometer (RESPECT) [14] with two optical channels. This mission will permit to strengthen and actualize the data of the BSUV program and develop the technology in Europe. In addition of these missions, several challenges will have to be addressed to respond to some needs in the industry and research community [3,4,6,8]: Technical Engineering Development:

- Improving design and analysis tools (uncertainty quantification included), such as CFD and material response models, to verify material response and qualification test conditions.
- Developing improved testing techniques to support traceability from ground to flight aerothermal environment conditions.

Table 1: Summary of the in-flight experiments for radiative studies

Mission	Year	Entry speed [km.s^{-1}]	Altitude range [km]	Spectral range [nm]	Spectral resolution [nm]	Focus
FIRE I	1964	11.5	70-89	300-600	4	Coupled ablation /radiation
FIRE II	1965	11.5	40-83	300-600	4	Coupled ablation /radiation
BSUV I	1990	3.5	38-70	200-400	1	UV diagnostic
BSUV II (UVDE)	1991	5.1	62-110	200-400	1	UV diagnostic
Ground observations (Stardust, ATV 1 and Hayabusa)	2006 2008 2010	above 12 7.8 above 12	High Uncertainties	300 - 2000	0.1 - 20	Global observation
EXPERT	Delayed	5	40-80	200-850	1.5	Build a database
QARMAN	2015	7.8	50-120	350-800	1	Payload demonstration /Build a database

- Designing tests that investigate material and system failure modes and use such data to develop improved system reliability analysis methodologies.

- Sustaining current material manufacturing capabilities and expertise to ensure that at least two proven TPS materials, for both the heat shield and back shell, are available for future Sample Return missions. Recertification or qualification of these materials needs to occur every few years.

Flight Instrumentation:

- Including TPS instrumentation in all reentry missions to generate a database of relevant flight data that will aid in the design of future entry missions as flight heritage is necessary for Technological Readiness Level ratings higher than 5.

- Multiply earth reentry TPS flight data to benefit sample return missions and ISS-orbit return.

In contrast of the above-mentioned programs, the QARMAN mission refers to a reentry from low earth orbit (LEO) with a speed of roughly 7.8 km.s-1 at 120 km of altitude. It is intended to be a gap-filler on the side of emission spectroscopy experiments. It will gather data in the important range between studies made for hypersonic/sub orbital atmospheric flight and lunar/sample return missions in the aspects of ablation and radiation studies. A mission aiming to tackle these issues named Skipper [15] was performed but unfortunately the vehicle failed in orbit before any scientific return. The platform was equipped with two spectrometers and 20 photometers in the aim of focusing the mission on ultra violet (UV) and vacuum ultra violet (VUV) wavelength ranges of the radiative flux. Even without the scientific return and without any detailed scientific publications, we can note the scientific interest, as one can understand the need of filling the gap between FIRE and BSUV programs. Tab. 1 summarizes the in-flight experiments for radiative studies to date and how QARMANs ES fits within the different missions.

The simulation of radiation and ablation are two highly complicated processes due to the numerous chemical components and energy levels to take into account. The approaches consist on either a decoupled or a coupled approach. The decoupled approach solves independently both processes and couples them back afterward. The coupled method, often more complex, solves directly the two processes within the same partial differential set of equations. The-state-of-the-art decoupled approach in modeling capabilities is an advanced collisional-radiative model where both thermochemical nonequilibrium and radiation are modeled [16, 17]. To understand what an in-flight ES could measure, emission spectrometry codes have to be used. Reference [18] presents an overview of the different available models and recommends the use of SPECAIR as a more reliable code than NEQAIR I&II, the historical standard. The author mentioned the uncertainties of the present models. At low pressure (high altitudes) possible departures from a Maxwellian distribution for the free elec-

trons are expected. This issue is an additional strong emphasis on the necessity to strengthen the models. In complement of the previous list, some additional specific questions and challenges can be addressed:

- Investigating TPS materials under LEO reentry conditions for the new generation of reentry vehicles.
- Investigating the effect of ablation products (high radiative CN products) on the radiative heat flux and the chemistry of the flow.
- Investigating specific emission spectra of the LEO return (atomic oxygen, Lyman-alpha, NO, OH, and N2+ wavelengths)
- Improving the existing tools to cover the rarefied flow field and the ionized conditions.

The scientific community needs to fill the gaps of the different numerical models (highly ionized plasma, coupled ablation and radiation) and develop new hardware/methodologies (flight experiments, high fidelity ground-to-flight extrapolation) to arrive to a better understanding of the reentry physic thus allowing greater endeavors in space missions.

4. Prediction of the Radiation Expected During the Reentry

An emission ES is an instrument enabling the characterization of a light source, for the present case, a plasma of air. The device measures the intensity of the light over a certain range of wavelengths. As observed in Fig. 4, a combination of two mirrors and one gratin permits to diffract the incoming coherent light source onto the detector to be analyzed independently according to the instrument sensitivity.

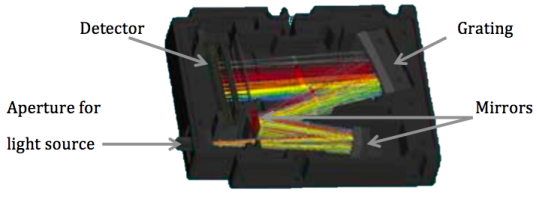

Figure 4: Components of an emission spectrometer

In order to assess the interest of radiation phenomenon, a spectrum of the most constraining trajectory conditions is presented in this part. The VKIs software Mutation and Stagline [16,17] was used to compute from the reentry conditions (Fig. 5) the temperatures of translation and vibration along with the chemical composition of the flow after the shock (Fig. 6 and Fig. 7).

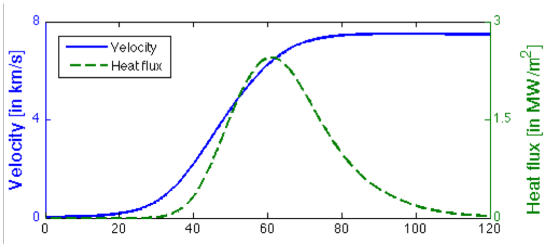

Figure 5: Velocity and heat flux profile versus altitude for the QARMAN mission

The software use state-of-the-art multi-temperature models to simulate the viscous flows along the stagnation-line of a blunt body. In the following example, the conditions are (QARMAN at 55km without ablation, 5.3km.s-1 and free stream conditions: 259K and 40 Pa).

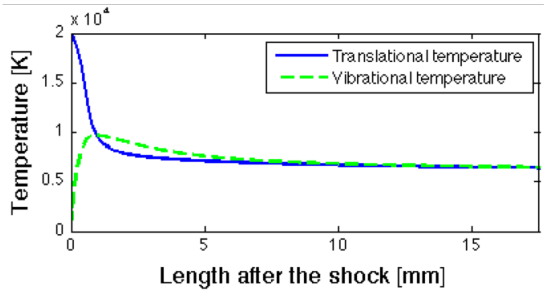

Figure 6: Profile of vibration and translation after the shock

Due to the small size/mass of the QARMAN vehicle, it allows observing the thermal-nonequilibrium part of the flow on a bigger fraction of the shock layer (i.e.: the part of the flow where the translational, vibrational, rotational and electronic temperatures are not all equal). In our case, we can observe this interesting part of the flow at a 10-20% of the stagnation line compare to only few percent on conventional missions. When this area is usually few centimeters thick on a shock layer several dozen of centimeters in length (i.e. ratio ¡ 1/10), we have in this case 4-6 mm of nonequilibrium for a shock layer of 16mm (i.e. a ratio ¿ 1/4). This high nonequilibrium fraction permits to observe spectra rich in diverse phenomena where more information is available.

The next step in the study of the radiative environ-

ment of the spacecraft is conducted using a radiation code named SPECAIR [18]. Calculating the radiation of air plasma, the program computing the emission and absorption coefficients of a number of atomic and electronic transitions, as well as the free-bound and free-free continua.

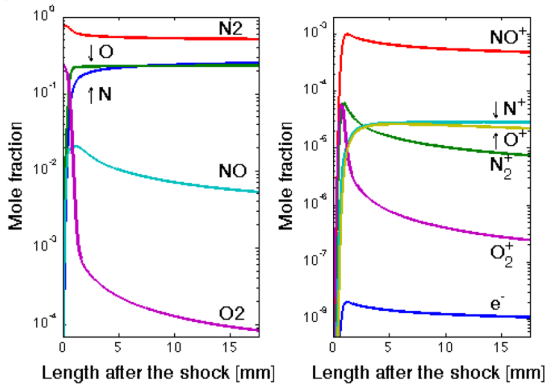

Figure 7: Chemical composition of the flow within the shock layer

Two important results could be extracted from that analysis. Fig. 8 shows with detail the components of the spectrum within the range [20-1200] nm for the altitude 55km of the QARMAN mission. Fig. 9 on the other hand shows a more compact view of the repartition of the total radiative flux depending on the different wavelength ranges to the total radiative flux (VUV, UV, VIS, IR-A and IR-B). Fig. 8 shows two interesting areas of the spectrum. Between 150nm and 500nm the spectrum is highly dominated by molecular systems (N2, N2+ and NO) and between 750nm and 1000nm, atomic lines dominate it (N and O). These results permit to respond to some of the challenges to be addressed by the scientific community by observing the phenomena of interest (I.e.: atomic oxygen, NO and N2+ wavelengths mentioned in Part 3).

As expected from the literature survey [18], the VUV range gathers the most important contributors to the total radiative flux when considering pure air plasma. Unfortunately, the devoted space of the experiment inside the QARMAN payload bay is 80x50x50 mm3. In such conditions, no VUV spectrometers are able to fit within this extremely constraining volume. By taking in account the amount of different phenomena and the relative intensity, the UV-VIS ranges are preferred. The next part explains the impact of ablation on the radiation flux and the solution identified to quantify it when the TPS material is not characterized.

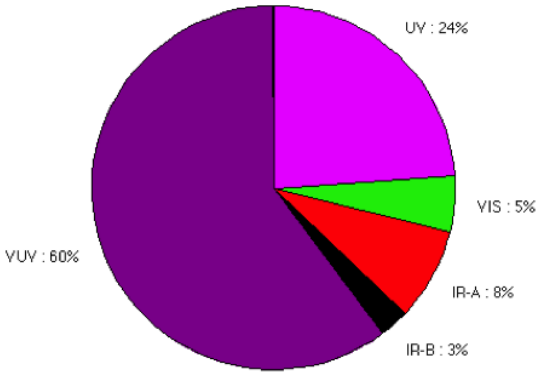

Figure 9: Repartition of the radiative flux into the different wavelength categories

5. New method to predict the contribution of the ablation products on the total radiation flux

To perform accurate spectroscopic measurements within an ablative environment, the physics of the optical path (OpP) pollution has to be understood. In this idea, a new technique was developed to clarify the science behind OpP pollution. The VKIs Plasmatron facility, an Inductive Coupled Plasma (ICP) torch, was used to test ablative samples (Cork P50: Cork + Phenolic Resin). The test conditions cover representative points of the QARMAN trajectory (Heat flux between 0.5 and 3 MW/m2). The samples were tested with the conventional design found in the literature [19]. The optical access is located at the bottom of a metallic cylinder, itself located bellow a protective layer of TPS. For the sake of predictions, a spectrometer different from QARMAN ones was used (wider spectral range: 190-1100nm instead of 350-800nm).

The test methodology permits to gain a deeper understanding of the OpP contamination behavior. Predictions of the absorption/emission can then be done to assess the total radiative heat flux. This method utilizes on a dual spectral acquisition system [20] presented in Fig. 10.

In this method, we are first reaching flight conditions by duplication the following parameters: static pressure, velocity gradient at the stagnation point and total enthalpy. The heat flux probe (calorimeter) permits in the following step to measure the corresponding cold wall heat flux (convention: 350K surface temperature).

The VKIs ICP torch produces an intense radiation source between the coils of the plasma generator (temperatures reaching more than 10000K). This radiation source would cause inherent troubles to conventional

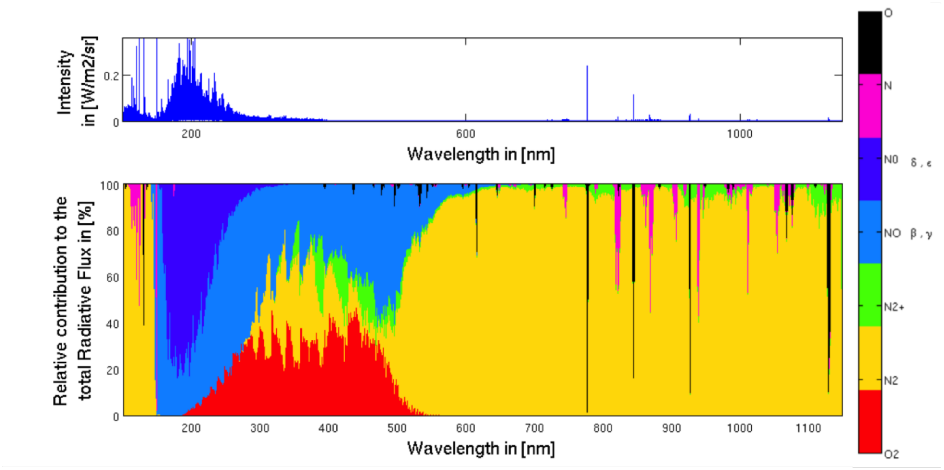

Figure 8: Identification of the contribution of atoms and molecules to the calculated spectrum (QARMAN at 55km without ablation, 5.3km.s-1 and free stream conditions: 259K and 40 Pa)

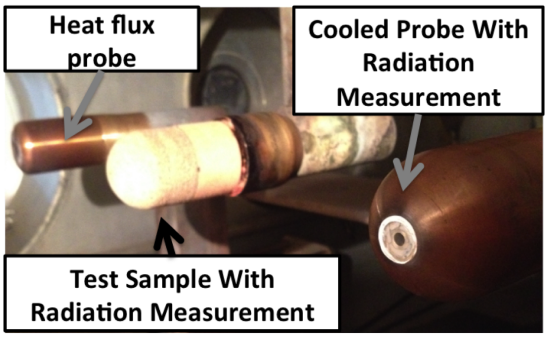

Figure 10: Dual spectral acquisition system setup at VKIs Plasmatron

radiation measurements with a conventional system.

Indeed, the hot boundary layer (BL) at the surface of the sample will emit and absorb radiation thus avoiding a distinguishing of both radiation sources. To solve this issue, the following step is dedicated to characterize the background radiation of the facility for the current test. Spectrum of the torch generator (on the stagnation line of the flow) is acquired with a cooled radiative probe (350K, no absorption of the BL). The measured spectrum is similar to the one of hot air plasma at 6000 K over 1 meter. The last step of the methodology consists on a new spectral measurement with the TPS sample at the same test conditions. In this case, the previous background measurement will act a reference to characterize the absorption characteristics of the hot ablative BL.

The test conditions for the case presented in this paper are 0.5MW/m2 for heat flux and 10mbar for static pressure. These settings allow testing the sample in conditions where pyrolysis contamination is dominant (i.e. the most constraining in the aspect of OpP pollution). The measurement lasted for 3 minutes until full blockage of the OpP and the effect of the OpP pollution appears after 30s. Fig. 11 can be produced by calculating the transmittance of the hot ablative BL in respect of the plasma generator in background. This parameter is calculated by making the difference of cold and ablative probe divided by 100. In this figure, one can observe the evolution of absorption and emission components over time. The correlation of this results with the temperature profile inside the sample [20] and the spectrum at each time step, we can identify three different phases, exposed hereafter. From 0 to 30s, the OpP pollution is negligible and only the emission from the hot BL is observed. The second phase occurs at relative low TPS material temperature (Temperature: 314.15K) corresponding to the phenol sublimation temperature. During this phase, absorption and emission of the pyrolysis gas in the OpP starts to corrupt the flowfield/boundary layer radiation. Pollution by absorption is increase with temperature as other molecules sublimate, (e.g. H2O and simple phenols). In the present example, the third phase appears far later than usual (high energy tests obstruct the OpP after few tens of seconds) due to the low energy nature of the test. It is identified by a strong attenuation of the signal all over the wavelength range. This massive absorption, starting at 155s in this case, leads to total obstruction of the OpP. This system can be considered as not suitable for any mission as even at low energy, the conventional design [19] is not suitable and our

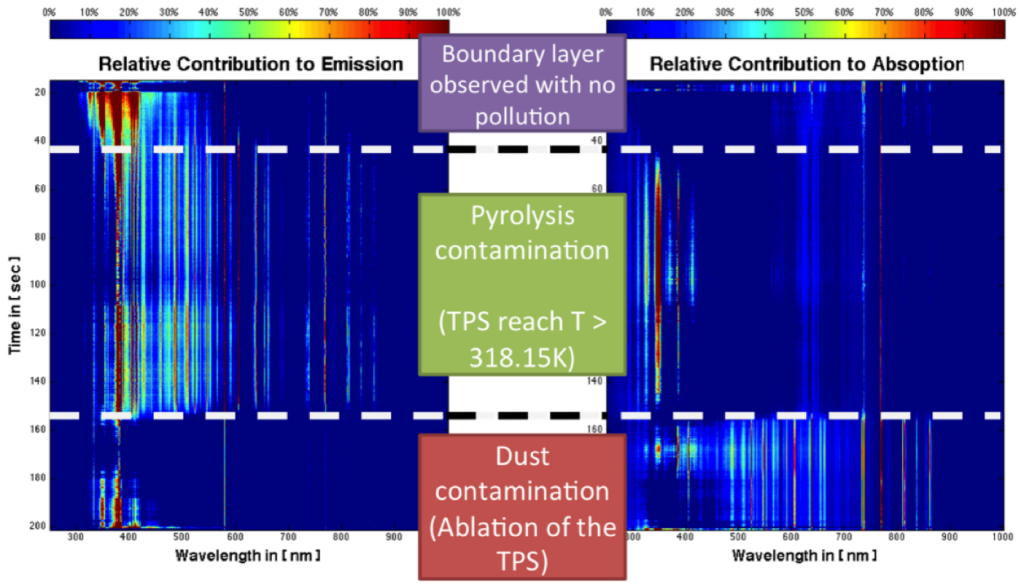

Figure 11: Contribution of the hot ablative boundary layer to the total radiative heat flux (Test conditions: 0.5MW/m2 for heat flux, 10mbar for static pressure, 5cm hemispherical probe and Cork P50 from Amorim as test article)

system is proposed allowing full measurement coverage of reentry mission. The prediction of the contribution of emission/absorption of the hot ablative BL permits to set optimal parameters for the ES payload of QARMAN. These parameters are altitude of measurements with best scientific return and acquisition time (to avoid saturation of the charge-coupled device (CCD) or under-exposure). In addition, the contribution of emission/absorption of the hot ablative BL enable to predict flight data with TPS material not characterized.

Fig. 12 shows such implementation in the case of air plasma at 6000K (with cold wall) representative of a typical LEO reentry. For the prediction, the methodology consist on simulation the radiation environment of the reentry vehicle with no ablation and a 350K wall temperature and then add the emission/absorption contribution of the hot/ablative boundary layer.

6. Calibration of a reentry emission spectrometer

The value of a scientific measurement is as good as its calibration. With this in mind, a look at the different parameters affecting the measurement of the ES is necessary. The conventional parameters affecting the response of the ES is linked to the quantum efficiency of CCDs pixels to the different wavelengths as well as the effect of light scattering inside it. These effects will give a variable response along the wavelength range with usually a lower value at each end of the range of observation.

Additional parameters appeared to be important in the case of QARMANs experiments. Pressure and temperature evolutions will affect the response of the payload. The pressure and temperature evolution will slightly change the shape of the optical elements thus affecting the focus of the light which results in a change in light intensity response and a wavelength shift/stretch. The temperature will also have an additional effect. Its evolution will also affect the quantum efficiency of the CCD by up to 50% over 30K in the UV range [21] and smaller changes at higher wavelengths. QARMAN being a small reentry platform, the payload bay and hence the ES is submitted to a transient heating reaching up to 10K/min. Fig. 13 shows the expected surface temperature of the ES during QARMANs reentry. The temperature profile calculated demonstrates the necessity of a dedicated calibration setup taking in account the expected heating.

During calibration, the payload is covered with heating panels controlled to duplicate the mission temperature environment. This assembly is located inside a vacuum chamber to set accordingly the pressure environment (Down to 1 Pa, 80Km of altitude) and avoid convective cooling. In the side of the calibration light source, a mini-arc (small plasma source)

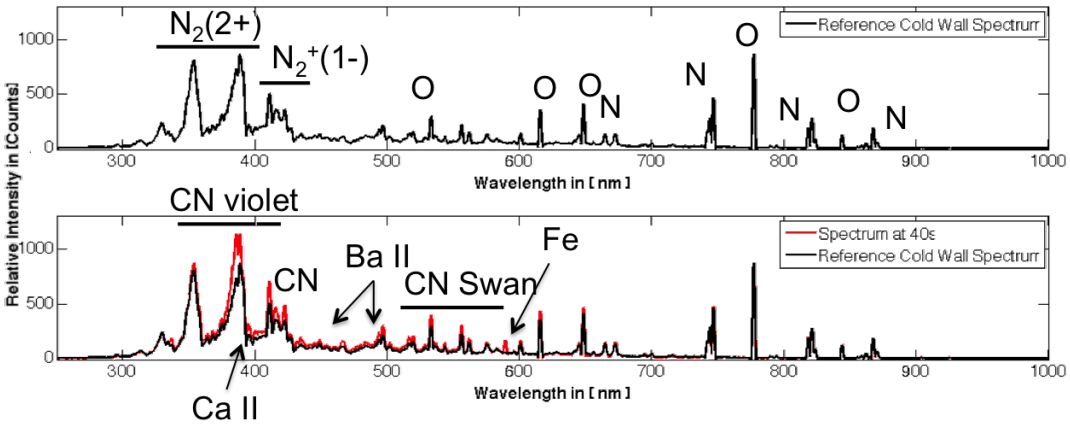

Figure 12: Calculated spectrum (6000K air plasma and cold wall, up) and overlay with the spectrum taking in account the contamination by absorption/emission of the hot ablative boundary layer (down, red)

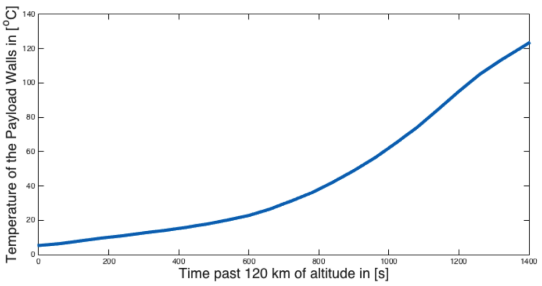

Figure 13: Calculated temperature profile on the paylaod

for the UV range is used while a tungsten lamp (grey body source) for the wavelengths above 400nm is preferred. The whole setup is presented in Fig. 14. More complex than traditional setups, it permits to get accurate scientific return. In addition, by analyzing the wavelength shift on the flight data, the ES temperature can be found to validate the thermocouple measurements inside the payload bay and the simulations. To that purpose, the evolution of noticeable atomic lines positions (ex. Oxygen 777nm) on the spectra will be tracked during flight reconstruction to identify the shift/stretch and come back on the temperature with the calibration data.

7. Conclusion

During the past years QARMAN vehicle went from feasibility to CDR level with an expected flight mid-2016. During this period, the scientific interest of the ES has raised in the view of the gaps in the different databases and the growing importance of the radiation flux assessment for the design of the new heat shields.

The integration of the payload remains possible thanks to the lightweight and compact new ES of the market. The sensitive point of such payload development is to predict the radiative flux with as much accuracy as possible to get an optimal scientific return. The efforts made through the experimental campaign and the calibration protocol gives all the keys to solve challenges linked to the ablation contamination and the effect of transient temperature profiles on the ES response. The efforts in the design of the payload and the methodology from preliminary analysis to calibration permit to use the developed technology for the QARMAN mission. It is then hoped to propose it for a wide variety of missions without constraining the platform on the interface side. The scientific return form QARMANs reentry is expected for end 2016 and additional test will be needed to complete the pre-flight efforts.

Acknowledgments

The research leading to the emission spectrometer payload development has received funding from AIRBUS DS through the CIFRE-ANRT Program. Research of T.E.M is is sponsored by the European Research Council Starting Grant #259354. Special thanks to Alexis Bourgoing, Franck Delattre, Jean-Marc Bouilly, Grgory Pinaud and Coumar Oudea for their support at AIRBUS DS.

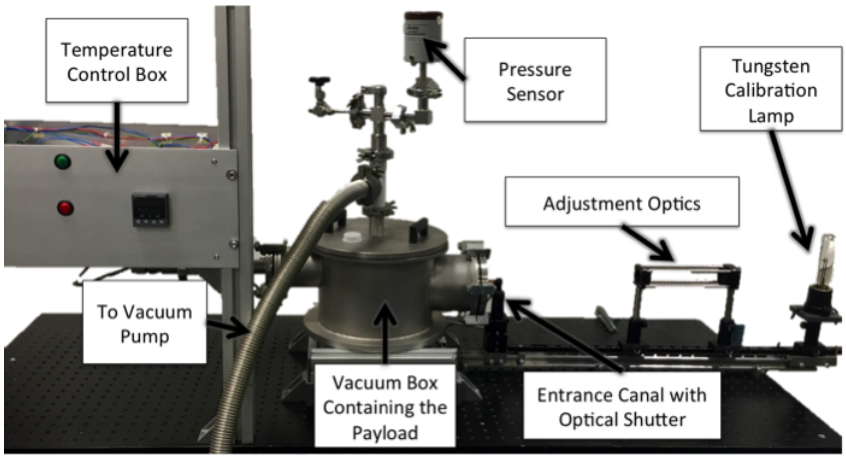

Figure 14: Calibration setup for QARMANs emission spectrometer payload

References

[1] I. Sakraker, et al., Qarman: an Atmospheric Entry Experiment on Cubesat Platform, 8th symposium on aerothermodynamics, ESA conference, Lisbon, Portugal, March 2015.

[2] L. Dell'Elce and G. Kerschen. Optimal propellantless rendezvous using diferential drag. Acta Astronautica, 109:112123, 2015. DOI: 10.1016/j.actaastro.2015.01.011.

[3] R. Venkatapathy, et al., Thermal Protection Systems Development, Testing, and Qualification for Atmospheric Probes and Sample Return Missions, JASR 9731, March 10, 2009.

[4] D. L. Cauchon, Radiative Heating Results from the FIRE II Flight Experiment at a Reentry Velocity of 11.4 Kilometers per Second, TM X1402, NASA, 1967.

[5] NASA-CR-170881, SRB thermal protection system materials test results in an archeated nitrogen environment, Lockheed Missiles and Space Co, 1979.

[6] D. Levin, et al., Theory of Radiation from Low Velocity Heated Air, AIAA-90-0133, 28th Aerospace Sciences Meeting, Reno , NV , January 1990.

[7] P. Erdman, et al., Measurements of Ultraviolet Radiation from a 5 Km/sec Bow Shock, AIAA Paper No. 92-2870, Nashville , TN , July 1992.

[8] D. A. Levin, et al., Examination of ultraviolet radiation theory for bow shock rocket experiments, AIAA Paper No. 92-2871, New York, 1992.

[9] D. A. Levin, et al., Comparison of Theory with Experiment for the Bow Shock Ultraviolet Rocket Flight, Journal of Thermophysics and Heat Transfer, Vol. 7, No. 1, Jan-March 1993.

[10] E. Venkatapathy, et al., Thermal Protection System Technologies for Enabling Future Return Missions, white paper to the NRC decadal primitive bodies sub-panel, 2009.

[11] Y. Takagi, Science Instruments on Hayabusa follow-on missions, JAXA, 2009

[12] M. A. Covington, Performance of a Lightweight Ablative Thermal Protection Material For the Stardust Mission Sample Return Capsule, NASA-NTRS, 2005.

[13] T. J. Kowal, Orion Flight Test-1 Thermal Protection System Instrumentation, NASA-NTRS, 2012.

[14] S. Lein, et al., Optical Emission Spectroscopic Experiments For In-Flight Entry Research, 8th International Planetary Probe Workshop, Portsmouth, Virginia 6-10 June 2011.

[15] D. Levin, et al., Skipper: an innovative U.S. and Russian university space science mission, Proc. SPIE Vol. 2217, p. 292-306, 1994.

[16] Munaf, Alessandro; Magin, Thierry E., Modeling of stagnation-line nonequilibrium flows by means of quantum based collisional models, Physics of Fluids 2014, 26, 097102.

[17] Scoggins, James B.; Soucasse, Laurent; Rivire, P.; Soufiane, Anouar; Magin, Thierry, Coupled flow, radiation, and ablation simulations of atmospheric entry vehicles using the hybrid statistical narrow band model, 45th AIAA Thermophysics Conference, Dallas, Texas, 2015, paper AIAA 2015-3112.

[18] C. Laux, Physico-Chemical Models for High Enthalpy and Plasma Flows, VKI-LS, 2002.

[19] F. Siebe, et al., Combined Sensor Assembly COMARS+ for Martian Atmospheric Entry, 9th International Planetary Probe Workshop, Toulouse, France, 16th-22nd June 2012.

[20] G. BAILET, et al., Reentry Platform for studying radiation, from Payload design to Qualification and Performances, 12th International Planetary Probe Workshop, Cologne, Germany, 13th-17th June 2015.

[21] L.-Y. Ling, et al., On the Influence of LED Temperature Shifts on Differential Optical Absorption Spectroscopy for Measuring NO2, Spectroscopy and Spectral Analysis, ol.32, No.1, p2886-2890, November, 2012.

Development of an ablation model for rarefied flows with application to meteor entry

Federico Bariselli

Aeronautics and Aerospace Department, von Karman Institute for Fluid Dynamics, Belgium, federico.bariselli@vki.ac.be

Supervisor: Thierry E. Magin

Associate Professor, Aeronautics and Aerospace Department, von Karman Institute for Fluid Dynamics, Belgium, thierry.magin@vki.ac.be

University Supervisor: Annick Hubin

Professor, Electrochemical and Surface Engineering Department, Vrije Universiteit Brussel, Belgium, anhubin@vub.ac.be

Abstract

Artificial space systems are not the only objects flying in our sky. About 50 tonnes of small meteoroids enter the terrestrial atmosphere every day. These bodies, from one meter diameter to micron-size grains, originate either from sublimating comets or from asteroids. In their rush to the ground, they intersect the atmosphere at velocities up to 72 km/s. As a meteoroid interacts with the atmosphere, its surface temperature can reach several thousands of Kelvin causing its ablation, i.e. melting and evaporation. Due to their small size and tremendous speeds, meteors often burn up at high altitudes, above 80 km, where the atmosphere is rarefied. Here, the gas cannot be treated as a continuous medium and the Navier-Stokes equations employed in Gas Dynamics fail. Moreover, due to the high energies involved, coupled physico-chemical phenomena (strong departure from thermo-chemical equilibrium, radiative heating, ionization and complex gas-surface interactions) occur both in gas and solid phases, making the prediction of these flows an extremely challenging task.

Recent efforts have been made by the Belgian Institute for Space Aeronomy to predict velocity, trajectory and mass of meteors. The Belgian RAdio Meteor Stations (BRAMS) experiment consists in a series of receivers spread all over Belgium to collect and standardize the meteor observations. Ground radio stations are able to detect the free electron concentration in the wake, which is directly influenced by ablation mechanisms. However, the interpretation of radio data currently relies on phenomenological methods, hence, poorly account for melting and evaporation of the material, chemistry in the meteor trail, and rarefied gas effects.

We propose to focus on developing comprehensive models for the description of the meteor phenomenon in the rarefied regime. The thesis work consists of four main segments. 1. Development of the physico-chemical models for the description of the ablation process. This will consist in an accurate description of both the gas-surface and gas phase chemical interactions. An ablative boundary condition will be developed. Transport and chemical kinetic properties of ablated vapours will be considered by constructing a database of relevant cross-sections. Moreover, both ionization and radiation cooling play a major role due to the extremely high kinetic energies involved during the meteoroid impact. Their contribution will be accounted with a step-by-step approach. 2. Implementation of the developed models in the framework of an open source Direct Simulation Monte Carlo (DSMC) software. We will benefit of the already well-established capabilities of the solver, while other features will be added: starting from the developed cross-section database, chemistry of ablated products will be implemented. 3. The theoretical/numerical modelling will be supported by experimental activity. Experimental characterization of the material response of meteorites samples collected during the Antarctic SAMBA expedition will be carried out in the VKI Plasmatron facility. Experiments will be followed by a multiscale analysis of the surface which will permit to gain a better understanding of the thermo-chemical mechanisms occurring. The experimental activity will allow for a validation of the ablation model by means of an iterative process which will lead to the refinement of the model itself. 4. In the last part, the developed tool will be used for the study of data from the BRAMS radar network. The BRAMS measurements will give access to a massive database of natural flight experiments which will help to validate the developed ablation models and, at the same time, will help the BRAMS team members in the interpretation of their data.

Keywords: atmospheric entry flows, rarefied flows, meteor, ablation, Direct Simulation Monte Carlo

Development of advanced gas-surface interaction models for reusable materials

Georgios Bellas-Chatzigeorgis

Aeronautics and Aerospace Department, von Karman Institute for Fluid Dynamics, Belgium, georgios.bellas.chatzigeorgis@vki.ac.be

Supervisor: Thierry E. Magin

Associate Professor, Aeronautics and Aerospace Department, von Karman Institute for Fluid Dynamics, Belgium, thierry.magin@vki.ac.be

University Supervisor: Paolo F. Barbante

Assistant Professor, Department of Mathematics, Politecnico di Milano, Italy, paolo.barbante@polimi.it

Abstract

A framework that provides the boundary condition for a chemically reacting wall to flow solvers has been implemented in a VKI code named *Mutation++*. It solves the mass balance at the wall taking into account the phenomenon of catalysis treated with two models; the *gamma* and the *elementary reaction* one. The gas-surface interaction framework has been coupled with a 1D Navier-Stokes solver.

Keywords: Catalysis, *Mutation++*, Gamma model, Finite Rate Chemistry model

1. Introduction

The design of the thermal protection system (TPS) for a spaceship during an atmospheric entry is a challenging task due to the multi-physics phenomena occurring in the shock layer of the space vehicle [1]. These phenomena include strong deviation from thermo-chemical equilibrium [25] , radiative heating [22] and gas-surface interaction (catalysis and ablation) between the vehicle's surface and the surrounding gas [8]. By correctly modeling them, one can more accurately predict the heat load to the vehicle. In this way the sizing of the TPS can be optimized and the available payload can be maximized.

Here we will focus on the phenomenon of catalysis in entry conditions. As the space vehicle enters an atmosphere, it converts its kinetic energy into thermal energy of the gas surrounding it. This thermal energy causes the molecules of the gas to dissociate converting part of the thermal energy into chemical and eventually cooling the gas. For vehicles such as the Space Shuttle, its thermal protection system acts as a catalyst of exothermic recombination reactions, which directly release part of the dissociation energy to the surface of the vehicle, negatively contributing to the total heat flux.

Three types of models have been used by the aerospace community in order to numerically study catalysis. The first one treats catalysis from a macroscopic point of view and is named gamma model [9]. It requires only the definition of a probability γ which expresses the probability for recombination to occur. Its simplicity has made the gamma model widely used in the study of thermal protection systems. The second approach, is a mesoscopic one and requires the definition of all the elementary processes that occur on the surface. Even though this approach is in principle more accurate than the previous one, these type of models for aerospace applications have still large uncertainties. The third type of models are the microscopic ones which study catalysis using molecular dynamics, direct simulation Monte Carlo and quantum chemistry calculations, but these approaches go beyond the scope of this report.

In parallel, catalysis is also being studied from an experimental point of view, using both ground and in-flight experiments [7; 30; 3]. These experiments are useful not only for their importance in practical applications, but also for the validation and calibration of the catalytic models described above.

In order to make the study of thermal protection materials more accessible to any CFD solver a gas-surface interaction framework has been developed in an open source code developed at the von Karman Institute for fluid dynamics named *Mutation++*, which provides directly the appropriate boundary conditions taking into account the gas-surface interaction phenomena. This framework will be presented below along with the currently implemented models for catalysis. Before that, the governing equations of the gas phase models need to be shown along with the necessary constitutive equations for the closure of the system. In the end, some preliminary results will be presented followed by the conclusions and future work.

2. Gas Phase Models

2.1. Governing Equations

The dynamical evolution of flowfield is governed by the Navier-Stokes equations:

$$\frac{\partial \rho_i}{\partial t} + \nabla \cdot (\rho_i \mathbf{u} + \mathbf{j}_i) = \dot{\omega}_i, \tag{1}$$

$$\frac{\partial \rho \mathbf{u}}{\partial t} + \nabla \cdot (\rho \mathbf{u} \otimes \mathbf{u} + p\underline{\underline{I}} + \underline{\underline{\tau}}) = \mathbf{0}, \tag{2}$$

$$\frac{\partial \rho E}{\partial t} + \nabla \cdot (\rho \mathbf{u} H + \underline{\underline{\tau}}\mathbf{u} + \mathbf{q}) = 0. \tag{3}$$

ρ_i is the partial density of species i, $\rho\mathbf{u}$ and ρE are momentum and total energy of the whole mixture. $\mathbf{j}_i$ is the diffusion flux and $\dot{\omega}_i$ is the chemical production/destruction term of the ith species. The identity matrix is symbolized with $\underline{\underline{I}}$, p is the mixture pressure, $\underline{\underline{\tau}}$ is the stress tensor and $\mathbf{q}$ is the heat flux. If Eqs. 1 are summed up over all the species in the mixture, the total continuity equation will be obtained, since $\sum_i \rho_i = \rho$. By solving the above equations along with the perfect gas law, $p_i = \rho_i R_i T$ the state of the fluid system is totally defined.

2.2. Transport

In order to close the Navier-Stokes equations (Section 2.1) expressions for diffusion flux, stress tensor and heat flux should be obtained. The transport properties are computed using the *Mutation++* library, developed by Scoggins and Magin [28] at the von Karman Institute for Fluid Dynamics. The diffusion flux is computed with the Stefan-Maxwell equations:

$$\frac{M}{\rho} \sum_k \left(\frac{x_i \mathbf{j_k}}{M_k \mathcal{D}_{ik}} - \frac{x_k \mathbf{j_i}}{M_i \mathcal{D}_{ik}} \right) = \nabla x_i \tag{4}$$

where ∇x_i is mole fraction gradient of species i. $\mathcal{D}_{ik}$ is the binary diffusion coefficient. The stress tensor reads classically:

$$\underline{\underline{\tau}} = -\mu[\nabla \mathbf{u} + (\nabla \mathbf{u}) - \frac{2}{3}\nabla \cdot \mathbf{u}\underline{\underline{I}}], \tag{5}$$

where μ is the shear viscosity and the heat flux:

$$\mathbf{q} = -\lambda \nabla T + \sum_i h_i \mathbf{j}_i \tag{6}$$

where λ is the thermal conductivity associated with the translational temperature T of the gas species and the second term is the diffusive heat flux. Both the viscosity and thermal conductivity have been computed by solving the linear transport systems as presented by [20].

3. Wall Phase Models

3.1. Mass Balance at the Interface

The Navier-Stokes equations in order to be solved require some boundary conditions. Here the general boundary condition for the case of a chemically reacting no slip wall will be presented. Firstly, since it is a no slip wall the tangent component of the velocity should be imposed to zero, $\mathbf{u}_t = \mathbf{0}$. Then additional information should be provided for the partial densities and energy at the wall. The conditions that will be applied should respect both the conservation of mass and energy. Integrating Eqs. 1 over a small volume and by forcing one of its dimensions to zero, and assuming steady state, one obtains:

$$(\rho_i \mathbf{u} + \mathbf{j}_i) \cdot \mathbf{n_w} = \dot{\omega}_{chem} + \dot{\Omega}_{surf}, \tag{7}$$

where $\mathbf{n}_w$ is the unit vector normal to the surface, $\dot{\omega}_{i,chem}$ is the mass of species i produced or destroyed per unit of area and unit time due to surface chemical reactions. The term $\dot{\Omega}_{surf}$ includes all the fluxes from the wall (eg. pyrolysis gas for ablation), but since they are not studied in this project are gathered into a single term which will be equal to zero. For a wall without mass blowing like in the case of catalysis, the normal velocity is equal to zero.

The above set of equations for all the gas species have to be solved to obtain the partial densities of the species at the wall. Coupled with the mass balance the energy balance should be also solved in order to correctly determine the temperature of the wall. The solution of the energy balance will also be provided by Mutation++ in the future, but for the time being the

assumption of no-slip isothermal wall has been imposed. It should be mentioned that the energy mass balance for catalysis will also take into account the thermal non-equilibrium effects and the β coefficient as described by [13]. The importance of thermal non-equilibrium effects for a catalytic wall has been studied by [18; 5].

Focus will be now given for the modeling of the term $\dot{\omega}_{i,chem}$ for the case of catalytic wall.

3.2. Gamma Model

The right hand side can be modeled using a phenomenological approach, the γ model, widely used in the aero-thermodynamics community [9]. In this model the recombination reactions are viewed macroscopically as:

$$A + A \rightarrow A_2, \tag{8}$$

where two atoms of A species are recombining into an A_2 molecule. For every category of this kind of reactions taken into account a probability for recombination needs to be defined. Therefore, the probability of recombination for species i, γ_i, is given as:

$$\gamma_i = \frac{M_{i,rec}}{M_i^{\downarrow}}, \tag{9}$$

where $M_i^{\downarrow}$ is the flux of species i impinging the surface and $M_{i,rec}$ is the flux of species recombining at the surface. This probability is the input parameter for this model. A fully catalytic wall has γ_i equal to 1, which means that all the particles of species i impinging the surface recombine at the wall. γ_i equal to 0 means that no reaction takes place and corresponds to a non-catalytic, or chemically inert wall. Anything between these two extreme cases is a partially catalytic wall. Knowing the probability γ_i, the right hand side of Eq. 7 is equal to [2]:

$$\dot{\omega}_{i,cat} = \gamma_i m_i M_i^{\downarrow} \tag{10}$$

When the translational energy modes of gas species close to the wall have a Maxwellian distribution function and there is no temperature slip, the impinging flux, $M_i^{\downarrow}$, is equal to [2]:

$$M_i^{\downarrow} = n_i \sqrt{\frac{kT_w}{2\pi m_i}} \tag{11}$$

where T_w is the wall temperature.

When the two recombining atoms are of the same species then the above approach is rigorous. Nonetheless, this is not the case for reactions such as:

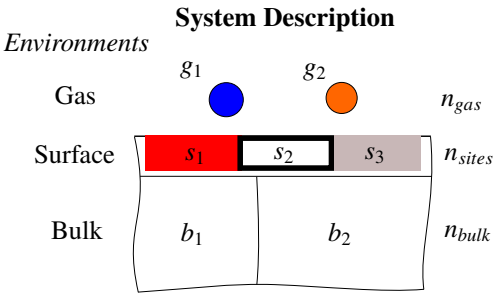

Figure 1: Description of the system for the elementary reactions model

$$A + B \rightarrow AB. \tag{12}$$

In this case one recombination probability for every different species is required for this reaction, meaning γ_A and γ_B should be provided. Then the fluxes of the A and B atoms are compared and the smallest one is chosen to be used for the computation of the catalytic wall production rate along with the appropriate γ. This approach ensures the conservation of elements on the surface. Another similar approach has been proposed by [27] for CO_2 recombination which will be also implemented in the future.

The γ coefficient for each recombination reaction can be given as a constant value or can be computed as function of temperature and pressure according to models suggested in the literature [15].

3.3. Elementary Reactions Model

Even thought the gamma approach is widely used in the aerothermodynamics community, a more rigorous way to describe the phenomenon of heterogeneous catalysis is by defining the elementary reactions that occur at the wall. This approach increases the complexity of the system, since it requires the definition of many parameters for the chemical reaction. Such parameters will be seen in the following sections, but they are mainly the coefficients of Arrhenius type reaction rates. Before defining each of the most important elementary reactions separately, some basic definitions for the model will be given.

3.3.1. Model Definitions

In order to formulate this model some basic definitions about the system itself should be given. The system in question can be seen in Fig. 1. Firstly, three distinct environments can be seen. The first one is the gas environment which is composed by n_{gas} chemically distinct species which participate in the surface

and the gas phase reactions. The rate of production and destruction of these species due to the surface are the ones needed in order to compute the term $\dot{\omega}_{i,chem}$ found in Eq. 7.

The second phase is the surface phase and it is composed of n_{sites} categories of active sites. Each category, s_i, covers a part of the surface and has a site density equal to S_i mole per square meter. By definition active sites are the places on the surface where all the surface chemical reactions take place. They can be empty or can accommodate a species from the gas phase. Not all gas species can be accommodated in all types of active sites. The number of different species that can be accommodated in a site i is denoted as $n_{(species\ in\ site\ i)}$. This accommodation is in reality the development of a chemical bond between the species and the surface. Then, the species are said to be adsorbed and will be denoted as A_{s_i}. This bond can be weak (van der Waals)-physisorption or strong (ionic or covalent)-chemisorption.

One chemical species in the gas phase should be considered different to the same one adsorbed on the surface at each site i. Chemical reactions are the mechanisms that convert one gas species to a surface one and vice versa. Therefore in order to fully define the surface, the total number of species that are needed is equal to:

$$n_{(surface\ species)} = \sum_{i=1}^{n_{sites}} n_{(species\ in\ site\ i)}. \tag{13}$$

The total number of each site S_i is conserved and it is a property of the material. Inert and porous areas of the surface can be included as sites without any chemical species assigned to them. For notation, if a species A has as subscript the symbol s it means that it is adsorbed into the active sites named s.

The last environment is the bulk environment which consists of n_{bulk} phases, but since it is used to describe mainly ablative reactions and porous materials it is not taken into account at all in this report [21].

The total number of species considered in this model ignoring the bulk are:

$$n = n_{gas} + n_{(surface\ species)}. \tag{14}$$

3.3.2. Adsorption

Adsorption is the elementary process where a gas species, mainly atom creates a chemical bond with one active site of the surface. Such a process can be seen in Fig. 2 and can be expressed as a chemical reaction as:

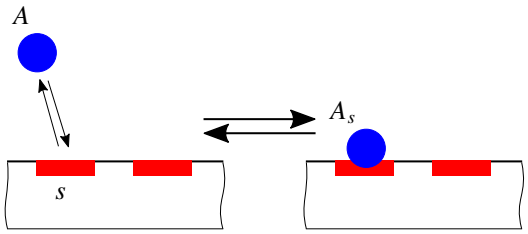

Figure 2: Adsorption/Desorption Mechanism.

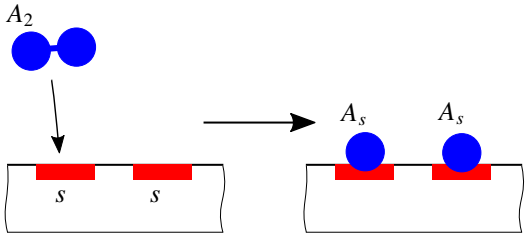

Figure 3: Dissociative Adsorption Mechanism.

$$A + s \rightarrow A_s. \tag{15}$$

For such kind of processes the reaction rate coefficient is given by the formula

$$k_{f,ads} = s_{ads} \sqrt{\frac{kT_w}{2\pi m_A}} \frac{1}{S_{tot}} e^{-\left(\frac{E_{ads}}{k_B T}\right)}, \tag{16}$$

where s_{ads} is a sticking coefficient and expresses the probability for an impinging atom to be adsorbed. It can be taken either as constant or an exponential function of the negative of temperature in order to take into account the fact that if an energetic atom contacts the surface, the probability of it to stick is decreased. For atoms there is no need to take into account any steric effect. Furthermore, adsorption is almost an instant process without the need of activation because of the large difference of energy between the gas and surface species. For this reason $E_{act} = 0$. S_{tot} is the total number of active sites on the surface.

Molecules have also a probability to be adsorbed by the surface, but they create a weak bond with it making their adsorption important only at very low temperatures. What is more likely to occur is the molecules to dissociate and then the atoms to be adsorbed. Such a process is called dissociative adsorption and can be seen schematically in Fig. 3. Its reaction reads

$$A_2 + 2s \rightarrow 2A_s \tag{17}$$

and the reaction rate coefficient as

$$k_{f,diss-ads} = s_{diss-ads}\sqrt{\frac{kT_w}{2\pi m_{A_2}}}\frac{1}{S_{tot}^2}e^{-\left(\frac{E_{ads}}{k_BT}\right)}, \quad (18)$$

Again the sticking coefficient $s_{diss-ads}$ is taken as constant or as a weak function of temperature and $E_{ads} = 0$, because we deal with a non activated reaction process.

Not all the molecules can be dissociatively adsorbed. For example O_2 is dissociatively adsorbed on a Cu surface, but N_2 is not. This is difference is associated to the vacancies of the orbitals of the atoms, to the energy of the bond between the N_2 atoms, as well as to the size of the N_2 molecule [4].

As a concluding remark, since we treat the surface from a mesoscopic point of view the mean field approximation is assumed meaning that all the adsorbed species are randomly distibuted on the surface and they do not interact between each other with a potential while they are adsorbed.

3.3.3. Desorption

Desorption or thermal desorption is the process where the adsorbed atoms on the surface have enough energy to vibrate sufficiently to break its bond with the surface without recombining. It is the reverse process of adsorption as it can be seen in Fig. 2 and its reaction is

$$A_s \rightarrow A + s \quad (19)$$

Desorption is an activated process, with activation energy E_{des} equal to the energy of the bond of the adsorbed atom with the surface. For a chemisorbed atom this energy can be high and therefore the process becomes important only for high temperatures. The rate coefficient of the desorption is give by the formula

$$k_{f,des} = v_d e^{-\left(\frac{E_{des}}{k_BT}\right)}, \quad (20)$$

with v_d expressing the attempts of the atoms to escape due to their vibrations on the surface. It can be imposed as a constant or get an approximation for it using transition state theory which gives $v_d = \frac{k_BT}{h}$.

3.3.4. Eley-Rideal Mechanism

The Eley-Rideal mechanism is the first of the two mechanisms which cause recombination on the surface. The presence of this mechanism was found by the fact that highly vibrationally excited molecules

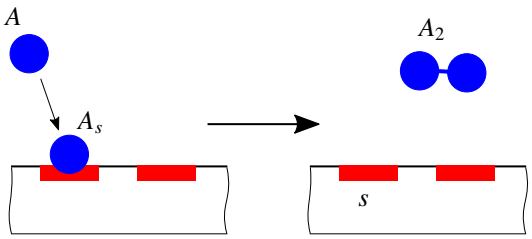

Figure 4: Eley-Rideal Mechanism.

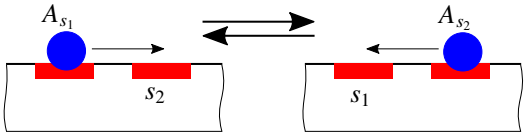

Figure 5: Surface Diffusion Mechanism.

were found over catalytic surfaces, something that could not be explained by the other recombination mechanism, the Langmuir-Hinshelwood.

The process describes the phenomenon when an atom from the gas phase impinges on an adsorbed atom and they recombine. The produced molecule is instantly released to the gas phase. The process can be seen in Fig. 4 and as a reaction:

$$A + A_s \rightarrow A_2 + s \quad (21)$$

This mechanism can be either activated or not depending on whether the resulting molecule has a stronger or weaker bond between its atoms compared to the bond between the atom and the surface before recombination [4]. Its rate coefficient is again of the Arrhenius type:

$$k_{f,E-R} = s_{E-R}\sqrt{\frac{kT_w}{2\pi m_A}}\frac{1}{S_{tot}}e^{-\left(\frac{E_{E-R}}{k_BT}\right)}. \quad (22)$$

s_{E-R} expresses the Eley-Rideal reaction efficiency and can be taken as a constant or a slightly increasing function with the temperature [4]. The reaction rate for this process is in fact the rate of impinging atoms on the surface, just like the case of adsorption, multiplied by a recombination probabily.

3.3.5. Surface Diffusion

If the surface in question consists of more than one categories of sites an adsorbed species may diffuse

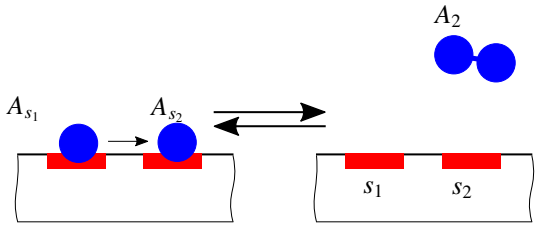

Figure 6: Langmuir-Hinshelwood Mechanism.

from one category of sites to another one. This process can be seen in Fig. 5 and as a reaction:

$$A_{s_1} + s_2 \rightarrow A_{s_2} + s_1 \tag{23}$$

Here emphasis will be given to the phenomenon where a physisorbed atom (A_{s_1}) diffuses to a chemisorption site (s_2) and gets chemisorbed. For such a process the reaction rate coefficient is given by the formula [11]:

$$k_{f,diff} = \begin{cases} 0 & \Lambda_D < d_{site} \\ \dfrac{1}{k_{f,des} s_2} & \Lambda_D > d_{chem} \\ \dfrac{1}{k_{f,des} s_{tot}} \left[\dfrac{v_D}{v_d} e^{\left(\frac{E_{des}-E_D}{k_B T}\right)} - \dfrac{1}{4} \right] & \text{else.} \end{cases} \tag{24}$$

Λ_D is the average distance an atom diffuses on the surface before it desorbes ($\Lambda_D = 2d_{site}\sqrt{\frac{v_d}{v_D}} e^{\left(\frac{E_{des}-E_D}{k_B T}\right)}$), $d_{site} = d_{phys}$ is the average radius of the sites, which is equal to the distance between physisorption sites, d_{chem} is the average distance between chemisorption sites, s_2 is the total number of chemisorption sites, v_D is the vibrational frequency of a physisorbed atom parallel to the surface and E_D is the activation energy for surface diffusion [16].

Without going into the details of this expression, it computes the probability of chemisorption to occur by comparing the average distance an atom travels on the surface before it thermally desorbs with the size of the site and the average distance between chemisorption sites. For this reason, it takes the value 0 if the sites are large, meaning that no chemisorption via diffusion is possible, 1 if the chemisorption sites are close to each other, or any other value in between.

3.3.6. Langmuir-Hinshelwood Mechanism

The last elementary reaction type that has been implemented so far is the mechanism of Langmuir-Hinshelwood. As it has been mentioned before, it is the second mechanism which produces molecules for the gas phase. These molecules are produced due to the sufficiently energetic collision of two already adsorbed atoms (Fig. 6):

$$A_{s_1} + A_{s_2} \rightarrow A_2 + s_1 + s_2 \tag{25}$$

For the reaction rate coefficient $k_{f,L-H}$ several approaches are available. The first one takes into account the effect of surface diffusion and the expression reads as:

$$k_{f,L-H} = \frac{k_D k_{f,E-R}}{k_{f,des}} \frac{1}{S_{tot}}. \tag{26}$$

This formula says that the probability for L-H recombination to occur is equal to three independent events to occur. Firstly, to have surface diffusion (k_D), not to have desorption ($1/k_{des}$) and lastly recombination to occur ($k_{f,E-R}$). This last event makes the assumption that the probability of recombination does not change whether the atom that impinges the adsorbed one comes from the gas or the surface phase.

Another approach for the reaction rate comes from the work of Marschall which suggest the following formula, since his model does not take into account the phenomenon of surface diffusion:

$$k_{f,L-H} = \sqrt{\frac{\pi k_B T}{2m_A}} \sqrt{\frac{A_v}{S_{tot}}} s_{L-H} e^{-\left(\frac{E_{L-H}}{k_B T}\right)}, \tag{27}$$

where A_V is the Avogadro number, s_{L-H} is the probability for the L-H recombination to occur and E_{L-H} is the activation energy of the reaction, which is assumed as a constant.

Other approaches close to the latter one are also available in the literature, but for different kind of metallic surfaces [4].

3.3.7. Steady State at the wall and Gamma Coefficient

The wall chemical production rates of both the gaseous and surface species are computed using the law of mass action [10] taking into account all the elementary reactions at the wall. For the surface species it is assumed that the surface coverage is in a study state, meaning that:

$$\frac{d[s]}{dt} = 0. \tag{28}$$

The above system is closed by applying the conservation of sites discussed in Section 3.3.1, and it is solved in *Mutation++* using the Newton method.

The atomic recombination coefficient γ used in the model of Section 3.2 can be calculated as an output of this model. As mentioned already, it is the fraction of the produced or destroyed species on the surface due to chemical reactions divided by the thermal flux of the atomic species impinging on the surface for recombination. For the recombination reaction of Eq. 8 by assuming the elementary reaction described above one gets:

$$\gamma_A = \frac{\dot{\omega}_{A,rec}}{M_A^{\downarrow}} = \frac{\dot{\omega}_{A,ads} + \dot{\omega}_{A,des} + \dot{\omega}_{A,E-R}}{M_A^{\downarrow}}, \qquad (29)$$

where M_A is half of the one dimensional thermal flux. At a steady state:

$$\gamma_A = \frac{\dot{\omega}_{A,rec}}{M_A^{\downarrow}} = \frac{2\left(\dot{\omega}_{A_2,E-R} + \dot{\omega}_{A_2,L-H}\right)}{M_A^{\downarrow}}. \qquad (30)$$

4. Numerical Methods

In order to test the implementation of the gas-surface interaction module in an efficient way, a special formulation of the Navier-Stokes equations, called dimensionally reduced Navier-Stokes equations (DRNSE) [17] is solved. This formulation simulates the flow field only on the stagnation line of the re-entry vehicle. The Navier-Stokes equations are written in spherical (r, θ, ϕ) coordinates. The flow is assumed to be axisymmetric and therefore $u_\phi = 0$ and $\partial/\partial\phi = 0$. The symmetry of the flow implies that u_r, p, T and ρ_i are symmetric (cosine) with respect to the stagnation line axis (located at $\theta = 0$) and u_θ is antisymmetric (sine) with respect to it. Furthermore, the Newtonian theory for pressure distribution of hypersonic flows is assumed. Finally, by taking the limit of $\theta \to 0$ the DRNSE equations [17] are obtained. The DRNSE system of equations is solved using the finite volume method in space, with an implicit Backward Euler method in time [14]. Detailed information about the numerical method can be found in [24]. For the simulations that will presented instead of using the Roe scheme for the convective fluxes the AUSM+up+AS scheme [19] was implemented. This change made the code more stable especially in the very low Mach number regime.

5. Results

5.1. Gamma Model

The first simulation to test the catalytic wall boundary was the OREX test case as it can be found in [2].

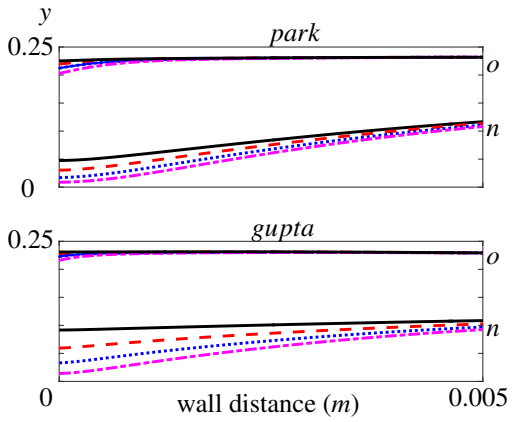

Figure 7: Mass Fraction profiles along the stagnation line close to the wall for the Park and Gupta chemical models. (***unbroken line***): $\gamma = 0$; (***dashed line***):$\gamma = 1 \cdot 10^{-3}$; (***dotted line***): $\gamma = 2 \cdot 10^{-3}$;(***dash-dotted line***): $\gamma = 3 \cdot 10^{-3}$.

The free stream conditions are seen in Table 1. This is an *air* 5 simulation, where at the wall only two recombination reactions are imposed, both with the same catalytic recombination probability. The two recombination reactions are the recombination of atomic oxygen and nitrogen to their molecular species. For the gas phase, two different chemical models are studied, the Park [26] and the Gupta models.

The mass fractions along the stagnation line of the atomic nitrogen and the atomic oxygen are shown (Fig. 7) parallel to the ones obtained in literature (Fig. 8, 9). The difference is associated to the fact that a stagnation line formulation is used for this project compared to the axisymmetric Navier-Stokes. In both the nitrogen and oxygen profiles, as the catalycity of the wall increases the profiles follow the same trend. Comparing the heat fluxes in Table 2, it can be observed that there is a difference in the heat fluxes also in the non catalytic case.

Comparing with other simulations of the conditions for the non catalytic case, Yamamoto (Park Model) computed a heat flux equal to $33 W/cm^2$ and Gupta (Gupta Model) heat flux equal to $26 W/cm^2$ which are close to our values. The experimental in-flight value,

Table 1: Boundary Conditions for the OREX test case.

T_{wall}	1458	K
p_∞	23.7	Pa
T_∞	248	K
u	5550.85	m/s

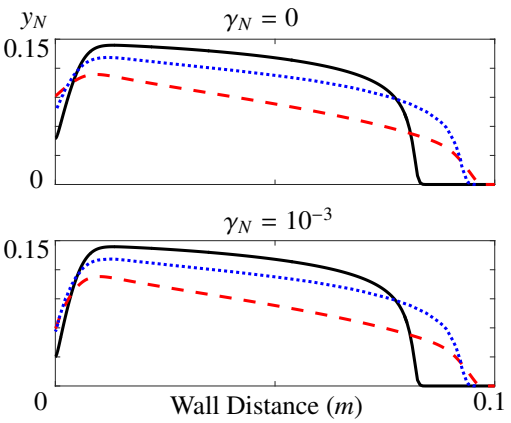

Figure 8: Mass fraction profiles for N comparing the chemical models for this project and the results of Barbante. (***unbroken line***): Park; (***dashed line***): Gupta; (***dotted line***): Barbante.

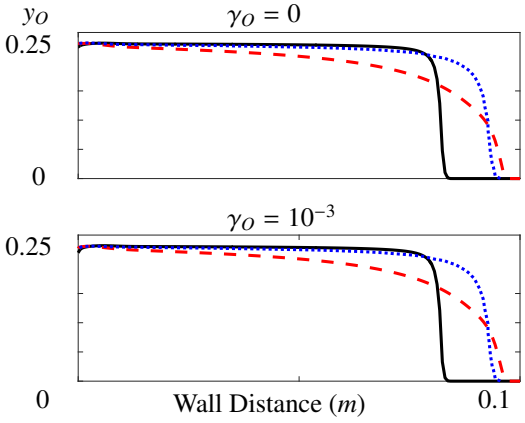

Figure 9: Mass fraction profiles for O comparing the chemical models for this project and the results of Barbante. (***unbroken line***): Park; (***dashed line***): Gupta; (***dotted line***): Barbante.

which was equal to $39 W/cm^2$, predicts a γ coefficient equal to $3 \cdot 10^{-3}$ for both the recombination reactions. As a future result, it would be recommended to take a different γ value for the two recombination reactions as a function of the wall temperature and compare the heat fluxes again.

5.2. Elementary Reactions Chemistry

In order to test the implementation of the elementary reaction model the approach of Guerra [11] has been followed, which studies the recombination of Nitrogen (N) on reaction-cured glass (RCG) made of Si. The advantage of his proposed approach is that it gives an analytical solution for the recombination probability γ as a function of temperature. This analytical solution is the reference to verify the implementation of his approach in *Mutation++*. To be obtained some assumptions have been made. Firstly, the concentration of N in the gas close to the surface is assumed constant and equal to $10^{21} 1/m^3$. Even though N recombines due to catalysis its concentration does not change and its value dictates the pressure in the flow field. The N_2 molecules that are produced are completely removed from the gas and their concentration is equal to zero. This assumption makes the dissociative adsorption as an non important elementary reaction and it is therefore ignored.

Table 2: Heat Flux Comparison for the Gupta and Park models with Barbante simulations [2].

Heat Flux (W/cm)	Barbante	Gupta	Park
Non-Catalytic	29	25	31
$\gamma = 1 \cdot 10^{-3}$	33	29	34
$\gamma = 2 \cdot 10^{-3}$	37	33	36
$\gamma = 3 \cdot 10^{-3}$	41	37	38

The surface is assumed to be composed of two categories of sites, the physisorption (p) and the chemisorption (c) sites. The physisorption sites are the areas of the surface where the atoms of N create only a Van der Waals bond with the surface. Almost all the surface is assumed to be covered with physisorption sites. The chemisorption sites exist due to imperfection of the crystal lattice of the surface and with them, the atoms create only a strong chemical bond with the surface. They cover usually a small fraction of the total surface. If an atom becomes chemisorbed, it cannot thermally desorb or diffuse without first recombining. This assumption can be weak in cases of high surface temperatures. The mechanism of diffusion from a physisorption to a chemisorption site is also taken into account. As far as the recombination reactions are concerned (E-R, L-H), they occur only at chemisorption sites.

The model described is summarized as the following set of reactions:

Table 3: Input Parameters for model [11] .

Parameter	Value	Units
$[N]$	10^{21}	$1/m^3$
S_{tot}	10^{20}	$1/m^2$
S_c	$2 \cdot 10^{17}$	$1/m^2$
d_p	10^{-10}	m
d_c	$2 \cdot 10^{-9}$	m
$s_{a,p}$	1	–
$E_{ads,p}$	0	J
v_d	10^{15}	$1/s$
$E_{des,p}$	$8.47 \cdot 10^{-20}$	J
$s_{a,c}$	1	–
$E_{ads,c}$	0	J
s_{E-R}	1	–
E_{E-R}	0	J
v_D	10^{12}	$1/s$
$E_{des,p}$	$4.23 \cdot 10^{-20}$	J

$$
\begin{aligned}
N + p &\xrightarrow{k_{f_p}} N_p \\
N_p &\xrightarrow{k_{f_{des}}} N + p \\
N + c &\xrightarrow{k_{f_c}} N_c \\
N + N_c &\xrightarrow{k_{f_{E-R}}} N_2 + c \\
N_p + c &\xrightarrow{k_{f_D}} N_c + p \\
N_p + N_c &\xrightarrow{k_{f_{L-H}}} N_2 + c + p
\end{aligned} \tag{31}
$$

The necessary parameters to get the reaction rates coefficients can be found in Table 3.

For the model above the function of γ to the surface temperature can be seen in Fig. 10. For details on the behavior of the system at all ranges of temperature and pressure more information can be found in [11].

Similar models to this for Si surfaces are available in [29]. In the future this model will be extended to take into account also the recombination on a surface made of Cu [4] to test the dependence of the γ coefficient on pressure as it has been observed by experiments in the Plasmatron facility.

6. Conclusions

A framework has been developed in *Mutation++* that is capable of providing the accurate boundary conditions for a chemically active wall. This report focuses on the gas-surface phenomenon of catalysis and how it can be treated from a macroscopic and a mesoscopic point of view. The implementation was coupled with an inexpensive formulation of the Navier-Stokes equations. The chosen test case was the OREX re-entry vehicle for the macroscopic point of view (γ model) of catalysis. The results were compared to similar results of the literature. The implementation of the mesoscopic catalyic was compared to an analytical approach proposed by Guerra.

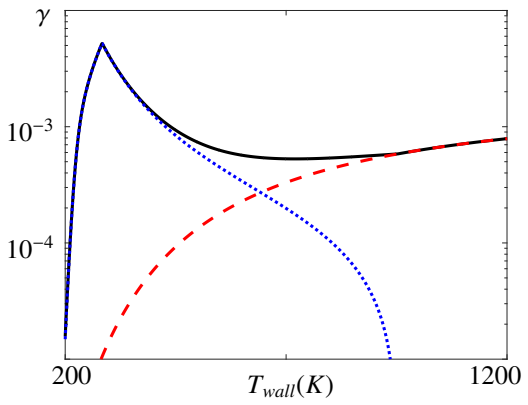

Figure 10: Recombination probability γ of N on a Si surface according to the model of [11]. (***unbroken line***): Total γ; (***dashed line***): Eley-Rideal Recombination γ_{E-R}; (***dotted line***): Langmuir-Hinshelwood Recombination γ_{L-H}.

The implementation can be easily extended to provide to the CFD solver the boundary conditions also for the cases of chemical equilibrium and finite rate ablation walls [6], by solving both the mass and energy balances on the surface coupled. *Mutation++* is currently being coupled with a two dimensional axisymmetric code named *Cosmic* [2], with which the IXV re-entry vehicle will be tested. Lastly, the mesoscopic model will be tested for more surfaces and will be validated with ground and in-flight experiments, taking into account also thermal non-equilibrium effects.

References

[1] J.D. Anderson. *Hypersonic and High-Temperature Gas Dynamics*. AIAA Education Series. American Institute of Aeronautics and Astronautics, 2006.

[2] P. F. Barbante. *Accurate and Efficient Modeling of High Temperature Nonequilibrium Air Flows*. PhD thesis, Université Libre de Bruxelles, 2001.

[3] M. Balat-Pichelin, V.L. Kovalev, A.F. Kolesnikov, and A.A. Krupnov. Effect of the incomplete accommodation of the het-

erogeneous recombination energy on heat fluxes to a quartz surface. *Fluid Dynamics*, 43(5):830–838, 2008.

[4] M. Barbato, S. Reggiani, C. Bruno and J. Muylaert. Model for Heterogeneous Catalysis on Metal Surfaces with Applications to Hypersonic Flows. *Thermophysics and Heat Transfer*, 14(3):412–420, 2000.

[5] G. Bellas-Chatzigeorgis, P. Barbante, T. E. Magin. Development of detailed chemistry models for boundary layer catalytic recombination. *8th European Symposium on Aerothermodynamics for Space Vehicles*, Lisbon, March 2015.

[6] B. Dias, A. Turchi, T. E. Magin Stagnation-Line Simulations of Meteor Ablation *AIAA 2015 Thermophysic Conference*, Dallas, TX, June 2015

[7] O. Chazot. Experimental studies on hypersonic stagnation point chemical environment. *RTO-EN-AVT-142 von Karman Institute Lecture Series: Experiment, Model and Simulation of Gas-Surface Interactions for Reactive Flows in Hypersonic Flights*, 2007.

[8] I. Chorkendorff and J.W. Niemantsverdriet. *Concepts of Modern Catalysis and Kinetics*. Wiley, 2006.

[9] R. Goulard. On catalytic recombination rates in hypersonic stagnation heat transfer. *Jet Propulsion*, 28:737–745, 1958.

[10] J.H. Ferziger and H.G. Kaper. *Mathematical theory of transport processes in gases*. North-Holland Pub. Co., 1972.

[11] V. Guerra. Analytical model of heterogeneous atomic recombination of silica-like surfaces. *IEEE Transaction on plasma science*, 5:35, 2007.

[12] V. Guerra and J. Loureiro. Dynamical Monte Carlo simulation of surface atomic recombination. *Plasma Sources Sci. Technol.*, 13:85, 2004.

[13] B. Halpern and D. E. Rosner. Chemical energy accommodation at catalyst surfaces. Flow reactor studies of the association of nitrogen atoms on metals at high temperatures. *Transactions of the Faraday Society*, 74:1883–1912, 1978.

[14] C. Hirsch. *Numerical Computation of Internal and External Flows: The Fundamentals of Computational Fluid Dynamics*. Elsevier Science, 2007.

[15] V. L. Kovalev and A. F. Kolesnikov. Experimental and Theoretical Simulation of Heteogeneous Catalysis in Aerothermochemistry (a Review). *Fluid Dynamics*, 40(5):669–693, 2005.

[16] Y. C. Kim and M. Boudart. Recombination of O, N and H Atoms on Silica: Kinetics and Mechanism. *Langmuir*, 7:2999-3005, 1991.

[17] A. Klomfass and S. Müller. A quasi-one dimensional approach for hypersonic stagnation-point flows. Technical report, RWTH Aachen, 1996.

[18] E. Kustova, E. Nagnibeda, I. Armenise and M. Capitelli. Nonequilibrium kinetics and heat transfer in O_2/O mixtures near catalytic surfaces. *Journal of Thermophysics and Heat Transfer*, 16:2:238–244, 2002.

[19] M.-S. Liou. A sequel to AUSM, Part II: AUSM+-up for all speeds. *Computational Physics*, 214(1):137–170, 2006.

[20] T.E. Magin. *A Model for Inductive Plasma Wind Tunnels*. PhD thesis, Université Libre de Bruxelles, 2004.

[21] J. Marschall and M. MacLean. Finite-Rate Surface Chemistry Model, I: Formulation and Reaction System Examples. *42nd AIAA Thermophysics Conference*, Honolulu, Hawaii, June 2011.

[22] M.F. Modest. *Radiative Heat Transfer*. Chemical, Petrochemical & Process. Academic Press, 2003.

[23] A. Munafò and T. E. Magin. Modeling of stagnation-line nonequilibrium flows by means of quantum based collisional models. *Physics of Fluids*, 26(9):–, 2014.

[24] A. Munafò. *Multi-Scale models and Computational methods for Aerothermodynamics*. PhD thesis, Ecole Central Paris, 2014.

[25] C. Park. *Nonequilibrium Hypersonic Aerothermodynamics*. Wiley, 1990.

[26] C. Park. Review of chemical-kinetic problems of future NASA missions. I: - earth entries. *Journal of Thermophysics and Heat Transfer*, 7-3:385–398, 1993.

[27] P. Rini and G. Degrez. Determination of effective recombination probability: Detailed aspects of a macroscopic methodology. *RTO-EN-AVT-142 von Karman Institute Lecture Series: Experiment, Model and Simulation of Gas-Surface Interactions for Reactive Flows in Hypersonic Flights*, 2007.

[28] J. B. Scoggins and T. E. Magin Development of Mutation^{++}: MUlticomponent Thermodynamics And Transport properties for Ionized Plasmas written in C++. *AIAA 2014-2966. 11th AIAA/ASME Joint Thermophysics and Heat Transfer Conference*, 2014.

[29] C. Sorensen, P. Valentini and T. E.Schwartzentruber. Uncertainty Analysis of Reaction Rates in a Finite-Rate Surface-Catalysis Model. *Journal of Thermophysics and Heat Transfer*, 26-3:407-416.

[30] J. Thoemel. *Surface catalysis in high enthalpy flows*. PhD thesis, RWTH Aachen, von Karman Institute for Fluid Dynamics, January 2013.

SPARK: Simplified plasma models based on reduced kinetics

Aurélie Bellemans

Aeronautics and Aerospace Department, von Karman Institute for Fluid Dynamics, Belgium, aurelie.bellemans@vki.ac.be

Supervisor: Thierry Magin

Associate Professor, Aeronautics and Aerospace Department, von Karman Institute for Fluid Dynamics, Belgium, thierry.magin@vki.ac.be

University Supervisor: Alessandro Parente

Associate Professor, Service d'Aéro-Thermo-Mécanique, Université Libre de Bruxelles, Belgium, alessandro.parente@ulb.ac.be

University Supervisor: Marc Massot

Professor, EM2C, CentraleSupélec, France, marc.massot@centralesupelec.fr

Abstract

Previous investigations have demonstrated the strength of Principal Component Analysis (PCA) for the reduction of complex and detailed chemistry models for plasma applications: starting from an electronic specific collisional-radiative model, a reduced argon system has been derived using Manifold Generated-PCA. In the present work we present how to optimize the reduction by using a newly developed clustering algorithm for MG-PCA.

Keywords: plasma, Principal Component Analysis (PCA), collisional-radiative, reduction, argon

1. Introduction

The simulation of plasma flows often remains restricted to zero-dimensional, or limited one-dimensional simulations because of its complexity and multi-scale aspects. A high number of species are involved through different kind of reactions such as dissociation and ionization reactions. Each of them have their own proper time scale and react at a different speeds. Some processes are already at equilibrium while others still react. Besides chemical non-equilibrium, we also have thermal non-equilibrium as translational, rotational, vibrational, and electron tempertures evolve distinctly during the process. During this PhD, we propose to investigate different chemistry reduction techniques to simplify the plasma kinetics of the system. These will lead to simplified calculations and considerably reduce the computational cost of heavy plasma simulations.

A first category of techniques is based on a time-scale separation. The dynamic system can be divided in a fast and a slow varying manifold. The goal is to project the fast reacting kinetics on the slow one, such as proposed by singular perturbation analysis and rate-controlled constrained equilibrium techniques. Examples can be found in the works of Kim [1] , Pope [2], Ren [3], Keck [4; 5] and Massot [6]. A possible alternative to the aforementioned methods is provided by more physics-based methods. Examples of this approach are the coarse-grained models proposed by Magin et al. [7], Munafò et al. [8; 9], Liu et al. [10; 11] and Panesi and Lani [12]. In the aforementioned papers the mechanism reduction is realized by lumping the internal energy levels in bins (where a distribution for the levels is prescribed). The work by Panesi and Lani [12] focuses on electronic excitation and ionization in air (ABBA model [13; 14; 15; 16]), while those by Magin et al. [7], Munafò et al. [8; 9], Liu et al. [10; 11] focus on the rovibrational kinetics of the $N_2(^1\Sigma_g^+)$-$N(^4S_u)$ system. Other examples of coarse-grained models for plasma flows are the works by Le et al. [17] and Guy et al. [18].

The other category of techniques is based on statis-

tical methods and has already been tested during this PhD work. Manifold-Generated Principal Component Analysis (MG-PCA) has been applied on collisional-radiative argon shock relaxation simulations. It has first been tested using the experimental test conditions as free stream parameters for the simulations. MG-PCA must be applied on a training data set containing the mass fractions of all species at every iteration of the simulation. As a fully calculated dataset is needed to train the PCA, we often start from a simple 0D or 1D shock tube simulation. Next an eigenvalue problem is solved on the covariance matrix of the data. The principal components are the variables containing the highest variance, and thus the highest eigenvalues. The system is projected on a basis formed by the principal variables to obtain a reduced system. There exist a global and a local formulation of the method. With local MG-PCA, the data is divided in several clusters and the reduction is applied on each of them. An important model reduction of 56 % could be obtained using the aforementioned local technique. In a next step, the pressure of the simulation has been lowered to 300 Pa to match re-entry conditions and better capture non-equilibrium features such as the depopulation of the excited argon states. Unfortunately, new techniques had to be developed to make the PCA work. The previous clustering algorithm for finding the local clusters was not detailed enough and could not divide the dataset according to the new non-equilibrium dynamics of the shock relaxation. In this paper we will present a new clustering algorithm to optimize MG-local-PCA and obtain a successful reduced model for simulation re-entry conditions.

2. Detailed chemistry modeling

The considered argon plasma is a 34 species mixture as described by Kapper [19] and Vlcek [20]. It contains 31 electronic levels of argon, 2 levels of ionized argon and electrons (Ar, Ar^+, e^-). The influence of doubly ionized argon, Ar^{++} has been neglected in this model. Contrary to a Multi-Temperature (MT) model where all electronic states are distributed according to a Maxwell-Boltzmann distribution, a Collisional-Radiative (CR) model accounts for a detailed description for every excited level. Ionization and excitation reactions by impact with electrons and the ground state are being considered within the collision model. Radiative losses between free-bound and bound-bound transitions have been taken into account. In the equations (1) to (6), the indices i and j stand for different excited states with $j > i$. The radiative effects have been modeled by the use of escape factors (Λ) as in equations (5) and (6). An escape factor of 1 corresponds to radiative transfer through an optically thin material, an escape factor of 0 to an optically thick material. The free-free transitions have been modeled through Bremsstrahlung emission of charged particles (Eq. 10) .

$$\mathrm{Ar(i)^+e^-} \underset{Fij}{\overset{Cij}{\rightleftharpoons}} \mathrm{Ar(j)^+e^-} \tag{1}$$

$$\mathrm{Ar(i) + Ar} \underset{Lij}{\overset{Kij}{\rightleftharpoons}} \mathrm{Ar(j) + Ar} \tag{2}$$

$$\mathrm{Ar(i) + e^-} \underset{Oi}{\overset{Si}{\rightleftharpoons}} \mathrm{Ar^+ + 2\,e^-} \tag{3}$$

$$\mathrm{Ar(i) + Ar_1} \underset{Wi}{\overset{Vi}{\rightleftharpoons}} \mathrm{Ar^+ + e^- + Ar_1} \tag{4}$$

$$\mathrm{Ar(i) + hv} \underset{\Lambda Aji}{\overset{(1-\Lambda)Aji}{\rightleftharpoons}} \mathrm{Ar(j)} \tag{5}$$

$$\mathrm{Ar(i) + hv} \underset{\Lambda Rji}{\overset{(1-\Lambda)Rji}{\rightleftharpoons}} \mathrm{Ar^+ + e^-} \tag{6}$$

The Euler flow equations have been modified to a 1D description in space by canceling the time-dependent term in the general differential form:

$$\frac{\partial Q}{\partial t} + \nabla \cdot \bar{\bar{F}} = \dot{\Omega} \tag{7}$$

In this expression Q is the vector of conserved quantities, P the tensor containing the fluxes of Q, and Ω the vector of source terms.

$$Q = \begin{pmatrix} \rho_1 \\ \vdots \\ \rho_N \\ \rho u \\ E \end{pmatrix}, F = \begin{pmatrix} \rho_1 u \\ \vdots \\ \rho_N u \\ \rho u^2 + p \\ uH \end{pmatrix}$$

Radiative source terms have to be added to the global and electronic energy conservation. Q_{radI}, represents the radiative power due to bound-bound transitions. These reactions are driven by the Einstein transition coefficients, Aji [s^{-1}]. Another radiative power term, Q_{radII}, has to be added for the conservation of electronic energy. It regroups the free-bound and free-free transitions. In the expressions 8 and 9, n_i represents the number density of species i, E_i stands for the energy of level i, and E_{Ar+} for the energy of the ionized

argon levels.

$$Q_{radI} = \sum (E_j - E_i) n_j A_{ji} \quad (8)$$

$$Q_{radII} = \sum (E_{Ar^+} - E_i) n_j R_{ji} + Q_{Brem} \quad (9)$$

$$Q_{Brem} = -1.42 \times 10^{-40} Z_{eff}^2 \sqrt{T_e} n_+ n_e \quad (10)$$

When canceling the time-dependent term one can retrieve the Euler equations for mass, momentum, energy and electron energy depending on the space variable x:

$$\frac{\partial}{\partial x}[\rho u y_i] = \omega_i \quad (11)$$

$$\frac{\partial}{\partial x}[\rho u^2 + p] = 0 \quad (12)$$

$$\frac{\partial}{\partial x}[\rho u (h + \frac{1}{2}u^2)] = -Q_{radI} \quad (13)$$

$$\frac{\partial}{\partial x}[\rho u y_e e^e] = \Omega_e - p_e \frac{\partial}{\partial x} u - Q_{radII} \quad (14)$$

In these expressions ρ is the total mass density, u the speed, y_i the mass fraction for every species i, ω_i the source term for each species, p the pressure and h the enthalpy of the mixture. The variables related to the electrons are: y_e the mass fraction of the electrons, e^e the electronic specific energy, Ω_e the electronic energy production and p_e the partial pressure of the electrons.

3. Principal Component Analysis

Manifold-Generated Principal Component Analysis (MG-PCA) has been introduced lately by Parente [21] as a mathematical method for reducing a dynamical system by projecting it on a base made up of its principal components. This reduction techniques has been derived from the classical PCA formulation and ameliorated with respect to error propagation during the variable reconstruction. In the works of Isaac [22] and Coussement [23], MG-PCA has been applied and verified on combustion applications. We will apply the reduction method on a CR model for argon plasma.

First of all, a full simulation must be performed to retrieve a training dataset composed of species mass fractions and mixture temperatures: $\mathbf{X} = [y_1, ..., y_N, T_h, T_e]$. As we consider an electronic specific model, two temperatures can be discerned: T_h, the temperature of the heavy species, and T_e, the temperature of the electrons. Our dataset is composed out of 36 variables for our specific argon case: 34 mass fractions and 2 temperatures. The flow speed, u, must not be taken into account during PCA.

3.1. Pre-processing

Before PCA is carried out, a pre-processing step has to be performed to remove outlier observations, and to center and scale the data. Centering allows focusing on fluctuations, while scaling is necessary to compare variables in different units and covering a very broad range of scales. Different scaling methods exist as it has been shown in previous works by Isaac [24] and Parente [21]. Table 1 shows the different scaling methods together with the corresponding scaling variable. Previous work by the authors[25] has determined the PARETO scaling method performs best for our application.

3.2. Model reduction

MG-PCA solves an eigenvalue problem om the covariance matrix of this dataset to obtain the eigenvalues, $\mathbf{L}$, and eigenvectors, $\mathbf{A}$ (Eq. 15). This matrix of eigenvectors can be truncated to a matrix $\mathbf{A}_q$ containing only the eigenvectors with the highest variance. When projecting the original dataset on this truncated matrix, one obtains the principal variables or principal components which correspond to the most important variables of the system as they change the most. When inverting relation 16 one can find back the original sample as shown in Eq.17

$$\mathbf{S} = \mathbf{A}\mathbf{L}\mathbf{A}^T \quad (15)$$

$$\mathbf{Z}_q = \mathbf{X}\mathbf{A}_q \quad (16)$$

$$\tilde{\mathbf{X}}_q = \mathbf{Z}_q \mathbf{A}_q^T \quad (17)$$

To control the error propagation during the reconstruction of the original sample, Manifold Generated PCA has been developed. The main idea is to reconstruct the non-transported variables (the non principal components), by using an optimal square and inverted subset of the eigenvector matrix $\mathbf{A}_q$, matrix $\mathbf{B}$:

$$\mathbf{B} = (\mathbf{A}_q^T)^{-1} = \mathbf{X}_q^+ \mathbf{Z}_q \quad (18)$$

In this equation $\mathbf{X}_q^+$ is the generalize inverse of $\mathbf{X}$, with $\mathbf{X}_q^+ = (\mathbf{X}_q^T \mathbf{X}_q)^{-1}$. The non-principal reconstructed variables, given by the vector $\tilde{\mathbf{X}}(Q-q)$, are reconstructed by multiplying the vector containing the principal components, $\mathbf{X}$(q), with this matrix $\mathbf{B}$ and the square subset of matrix $\mathbf{A}$(Q-q)$_q$:

$$\tilde{\mathbf{X}}(Q-q) = \mathbf{X}(q)\mathbf{B}\mathbf{A}(Q-q)_q^T \quad (19)$$

There exist different criteria to retrieve these principal variables as explained by Parente [21]. The results

Scaling technique	Abbr.	Scaling variable
Auto	*STD*	s_j (standard deviation)
Level	*LEVEL*	$\bar{x}_j$ (mean value)
Range	*RANGE*	$max(x_j) - min(x_j)$
Max	*MAX*	$max(x_j)$
PARETO	*PARETO*	$\sqrt{s_j}$
VAriable STability	*VAST*	$s_j^2/\bar{x}_j$

Table 1: Scaling techniques for MG-PCA data pre-processing.

of the comparison between the different principal variable extraction methods can be found back int Section IV. The different PV extraction methods are:

- B4 Forward method: PCA is performed on the matrix containing the original dataset. The criterion to retain the principal variables depends on $l^* = 0.7 \cdot \bar{l}$. In this expression $\bar{l}$ is the average eigenvalue size. If Q1 components have an eigenvalue less than l^*, the remaining Q-Q1 components are analysed starting with the first component.
- B2 Backward method: This method is similar to the B2 forward method. When analysing the remaining Q-Q1 eigenvalues, the criterion l^* is applied on the last component.
- M2 Backward method: PCA is performed on the original dataset, containing Q variables, to evaluate the eigenvalues of the covariance matrix. A criterion is chosen to retain q PCs scores in a matrix $\mathbf{Z}_q$. The idea is to find a matrix $\tilde{\mathbf{Z}}$ containing m variables (with $q \leq Q$) which will reproduce $\mathbf{Z}_q$ in the best way. To do so the M2 Backward method finds the subset of variables minimizing the following relation:

$$M_2 = tr(\mathbf{Z}_q^T \mathbf{Z}_q + \tilde{\mathbf{Z}}^T \tilde{\mathbf{Z}} - 2\sum) \tag{20}$$

  In this expression $\sum$ is the matrix of singular values from the singular values form the singular value decomposition of $\tilde{\mathbf{Z}}^T \mathbf{Z}_q$
- Mc Cabe criterion: McCabe proposes 3 criteria to select the principal variables. These criteria are based on the fact principal components satisfy some optimal criteria. A subset of the original variables that optimizes one of these criteria is selected as a set of McCabe principal variables.

If $\mathbf{X}(1)$ and $\mathbf{X}(2)$ are subsets of the set of variables $\mathbf{X}$ and the covariance matrix $\mathbf{S}$ can be decomposed as:

$$\mathbf{S} = \begin{bmatrix} \mathbf{S}_{11} & \mathbf{S}_{12} \\ \mathbf{S}_{21} & \mathbf{S}_{22} \end{bmatrix} \tag{21}$$

One can define the partial covariance matrix:

$$\mathbf{S}_{22,1} = \mathbf{S}_{22} - \mathbf{S}_{21}\mathbf{S}_{11}^{-1}\mathbf{S}_{12} \tag{22}$$

which appears in the 3 selection criteria together with its eigenvalues δ_k:

$$MC1 = max|\mathbf{S}_{11}| = min|\mathbf{S}_{22,1}| = min\prod_{k=1}^{m}(2\delta_k) \tag{23}$$

$$MC2 = min|tr(\mathbf{S}_{22,1})| = min\prod_{k=1}^{m}\delta_k \tag{24}$$

$$MC3 = min|\mathbf{S}_{22,1}|^2 = min\prod_{k=1}^{m}\delta_k^2 \tag{25}$$

3.3. MG-local-PCA

There exist two formulations of the MG-PCA method. Up to now we only described the global formulation of the method, i.e. MG-PCA has been applied to the entire dataset. Another approach is to divide the dataset in several bins or clusters, and to apply the reduction technique locally on each of them. This technique is called MG-local-PCA. Consequently a better reduction will be obtained as each bin has its optimized base. The same principal variables are transported from one cluster to another to minimize the number of equations to be solved, and to avoid numerical issues at the cluster borders. To define the clusters a conditioning variable, such as the mixture temperature for example, is used. This conditioning variable should well characterize the state-space. During *a priori* model evaluation, different variables will be tested for clustering. Candidates are

the temperatures, species mass fractions, and the variable source terms. This local formulation of MG-PCA has already been tested on combustion cases as investigated by Isaac [24] and Coussement [23]. In the work of Coussement [26], MG-local-PCA has successfully been applied on DNS simulations of flame vortex interactions.

3.4. Clustering algorithms for MG-local-PCA

Local MG-PCA divides the data in clusters and applies the reduction technique in each of them. Good clustering of the data is essential for making the reduced model work. The same principal variables are transported in each cluster to ensure continuity at the borders, and to limit the number of governing equations. Parente et al. [27] have developed a clustering algorithm based on the behavior of a monotonic increasing variable. An example of such a variable is the mixture temperature, or a species mass fraction. In this algorithm, the number of principal variables is chosen beforehand, and the number of clusters is consequently being determined to ensure the smallest reconstruction error.

A different approach is considered in the present work. Contrary to the method of Parente[27], a combination of various conditioning variables is used for determining the clusters: the electron temperature and the source terms. Choosing the electron temperature is a logical choice as it does well represent the chemistry occurring after the shock. The shock relaxation zone can be divided in 5 distinct regions according to the electron temperature as shown in Figure 3. The cluster borders are chosen at the extrema of the electron temperature as shown in Figure 2.

- **Zone 1:** Production of priming cold electrons through ionization by heavy-particle impact, $Ar(i) + Ar(1) \rightleftharpoons Ar^+ + e^- + Ar(1)$.
- **Zone 2:** Once enough priming electrons are produced, Ar atoms start undergo ionization through electron impact reactions, $Ar(i)+e^- \rightleftharpoons Ar^+ + e^- + e^-$. Starting from this zone, electron impact processes become dominant over those induced by heavy-particle collisions.
- **Zone 3:** The free-electron temperature slowly rises to due to the combined effects of elastic collisions with heavy-particles (which tend to heat up the electron gas), and inelastic and ionizing collisions (which tend to deplete the energy content of free-electrons).

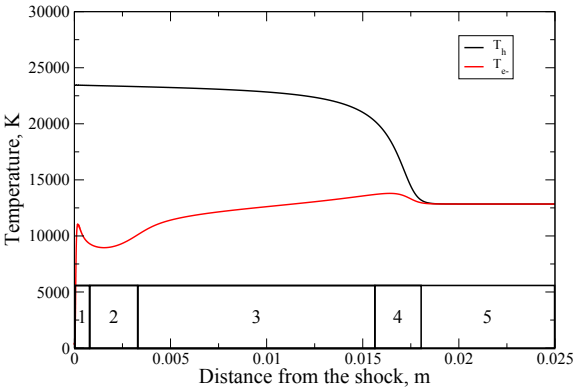

Figure 3: Detailing the shock structure in 5 zones according to the electron temperature. Pre-shock conditions: Ma= 15.9, T=293.6 K, p=685.3 Pa. (red: electron temperature, black: heavy species temperature)

- **Zone 4:** Electron avalanche. The ionization of Ar by electron impact continues and stimulates the further productions of free-electrons. This leads to an avalanche behavior which is finally balanced by three-body recombination of Ar^+ ions.
- **Zone 5:** Thermal equilibrium between heavy-particles and free-electrons. In this zone, the plasma can be described by one single temperature. This temperature keeps decreasing because of the radiative transitions within the plasma.

The source terms are also excellent candidates for determining clusters. They have been plotted against the post-shock distance x, the heavy species temperature T_h, and the electron temperature T_{e-} for a detailed analysis. Most of the species have a similar behavior and thus a similar source term. In Figure 1 we plotted two source terms in function of x and T_h respectively. The extrema of those function have again been used for determining the cluster borders. Figure 2 shows the cluster borders in function of the electron temperature evolution. One can notice the clustering of the data corresponds well to the chemistry explained in the previous paragraph.

4. Results

The data has been clustered according to the source terms and the electron temperature as explained previously. An addition cluster border has been defined at thermal equilibrium where both the electron and

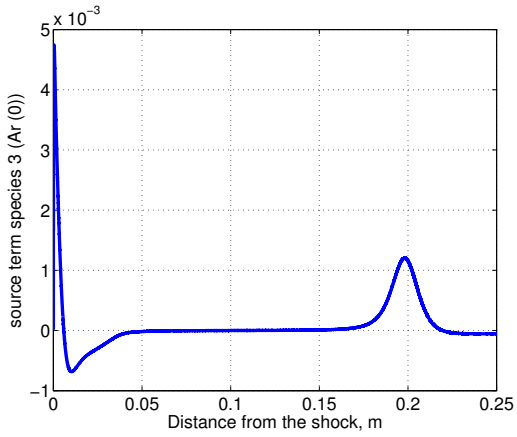

(a) Sourceterm for Ar(0).

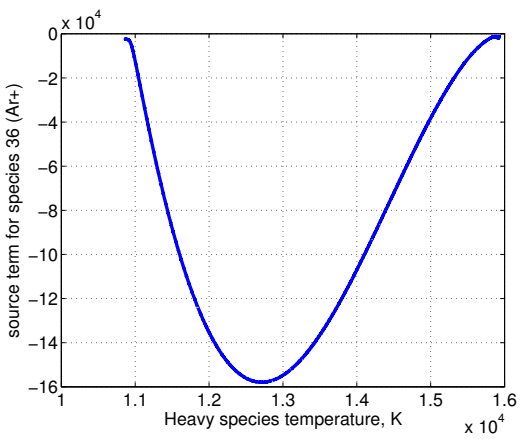

(b) Sourceterm for Ar^+

Figure 1: Clustering based on the extrema of the source terms

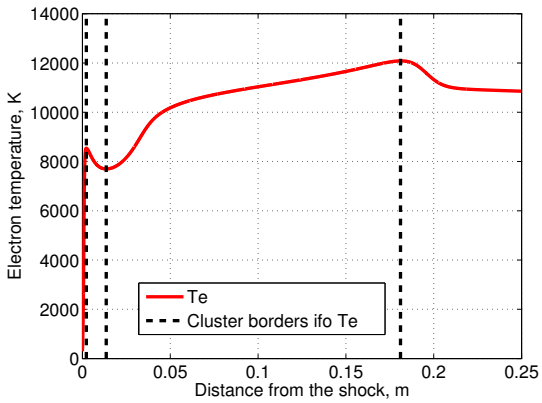

(a) Clustering on electron temperature

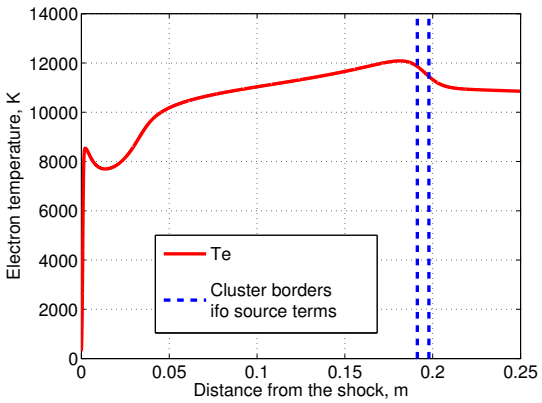

(b) Clustering on sourceterms

Figure 2: Clustering algorithm based on extrema of T_{e-} and the sourceterms

heavy species temperatures meet. In the end a system with 6 separate clusters is obtained. MG-local-PCA works well up to 18 retained variables out of 34. This results in a model reduction of 47 %. Table 2 shows the retained principal components during the PCA analysis. It's important to notice the electrons are being neglected and are thus not important as a variable for the reduction. This is not intuitive as ionization reactions are imporant reactions and produce a lot of electrons during the relaxation process.

The temperature evolution during the shock relaxation is shown in Figure 4a for the full model (full lines) and the reduced PCA model (dotted lines). Figure 4b shows the population distribution in function of the energy of each excited state. The depopulation of the higher lying states is clearly visible with the reduced model. There can be concluded the reduced PCA model is able to retrieve detailed chemistry information.

5. Conclusion

Some important goals have already been achieved during this PhD project. We were able to demonstrate the applicability of the PCA reduction techniques developed for combustion applications to plasma. Manifold Generated Principal Component Analysis (MG-PCA) has successfully been applied on a 34 species argon reacting system. The technique has proven its ability to retrieve detailed chemistry

Method	var	Retained principal components (PC's)
local	18/34	2 3 4 5 6 7 8 11 13 16 17 18 20 21 22 24 33 34

Table 2: Retained principal components after local MG-PCA. Principal components: 1= y_{e-}, 2= $y_{Ar(0)}$, 32= $y_{Ar(31)}$, 33=$y_{Ar^+(1)}$, 34=$y_{Ar^+(2)}$

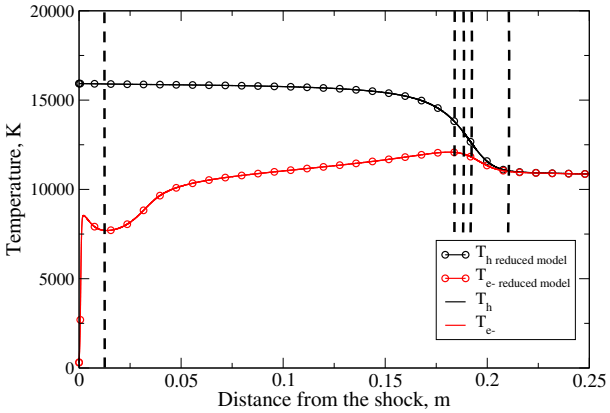

(a) Local MG-PCA. Clusters: 6.

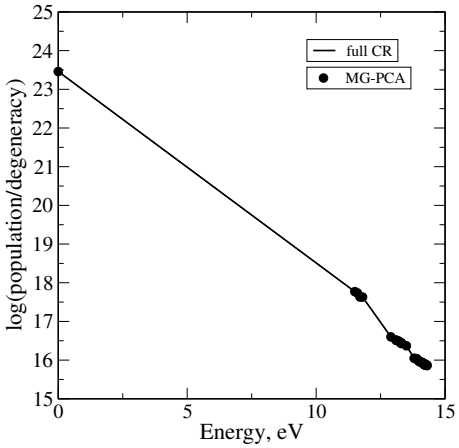

(b) Population/degeneracy in function of the energy levels for the 31 excited states of argon.

Figure 4: Local MG-PCA Principal variable extraction method: B2 Backward Method. Scaling: PARETO.

features such as temperatures, concentrations, and the depopulation of the excited argon states. The Local MG-PCA technique has also been optimized by adding an automatic clustering algorithm using the electron temperature and source terms for determining bins. Using this new clustering algorithm we were able to retrieve a model reduction of 47% when using re-entry free-stream conditions in the simulation.

6. Future work

Future work will focus on the comparison of the PCA techniques with other reduction methods. A modified multi-temperature model is being developed regrouping all excited states as one species. This will lead to a very simplified model which transforms the 34-species model in a 4-species model. An additional temperature will be considered for the excited states and will be solved separately. Future investigations will determine if PCA is still competitive with other reduction approaches.

Acknowledgments

The research of A. Bellemans, is sponsored by the Belgian FRIA-FNRS grant. The authors wish to acknowledge the European Research Council, Starting Grant No. 259354 , for the research of Prof. T.E. Magin.

References

[1] J. Kim, S. B. Pope, Effects of combined dimension reduction and tabulation on the simulations of a turbulent premixed flame using a large-eddy simulation/probability density funcion method, Combustion Theory and Modelling 18 (3) (2014) 388–413.

[2] S. B. Pope, The computation of constrained and unconstrained equilibrium compositions of ideal gas mixtures using gibbs function continuation, FDA 03-02.

[3] Z. Ren, S. B. Pope, A. Vladimirsky, J. M. Guckenheimer, The invariant constrained equilibrium edge preimage curve method for the dimension reduction of chemical kinetics, The Journal of Chemical Physics 124 (2006) 114111.

[4] J. C. Keck, Rate-controlled constrained equilibrium theory of chemical reactions, AIP Conf. Proc. 1033 (2008) 329 – 334. doi:http://dx.doi.org/10.1063/1.2979054.

[5] J. C. Keck, Rate-controlled constrained equilibrium theory of chemical reactions in complex systems, Prog. Energy Combust. Sci. 16 (1990) 125–154.

[6] M. Massot, Singular perturbation analysis for the reduction of complex chemistry in gaseous mixtures using the entropic structure, Comptes Rendus Mathematique 335 (1) (2002) 93 – 98.
[7] T. Magin, M. Panesi, A. Bourdon, R. Jaffe, D. W. Schwenke, Coarse-graining model for internal energy excitation and dissociation of molecular nitrogen, Chem. Phys. 398 (90) (2012) 90 – 95.
[8] A. Munafò, M. Panesi, T. E. Magin, Boltzmann rovibrational collisional coarse-grained model for internal energy excitation and dissociation in hypersonic flows, Phys. Rev. E 89 (2) (2014) 023001.
[9] A. Munafò, T. E. Magin, Modeling of stagnation-line nonequilibrium flows by means of quantum based collisional models, Phys. Fluids 26 (9) (2014) 097102.
[10] Y. Liu, M. Vinokur, M. Panesi, T. E. Magin, A multi-group maximum entropy model for thermo-chemical nonequilibrium, AIAA Paper 2010–4332, 10th AIAA/ASME Joint Thermophysics and Heat Transfer Conference, Chicago, IL (2010).
[11] Y. Liu, M. Panesi, M. Vinokur, P. Clarke, Microscopic simulation and macroscopic modeling of thermal and chemical non-equilibrium gases, AIAA Paper 2013–3146, 44th AIAA Thermophysics Conference, San Diego, CA (2013).
[12] M. Panesi, A. Lani, Collisional radiative coarse-grain model for ionization in air, Phys. Fluids 25 (5) (2013) 057101.
[13] A. Bultel, B. G. Chéron, A. Bourdon, O. Motapon, I. F. Schneider, Collisional-radiative model in air for earth re-entry problems, Phys. Plasmas 13 (4) (2006) 043502.
[14] M. Panesi, T. E. Magin, A. Bourdon, A. Bultel, O. Chazot, Fire II flight experiment analysis by means of a collisional-radiative model, J. Thermophys. Heat Transfer 23 (2) (2009) 236–248.
[15] M. Panesi, T. E. Magin, A. Bourdon, A. Bultel, O. Chazot, Electronic excitation of atoms and molecules for the FIRE II flight experiment, J. Thermophys. Heat Transfer 25 (3) (2011) 361–374.
[16] A. Munafò, A. Lani, A. Bultel, M. Panesi, Modeling of non-equilibrium phenomena in expanding flows by means of a collisional-radiative model, Phys. Plasmas 20 (7) (2013) 073501.
[17] H. P. Le, A. R. Karagozian, J. L. Cambie, Complexity reduction of collisional-radiative kinetics for atomic plasma, Phys. Plasmas 20 (12) (2013) 123304.
[18] A. Guy, A. Bourdon, M.-Y. Perrin, Consistent multi-internal-temperatures models for nonequilibrium nozzle flows, Chem. Phys. 420 (2013) 15–24.
[19] M. G. Kapper, Ionizing shocks in argon. part 2: Transient and multi-dimensional effects, J. Appl. Phys. 109 (11) (2011) 113309.
[20] J. Vlcek, A collisional-radiative model applicable to argon discharges over a wide range of conditions. i: Formulation and basic data, J. Phys. D 22 (1989) 623–631.
[21] A. Parente, J. Sutherland, Prinicpal component analysis of turbulent combustion data: Data pre-processing and manifold sensitivity, Combustion and Flame 160 (2) (2013) 340–350.
[22] B. Isaac, Reduced-order modelling for reacting flows based on principal component analysis, Ph.D. thesis, University of Utah (2014s).
[23] A. Coussement, A. Parente, O. Gicquel, Mg-local-pca method fo reduced order combustion modeling, Proceedings of the Combustion Institute 34 (1) (2013) 1117–1123.
[24] B. Isaac, A. Coussement, O. Gicquel, P. J. Smith, A. Parente, Reduced-order pca models for chemical reacting flows, Combustion and Flame 161 (11) (2014) 2785 – 2800.
[25] A. Bellemans, A. Munafò, T. Magin, A. Parente, G. Degrez, Developement of reduced chemistry models for high enthalpy and plasma flows, in: AIAA Aviation Conference, Atlanta, USA, 2014.
[26] A. Coussement, O. Gicquel, A. Parente, Kernel density weighted principal component analysis of combustion processes, Combustion and Flame 159 (9) (2012) 2844 – 2855.
[27] A. Parente, J. C. Sutherland, L. Tognotti, P. J. Smith, Identification of low-dimensional manifolds in turbulent flames, Proc. Combust. Inst. 32 (1).

Rebuilding freestream atmospheric conditions using surface pressure and heat flux data

Andrea F. Cortesi

CARDAMOM Team, INRIA Bordeaux Sud-Ouest, France, andrea.cortesi@inria.fr

Supervisor: Thierry E. Magin

Associate Professor, Aeronautics and Aerospace Department, von Karman Institute for Fluid Dynamics, Belgium, magin@vki.ac.be

University Supervisor: Pietro M. Congedo

Research Scientist, CARDAMOM Team, INRIA Bordeaux Sud-Ouest, France, pietro.congedo@inria.fr

Abstract

This paper proposes a technique for the reconstruction of freestream atmospheric quantities from entry measurements of both pressure and heat flux in the vehicle forebody surface. The proposed approach is able to give both freestream mean values and uncertainty bounds that take into account measurements errors as well as uncertainties in the flow model parameters. It exploits pressure and heat flux measurements given by Flush Air Data Systems at the stagnation point of the entry vehicle. This expensive Bayesian reconstruction algorithm is accelerated by a surrogate model for the quantities of interest, namely pressure and heat flux at the stagnation point. An application to the entry trajectory of the EXPERT space vehicle is discussed.

Keywords: Atmospheric Reentry Flows, Freestream rebuilding, Surrogate Modeling, Uncertainty Quantification, Inverse Problems, Bayesian Inference

1. Introduction

The design of the entry system of a space vehicle requires accurate predictions of atmospheric conditions and vehicle aerothermodynamics. Since the variability of atmospheric conditions has important implications for EDL (Entry, Descent and Landing) mission design and performance, post-flight reconstruction is essential. Accurately replicating entry conditions in ground test facilities is notoriously difficult and the lack of knowledge about atmospheric models affects also computational fluid dynamics (CFD) simulations, since they need proper boundary conditions to give reliable predictions. Therefore in-flight measurements must be fully exploited to gain knowledge on both the vehicle response to the planetary environment and the atmospheric flight conditions, which must be reconstructed accurately to validate or improve ground predictions, reducing their uncertainty bounds.

The problem of accurately rebuilding atmospheric conditions upstream the shock starting from surface measurements is an inverse problem that requires accurate but sometimes costly methods to be solved. One classical reconstruction technique is based on linear accelerations and angular rotation measured by the Inertial Measurement Unit (IMU), which is part of the standard instrumentation on entry vehicles. However, while such flight data are ideally suited for the entry trajectory reconstruction (4), they may not suffice to accurately characterize the atmospheric environment (22), since the do not include any direct information about the flow around the capsule.

On some vehicles a Flush Air Data System (FADS) is also available, consisting of pressure taps and thermal sensors integrated into the thermal protection system (TPS). Normally FADS measurements consist of pressure and heat flux data at several points of the vehicle heat shield. This system is able to provide measurements that are complementary to those given by IMU, since they contain information about the flow and the atmospheric environment to which the vehicle surface is exposed. Van Hove and Karatekin (23)

described a methodology for reconstructing the atmospheric flight environment using both IMU measurements and FADS pressure data. It relies on approximate analytical relations for the stagnation pressure and includes modifications to include high-temperature effects (chemical reactions). Uncertainties can be estimated using a Monte Carlo approach. Other freestream reconstruction techniques that use surface pressure measurements can be found in literature, such as in Refs. (24; 16; 10; 8; 5). Predictions of the pressure flight data, required to solve the inverse problem required to reconstruct atmospheric freestream conditions, have been obtained from wind tunnel testing and/or flow modeling. However, heat flux is more challenging to predict and its measurements are normally associated with higher errors. For these reasons heat flux measurements have not been used for atmospheric reconstruction.

In a recent work, Tryoen et al.(21) proposed a novel strategy for rebuilding freestream conditions starting from both stagnation pressure and heat flux measures, trying in this way to exploit all the information given by the FADS. They applied the technique to one point of the entry trajectory of the European Experimental Reentry Test-Bed (EXPERT) vehicle. This method is based on Bayesian inference (9), which is an approach capable of exploiting the results of complex forward Computational Fluid Dynamics (CFD) simulations and Uncertainty Quantification (UQ) to reconstruct the freestream conditions. This approach allows to consider the complex high temperature effects of hypersonic flows, such as thermochemical non equilibrium, radiation, ablation, and catalysis, and to take into account measurement errors, uncertainties on chemical model parameters and also model uncertainties. In the context of this technique the inverse problem is solved with a statistical approach. Results are the posterior conditional probabilities of the quantities that need to be reconstructed given the measurements. The problem with Bayesian inference is that the Markov Chain Monte Carlo algorithm used to sample the posterior distribution of the rebuilt parameters requires several evaluations of the forward problem, which can be prohibitive from a computational point of view in the case of expensive CFD computations. They used the polynomial chaos (PC) expansion(11; 2) as a metamodel to accelerate the resolution of the Bayesian inverse problem. In particular, they have shown that the PC response surface computed with a non intrusive spectral projection approach was not sufficiently accurate for the stagnation heat flux, featuring also non-physical negative solutions. Hence they were not able to provide solutions of the inverse problem by exploiting also heat flux informations.

The objective of this work is to improve the methodology proposed in Ref. (21) in order to be able of truly exploiting also the information about the heat flux for the freestream characterization.

2. Formulation of the Bayesian inverse problem for rebuilding the freestream conditions

Let us consider to rebuild unknown freestream pressure and Mach number $\boldsymbol{m} = \{p_\infty, M_\infty\}$ starting from experimental (*i.e.* noisy) measurements given by pressure and heat flux sensors located at the stagnation point $\boldsymbol{d} = \{p_{st}, q_{st}\}$. Furthermore, let us consider that some parameters c in the physico-chemical model are affected by uncertainties. The Bayesian setting allows to rigorously treat inverse problems with noisy data and uncertain forward models. The output of the inverse problem in this stochastic framework is no more a single value but a probability distribution that encompasses all available information about measurements and parameters.

Uncertainties on the model parameters $\boldsymbol{c}$ are considered to be known and to be independent, hence they can be assumed to follow the distribution $p_c(\boldsymbol{c}) = p_\gamma(\gamma) \prod_{r=1}^{4} p_{k_r}(k_r)$.

Bayes rule can be used to define the posterior probability density for the freestream quantities given n measurements of the stagnation data $\{\boldsymbol{d}_1, \ldots, \boldsymbol{d}_n\}$:

$$p(\boldsymbol{m}, \boldsymbol{c}|\boldsymbol{d}_1, \ldots, \boldsymbol{d}_n) = \frac{p(\boldsymbol{d}_1, \ldots, \boldsymbol{d}_n|\boldsymbol{m}, \boldsymbol{c})\, p_m(\boldsymbol{m}) p_c(\boldsymbol{c})}{\int p(\boldsymbol{d}_1, \ldots, \boldsymbol{d}_n|\boldsymbol{m}, \boldsymbol{c})\, p_m(\boldsymbol{m}) p_c(\boldsymbol{c})\, \mathrm{d}\boldsymbol{m}\mathrm{d}\boldsymbol{c}} \tag{1}$$

The prior distribution $p_m(\boldsymbol{m})$ represents the degree of belief about possible freestream values before observing the data. These distributions are assumed to be uninformative uniform that only impose upper and lower bounds to the quantities. Measurements enter the formulation through the likelihood distribution $p(\boldsymbol{d}_1, \ldots, \boldsymbol{d}_n|\boldsymbol{m}, \boldsymbol{c})$, which is the conditioned probability of the observations given $\boldsymbol{m}$ and $\boldsymbol{c}$. Measurements can be assumed independent and affected by independent additive errors $\boldsymbol{\eta}$:

$$\boldsymbol{d}_j = \boldsymbol{f}(\boldsymbol{m}, \boldsymbol{c}) + \boldsymbol{\eta}_j \qquad j = 1, \ldots, n \tag{2}$$

In this way the likelihood distribution becomes

$$p(\boldsymbol{d}_1, \ldots, \boldsymbol{d}_n|\boldsymbol{m}, \boldsymbol{c}) = \prod_{j=1}^{n} p_{d_j}(\boldsymbol{d}_j|\boldsymbol{m}, \boldsymbol{c}) = \prod_{j=1}^{n} p_{\eta_j}(\boldsymbol{d}_j - \boldsymbol{f}(\boldsymbol{m}, \boldsymbol{c})) \tag{3}$$

This equation shows that evaluations of the computationally costly forward CFD model are involved in the solution of the inverse problem through the likelihood. This could lead to a prohibitive computational effort to obtain the inverse solution, since, as it will be shown later, the algorithm to sample from the posterior probability requires several evaluations of the likelihood. Hence a cheap surrogate model (or metamodel) $\hat{f}$, described in Section 2.2, can be usefully used to replace the expensive forward CFD evaluation. Since the employment of a metamodel to accelerate the inverse problem resolution introduces a further source of discrepancy between predictions and measurements, it should be taken into account in the likelihood distribution to improve the accuracy and the conservativeness of the posterior distribution. A straightforward way of doing it is by adding a second independent error term in the expression of the observed data

$$\boldsymbol{d}_j = \hat{\boldsymbol{f}}(\boldsymbol{m}, \boldsymbol{c}) + \boldsymbol{\eta}_j + \boldsymbol{\delta}_j \qquad j = 1, \dots, n \tag{4}$$

Considering p_{st} and q_{st} as independent, it is common to assume that errors are realizations of a Gaussian random variable $\boldsymbol{\eta}_j \sim \mathcal{N}(0, \Gamma)$, where $\Gamma = \mathrm{diag}(\sigma^2_{p_{st}}, \sigma^2_{q_{st}})$, with $\sigma_{p_{st}}$ and $\sigma_{p_{st}}$ representing measurement errors. The same model can be adopted for metamodeling errors, thus leading to $\boldsymbol{\delta}_j \sim \mathcal{N}(0, G)$, where $G = \mathrm{diag}(\mathrm{CV}^2_{p_{st}}, \mathrm{CV}^2_{q_{st}})$ includes global cross validation error estimates (see Sec. 2.2.1). In this case the likelihood distribution becomes

$$p(\boldsymbol{d}_1, \dots, \boldsymbol{d}_n | \boldsymbol{m}, \boldsymbol{c}) = \prod_{j=1}^{n} p_{\eta_j + \delta_j}(\boldsymbol{d}_j - \hat{\boldsymbol{f}}(\boldsymbol{m}, \boldsymbol{c})) \tag{5}$$

where $p_{\eta_j+\delta_j}$ is the Gaussian probability density of the sum of measurement and metamodeling errors:

$$\boldsymbol{\eta}_j + \boldsymbol{\delta}_j \sim \mathcal{N}(0, \Gamma) + \mathcal{N}(0, G) = \mathcal{N}(0, \Gamma + G) \tag{6}$$

2.1. Sampling the posterior distribution

As already mentioned, the result of Bayesian inference is not a single value for the solution, but a posterior probability distribution that encompasses all the informations about the prior distributions, parameters uncertainties and measurement errors. In order to compute means, moments and other statistical indicators of the posterior, often the only possible way is by drawing samples. The expression obtained for the posterior distribution in Eq. 1 is difficult to be evaluated, since the integral constituting the normalization constant is not easily computable, thus it is normally assumed to start from the normalized posterior

$$p(\boldsymbol{m}, \boldsymbol{c} | \boldsymbol{d}_1, \dots, \boldsymbol{d}_n) \propto p(\boldsymbol{d}_1, \dots, \boldsymbol{d}_n | \boldsymbol{m}, \boldsymbol{c})\, p_m(\boldsymbol{m}) p_c(\boldsymbol{c}) \tag{7}$$

Then the marginal distribution of the freestream conditions given the measures can be obtained as

$$p(\boldsymbol{m} | \boldsymbol{d}_1, \dots, \boldsymbol{d}_n) \propto \int p(\boldsymbol{m}, \boldsymbol{c} | \boldsymbol{d}_1, \dots, \boldsymbol{d}_n) d\boldsymbol{c} \tag{8}$$

Markov Chain Monte Carlo (MCMC) (6) is a class of methods used to draw samples from probability distributions. In this work the Metropolis-Hastings algorithm with single-site updating and Gaussian proposal density has been used to draw samples from the normalized posterior distribution. The following algorithm has been used.

1. Initialize the chain state $\boldsymbol{m}^{k=0} = \{\mu(p_\infty), \mu(M_\infty)\}$ and $\boldsymbol{c}^{k=0} = \{\mu(c_i)\}$
2. For each random variable x_i, with $\boldsymbol{x} = \{\boldsymbol{m}, \boldsymbol{c}\}$, generate $\boldsymbol{x}^{k,i}_{-i}$ and a candidate $\tilde{x}_i$ and call $\tilde{\boldsymbol{x}}^{k,i} = \{\boldsymbol{x}^{k,i}_{-i}, \tilde{x}_i\}$
3. Evaluate the acceptance rate

$$\alpha(\boldsymbol{x}^{k-1}, \tilde{\boldsymbol{x}}^{k,i}) = \min\left\{1, \frac{p(\boldsymbol{d}_1, \dots, \boldsymbol{d}_n | \tilde{\boldsymbol{x}}^{k,i}) p_x(\tilde{\boldsymbol{x}}^{k,i}))}{p(\boldsymbol{d}_1, \dots, \boldsymbol{d}_n | \boldsymbol{x}^{k-1}) p_x(\boldsymbol{x}^{k-1}))}\right\} \tag{9}$$

4. Generate $u^{k,i} \sim \mathcal{U}(0, 1)$ and perform the acceptance test: if $u^{k,i} < \alpha(\boldsymbol{x}^{k-1}, \tilde{\boldsymbol{x}}^{k,i})$ then $x^k_i = \tilde{x}_i$, else $x^k_i = x^{k-1}_i$.
5. $k = k + 1$ and go to step 2, while $k < N_{MCMC}$

This algorithm produces a Markov Chain that converges to a stationary distribution that coincides with the posterior distribution, independently of the initial state. Means and variances of the rebuilt quantities can be estimated in the usual way, remembering to neglect the first b iterations of the chain, where b is usually called *burn-in* time.

$$\mu(m_i) = \frac{1}{N_{MCMC} - b} \sum_{k=b+1}^{N_{MCMC}} m^k_i \tag{10}$$

$$\sigma^2(m_i) = \frac{1}{N_{MCMC} - b - 1} \sum_{k=b+1}^{N_{MCMC}} (m^k_i - \mu(m_i))^2 \tag{11}$$

Finally the marginal distributions of $\boldsymbol{m} = \{p_\infty, M_\infty\}$ can be estimated by kernel density estimation from the MCMC sample.

2.2. Kriging surrogate model

Kriging interpolation(14; 20; 3) is a well-known technique for building a surrogate model for a function of interest. The main idea of Kriging method is to consider the function of interest as a realization of a stationary Gaussian stochastic process $F(\boldsymbol{x})$.

$$F(\boldsymbol{x}) = \mathcal{N}(\mu_k(\boldsymbol{x}), s_k(\boldsymbol{x})) \tag{12}$$

In universal Kriging, the stochastic process can be written in the form of the sum of a deterministic regression model and a stochastic departure term

$$F(\boldsymbol{x}) = \sum_{j=1}^{n} \beta_j y_j(\boldsymbol{x}) + Z(\boldsymbol{x}) \tag{13}$$

where $y_j(\boldsymbol{x})$ are linearly independent known functions, β_j are unknown weights, and $Z(\boldsymbol{x})$ is a Gaussian process with zero mean and covariance $k(\boldsymbol{u}, \boldsymbol{v})$. The departure term is assumed to be correlated as a function of the distance between different points, using for example a Gaussian, exponential or Matèrn correlation function (19). The parameters of the correlation function, such as the variance σ and the correlation lengths $\boldsymbol{l} = \{l_j\}_{j=1}^{N}$, called *hyperparameters*, can be estimated by using the maximum likelihood method, and enter as known parameter in the construction of the Kriging surface.

The aim of the method is to build an interpolation of the function of interest in the form

$$\hat{f}(\boldsymbol{x}) = \sum_{i=1}^{N_s} f(\boldsymbol{x}_i)\lambda_i(\boldsymbol{x}) \tag{14}$$

where $\boldsymbol{f}_{obs} = (f(\boldsymbol{x}_1), \ldots, f(\boldsymbol{x}_{N_s}))^T$ are the observation of the function at the N_s training points and $\lambda_i(\boldsymbol{x})$ are unknown weights. This can be done by computing the best unbiased linear predictor, which is obtained by minimizing the mean square error between the model and the predictor $MSE = E[F(\boldsymbol{x}) - \hat{f}(\boldsymbol{x})]^2$ under the constraint of unbiasedness $E[F(\boldsymbol{x})] = E[\hat{f}(\boldsymbol{x})]$. By solving this minimization problem, it is possible to obtain the mean of the stochastic process, which interpolates the observations of the real functions, and that can be used as a metamodel for the original function

$$\hat{f}(\boldsymbol{x}) = \mu_k(\boldsymbol{x}) = \boldsymbol{y}^T(\boldsymbol{x})\boldsymbol{\beta} + \boldsymbol{c}(\boldsymbol{x})^T C^{-1}(\boldsymbol{f}_{obs} - Y^T\boldsymbol{\beta}) \quad \text{with} \quad \boldsymbol{\beta} = (Y^T C^{-1} Y)^{-1} Y^T C^{-1} \boldsymbol{f}_{obs} \tag{15}$$

where $\boldsymbol{y}(\boldsymbol{x}) = (y_1(\boldsymbol{x}), \ldots, y_n(\boldsymbol{x}))^T$ is the vector of basis functions, Y is a matrix whose elements are the evaluation of the i-th basis function at the j-th training point $Y_{ij} = y_i(\boldsymbol{x}_j)$, $\boldsymbol{c}(\boldsymbol{x})$ is the vector of correlations between the point $\boldsymbol{x}$ and each training point and C is the matrix of correlations among training points.

Often, in practical applications where there is a lack of proper *a priori* knowledge about the evolution of the quantity of interest, it can be difficult to determine relevant basis functions for the regression term in Equation 13. Hence the simpler model called *ordinary Kriging* is used, in which $y_1(\boldsymbol{x}) = 1$ and $y_j(\boldsymbol{x}) = 0$ for $j \neq 1$, hence only β_1 needs to be determined. In this work the implementation of Kriging method included in the ForK library (13) has been used.

2.2.1. Metamodeling error estimation

In literature there can be found many error measures to assess the quality of a surrogate model. One of the most popular among these methods is *leave-one-out* generalized cross-validation (15; 7) (CV). It consists in fitting the Kriging surrogate model on $N_s - 1$ points, by leaving out one training point at a time, then the response is predicted at this point with the metamodel. Then the CV error can be defined as

$$\mathrm{CV} = \sqrt{\frac{1}{N_s}\sum_{i=1}^{N_s}\left(f_i - \hat{f}_i^{(-i)}\right)^2} \tag{16}$$

where f_i is the training point observed response, while $\hat{f}_i^{(-i)}$ is the prediction at the left-out point using the surrogate built from all the other points. The CV error can be used to estimate the actual root mean squared error of the approximation. Although being relatively expensive for Kriging, this error estimate is supposed to perform quite accurately.

3. Application to EXPERT reentry

The physical context concerned in this work is the hypersonic high-temperature reacting aerodynamic flow that invests the nose of the EXPERT space vehicle during its reentry trajectory in Earth atmosphere. The deterministic CFD forward problem consists in computing the quantities of interest, which are the quantities measured by the flush air-data system (FADS), namely the pressure p_{st} and the heat flux q_{st} at the stagnation point. In this work two different points in the entry trajectory of the vehicle are investigated. For each point, nominal freestream conditions are described in table 1. The point at higher altitudes is known to exhibit chemical non-equilibrium effects, while in the lower part of the trajectory the chemistry tends to go towards the equilibrium.

Altitude, Km	T_∞, K	p_∞, Pa	M_∞
60	245.5	20.3	15.5
30	220.0	1200	12.3

Table 1: Freestream conditions for two points of the trajectory of the EXPERT vehicle.

The set of equations used to describe the phenomena is a combined physico-chemical model, developed by Barbante (1), able to simulate hypersonic high-temperature reacting flows. Two-dimensional axisymmetric Navier-Stokes equations, supplied with adequate boundary conditions, are combined with the chemical mechanism introduced by Park et al. (18) applied to a mixture of five species air (N, O, NO, N_2 and O_2). Furthermore, the catalyticity of the vehicle surface is taken into account, and it is modeled as a catalytic wall at radiative equilibrium. Hence the input parameters for the forward CFD code freestream pressure and Mach number (p_∞ and M_∞), the catalytic recombination coefficient γ and the reaction rate coefficients k_r of the r chemical reactions. To simulate the forward problem, we use the COSMIC code developed by Barbante (1). This solver was designed to approximate hypersonic flow models where chemical non-equilibrium effects need to be accounted for. It includes a hybrid upwind splitting scheme, the hybridization of the van Leer scheme (12) and the Osher scheme (17) and includes a carbuncle fix. An axisymmetric condition is imposed on the symmetry axis, while the wall of the body is modeled by a partially catalytic wall at radiative equilibrium.

Concerning uncertainty characterization, uncertainties are associated to the freestream conditions and some parameters of the chemical model (globally seven uncertain parameters). In particular, the unknown freestream quantities p_∞ and M_∞ are assumed to follow uninformative uniform prior distributions, and uniform epistemic uncertainty is associated also to the catalytic recombination coefficient γ, as described in Table 2. The uncertainties on p_∞ and M_∞ are respectively of 20% and 12%. These values are chosen such that the relative deviations on the stagnation values p_{st} and q_{st} will be roughly of the order of 20%, as will be presented in section 3.1 with the results of the forward uncertainty propagation. Uncertainty is also taken into account on four reactions rates coefficients k_r of four chemical dissociation processes, and they are assumed distributed with log-normal distributions (see Table 3).

Variable	Min (neq)	Max (neq)	Min (eq)	Max (eq)
p_∞, Pa	16.3	24.3	960	1440
M_∞	13.7	17.3	10.9	13.7
γ	0.001	0.002	0.001	0.002

Table 2: Prior uniform distributions of freestream conditions and uncertainties associated to the catalytic recombination constant.

Gas reaction	Distribution of $\log_{10} k_r$	σ_r
$NO + O \rightarrow N + O + O$	Normal	0.12
$NO + N \rightarrow N + O + N$	Normal	0.12
$O_2 + N_2 \rightarrow 2O + N_2$	Normal	0.10
$O_2 + O \rightarrow 2O + O$	Normal	0.10

Table 3: Uncertainties on gas reaction rates.

When solving the inverse problem, measurement uncertainties on the pressure and heat flux at the stagnation point should also be considered. Unfortunately, since the EXPERT vehicle has not been launched to date, synthetic data are generated by perturbing mean data with an artificial noise. More details are provided in Section 3.1.

3.1. Results

In this section some results are shown, following the procedure used to compute the final mean values and uncertainty bounds of the rebuilt quantities. Firstly, suitable surrogate models must be constructed for the quantities of interest. To accomplish this goal, several CFD simulations need to be performed with different perturbed values of uncertain parameters. The set of values of uncertain parameter is called *design of experiments*, and it consists in a set of *training points* in the stochastic space of the uncertain variables to which CFD simulations associate values for the quantities of interest. For Kriging metamodels, a classical and efficient way to select the design of experiments is to use the Latin Hypercubes Sampling (LHS) technique (20). In this work, three sets of LHS training point of increasing size are take into account for each trajectory point, for sake of convergence analysis. Kriging metamodels are trained on each set for both stagnation pressure and heat flux, and the metamodel assessment is performed. Obtained values of cross-validation error measures are reported in tables 4 and 5 and are compared with the actual root mean squared error (aRMSE) (7), which is the actual global difference existing between the metamodel and the real model response. It has been computed on a LHS

plan of 3600 points. It is worth noticing that in practical applications the aRMSE value is usually not accessible due to the high computational cost involved in its computation. Results show convergence of the meta-

LHS pts.	aRMSE p_{st}	CV p_{st}	aRMSE q_{st}	CV q_{st}
120	50.578	47.712	2.392e4	2.074e4
680	14.918	15.724	1.831e4	1.721e4
3060	11.095	10.823	1.504e4	1.451e4

Table 4: Error measures for the stagnation pressure p_{st} [Pa] and the stagnation heat flux q_{st} [W/m^2] at the nonequilibrium point at 60km altitude

LHS pts.	aRMSE p_{st}	CV p_{st}	aRMSE q_{st}	CV q_{st}
120	1.9387e4	2.335e4	2.9538e5	3.455e5
680	4.4595e3	4.693e3	1.5498e5	1.576e5
3060	1.1188e3	1.133e3	7.7408e4	7.732e4

Table 5: Error measures for the stagnation pressure p_{st} [Pa] and the stagnation heat flux q_{st} [W/m^2] at the equilibrium point at 30km altitude

modeling error when increasing the number of training points for both the quantities of interest in both the considered inflow conditions. It can be noticed that errors associated to the stagnation pressure are lower with respect to the ones associated to the heat flux, due to the higher complexity of this last function. Relative global errors can be computed by dividing values in Tables 4 and 5 by mean values of the QoIs reported in Tables 6 and 7. This shows that metamodeling errors are quite low, being in the order of 5% for the heat flux and less than 1% for the pressure for both trajectory points for the LHS3060 training plan. It is also worth noticing that for this application the CV error estimation is able to predict very well the value of the actual RMSE, as can be seen in Tables 4 and 5.

Exploiting the very reduced cost of evaluating the surrogate model, a simple Monte Carlo (MC) sampling technique can be applied to the Kriging response surfaces in order to perform a forward uncertainty propagation and compute the statistics of the quantities of interest. Mean and variance of p_{st} and q_{st}, computed on a set of one million of MC points, are reported in Table 6 and 7 for the two trajectory points. Results show in general a good convergence for the mean values, especially for the stagnation pressure. Also the values of deviation can be considered at convergence, but with less accuracy. It can be notice that, as expected, the mean heat flux value is higher at 30km, since this altitude is close to the peak heating point.

		LHS120	LHS680	LHS3060
p_{st} [Pa]	μ	$6.498 \cdot 10^3$	$6.499 \cdot 10^3$	$6.499 \cdot 10^3$
	σ	$1.142 \cdot 10^3$	$1.155 \cdot 10^3$	$1.156 \cdot 10^3$
q_{st} [W/m^2]	μ	$2.877 \cdot 10^5$	$2.869 \cdot 10^5$	$2.879 \cdot 10^5$
	σ	$5.649 \cdot 10^4$	$5.898 \cdot 10^4$	$6.011 \cdot 10^4$

Table 6: Mean value and variance of the quantities of interest computed with the Kriging surrogates built on grids of different size, non-equilibrium case.

		LHS120	LHS680	LHS3060
p_{st} [Pa]	μ	$2.429 \cdot 10^5$	$2.429 \cdot 10^5$	$2.429 \cdot 10^5$
	σ	$3.082 \cdot 10^4$	$4.067 \cdot 10^4$	$4.245 \cdot 10^4$
q_{st} [W/m^2]	μ	$1.216 \cdot 10^6$	$1.219 \cdot 10^6$	$1.217 \cdot 10^6$
	σ	$2.432 \cdot 10^5$	$3.367 \cdot 10^5$	$3.748 \cdot 10^5$

Table 7: Mean value and variance of the quantities of interest computed with the Kriging surrogates built on grids of different size, equilibrium case.

Now that metamodels have been tested, it is possible to proceed with the computation of inverse problem solutions. Since flight data for the EXPERT vehicle do not exist, a set of ten artificial stagnation measurements is created, starting from the mean values of p_{st} and q_{st}, reported in table 6 and 7, and perturbing them with independent samples form a known artificial noise of standard deviation $\sigma_n = \{10\%\mu_{p_{st}}, 20\%\mu_{q_{st}}\}$.

At this point, it is possible to run the Metropolis-Hastings MCMC algorithm to draw samples from the posterior distributions of freestream quantities given the stagnation measurements. The posterior PDFs obtained with the MCMC algorithm are reported in Figure 1 and 2, respectively for the two trajectory points. Results obtained with the Kriging response surfaces built on three different experimental designs are compared. Some differences between the different PDFs are noticeable. In general it is likely that they are also due to the intrinsic randomness of the MCMC process. Probably this can affect the PDFs more than the differences between response surfaces, since metamodeling errors are quite low. However in general the three results can be considered in good convergence. In Tab 8 and 9, mean values and standard deviations associated to these PDFs are reported. It is possible to say that, based on the 10% deviation due to measurement noise on p_{st} and the 20% on q_{st}, the resulting

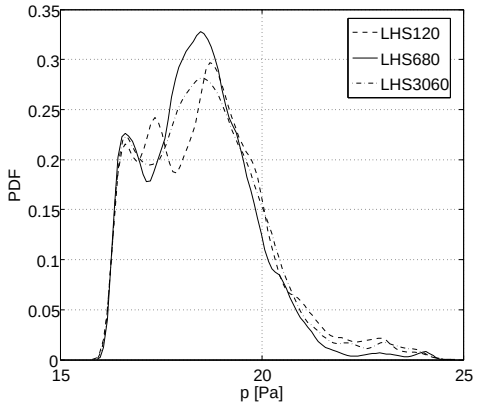

(a) Pressure

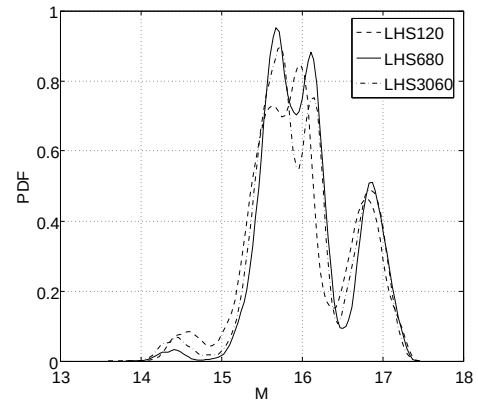

(b) Mach number

Figure 1: Posterior probability distribution functions of the freestream pressure and Mach number rebuilt with MCMC, accounting for metamodeling errors, 60km case.

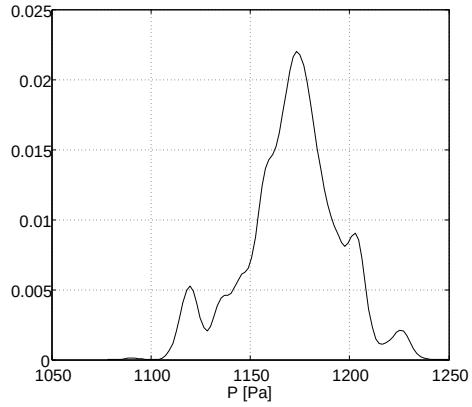

(a) Pressure

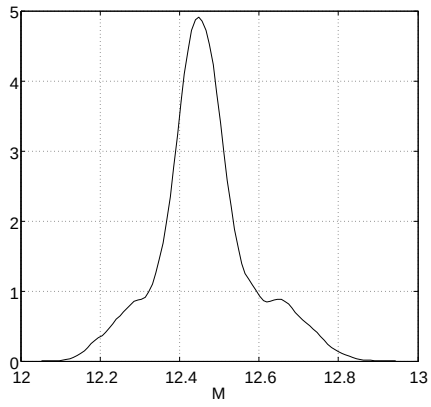

(b) Mach number

Figure 2: Posterior probability distribution functions of the freestream pressure and Mach number rebuilt with MCMC, accounting for metamodeling errors, 30km case.

1σ uncertainties on p_∞ and M_∞, computed from Table 8 and 9 , are respectively about 8% and 4% for the 60km altitude case. The 2% measurement noise on p_{st} and the 10% on q_{st} at 30km altitude lead instead to respectively 2% and 1% 1σ uncertainties on p_∞ and M_∞. In this case just results obtained with the LHS3060 metamodel are reported, because the ones obtained with less training points are affected by some small spurious oscillations that spoil the rebuilt PDFs. The uncertainty associated to the posterior estimation is lower for the Mach number, as it is about the half of the one associated to the freestream pressure. Even in these results, differences noticed while using different surrogate models are due to the combined effect of metamodel accuracies and the randomness in the convergence of the chains. Probably this second aspect should be firstly improved in order to increase the accuracy of the global result of the Bayesian inference.

The difference between PDFs obtained with classical MCMC sampling and the ones with the inclusion of the metamodeling error are not reported for brevity. In practice, comparisons show that, when accounting for the CV error estimate, the result is more conservative, showing a slightly higher probability towards the tails of the probability distribution. However, since the CV is quite low for this application, the differences are relatively small and partially lost in the numerical noise produced by the randomness of the MCMC algorithm itself.

		LHS120	LHS680	LHS3060
p_∞ [Pa]	μ	18.6524	18.4544	18.5672
	σ	1.5272	1.3034	1.4325
M_∞	μ	15.9599	16.0527	16.0198
	σ	0.62243	0.54363	0.58341

Table 8: Mean values and standard deviations of the freestream quantities rebuilt with MCMC algorithm exploiting the Kriging surrogates built on different experimental designs, 60km case.

		LHS120	LHS680	LHS3060
p_∞ [Pa]	μ	–	–	1170.97
	σ	–	–	23.5891
M_∞	μ	–	–	12.4634
	σ	–	–	0.11546

Table 9: Mean values and standard deviations of the freestream quantities rebuilt with MCMC algorithm exploiting the Kriging surrogates built on different experimental designs, 30km case.

Concerning the physical interpretation of these results, it seems that the PDFs of the rebuilt quantities feature a quite large support. This makes someway questionable how much robust and reliable the numerical prediction could be. However it has to be recalled that the relatively large variance of the rebuilt quantities includes the effects of all the uncertainties and error measurements accounted in the Bayesian inference. The importance of the analysis presented in this work seems even more important, since the assessment of the uncertainty associated to the rebuilt quantities could lead to specific investigation for trying to reduce the experimental uncertainties of the measurements at the stagnation point.

4. Conclusions and developments

This paper deals with a rebuilding methodology of the freestream pressure and Mach number of a hypersonic high-temperature reentry problem of a space vehicle, using both stagnation pressure and heat flux measurements. The use of heat flux data in the inference of freestream quantities is not a common practice in literature. An application is proposed in the context of the atmospheric entry of the EXPERT vehicle.

Prior uncertainties in the freestream values and chemical reaction rates are firstly propagated into the forward CFD problem by performing the simulations of the flow in different perturbed points in the stochastic space chosen with Latin Hypercubes Sampling. Then, this solutions at the training points are used to build ordinary Kriging interpolations of the quantities of interest. The quality of the metamodels is assessed with two different global error measures: the actual root mean squared error and a leave-one-out generalized cross validation estimation technique. Results show a convergence of the metamodeling error when increasing the size of the training set. The metamodels are firstly used to perform a Monte Carlo forward uncertainty propagation to obtain mean values and deviations of the quantities of interest in both the nominal trajectory conditions taken into account in this work.

A backward uncertainty propagation method is then proposed to solve the inverse problem by taking into account uncertainties on model parameters and measurement errors. A Bayesian framework is adopted and a Markov Chain Mont Carlo algorithm is used to sample the posterior distribution of the freestream quantities given some measurements of stagnations pressure and heat flux. The Kriging metamodel for the quantities of interest is used to accelerate the MCMC Metropolis-Hastings algorithm. A simple technique is proposed in order to take into account the metamodeling error during the inference process. When imposing some synthetic data on the pressure and the heat flux at the stagnation point, a large support of the PDF is observed on the rebuilt quantities, which shows the importance of considering uncertainties for correctly controlling the trajectory.

Future works will be oriented to the application of the proposed methods to real flight data. Moreover, the variability of the rebuilt quantities with respect to different types of measurements will be explored. An important aspect to be analyzed could be the determination of sensors accuracy needed to achieve a prescribed level of uncertainty on the rebuilt freestream quantities.

5. Acknowledgments

Andrea F. Cortesi has been supported by DGA (Direction Générale de l'Armement) from French Government.

References

[1] Barbante, P. *Accurate and efficient modelling of high temperature non-equilibrium air flows*. PhD thesis, Von Karman Institute, 2001.

[2] Congedo, P., Corre, C., and Martinez, J.-M. Shape optimization of an airfoil in a bzt flow with multiple-source uncertainties. *Computer Methods in Applied Mechanics and Engineering 200*, 1 (2011), 216–232.

[3] Cressie, N. A. C. *Statistics for spatial data*. John Wiley & Sons, 1993.

[4] Desai, P. N., Prince, J. L., Queen, E. M., Schoenenberger, M. M., Cruz, J. R., and Grover, M. R. Entry, descent and landing performance of the mars phoenix lander. *Journal of Spacecraft and Rockets 48*, 5 (2011), 798 – 808.

[5] Dutta, S., and Braun, R. D. Statistical entry, descent, and landing performance reconstruction of the mars science laboratory. *Journal of Spacecraft and Rockets 51*, 4 (2014), 1048 – 1061.

[6] Gilks, W. R., Richardson, S., and Spiegelhalter, D. J. *Markov Chain Monte Carlo in practice*. Chapman & Hall/CRC Interdisciplinary Statistics, 1996.

[7] Goel, T., Hafkta, R. T., and Shyy, W. Comparing error estimation measures for polynomial and kriging approximation of noise-free functions. *Structural and multidisciplinary optimization **38*** (2009), 429 – 442.

[8] Häuser, J., Dai, W., Koppenwallner, G., and Muylaert, J. Inverse problem solution for determining spacecraft orientation from pressure measurements. *Proceedings of the Fifth European Symposium on Aerothermodynamics for Space Vehicles ESA SP-563* (2004), 1 – 30.

[9] Kaipio, J., and Somersalo, E. *Statistical and computational inverse problems*, vol. 160 of *Applied Mathematical Sciences*. Springer, 2010.

[10] Koppenwallner, G. Controlled hypersonic flight air data system and flight instrumentation. *Flight Experiments for Hypersonic Vehicle Development, Educational Notes RTO-EN-AVT-130*, 17 (2007), 1 – 30.

[11] Le Maître, O. P., and Knio, O. M. *Spectral methods for uncertainty quantification*. Springer, 2010.

[12] Leer, B. V. Towards the ultimate conservative difference scheme. V. A second-order sequel to godunov's method. *Journal of Computational Physics 32*, 1 (1979), 101–136.

[13] Lockwood, B. A. http://w3.uwyo.edu/~blockwoo/ForKlib/index.html.

[14] Matheron, G. *The theory of regionalised variables and its applications*. PhD thesis, École Nationale Supérieure des Mines, 1971.

[15] Meckesheimer, M., Barton, R. R., Simpson, T. W., and Booker, A. Computationally inexpensive metamodel assessment strategies. *AIAA Journal **40***, 10 (2002), 2053 – 2060.

[16] Müller-Eigner, R., Koppenwallner, G., and Fritsche, B. Pressure and heat flux measurement with RAFLEX II during MIRKA re-entry. *Third European Symposium on Aerothermodynamics for Space Vehicles ESA SP-426* (1999), 685 – 694.

[17] Osher, S., and Solomon, F. Upwind Difference Schemes for Hyperbolic Systems of Conservation Laws. *Mathematics of Computation 38*, 158 (1982), 339–374.

[18] Park, C., Jaffe, R., and Partridge, H. Chemical-kinetic parameters of hyperbolic earth entry. *Journal of Thermophysics and Heat Transfer **15***, 1 (2001), 76 – 90.

[19] Picheny, V. *Improving accuracy and compensating for uncertainty in surrogate modeling*. PhD thesis, École Nationale Supérieure des Mines, 2009.

[20] Sacks, J., Welch, W. J., Mitchell, T. J., and Wynn, H. P. Design and analysis of computer experiments. *Statistical sciences **4***, 4 (1989), 409 – 435.

[21] Tryoen, J., Congedo, P. M., Abgrall, R., Villedieu, N., and Magin, T. Bayesian-based method with metamodels for re-building freestream conditions in atmospheric entry flows. *AIAA Journal **52***, 10 (2014), 2190 – 2197.

[22] Van Hove, B., and Karatekin, O. Mars entry, descent, and landing reconstruction from flight data: uncertainty quantification.

[23] Van Hove, B., and Karatekin, O. Mars atmosphere reconstruction using a flush air data system on the exomars entry, descent and landing demonstrator module. *10th International Planetary Probe Workshop* (2013).

[24] zur Nieden, P., and Olivier, H. Determination of atmospheric densities from reentry data flight data. *Journal of Spacecraft and Rockets **44***, 2 (2007), 332 – 337.

Investigations on the reproduction of planetary re-entry flights in high enthalpy and plasma wind tunnels

Ana Isabel del Val Benítez

Aeronautics and Aerospace Department, von Karman Institute for Fluid Dynamics, Belgium, ana.isabel.del.val.benitez@vki.ac.be

Supervisor: Olivier Chazot

Professor, Aeronautics and Aerospace Department, von Karman Institute for Fluid Dynamics, Belgium, olivier.chazot@vki.ac.be

University Supervisor: Gaëtan Kerschen

Professor, Aerospace and Mechanical Engineering Department, Université de Liège, Belgium, g.kerschen@ulg.ac.be

Abstract

Ground testing plays a main role in the Thermal Protection System (TPS) design. It can be carried out in high enthalpy, arcjets or Inductively-Coupled Plasma (ICP) facilities, involving different flow characteristics and regimes. The duplication of the flight conditions on ground requires the application of a dedicated extrapolation methodology known as the Local Heat Transfer Simulation (LHTS) which will be described in the following sections together with the goal of defining a testing strategy for the Hayabusa mission in the VKI Plasmatron.

Keywords: Ground testing, plasma flows, LHTS, atmospheric entry

1. Introduction

Space exploration represents one of the greatest technological and design endeavours of our time in which interplanetary manned missions to Mars and return-sample missions from asteroids are some of the challenges to be faced in the near future. One of the critical steps, in the overall mission scenario, is the particular design of the Thermal Protection System (TPS).

Thermal Protection Systems have been continuously used in aerospace vehicles since the very beginning of the Space Era. Although the use of the TPS is not a new business, the efficient design of it regarding a better understanding of all the different physical phenomena involved on this delicate part of the journey is a matter of recent study. Ground testing plays a main role in the development of efficient TPS and its understanding is essential for Space exploration. Supersonic ground testing is associated to high enthalpy levels due to high speed re-entry trajectories concerning future interplanetary missions aiming at bringing back asteroid samples to Earth and manned missions to the Moon and Mars. As the ground testing of high speed re-entry missions requires the use of high speed flows in plasma facilities, the applicability of the LHTS methodology to supersonic plasma flows in ICP facilities has to be determined in order to be able to reach higher heat flux values.

The purpose of this study is the development and assessment of a ground testing strategy extended to all types of facilities within the LHTS frame, focusing on its applicability to supersonic plasma facilities.

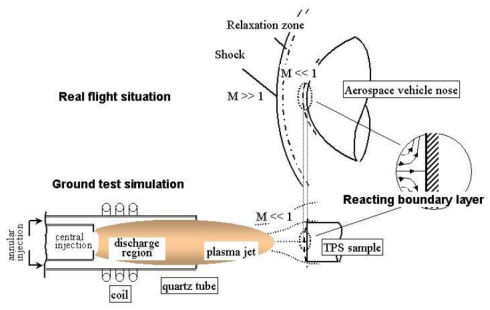

Figure 1: Application of the LHTS in subsonic regime

2. Ground testing methodology, facilities and numerical tools

To enable the study of the reproduction of re-entry flights, a ground testing methodology has to be followed together with experiments and numerical approximations to validate the ground testing strategy adopted.

2.1. LHTS methodology

The LHTS methodology is often used to identify the set of flight conditions, such as altitude, velocity and vehicle size, which allow to match the boundary layer near the stagnation point of the space vehicle to the environment the sample is exposed to during the ground test.

Lees [1] and Fay and Riddell [2] have laid down the general formulation of the boundary layer equations for the case of a dissociating gas using the usual Howarth-Mangler transformations. This general formulation reviewed by Solano [3] paved the way to the LHTS methodology presented by Kolesnikov [4]. The following expression was obtained by Fay and Riddell

$$q_w = 0.763 Pr^{-0.6} (\rho_w \mu_w)^{0.1} (\rho_e \mu_e)^{0.4} (H_e - H_w) \sqrt{\beta_e} \qquad (1)$$

and it allows to reduce the problem to the matching of three different parameters such as pressure, enthalpy and velocity gradient referred to the outer edge of the boundary layer when ordinary molecular conduction and diffusion are the only physical phenomena taken into account on the heat transfer. Goulard [5] on his studies developed an equivalent formulation implementing the effects of catalytic walls on the heat transfer considering finite recombination rates for the boundary layer chemistry which has been also studied numerically and experimentally by Bellas et al. [6] and Viladegut et al. [7], respectively.

The applicability of the LHTS methodology has been proven not only for different flow regimes(subsonic and hypersonic) found in [10] but also when other physical phenomena are implemented on the formulation as shown by Turchi et al. [8] by considering ablative material tests.

If one only consider the stagnation region, the applicability of the LHTS methodology allows to the experimental assessment of a ground testing strategy conducted at VKI Plasmatron for subsonic plasma flows (as shown in Fig. 1) by Barbante and Chazot [9]. This shows that the boundary layers profiles from the hypersonic flow are very well duplicated with the subsonic plasma flow, when matching the characteristics parameters at the edge of the boundary layer as described by the conservation and momentum equations together with a velocity gradient model:

$$h_\infty^{\mathrm{f}} + \frac{1}{2} V_\infty^{\mathrm{f2}} = H_{\mathrm{e}}^{\mathrm{t}} \qquad (2)$$

$$p_\infty^{\mathrm{f}} + \rho_\infty^{\mathrm{f}} V_2^{\mathrm{f2}} = p_{\mathrm{e}}^{\mathrm{t}} \qquad (3)$$

$$\beta_{\mathrm{e}}^{\mathrm{f}} = \beta_{\mathrm{e}}^{\mathrm{t}} \qquad (4)$$

New interplanetary trajectories associated with high speed re-entry, like the one of Hayabusa, push the LHTS applicability to its limits and supersonic plasma flows in ICP facilities become the target of our study. LTHS applicability has to be proven then for a different flow regime (supersonic flows) to achieve such high enthalpy levels on ICP facilities and arcjets.

2.2. VKI Plasmatron facility

The Plasmatron facility is a plasma wind tunnel equipped with a 160mm diameter Inductively-Coupled Plasma (ICP) torch powered by a high frequency, high power, high voltage (400kHz, 1.2MW, 2kV) generator [10]. The gas is heated by induction through a coil, this leads to high purity of the plasma flows generated due to the absence of electrodes and their associated erosion.

The ICP Plasmatron facility it is then used to reproduce the aerothermodynamic environment to which a (re)entry capsule is exposed, creating a high enthalpy and highly dissociated subsonic or supersonic gas flow.

For the particular case of supersonic operation, the working principle is the same and the flow is accelerated and expanded through a 35mm throat convergent nozzle placed at the exit of the torch. The plasma flow then reaches Mach 1 at the exit and it expands freely afterwards impinging on the surface of the test probe.

As for the measurements associated to this facility, the heat flux and the stagnation pressure can be measured by means of a copper calorimeter mounted in the center of the front face of a copper water-cooled probe and a Pitot probe, respectively. The cold wall stagnation point can be then measured by the cooling water mass flow, controlled by a calibrated rotameter and the inlet/outlet temperature difference, measured by two type-E thermocouples. The heat flux can be measured with an accuracy of ±10%. As for the stagnation pressure, a water-cooled Pitot probe is used to perform the pressure measurements, the accuracy is

of ±0.2%. The Plasmatron chamber is also equipped with an absolute pressure transducer that measures the static pressure with ± 2Pa accuracy.

2.3. *Numerical tools*

Different numerical tools are used to perform the flight-to-ground extrapolation and determine the testing conditions and the probe size needed for the Plasmatron tests. Those tools are explained below:

2.3.1. *CABARET code*

The **C**onserv**A**tion **B**alance equation code for **A**tmosphe**R**ic **E**n**T**ry, CABARET, was developed during my Master Thesis stay at VKI in 2014 [11]. It consists on a rebuilding code for free stream conditions in high enthalpy facilities such as the Plasmatron and Longshot. For doing so, a set of inputs are necessary (see Fig. 2). These inputs come from the different measurements performed in the facilities such as the heat flux and the pressure at the wall and the pressure in the reservoir, in the case of the Plasmatron, or the free stream pressure in the case of the Longshot [12].



Figure 2: Schematic view of the inputs/outputs of CABARET for Plasmatron

The details and assumptions behind the code can be found in the conference paper [11].

2.3.2. *ICP code*

The ICP code is a compressible flow solver capable of simulating plasma flows from the incompressible to the supersonic regime in the framework of the COOLFluiD platform [13]. The numerical solver allows for the simulation of expansion and shock waves, but also for low speed flows. Hence, it could be referred to as an all-speed solver [14] (see Fig. 3).

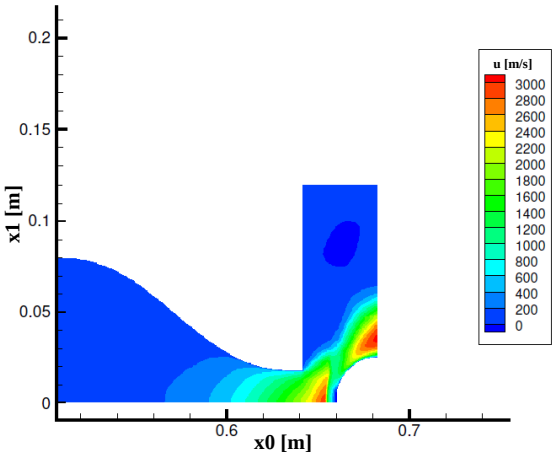

Figure 3: Velocity distribution in supersonic plasma flow in Plasmatron facility (Probe radius: 25mm, plasma power: 80kW, mass flow: 5g/s, reservoir pressure: 15550Pa, static pressure in the chamber: 1200Pa)

3. The Hayabusa mission

Hayabusa is the name of an unmanned spacecraft developed by the Japanese Aerospace Exploration Agency (JAXA) to return a sample of material from a small near-Earth asteroid named 25143 Itokawa to Earth for further analysis. Hayabusa studied the asteroid's shape, spin, topography, colour, composition, density, and history. In November 2005, it landed on the asteroid and collected samples in the form of tiny grains of asteroidal material, which were returned to Earth aboard the spacecraft on 13 June 2010.

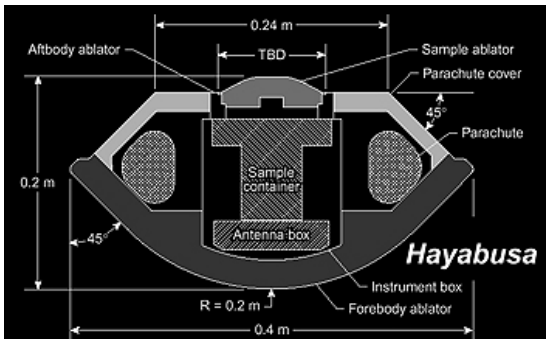

Figure 4: Hayabusa re-entry capsule

The Hayabusa re-entry in 2010 was only the second flight test of a thermal protection system (TPS) under the severe conditions of a hyperbolic re-entry, the first being Stardust in 2006. The successful observation of the Hayabusa re-entry offers a variety of real flight

data sets that allow for the analysis of ground testing as well as numerical simulation currently used as design tools for future hypersonic re-entry vehicles.

This study will be focused on one point of the re-entry trajectory, in particular:

Table 1: Hayabusa flight data

13:52:20 UTC 1s after peak heating	
Nose radius	$200mm$
Total enthalpy	$54.5MJ/kg$
Velocity	$10440m/s$
Altitude	$56.4km$
Density	$5x10^{-4}kg/m^3$
Pressure	$38Pa$
Temperature	$258K$
Mach number	32.4

For this specific point, CFD simulations of the stagnation line ahead of the capsule were carried out at VKI using the in-house stagnation line code [15] in order to obtain one of the parameters that needs to be reproduced according to the LHTS framework. This parameter is the velocity gradient at the edge of the boundary layer. As seen in Eq. 2 and Eq. 3, the free stream conditions of the flight can be used to determine the total enthalpy and the pressure at the boundary layer edge, while a model is needed to compute the velocity gradient, most of them including boundary layer edge parameters such as density and pressure.

Using the stagnation line code, the flow properties can be computed along the stagnation line and the velocity gradient can be extracted to continue with the ground testing strategy.

4. Preliminary results

As mentioned in the previous section, a computation of the stagnation line flow properties was carried out using the stagnation line code developed by Munafò [15] applied to the trajectory point exposed before.

From this computation, the interest is focused on the velocity gradient distribution along the stagnation line for extracting the value at the boundary layer edge for a correct ground testing duplication. The velocity gradient distribution results:

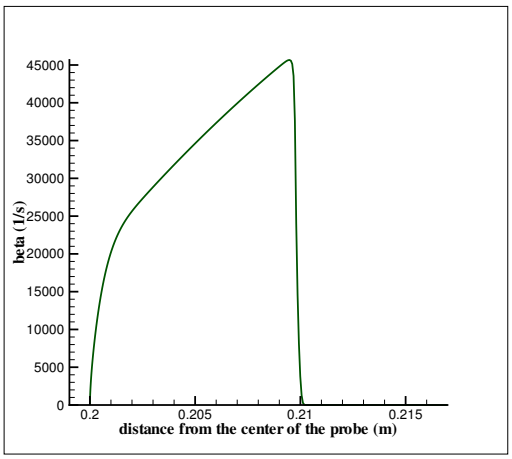

Figure 5: Velocity gradient distribution along the stagnation line of the Hayabusa re-entry probe

For extracting the boundary layer edge value, a look at the temperature distribution has to be taken in order to locate the boundary layer edge defined where the temperature starts to decrease close to the wall:

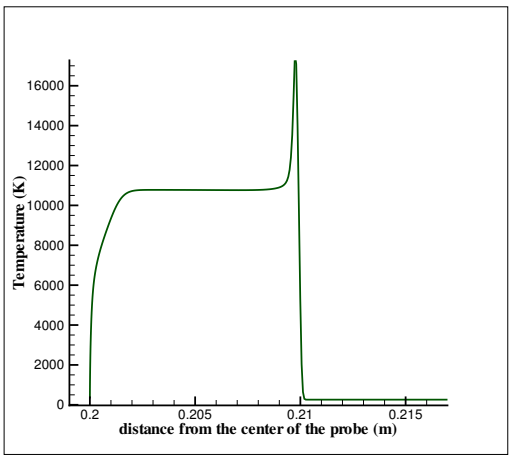

Figure 6: Temperature distribution along the stagnation line of the Hayabusa re-entry probe

As a result, the three independent parameters to be matched in the ground testing facility are:

Table 2: LHTS parameters to be duplicated

Total enthalpy	$54.5MJ/kg$
Stagnation pressure	$54534.8Pa$
Velocity gradient	$24000s^{-1}$

These parameters lead the way to determining the ground testing conditions using Eq. 2, Eq. 3 and Eq.

4 by adopting a model for the velocity gradient, in this case, the Modified Newtonian Theory, explained in [11]. As the size of the model is not known a priori, a parametric study on this variable has been conducted to see how it changes the flow regime and therefore, the Plasmatron configuration for the tests:

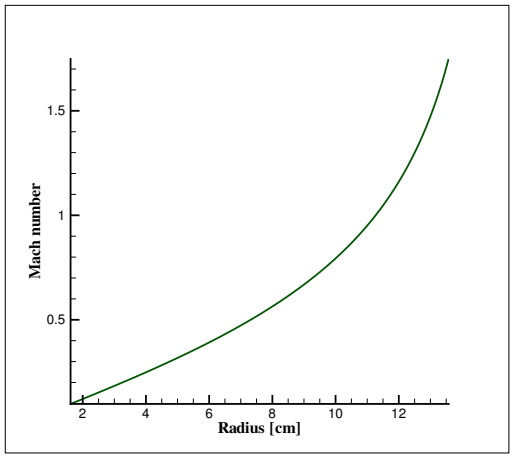

Figure 7: Mach number of the free stream related to the size of the probe

If we take a look now to the free stream pressure, also changing with the size of the probe:

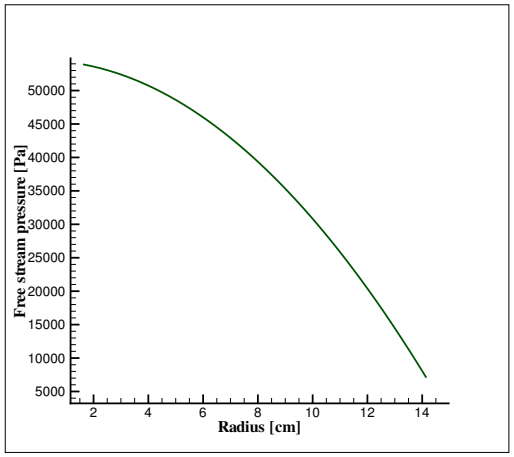

Figure 8: Free stream pressure related to the size of the probe

As the size of the probe increases, the flow regime changes from subsonic to supersonic, and the pressure drops. When taking into account the working envelope of the Plasmatron [16], one can notice that high values of pressure associated with high values of the heat flux are not achievable yet in this facility. This is the case of the Hayabusa probe due to the high-speed re-entry at 10km/s approx. Due to this, a size of a 12cm of local radius has been selected for the ground testing which gives us the free stream conditions for the Plasmatron (exposed below) by using the CABARET code described previously in Sec. 2:

Table 3: Hayabusa ground testing conditions

Temperature	$9730.43K$
Pressure	$20391.47Pa$
Velocity	$3125.9m/s$
Mach number	1.18

As can be appreciated, the flow is supersonic, therefore, the supersonic configuration of the Plasmatron with the sonic nozzle will have to be used.

The size of the probe obtained until this point of the research is the supersonic equivalent sphere for high Reynolds number flows which means that it is supposed to create the same boundary layer conditions in the stagnation region as the actual flight under high Reynolds number flows condition. As the Plasmatron operates with a low Reynolds number plasma flows, an iterative method is needed in order to compute the final model size for the Plasmatron by following the equation:

$$R_{eff,S} = \frac{R_m}{f(NDP)} \tag{5}$$

Where $R_{eff,S}$ is the equivalent supersonic radius of the probe and R_m is the equivalent radius of the Plasmatron model. The NDPs (Non-Dimensional Parameters), describe the flow characteristics at the stagnation line in front of the hemispherical probe of the Plasmatron and are one of the outputs of the ICP computations [17]. One can now compute the radius of the model with the function of the NDPs which comes from solving the flow in the Plasmatron using the ICP code described in Sec. 2. This part is now undergoing.

5. Conclusion

Space exploration leads to extreme challenges as it aims to investigate planets and asteroids in the Solar System and return samples for analysis. Our access to Space is now being enhanced through the development of many different vehicles. The correct understanding of all the physical phenomena involved in every step that makes a mission being successful is essential for avoiding economic and scientific risks, aside from human lives involved in manned missions.

Ground testing represents one of the crucial points for the optimization and qualification of the Thermal Protection System (TPS) design. The importance of ground testing lies not only on the qualification step of the design as is usually associated with, but it is also needed along the optimization process.

In this study, the LHTS framework presents the key parameters to correctly duplicate the re-entry flight. For this purpose, the computation of the duplication parameters is of vital importance. The CABARET codes provides the free stream conditions that have to be reached in the Plasmatron for duplicating the key parameters at the boundary layer edge of our sample. The ICP code redefine the size of the probe for low Reynolds number flows. These tools provide the ground testing conditions needed for the supersonic Plasmatron tests if they remain in its working envelope.

The duplication of the Hayabusa flight in an ICP facility will help to understand our current extrapolation methodologies as well as provide data regarding the material and the thermal environment of the capsule that can be compared to the actual flight.

References

[1] L. Lees, Laminar Heat Transfer over Blunt-Nosed at Hypersonic Flight Speeds, J. Jet Propulsion 26(4), 259-269.

[2] J. Fay, F. Riddell, Theory of Stagnation Point Heat Transfer in Dissociated Air, Journal of the Aerospace Sciences 25.

[3] P. Solano López, Plasmatron Testing Conditions Characterization, Tech. rep., von Karman Institute for Fluid Dynamics, Rhode-St-Genèse, Belgium (2014).

[4] A. F. Kolesnikov, The Concept of Local Simulation for Stagnation Point Heat Transfer in Hypersonic Flows: Applications and Validation, in: 21st AIAA Aerodynamic Measurement Technology and Ground Testing Conference, no. June, 2000.

[5] R. Goulard, On Catalytic Recombination Rates in Hypersonic Stagnation Heat Transfer, in: ARS 12th Annual Meeting, New York, 1958.

[6] G. Bellas-Chatzigeorgis, P. Barbante, T. Magin, Development of Detailed Chemistry Models for Boundary Layer Catalytic Recombination, in: 8th European Symposium on Aerothermodynamics for Space Vehicles, 94423, Lisbon, Portugal, 2-6 March, 2015.

[7] A. Viladegut, F. Panerai, O. Chazot, T. Pichon, P. Bertrand, C. Verdy, C. Coddet, Flying Catalysis in Lifting Atmospheric Entry: Design and Integration of the IXV Catalysis Experiment, in: 8th European Symposium on Aerothermodynamics for Space Vehicles, 84839, Lisbon, Portugal, 2-6 March, 2015.

[8] A. Turchi, J. J. Matesanz Saiz, T. Magin, O. Chazot, On the Flight Extrapolation of Stagnation-Point Ablative Material Plasma Wind Tunnel Tests, in: 8th European Symposium on Aerothermodynamics for Space Vehicles, ESA, Lisbon, Portugal, 2015.

[9] P. F. Barbante, O. Chazot, Flight Extrapolation of Plasma Wind Tunnel Stagnation Region Flowfield, Journal of Thermophysics and Heat Transfer 20 (3) (2006) 493–499.

[10] B. Bottin, O. Chazot, M. Carbonaro, V. Van der Haegen, S. Paris, The VKI Plasmatron Characteristics and Performance, Tech. rep., von Karman Institute for Fluid Dynamics, Rhode-St-Genèse, Belgium.

[11] A. del Val Benitez, T. Magin, B. Dias, O. Chazot, Characterization of Ground Testing Conditions in High Enthalpy and Plasma Wind Tunnels for Aerospace Missions, in: 8th European Symposium on Aerothermodynamics for Space Vehicles, Lisbon, Portugal, 2-6 March, 2015.

[12] G. Grossir, Longshot Hypersonic Wind Tunnel Flow Characterization and Boundary Layer Stability Investigations, Ph.D. thesis, VKI & ULB (2015).

[13] A. Lani, T. Quintino, D. Kimpe, H. Deconinck, S. Vandewalle, S. Poedts, COOLFluid: a high-performance multilayer architecture for solving PDE, in: POOSC'05 - 4th Workshop on Parallel High Performance Object Oriented Scientific Computating - 19th European Conference on Object Oriented Programming, Glasgow, UK, July, 2005.

[14] V. Van der Haegen, Development of an All-Speed Approximate Riemann Solver Applied to Supersonic Plasmas, Tech. rep., von Karman Institute for Fluid Dynamics, Rhode-St-Genèse, Belgium (2013).

[15] A. Munafò, T. E. Magin, Modeling of stagnation-line nonequilibrium flows by means of quantum based collisional models, Physics of Fluids 26 (9) (2014) 097102.

[16] D. Guariglia, B. Helber, O. Chazot, Very High Heat-Flux Measurements in Plasmatron with Subsonic and Supersonic Plasma Flow, in: 8th European Symposium on Aerothermodynamics for Space Vehicles, Lisbon, Portugal, 2-6 March, 2015.

[17] I. Sakraker, A. Turchi, O. Chazot, Hypersonic Aerothermochemistry Duplication in Ground Plasma Facilities : A Flight-to-Ground Approach, Journal of Spacecraft and Rockets, doi: 10.2514/1.A33137.

Simulation of the atmospheric entry of meteors with application to radio detection

Bruno Dias

Aeronautics and Aerospace Department, von Karman Institute for Fluid Dynamics, Belgium, bruno.ricardo.barros.dias@vki.ac.be

Supervisor: Thierry E. Magin

Associate Professor, Aeronautics and Aerospace Department, von Karman Institute for Fluid Dynamics, Belgium, magin@vki.ac.be

University Supervisor: Philippe Chatelain

Assistant professor, Thermodynamics and fluid mechanics - TFL, Université catholique de Louvain, Belgium, philippe.chatelain@uclouvain.be

Abstract

The intersection of meteoroid orbits with the Earth is the responsible for a significant amount of mass injection into the planet atmosphere everyday. In the present work we focus on low entry-velocity meteors, at altitudes of 50 km, to study their ablation with a strategy based on an aerospace-engineering-derived approach (i.e., steady-state CFD with surface ablation model). Numerical results are shown for an flow field considering ablation of the meteor and radiation of air species.

Keywords: Atmospheric entry, meteors, ablation, radiation.

1. Introduction

Meteoroids are space debris traveling at high velocities, product of asteroids or comets fragmentation. Earth's atmosphere is daily bombarded by thousands of meteoroids, almost 50 tonnes per day, whose entry velocity can vary between 11.5 km/s to 72 km/s depending on the orbit [1]. When these objects interact with the Earth's atmosphere the surface temperature can reach several thousands of kelvins causing the melting and/or the ablation of the meteoroid. This phenomenon is commonly known as meteor. Overall, this process leads to a huge amount of mass deposition in the upper atmosphere. The latter is the main reason of the growing interest in studying the ablation of these space objects.

During the meteoroid disintegration, ablation products interact with the ionized gas surrounding the meteoroids and are driven to the wake giving a signature that can be detected by radars.[2] Recent efforts have been made by the Belgian Institute for Space Aeronomy in order to predict velocity and trajectory of the meteors, by means of an innovative technique based on radio waves.[3] The Belgian Radio Meteor Stations (BRAMS)[4] experiment, consists in a series of receivers spread all over Belgium to study the meteor atmospheric entry, to collect and standardize the meteor observation data. In brief, a signal sent by a transmitter, is first reflected by the free electrons in the trail of the meteor, and then captured by the ground receivers (Forward Scattering technique) allowing for the study of the meteor atmospheric entry. One of the main objective of this project is the computation of the meteoroid flux densities. However, this quantity is hardly quantifiable from the lone radar observation, and it is necessary to rely on comparison with numerical models to have an estimate of it. In this scenario, the necessity of having the capability to numerically reproduce the meteor entry finds its room.

The classical meteor ablation process proposed in Ref. [5] is described as "... the mass loss rate is proportional to the kinetic energy imparted to the meteoroid [...] ablation begins when the surface of the meteoroid reaches the boiling point." Ref. [6] concluded that the model given in Ref. [5] is not valid for low dense atmosphere and the ablation may start

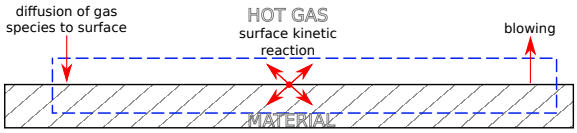

Figure 1: Illustration surface mass balance

before the boiling temperatures is reached. They proposed an ablation model using a Knudsen-Langmuir formula coupled with Clausius-Clapeyron. Ref. [7] computes the mass-loss rate with the Langmuir evaporation where "... the rate of evaporation into a vacuum is equal to the rate of evaporation needed to balance the rate of uptake of a species i in a closed system."

The approaches mentioned above are used to study of the mass deposition in the atmosphere. However, since they were conceived to study the ablation of small particles in the upper atmosphere, they usually rely on a zero dimensional approach and lack of an accurate treatment of the particle interaction with the atmosphere from the fluid dynamic point of view. Therefore, for meteoroids big enough to survive this first phase of the atmospheric entry, a different approach has to be sought.

The von Karman Institute (VKI) has a recognized expertise in hypersonic re-entry studies, and recently focused on the study of the ablation of thermal protection system (TPS) materials. Several experiments, to understand the material behavior, have been conducted in the VKI Plasmatron facility[8; 9] and complemented by numerical analysis to extrapolate experimental results to flight conditions.[10] In this work we propose to study the meteor ablation with a numerical approach similar to those used in the aerospace community to model the gas-surface interaction over TPS materials[11; 12]. A multiphase equilibrium solver, coupled with a 1-D Stagnation-Line CFD solver with an integrated ablative boundary condition is used in the course of this analyses.

2. Gas Surface Interaction

The interaction between the surface and the flow coming from the shock layer can be modeled by limiting the control volume to a infinitesimal thin lamina where the surface is located. The mass conservation for the generic species i can be written in terms of a surface mass balance (SMB) (see Fig. 1):

$$J_{i,w} + \sum_{r=1}^{N_r} \omega_i^r = (\rho v)_w y_{i,w} \quad \forall\, i \in N_s \tag{1}$$

on the left-hand side the mass diffusion of the species and the surface reaction term are present; whereas the term on the right-hand side corresponds to mass blowing due to the surface ablation. In Eq. 1 the subscript w indicates the gas phase at the wall, N_s is the set of species and N_r corresponds to the number of surface reactions involving the species i. In this kind of approach, assuming that a suitable model to compute the surface reactions is available, all the fluxes are known from the flow field calculation. In some cases (e.g., carbon-based TPS ablation modeling), finite-rate chemistry data for the major interactions between the gas and the solid phase are available. Therefore, a finite-rate model can be used in order to calculate the production term in Eq. 1[13]. However, this approach is not always feasible due to the lack of specific data when more exotic surface are considered. In this case, a possible solution is then to consider the heterogeneous mixture (hot gas phase and material surface) to be in thermochemical equilibrium at the local conditions of pressure and temperature [14]. When such an equilibrium approach is considered, it is useful to rewrite Eq. 1 in terms of elements. The elemental mass fraction and the elemental mass diffusion are given by the following relations:

$$y_{k,w} = \sum_{i=1}^{Ns} \alpha_{ki} y_{i,w} \qquad \forall\, k \in \varepsilon \tag{2}$$

$$J_{k,w} = \sum_{i=1}^{Ns} \alpha_{ki} J_{i,w} \qquad \forall\, k \in \varepsilon \tag{3}$$

where ε represents the set of elements. The mass fraction of element k in species i is expressed as:

$$\alpha_{ki} = \sigma_{ik} \frac{M_k}{M_i} \tag{4}$$

where σ_{ik} is the formation matrix coefficient of element k in species i and M the molecular weight. Then, by summing the production term over all the species, one obtains:

$$\dot{m} = \sum_{i=1}^{Ns} \sum_{r=1}^{N_r} \omega_i^r \tag{5}$$

and the elemental SMB reads as:

$$J_{k,w} + \dot{m} y_{k,s} = (\rho v)_w\, y_{k,w} \quad \forall\, k \in \varepsilon \tag{6}$$

where $(\rho v)_w$ is the gas blowing, $y_{k,w}$ is the mass fraction of element k in the gaseous mixture at the wall, $y_{k,s}$ is the elemental mass fraction of the solid, $\dot{m}$ is the mass blowing rate and $J_{k,w}$ is the elemental mass

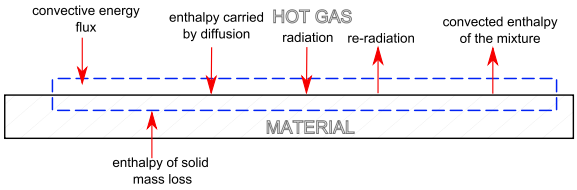

Figure 2: Illustration surface energy balance

diffusion. By summing Eq. 6 over all elements, one obtains:

$$\sum_{k=1}^{\varepsilon} J_{k,w} + \sum_{k=1}^{\varepsilon} \dot{m} y_{k,s} = \sum_{k=1}^{\varepsilon} (\rho v)_w \, y_{k,w} \Rightarrow$$
$$\Rightarrow \dot{m} = (\rho v)_w$$

and finally the mass blowing rate can be computed as:

$$\dot{m} = \frac{J_{k,w}}{(y_{k,w} - y_{k,s})} \quad \forall \, k \in \varepsilon \tag{7}$$

where the elemental composition of the solid phase, $y_{k,s}$, is known and the elemental composition of the gas can be computed by solving a multiphase equilibrium problem. Once the equilibrium gas composition is known and the mass blowing rate, $\dot{m}$, is computed, the surface blowing velocity can be easily obtained as:

$$v_w = \frac{\dot{m}}{\rho_w} \tag{8}$$

where ρ_w is the density of the mixture in gas phase at the wall. Finally the recession velocity, $\dot{s}$, can be computed as:

$$\dot{s} = \frac{\dot{m}}{\rho_s} \tag{9}$$

being ρ_s the density of the solid phase.

Analogously one can consider a balance of energy fluxes entering and exiting the surface, as shown by Fig. 2. The surface energy balance (SEB) is described by:

$$\lambda \nabla T_w + \sum_{i=1}^{N_s} h_i \rho_i V_i + q_{rad,in} + \dot{m} h_c = q_{rad,out} + \dot{m} h_w \tag{10}$$

where the terms on the left side represent the incoming conductive heat flux, diffusive heat flux, shock layer radiation and the energy of the solid due to mass loss. On the right side the fluxes leaving the surface are represented by the re-radiation of the material[1] and the energy of the gases produced during ablation. In this specific case the heat conduction inside the material is neglected, otherwise, an extra term would be included in the right side. By solving this non-linear equation, one can estimate the surface temperature T_w.

It is worth noting that the considered approach provides the most rigorous possible application of equilibrium ablation [15]. It represents a fully coupled approach, and has not to be confused with the simplified uncoupled so called B' approach [16]. In the latter, in fact, additional assumptions are made in the mass diffusion flux through the boundary layer and CFD data obtained in the form of transfer coefficients (obtained non-ablative CFD simulations) are used in the resolution of the simplified surface mass balance and surface energy balance.

2.1. Multiphase Equilibrium Solver

Meteors are commonly composed by several species. Accurate chemical equilibrium solutions are necessary to have a proper estimation of the therm $y_{k,w}$ in Eq. 7. As it is possible to observe from Table 1, Meteor A (also referred as Ordinary Chondrites) is composed by four elements. The solid composition of Meteor A differs slightly from Ref. [7] as consequence of the lack of data of the solid species in the thermodynamic database, used in the course of this project. When such materials are considered it becomes harder to estimate the surface behavior under heat loads. For Thermal Protection Systems composed by a single element, such as carbon graphite, the material response modeling is rather easy. On the other hand, when these materials contain multiple elements, that have dissimilar ablation behaviors, this response modeling becomes more complex. The thermochemistry ablation of multiple surface elements problem was first addressed by Ref. [16]. In this work the author dealt with this problem by constraining the surface element ratios. In the case where the gas elemental composition is not the same as the condensed elemental composition, it is hard to understand how to treat the elements that are still in the condensed phase, thus, how to compute the mass blowing rate. By applying the constraint, it is possible to assume that all elements are removed, from the condensed phase, with the same rate. Therefore, the ratio of the ablation elements in the gas phase is the same as the in-depth elemental composition.

By starting with a solid composed by SiO_2 and MgO where the element composition is:

- Si: 0.232

[1] the surface radiation can be computed by $\sigma \epsilon T_w^4$

- Mg: 0.152
- O: 0.616

More recently an equilibrium multiphase solver based on the Gibbs function continuation method was developed at VKI by Ref. [18] and implemented inside a physico-chemical library *MUlticomponent Thermodynamic And Transport properties for IONized plasmas in C++* (Mutation^{++}). The solver proved to be very robust by converting the minimization of the mixture Gibbs free energy into a initial value problem which can be easily integrated. Furthermore, the solver has the capability of imposing any constraint in order to treat multiple surface components. As an example of the use of this solver, constraint of the condensed elements of Meteor A: $x_{\mathrm{Si}}/x_{\mathrm{Mg}}$ = const is imposed. In brief the ratio between each element in the condensed phase is always respected. By doing this, it can be ensured that in the case of ablation all the surface elements are changing phase with the same rate and the surface composition is always clearly defined. It is not clear that the occurrence of this event might or might not represent the reality. Experimental analyses is needed to validate such observations. However, at the steady-state it is assumed that all condensed elements are removed with the same rate.

Figure 3 shows the equilibrium elemental gas composition resulting from an equilibrium calculation of Meteor A on an Earth atmosphere shown by Table 2. A comparison is made between with the constraint imposed and without constraint with Mutation^{++} For temperatures lower than 2400 K only air elements can be found in the equilibrium gas composition. With the increase of temperature, the species that belong to the meteor composition start to be found in the equilibrium gas phase. From the mixture without constraint the element Si is the first to be completely removed from the solid phase, remaining only Mg in the condensed composition.

It is clear that the ratio between the elements is not respected. Consequently, at higher temperatures the composition of condensed phase does not have the same behavior than at lower temperatures. With the constraint the ratio is respected and the elements evaporate with the same rate.

From chemical equilibrium, with the increase of pressure, a higher surface temperature is needed to obtain the same mass blowing rate. As an indication the non dimensional mass blowing is shown by Fig. 4 for the same mixture with equilibrium constraint shown in Fig. 3. For sake of clearness the non dimensional mass blowing tables are not used in this paper as mentioned previously.

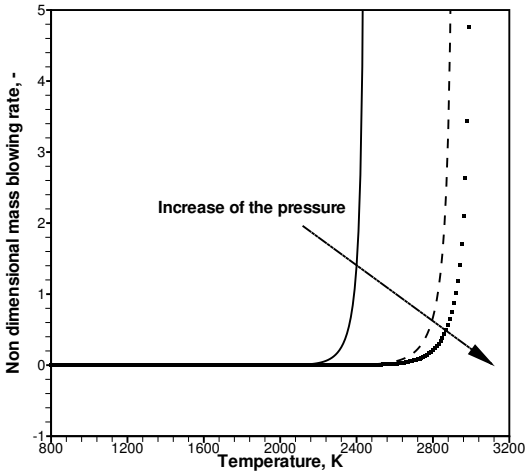

Figure 4: Non dimensional mass blowing rate constraint equilibrium composition vs Temperature; —— 0.01 atm, - - - 0.5 atm, ■ 1 atm

3. Flow Field Modeling

3.1. MUlticomponent Thermodynamic And Transport properties for IONized plasmas in C++ (Mutation^{++})

In order to close the governing equations, thermodynamic and transport properties of the flow field need to be calculated. These properties are computed by a library called Mutation^{++}, built at VKI by Ref. [19], able to compute thermodynamic properties using NASA database [20; 21] or Rigid Rotor Harmonic Oscillator model. The transport properties are computed by the Chapman-Enskog expansion derived from Kinetic Theory [22]. These properties requires a priori information related with the collision integrals, $Q_{ij}^{(l,s)}$, which is described by the potential interaction during an elastic collision between two particles.

As an example the following results concern a mixture composed by only gaseous species of Meteor A in an atmospheric environment, shown by Table 2. These gaseous species were computed by taking the elemental composition at 2600 K for the constrained and unconstrained equilibrium, from the Fig. 3. By doing this it is possible to compute thermodynamic and transport properties of a gaseous mixture produced by ablation with the respective wall temperature. These analyses help to understand the influence of the constraint equilibrium in the computation of the

Table 1: Meteors surface properties

#	Classification	Composition[a]		Elemental composition[a]		Density [kg/m^3]
A	Ordinary Chondrites[b]	SiO_2 MgO	0.606 0.394	Si Mg O	0.232 0.152 0.616	2800

[a] Mole fractions are shown.
[b] Composition was obtained from the "Department of Earth and Planetary Science, University in St. Louis; Washington"[17]

Table 2: Mixture Gaseous species.

Ablation products	Meteor A	Si	SiO	SiO_2	Mg	MgO						
Air species		e^-	N	N^+	O	O+	NO	N_2	N_2^+	O_2	O_2^+	NO^+

thermodynamic and transport properties. The accuracy of such properties become important to evaluated the mass blowing rate, where for instance, the mass diffusion flux is an important parameter in Eq. 7.

3.1.1. Thermodynamic Properties

An example of a thermodynamic property, calculated by Mutation^{++} with RRHO model, is presented in Fig. 5 which shows the equilibrium composition in function of the temperature. From Fig. 5 it is possible to see the effect of the constraint in the composition. It is visible the difference of both cases, i.e., for constrained equilibrium the concentration of the ablation species is significantly smaller than the previous case. With the increase of the temperature, it is possible to see the evaluation of the composition, where in the case that "*reactions*" are considered, one can see the how the species behave by diffusing in the boundary layer where high temperatures are expected. Another relevant thermodynamic property is the equilibrium specific heat at constant pressure shown by Fig. 6. Since this property is related with the composition, mentioned before, Fig. 6 shows the effect of the constraint in the Cp. For higher temperatures, Cp it is significantly higher for the constraint equilibrium case. This difference will have an influence on the total energy governing equation to model the flow field.

3.1.2. Transport Properties

The following results concern the transport properties mentioned above. It is important to refer that the Mutation^{++} computes this properties by the rigorous expansion of the Champman-Enknog formulation. The calculation of the collision integrals of air

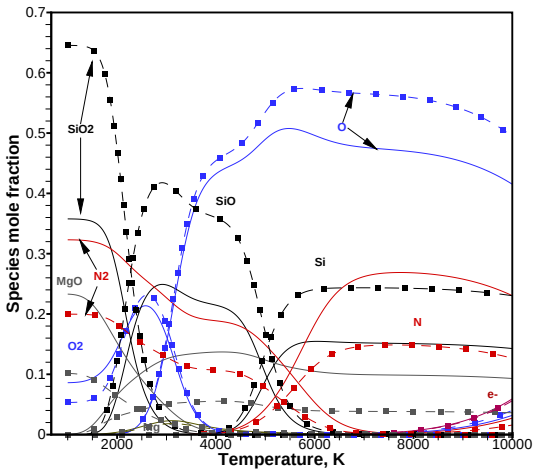

Figure 5: Composition vs Temperature, 0.09 atm: —— constrained mixture, -■- unconstrained equilibrium Mutation^{++}

11 species were based on the data presented by Ref. [23] and the meteor species (Si, SiO, SiO_2, Fe, FeO, Mg, MgO) based on Lennard-Jones potential (Table 3).

Having a similar analysis from the thermodynamic properties, Fig. 7, also shows an comparison from the unconstrained and constrained equilibrium mixture. Figure 7 shows the dynamic viscosity for the case where the equilibrium mixture doesn't have any constraint. By comparing the viscosity from Mutation^{++} with and without constraint, Fig. 7, it is visible the difference in this property due to the equilibrium constraint. This difference will influence the computa-

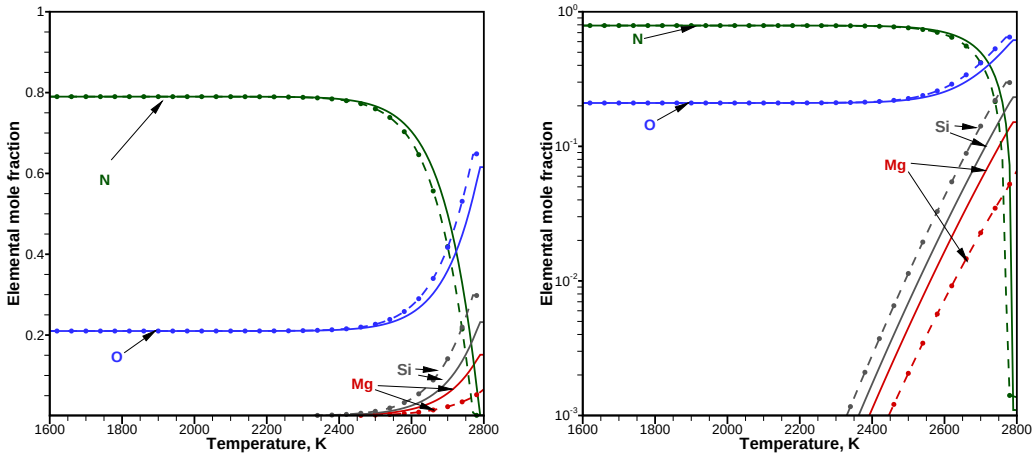

(a) Multi species surface equilibrium constraint vs unconstrained

(b) Multi species surface equilibrium constraint vs unconstrained (log scale)

Figure 3: Gaseous Elemental mole fraction vs Temperature, 0.09 atm; —— constrained, – • – unconstrained equilibrium Mutation^{++}

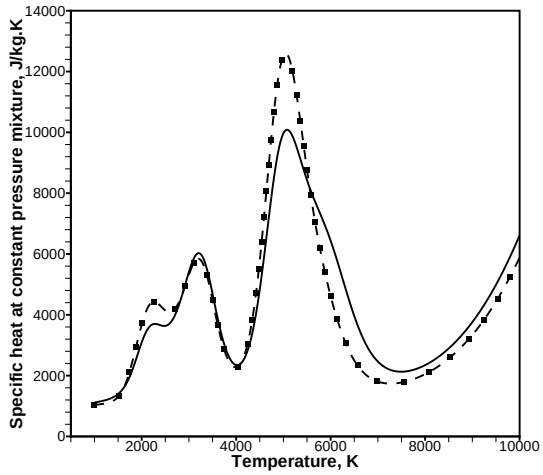

Figure 6: Specific heat at constant pressure gases species mixture vs Temperature, 0.09 atm: —— constrained mixture, -■- unconstrained equilibrium Mutation^{++}

tion of the shear stresses, for instances, in the Navier-Stokes equations.

3.2. *Flow field radiation*

The intensive light observed during a meteor entry is mainly due to the radiation of the air and metallic species, where the latter are coming from ablation products. Coupling radiation with flow field solver can become computationally expensive due to

Interactions	ε/K [K]	σ [Å]	ref
Fe-Fe	7556	2.467	[24]
FeO-FeO	150	4.436	[24]
Mg-Mg	1614	2.926	[25]
MgO-MgO	150	4.454	[24]
Si-Si	3036	2.91	[25]
SiO-SiO	569	3.374	[25]
SiO_2-SiO_2	2954	3.706	[25]

Table 3: Parameters of the Lennard-Jones potential for neutral-neutral interaction

the complex spectral nature of the species. Recently, Ref. [26] presented an hybrid statistical narrow band model (HSNB) showing an accurate description of the radiative flux with low CPU cost for non-ablating materials. Later Ref. [27] extended this approach for ablative TPS material.

By solving the radiative transfer equations (RTE)[2] one can determine the spectral radiative intensity, therefore, the radiative source terms, $\mathcal{P}^{rad}$ and $\mathcal{P}^{rad,VE}$ and $\dot{\omega}_i^{rad}$. The production or destruction of species, $\dot{\omega}_i^{rad}$, due to radiative processes such as photoionization and photodissociation and the radiative source terms are shown in detail by Ref. [27].

Solving the RTE by conventional methods such as Line-by-Line (LBL) becomes very computational ex-

[2]In this work the RTE is solved by using a tangent slab method.

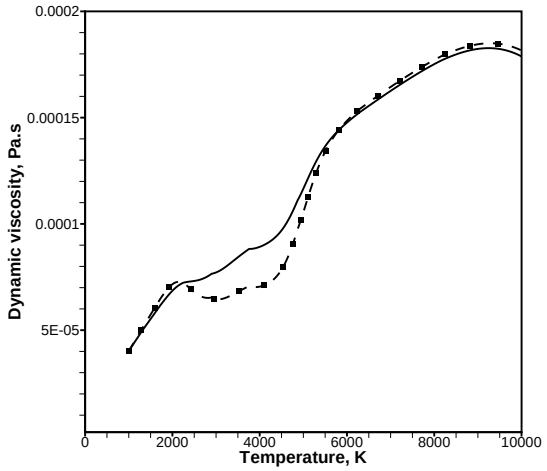

Figure 7: Dynamic viscosity gases species mixture vs Temperature, 0.09 atm: —— constrained mixture, -■- unconstrained equilibrium Mutation^{++}

pensive for complex molecular spectra. The feature of the HSNB is that if the radiative mechanisms are statistically uncorrelated one can divide the spectra into narrow bands and compute the intensity in terms of averages. The different mechanism can be separated in two 3 contributions: -opticallly thick molecular systems, - optically thin molecular systems and continua, - atomic lines. Due to the weak spectral density of atomic lines, this contribution has to be solved by LBL methods. Ref. [28] presents an atomic spectral mesh to optimize to the LBN method for atomic lines. Details about the HSNB can be found in Refs. [26; 27].

4. Numerical tools

The flow governing equations are modeled through a CFD solver where the gas-surface interaction boundary condition, explained in previous sections, is implemented. Moreover the flow properties are computed with Mutation^{++} through the CFD solver.

4.1. Stagnation-Line Code CFD Solver

The 1D Stagnation-Line solver developed at the VKI by Ref. [29], resolves the Navier-Stokes equations along the stagnation line for blunt bodies considering spherical or cylindrical bodies.

The methodology used is presented by Ref. [30], where the number of independent space variables of the governing equations, are reduced to a quasi one-dimensional equations. This model leads to an efficient way to calculate hypersonic flows with low computational cost. In this code the two-dimensional Navier-Stokes equations are simplified to a one-dimensional approximation for the stagnation streamline by a system called "Dimensionally Reduced Navier Stokes Equations" (DRNSE). Since the flow field is symmetric, u, p, T, y_i are symmetric to the axis, on the opposite v behaves anti-symmetric, therefore:

$$\begin{aligned} u &= \bar{u}(r)cos\,\theta \\ v &= \bar{v}(r)sin\,\theta \\ p - p_\infty &= \bar{p}(r)cos^2\,\theta \\ T^{(tr)} &= \bar{T}^{(tr)}(r) \\ y_i &= \bar{y}_i(r) \end{aligned}$$

where v and u are radial and axial velocities, respectively, r is the distance from the center of the body and θ is the angle measured with respect to the stagnation-line. The one-dimensional set of equations are written in the conservative form to allow the use of shock-capturing techniques and the use of time-marching techniques to reach steady-state conditions. The spatial discretization is done by finite volume method and the time integration is computed by a Backward-Euler method. The stagnation-line equations read as:

$$\frac{\partial}{\partial t}\mathbf{U} + \frac{\partial}{\partial r}\mathbf{F^{inv}} + \frac{\partial}{\partial r}\mathbf{F^{vis}} + \frac{\mathbf{G^{inv}} + \mathbf{G^{vis}}}{r} = \mathbf{S^c} + \mathbf{S^r}$$

Where $\mathbf{U}$ denotes the volume-specific balance quantities, $\mathbf{F^{inv}}$ are the inviscid fluxes, $\mathbf{F^{vis}}$ the viscous terms, $\mathbf{S^c}$ and $\mathbf{S^r}$ are respectively the chemical and radiative source terms:

$$
\begin{aligned}
\mathbf{U} &= \left[\rho_i,\ \rho u,\ \rho v,\ \rho E,\ \rho e^{VE}\right]^T \\
\mathbf{F^{inv}} &= \left[\rho_i u,\ \rho u^2 + p,\ \rho uv,\ \rho uH,\ \rho u e^{VE}\right]^T \\
\mathbf{F^{vis}} &= \left[\mathrm{J}_{ri},\ \bar{\tau}_{rr},\ \bar{\tau}_{r\theta},\ q_r + \bar{\tau}_{rr}u,\ q_r^{VE}\right]^T \\
\mathbf{G^{inv}} &= \left[2\rho_i(u+v),\ 2\rho u(u+v),\ 3\rho v(u+v) - 2\bar{p},\ 2\rho H(u+v),\ \rho e^{VE}\right]^T \\
\mathbf{G^{vis}} &= \left[\mathrm{J}_{ri},\ 2(\bar{\tau}_{rr} - \bar{\tau}_{\theta\theta} + \bar{\tau}_{r\theta}),\ -\bar{\tau}_{\theta\theta} + 3\bar{\tau}_{r\theta},\ 2(q_r + \bar{\tau}_{rr}u + \bar{\tau}_{\theta\theta}u + \bar{\tau}_{r\theta}v),\ 2q_r^{VE}\right]^T \\
\mathbf{S^c} &= \left[\dot{\omega}_i^{\mathbf{c}},\ 0,\ 0,\ 0,\ \Omega^{VE}\right]^T \\
\mathbf{S^r} &= \left[\dot{\omega}_i^{\mathbf{rad}},\ 0,\ 0,\ \mathcal{P}^{rad},\ \mathcal{P}^{rad,VE}\right]^T
\end{aligned}
$$

The variables $\mathbf{G^{inv}}$ and $\mathbf{G^{vis}}$ are respectively inviscid and viscous source terms arising from the DRNSE transformation. The therm ρe^{VE} stands for vibrational-electronic-electron energy. Details regarding the radial heat fluxes, q_r and q_r^{VE} as well the energy transfer source term, Ω^{VE} are give by Ref. [27]. The boundary conditions for ablation cases are:

$$
\text{Free} - \text{stream} : \begin{cases} u &= u_\infty \\ T &= T_\infty \\ v &= -u_\infty \\ y_i &= y_{i,\infty} \end{cases}
$$

$$
\text{Stagn.} - \text{point} : \begin{cases} u &= -v_{blowing} \\ T &= T_w \\ v &= 0 \\ y_i &= y_{i,w} \end{cases}
$$

These boundary conditions describe the supersonic inlet free stream, and an ablation isothermal reacting wall.

Numerous studies have been made, at VKI, using this solver to analyze gas-surface interactions of carbon based Thermal Protection System (TPS). Ref. [10] implemented an ablative boundary condition with finite-rate chemistry[31] and studied the thermochemical ablation of TPS material showing good agreement with experimental results performed at the VKI. More recently Ref. [32] used the capabilities of this solver to study the effect of catalytic recombination in the boundary layer.

5. Results

The ablation of Meteor A type was analysed (Table 2). The particle in consideration has a 1 cm radius entering at 15 km/s at an altitude of 50 km. This altitude was chosen to ensure that the particle can still be treated in the continuum regime.

The boundary conditions (SMB and SEB) described previously were imposed. The ablation species injected into the flow field were considered frozen due to the lack of specific data on their chemical reaction rates. Differently, air species were modeled with finite rate chemistry with reaction rates taken from Ref. [33]. Two-temperature model was used during the course of these simulations, i.e., T = T_{rot} and T_{vib} =T_{ele}.

From Fig. 8 it is possible to see three distinct results with different properties. The label "Flow" stands for a simulations disregarding ablation of meteor, i.e., only air species are considered. The simulation labeled "Flow/Ablation" represents the a simulation considering the ablative boundary conditions described previously. Finally the simulation "Flow/Coupled" represents the coupling of ablation and radiation also described previously. All simulations present a highest translational temperature around 75000 K after the shock wave proceeded by a sharp drop to an plateau around 15000 K (Fig. 8(a)). The location of the shock wave differs considerably from the fist simulations and the last two (Fig. 8(b)). This difference is due to the high injection of ablation products into the boundary layer. This effect is visible from the small plateau, in the temperature profile, near the stagnation point. From the last two simulations no significant differences are observable. Nonetheless by observing Fig. 8(b) it is noticed a difference in the internal temperatures in the free-stream,i.e., in the case of radiation coupled with ablation a thermal non-equilibrium is observed in front of the shock.

In Fig. 9 the composition along the stagnation streamline for the latter simulation is shown. As it is possible to see from Fig. 9(a) the concentration of the ablation products at the surface is predominant. With the highest concentration being SiO followed by

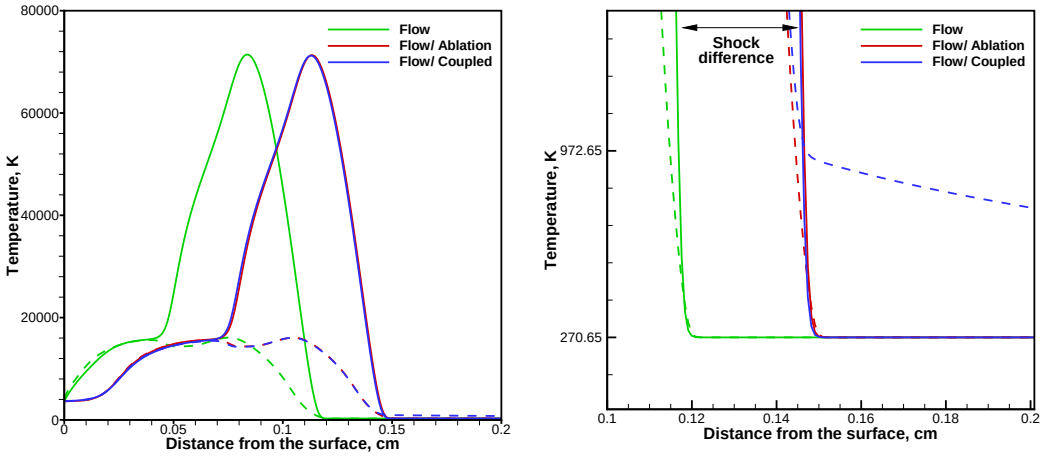

(a) Temperature profile

(b) Temperature profile (zoom)

Figure 8: Temperature profile along the stagnation streamline

O which is also a product from ablation according to the chemical equilibrium solution. By analyzing Fig. 9(b) it is visible a great concentration of e^- along the streamline.

By solving Eqs. 7 and 10 for the latter simulation one could obtain a mass blowing rate of 9.54 $kg/m^2/s$ and a wall temperature of 3645 K.

6. Conclusion

A model to study the meteor ablation at low altitude (up to 70 km) has been proposed and implemented. The model takes the clue from the strategy used to evaluate the gas-surface interaction on the heat shields of re-entry capsules: i) accurate CFD solution of the steady-state flow field; ii) ablative boundary condition based on the mass flux balance at the meteor surface; iii) heterogeneous equilibrium chemistry to compute the gas composition at the surface; iv) ablation products are considered frozen in the flow field. Where in the point iii), due to the multiple constituents of the meteors, required to add additional constrains (i.e., solid phase elemental ratio) for the multiphase equilibrium computation to be consistent with the steady-state hypothesis. These additional constrains have been shown to have a strong impact on the computed surface equilibrium computation. It has been shown that by computing the surface energy balance it was possible to obtain high temperatures at the surface leading to the sublimation of the material. This effect leads to a considerable mass blowing rate and subsequently an enormous injection of ablation products into the boundary layer affecting the position of the shock wave.

By coupling radiation with the flow field, no significant effects were observed which can be due to two main reasons: - only radiation of air species were considered; - the shock layer is considerably small. In other words radiation might become more predominant for bigger objects and the inclusion of the radiative properties for metallic species might change significantly the shock layer structure. It is well known that the bright light observed during a meteor entry is mainly due to the radiation of Na. Nonetheless some thermal non-equilibrium effects were observed in the free-stream due to the precursor effect. This effect is due to the crossing of photons through the shock wave leading to photoionization of the neutral species in the free-stream. This effect can become stronger for higher entry velocities. It has also been observed a considerable amount of e^- in the shock layer. This result might not represent the reality since at this range of temperatures it is important to consider double ionized species such as N^{++} and O^{++} as shown by Ref. [34].

For detection purposes, to study the electron concentration in the wake is essential. The model presented in this paper can easily be integrated into a multi dimensional CFD solver in order to study the wake of meteors, consequently, the electron concentration in the trail. Moreover reactions rates of the ablation species with air species are required to understand the influence of ablation in the electron concentration. Further comparisons with this model and

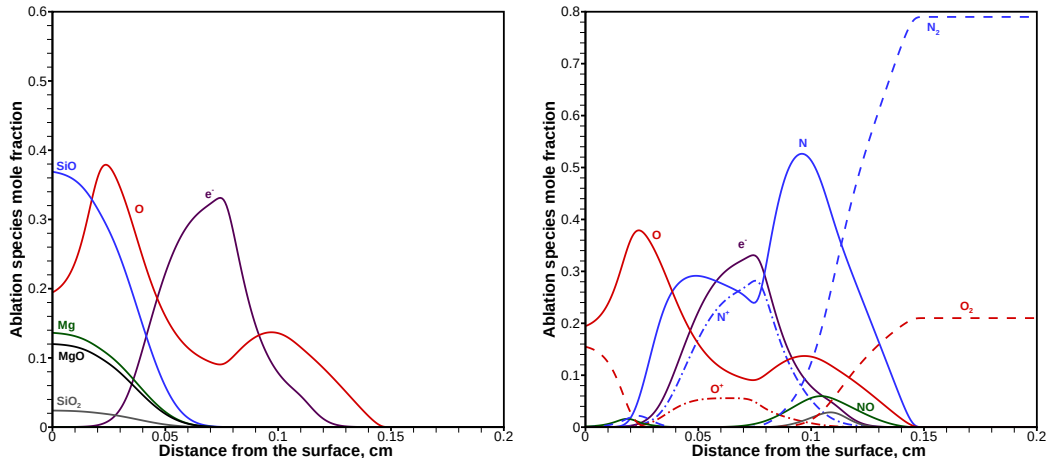

(a) Ablation products (b) Air species

Figure 9: Species mole fraction along the stagnation streamline

meteor observations will be done in the future.

Acknowledgments

The continuous support given by Alessandro Turchi and J.B. Scoggins is gratefully acknowledged. The author also acknowledges the fruitful discussions with Prof. Aldo Frezzotti and Federico Bariselli. The first author acknowledges support through a fellowship from the Fond pour la formation ‘a la Recherche dans lIndustrie et dans lAgriculture .

References

[1] C. Park, The Flow Around Tunguska Meteor, in: 43rd AIAA Thermophysics Conference, New Orleans, Louisiana, 2012, aIAA 2012-3000.

[2] J. Zinn, D. Judd, D. ReVelle, Leonid meteor ablation, energy exchange, and trail morphology, Advances in Space Research 33 (9) (2004) 1466–1474.

[3] Z. Ceplecha, J. Borovicka, W. Elford, D. ReVelle, R. Hawkes, V. Porubcan, M. Simek, Meteor phenomena and bodies, Space Science Reviews 84 (3-4) (1998) 327–471.

[4] Belgian Institute for Space Aeronomy, BRAMS (Belgian RAdio Meteor Stations), `http://brams.aeronomie.be/pages/home`.

[5] V. A. Bronshten, Physics of Meteoric Phenomena, D. Reidel Pub. Co., 1983.

[6] M. Campbell-Brown, D. Koschny, J. Zender, O. Witasse, Model of the Ablation of Faint Meteors, Astronomy & Astrophysics 418 (2) (2004) 751–758.

[7] T. Vondrak, J. M. Plane, S. Broadley, D. Janches, A Chemical Model of Meteoric Ablation, Atmospheric Chemistry and Physics 8 (23) (2008) 7015–7031.

[8] A. Turchi, B. Helber, A. Munafò, T. Magin, Development and testing of an ablation model based on plasma wind tunnel experiments, AIAA Paper 2014–2125, 11th AIAA/ASME Joint Thermophysics and Heat Transfer Conference, Atlanta, Georgia, June 16-20 (2014).

[9] B. Helber, A. Turchi, O. Chazot, T. Magin, Physico-chemistry of cn in the boundary layer of graphite in nitrogen plasmas, AIAA Paper 2015–2668, 45th AIAA Thermophysics Conference, Dallas, Texas, June 22-26 (2015).

[10] A. Turchi, J. J. Matesanz Saiz, T. Magin, O. Chazot, On the flight extrapolation of stagnation-point ablative material plasma wind tunnel tests, in: Proceedings of 8th European Symposium on Aerothermodynamics for Space Vehicles, May 2015, ESTEC, Noordwijk, The Netherlands, 2015, to appear on ESA SP-XXX.

[11] F. Milos, D. J. Rasky, Review of numerical procedures for computational surface thermochemistry, Journal of Thermophysics and Heat Transfer 8 (1) (1994) 24–34.

[12] J. A. Keenan, Thermo-chemical ablation of heat shields under earth re-entry conditions, Ph.D. thesis, North Carolina State University, Raleigh, North Carolina (1994).

[13] A. Turchi, A Gas-Surface Interaction Model for the Numerical Study of Rocket nozzle flows over pyrolyzing ablative materials, Ph.D. thesis, Università degli Studi di Roma “La Sapienza” (2013).

[14] D. Bianchi, F. Nasuti, E. Martelli, Navier-stokes simulations of hypersonic flows with coupled graphite ablation, Journal of Spacecraft and Rockets 47 (4) (2010) 554–562.

[15] C. O. Johnston, P. A. Gnoffo, A. Mazaheri, Study of ablation-flowfield coupling relevant to the orion heatshield, Journal of Thermophysics and Heat Transfer 26 (2) (2012) 213–221.

[16] F. S. Milos, Y.-K. Chen, Comprehensive model for multicomponent ablation thermochemistry, in: AIAA, Aerospace Sciences Meeting & Exhibit, 35th,, Reno, NV, 1997, aIAA 97-0141. doi:10.2514/6.2011-3758.

[17] W. University in St. Louis, `http://meteorites.wustl.edu/metcomp/index.htm`.

[18] J. Scoggins, T. Magin, The gibbs function continuation method for linearly constrained multiphase equilibria, Under Review.

[19] J. Scoggins, Development of Mutation++: MUlticomponent Thermodynamics And Transport properties for IONized gases library in C++, VKI PhD Symposium (2013).

[20] B. J. McBride, S. Gordon, Computer Program for Calculation of Complex Chemical Equilibrium Compositions and Applications II. User's Manual and Program Description, NASA RP-1311-P2, Lewis Research Center, Cleveland, Ohio (Jun. 1996).

[21] B. J. McBride, S. Gordon, M. A. Reno, Thermodynamic data for fifty reference elements, NASA TP-3287-REV1, Glenn Research Center, Cleveland, Ohio (February 2001).

[22] T. E. Magin, A Model for Inductive Plasma Wind Tunnels, Ph.D. thesis, Universitè Libre de Bruxelles (2004).

[23] M. Capitelli, C. Gorse, S. Longo, D. Giordano, Collision Integrals of High-Temperature Air Species, Journal of Thermophysics and Heat Transfer 14 (2) (2000) 259–268.

[24] B. C. McGee, M. L. Hobbs, M. R. Baer, Exponential 6 Parameterization for the JCZ3-EOS, SAND98-1191, Sandia National Laboratories (1998).

[25] R. A. Svehla, Estimated Viscosities and Thermal Conductivities of Gases at High Temperatures, NASA TR R-132, Lewis Research Center, Cleveland, Ohio (1962).

[26] J. Lamet, P. Rivière, M. Perrin, A. Soufiani, Narrow-band model for nonequilibrium air plasma radiation, Journal of Quantitative Spectroscopy and Radiative Transfer 111 (1) (2010) 87–104.

[27] J. Scoggins, L. Soucasse, P. Riviere, S. Soufiani, T. Magin, Coupled flow, radiation, and ablation simulations of atmospheric entry vehicles using the hybrid statistical narrow band model, AIAA Paper 2015–3112, 45th AIAA Thermophysics Conference, Dallas, Texas, June 22-26 (2015).

[28] J. Scoggins, L. Soucasse, P. Riviere, S. Soufiani, T. Magin, An adaptive hybrid statistical narrow band model for coupled, in: Proceedings of 8th European Symposium on Aerothermodynamics for Space Vehicles, May 2015, ESTEC, Noordwijk, The Netherlands, 2015, to appear on ESA SP-XXX.

[29] A. Munafò, Multi-Scale Models and Computational Methods for Aerothermodynamics, Ph.D. thesis, Ecole Central Paris (2014).

[30] A. Klomfass, S. Muller, A Quasi-One Dimensional Approach for Hypersonic Stagnation-Point Flows, Tech. rep., RWTH Aachen (2000).

[31] D. Bianchi, A. Turchi, M. Nasuti, F.and Onofri, Chemical erosion of carbon-phenolic rocket nozzles with finite-rate surface chemistry, Journal of Propulsion and Power 29 (5) (2013) 1220–1230.

[32] G. Bellas-Chatzigeorgis, P. F. Barbante, T. E. Magin, Development of detailed chemistry models for boundary layer catalytic recombination, in: Proceedings of 8th European Symposium on Aerothermodynamics for Space Vehicles, May 2015, ESTEC, Noordwijk, The Netherlands, 2015, to appear on ESA SP-XXX.

[33] C. Park, R. Jaffe, H. Partridge, Chemical-kinetic parameters of hyperbolic earth entry, Journal of Thermophysics and Heat Transfer 15 (1) (2001) 76–90. doi:10.2514/2.6517.

[34] C. Johnston, A. Brandis, Aerothermodynamic Characteristics of 16-22 km/s Earth Entry, in: 45th AIAA Thermophysics Conference, no. AIAA 2015-3110, American Institute of Aeronautics and Astronautics, Dallas, TX, 2015.

Non-linear extensions of global flow stability theory

Koen J. Groot

Aeronautics and Aerospace Department, von Karman Institute for Fluid Dynamics, Belgium, koen.groot@vki.ac.be

Aerodynamics Section (AWEP), Delft University of Technology, The Netherlands, k.j.groot@tudelft.nl

Supervisors: Olivier Chazot and Fabio Pinna

Professor, Aeronautics and Aerospace Department, von Karman Institute for Fluid Dynamics, Belgium, chazot@vki.ac.be

Research Engineer, Aeronautics and Aerospace Department, von Karman Institute for Fluid Dynamics, Belgium, fabio.pinna@vki.ac.be

University Supervisor: Bas W. van Oudheusden

Associate Professor, Aerodynamics Section (AWEP), Delft University of Technology, The Netherlands, b.w.vanoudheusden@tudelft.nl.

University Promotor: Fulvio Scarano

Professor, Aerodynamics Section (AWEP), Delft University of Technology, The Netherlands, f.scarano@tudelft.nl.

Abstract

The project's goal is to incorporate non-linearities in global stability approaches, which requires eigensolutions *a priori*. Streamwise BiGlobal problems are sensitive to in-/outflow boundary conditions (BCs) and are therefore thus far avoided for practical applications. BCs for spanwise problems are well-posed; these problems' feasibility applied to experimental micro-ramp wake base flows was investigated. Results agree with experiments accounting for "branch bifurcations."

Keywords: laminar-to-turbulent transition, e^N-method, BiGlobal stability, micro-ramp wake

1. Introduction

Laminar-to-turbulent transition of flows causes an increase in the local skin friction and heat transfer. Therefore taking into account this phenomenon is important for the design of airliners, regarding their fuel consumption, and re-entry vehicles, with respect to their thermal protection systems. The classical numerical approach to this phenomenon, originally proposed in 1956 by Van Ingen [1], is the combination of Linear Stability Theory (LST), which determines the growth rate of the eigenmodes (Tollmien-Schlichting (TS) waves) that live on a laminar flow, and the semi-empirical e^N-method, which establishes a correlation between the transition "location" and the total growth (or: gain) that the eigenmodes undergo.

The different mechanisms involved in the transition phenomenon are shown in Fig. 1. Disturbances are entrained into the boundary layer via *receptivity mechanisms*. Thereafter the perturbations experience an amplification phase before they breakdown and lead to a turbulent state. The kind of amplification will strongly dependent on the disturbance environment. For small perturbations, the most unstable exponentially growing eigenmode will become dominant and lead to parametric instability (path A). However, for larger initial disturbance levels, multiple eigenmodes can have relatively large amplitudes yielding that their linear superposition displays algebraic *transient growth* (paths B and C). For even larger environmental disturbances, strong non-linearities can set in very early, thereby "by-passing" the aforementioned linear growth mechanisms (paths D and E). Another interpretation of the *by-pass mechanisms* is that they by-pass the current knowledge of what is going on.

The final evolution of the perturbations is highly non-linear. The success of the classical approach that only accounts for linear growth therefore seems sur-

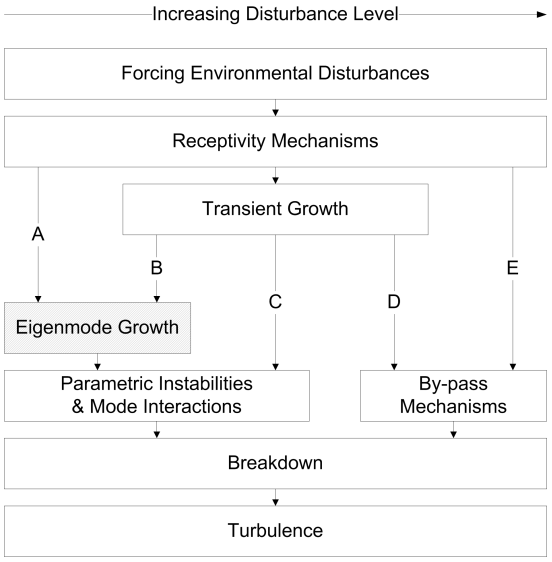

Figure 1: Mechanisms leading to turbulence for different disturbance levels. Original by Reshotko [2].

prising. The omission of non-linear effects is argued to be reasonable with respect to the small spatial extent where they are dominant. The goal of the current PhD project is to extend this approach to include more physics, most prominently: the non-linear mechanisms. The first effect that can be taken into account is eigenmode interaction. Methods that can take these interactions into account fully are able to incorporate the transient growth, by-pass and breakdown mechanisms as well. An important problem is that, as an apparent snowball effect, the receptivity mechanisms have to be accounted for in that case as well, which is equivalent to effectively handling the butterfly effect inherently associated with chaos. This is what makes improving transition analysis very difficult.

In addition to the distinction between the different mechanisms involved, it is important to distinguish different kinds of perturbations. As indicated in Fig. 2, *absolute instabilities* (a) remain finite at the location of their generating source, while *convective instabilities* (b) move away. Due to their definite direction of movement, the convective instabilities can be analysed using parabolized approaches (posing an initial-value problem in space), while it is more convenient to apply an elliptic approach (posing a boundary-value problem in space) to the absolute instabilities.

In what follows, first the two-dimensional generalization of the classical linear stability method is elaborated on followed by the non-linear extension thereof in Section 2. The linear problem has been focused upon up to now, because that provides the initial conditions for the non-linear problem. The generalization implies the solutions are given in 2 spatial dimensions. The solution plane is oriented in either the streamwise or spanwise direction. The former case is referred to as the *BiGlobal* (or streamwise BiGlobal) stability framework and is to be associated with the aforementioned elliptic approach. The latter case is referred to as the *BiLocal* (or spanwise BiGlobal) stability framework. In this case, the perturbation propagation direction is treated infinitely, thereby avoiding problems with in-/outflow boundary conditions.

This motivated focusing on the spanwise BiGlobal stability problem for practical applications. In particular, the method is applied to the approximately two-dimensional vortex pair observed in the wakes of micro-ramps. The base flows required for the stability analysis are obtained mainly by experimental measurement means, as elaborated upon in Section 3, which is a controversial practice in the field of stability analysis, of which the set-up is discussed in Section 4. The main focus was therefore on the stability results' sensitivity to the used base flows to assess the feasibility of the approach. The most unstable modes and involved qualitative errors, *branch bifurcation*, are discussed in Sections 5 and 6, respectively. The treatment is concluded in Section 7.

2. Stability Theory

As indicated, perturbations are the main interest. Therefore the instantaneous flow q is decomposed into a perturbation q' and *steady* base flow $\overline{Q}$:

$$q(x,y,z,t) = \overline{Q}(x,y,z) + q'(x,y,z,t), \qquad (1)$$

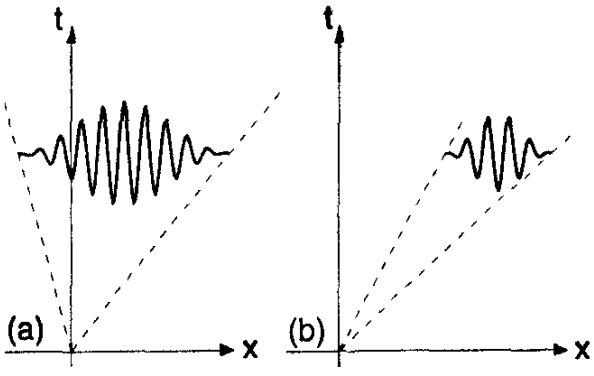

Figure 2: Evolution in space and time of an absolute (a) and convective (b) instability. Original image by Schmid & Henningson [3].

Substituting Eq. 1 into the Navier-Stokes equations yields the *non-linear perturbation equations* for q' from which the combination of terms involving $\overline{Q}$ only (forming steady Navier-Stokes) can be dropped, i.e. $\overline{Q}$ is a physical flow. In the linear theory, the perturbations are assumed to be negligibly small with respect to the base flow terms, allowing the linearisation of the latter equations, resulting in *linearized Navier-Stokes*.

The latter equations are still rather expensive to solve. They are therefore simplified regarding the dimensionality of the base flow. Partial Differential Equation (PDE) theory dictates that the solution must vary "generally" in the directions in which the coefficients, here $\overline{Q}$, vary. The solutions behave exponentially in the remaining directions and time. Regarding boundary layer flow, the streamwise development is classically neglected as opposed to the more prominent wall-normal gradients. This yields the classical (LST) ansatz:

$$q' = \tilde{q}(y)e^{i(\alpha x+\beta z-\omega t)} + c.c., \tag{2}$$

where $\tilde{q}$ denotes the perturbation amplitude, α and β are the stream- and spanwise wavenumbers, ω is the frequency and $c.c.$ abbreviates complex conjugate.

The assumption that the base flow is homogeneous in the x- and z-directions implies, through mass conservation and the no-penetration boundary condition, that the wall-normal velocity component is zero and is therefore also referred to as the *parallel flow assumption*. See the monograph of Mack [4] for an extensive elaboration on LST.

In flows like separation bubbles or those over backward facing steps this assumption breaks down. Another direction has to be considered inhomogeneous, leading to the (streamwise) BiGlobal ansatz (see the review of Theofilis [5]):

$$q' = \tilde{q}(x, y)e^{i(\beta z-\omega t)} + c.c. \tag{3}$$

Inserting either Eq. 2 or 3 into linearized Navier-Stokes leads to the LST or BiGlobal *stability equations* which form eigen-boundary-value problems. Deriving the BiGlobal stability equations for a compressible flow is difficult because of their length. The automatic derivation tools in the VKI Extensible Stability and Transition Analysis (VESTA) toolkit were created with the purpose of tackling this problem. The first error free compressible BiGlobal system was reported by Pinna & Groot [6].

The extension to non-linear perturbation dynamics lies in considering the non-linear perturbation equations. In the non-linear case, one can no longer separate the eigenmodes in the ansatz; they ought to be superposed, thereby allowing them to interact. This leads to the following Wentzel-Kramers-Brillouin-Jeffreys (WKBJ) ansatz (see Holmes [7]):

$$q' = \sum_{m=0}^{N_m} A_m\tilde{q}_m(x, y, t)e^{i\left(m\beta z-\int_0^t \omega_m(\tau)d\tau\right)} + c.c., \tag{4}$$

where τ is the dummy time variable, $\{\omega_m, \tilde{q}_m\}$ are the BiGlobal eigensolutions and $\{A_m\}$ are their associated amplitudes. Inserting Eq. 4 into the governing equations and balancing the harmonics yields a system of systems of equations for the harmonics that forms an initial-value problem that can be solved by a time marching procedure.

The BiGlobal eigensolutions are used to set the initial condition of this initial-value problem. Therefore the linear problem has to be considered before the non-linear one can be dealt with. In this project, regarding the streamwise linear BiGlobal analysis, a large amount of attention was spent on the boundary layer, which logically followed from a tool verification case. In the previous proceedings, it was elaborated that this problem is very difficult because of the sensitivity of the problem to the in- and outflow boundary conditions. That treatment was analogous to the publication of Groot, Pinna & Van Oudheusden [8].

When treating the spanwise z-coordinate as inhomogeneous, instead of the streamwise x-coordinate, the analysis is referred to as BiLocal or spanwise BiGlobal as opposed to (streamwise) BiGlobal. In that case, ansatz (3) (and (4)) has to be adjusted to:

$$q' = \tilde{q}(z, y)e^{i(\alpha x-\omega t)} + c.c. \tag{5}$$

Defining $\lambda = 2\pi/\alpha$ as the streamwise wavelength. This is the problem that will be focused on for the remainder of this treatment. The *temporal approach* is considered implying that a real value for λ is specified and ω is solved for as the usually complex eigenvalue. When $\omega_i > 0$, the eigensolution under consideration is unstable and ω_i is the temporal exponential growth rate.

It is however important to note that temporal instability does not necessarily imply that the perturbation, described by ansatz (5), will grow with the rate ω_i at a *fixed* x-location in time. In other words, it does not imply that the instability is absolute. For that to be possible, it is necessary that the group speed $c_g = d\omega/d\alpha$ be zero for a specific α or λ, see Briggs [9]. Otherwise, it might well be the case that the perturbation

decays in time at the fixed x-location under consideration, but grows (with exponential growth rate ω_i) as it propagates/convects away; this is a feature associated to the streamwise Galilean invariance implied by using ansatz (5). This becomes clear when performing the α-Fourier inversion integral, i.e. superposing α-harmonics, to reconstruct the initial condition or applied forcing in space or time, respectively.

This PhD project is mainly executed at the High Speed Laboratory (HSL) of Delft University of Technology (TUD) where the main research expertise is executing Particle Image Velocity (PIV) experimental measurements. Several flow cases under investigation are two-dimensional in the spanwise-wall-normal zy-plane and therefore suitable for analysis with the spanwise BiGlobal approach. To let the stability analysis correspond most to the experimental circumstances, it is logical to use the base flows obtained by constructing a time-averaged field from tomographic PIV data. However, those fields contain errors associated to the residual perturbations (a finite amount of instantaneous snapshots is used to construct the time-average), let alone those corresponding to structural measurement errors and noise. One could argue that these time-averaged flows do not satisfy steady Navier-Stokes; which, as mentioned earlier, is an inherent assumption underlying stability theory. Numerical stability analysis campaigns were therefore set up to investigate the feasibility of using this kind of base flows;[1] one regarding the primary instability of the vortex pair in a micro-ramp's wake and another for the secondary instability of cross flow vortices (both incompressible flow circumstances). The former case is elaborated upon here and is analogous to the presentation given for the Global Flow Instability and Control symposium (Crete VI) and currently awaiting acceptance of publication by Groot *et al.* [10]. The approach is deemed feasible when yielding agreement with the experimental observations and when qualitatively comparing to analyses of computational base flows, deeper investigations have to be undertaken to verify whether the approach converges with the PIV post-processing parameters.

3. Micro-Ramp Wake Base Flows

Micro-ramps are millimeter sized vortex generators that are applied to suppress shock-wave/boundary-layer interaction, encoutered in supersonic internal flows like supersonic inlet cones. An isometric schematic of the geometry of the currently used micro-ramp and the laminar base flow is shown in Fig. 3. The micro-ramp is symmetric about the (center) xy-plane, it is placed at $290mm$ from the elliptical leading edge and it's height $h = 2mm$. It is $2h$ wide and $2.25h$ long. The freestream velocity $\overline{U}_e = 5m/s$. The associated Reynolds numbers are $Re_h = 685$ and $Re_{hh} = 470$. $Re_{hh}/Re_h = \overline{U}_{ud}(h)/\overline{U}_e$, where $\overline{U}_{ud}(y)$ is the undisturbed Blasius profile.

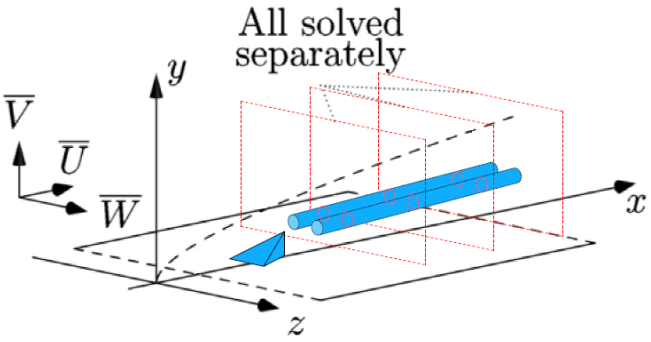

Figure 3: Schematic of the micro-ramp geometry, the induced vortex pair and the spanwise planes for the stability analysis.

The ramp generates two steady counter-rotating streamwise vortices that cause a relatively strong upwash along the center plane. Both computational and experimental efforts were undertaken to resolve the base flow. First of all, the computational results are laminar Navier-Stokes (NS) simulations on the half domain, taking into account the base flow's symmetry. The domain spans $(z, y) = [-5.43h, 0] \times [0, 13.4h]$. The geometry is discretized using a second order finite volume method and fourth order Runge-Kutta is used in time; see Zhang *et al.* [11] for the high-speed equivalents of these simulations. The simulations were stopped when the equations' residual dropped four orders of magnitude. The magnitude of residual perturbations in the computational base flows is therefore argued to be $O(10^{-4})$. Four different spatial resolutions were used having $(N_x, N_y, N_z) = (444, 79, 62)$ (coarse), $(475, 97, 85)$ (nominal), $(530, 110, 133)$ (dense) and $(465, 163, 128)$ (dense plane) nodes. The spatial resolution and stopping criterion correspond to relatively low computational cost; especially with respect to the cost of DNS. Multiple spatial resolutions, which were argued to cause the most significant changes in the base flow, were used to check the corresponding changes in the stability results. It should be emphasized that the computational base flow cases are used only for qualitative

[1] Strictly speaking, the experimental base flows should be referred to as mean flows, but they are not for text uniformity.

verification purposes in the strict sense that the stability results of the computational and experimental base flows are not compared. The computational base flow cases were set up separately to verify the general behaviour of the corresponding solutions; no significant effort was undertaken to exactly replicate the flow conditions and therefore different quantitative results were expected *a priori*.

The tomo-PIV experiments, performed by Ye *et al.* [12] have a sampling frequency of 1.5 $[Hz]$. The base flows were conceived using 100 and 200 instantaneous snapshots. By using more snapshots to generate the base flow, the perturbations present in the instantaneous flow are gradually filtered out. Given that the perturbations have a mean amplitude equal to $0.1\overline{U}_e$, using 100 and 200 frames for the construction correspond to an estimated error/residual perturbation magnitude of $0.1/\sqrt{100} = 1.0 \cdot 10^{-2}$ and $0.1/\sqrt{200} = 0.7 \cdot 10^{-2}$ with respect to $\overline{U}_e$. Furthermore, two different cross-correlation volumes were used of which the height is the most important parameter; taken to be $0.50h$ ("large") and $0.29h$ ("small"). In the other directions, the volumes were taken $0.50h \times 0.50h$ and $0.68h \times 0.68h$, respectively. From now on, the former window sizes will be indicated by talking about the "large PIV" and "small PIV" cases. Taking the combinations of these parameters ultimately leads to distinguishing 4 experimental base flows. When increasing the volume height, a larger spatial average is taken when reconstructing the instantaneous flow snapshot, which means that the overall fields are smoother and the corresponding shear less. Decreasing the height, on the other hand, corresponds to having a higher spatial resolution. This comes at a cost, however, because a smaller window size will lead to using less particles to perform the instantaneous flow reconstruction and hence reduces accuracy.

The three-dimensional velocity field is measured on the domain $(z, y) = [-5.43h, 5.43h] \times [0, 3h]$, so vertically up to $3h$, while $\delta_{99} \approx 2.4h$ at the farthest considered location in x. This causes problems for the stability calculations, as the eigenmodes require a high domain to sufficiently decay before encountering the upper boundary. Therefore, the freestream is extrapolated with the Blasius solution using a cosine weight in an overlap region. Using several combinations of the sizes and positions of this region caused $O(10^{-5})$, i.e. insignificant, differences in the eigenvalues.

In Figs. 4 to 6, the magnitude of the in-plane $\overline{U}$-shear (i.e. the Pythagorean sum of the wall-normal and spanwise shear in the $\overline{U}$-component),

$$\sqrt{(\partial\overline{U}/\partial z)^2 + (\partial\overline{U}/\partial y)^2}, \tag{6}$$

is shown for the tomo-PIV and NS base flows, respectively. In the remainder the magnitude of the in-plane $\overline{U}$-shear will be abbreviated by "$\overline{U}$-shear". Several important differences can be identified directly.

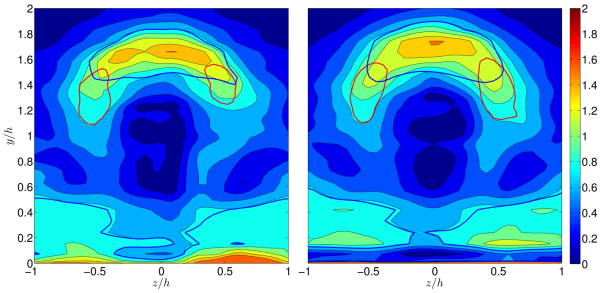

Figure 4: Pythagorean sum of the wall-normal and spanwise $\overline{U}$-shear (abbreviated with $\overline{U}$-shear) for the small investigation window using (left) 100 and (right) 200 frames. Red and blue contours respectively indicate where the z- and y-shear levels attain 50% of the maximum y-shear.

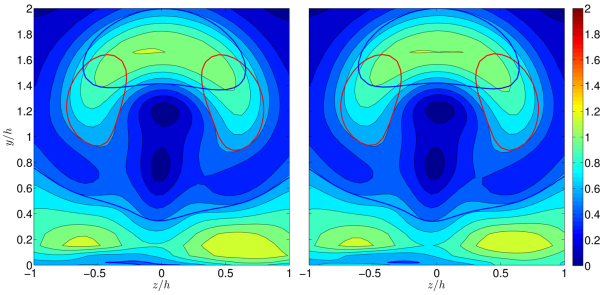

Figure 5: As Fig. 4, for the large investigation window using (left) 100 and (right) 200 frames.

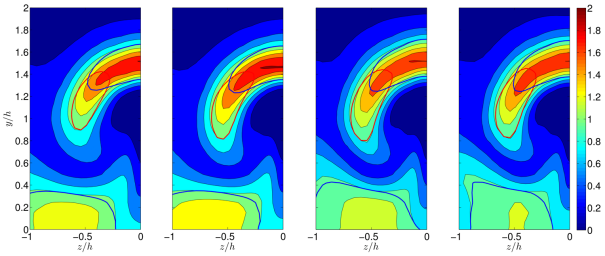

Figure 6: $\overline{U}$-shear for the (far left) coarse, (center left) nominal, (center right) dense and (far right) dense plane NS base flows. Red and blue contours same as in Fig. 4.

First of all, the shear levels in the small and large PIV base flow cases are significantly less (about 76% and 57%, respectively) than those in the NS cases.

As the shear magnitude is proportional to the production of the perturbations, the associated growth rates are expected to be different correspondingly. Furthermore, large differences can be observed in the shear near the wall. In the small PIV cases this is particularly apparent as in those cases the effect of laser reflections off the wall is not smoothed out. A discrepancy that is less clearly visible is the height of the maximum $\overline{U}$-shear, i.e. the inflexion point in the center $\overline{U}$-profile. In the PIV cases, it lies consistently about 10% higher than the NS cases. From these observations it follows that trivial differences in the computational and experimental stability results should occur; the flow conditions are not the same. Equating the latter will be done in future efforts.

4. BiGlobal Stability Problem Set-Up

Regarding the incompressible flow regime, the perturbation amplitudes $\tilde{q}$ consist of the velocity components $\tilde{u}$, $\tilde{v}$, $\tilde{w}$ in the x-, y- and z-direction, respectively, and the pressure $\tilde{p}$. The wave with maximal ω_i, with respect to λ, grows fastest in time and is to be compared to the experimental instantaneous signal. The corresponding λ is referred to as the most unstable wavelength.

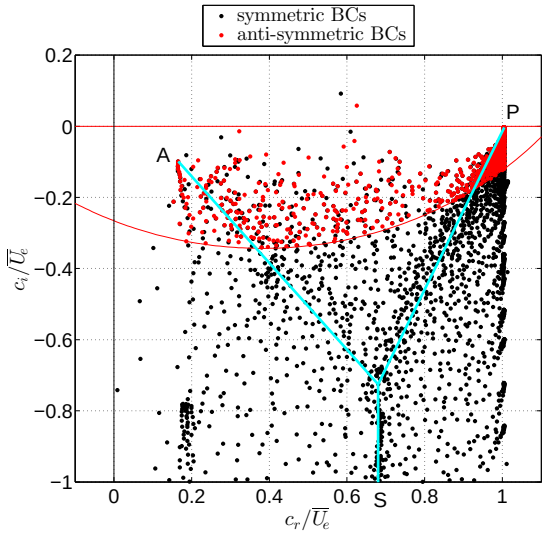

Figure 7: c-spectra corresponding to the nominal NS case at $x = 10h$, having set $\lambda = 4h$ and using symmetric and anti-symmetric boundary conditions along the centerline. The conventional APS branch structure is highlighted. The red line indicates the boundary of the region up to which the anti-symmetric modes were calculated.

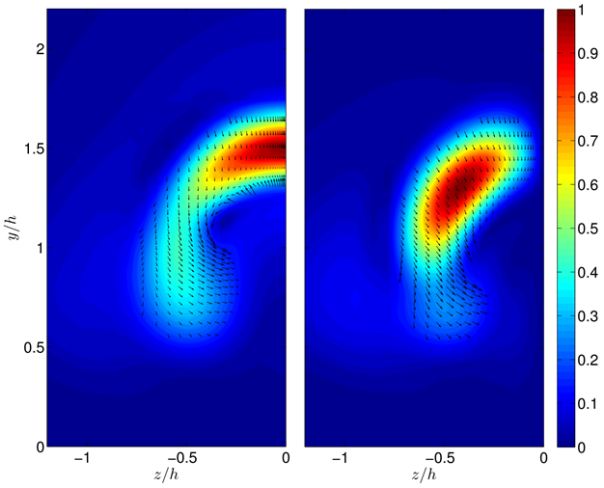

Figure 8: (left) $|\tilde{u}|$ distribution for the unstable symmetric mode and (right) the unstable sinuous mode in the spectrum. The arrows display the in-plane wave propagation direction, i.e. the phase's gradient.

Two downstream planes are considered for the stability analysis, at $5h$ and $10h$ behind the ramp. These stations were chosen so to lie slightly upstream of where the KH-structures are observed, so to minimize the effect of their presence, but close enough for the stability results to reasonably correspond to the experimentally observed behaviour. The problem is solved using a Chebyshev spectral collocation method, using mappings to densely resolve the perturbation amplitudes dominant in the shear regions introduced by the ramp. Wall conditions, as discussed by Groot *et al.*[8] are applied on the solid boundary. Dirichlet conditions are used for all amplitudes on the top boundary as it is located high enough and as it resolves the additive-constant non-uniqueness problem with the pressure. At the far-field boundaries for large $|z|$, the velocity amplitudes are set equal to zero, while homogeneous Neumann conditions are used for the pressure.[2] Using $N_z \times N_y = 60 \times 60$ nodes in the cases where the whole z-domain is considered yields eigenvalue convergence with errors of $O(10^{-4})$.

Fig. 7 displays the c-spectra ($c \equiv \omega/\alpha$) retrieved using symmetric and anti-symmetric boundary conditions along the centerline for the spanwise plane at $x = 10h$ and having set $\lambda = 4h$. A multitude of overlapping APS-like branch structures is retrieved, remi-

[2]Using compatibility conditions for the pressure yielded virtually indistinguishable results, also in the cases where the pressure amplitude attained a small, but significant, magnitude near the boundaries.

niscent of the spectrum shape for Poiseuille flow, corresponding to the spanwise harmonics of the classical one-dimensional equivalent. Two modes, one symmetric (varicose) and the other anti-symmetric (sinuous), are found to be unstable for these parameter combinations. The symmetric mode is from now on referred to as the Kelvin-Helmholtz mode (KH-mode). It has to be noted that, when sufficiently increasing λ, the sinuous mode becomes more unstable than the KH-mode. However, the most (ω_i-)unstable sinuous mode for all interesting λ is less unstable than the most unstable varicose mode. Here, the KH-mode is focused on, as that is observed in the instantaneous PIV images.

5. Analysis of Most Unstable Modes

Figs. 9 and 10 show the ω_i-branches as a function of λ for the $x = 5h$ and $10h$ stations, respectively. All branches agree qualitatively, both experimental and computational branches show the same trend for the considered range of λ. The most-ω_i-unstable modes are ordered in a consistent manner for both stations. Fixing the frame number, the small PIV base flows yield more unstable modes. This is linked to the different magnitude of the $\overline{U}$-shear in these cases. On the other hand, the small and large 200 frame PIV cases are more unstable than the respective 100 frame cases.

Regarding the most unstable wavelengths per case, the NS cases yield a value around $2.2h$ and $2.6h$ for the $x = 5h$ and $10h$ stations, respectively. The large PIV cases have a longer most unstable wavelength than the small PIV cases. These values lie very close to the experimentally observed range, $\lambda/h = 3.5 \pm 0.5$, with the exception of the $x = 10h$ large PIV cases. This range is determined by considering the most upstream hairpins, in the range $x = 10h$ to $15h$, of which an indication is given in Fig. 11. In the $x = 10h$ case, the most unstable seems to converge to the experimentally observed value from above. These results deem the feasibility of the approach to be verified.

A two-dimensional comparison of the most unstable eigenmodes is shown in Fig. 12; it clearly shows the arc shape of the perturbation, which can be divided into an upper part and leg parts. This upper part is asymmetric in the large PIV cases, while it is so to a lesser extent in the small PIV cases. This is due to the asymmetry that can also be spotted in the $\overline{U}$-shear plotted in Figs. 4 and 5. The leg parts change significantly with the base flow parameters. This base flow dependency of the legs is also observed in the computational cases.

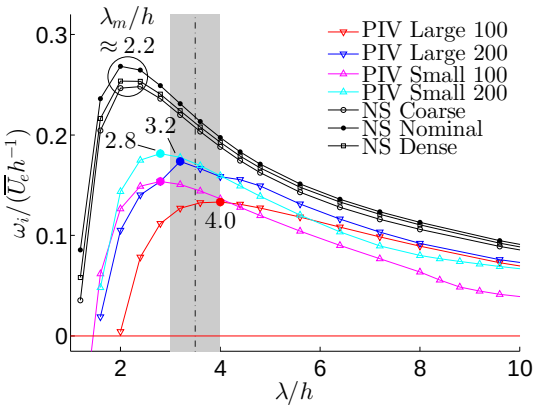

Figure 9: Growth rate versus wavelength branches for the different base flow at the $x = 5h$ station. The dashed-dotted line corresponds to the experimentally observed wavelength, $3.5h$, and the gray region indicates the uncertainty thereof, $\pm 0.5h$.

A three-dimensional comparison of the most unstable eigenmodes is shown in Fig. 11, comparing also against the experimentally observed structures for the considered parameter values. For the Q-criterion to make sense, the perturbation is to be superimposed on the base flow, requiring the specification of an amplitude. Based on the maximal perturbation amplitude found in the experiments, the amplitude $\max|\tilde{u}|/\overline{U}_e$ was set to 20%. The latter is taken constant in x. Two clear distinctions with the experimental case can be identified. First, the upper parts and legs of the hairpins have a longer streamwise extent than in the experiment. For the used amplitude, the different hairpins are disconnected. Second, in between the hairpins, one consistently observes a disconnected vortical structure. For some plotting parameter combinations this makes the overall structures appear like a

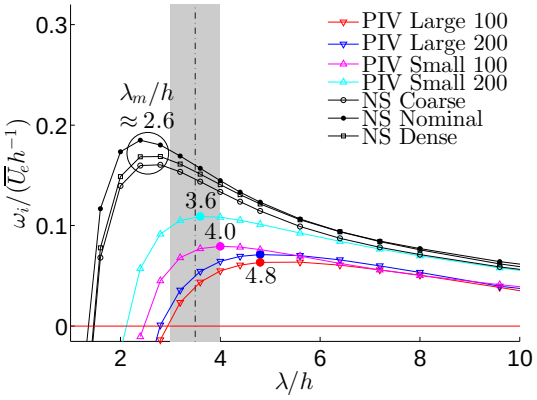

Figure 10: As Fig. 9, for the $x = 10h$ station.

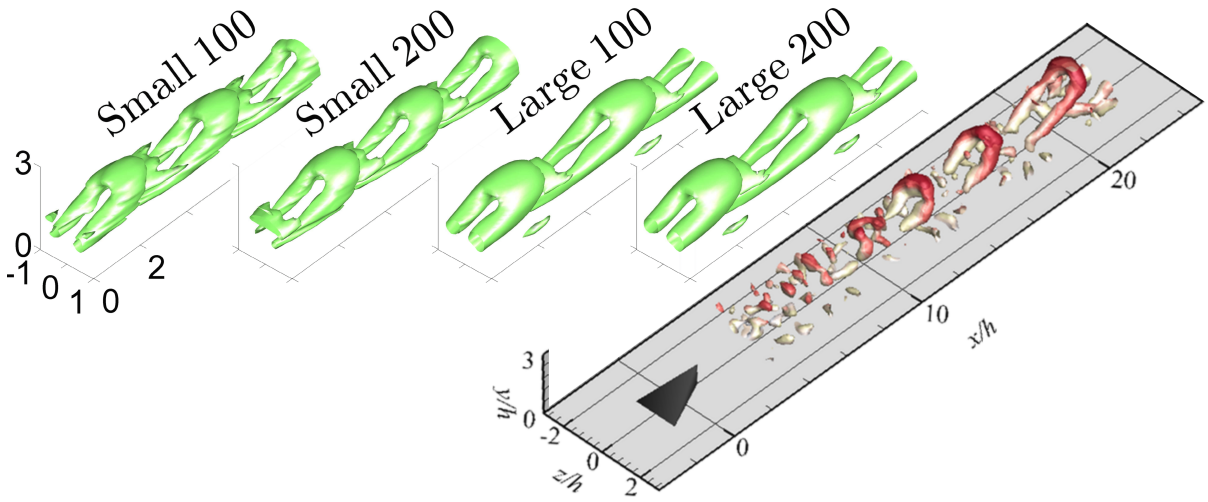

Figure 11: Experimentally observed hairpins (far right) together with the Q-criterion (5% of the maximum Q-level) of the most unstable KH-modes setting the maximum $|\tilde{u}|/\overline{U}_e = 0.2$. All dimensions are in units of h.

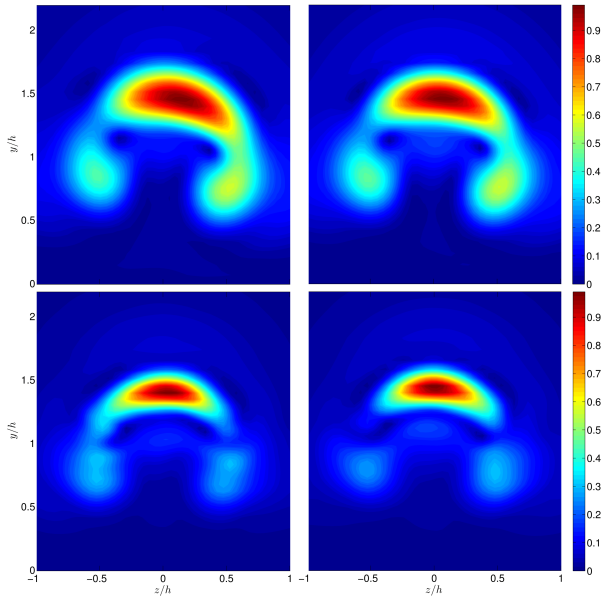

Figure 12: $|\tilde{u}|/\max|\tilde{u}|$ amplitude profiles of the most unstable eigenmodes corresponding to the large 100 (top left), large 200 (top right), small 100 (bottom left) and small 200 (bottom right) cases, at $x = 5h$.

duckling, the additional structure forming the "beak". Despite these matters, the structures are argued to correspond quite well to the experimentally observed signal.

Regarding the large perturbation amplitude, one possible cause of the discrepancies is the finite amplitude dynamics in the experiments.

6. Branch Bifurcations

Despite the good agreement, some strong words of caution are in place. This becomes most apparent when regarding the c-branches as opposed to the λ-ω_i curves, because the parametric branches movement is very limited in the c-plane. The c-branches are shown in Figs. 13 and 14 for the $x = 5h$ and $x = 10h$ stations, respectively. First focusing on Fig. 13, the black curves corresponding to the NS cases lie quite closely together for λ smaller than the c_i maximum. The branches corresponding to the denser resolved cases diverge thereafter. For the current purposes these computational results are deemed to be representative as qualitative references. Regarding the PIV base flow results, it is clear that the branches' shape can change qualitatively. The large PIV branches behave quite similarly, except for an apparent c_r-shift. The big difference occurs when regarding the small PIV base flows.Whereas the number of frames did not yield that large a difference in the large PIV cases, here it does. For 200 frames, the overall shape of the branch is most similar to the computational cases, but

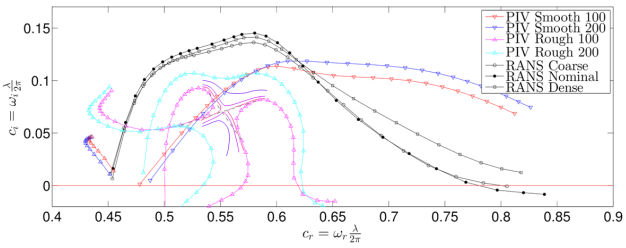

Figure 13: c-branches (growth *speed* versus wavespeed) with varying λ for the different base flows at the $x = 5h$ plane.

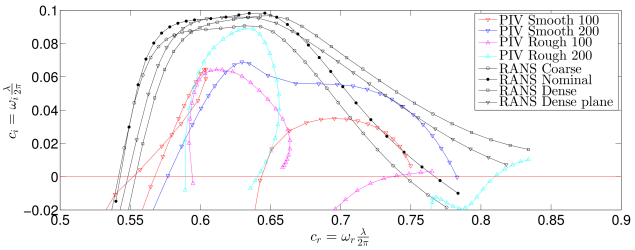

Figure 14: c-branches with varying λ for the different base flows at the $x = 10h$ plane.

an extra branch appears that ends at $c \approx 0.45 + 0.1i$ for $\lambda = 32h$. For the 100 frame case, this new branch has entangled itself with the one pertaining most to the KH-instability, forming two branches of which each respectively corresponds to the KH-branch at either smaller or larger values of λ. It must be noted that the new branch is also present in the large cases as can be seen to the left in Fig. 13; there it is far enough not to influence the KH-branch's shape.

To clarify the process the branches have undergone going from the 100 to 200 frame case, some conceptual branch parts are drawn in Fig. 13. As the number of frames is increased beyond 100, the magenta branches move together and at a certain number touch, or *pinch*. This means, theoretically, that for a certain value of λ a double eigenvalue should be present in the spectrum; the branches have *synchronized*. Practically, this will be hard to obtain exactly, regarding the discrete nature of the number of frames. Increasing the number of frames beyond the occurrence of this special feature, the branches have *bifurcated*, joining the different heads and tails. This is referred to here as a "branch bifurcation". Increasing the number of frames further up to 200, the branches move so to ultimately coincide with the cyan ones. Although this feature is very interesting to consider theoretically, it is a non-physical feature most probably corresponding to the residual perturbations in the base flows. Increasing the number of instantaneous fields to construct the base flow is instrumental to solving this problem. In the current case, the bifurcations occur at wavelengths significantly larger than the most unstable ones; they do not significantly affect the most unstable wavelength. These features are to be taken very seriously, though, as they could have a major influence in other cases.

Regarding Fig. 14, the same can be observed, but is even more predominant. It has to be noted that the sharp cusp in the branch corresponding to the 100 frame large PIV case has been thoroughly probed on invariance with stability grid resolution, boundary conditions on $\tilde{p}$ at the large $|z|$ far field boundaries and the spanwise domain length. This is argued to be the case because at $x = 10h$ the $\overline{U}$-shear in the base flow is smaller than at the $x = 5h$ station, so the additional shear induced by the residual perturbations is relatively larger. By increasing the number of frames from 100 to 200, a bifurcation has occurred in the large PIV cases. This might indicate that the structural wall-reflection errors—much less present in this base flow kind—might not be principally important for the branch bifurcations. The small PIV branches do not seem to have undergone a bifurcation when increasing the number of frames from 100 to 200 frames. Despite this, they display a part where the wavespeed decreases with λ. This is taken as a sign that a bifurcation might take place for a larger number of frames. Furthermore, it must be noted that the 200 frame small PIV case already attains a comparable c_i maximum as the computational cases, despite the fact that the shear in the base flow is smaller than in the NS cases. Overall, it is clear that more instantaneous frames are required to let the branches converge. Future investigations will focus on this.

7. Conclusion

The goal of the overarching PhD project is to extend the stability approaches used for transition prediction to include more physics, e.g. base flow dimensionality and non-linear mechanisms. The base flow dimensionality is included by considering the BiGlobal stability framework, which in turn can be extended to incorporate non-linear behaviour. The non-linear approach requires the solution of the linear problem as an initial condition and therefore the linear BiGlobal eigenvalue problem was focussed on mainly up to this stage in the project.

The stability of micro-ramp wakes is analysed using the spanwise BiGlobal analysis, avoiding concep-

tual problems with in-/outflow boundary conditions associated to the streamwise analysis. The goal was to find the hairpin shaped Kelvin-Helmholtz (KH) waves observed in instantaneous tomographic Particle Image Velocimetry (PIV) measurements. The study focused on the feasibility of using base flows conceived by constructing the mean of the latter instantaneous images; many such base flows are available at the local institution, yielding opportunities to collaborate. The main verification parameter was taken to be the streamwise wavelength found in the PIV measurements, determined to be 3.5 ± 0.5 micro-ramp heights. Furthermore, a strictly qualitative sanity check is performed with computational base flows, Navier-Stokes (NS) solutions.

Restricting the attention to the symmetric/varicose mode, branches were constructed by varying the streamwise wavelength. Representing these branches in a temporal growth rate versus wavelength graph yielded qualitative agreement for the different base flows, both computational and experimental. The most unstable wavelength was determined regarding the maximum temporal growth rate. These maxima were found to be ordered logically with respect to the magnitude and position of the shear layers in the different base flows. The PIV base flows resolving the shear best, using a small volume height, yield the most unstable branches. This leads to the conclusion that resolving the shear layer has high priority regarding the stability results with the PIV base flow parameters. Furthermore, with some exceptions, the most unstable wavelengths were found to correspond to the experimentally observed range thereof. Regarding these facts, the feasibility of the approach is deemed to be verified. Branch bifurcations cause qualitative difference in the spectral information. These differences were found to occur "far away" from the most unstable wavelength.

Looking at the eigenfunctions of the most unstable waves, they all have a typical hairpin shape. Although the upper part of the arc is relatively well-defined, the leg parts still change with the considered base flow parameter changes. Differing features in the Q-criterion structures as opposed to the experiment include the streamwise extent and consistent disconnected structures in between two subsequent hairpins. Despite these features, the structures agree qualitatively.

Acknowledgments

KJG wishes to express his gratitude to the supervisors and professors for their advice and guidance and acknowledge the AWEP department of TUD for the financial support.

References

[1] J. L. Van Ingen, The e^n-method for transition prediction. historical review of work at tu delft, in: 38th Fluid Dynamics Conference & Exhibit, no. 2008-3830, AIAA, ISBN: 978-1-60086-989-1, Seattle, Washington, 2008.

[2] E. Reshotko, Paths to transition in wall layers, in: Advances in laminar-turbulent transition modeling, Von Kármán Institute for Fluid Dyanmics, ISBN: 978-92-837-0900-6, 2008.

[3] P. J. Schmid, D. S. Henningson, Stability and Transition in Shear Flows, Springer Verlag, New York, ISBN: 0-387-98985-4, 2001.

[4] L. Mack, Special course on stability and transition of laminar flow, in: AGARD, Special Course of Stability and Transition of Laminar Flows, North Atlantic Treaty Organization, ISBN: 92-835-0355-4, 1984.

[5] V. Theofilis, Global linear instability, Annual Review of Fluid Mechanics 43 (1) (2011) 319–352.

[6] F. Pinna, K. J. Groot, Automatic derivation of stability equations in arbitrary coordinates and different flow regimes, in: 44th AIAA Fluid Dynamics Conference, AIAA, ISBN: 978-1-62410-289-9, 2014.

[7] M. H. Holmes, Introduction to Perturbation Methods, Texts in Applied Mathematics, Springer, ISBN: 978-0-387-94203-2, 1995.

[8] K. J. Groot, F. Pinna, B. W. van Oudheusden, On closing the streamwise biglobal stability problem: the effect of boundary conditions, in: 8th IUTAM-ABCM Symposium on Laminar-Turbulent Transition, Elsevier, Rio de Janeiro, 2014.

[9] R. Briggs, Electron-stream interaction with plasmas, Research Monogrph No. 29. Cambridge, Mass: M.I.T. Press, ISBN: 9780262523509, 1964.

[10] K. J. Groot, Q. Ye, Y. Zhang, F. Pinna, B. W. van Oudheusden, Biglobal stability analysis of micro-ramp wakes using piv base flows, in: To be accepted for publication, 2016.

[11] Y. Zhang, H. Tan, M. Du, D. Wang, Control of shock/boundary-layer interaction for hypersonic inlets by highly swept microramps, Journal of Propulsion and Power 31 (1) (2015) 133–143.

[12] Q. Ye, F. F. J. Schrijer, F. Scarano, Geometry effect of isolated roughness on boundary layer transition investigated by tomographic piv, in: 9th International Symposium on Turbulence and Shear Flow Phenomena, University of Melbourne, Australia, 2015.

Numerical investigation of hypersonic boundary-layer stability in the presence of ablation phenomena

Fernando Miró Miró

Aeronautics and Aerospace Department, von Karman Institute for Fluid Dynamics, Belgium, fernando.miro.miro@vki.ac.be

Supervisor: Olivier Chazot

Head of Department, Aeronautics and Aerospace Department, von Karman Institute for Fluid Dynamics, Belgium, olivier.chazot@vki.ac.be

University Supervisor: Gérard Degrez

Dean of Faculty, École Polytechnique de Bruxelles, Université Libre de Bruxelles, Belgium, gerard.degrez@ulb.ac.be

Abstract

The study of entry flows is of crucial importance in the current aerospace context. The uncertainty still existing around the behavior of fluids in such flows is a major drawback when designing space vehicles that include an atmospheric entry in their mission. Oversizing of the Thermal Protection System (TPS) is the way to make the vehicles safe despite this uncertainty, but it penalizes the mission objectives due to heavy non-optimal TPS designs. This compromises the propulsion unit, and therefore a weight that could be allocated to the payload is lost. A better understanding of the interaction between the flow and the TPS material would allow optimizing the designs. Laminar-to-turbulent transition phenomena play a big role in the oversizing, since not knowing its location in the boundary layer leads to the use of great safety coefficients for TPS thicknesses. Transition is a complex phenomenon, not well understood in hypersonic regime. Including gas-surface phenomena like ablation, it becomes even more intricate, and its study is difficult because of all the interacting parameters. The research proposal aims to investigate the transition phenomena in this complex scenario with flow stability calculations. It allows physical based approaches to develop an understanding of the effect that TPS pyrolysis and ablation has on boundary-layer transition in hypersonic regime. This will be done through boundary-layer stability analysis, combined with semi-empirical methods such as the e^N method. The VESTA toolkit will be extended in order to include such phenomena. It is made possible thanks to the collaboration between VKI and CenAero who have developed complementary expertise. It is also relevant with the need expressed by aerospace research and industry.

Keywords: Stability, Transition, Ablation, LST.

Assessment of gas-surface interaction modeling for lifting body re-entry flight design

Alan Viladegut

Aeronautics and Aerospace Department, von Karman Institute for Fluid Dynamics, Belgium, alan.viladegut@vki.ac.be

Supervisor: Olivier Chazot

Professor, Aeronautics and Aerospace Department, von Karman Institute for Fluid Dynamics, Belgium, olivier.chazot@vki.ac.be

University Supervisor: Roberto M. Flores

Professor, Aerospace Department, Universitat Politècnica de Catalunya (UPC), Spain, rflores@cimne.upc.edu

Abstract

Atomic recombination is an important process to consider when computing the heat flux transferred to the wall of a re-entry vehicle. Two chemical processes are responsible of the species diffusion within the boundary layer surrounding the non-ablating wall of the Thermal Protection Sustem: gas phase reactions and catalytic recombination at the surface. The coupling between them is not normally taken into account when determining the catalytic recombination coefficient (γ) in plasma facilities. This work aims to demonstrate the influence of the flow characteristics on the catalytic measurements carried out in the VKI Plasmatron facility and to show that chemical coupling is a topic that needs to be addressed when developing ground-to-flight extrapolation methodologies. Recombination coefficient measurements at off-stagnation point configuration on a linear copper calorimeter are provided. An evolution from high-catalytic to non-catalytic due to the boundary layer growth throughout the probe and due to the increase of pressure is observed. A discussion about the possible limitations of the γ-model used for the computations is also provided.

Keywords: Catalysis, Plasmatron, recombination coefficient, off-stagnation point, flat plate.

1. Introduction

Space vehicles re-entering an atmosphere at hypersonic velocities face extreme heat flux conditions. A bow shock wave appears in front of the vehicle after which molecules dissociate into atoms and the gas becomes a mixture of several species. Diffusive effects are confined inside a thin boundary layer close to the body. The processes involved within this layer are responsible for the energy balance at the wall of the Thermal Protection System (TPS). If conduction inside the TPS is neglected, both convective and diffusive heatings should be compensated by radiative heat flux. An accurate characterization of the flow diffusive properties and an appropriate gas-surface interaction model is necessary for both payload integrity and overall mission efficiency.

The diffusive heat flux is defined in Eq. 1, where $\vec{J}_{iw}$ and $h_{i,w}$ are both the diffusive flux and enthalpy of species i in a non-ablating material. $\vec{J}_{iw}$ is only driven by the wall catalytic properties through the boundary condition of the species conservation equation defined in Eq. 2 for first order reactions and following Fick's law in the case of binary mixtures, with ρ_w being the gas density at the wall, c_i and D_i are the mass fraction and mass diffusion coefficient of species i respectively, and η is the coordinate perpendicular to the wall. This relation imposes the species diffusion velocity at the wall to match the speed of the catalytic reaction, characterized by the reaction rate constant $k_{i,cat}$. Thus, the species production/depletion rates due to catalytic activity is a balance between species diffusing to the surface and the chemical kinetics enhanced by the material properties of the wall.

$$\vec{q}_d = \sum_i^{N_s} \vec{J}_{iw} h_{i,w} \tag{1}$$

$$\vec{J}_{iw} \cdot \vec{n} = k_{i,cat} \rho_w c_{i,w} = \rho_w D_i \left. \frac{\partial c_i}{\partial \eta} \right|_w \tag{2}$$

Many efforts have been made since the late 50's to account for chemical reactions in hypersonic boundary layers. Lees [1] introduced in 1956 the relevance of the Lewis number ($Le = \rho D c_p / \lambda$) in both frozen and equilibrium boundary layers. Then, in 1958, Fay and Riddell [2] gave a mathematical expression that is still in use for flight extrapolation methodologies such as the Local Heat Transfer Simulation developed at the Institute of Problems in Mechanics (IPM) by Kolesnikov [3] and adapted at the von Karman Institute (VKI) [4]. Also in 1958, Goulard [5] extended the conservative assumption of full recombination at the wall used by Lees and Fay and Riddell to a finite catalytic activity under frozen boundary layers, being the first to introduce the concept of catalytic recombination coefficient (γ) for re-entry applications. This coefficient is defined for an elementary reaction in Eq. 3, where k_B is the Boltzmann's constant, T_w the temperature at the surface and m_i the mass particle. The recombination coefficient is widely used in non-equilibrium CFD calculations for TPS design, and its influence in a cold wall stagnation point heat flux can be seen in Fig. 1 from the non-catalytic ($\gamma \to 0$) to the full-catalytic ($\gamma \to 1$) conditions.

$$\gamma_i = k_{i,cat} \sqrt{\frac{2\pi m_i}{k_B T_w}} \tag{3}$$

Despite the fact that space vehicles are equipped with low catalytic materials, the full-catalytic assumption is still included in the design phase, leading to oversized TPS and adding constraints in both payload and mission efficiency. The main reason explaining the adoption of such a conservative assumption is the lack of accuracy in the determination of the recombination coefficient for different materials, with the minimum uncertainty found in literature nowadays being ±30% by Balat-Pichelin et al. [6; 7]. Then, more accurate catalytic measurements are required in order to relax the full-catalytic assumption.

The general objective of this work is to understand the link between what we are able to test on ground and what is really happening during a re-entry in the frame of a vehicle equipped with reusable TPS. For that, it is necessary to start with an appropriate enthalpy characterization of the VKI-Plasmatron facility

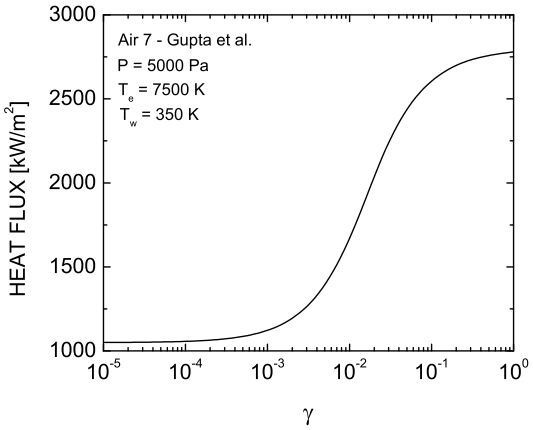

Figure 1: Stagnation point heat flux variation from non-catalytic to full-catalytic cold wall (obtained with the VKI non-equilibrium boundary layer code).

using a reference catalytic model, which was already shown in [8]. Then, we should identify the parameters that have an impact on the experimentally determined catalysis. This is the key to define our capabilities and limitations when measuring the recombination coefficient. Indeed, the present work shows that one of these limits could be the presence of gas-phase recombination in the bulk of the boundary layer. Results from two testing campaigns at both stagnation and off-stagnation point configurations in the Plasmatron demonstrate that the flow configuration, and hence the amount of volume recombination, have a non-negligible impact on the measured recombination coefficient. This conclusion poses the following questions:

- What are we really measuring?
- What should we understand from our modeling?
- How do we build an appropriate flight extrapolation technique?

In the lines that follow, a theoretical analysis is explained where both volume and surface recombinations are considered to compute the heat flux. Then, the recombination coefficient measurements on a cold wall copper calorimeter at stagnation point configuration for two different radii are presented. Results show discrepancies between the two configurations. Then, a similar methodology is applied to extract γ at off-stagnation point on a linear copper calorimeter installed on a flat plate. In this case, the recombination

coefficient distribution along the streamwise direction is obtained and it seems to be reduced throughout the flat plate. The results of both testing campaigns are consistent with the fact that the increase of volume reactions reduces the value of γ. Finally, some considerations on how to proceed with flight extrapolation techniques are discussed when considering the recombination coefficient that should be imposed at the wall of the vehicle.

2. Catalysis determination in non-equilibrium flows

The recombination coefficient γ is a chemical parameter that only depends on the wall temperature conditions for first order reactions. Its experimental determination is suitable for binary mixtures with no gas phase atomic recombination (frozen flow). Indeed, these ideal testing conditions are obtained by Balat-Pichelin [9; 6; 7], Driver [10; 11] and Fletcher [12] due to the low pressure environment provided by their facilities (only a few pascals). However, the measurement of γ in larger plasma facilities is also of interest since their testing conditions are much closer to the real flight. In fact, Inductively Coupled Plasma (ICP) facilities such as the VKI Plasmatron are designed to operate at higher pressures, meaning that the presence of gas phase atomic recombination is likely to occur. This is a limitation inherent to the facility for TPS catalysis determination purposes and its comprehension is a major concern for both the ground-to-flight extrapolation activities being developed at VKI and the further validation of catalytic models. This situation makes the catalytic determination in relatively high pressure conditions a challenging task that should no longer be ignored.

To illustrate the problem regarding catalytic measurements in plasma facilities, it is worth to consider the work of Rosner [13], in which Broadwell's conductivity cell model [14] is generalized to include first order atom recombination at a cold surface of arbitrary catalytic activity. The flow within two parallel plates separated by a distance δ and enclosing a partially dissociated gas is analyzed. One of the plates is hot and under Local Thermodynamic Equilibrium (LTE) conditions, while the other one is cold and with finite catalytic properties. Three non-dimensional parameters appear in the problem: Da_g, Da_w and H. The parameter Da_g is the gas-phase Damköhler number, defined as the ratio between the characteristic diffusion time δ^2/D_{12} and the characteristic chemical relaxation time τ. The Da_w is the wall Damköhler number defined as $k_{cat}\delta/D_{12}$ and introduces the chemical kinetics for recombination at the cold wall through k_{cat}, with $Da_w \to 0$ and $Da_w \to \infty$ being the reaction limited and diffusion limited regimes respectively. The parameter H is a measure of the maximum possible enthalpy change $\Delta h_{chem,eq}$ across the cell as compared to the enthalpy change under frozen conditions Δh_f for the given temperature difference $T_{hot} - T_{cold}$ imposed by the two plates. The Nusselt number (Nu) based on the temperature change between the plates across the film thickness δ is shown in Eq. 4, where ϕ is defined in Eq. 5 and $\xi = \sqrt{Da_g(1+H)}$.

$$Nu = 1 + \phi H \tag{4}$$

$$\phi = 1 - \left\{ 1 + Da_w - \frac{1 - \xi coth\xi}{1 + H} \right\}^{-1} \tag{5}$$

The surface of $Nu = f(Da_g, Da_w)$ is shown in Fig. 2 for $H = 9$. The heat flux transferred to the cold wall increases with both Damköhler numbers. However, one may notice that for large Da_g, there are less atoms available close to the surface due to the presence of gas-phase recombination, leading to a heat flux that is less sensitive to the wall catalytic reactions. This fact has an important consequence when determining a catalytic recombination coefficient based on calorimetric measurements in plasma wind tunnels because uncertainties associated with measuring instruments, data processing and chemical models may lead to an experimentally determined catalytic activity that is far from reality. This is the reason why the suitable conditions for catalysis determination are under very low pressure environments, where collisions between atoms is unlikely to occur and the frozen flow conditions ($Da_g \to 0$) are achieved. Then, since it is not always possible to test at this favorable flow conditions in large high enthalpy facilities such as the Plasmatron, catalytic recombination coefficient measurements might seem influenced by not low enough pressure conditions, sample geometry and diameter at stagnation point configuration, plasma freestream enthalpy or any other flow parameter defining the non-equilibrium boundary layer characteristics (Da_g). This fact would lead either to inaccurate heat flux predictions if measurements of γ were directly imposed in the CFD codes, or to the incapability to validate finite rate chemistry models.

The procedure to determine the recombination coefficient on a catalytic sample in the Plasmatron facility relies on both a heat flux measurement and an

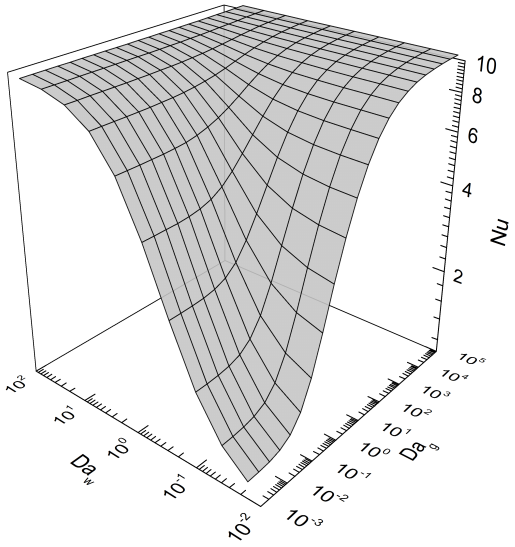

Figure 2: Nu number as a function of Da_g and Da_w for $H = 9$ [13].

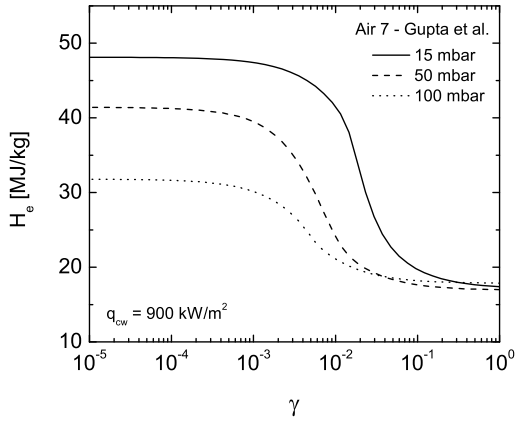

Figure 3: Static pressure effect on the relation between rebuilt enthalpy and recombination coefficient.

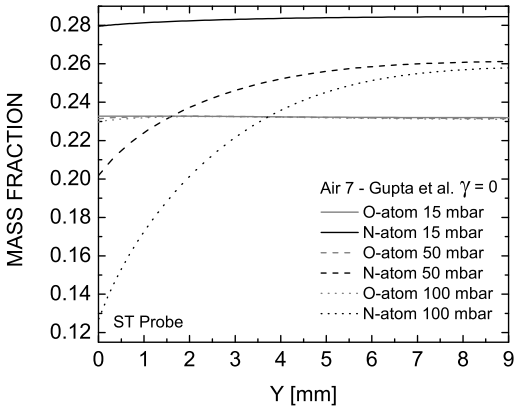

Figure 4: Example of the static pressure effect on the species profiles under non-catalytic conditions for $\dot{q}_{cw} = 900$ kW/m^2.

accurate numerical rebuilding of the boundary layer outer edge enthalpy (H_e) conditions for given static pressure (P_s), gas mass flow ($\dot{m}$) and electric power (PW). The Da_g can be modified by changing the diffusion characteristics of the boundary layer with P_s and/or the probe configuration. The evolution of the rebuilt H_e and γ from non-catalytic to full-catalytic conditions is shown in Fig. 3 for different static pressures and equal cold wall heat flux. Following a logic similar to the exposition above, one notices that the rebuilt H_e is less sensitive to the catalytic activity of the surface when P_s is increased; which, in turn, modifies the boundary layer thickness. Indeed, this change in sensitivity could be due to the larger gas-phase recombination at higher pressures as confirmed by the non-catalytic species profiles shown in Fig. 4 under a heat flux of 900 kW/m^2. Then, when trying to determine the recombination coefficient using the H_e as input, one should expect a reduction of the wall catalytic activity observed in the sample at higher pressures. This is already observed by Panerai [15] over TPS samples and by the author during the development of a reference catalytic model for copper on an *ESA-Standard* probe [8]. This means that, although the recombination coefficient is only temperature dependent, its determination seems to be influenced by the flow surrounding the sample and additional variables might need to be taken into account.

3. The VKI-Plasmatron facility

Plasma facilities are used to reproduce the high temperature environment encountered during re-entry. ICP wind tunnels are suited for catalytic studies due to the gas purity they provide. The VKI-Plasmatron is a 1.2 MW ICP facility able to use 2 kV at 400 kHZ to create the plasma and expand it into a 2.5 m long and 1.4 m diameter test chamber through a 160 mm diameter torch. A scheme of the facility can be seen in Fig. 5. It can operate with different gases at both subsonic and supersonic regimes, with Air, N_2 and CO_2 being the most commonly used. Test samples are normally located at 445 mm from the torch exit. This is a standard configuration for most of the subsonic

tests. A heat exchanger is placed behind the chamber and it is connected to the cooling system to ensure the appropriate gas temperature reduction before particles get into the vacuum pumps. All metal surfaces exposed to the plasma must be cooled down to prevent them from melting.

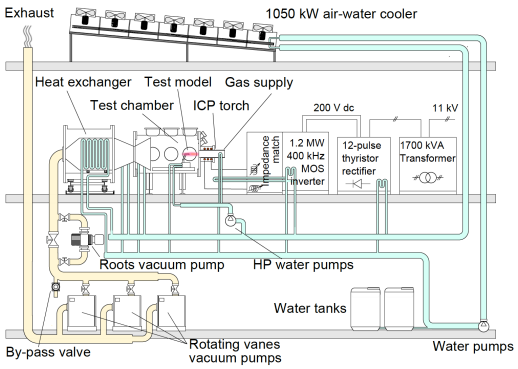

Figure 5: The VKI-Plasmatron Facility.

Pressure ports allow different pressure measurements. Static pressure is measured at the top of the chamber with an absolute pressure transducer (Membranovac DM 12, Leybold Vacuum, OC Oerlikon Corporation AG, Switzerland) with ±0.7hPa accuracy. Dynamic pressure P_{dyn} data is taken with a variable reluctance pressure transducer (DP-15, Valydine Engineering Corp, Northridge, CA USA) of ±0.2% uncertainty that is installed on a probe at stagnation point configuration. Due to torch instabilities, uncertainties increase to ±2% for both P_s and P_{dyn}.

3.1. Catalytic measurements at Stagnation Point

An in-house developed stagnation line boundary layer code (*CERBOULA*) is used in combination with Plasmatron measurements to determine surface catalysis. This solver assumes thermal equilibrium and chemical non-equilibrium around an axisymmetric body to establish the relation between the outer edge enthalpy and wall catalysis from non-catalytic to full-catalytic shown in Fig. 3, if cold wall heat flux ($\dot{q}_{cw}$), pressure and wall temperature measurements are provided. LTE is assumed at the outer edge, which is reasonable far from the torch exit for a broad range of pressures. Different chemical models and gas mixtures are available in the code for data post-processing [16; 17; 18]. Diffusion fluxes are modeled following the Stefan-Maxwell equations. The surface boundary condition for species equations implemented in *CERBOULA* is based on the recombination coefficient γ and related to the reaction rate constant of the catalytic process $k_{i,cat}$ through Eq. 6. This relation considers the Chapman-Enskog perturbation term for non-Maxwellian distribution close to the wall [19]. The species mass flux leaving the surface due to catalytic reactions ($\vec{J}_{i,cat}$) is computed with the relation given in Eq. 7 for each species i, where n_i is the particle density of species i. Only the recombination reactions N+N $\rightarrow$ N_2 and O+O $\rightarrow$ O_2 are considered on the surface under the assumption $\gamma_N = \gamma_O$ for an air mixture.

$$k_{i,cat} = \frac{2\gamma_i}{2-\gamma_i}\sqrt{\frac{k_B T_w}{2\pi m_i}} \tag{6}$$

$$\vec{J}_{i,cat} \cdot \vec{n} = k_{i,cat} m_i n_i \tag{7}$$

Since H_e is unknown during the test, the same code can be used to define enthalpy conditions by introducing a reference recombination coefficient defined on a reference material and probe configuration (γ_{ref}). A water cooled copper calorimeter of 14mm in diameter is normally used to measure $\dot{q}_{cw}$ for H_e rebuilding. It is installed at the center of a water cooled 50 mm diameter holder with 11.75 mm radii on the edge (*ESA-Standard* probe). The calorimeter is insulated from the holder cooling circuit with the teflon ring shown in Fig. 6. Heat flux is measured considering that all the energy is transferred to the water circulating inside the calorimeter by Eq. 8, where T_{in} and T_{out} are the inlet and outlet temperatures measured with type-E thermocouples, $\dot{m}_w$ and c_p are the water mass flow and specific heat respectively and A is the area of the surface exposed to the plasma.



Figure 6: Copper calorimeter and insulating teflon ring.

$$\dot{q}_{cw} = \frac{\dot{m} c_p \left(T_{out} - T_{in}\right)}{A} \tag{8}$$

The determination of copper recombination coefficient at 350 K in VKI is done through the Mini-Max methodology, which is applied by the author [8] for different Plasmatron powers (i.e different H_e) and pressures on the *ESA-Standard* probe. Results suggested that the influence of H_e on the recombination coefficient can be neglected at this configuration. The average values among different powers are γ_{ref} = 0.0265 and γ_{ref} = 0.0156 at 50 and 100 mbar respectively. A reduction of the catalytic efficiency is obtained with the increase in pressure as expected from Fig. 3. These values will be further used to rebuild the outer edge enthalpy conditions of the plasma. To mention that Fletcher [12] measured the O-atom recombination coefficient as 0.027 in an ICP facility using LIF methods and Cauquot [20] 0.025 on Cu_2O in a microwave plasma reactor. These values are also within the range given by Driver [11].

Following the research on the impact of gas-phase atom recombination over the determined catalysis in the Plasmatron, copper catalysis has been determined on another probe size [8]. The *Equilibrium* probe consists on a 115 mm diameter holder with 15 mm rounded corners and a copper calorimeter at the center. The increase of the size leads to a thicker stagnation point boundary layer, increasing the characteristic Da_g, and enhancing the volume recombination of the species. A catalytic activity reduction on the *Equilibrium* probe is observed in Fig. 7 when compared to the reference *ESA-Standard* (γ_{ref}). Indeed, this is consistent with the presence of less atomic species in the bulk of the boundary layer.

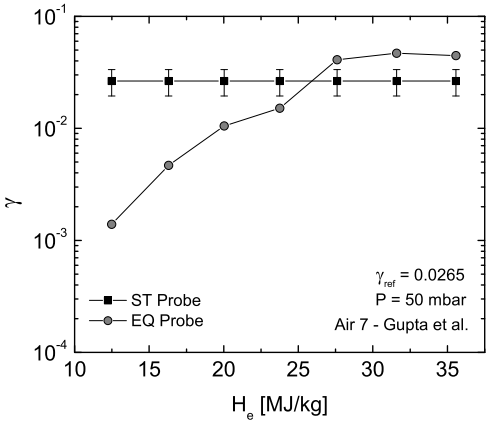

Figure 7: Recombination coefficient comparison between *ESA-Standard* and *Equilibrium* probes [8].

3.2. Extension to Off-Stagnation Point

A 240 mm long by 200 mm wide and 25 mm thick water cooled copper flat plate holder has been designed and manufactured at VKI in order to perform tests at off-stagnation point configuration [21; 22]. It contains a groove of 190 mm by 30 mm to install the linear copper calorimeter shown in Fig. 8 and measure the heat flux distribution at off-stagnation point configuration. This calorimeter consists of 8 consecutive heat flux sensors insulated one from each other but sharing a water pipe circuit. This configuration has already been used for the validation of an off-stagnation point testing methodology in VKI [23]. A total of 9 type-E thermocouples measure the water temperature at each inlet and outlet, leading to 8 heat flux measuring points. Tests with C/SiC and Mullite samples have been carried out for the design of the CATalytic Experiment (CATE) that was on board of IXV [24].

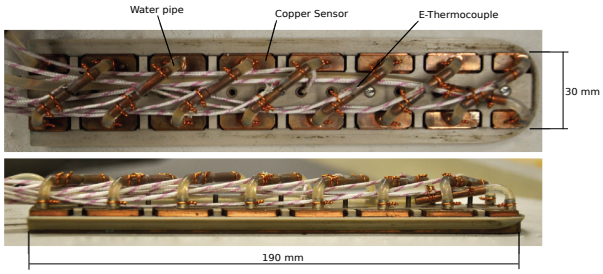

Figure 8: The flat plate calorimeter.

In this work, the flat plate is used in combination with non-equilibrium Navier-Stokes CFD simualtions for catalysis determination at off-stagnation point by following the same strategy used at stagnation point. The solver used for that purpose is CFD++ 14.1.1 from *Metacomp Technologies*. The 2D flow is solved in a mesh with 14,950 quadrilateral cells. The leading edge of the plate is located at 445 mm from the Plasmatron torch exit and consists on a rounded nose of 12.5 mm radius, with the stagnation line being the symmetry plane for the simulation. The flow inlet of the mesh is located at 287.5 mm from the leading edge of the flat plate. Velocity, temperature and species profiles, defined from stagnation point rebuilding with *CERBOULA* and extrapolated from ICP simulations of the Plasmatron chamber under LTE conditions, are imposed at this location. Static pressure is defined at the upper and rear outlets of the mesh. The wall of the flat plate is assumed at 350 K for cold wall copper heat flux and the same recombination coefficient is imposed for both O+O $\rightarrow$ O_2 and N+N $\rightarrow$ N_2 reactions, with non-catalytic conditions being imposed for

the rest of the reactions. The 7 species Air model and Gupta et al. [16] chemical model are used to solve the species equations. The flow is assumed laminar since the typical Reynolds numbers obtained in the Plasmatron in this configuration are below 100.

4. Experimental Campaign

Two pressure conditions are considered for catalytic measurement purposes at off-stagnation point: (*a*) 50 mbar and (*b*) 100 mbar. These pressures are chosen so catalysis values can be compared with the ones provided by the reference configuration (γ_{ref}) at stagnation point. The Plasmatron power applied to the coil is 221 kW at 50 mbar and 188 kW at 100 mbar, leading both to a reference cold wall heat flux of 900 kW/m^2 on the *ESA-Standard* probe. The air mass flow is 16g/s and it is kept constant with a rotameter. The outer edge enthalpy rebuilding procedure using γ_{ref} leads to the reference stagnation point freestream conditions listed in Table 1. Based on these measurements, an extrapolation of the flowfield at the inlet of the CFD++ computational domain is carried out through ICP simulations. Temperature and horizontal velocity profiles imposed in CFD++ are shown in Fig. 9 and 10 for conditions (*a*) and (*b*) assuming 50% efficiency for the power transferred to the plasma.

Table 1: Rebuilt stagnation point boundary layer outer edge conditions.

Test	H_e MJ/kg	T_e K	U_e m/s
a	19.31	5628	234
b	19.91	5841	103

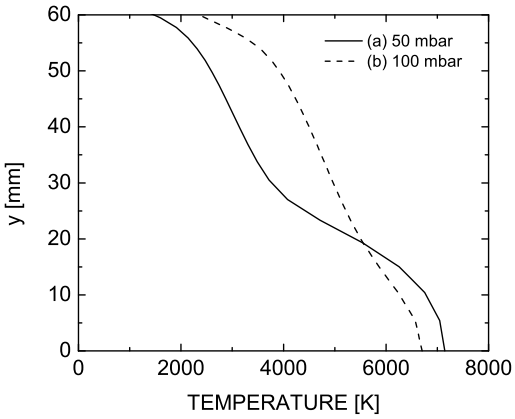

Figure 9: Temperature profiles generated with ICP simulations and imposed as inlet boundary condition in CFD++ computations.

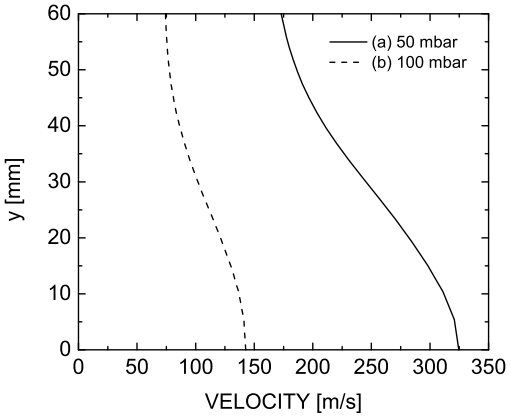

Figure 10: Velocity profiles generated with ICP simulations and imposed as inlet boundary condition in CFD++ computations.

The 9 thermocouples distributed along the calorimeter measure the temperature of the water that is constantly flowing through the pipe. These thermocouples are connected to the data acquisition system and measurements are recorded at 1 Hz. The location of the thermocouples from the leading edge is specified in Table 2 together with the averaged temperatures during plasma exposition for the two testing conditions. The water temperature distribution throughout the plate is shown in Fig. 11. A logarithmic interpolation in the form $T(x) = A\ln(x) + B$ has been carried out over the experimental points in order to avoid discontinuities in the heat flux distribution following Eq. 9, where $d = 30$ mm is the calorimeter wide, and $\dot{m}_{H_2O} = 5.093$ g/s is the water mass flow circulating through the pipe of the calorimeter that is also kept constant with a rotameter. Constants A and B are provided in Table 3 together with the R^2 of the fitting.

$$\dot{q}_w(x) = \frac{c_p \dot{m}_{H_2O}}{d} \frac{\partial T}{\partial x}(x) \tag{9}$$

The heat flux distributions along the flat plate are shown in Fig. 12 and 13 for conditions (*a*) and (*b*), respectively. An accuracy of ±10% is normally given by Eq. 10 with uncertainties over measured quantities provided in Table 4. Plotting both the full-catalytic and the non-catalytic numerical heat fluxes shows an evolution of the wall catalycity of the experimental curve. This is consistent with the analysis exposed

Table 2: Thermocouples location and temperature measurements along the linear calorimeter ($x = 0$ is the leading edge of the flat plate holder).

i	1	2	3	4	5	6	7	8	9
x_i [mm]	49	62	88	113	139	165	190	216	229
$T_i^{(a)}$ [°C]	21.65	32.70	43.28	49.18	50.99	55.21	59.53	64.42	67.65
$T_i^{(b)}$ [°C]	19.88	28.84	38.02	41.87	42.25	45.02	47.47	51.08	51.40

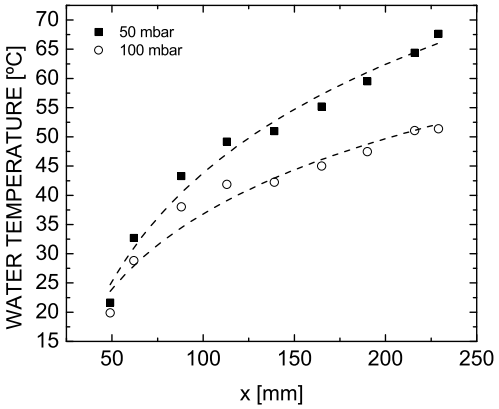

Figure 11: Water temperature distribution along the linear calorimeter.

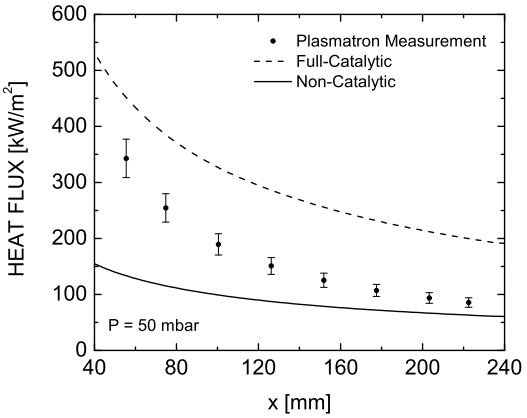

Figure 12: Heat flux distribution along the calorimeter at 50mbar.

Table 3: Coefficients of temperature logarithmic fittings $T(x) = A\ln(x) + B$.

Test	A	B	R^2
a	26.801	-79.601	0.9795
b	18.571	-48.704	0.9554

Table 4: Uncertainties of measured quantities.

Measured Quantity	Uncertainty
$\dot{m}$	±0.5 mg/s
ΔT	±0.8 K
c_p	±0.1 $Jkg^{-1}K^{-1}$
A	±4.4 mm^2

in Sec. 2. Indeed, the increase of the boundary layer thickness leads to a higher Da_g along the plate, which explains why the experimentally observed catalysis is reduced. In addition, the catalytic reduction that was observed when increasing pressure at stagnation point is observed again at off-stagnation point.

$$\frac{\delta\dot{q}_w}{\dot{q}_w} = \sqrt{\left(\frac{\delta\dot{m}}{\dot{m}}\right)^2 + \left(\frac{\delta c_p}{c_p}\right)^2 + \left(\frac{\delta(T_{out} - T_{in})}{T_{out} - T_{in}}\right)^2 + \left(\frac{\delta A}{A}\right)^2} \tag{10}$$

5. Discussion of the Results

The results reported in this paper show that the flow environment has a non-negligible influence on the determination of the wall catalytic activity in the VKI-Plasmatron facility. The same conclusions that were obtained at stagnation point with the 115mm *Equilibrium* probe also apply at off-stagnation point configuration. Indeed, the increase of either pressure or boundary layer thickness tend to reduce the wall catalytic activity. To illustrate this phenomenon on the flat plate, a heat flux abacus between non-catalytic and full-catalytic conditions is generated using CFD++ computations and the evolution with x of the experimentally determined recombination coefficient is clear in Fig. 14 at 50 and 100 mbar. This would be a rather unexpected result considering that the γ-model implemented in both solvers assumes the recombination process as a first order elementary reaction (only temperature dependent). Then, the influ-

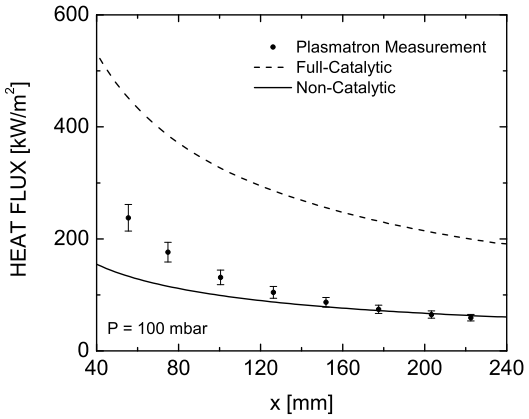

Figure 13: Heat flux distribution along the calorimeter at 100mbar.

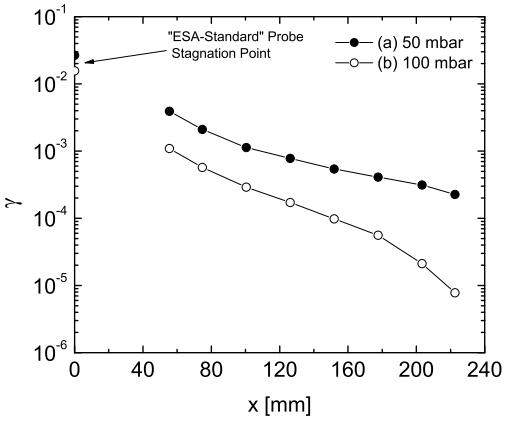

Figure 14: Recombination coefficient distribution along the linear calorimeter.

ence of the gas phase recombination on the surface chemistry characterization is confirmed.

One explanation is that the increase in static pressure enhances the atomic species depletion within the bulk of the boundary layer through gas-phase recombination enhancement, turning the heat flux measurement less sensitive to catalysis and making the determination of catalytic reactivities more difficult for the experimentalist.

Another interpretation is that the level of description used in such a γ-model is not accurate enough to properly describe the catalytic mechanism. One solution is the inclusion of new flow variables such as pressure and boundary layer thickness to keep using this simplistic approach, losing most of the physics at the wall in exchange of accurate heat flux calculations. This could be appropriate for engineers that require simple solutions to design the TPS.

It is important to remark that experimental evidence is consistent with finite-rate chemistry models such as the one proposed by Marschall et al. [25; 26], where the oxygen loss efficiency is reduced with the increase of pressure at the same surface temperature due to the activation of Langmuir-Hinshelwood recombination mechanism, which is not a first order process. Indeed, higher pressure conditions lead to a higher surface coverage so the Eley-Rideal mechanism overcomes the Langmuir-Hinshelwood process, turning into a catalytic reduction. Although the model is applied for a very wide range of surface temperatures (from 500 to 3500K), the fact that copper is highly catalytic may activate the L-H mechanism at lower temperatures (around 350K).

To conclude, the next steps of this research are the definition of a ground-to-flight extrapolation methodology taking into account the geometric factor influencing the measured recombination coefficient. This study is in the framework of the CATalytic Experiment (CATE) [24] (which was under the lead of VKI) that was on board of the Intermediate eXperimental Vehicle (IXV). The experiment provided surface temperature measurements during the re-entry of IXV over a high-catalytic patch that was coated over the baseline ceramic material. With the main objective of the catalytic jump being the demonstration that the full-catalytic assumtion shall not be used in ceramic based materials, in VKI we want to learn how to extract the in-flight catalysis for aerothermodynamic model validation. For that, we need to know how to extrapolate to flight in off-stagnation point.

References

[1] L. Lees, Laminar Heat Transfer Over Blunt-Nosed Bodies at Hypersonic Flight Speeds, Jet Propulsion 26, No. 4 (1956) 259–269.

[2] J. A. Fay, F. R. Riddell, Theory of Stagnation Point Heat Transfer in Dissociated Air, Journal of the Aeronautical Sciences 25, No. 2 (1958) 73–85.

[3] A. Kolesnikov, The Concept of Local Simulation for Stagnation Point Heat Transfer in Hypersonic Flows: Application and Validation, AIAA Paper 2000-2515.

[4] P. F. Barbante, O. Chazot, Flight Extrapolation of Plasma Wind Tunnel Stagnation Region Flowfield, Journal of Thermophysics and Heat Transfer 20, No. 3 (2006) 493–499.

[5] R. Goulard, On Catalytic Recombination Rates in Hypersonic Stagnation Heat Transfer, Jet Propulsion 28, No. 11 (1958) 737–745.

[6] M. Balat-Pichelin, L. Bedra, O. Gerasimova, P. Boubert, Recombination of Atomic Oxygen on $\alpha - Al_2O_3$ at High Tem-

perature Under Air Microwave-Induced Plasma, Chemical Physics 340 (2007) 217–226.
[7] M. Balat-Pichelin, J. Badie, R. Berjoan, P. Boubert, Recombination Coefficient of Atomic Oxygen on Ceramic Materials Under Earth Re-Entry Conditions by Optical Emission Spectroscopy, Chemical Physics 291 (2003) 181–194.
[8] A. Viladegut, O. Chazot, Enthalpy characterization and assessment of copper catalysis determination in inductively coupled plasma facility, in: 45th AIAA Thermophysics Conference, AIAA, Dallas, Texas, 22-26 June, 2015.
[9] M. Balat-Pichelin, M. Czerniak, J. Badie, Thermal and Chemical Approaches for Oxygen Catalytic Recombination Evaluation on Ceramic Materials at High Temperature, Applied Surface Science 120 (1997) 225–238.
[10] A. Nawaz, D. Driver, I. Terrazas-Salinas, S. Sepka, Surface catalysis and oxidation on stagnation point heat flux measurements in high enthalpy arc jets, in: 44th AIAA Thermophysics Conference, AIAA 2013-3138, San Diego CA, United States, June 24-27, 2013.
[11] D. M. Driver, S. Sepka, Side arm reactor study of copper catalysis, in: 45th AIAA Thermophysics Conference, AIAA, Dallas, Texas, 22-26 June, 2015.
[12] J. M. Meyers, W. P. Owens, D. G. Fletcher, Surface catalyzed reaction efficiencies in nitrogen and oxygen plasmas from laser induced fluorescence measurements, in: 44th AIAA Thermophysics Conference, AIAA 2013-3139, San Diego CA, United States, June 24-27, 2013.
[13] D. E. Rosner, Scale Effects and Correlations in Nonequilibrium Convective Heat Transfer, AIAA Journal 1, No. 7 (July 1963) 1550–1555.
[14] J. E. Broadwell, A Simple Model of the Non-Equilibrium Dissociation of a Gas in Couette and Boundary Layer Flows, Journal of Fluid Mechanics 4 (1958) 113–139.
[15] F. Panerai, Aerothermochemistry Characterization of Thermal Protection Systems, Ph.D. thesis, von Karman Institute for Fluid Dynamics / Università Degli Studi Di Perugia (2012).
[16] R. N. Gupta, J. M. Yos, R. A. Thompson, K.-P. Lee, A Review of Reaction Rates and Thermodynamic and Transport Properties for an 11-Species Air Model for Chemical and Thermal Nonequilibrium Calculations to 30000K, NASA Reference Publication 1232.
[17] C. Park, Nonequilibrium Hypersonic Aerothermodynamics, Wiley-Interscience, John Wiley & Sons, 1990.
[18] M. G. Dunn, S.-W. Kang, Theoretical and Experimental Studies of Reentry Plasmas, Contractor Report 2232, NASA Langley Research Center, Hampton, VA, USA. Prepared by Cornell Aeronautical Laboratory, Inc. Buffalo, NY, 14221.
[19] P. F. Barbante, Accurate and Efficient Modelling of High Temperature Nonequilibrium Air Flows, Ph.D. thesis, von Karman Institute for Fluid Dynamics / Université Libre de Bruxelles (2001).
[20] P. Cauquot, S. Cavadias, J. Amouroux, Thermal Energy Accomodation from Oxygen Atoms Recombination on Metallic Surfaces, Journal of Thermophysics and Heat Transfer 12, No. 2 (April-June 1998) 206–213.
[21] A. Vanaerschot, Development of a Flat Plate Probe for Off-Stagnation Testig of Space Reentry Vehicles, Final year project, Faculteit Ingenieurswetenschappen - Katholieke Universiteit Leuven (2009-2010).
[22] A. Braun, Validation of a methodology for Off-Stagnation Point Testing, Study thesis, Von Karma Institute, Institute for Space Systems - Stuttgart University (2011).
[23] A. Viladegut, O. Chazot, Off-Stagnation Point Testing in Plasma Facility, Progress in Flight Physics, Volume 7, Advances in Aerospace Sciences, EUCASS Book Series.
[24] A. Viladegut, F. Panerai, O. Chazot, T. Pichon, P. Bertrand, C. Verdy, C. Coddet, Flying catalysis in lifting atmospheric entry: Design and integration of the ixv catalysis experiment, in: 8th European Symposium on Aerothermodynamics for Space Vehicles, ESA, Lisbon, Portugal, 2-6 March, 2015.
[25] J. Marschall, M. MacLean, Finite-rate surface chemistry model, i: Formulation and reaction system examples, in: 42nd AIAA Thermophysics Conference, AIAA 2011-3783, Honolulu, Hawaii, 27-30 June 2011.
[26] M. MacLean, J. Marschall, D. M. Driver, Finite-rate surface chemistry model, ii: Coupling to viscous navier-stokes code, in: 42nd AIAA Thermophysics Conference, AIAA 2011-3784, Honolulu, Hawaii, 27-30 June 2011.

GROUND AND FLIGHT EXPERIMENTS

Aerodynamic design methodology for supersonic internal passages

Jorge Sousa

Aeronautics and Aerospace Department, von Karman Institute for Fluid Dynamics, Belgium, jorge.sousa@vki.ac.be

Supervisor: Guillermo Paniagua

Adjunct Professor, Aeronautics and Aerospace Department, von Karman Institute for Fluid Dynamics, Belgium, gpaniagua@vki.ac.be

University Supervisor: Iskender Gokalp

Director of the ICARE laboratory, Université d Orleans, France, iskender.gokalp@cnrs-orleans.fr

Abstract

Fluid machinery operating in the supersonic regime unveil avenues towards more compact technology. However, internal supersonic flows are associated with high aerodynamic and thermal penalties, which usually prevent their practical implementation. Indeed, both shock losses and the limited operational range represent particular challenges to aerodynamic designers that should be taken into account at the initial phase of the design process. This paper presents a design methodology for supersonic passages based on direct evaluations of the velocity field using the method of characteristics and computation of entropy generation across shock waves. This meshless function evaluation tool is then coupled to an optimization scheme, based on evolutionary algorithms that minimize the entropy generation across the supersonic passage. Finally, we assessed the results with 3D Reynolds Averaged Navier Stokes calculations.

Keywords: Turbine design; Supersonic internal flow; Method of characteristics; Optimization

1. Introduction

The specific power extraction in fluid machinery scales with the specific mass flow, reaching a maximum at sonic conditions. Based on the conservation of momentum through a fluid machine it follows that the specific power increases with the flow velocity. Consequently we are compelled to explore supersonic internal rotating passages. The design of such supersonic internal passages is governed by the existence of large shock losses and restricted operational range [1; 2]. In the 1950's, the research was focused on steam turbine applications [2] and rocket propulsion systems [3]. Nowadays, supersonic turbines with a subsonic axial Mach number are being used in several applications: [1]

- Organic fluid Rankine cycles, in thermo-solar plants or waste heat energy recovery systems [4].
- Fast start up gas turbine [5].
- Turbopump turbines, as in the rocket engine Vulcain [3].

In the quest to develop more efficient and compact fluid machinery we are designing internal passages with supersonic inlet axial conditions. These types of turbines are suitable for fluid machines that follow the modified Brayton cycles, with an isothermal heat addition process where the combustor presents a convergent shape [7,8]. In those engines, the turbine inlet Mach number is limited to values below unity [9], because those authors were unaware of the possible uses of turbines with supersonic inlet flows. By contrast, in a previous publication, we had explored the performance of a turbine passage that was designed considering the starting capabilities, and coolability, of the airfoil [10]. The presence of the blunt leading edge, was responsible for strong leading edge shock waves and, consequently, led to the reduction of isentropic efficiency. Figure 1a depicts the iso-Mach contour

[1] This work was previously published on the Entropy journal (Entropy 2015, 17(8), 5593-5610; doi:10.3390/e17085593).

at mid-span for a supersonic turbine design, whereas Figure 1c shows the Mach number distribution along the pressure and suction side. Both representations prove the existence of supersonic flow in the passage. On the other hand, Figure 1b represents the attempt to use a conventional design with the same supersonic inlet Mach number. As a consequence of the high area contraction associated with this design, supersonic flow is not established in the passage (unstarted configuration). Hence, a normal shock wave occurs in the inlet of the numerical domain. As shown by the Mach number distribution (Figure 1c-bottom) only subsonic flow exists along the conventional design profile. In an engine application, such a design would lead to a tremendous entropy rise (s 440 KJ/(Kg K)) and eventually this shock wave would evolve towards the combustor. The present publication proposes a new approach to optimize the design of supersonic passages.

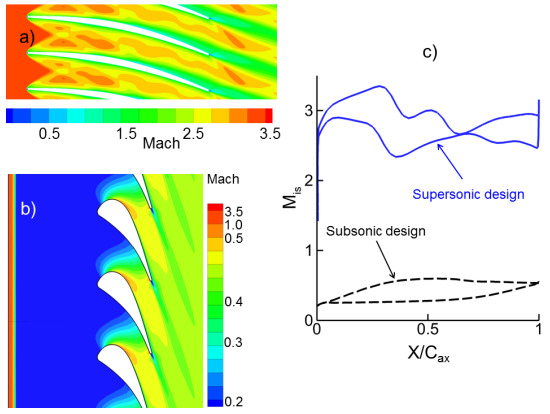

Figure 1: (a) Mach number iso-contour in a supersonic passage; (b) Mach number iso-contour in a subsonic passage; (c) Isentropic Mach number distribution along the two passages.

In the present paper, we present a new design methodology, which was evaluated with distinct design choices/objectives. The optimized geometries were ultimately assessed using Reynolds-Averaged Navier-Stokes calculations. Figure 2a shows the specific mass flow in function of the inlet Mach number. The supersonic operation allows three times more specific mass flow rate than the subsonic operation. Therefore, the frontal area of the turbine could be reduced, enabling more compact designs. Figure 2b depicts the main flow patterns that are present in a supersonic bladed passage. The blockage caused by the airfoil leading edges is responsible for the generation of a detached oblique shock wave that propagates through successive reflections along the passage. The shock waves cause an abrupt flow deviation, deceleration and entropy rise.

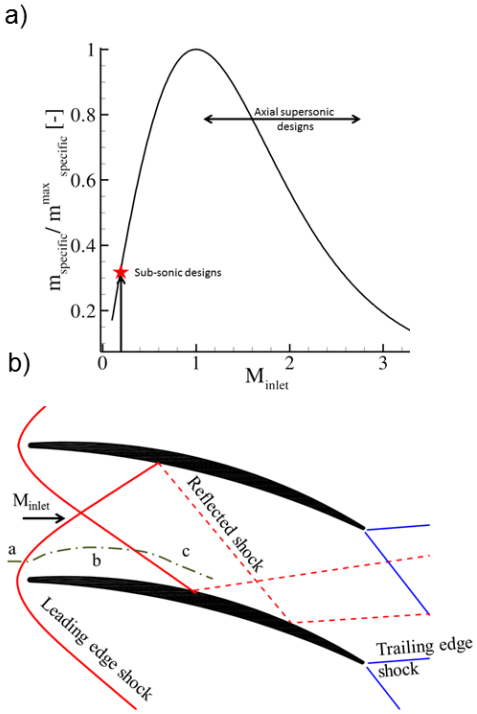

Figure 2: (a) Normalized specific mass flow rate at different inlet Mach number; (b) Flow pattern in a supersonic bladed passage.

1.1. Allowable Turning through Supersonic Passages

The possible turning across bladed supersonic passages is restrained by the supersonic starting. At the beginning of the operation of a supersonic fluid machine, the flow will need to transit from a subsonic to a supersonic condition. During this unsteady starting process, a normal shock wave travels across the passage separating the subsonic from the supersonic domain. If this shock wave cannot be swallowed through the throat, the passage becomes unstarted. This results in tremendous aerodynamic losses and forces that jeopardize the aerodynamic and mechanical operation of the fluid machine. Kantrowitz and Donaldson [1] demonstrated that when this starting normal shock stands momentarily in front of the passage, flow with the post-normal shock conditions (M_2), as defined by Equation 1, enter the passage.

$$M_2^2 = \frac{(\gamma - 1)M_1^2 + 2}{2\gamma M_1^2 - (\gamma - 1)} \quad (1)$$

In order to ensure a started configuration, the entire subsonic mass flow rate must be allowed to proceed

through the throat. Consequently, the area contraction of the converging passage must stand above the isentropic limit for the post shock flow conditions (at M_2). Equation 2 defines this isentropic area limitation, which is an exclusive function of the downstream subsonic Mach number (M2) and the fluid properties.

$$\frac{A_{out}}{A_{in}} = \frac{1}{M_{out}}\left(\frac{2(1+(\gamma-1)/2)M_{out}^2}{\gamma+2}\right)^{(-(\gamma+1)/(2(\gamma-1)))} \quad (2)$$

Substituting Equation 1 into Equation 2 we define the Kantrowitz limit that ensures a started operation for any area reduction with contraction ratios larger than what is computed by Equation 2. The cross sectional area (A) of a perfectly axial machine is specified by the throat times the channel height (H), the area can then be expressed in function of the pitch (g), and the outlet metal angle (): $A = gcos(\alpha)H$.

$$\frac{A_{out}}{A_{in}} = \frac{gH_{out}cos(\alpha_{out})}{gH_{in}cos(\alpha_{in})} \quad (3)$$
$$> \frac{1}{M_{out}}\left(\frac{2(1+(\gamma-1)/2)M_{out}^2}{\gamma+2}\right)^{(-(\gamma+1)/(2(\gamma-1)))}$$

For a given inlet condition, the maximum possible outlet angle to ensure a started configuration can be evaluated using Equation 3. Figure 3 plots the maximum possible throat angle for a certain inlet Mach number (M1) and inlet angle. Let us consider a fully inlet axial flow ($\alpha_{inlet} = 0$) when Mref = Minlet = 2.0. The maximum turning through this particular passage would be limited to 34 (deg.). In case the inlet Mach number would be augmented by 50%, a much higher turning could be achieved (α_{throat} could be 44 deg.). Conversely, for the same inlet Mach number, an increase of inlet flow angle allows an increase of the turning.

2. Numerical Flow Analysis Method

2.1. Leading Edge Shock Modeling

The leading edge shock waves were predicted using the empirical method developed by Moeckel [6] for inlet Mach numbers ranging between 1.1 and 3.5. Moeckel validated this approach for several leading edge shapes, including conical, spherical and projectile shapes. Fig. 4 sketches the shape of the leading edge shock wave, where point SB represents the sonic point on the airfoil surface while angle θ is the detachment angle for the incoming Mach number (M1). The detached shock approximates to an asymptotic

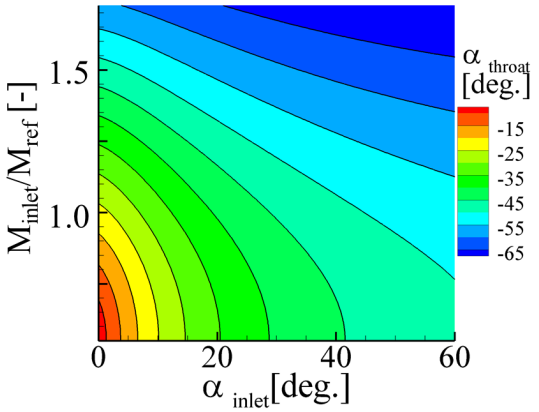

Figure 3: Maximum blade turning in function of the inlet angle (α_{inlet}) and inlet Mach number (M_{inlet}) according to the Kantrowitz limit.

line for large distances from the leading edge. Hence, Moeckel proposed the use of a simple curve with the characteristics of a hyperbola represented by Equation 4 to define the wave shape. 4

$$y_{shock} = \frac{(x_{shock}^2 - x_0^2)^{1/2}}{\mu} \quad (4)$$

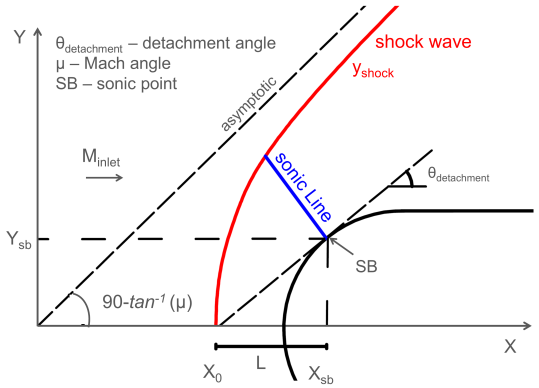

Figure 4: Prediction of the leading edge shock stand off distance (X_0), sonic line and wave shape.

In the current research the shape of the leading edge shock wave was compared with the CFD results at numerous inlet Mach numbers. Fig. 5a presents a good agreement between the predicted shock wave (the red line), and with the CFD results visualized with numerical Schlieren (in grayscale). Fig. 5b displays the entropy variation along the pitch-wise direction, across one passage (g, pitch) at three inlet Mach numbers. Most of the entropy is generated at the edge of the passage (Y = 0, or Y = g), where the leading edge shock

is normal. Higher Mach numbers result in steeper gradients along the pitch-wise direction and a larger overall entropy generation.

2.2. Method of Characteristics

The method of characteristics (MOC) is a meshless approach with reduced computational demand. The procedure is applicable to the solution of any second-order hyperbolic partial differential equation [7]. Hence, it is suitable to solve a steady, two dimensional and irrotational flow. The resulting system of three equations (Eq. 5-7) has three unknowns: Φ_{xx} Φ_{xy} Φ_{yy}. (Φ being the velocity potential).

$$\left(1-\frac{u^2}{C^2}\right)\Phi_{xx}+\left(1-\frac{v^2}{C^2}\right)\Phi_{xy}-\frac{2uv}{C^2}\Phi_{xy}=0 \quad (5)$$

$$d\Phi_x=\Phi_{xx}dx+\Phi_{xy}dy \quad (6)$$

$$d\Phi_y=\Phi_{xy}dx+\Phi_{yy}dy \quad (7)$$

The following step involves the determination of the direction along which the quantity Φ_{xy} is undetermined. These directions, known as characteristic lines represent the zone where the derivative of the velocity is discontinuous. The slope of this characteristics line at a certain point in the flow field can be determined with Eq. 8.

$$\left(\frac{dy}{dx}\right)_{char}=tan(\theta\pm\mu) \quad (8)$$

where μ is the Mach angle given by $\mu=sin^{-1}(1/M)$ and θ is the flow direction at the evaluated location. Eq. 8 stipulates that there are two characteristic lines passing through any point in the flow field. A left running characteristic that passes above the streamline ($\theta+\mu$ known as C_+) and a right running one that passes below the streamline ($\theta-\mu$ known as C_-). Along each of the characteristic line the flow properties are defined by the algebraic compatibility equations [7]:

$$\theta+\nu(M)=const=K_- \quad (along \quad C_-) \quad (9)$$

$$\theta-\nu(M)=const=K_+ \quad (along \quad C_+) \quad (10)$$

$\nu(M)$ is the Prandtl-Meyer function for a certain local Mach number (M). In Figure 6 a), the lattice of characteristics begins at the sonic line. The location and angle of this sonic line is obtained from the empirical method proposed by Moeckel [6] as previously described. In order to avoid the singularity at M=1 the flow velocity is set slightly above the sonic conditions (M=1.1). The calculations can then proceed in a marching manner.

- In point 3: Two characteristics of opposite family (originated from two known points: 1 and 2) intersect at point 3. Since the along the characteristic lines K_+ and K_- are invariant, the flow conditions in point 3 are retrieved by imposing: $(K_-)_3=(K_-)_1$ and $(K_+)_3=(K_+)_2$.
- In point 5: When a boundary condition such as a solid wall is intersected the flow direction should be equivalent to the wall curvature. Since, $(K_+)_4=(K_+)_5$ and $\theta_5=\theta_{wall}$ point 5 can be directly computed.
- Point 7: Represents the intersection with an upstream shock wave. The post shock conditions are estimated in an iterative manner by imposing $(K_-)_6=(K_-)_7$ and the oblique shock equations are use to find β_{shock} for the respective M_{inlet}, that respects this equality [7].

When a characteristic intersects a downstream shock wave the oblique shock equations are used to estimate the post shock conditions, from where the marching method can be reestablished. The entropy jump across the shock wave is evaluated at discrete locations.

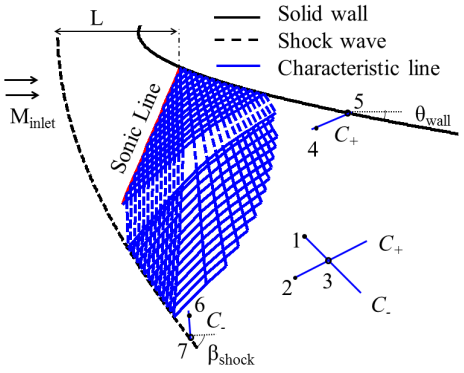

Figure 6: a) Different unit processes within the characteristic net of a 2D steady and irrotational flow. b) Prior and post shock flow properties at the intersection with a characteristic line.

2.3. Assessment of the Method of Characteristics

The proposed flow evaluation tool was compared with current Reynolds-average Navier Stokes equations (RANS) methodologies. In particular, we used the commercial solver CFD++ version 14.1 developed by Metacomp Technologies, Agoura Hills, USA. Figure 7 displays the geometry investigated and the lattice of characteristics across the supersonic passage. The dotted (red) symbols over the shock waves

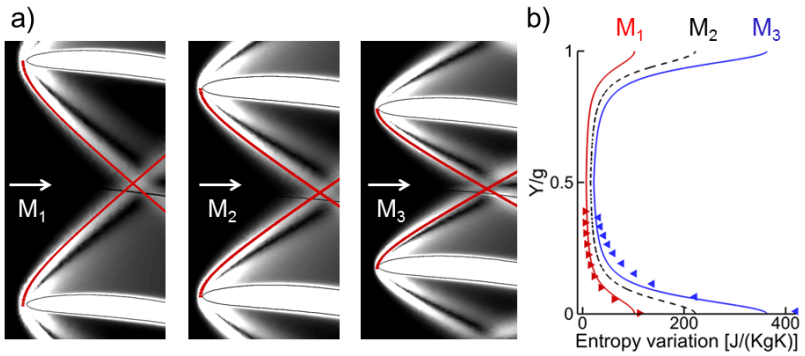

Figure 5: a) Numerical Schlieren at different inlet Mach numbers, red line represents the predicted/modeled leading edge shock wave, b) leading edge shock losses prediction along the pitch-wise direction at three inlet Mach numbers and comparison with CFD results.

represent the points where a characteristic crossed a shock wave. At these locations the oblique shock equations are used to compute the post shock flow conditions, and the entropy generation at each point. The area average entropy is then computed for each shock wave. The dots located at the passage outlet indicate where the outlet flow properties were evaluated. The numerical Schlieren visualization of the CFD results compares well with the present predictions.

Fig. 8 presents the isentropic Mach number distribution along the pressure side and suction side using three different approaches: The 2D method of characteristics, 3D Euler simulations, 3D Reynolds Averaged Navier-Stokes simulations. The three methods present similar values within 2% of the reference Mach number (M_{ref}) except in the rear suction side. At $x/C_{ax} = 0.75$ the leading edge shock wave from the neighboring airfoil impacts with the boundary layer and therefore a separation bubble appeared, which results in a smoother variation of the Mach number, as described by the RANS simulations. By contrast, both Euler and MOC were unable to capture such a shock-boundary layer interaction and therefore they present a very steep variation. The comparison of the Euler and RANS results allowed to quantify the viscous contribution to the entropy generation. In the present case, at high inlet supersonic conditions, the viscous effects only increased the total losses by 5%. In fact the prime contribution to the entropy generation was the shock loss, responsible for 70% of the total amount of entropy rises. The remaining 30% was split between profile, mixing and secondary loss. Consequently, in the present case, the method of characteristics, which neglects the viscous contribution, is an appropriate tool to optimize the airfoil profile, towards more efficient designs.

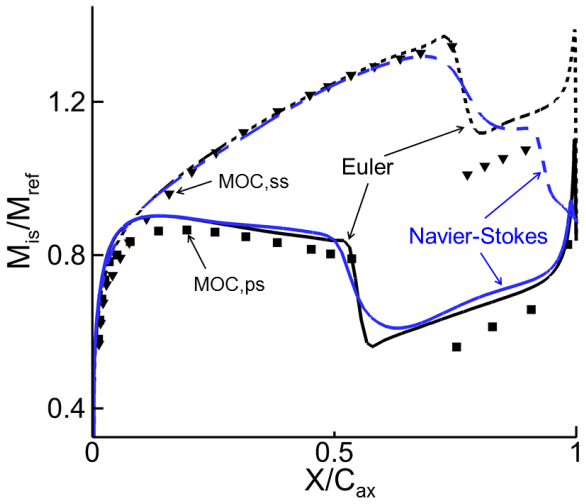

Figure 8: . Comparison of the isentropic Mach number distribution using the 2D Method of Characteristics (MOC), 3D non-viscous simulations (Euler), and 3D Reynolds Averaged Navier-Stokes simulations (RANS) at mid span.

Table 1 compares the total pressure ratio and the averaged outlet flow angle and Mach number computed with both methods. From all the quantities of interest, the outlet flow angle is the one with the highest absolute deviation, close to 2 deg.. The computational time for both methods is also compared, where the proposed methodology requires only 0.5% of the computational time of 3D RANS simulations. The viscous effects, such as the boundary layers and the additional mixing processes, are only present in the RANS simulation and therefore contribute to the 4.7% discrepancy between both methods.

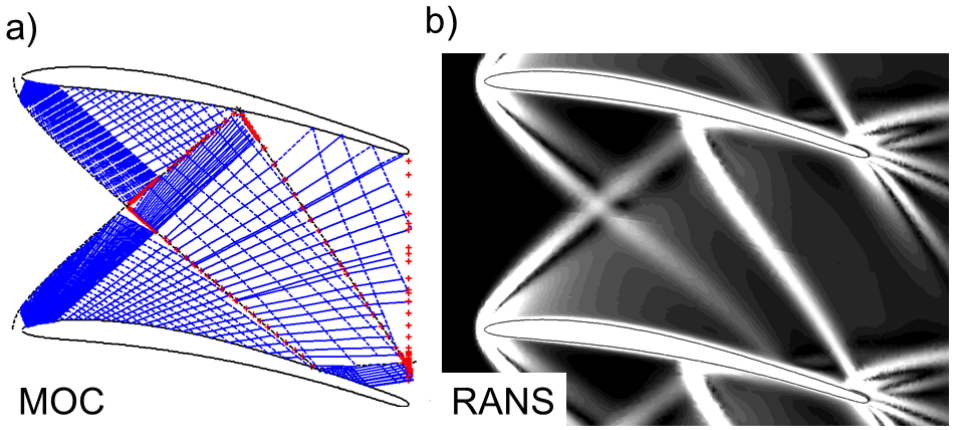

Figure 7: (a) Illustration of the characteristic net and the empirically predicted shock waves. (b) Numerical Schlieren visualization obtained with 3D RANS simulations.

	P_{0out}/P_{0in}	M_{out}	α_{out}	Time
Error	+4.7%	0.6%	2 [deg.]	-99.5%

Table 1: Comparison of the turbine outlet flow conditions computed with RANS and MOC simulations and the respective computational time

3. Supersonic Design Approach

3.1. Geometrical Parameterization

The design procedure begins by defining the chord to pitch ratio and inlet-outlet metal angles. The camber line is constructed with a quadratic Bezier curve, where the first and last control points are placed at the leading and trailing edge. Sharp leading edges are not allowed due to mechanical consideration. In order to reduce the leading edge shocks, several authors [8; 9] proposed wedge-type geometries. Figure 9 represents our proposed leading edge parameterization. The free design parameters are:

- the leading/ trailing edge thicknesses ($T_{1,le}/T_{1,te}$)
- the second leading/ trailing edge thickness ($T_{2,le}/T_{2,te}$)
- and the wedge leading/ trailing edge angle (α_{le}/α_{te})

The suction and pressure side are then built with Bezier curves. As illustrated in Figure 10, the control points are equally spaced in the axial direction and are then defined by its normal distance (thickness) to the camber line. The number of control points to define PS and SS, which is a free design parameter, is four in the present work. The proposed parameterization guarantees continuity in the local curvature of the leading up to the trailing edge of the airfoil.

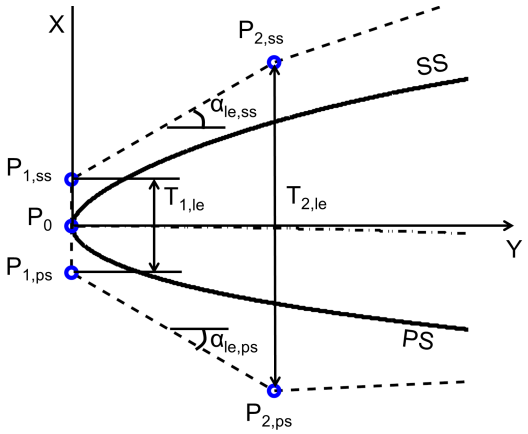

Figure 9: Leading edge parametrization

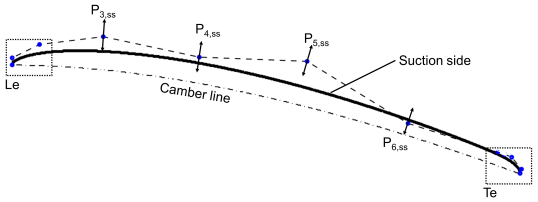

Figure 10: Suction side parametrization. Four control points can be modified by controlling its distance to the camber line

3.2. Optimization Approach

Evolutionary Algorithms (EA) were proposed and developed by Holland [10] in the 1970s. These algorithms follow the Darwinian theory of evolution, where several individuals form a population that evolves in time, following successive adaptations to the environment. The better fitted individuals have more likelihood to be retained (survive) and, thus, to reproduce. The population diversity and evolution is a consequence of mutation, crossover and finally of natural selection. In contrast to gradient based methods, evolutionary algorithms do not require having a continuous objective function, and additionally are more tolerant to noise [11]. Additionally, they are able to identify the global optima and avoid getting captured in a local minimum. The main drawback of evolutionary algorithms is the broad number of function evaluations required. However, as proposed in the present research, this issue can be addressed by using a fast flow evaluation tool to compute the objective function. The chosen optimization strategy is the differential evolution approach named DE/rand/1 proposed by Storn and Price [12]. This scheme is commonly used in turbomachinery applications [13] and the MATLAB code is openly available from Reference [14]. The weighting factor was set to F = 0.6, while the crossover probability to CR = 0.9. The differential evolution is a population based, stochastic function minimizer. As shown in 11, each time the method requires the evaluation of the objective function for a certain individual (in this case a certain passage), the method of characteristics is called within the optimization loop.

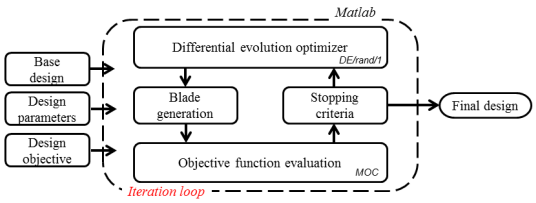

Figure 11: Flow chart with the design/ optimization process. Process begins with the definition of a base design, the design parameters and the design objective. Within the iteration loop, a differential evolution algorithm tries to find the most suitable design.

Several design options can be targeted depending on the chosen objective function. Additionally, several constrains can be imposed, such as a minimum mechanical thickness or a certain minimum flow turning. The original population is randomly generated based on an initial geometry, where 10 different design variables were free to be modified within the limiting bounds summarized in Table 2. The control points of the initial geometry correspond to the mean level of these values.

Parameter	Limits SS	Limit PS
α_{le} [deg.]	22.5 - 27.5	22.5 - 27.5
P_3 [mm]	1.04 - 2.4	-1.9 - 6.1
P_4 [mm]	1.29 - 4.9	-4.4 - 3.6
P_5 [mm]	1.6 - 8.6	-3.1 - 4.9
P_6 [mm]	-1.8 - 6.2	-3.2 - 4.8

Table 2: Bounded design space used by the optimizer

3.3. Results of the Optimization Procedure

3.3.1. Minimum loss

The first test case aimed the minimization of entropy production across the leading edge and reflected shock waves. Figure 12 displays the entropy evolution during the optimization process. After 36 iterations, the entropy generated by the supersonic passage was reduced by 15%. The initial and the optimized geometries were evaluated with a RANS solver. The 3D calculations demonstrated the superiority of the optimized geometry. The outlet entropy was reduced by 3.8 [J/(KgK)] representing a reduction of 6% of the total entropy production.

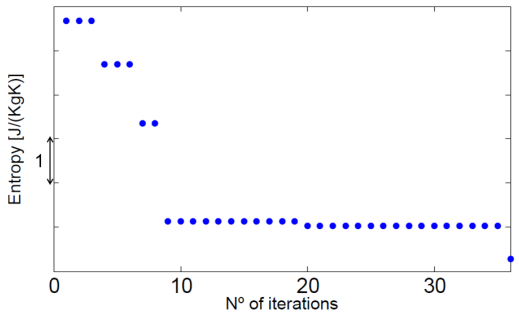

Figure 12: Entropy level at each iteration of the optimization process

Fig.13 depicts the initial geometry (solid line) and the final optimized design (dashed line). The first thickness ($T_{1,le}$) was not altered to ensure a minimum leading edge thickness. Instead, the wedge angle ($\alpha_{le,ss}$) was slightly reduced by 2.5 deg., and the second leading edge thickness ($T_{2,le}$) was lowered by 16%.

Fig. 14 plots the isentropic Mach number distribution along the suction and pressure side of the passage

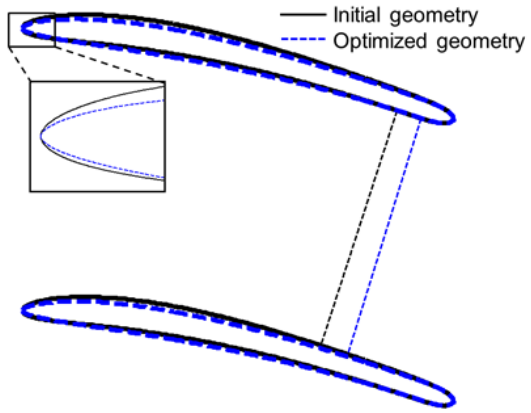

Figure 13: a) Illustration of the initial profile shape (solid line) and the optimized one (dashed line) for minimum shock losses with detailed illustration of the leading edge modification. b) Thickness variation along the axial direction for both geometries

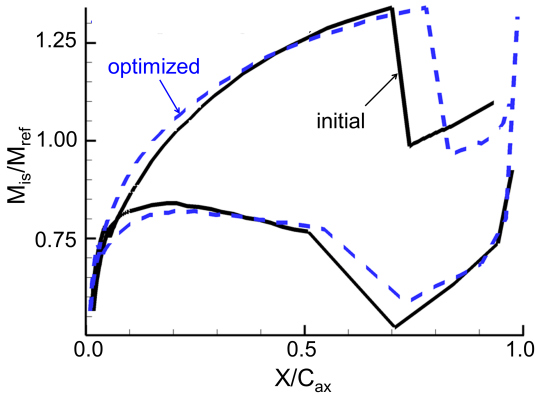

Figure 14: Isentropic Mach number distribution for the initial and the optimized geometry for minimum shock losses, $M_{ref} = 2.0$.

for both geometries. As illustrated in Fig.7, the right and left running shock waves generated at the leading edge impact at the suction and pressure side, respectively, as represented by the two discontinuities in the velocity field in suction and pressure side. The main differences between the initial and optimized designs are two-fold:

- A higher loading at the leading edge on the optimized geometry due to the greater flow acceleration on the suction side. The smoother acceleration along the pressure side helped to reduce the flow deceleration prior to the shock impact.
- Due to the smaller wedge angle of the leading edge, the shock waves have a higher inclination angle, which directly implies lower losses. As a consequence, the shock impact on the suction and pressure side occurs further downstream (10% of the suction side). Because the Mach number before the shock impingement is detrimental to the intensity of the reflected shock, the optimizer tried to reduce the upstream Mach number by modifying the suction side shape.

3.3.2. Imposed Mach Number Distribution

In this case the designer imposes a target velocity (or Mach number) distribution along the suction and pressure side of the passage. The optimizer will iteratively adjust the geometrical parameters and evaluate the overall difference in velocity between the target and the current profile. In this particular case the objective function is the minimization of such difference.

Fig. 15 a) displays the initial velocity profile (solid line) as well the target one (circular symbols). The target geometry was predefined to turn the flow more in the frontal part of the passage, where the boundary layer should be thinner, i.e., the target loading was increased in the front part. The rear suction side Mach number was decreased to reduce the pressure jump across the reflected shock. The optimizer required 15 iterations to obtain the optimized geometry displayed in dashed lines. Fig. 15 b) compares the geometry of the initial profile and the modified one. One can observe that due to the higher targeted loading after the leading edge, both the suction and pressure side presents a higher curvature level. Additionally, due to the higher intended Mach number after the shock interactions, both the suction and pressure side present a more pronounced concave shape, that enhances the flow acceleration in this region.

4. Conclusion

This paper presents a design methodology for two-dimensional supersonic internal flow passages. The proposed design methodology provides a detailed parameterization of the leading edge where the greater part of the shock losses is generated. Additionally, the use of Bezier curves assures the curvature continuity from the leading to the trailing edge. The performance of the supersonic passage is evaluated by the method of characteristics. This flow evaluation tool was then coupled with an optimization routine with different design targets, one minimizing the entropy generation and another imposing a certain of the velocity distribution across the passage as objective function. The accuracy of the design method was then assessed with

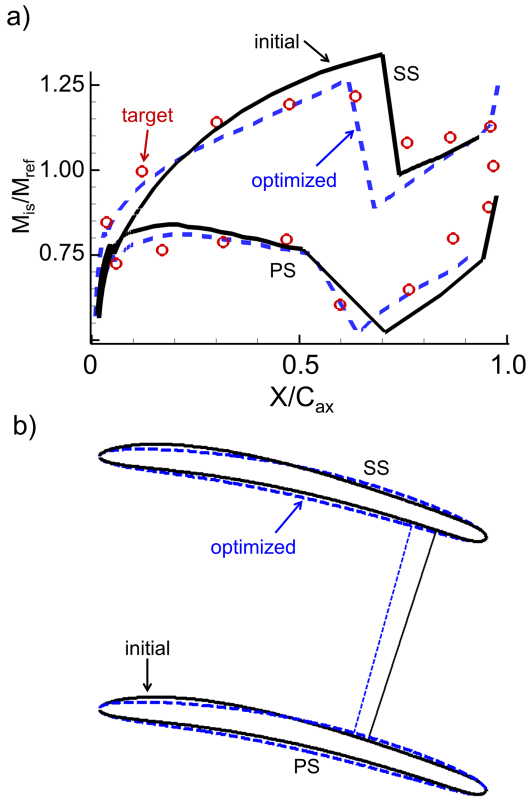

Figure 15: a) Representation of the target Mach number distribution and respective initial and the optimized geometry. b) Illustration of the initial profile shape and the optimized one that better fits the imposed Mach number distribution, $M_{ref} = 2.0$

3D Navier-Stokes solution, where the discrepancy between both methods was below 4.7% in predicting the losses. Additionally, the developed methodology requires only 0.5% of the Navier-Stokes computational time. This becomes of fundamental importance when using optimization algorithms, as implemented in the present work. The numerical study yielded a deeper insight on the physics of supersonic flow passages and their design optimization. The research provides the knowledge to guide designers of future ultra-compact fluid machinery.

Acknowledgments

This work was conducted at the von Karman Institute for Fluid Dynamics, Belgium in cooperation with Turbomeca, and the University of Orleans, France. This research was funded by a Ph.D. CIFRE grant of the French Agency ANRT.

This work was previously published on the Entropy journal (Entropy 2015, 17(8), 5593-5610; doi:10.3390/e17085593).

References

[1] A. Kantrowitz, C. Donaldson, Preliminary investigation of supersonic diffusers, Tech. rep., NACA (1945).

[2] A. Ferri, Perliminary analysis of axial-flow compressor having supersonic velocity at the entrance of the stator, Tech. rep., NACA RM L6G06 (1949).

[3] U. Wahlen, The aerodynamic design and testing of a supersonic turbine for rocket engine application, in: 3rd European Conference on Turbomachinery: Fluid dynamics and Thermodynamics, 1999.

[4] A. Verneau, Supersonic turbines for organic fluid rankine cycles from 3 to 1300 kw, in: von Karman Institute Lecture Series on "Small High Pressure Ratio Turbines", 1987.

[5] R. Binsley, J. Boynton, Aerodynamic design and verification of a two-stage turbine with a supersonic first stage, Journal of Engineering for Power 100 (1978) 197–202.

[6] W. E. Moeckel, Approximate method for prediction form and location of detached shock waves ahead of plane or axially symmetric bodies, Tech. rep., NACA (1921).

[7] J. D. Anderson, Modern compressible flow: with historical perspective, McGraw Hill Higher Education, 2004.

[8] S. Senoo, Development of design method for supersonic turbine aerofoils near the tip of long blades in steam turbines: Part 1overall configuration, in: ASME Turbo Expo 2012: Turbine Technical Conference and Exposition, American Society of Mechanical Engineers, pp. 355–365.

[9] R. Dvorak, P. Safarik, M. Luxa, D. Simurda, Optimizing the tip section profiles of a steam turbine blade, in: Proceedings of the ASME 2013 Turbine Blade Tip Symposium, 2013.

[10] J. Holland, Adaptation in natural and artificial systems, Generic, MIT (1975).

[11] T. Verstraete, Cado: a computer aided design and optimization tool for turbomachinery applications, in: 2nd Int. Conf. on Engineering Optimization, Lisbon, Portugal, September, pp. 6–9.

[12] R. Storn, K. Price, Differential evolution a simple and efficient heuristic for global optimization over continuous spaces, Journal of global optimization 11 (4) (1997) 341–359.
[13] S. Das, P. N. Suganthan, Differential evolution: a survey of the state-of-the-art, Evolutionary Computation, IEEE Transactions on 15 (1) (2011) 4–31.
[14] B. University, Differential evolution (de).
URL http://www1.icsi.berkeley.edu/ storn/code.html

Experimental investigation of roughness induced transition phenomena at hypersonic Mach numbers

Zdeněk Ilich

Aeronautics and Aerospace Department, von Karman Institute for Fluid Dynamics, Belgium, zdenek.ilich@vki.ac.be

Supervisor: Olivier Chazot

Professor, Aeronautics and Aerospace Department, von Karman Institute for Fluid Dynamics, Belgium, chazot@vki.ac.be

University Supervisor: Herbert Olivier

Professor, Shock Wave Laboratory, RWTH Aachen University, Germany, olivier@swl.rwth-aachen.de

Abstract

This report briefly outlines the proposed research of hypersonic boundary-layer transition with roughness effects. The preliminary description of the transition experiments is presented and corresponding requirements and challenges are pointed out.

Keywords: Hypersonic, boundary layer, transition, roughness.

1. Introduction and motivation

The boundary-layer transition from laminar-to-turbulent flow has been extensively investigated for several decades. Due to the high level of complexity, this problem still employs minds of researchers from theoretical, numerical and experimental branches. Yet, a lot of questions remain unanswered. This is especially true for regimes with large Mach numbers. The ability to accurate predict the transition process in the hypersonic regime is the crucial task for the design of space vehicles exposed to the atmospheric re-entry (Fig. 1). Indeed, the boundary-layer transition has a strong effect on the estimation of heat fluxes into a vehicle surface, which are typically large and may cause a structural damage. This fact identifies transition as one of the potential mission killers.

Despite the ongoing progress in the numerical modelling, an experiment is still an indispensable part of the aerodynamic research since it provides insight to physics of phenomena and data for a validation. On the other hand, experimental work is expensive through its requirements to facilities, operating costs, instrumentations and personnel. This is particularly true for hypersonics. In the light of this, the equipment of the VKI laboratory seems to be a unique occasion to perform the experimental investigation of the boundary-layer transition under conditions partially corresponding to the atmospheric re-entry. Instability and transition measurements on a smooth slender cone article have been already performed by Grossir (2015) in the VKI Longshot gun tunnel [1]. This work demonstrates ability of this facility to be used for such experiments.



Figure 1: The European space agency's IXV demonstrator successfully flown in 2015 (with kind permission of Mourad Cherfi)

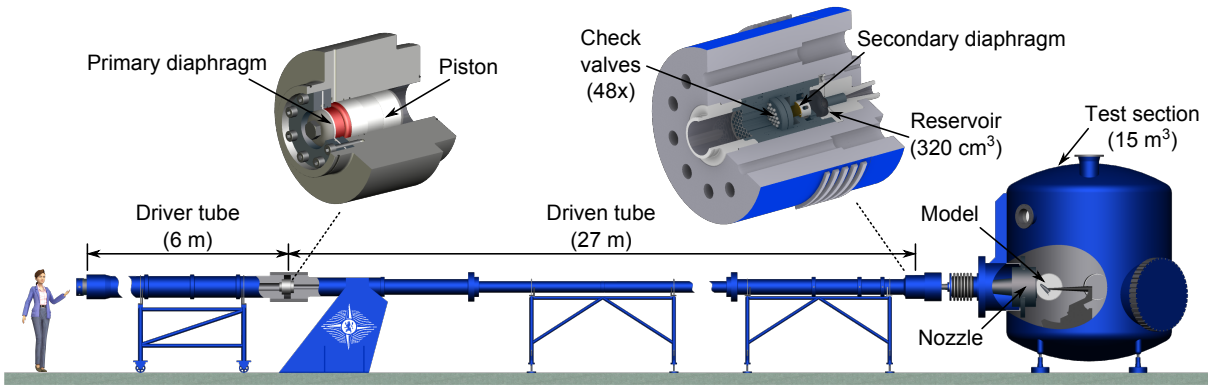

Figure 2: The VKI Longshot hypersonic gun tunnel

2. Objectives

It is well known that the transition process on a real vehicle configuration is influenced by a large number of parameters (e.g. wall curvature and temperature, nose bluntness, angle of attack (AoA), etc.). In case of atmospheric re-entry vehicles equipped with ablating thermal protection systems (TPS), these effects can be related to the ablation of a surface material. Indeed, the ablation leads to changes in a body surface toward a blunter shape, changes in surface roughness, blowing of pyrolysis gases into the boundary layer, chemical reactions and so forth. It is not possible to reproduce all these phenomena in a single ground facility. Since the VKI Longshot facility allows partial duplication of the re-entry conditions in terms of Mach and Reynolds numbers, the effects belonging to the aerodynamic part of the real flow can be investigated.

The present work will focus on the ablation-induced roughness and bluntness effects since it is still an open research problem. The numerical treatment of roughness increases computational cost and complexity significantly and therefore experimental results are clearly needed [2]. The idea is to utilize data from the VKI Plasmatron facility and available flight data (e.g. characterization of roughness) to setup transition experiments in the Longshot wind tunnel.

For the design of a space-vehicle TPS, the effects of roughness on the boundary-layer transition and turbulent heating are estimated through approximate engineering correlations and methods since no physic-based theory is currently available. The present work aims to obtain not only other data for such empirical correlations but mainly to provide information that could help to physically understand this transition process and instability behaviour inside the boundary layer.

3. Experiment – layout and challenges

3.1. Facility

The VKI Longshot hypersonic wind tunnel (Fig. 2) belongs to the gun tunnel family. It is designed to provide hypersonic short duration (about 20 ms) flows of large Reynolds numbers[1] whereas stagnation temperatures remain low enough not to have high-temperature gas effects such as dissociation of the test gas [1]. Thus, the Longshot wind tunnel is sometimes referred as a “cold hypersonic” facility. Nowadays, nitrogen is used as a test and driver gas. The state-of-the-art Longshot wind tunnel with its detailed description can be found in [1].

The quality of free-stream conditions, which should at least partially correspond to environments occurring during a flight, is of main interest for every test in wind tunnels. This is special true for boundary-layer transition experiments where an additional requirement of low disturbance levels appears. The effect of free-stream disturbances on the boundary-layer transition is well-known even though the receptivity mechanisms by which the disturbances enter a boundary layer are still poorly understood [3].

It is possible to distinguish three main origins (modes) of wind tunnel disturbance levels [4]: *vorticity* (velocity fluctuation), *entropy fluctuations* (temperature/entropy spottiness) and *pressure fluctuations* (often referred to as noise levels). The latter ones, which are believed to mainly come from a turbulent boundary layer developed on the nozzle wall, are usually identify to be dominant in supersonic and hypersonic wind tunnels ($M_\infty > 2.5$). Since the flight

[1] The final test conditions depend on initial parameters according a desired test regime and on a nozzle used. General range is $Re_{\infty,unit} = (3 - 13) \cdot 10^6$ /m.

noise levels are much lower than wind-tunnel ones [3], many efforts have been made to design "quiet" wind tunnels [5]. In conventional hypersonic ground-test facilities such as the VKI Longshot tunnel[2], it is necessary to characterize the disturbance levels as much as possible (i.e. their amplitude, spectrum and direction) in order to allow correct interpretation of the acquired data.

To improve the measurement of parameters that enter to the rebuilding method for determination of the free-stream properties [1], a new family of probes has been designed. In Fig. 3 A and B, the stagnation pressure and heat flux probes are presented, respectively.

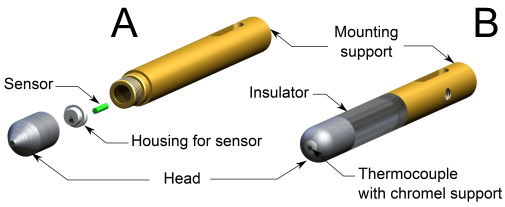

Figure 3: The stagnation probes of: A) pitot pressure B) heat flux

A new fast-response acoustic probe (similar to one in Fig. 3 A, but with a flush-mounted piezoelectric pressure sensor) aims to obtain a spectrum of free-stream noise by measuring pitot pressure fluctuation. The design details of the probes can be found in [6].

Nevertheless, it has been shown that the shock interaction with one of three types of disturbance waves creates all of them downstream from the shock wave [7], [8]. Thus the noise measured by the acoustic probe may not be the same as in the free-stream and the pitot pressure fluctuations alone are not sufficient to perform a modal analysis.

3.2. Roughness

Surface roughness may significantly influence the transition process such as leading from natural to bypass transition (eigenmode growth is bypass). In most cases the effect of roughness causes early boundary-layer transition when compared to a smooth surface [9][3].

The common division of roughness is depicted in Fig. 4 where two main classes can be distinguished: *isolated roughness* (each protuberance can be considered separately) and *distributed roughness* (patterned or sandpaper-like) [9], [11].

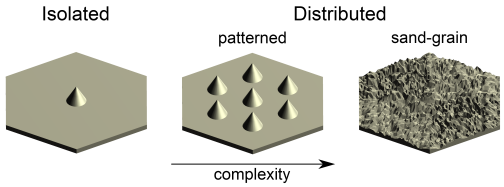

Figure 4: Types of roughness

An increasing complexity from left to right and corresponding difficulties of roughness characterization can be noticed. Whereas the isolated roughness can be described by height and shape of its elements (additionally by their spacing for the patterned one), the distributed sand-grain roughness has to be characterized statistically using various methods as an optical measurement of surface followed by topological analysis [12] or simply using a specific-size grid for sand grains.

The *ablation-induced roughness* has statistical character of the distributed "sand-grain" type with a relatively wide range of element heights [13] illustrated in Fig. 5. The characterization of the in-flight distributed roughness profile has significant uncertainty since the size of the roughness elements developed during the ablation is not constant over the surface at any instant in time. The typical ablating TPS of re-entry vehicles, such as those made using graphite or phenolic impregnated carbon ablator (PICA), first experiences a laminar-flow ablation at high altitudes (low Re). This leads to the formation of a distributed micro-roughness pattern, which may cause transition at lower altitudes as Reynolds number increases. The ablation-induced roughness is characteristic of the TPS material (its composition and variability) and fabrication process [12], [13].

3.3. Conceptual setup and measurement techniques

This work mainly builds on the previous experiments already carried out in the VKI Longshot facility [1] and also in the H3 hypersonic blowdown wind tunnel [14], [15]. They have used a 7° half-angle cone as a test article that has several advantages against a flat plate [1] and is considered to be used also for the present experiments.

The common measurement techniques used in the Longshot wind tunnel are flush-mounted *pressure*

[2]Noise levels have been estimated to be about 7% at the nozzle exit [1].

[3]However, recent direct numerical simulation (DNS) results followed by experimental investigation [10] have shown that 2D roughness elements may stabilize the second mode that is the most dominant in a hypersonic boundary layer and thus delay transition.

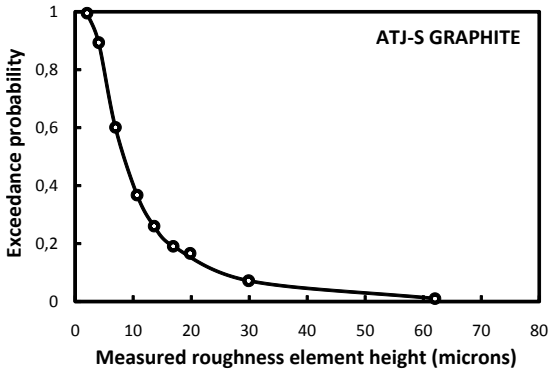

Figure 5: Roughness character of ablated graphite surface, replotted from [13]

transducers on the cone wall (wall pressure distribution and wall pressure fluctuations), *coaxial thermocouples* (wall heat fluxes - determination of the transition location) and the novel *LIF-based Schlieren method*. Except the Schlieren method, they all represent discrete measurements on the wall. Therefore methods that would allow either probing the boundary layer or measurement in continuous fashion in space (both with sufficiently high frequency[4]) are of main interest.

The implementation of standard techniques used in the H3 wind tunnel to the Longshot facility is not straightforward. The *Infrared thermography* allowing a determination of the wall heat fluxes requires a fast infrared camera in order to acquire more than one image during a run with decaying free-stream conditions. Such a camera is not currently available at the VKI[5]. The *Hot-wire anemometry* in hypersonic flow is sensitive to mass flux (ρu) and total temperature. It has been employed for free-stream characterisation in the H3 tunnel although the frequency response was limited up to 10 kHz [14]. Despite of some attempts with hot-wire probes made in the past [16], the implementation of this technique to the Longshot test environment remains a challenge.

Optical methods, which are in continuous progress, represent an interesting option of a fast non-intrusive measurement of wide range of flow properties. Unfortunately, they are very often cost-prohibitive. The most promising ones are FLDI (*Focused Laser Differential Interferometry*) [17], LIF (*Laser Induced Fluorescence*) [18] and DLAS (*Diode Laser Absorption Spectroscopy*) [19]. However, the latter is limited to experiments using CO_2 as the test gas (Martian reentries).

[4]The frequency of disturbances within the boundary layer (corresponding to the second mode waves) are measured by the wall pressure sensors to be about 200 kHz. Their initial development and harmonics are much higher [1].

[5]The currently available camera FLIR SC 3000 has an image frequency of 50/60 Hz non-interlaced at 14bit full resolution (320 × 240 pixels).

4. Conclusion

The present work aims to carry out the transition and stability measurement in the VKI Longshot tunnel in order to study roughness effects. Despite effort that has been made, this remains a challenging task through its requirements to precise characterization of free-stream conditions (including disturbance levels), manufacture the distributed roughness and measurement techniques that have to be involved.

References

[1] G. Grossir, Longshot hypersonic wind tunnel flow characterization and boundary layer stability investigations, Ph.D. thesis, von Karman Institute for Fluid Dynamics - Université Libre de Bruxelles (July 2015).

[2] C. H. Mortensen, Effects of thermochemical nonequilibrium on hypersonic boundary-layer instability in the presence of surface ablation or isolated two-dimensional roughness, Ph.D. thesis, University of California (2015).

[3] S. P. Schneider, Effects of high-speed tunnel noise on laminar-turbulent transition, Journal of Spacecraft and Rockets 38 (3) (2001) 323–333.

[4] S. R. Pate, Effects of wind tunnel disturbances on boundary-layer transition with emphasis on radiated noise: a review, in: 11th AIAA Aerodynamic testing conference, no. AIAA paper 1980-0431, 1980.

[5] I. E. Beckwith, Development of a high Reynolds number quiet tunnel for transition research, AIAA Journal 13 (3) (1975) 300–306.

[6] G. Grossir, Z. Ilich, Intrusive measurement techniques, Technical Note 3100, VKI (2015).

[7] H. S. Ribner, Spectra of noise and amplified turbulence emanating from shock-turbulence interaction, AIAA Journal 25 (3) (1987) 436–442.

[8] T. Schilden, W. Schröder, S. R. C. Ali, R. Radespiel, Interaction of acoustic and entropy waves with shocks, in: 44th AIAA Fluid Dynamics conference, no. AIAA paper 2014-2352, 2014.

[9] S. P. Schneider, Effects of roughness on hypersonic boundary layer transition, Journal of Spacecraft and Rockets 45 (2) (2008) 193–209.

[10] K. Fong, X. Wang, Y. Huang, X. Zhong, G. McKiernan, R. Fisher, S. Schneider, Second mode suppression in hypersonic boundary layer by roughness, AIAA Journal 53 (10) (2015) 3138 –3144.

[11] M. S. Holden, E. P. Mundy, M. MacLean, Heat transfer measurements to examine surface roughness and blowing effects in hypersonic flows, in: 49th AIAA Aerospace Sciences Meeting including the New Horizons Forum and Aerospace Exposition, 2011.

[12] D. C. Reda, M. C. Wilder, D. K. Prabhu, Transition experiments on slightly blunted cones with distributed roughness in hypersonic flight, AIAA Journal 50 (10) (2012) 2248–2254.

[13] R. B. Dirling, On the relation between material variability and surface roughness, in: 18th AIAA Structures, Structural Dynamics and Materials Conference, no. AIAA paper 1977-0402, 1977.

[14] D. Masutti, Ground testing investigation of hypersonic transition phenomenon for a re-entry vehicle, Ph.D. thesis, von Karman Institute for Fluid Dynamics - Technische Universiteit Delft (2013).

[15] M. K. Gkolia, Development of testing strategy for study of ablation-transition phenomena in hypersonic regime, PR 2015-18, von Karman Institute for Fluid Dynamics (June 2015).

[16] E. Backx, A study of the turbulent boundary layer at Mach 15 and 19.8 on the wall of a conical nozzle, Ph.D. thesis, von Karman Institute for Fluid Dynamics - KU Leuven (1975).

[17] N. J. Parziale, Slender-body hypervelocity boundary-layer instability, Ph.D. thesis, California Institute of Technology (May 2013).

[18] T. J. McIntyre, H. Kleine, A. F. P. Houwing, Optical imaging techniques for hypersonic impulse facilities, The Aeronautical Journal 111 (2007) 1–16.

[19] J. Meyers, Tunable diode laser absorption spectroscopy characterization of impulse hypervelocity co_2 flows, Ph. D. thesis, von Karman Institute for Fluid Dynamics - Université Libre de Bruxelles (2009).

MULTIPHASE FLOWS

The characterization of turbulence in high speed, compressible and complex industrial flows

Elissavet Boufidi

Turbomachinery and Propulsion Department, von Karman Institute for Fluid Dynamics, Belgium, boufidi@vki.ac.be

Supervisor: Fabrizio Fontaneto

Assistant Professor, Turbomachinery and Propulsion Department, von Karman Institute for Fluid Dynamics, Belgium, fontaneto@vki.ac.be

University Supervisor: Tony Arts

Professor, Head of Department, Turbomachinery and Propulsion Department, von Karman Institute for Fluid Dynamics, Belgium, iMMC, Université Catholique de Louvain, Belgium, arts@vki.ac.be

Abstract

This project aims to contribute to the understanding of turbulence mechanisms in complex industrial flows, by developing a measurement methodology that can be reliably applied in compressible, high-temperature flows, typical of aero engines. The methodology will be based on the use of Hot Wire Anemometry and Fast Response Aerodynamic Pressure Probes, and once established, will be applied to a number of test cases with realistic flow conditions.

Keywords: turbulence, turbomachinery, compressible flow, Hot Wire Anemometry, time-resolved pressure measurements

1. Introduction

Flow turbulence has a strong effect in many phenomena, like the boundary layer development on a surface, the convective heat transfer, the mixing of jets and the kinetics of chemical reactions. As a result, a rigorous characterization of flow turbulence (i.e. turbulence intensity, time and length scales, even spectrum) is important for many industrial applications. The importance of the whole turbulence spectrum for the prediction of turbulence effects in laminar boundary layer transition and heat transfer is illustrated by Mayle et al. [1]. In high pressure turbines (HPT) the freestream turbulence is one of the main parameters defining the heat transfer process and magnitude to the vanes [2]. In low pressure turbines (LPT) the freestream turbulence intensity and length scales are critical for the boundary layer transition and/or separation along the blade surfaces, and therefore for the components losses [3]. Relevant and accurate information on turbulent quantities in engine conditions is thus significant for the successful, reliable and cost-effective design of these components.

Considering the high specific cost of experimental facilities (manufacturing,operation), and the advances in computer performance, high-fidelity CFD is substituting more and more experimental investigations, becoming as well a widely used investigation tool. But the quality and validity of simulations strongly depend on the accuracy of the used boundary conditions, which from the point of view of turbulence normally coincide with imposing the turbulent kinetic energy and length scales at some borders of the computational domain [4; 5]. Since this information is rarely completely known, researchers often calibrate the turbulence inlet conditions on a specific experimental case, by systematically varying those values until the results of the simulation reach a good agreement with the experimental data. Two such examples can be found in [6], where Ong and Miller gradually change the inlet turbulence intensity to predict the spreading of a hot gas through a HPT vane passage, and in [7], where Aalburg et al. vary the inlet turbulence length scale to correctly predict the velocity distribution across the bend of a diffuser. Another source

of uncertainty often lies in the experimental test cases employed to calibrate the turbulence models: the typical laboratory cases usually used can be significantly different from the actual flows. As Tucker [4] states, "there is need for improved measurements with well defined boundary conditions that have Reynolds stress and even spectral information, at Reynolds and Mach numbers that connect with typically powerful turbomachinery systems". Such a lack has to be addressed to the limitations of established experimental techniques and the difficulties of their application to realistic flow conditions.

The goal of this research project is to strongly contribute to the understanding of real turbulence, such as in compressible, high speed, complex industrial flows. Experimental information that is not yet available today will be acquired to lead to the description of complex flow phenomena and provide a reliable experimental database of turbulent quantities for the validation of turbulence models and the definition of boundary conditions for high-fidelity CFD. This will be achieved through the development of a reliable experimental methodology, based on the use of Hot Wire Anemometry (HWA) and Fast Response Aerodynamic Pressure Probes (FRAPPs), which will allow measurements in engine flow conditions.

2. Measurement techniques

2.1. Hot Wire Anemometry

HWA is among the most popular techniques for measuring velocity fluctuations, and therefore turbulence, due to its high spatial resolution (wire diameters as small as 5 μm), high frequency response (up to 50 kHz) and good signal to noise ratio [8]. An example of a HWA probe is given in Figure 1. Despite its extended use for many years, (the first works date back to the beginning of the 20th century), its application to certain flow regimes like high subsonic and low density flows is still limited. The particularities and limitations in the application of HWA in different flows are well summarized in a review article by Stainback and Nagabushana [9], where the following flow regimes are distinguished (in terms of Mach number):

- subsonic incompressible flow ($M < 0.3$)
- subsonic compressible, transonic and low supersonic flow ($0.3 < M < 1.4$)
- high supersonic and hypersonic flow ($M > 1.4$)

within which one can distinguish the following subregimes (in terms of Knudsen number):

- continuum flow ($Kn < 0.01$)
- slip flow ($0.01 < Kn < 0.1$)
- free molecular flow ($Kn > 0.1$)

The Knudsen number is defined as the ratio of the molecular mean free path length to a characteristic length of the flow (the wire diameter in the Hot Wire case), and it expresses the deviation from the continuum flow.

In the general case, a Hot Wire is sensitive to density, velocity and total temperature fluctuations, and decoupling each effect from the others is not necessarily straightforward. It is well known that in incompressible ($M < 0.3$) and supersonic flows ($M > 1.4$), the sensitivities of the wire to density and velocity are equal, which facilitates the decoupling [9; 10; 11]. But this is not the case in the high subsonic and transonic ranges. Moreover, it has been observed by many researchers that in low density flows, the compressibility effect extends to a much lower value than the typical incompressibility limit of $M = 0.3$ [9]. Spangenberg [12] was the first to attribute this effect to gas rarefaction, since in low density flows, the Hot Wire often operates in slip flow, due to its small diameter. For those reasons, the HWA has been one of the main research tools in turbulence for either incompressible or supersonic continuum flows, but even today, few studies exist in high subsonic/transonic and subsonic slip flows.



Figure 1: Single-sensor hot-wire anemometer probe

A characteristic example highlighting the limitations of HWA in certain flow ranges is the case of LPTs. At engine representative conditions, the flow in the LPT features high subsonic Mach and low Reynolds number (especially at cruise conditions). Though turbulence measurements using HWA in low

speed testing (incompressible exit Mach numbers) have been performed by different researchers downstream of linear cascades (Hodson [13] and Graveline and Sjolander [14] between two adjacent blades, Satta et al. [15] accross the wake), no detailed turbulence investigation has been performed so far at engine representative conditions. This is due to the HWA limitations in high subsonic slip flows. Extensions to the applicability of HWA in such conditions have been proposed by researchers like Cukurel et al. [16] and Boyle et al. [17], but further studies are required before a general measurement methodology can be established.

2.2. Fast Response Aerodynamic Pressure Probes

The Hot Wire is a fragile instrument (wire diameter of the order of 5-10 μm) which can not withstand the non-clean environment and high temperatures of an aero-engine. This led to the development of Fast Response Aerodynamic Pressure Probes (FRAPPs) for time-resolved pressure measurements. An example of a FRAPP is given in Figure 2. When dealing with extreme measurement conditions, FRAPPs have demonstrated a high degree of robustness and a wide range of applicability [18; 19; 20]. Recent technology improvements allowed the creation of FRAPPs which can withstand temperatures above 900 °C, with a sensor bandwidth of 300 kHz, like the cooled FRAPP used by Mersinligil et al. in [21]. Nevertheless, in order to measure turbulence quantities a link must be established between time-resolved pressure and velocity fluctuations. The first attempt was realized by Heneka [22] already in 1983 using a four-hole wedge pressure probe. Since then, researchers have focused mainly on single or dual-sensor probes in order to reduce the measurement volume and increase the accuracy. Porreca et al. [23] demonstrated the use of dual-sensor probes in virtual four sensor mode to measure turbulence in incompressible flows. Wallace and Davies [24] proposed a methodology to relate velocity fluctuations to total pressure for incompressible and compressible flows, assuming isotropic turbulence. Anyway, this methodology is still neglecting density fluctuations, also in compressible flows, and it was only validated at ambient conditions, with the authors underlining that it should not be taken as a universal relation. The methodology of Wallace and Davies has since been used by various researchers like Persico et al. [25] and Lengani et al. [26] in turbomachinery flows, providing satisfying qualitative results, but without verifying the validity of the assumptions at their conditions.



Figure 2: Single-sensor fast response aerodynamic pressure probe

3. Research Methodology

For the reasons previously stated (robustness, high frequency response), FRAPPs (eventually cooled) are the appropriate tool to use in real-life flows. But the link between fluctuating velocities (turbulence) and time-resolved pressures has only been demonstrated in very particular environments. Its extension to high speed and low density flows is needed, using HWA as a reference tool, to give access to a much better and more accurate definition of turbulence characteristics in real life conditions. In this context, the HWA technique should also be thoroughly reconsidered to enhance its application to high subsonic/transonic and low density flows. A versatile calibration facility will be developed, that will operate in a wide range of subsonic Mach numbers and sub-atmospheric pressures and that will be able to set independently the velocity, density and total temperature of the flow. This will allow to experimentally define the sensitivities of the HW to each flow parameter and extend already existing, but limited, calibration procedures to retrieve the true velocity fluctuations in high subsonic and low density flows. Efforts will be placed on the facilitation of this retrieval, either by different probe designs or processing methodologies. This is particularly important in low density flows, where the sensitivity to velocity is significantly lower compared to the sensitivity to density, which further complicates the velocity fluctuations decoupling. In order to reduce the sensitivity to total temperature, the adoption of new materials might allow the sensor operation at higher temperatures. The calibration facility will also be used for the investigation of the link between pressure and velocity fluctuations, using HWA as a reference tool. For this purpose, a research probe will be designed at this stage. The latter will be equipped with both a HWA and a FRAPP sensor, allowing for synchronous acquisitions in the same measurement point of the flow field. The different methodologies

proposed so far, will be then examined in compressible and low density conditions and their applicability range will be defined. Ideally, an extension will be added to the already-existing methodologies. The effect of the anisotropy of turbulence on the correlations will also be examined and assessed.

Once a reliable measurement methodology with a defined application range has been established for both measurement techniques (HWA, FRAPPs), tests will be performed behind the T106 LPT linear cascade in the S1/C wind tunnel of the von Karman Institute for Fluid Dynamics (VKI). Such a facility is able to reproduce engine representative LPT conditions (low Reynolds and high Mach number), with a turbulence topology much closer to reality, thanks to the simulation of incoming wakes from preceding bladerows. Since the flow temperature is ambient and since it is a clean wind tunnel flow, HWA can still be applied. This will provide the opportunity to further validate the link between velocity and pressure fluctuations in conditions close to reality. Moreover, this test case is of special interest to a number of researchers dealing with high fidelity CFD. The T106 airfoil is a well-studied test case, but since no detailed turbulence investigation exists in the wake of a LPT blade in high speed testing, this study will already constitute a significant contribution. Finally, the FRAPP measurement methodology will be extended to real engine flows. Considering the current capabilities of cooled FRAPPs [21], high temperature flows can also be addressed. This will provide the opportunity to carry out a turbulence analysis at the exit of a combustion chamber or an afterburner, where very limited experimental data (if any) exist due to the harsh conditions.

4. Conclusion

The principal motivation for this research project is to acquire and analyze the turbulence characteristics in complex flows, where this kind of information is limited or even not-existent today. This will provide a deeper insight in complex flow phenomena which are still interpreted based on data acquired for simplified configurations and flow conditions. Compressible, high speed and high temperature flows are among those complex cases and will be targeted in the present project. Due to the complex nature of turbulence, demanding measurements are required to obtain sufficient information. High frequency response, high spatial resolution and sufficient measurement time are necessary. The lack of experimental data on turbulence in environments such as real turbomachinery and combustor flows is mainly due to the limitations of suitable experimental techniques.

References

[1] R. E. Mayle, K. Dullenkopf, A. Schultz, The Turbulence that Matters, Journal of Turbomachinery 120 (1998) 402–409.

[2] T. Arts, M. Lambert de Rouvroit, Aero-Thermal Investigation of a Two-Dimensional Highly Loaded Transonic Turbine Nozzle Guide Vane: A Test Case for Inviscid and Viscous Flow Calculations, Journal of Turbomachinery 114 (1) (1992) 147–154.

[3] R. E. Mayle, The Role of Laminar-Turbulent Transition in Gas Turbine Engines, Journal of Turbomachinery 113 (1991) 509–536.

[4] P. Tucker, Trends in Turbomachinery Turbulence Treatments, Progress in Aerospace Sciences 63 (2013) 1–32.

[5] J. Denton, Some Limitations of Turbomachinery CFD, in: ASME Turbo Expo 2010: Power for Land, Sea and Air, no. GT2010-22540, Glasgow, UK, 2010.

[6] J. Ong, R. Miller, Hot streak and vane coolant migration in a downstream rotor, Journal of Turbomachinery 134 (5) (2012) 051002.

[7] C. Aalburg, A. Simpson, M. Schmitz, V. Michelassi, S. Evangelisti, E. Belardini, V. Ballarini, Design and Testing of Multistage Centrifugal Compressors with Small Diffusion Ratios, Journal of Turbomachinery 134 (4) (2012) 041019.

[8] H. H. Bruun, Hot-Wire Anemometry: Principles and Signal Analysis, Oxford University Press, 1995.

[9] P. Stainback, K. Nagabushana, Review of Hot-Wire Anemometry and the Range of Their Applicability, in: A. F. E. Division (Ed.), Third International Symposium on Thermal Anemometry, Vol. 167, 1993, pp. 93–134.

[10] L. S. G. Kovazsnay, Turbulence in Supersonic Flow, Journal of the Aeronautical Sciences 120 (10) (1953) 657–674.

[11] M. Morkovin, Fluctuations and hot-wire anemometry in compressible flows, AGARDograph 24 (1956).

[12] W. G. Spangenberg, Heat-Loss Characteristics of Hot-Wire Anemometers at Various Densities in Transonic and Supersonic Flow, Technical Note 3381, NASA (1955).

[13] H. P. Hodson, Measurements of Wake-Generated Unsteadiness in the Rotor Passages of Axial Flow Turbines, Journal of Engineering for Gas Turbines and Power 107 (1985) 467–476.

[14] J. R. S. Graveline, S. A. Sjolander, A spectral study of a moderately loaded low-pressure turbine airfoil part 1: Identifying frequencies affecting by-pass transition, Journal of Turbomachinery 135 (2013) 041016.

[15] F. Satta, M. Ubaldi, P. Zunino, Unsteady Inflow Effects on the Wake Shed from a High-Lift LPT Blade Subjected to Boundary Layer Laminar Separation, Journal of Thermal Science 21 (97-108).

[16] B.Cukurel, S. Acarer, T. Arts, A Novel Perpesctive to High-Speed Cross-Hot-Wire Calibration Methodology, Experiments in Fluids 53 (4) (2012) 1073–1085.

[17] R. Boyle, B. L. Lucci, Aerodynamic performance and turbulence measurements in a turbine vane cascade, in: ASME Turbo Expo 2002: Power for Land, Sea and Air, no. GT2002-30434, Amsterdam, The Netherlands, 2002.

[18] A. J. L. Ainsworth, R. W., J. J. M. Batt, The Development of Fast Response Aerodynamic Probes for Flow Measurements in Turbomachinery, Journal of Turbomachinery 117 (4) (1994) 625–634.

[19] P. Kupferschmied, P. Koppel, W. Gizzi, C. Roduner, G. Gyarmathy, Time-Resolved Flow Measurements with Fast-Response Aerodynamic Probes in Turbomachines, Measurement Science and Technology 11 (2000) 1036–1054.

[20] C. H. Sieverding, T. Arts, R. D?nos, J. F. Brouckaert, Measurement Techniques for Unsteady Flows in Turbomachines, Experiments in Fluids 28 (2000) 285–321.

[21] M. Mersinligil, J. Desset, J. Brouckaert, High-Temperature High-Frequency Turbine Exit Flow Field Measurements in a Military Engine with a Cooled Unsteady Total Pressure Probe, in: Proceedings of the Institution of Mechanical Engineers, Part A: Journal of Power and Energy, Vol. 225, 2011, pp. 954–963.

[22] A. Heneka, Instantaneous Three-Dimensional Flow Measurements with a Four-Hole Wedge Probe, in: Proceedings of 7th Symposium on Measuring techniques for Transonic and Supersonic Flow in Cascades and Turbomachinery, Aachen, Germany, 1983.

[23] L. Porreca, M. Hollestein, A. I. Kalfas, R. S. Abhari, Turbulence Measurements and Analysis in a Multistage Axial Turbine, Journal of Propulsion and Power 23 (2007) 227–234.

[24] J. D. Wallace, M. R. D. Davies, Turbulence Measurement with a Calibrated Pitot Mounted Pressure Transducer, in: Proceedings of 13th Symposium on Measuring techniques for Transonic and Supersonic Flow in Cascades and Turbomachinery, Zurich, Switzerland, 1996.

[25] G. Persico, P. Gaetani, B. Paradiso, Estimation of Turbulence by Single-Sensor Pressure Probes, in: Proceedings of the XIX Biannual Symposium on Measuring Techniques in Turbomachinery Transonic and Supersonic Flow in Cascades and Turbomachines, 2008.

[26] D. Lengani, B. Paradiso, A. Marn, A Method for the Determination of Turbulence Intensity by Means of a Fast Response Pressure Probe and its Application in a LP Turbine, Journal of Thermal Sciences 21 (2012) 21–31.

Turbulent heat transfer of separated flows at low Prandtl numbers

Sophia Buckingham

Environmental and Applied Fluid Dynamics Department, von Karman Institute for Fluid Dynamics, Belgium, sophia.buckingham@vki.ac.be

Supervisor: Tamas Regert

Associate Professor, Environmental and Applied Fluid Dynamics Department, von Karman Institute for Fluid Dynamics, Belgium, tamas.regert@vki.ac.be

University Supervisors: Yann Bartosiewicz, Grégoire Winckelmans

Professor, Institute of Mechanics, Materials and Civil Engineering, Université catholique de Louvain, Belgium, yann.bartosiewicz@uclouvain.be, gregoire.winckelmans@uclouvain.be

Abstract

The turbulent heat transfer of low Prandtl fluids is investigated in separated flows. Large-eddy simulations of the flow over a backward-facing step aim at producing reference data that can be used to validate turbulent heat transfer models that are adequate to these types of fluids. The temperature perturbation method is used to generate turbulent inflow conditions for LES/DNS simulations in OpenFOAM. A gas mixture experiment is planned in order to validate the LES at a moderately low Prandtl number and help improve our understanding of the physics involved.

Keywords: low Prandtl fluids, turbulence generation, large eddy simulation, turbulent heat transfer modeling.

1. Motivation

A major challenge in the CFD analysis of the reactor pool flow, is the modeling of the turbulent heat transfer in the low Prandtl number LBE coolant. The classical Reynolds analogy, which forms the basis of the turbulent Prandtl concept in CFD simulations, fails to correctly predict the local heat transfer of these fluids. This leads to incorrect predictions of the temperature field and thus thermal stresses, which may jeopardize the structural integrity of the reactor components. Up to now, studies on models for liquid metal heat transfer have mainly relied on developed flow in confined channels for validation. These are however, not representative of the turbulent thermal behavior of pool flows. In order to obtain relevant results with CFD models, specific research on this topic is necessary.

2. Objectives

To compensate for this lack of validation data, the aim of this project is to generate a Large-Eddy Simulation (LES) validation database for non-confined separated flows at low Prandtl numbers. To represent the complex flow that is present in pool flows, the test case chosen for this is the backward-facing step (BFS) shown in Fig. 1, as it exhibits a detached shear-layer and a recirculation zone.

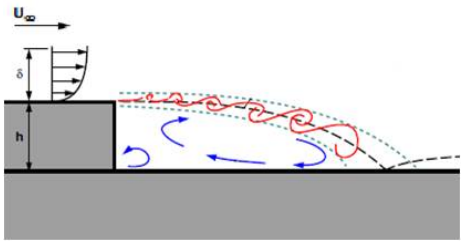

Figure 1: Test case: backward-facing step

To fulfill this objective, firstly an efficient wall-resolved LES of the BFS should be set-up to provide reference data across a range of low Prandtl numbers. A typical Reynolds number based on the step height of about 5000 will be simulated for the computational

cost to remain reasonable.

Secondly, the aim is to perform measurements of a moderately low Prandtl number gas over this same BFS configuration. A gas mixture of Helium and Xenon has been selected, enabling to reach values from 0.67 to 0.2 [1].

3. Methodology

3.1. Gas mixture experiment

Introducing additional transport equations requires determining new model coefficients. As heavy liquid metals (HLM) are opaque, the well-developed experimental techniques used in transparent fluids are not applicable. Among the measurement methods adapted to HLM experiments, none of them is able to measure simultaneously fluctuating velocities and temperatures. These correlated quantities are precisely the information required to calculate Reynolds stresses and turbulent heat fluxes that appear in the modeling equations. A transparent low Prandtl number gas flow experiment provides the solution.

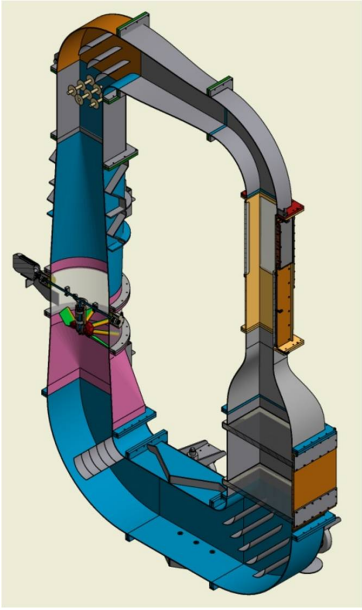

Figure 2: He-Xe wind tunnel design

A closed-loop sealed wind tunnel shown in Fig. 2 is being designed at VKI to accommodate wall bounded test cases. One of the test sections will be specifically prepared to test the BFS in a non-confined configuration. Simultaneous measurements of velocity and temperature will be performed using a Helium-Xenon gas mixture over the BFS. Several measurement techniques are under investigation among which the possibility of using hot-wire anemometry in constant temperature mode. Converting the calibration data acquired across the temperature and velocity range of interest into Reynolds as function of Nusselt number, provides the unknown wire temperature needed to deduce the wire's sensitivities to velocity and temperature. From a sensitivity analysis, it should be possible to deduce fluctuating quantities.

Other techniques that would combine for instance Laser-Doppler Velocimetry with fast-response temperature sensors are also of interest, but the effect of the seeding on the gas properties and in particular its Prandtl number should be carefully considered.

3.2. LES/DNS simulation of a BFS

The proper specification of turbulent inflow conditions for both LES and Direct Numerical Simulation (DNS) remains a considerable challenge and is not possible at the current state-of-the-art. As a result, the flow needs to adjust until equilibrium is reached. The key requirement for a turbulent inflow technique is to be as efficient as possible in order minimize this recovery length and thus reduce the computational cost.

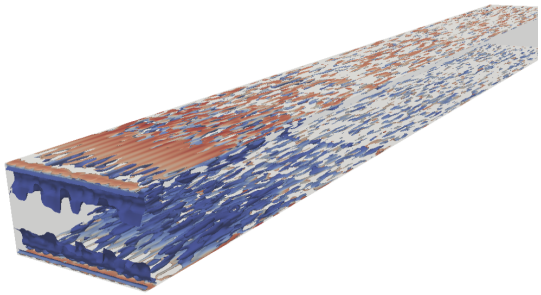

Figure 3: Buoyancy induced turbulent structures

An alternative to the classical velocity perturbations is the inclusion of random temperature perturbations. This technique relies on the principle that the seeded perturbations can generate turbulence through local buoyancy effects. The cell perturbation method developed for atmospheric flows [2] applies pseudo-random perturbations to tridimensional cells of grid points, distributed over a buffer region that extends over three streamwise cells all along the inlet boundary. In this work, the cell perturbation method is implemented in the incompressible buoyant solver of OpenFOAM. Reference data is first obtained for a periodic channel flow, before testing the technique on

an inlet/outlet channel. Preliminary results shown in Fig. 3 depict the creation of three-dimensional motions that eventually form turbulent structures.

Ongoing work consists in optimizing the parameters that govern the temperature perturbation process. To minimize the recovery length, these should be adjusted to provide an amount of energy comparable to the mechanical energy that is naturally produced by turbulence. The results will be compared to techniques that are more commonly used to generate turbulent inflow conditions, such as a synthetic digital filter method [3]. The development distance is estimated based on the recovery length of the wall shear stress. Mean velocity profiles and Reynolds stresses are compared with the periodic results obtained previously.

3.3. Turbulent heat transfer modeling

The limitations of the commonly used eddy diffusivity approach have become more evident especially when applied to model low Prandtl fluids. In an effort to validate more accurate closures within CFD codes used for innovative reactors, the following more advanced turbulent heat transfer models have been previously implemented in OpenFOAM and will be confronted to the LES data generated over the BFS.

The Algebraic-Heat Flux Model (AHFM) is equipped with an algebraic formulation for the turbulent heat flux [4]. This formulation is function of the temperature variance for which a separated transport equation is solved. The latest model correlations proposed as an outcome of the THINS project [5] will be incorporated in the model, bringing significant improvements in the heat transfer predictions across a wide range of flow regimes.

The use of a four equation model [6] involves two additional transport equations for both the temperature variance and its dissipation. Further calibration of the default constants is required in different flow conditions.

Finally, these models could be used in conjunction to appropriate near-wall modeling. LES channel flow simulations performed at low Prandtl numbers up to a friction Reynolds number of 2000 [7], have shown that the temperature profile exhibits a certain level of universality. This new temperature wall function will be tested, in order to reduce the simulation cost and allow for more affordable RANS simulations at reactor scale.

Acknowledgments

This research work is funded by the European Horizon 2020 project MYRTE (662186).

References

[1] J. Liu and G. Ahlers, Rayleigh-Benard convection in binary-gas mixtures: Thermophysical properties and the onset of convection, Phys. Rev. 55 (6) (1997) 6950–6968.

[2] D. Munoz-Esparza, B. Kosovic, B. Mirocha and J. van Beeck, Bridging the transition from mesoscale to microscale turbulence in numerical weather prediction models, Boundary-Layer Meteorology 153 (035102) (2014) 409–440.

[3] Z. T. Xie and I. P. Castro, Efficient generation of inflow conditions for large eddy simulation of street-scale flow, Flow Turb. Combust 81 (2008) 449–470.

[4] S. Kenjeres, S. B. Gunarjo and K. Hanjalic, Contribution to elliptic relaxation modelling of turbulent natural and mixed convection, Int. J. Heat Fluid Flow 26 (4) (2005) 569–586.

[5] A. Shams, F. Roelofs, E. Baglietto, S. Lardeau, S. Kenjeres , Assessment and calibration of an algebraic turbulent heat flux model for low-Prandtl fluids, Int. J. of Heat and Mass Transfer 79 (2014) 589–601.

[6] S. Manservisi and F. Menghini, A CFD four parameter heat transfer turbulence model for engineering applications in heavy liquid metals, Int. J. of Heat and Mass Transfer 69 (2014) 312–326.

[7] M. Duponcheel, L. Bricteux, M. Manconi, G. Winckelmans, Y. Bartosiewicz, Assessment of RANS and improved near-wall modelling for forced convection at low Prandtl numbers based on LES up to Re_τ =2000, Int. J. of Heat and Mass Transfer 75 (2014) 470–482.

Splash plate nozzle design optimization

De Cock Nicolas

Environmental and Applied Fluid Dynamics Department, von Karman Institute for Fluid Dynamics, Belgium, nicolas.decock@vki.ac.be

Supervisor : Vetrano M. Rosaria

Assistant Professor, Environmental and Applied Fluid Dynamics Department, von Karman Institute for Fluid Dynamics, Belgium, vetrano@vki.ac.be

University Supervisor : Lebeau Frédéric

Professor, Gembloux Agro-Bio Tech, ULg, Belgium, f.lebeau@ulg.ac.be

Abstract

Optimization of the droplet spectra of the agricultural spray may increase the spray application efficiency. The optimal spray would contain only the most efficient droplets in term of speed and size. Therefore, this paper is presenting the first steps of the design of a narrow span nozzle in order to produce an optimized spray. The starting geometry is a splash plate nozzle with a disk ending with structures (i.e. tooth, grooves, and needles) that would separate the liquid sheet into jets. These jets would be in the Rayleigh regime which has the advantage of producing narrower droplet spectra than liquid sheet break-up. The present project aims to design a hydraulic nozzle producing a spray with a narrow drop size distribution in order to increase the agricultural spray application efficiency. In the present paper the first project steps are presented.

Keywords: Agricultural spray, drop size distribution, hydraulic nozzle, Rayleigh break-up, CFD

1. Introduction

1.1. Context

Spray application is a key process in crop protection to ensure that high yields are obtained while minimizing adverse environmental and health impacts of plant protection products. During this process, the agricultural mixture is fragmented by passing through a nozzle generating a cloud of droplets.

It has been proved that the spray droplet size distribution significantly affects the global deposition process efficiency [1]. Indeed, smaller droplets have a higher drift potential [2] leading to potential product losses in air, water and soil [3]. Whilst, larger droplets, with a higher kinematic energy, are more prone to splash while impacting the target and then may reduce the target retention efficiency [4] (Fig. 1). Therefore, an ideal agricultural spray would include only medium size droplets, i.e. ranging between 200 and 300 μm for weed treatment. The droplet sizes and speeds constitutive of a spray result from the interactions between the physical properties of the liquid, the operating conditions and the nozzle geometry [5]. During the past decades, multiple researches have been performed on the effect of the liquid physical properties [6] [7] [8] as well as the nozzle type [9]. The need of a narrow drop size distribution stimulated the development of devices for spray generation using centrifugal forces such as the rotary atomizers. These atomizers produce a significantly narrower drop size distribution than the hydraulic nozzles usually used in field treatment [10]. Despite the quality of the produced sprays, the rotary atomizers are not hardly used for field spray application because of their bulkiness. However, they remain an interesting study case as a way to produce sprays with narrow drop size distribution. The contrast in the drop size distribution between the hydraulic nozzles and the rotary atomizers derives from the different breakup modes occuring with the two atomizers types. Rotary atomizers produce round liquid jets of uniform sizes at the exit of the rotating part, then these jets break in droplets by the Rayleigh-Plateau mode

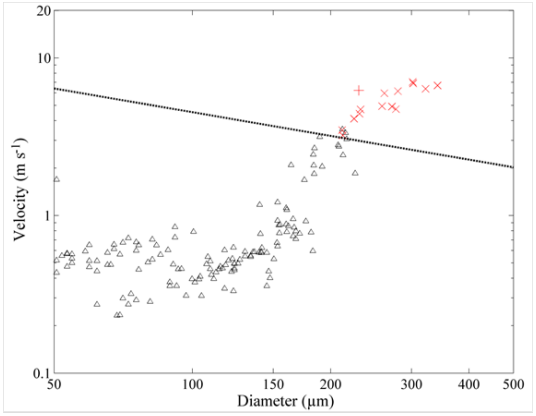

FIGURE 1: Behavior of the droplets while impacting a superhydrophobic surface in function of their diameter and velocity [4]. The triangles and the crosses correspond to droplet adhesion and droplet splashing respectively.

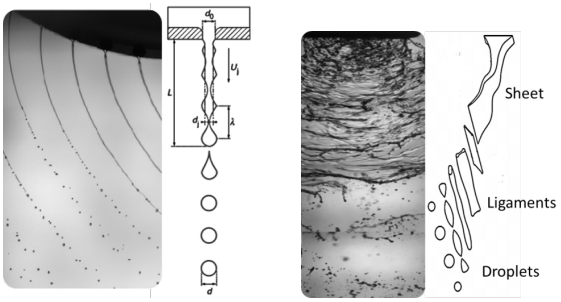

(a) Capillary breakup (b) Sheet breakup

FIGURE 2: Ilustration of the two breakup modes occuring at the exit of a rotary atomizer (a) and a hydraulic nozzle (b).

(Fig. 2a). Whilst, the hydraulic nozzles produce a liquid sheet that break-up in ligaments which, in turn, break-up in to droplets of various sizes (Fig. 2b).

1.2. Rayleigh-Plateau Breakup

The Rayleigh-Plateau breakup regime occurs when a cylindrical jet is discharged into gas with a low inertia in respect with its capillary forces. Therefore the Weber number is used as criterion to set the limits of the Rayleigh-Plateau regime [11]. The We_L has to be higher than 8 and the gaseous Weber number We_G has to be lower than 0.4. With We_G and We_L defined as :

$$We_L = \frac{\rho_L U_L^2 d}{\sigma} \tag{1}$$

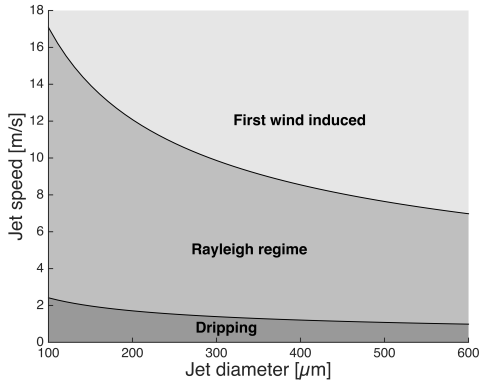

FIGURE 3: Breakup regimes of a cylindrical water jet in still air.

$$We_G = \frac{\rho_G U_L^2 d}{\sigma} \tag{2}$$

where ρ_L and ρ_G the liquid and the gas density respectively, U_L^2 is the liquid speed, d is the jet diameter, σ is the surface tension

These Weber numbers correspond to low Reynolds and Ohnesorge numbers. Theoretical developments realized by Rayleigh [12] showed that the growth of the most unstable perturbation breaks the jet in droplets of 1.89 times the jet diameter. Therefore the jet breakup can be controlled by triggered by stimulating the most unstable wavelength, e.g. using acoustic waves generated by piezoelectric element with the adequate wavenumber [13]. The Rayleigh break-up domain correspond to low speed and jet size as shown on the Fig 3 for the case of a water jet discharging in air. This diagram shows that using the Rayleigh breakup regime, droplets of 300m with a speed of 13 m/s can be produced.

1.3. Goals

The present project aims to design a hydraulic nozzle producing a spray with a narrow drop size distribution in order to increase the agricultural spray application efficiency. The starting design of this nozzle will be a splash plate nozzle (Fig. 4) for which the plate will be modified in order to split the liquid sheet formed on the plate into multiple jets at its end. The jets would be in the Rayleigh-Plateau regime and then generate a narrow drop size distribution. For agricultural spraying the common flow rate is around 1 l/min and the droplet diameters would be ranging between 200-300 μm. Thus, it requires roughly 60 to 90 jets of

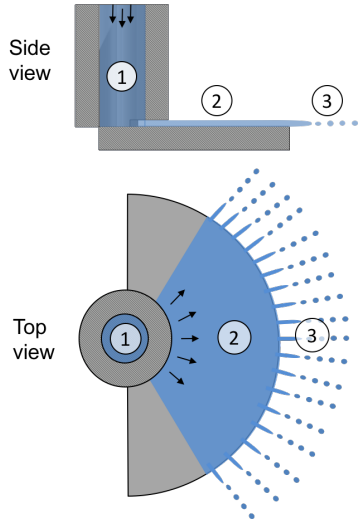

FIGURE 4: Illustration of the nozzle with the three main regions : the nozzle pipe (1), the disk (2), the disk edges (3).

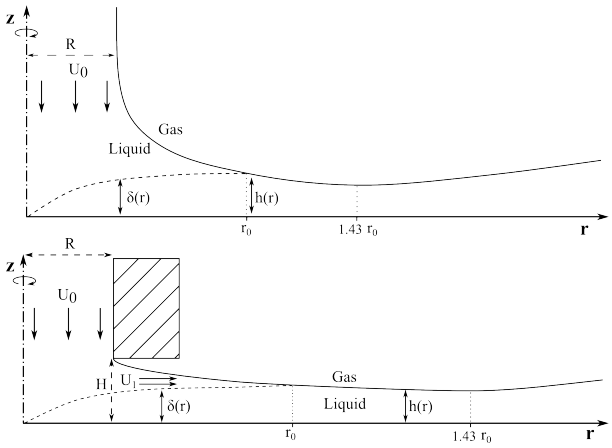

FIGURE 5: Half radial cut of the radial flow created by a impact of a round jet on a horizontal plate (top) and thin cylindrical opening (bottom). With r the radial distance, R the jet radius, H the distance between the nozzle and the plate, U_0 jet mean velocity, U_1 the main stream velocity, $h(r)$ the liquid film thickness, $U(r)$ the interface speed and $\delta(r)$ the boundary layer thickness.

100-150 μm with a speed of 10 to 15 m/s in order to deliver the adequate flow rate.

The splash plate nozzle geometry can be simplified as a pipe ending perpendicularly on a horizontal disk. The flow will create a liquid sheet on the disk then at the exit of the disk a liquid sheet or multiple jets will be formed. Three main regions of the nozzle can be distinguished : the nozzle pipe end, the disk, the disk border. In the two first regions the objective will be to generate a homogeneous flow with the right properties in term of speed and thickness. Then at the disk border specific structures (teeth, grooves, and channels) will be used in order to separate the liquid sheet in to multiple jets.

2. Flow dispersion on the disk

2.1. Flow description

The radial spread of a liquid film created by a round jet impact on a surface (Fig. 5a) occurs in numerous applications including mass and heat transfer. Surface cooling using an impinging water jet has been studied by [14], [15], [16]. Spray formation by fire sprinker [17; 18; 19] or plate nozzle [20; 21; 22] involves a liquid film as the first step of a spray formation. The governing parameters of the spray formation process are the thickness and the velocity of the liquid layer. [18] proposed a sprinkler spray model which combines a film flow dynamic model based on analytical solution of [23] with an atomization model. One way to increase the flow speed without increasing the flow rate is to constraint the liquid by bringing the nozzle closer to the plate (Fig. 5b). The flow formation changes from the impact free jet to the discharge of a thin cylindrical opening.

The hydrodynamics of the impact of an axisymmetric liquid jet on a normal surface has been theoretically studied by [23]. who provided an analytical solution of the liquid layer thickness $h(r)$ and surface speed $U(r)$ in respect with the radial distance from the jet centre r, the liquid kinematic viscosity ν, the jet volumetric flow rate Q and the jet radius R. His solution is realized using a self similarity solution and the momentum integral solutions. He distinguished three main regions in the flow. The first one begins at stagnation point where the boundary layer starts growing and it finishes at $r = r_0$ where the whole flow is within the boundary layer. In the second region, the boundary layer is fully developed. The liquid layer thickness is controlled by both radial dispersion and viscous wall effects. The liquid layer thickness is decreasing until $r = 1.43\, r_0$ and then it increases. Measurements of the liquid layer thickness and the velocity profile realized by [24] and [25] using needle probe and laser doppler velocimeter show a good agreement with the solution proposed by Watson.

When the nozzle is close to the plate (Fig. 5b), the

water is discharging through a thin cylindrical opening creating a thin liquid layer spreading radially. At the inner corner of the constriction, the flow is separating leading to an actual discharging area smaller than $2\pi RH$. [26] performed 2D numerical computations using the free-streamline theory on right-angle elbows with geometrical ratio, upstream to downstream channel width, ranging from 0.01 to 1.2. They compute the contraction coefficient (C_c) defined as the ratio of the asymptotic stream width downstream of the corner to the upstream channel width. The C_c was decreasing with the geometrical ratio. [27] investigated the effect of the elbow angle on the contraction coefficient showing that C_c was decreasing with the elbow angle. Their computations of the C_c has been validated by [28] who solved the Euler equations of the flow at a corner using a Lagrangian model based on smoothed particle hydrodynamics method.
The goal of this paper is to provide an analytical description of the thickness and the velocity of a thin liquid layer generated by radial flow generated by a thin cylindrical opening. The solution combines the analytical solution given by Watson and a correlation expression the flow acceleration due to the flow separation in respect with the geometrical ratio. The paper is structured as follows : in § 2.2.1 the theoretical development proposed by Watson for a round jet spreading radially is presented ; in § 2.2.2 presents the theoretical extension to a radial flow of the Watson solution ; in § 2.3 presents the numerical computations used to find the relationship between the geometrical ratio and the flow acceleration ; finally, in § 2.4 the validity and the quality of the proposed model is discussed.

2.2. Theoretical developments

2.2.1. Flow created by a round liquid jet impacting on a horizontal plate

This axisymmetric flow can be described as a thin layer by the following equations :

$$\frac{\partial(ru)}{\partial r} + \frac{\partial(rw)}{\partial z} = 0 \tag{3}$$

$$u\left(\frac{\partial u}{\partial r}\right) + w\left(\frac{\partial u}{\partial z}\right) = \nu\left(\frac{\partial^2 u}{\partial z^2}\right) \tag{4}$$

where r is the radial distance from the jet center, z is the distance upward from the plate, u and w are the corresponding velocity components, ν is the kinematic viscosity.

The hypothesis are : a no slip condition at the plate 5), the shear stress at the free surface is negligible (eq. 6) and the flow rate along the radial axis is constant (eq. 7).

$$u = w = 0 \quad \text{at} \quad z = 0 \tag{5}$$

$$\frac{\partial u}{\partial z} = 0 \quad \text{on} \quad z = h(r) \tag{6}$$

$$Q = 2\pi r \int_0^{h(r)} u \, \mathrm{d}z \tag{7}$$

The velocity profile in the axial direction u can be rewritten as function of the velocity at the free surface $U(r)$ and a similarity solution $f(\eta)$:

$$u = U(r) f(\eta) \tag{8}$$

where

$$\eta = \frac{z}{h(r)} \tag{9}$$

From the equations 5, 6 and 7, the boundary conditions of the similarity solution $f(\eta)$ are :

$$f(0) = 0, \; f(1) = 1, \; f'(1) = 0 \tag{10}$$

Then, the flow rate along the radial direction given by the equation 7 can be rewritten as :

$$Q = 2\pi r U h \int_0^1 f(\eta) \, \mathrm{d}\eta \tag{11}$$

Therefore, rUh has to be constant and the equation 3 becomes :

$$w = \frac{\partial h}{\partial r} U \eta f(\eta) \tag{12}$$

Then the equation of motion 4 turns into :

$$\nu f''(\eta) = \frac{\partial U}{\partial r} h^2 \eta f(\eta) \tag{13}$$

From which $U'h^2$ is constant if there is a similarity solution. Therefore $f(\eta)$ is only dependant on η and f'' is ≤ 0 since the shearing stress is greatest at the plate. It's convenient to write :

$$\frac{\partial U}{\partial r} h^2 = -\frac{3}{2} c^2 \nu \tag{14}$$

$$2f'' = -3c^2 f^2 \tag{15}$$

After integration of 15 and using the boundary conditions defined in 10 it becomes :

$$f'^2 = c^2 \left(1 - f^3\right) \tag{16}$$

$$c\eta = \int_0^f \frac{1}{\sqrt{1 - x^3}} \, \mathrm{d}x \tag{17}$$

where x is an integration variable.

Since $f(1) = 1$ and using the beta theorem :

$$c = \int_0^1 \frac{1}{\sqrt{1-x^3}}\,\mathrm{d}x = 1.402 \tag{18}$$

Then,

$$\int_0^1 f(\eta)\,\mathrm{d}\eta = \frac{1}{c}\int_0^1 \frac{1}{\sqrt{f(1-f^3)}}\,\mathrm{d}f = \frac{2\pi}{3\sqrt{3}c^2} \tag{19}$$

Finally, the constant flow equation 11 can be rewritten as :

$$rUh = \frac{3\sqrt{3}c^2 Q}{4\pi^2} \tag{20}$$

Using the equations 14 and 20, $U(r)$ and $h(r)$ can be expressed as :

$$U(r) = \frac{27c^2Q^2}{8\pi^4\nu(r^3+l^3)} \tag{21}$$

$$h(r) = \frac{2\pi^2\nu(r^3+l^3)}{3\sqrt{3}Qr} \tag{22}$$

where l is a constant length arising from the integration of $\frac{\partial U}{\partial r}$ in the equation 14. The value of l will be determined later using the boundary development region equations knowing that $h(r_0) = \delta$.

In the first region, the speed outside the boundary layer is equal to jet speed since the boundary layer is not fully developed. Therefore, the speed outside the boundary layer is considered as equal to speed of the jet U_0 which is equal to :

$$U_0 = \frac{Q}{\pi R^2} \tag{23}$$

with R the jet radius.

Inside the boundary layer, the velocity profile is defined by the similarity function $f(\eta)$:

$$u = U_0\, f\left(\frac{z}{\delta}\right) \quad \text{with} \quad u = U_0 \quad \text{when} \quad z \geq \delta(r) \tag{24}$$

The momentum integral equation is equal to :

$$\left(\frac{d}{dr}+\frac{1}{r}\right)\int_0^\delta (U_0\,u - u^2)\,\mathrm{d}z = \nu\left(\frac{\partial u}{\partial z}\right)_{z=0} \tag{25}$$

Because of equation 24, it can be rewritten :

$$\left(\frac{\mathrm{d}}{\mathrm{d}r}+\frac{1}{r}\right)U_0^2\,\delta\int_0^1 (f-f^2)\,\mathrm{d}\eta = \frac{\nu U_0\,c}{\delta} \tag{26}$$

$$\left(\frac{\mathrm{d}\delta}{\mathrm{d}r}+\frac{\delta}{r}\right)\frac{2U_0^2\left(\pi - c\sqrt{3}\right)}{3\sqrt{3}c^2} = \frac{\nu U_0\,c}{\delta} \tag{27}$$

Integration of equation 27 gives :

$$r^2\delta^2 = \frac{c^3\sqrt{3}\nu r^3}{\pi - c\sqrt{3}U_0} \tag{28}$$

$$\delta = \sqrt{\frac{\sqrt{3}c^3\nu r}{\left(\pi - c\sqrt{3}\right)U_0}} \tag{29}$$

The constant flow rate expression given by equation 7 can be rewritten as :

$$Q = 2\pi r\left(U_0\delta\int_0^1 f(\eta)\,d\eta + U_0(h-\delta)\right) \tag{30}$$

From which h can be derived :

$$h(r) = \frac{R^2}{2r} + \left(1 - \frac{2\pi}{3\sqrt{3}c^2}\right)\delta \tag{31}$$

Then, the expression of h is the sum of two effects : the radial dispersion of the flow and the displacement thickness of the boundary layer. This expression is valid until the whole flow is within the boundary layer, *i.e.* when $r \leq r_0$. The r_0 value is determined by founding the location where the boundary layer volume flux is equal to the inlet volume flux :

$$r_0 U_0 \delta(r_0) = \frac{3\sqrt{3}c^2 Q}{4\pi^2} \tag{32}$$

Using equation 29, r_0 is equal to :

$$r_0 = 0.3155\sqrt[3]{\frac{QR^2}{\nu}} \tag{33}$$

Since U is equal to U_0 when $r = r_0$. Therefore the value of l can be found using equations 20 and 33 :

$$l = 0.5673\sqrt[3]{\frac{QR^2}{\nu}} \tag{34}$$

Finally, the equations describing the liquid layer thickness are equations 31 when $r \leq r_0$ and 22 when $r > r_0$. The surface speed is equal to the initial velocity U_0 when $r \leq r_0$ and then it is given by the equation 21 when $r > r_0$.

2.2.2. Radial flow of a thin liquid film

When the gap, H, between the jet nozzle and the plate is reducing the discharging area may be smaller than the inlet area leading to an increase of the main flow speed downstream of the thin cylindrical opening (figure 5b). Moreover, a flow separation is occurring at the nozzle inner corner leading to the contraction of the streamline which consequently decrease the actual

discharging area. The main flow speed changes from U_0 in the inlet pipe to U_1 downstream of the jet impact region. This increase of speed is defined here as $\frac{1}{\alpha}$. Therefore, U_1 reads as :

$$\alpha = \frac{U_0}{U_1} = \frac{2HC_C}{R} \tag{35}$$

$$U_1\alpha = U_0 \tag{36}$$

The expression of α should lies between 0 and 1 and it should depends on $\frac{H}{R}$, defined as the opening ratio. Making the hypothesis that the downstream flow can be described by the Watson's model taking in account this main flow acceleration, the height and the surface speed of the liquid layer can be rewritten adding the new variable α. When $r \leq r_0$, the equations 29, 31 and 34 become :

$$\delta = \sqrt{\frac{\alpha\sqrt{3}c^3\nu r}{(\pi - c\sqrt{3})U_0}} \tag{37}$$

$$h(r) = \frac{\alpha R^2}{2r} + \left(1 - \frac{2\pi}{3\sqrt{3}c^2}\right)\delta \tag{38}$$

$$r_0 = 0.3155\sqrt[3]{\frac{\alpha QR^2}{\nu}} \tag{39}$$

When $r > r_0$, the equations 21, 22 and 34 become :

$$U(r) = \frac{27c^2Q^2}{8\pi^4\nu(r^3 + l^3)} \tag{40}$$

$$h(r) = \frac{2\pi^2\nu(r^3 + l^3)}{3\sqrt{3}Qr} \tag{41}$$

$$l = 0.5673\sqrt[3]{\frac{\alpha QR^2}{\nu}} \tag{42}$$

In this set of equation only l is affected by the velocity increase of the main flow.

2.3. Numerical modelling

2.3.1. Computational domain

Since the flow generated by a thin cylindrical opening is axisymmetric, the computational domain was two-dimensional (Fig. 6). In the radial direction, the domain was starting at the middle of the inlet pipe and it was ending at $r = 3.5\,r_0$. The height of the domain at the top of the plate was set at four time the inlet radius and the height of the inlet was set at three times the inlet radius.

The computational grid was a wedge (Fig. 6) with an opening angle of 5° and 1 cell thick running along

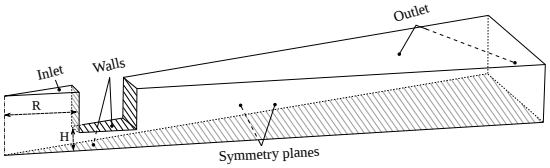

FIGURE 6: Computational domain used to simulate the flow generated by a thin cylindrical opening with the associated boundary conditions.

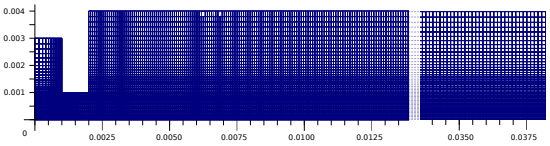

FIGURE 7: Example of mesh for a nozzle with a radius of 1 *mm* and a height of 1 *mm*. The dimensions are given in meters.

the plane of symmetry. The mesh resolution was adapted to each geometry using an automatic routine. A mesh refinement region was set at the exit of the inlet. In this region, the z resolution was set as $\Delta z = min\left(\frac{H}{25}, \frac{R}{75}\right)$ and the r resolution is set as $\Delta r = \frac{R}{15}$. The cell size was growing with the distance from the inlet centre. The maximal cell aspect ratio was 5 and the cell-to-cell expansion ratio was no exceeding 1.1. The number of cells was ranging from 50 000 to 250 000 for the largest geometry. An example of mesh is illustrated by the Fig. 7.

2.3.2. Computational parameters

Numerical simulations were performed in order to retrieve the value of α. The effect of the relative gap on the flow acceleration were studied for relative opening ranging from 0.2 to 3. Two different inlet radius R were tested 1 and 2 *mm* and two flow rates Q : 3 and 6 $l\,min^{-1}$. The thickness of the inlet pipe wall was 1mm defining the length of the restriction. The fluids used for the simulations were water and air at $20°C$ with the following properties : $\rho_{water} = 998\ kg^1\,m^{-3}$, $\nu_{water} = 1\ 10^{-6}\,m^2s^{-1}$, $\rho_{air} = 1.2\ kg^1\,m^{-3}$ and $\nu_{air} = 15\ 10^{-6}\,m^2s^{-1}$. The surface tension effects were neglected.

2.3.3. Boundary conditions

The inlet boundary was set with an uniform velocity equal to $U_0 = \frac{Q}{\pi R^2}$, a normal gradient of pressure equal to 0 and a liquid fraction ϕ equal to 1. The wall boundaries were set as no slip, zero normal gradients

for ϕ and the pressure. The outlet was set at atmospheric pressure with no liquid backflow. Axisymmetric boundary conditions were set the for the front and back plans of the domain.

2.3.4. Numerical method

The InterFoam solver from the *OpenFOAM C++* toolbox has been used to perform numerical simulations. InterFoam is a Volume Of Fluid (VOF) solver for incompressible two-phase flow. This solver provided good results for inertia-dominated flows with large fluid density ratios ($\geq 10^3$), such as round jet impact [29]. The governing equations are discretised and solved using the finite volume method and the PISO algorithm respectively. The diffusion terms were discretized using a second order central difference scheme. All the cases were considered in a laminar mode. Therefore, no extra turbulence model has been used. The computations were unsteady and the time step was controlled by the Courant number set at 0.45. Consequently, the results presented in the next section are an averaged solution of the flow over a certain time interval at the steady state.

2.3.5. Post processing

The liquid layer thickness $h(r)$ was computed by integrating the liquid fraction ϕ over the z direction : $h(r) = \int \phi(r)\, \mathrm{d}z$. The surface speed was computed at the location where $\phi = 0.5$ using a linear interpolation. In order to present results in a concise way, the radial distance, the height and the surface speed profiles are expressed in non dimensional way : $r^* = r\sqrt[3]{\frac{\nu}{\alpha Q R^2}}$, $h^* = h(r)\sqrt[3]{\frac{Q}{\alpha^2 \nu R^4}}$ and $U^* = 10\left(\frac{\alpha U(r)}{U_0}\right)$.

α_{obs} was computed using the equation 35. U_1 was computed as the average of the main flow velocity from $r = 0$ until $r = r_0$. Moreover, three extra values of α were computed by fitting. The liquid sheet thickness equations 38 and 41 were reduced to two simpler expressions depending on the radial distance r and on four coefficients a, b, d and e. For each case, the values of the four coefficients were retrieved by fitting the equation 43 on the thickness profile $h(r)$ from the numerical data.

$$h(r) = \begin{cases} \frac{a}{r} + b\sqrt{r}, & r \leq r_0 \\ \frac{d(r^3+e)}{r}, & r > r_0. \end{cases} \tag{43}$$

Then, from the equations 37, 38 and 42, three expressions of α were obtained :

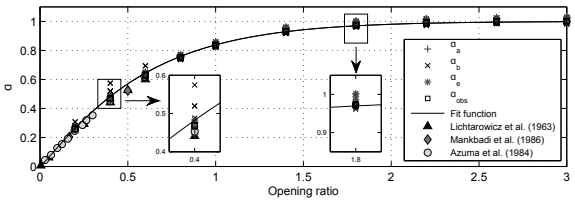

FIGURE 8: Comparison of the value of α retrieved from the post processing or found in the literature in respect with the relative gap.

$$\begin{cases} \alpha_a = \frac{2a}{R^2} \\ \alpha_b = \left(\frac{b\sqrt{U_0}}{0.9955\sqrt{\nu}}\right)^2 \\ \alpha_e = \frac{e\nu}{0.1826\, Q R^2} \end{cases} \tag{44}$$

There is no expression for α_d since d is independent of α. Finally, some flow acceleration for similar flow available in the literature are used for comparison. [26] and [30] computed the contraction coefficient for a 90° elbow with several ratios upstream to downstream. [31] realized measurements of the flow velocity at the exit of a circular inlet for small opening ratios.

2.3.6. Model quality

The quality of the analytical model given by the equations 38 and 41 was assessed by computing the Normalised Root Mean Square Deviation (NRMSD) using the numerical data as observed values. The NRMSD was computed as :

$$NRMSD = \frac{\sqrt{\frac{1}{n}\sum_{i=1}^{n}\left(\hat{Y}_i - Y_i\right)^2}}{(Y_{max} - Y_{min})} \tag{45}$$

where n is the number of observation, $\hat{Y}_i$ are the values predicted by the model, Y_i are the observed values and $(Y_{max} - Y_{min})$ is the amplitude of the variation within the dataset.

2.4. Results and discussion

Comparison of the different α in respect with the relative gap is presented on the Fig. 8. α is increasing with the opening ratio until the asymptotic value of 1 is reached. For most of the cases the different values of α are close to each other. Therefore, taking in account the flow acceleration allows to extend the set of equation from the jet flow to the thin cylindrical opening flow. When the opening ratio is small, i. e. < 1.5, there are discrepancies between the different values of

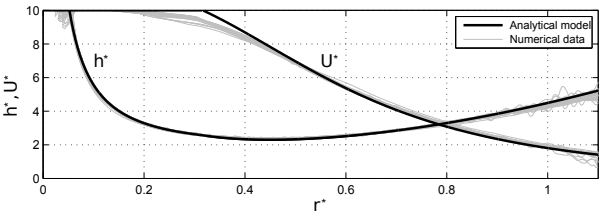

FIGURE 9: Comparison between between the numerical data from all the cases and the model prediction for the surface velocity and liquid thickness in respect with the radial distance.

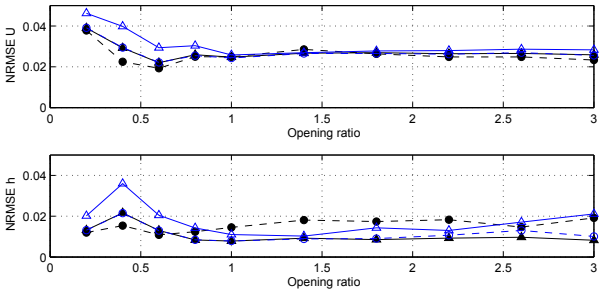

FIGURE 10: NRMSD on the interface velocity (top) and the liquid sheet thickness (bottom) predictions in respect with the relative opening ratio. Each marker corresponds to a specific radius/flow rate combination : - - △ - - is for $R = 1\,mm$ & $Q = 3\,l/min$, —○— is for $R = 2\,mm$ & $Q = 6\,l/min$, —▲— is for is for $R = 2\,mm$ & $Q = 3\,l/min$ and - - ● - is for $R = 2\,mm$ & $Q = 6\,l/min$.

α and α_b. α_b is larger than the other values of α showing that the displacement thickness induced by the boundary layer development is larger than expected. For these cases, close to the inlet the velocity outside boundary layer is not equal to the free stream velocity everywhere. Indeed, the velocity is lower close to the liquid/air interface. Therefore, the liquid height is higher than expected to compensate this deficit of speed. When the opening ratio is large, i.e. > 1.5, α is close to one, therefore the flow is close to the free jet impact flow. The comparisons with the measurements of [31] show good agreement as well as the theoretical contraction coefficients computed by [26] and [30]. From these results, α can be expressed in respect with the opening ratio $\frac{H}{R}$ as :

$$\alpha = \left(1 - e^{-1.82\left(\frac{H}{R}\right)^{1.11}}\right) \tag{46}$$

The Fig. 9 compares the numerical data from all the cases and the model prediction for the surface velocity and liquid thickness in respect with the radial distance. The reduction to a non dimensional expression of $U(r)$ and $h(r)$ was realized using the expression of α given by the equation 46. After, the reduction to the non dimensional expression all the curves are really close to each other showing that the flow equations with α are describing on the downstream flow well the effect of the gap between the inlet and the plate. For the surface speed $U(r)$ when $0.3 < r^* < 0.4$, the observed values are lower than the predicted one because the velocity profile was decreasing close to the interface liquid/air. For the liquid layer thickness $h(r)$, the prediction and the observed data are really close to each other.

The NRMSD on the liquid sheet thickness and interface velocity prediction in respect with the relative opening ratio are presented on the Fig. 10. For both the surface height and the surface speed, the NRMSD is larger when the opening ratio is smaller than 1. Then, when the opening ratio is larger than 1 the NRMSD is equal to 3% for the surface speed and to 2% for the liquid layer thickness. There is no significative difference between the different cases.

3. Disk border

The Fig. 11 shows the different structures used on the border of the disk in order to generate cylindrical jets. The pictures come from preliminary tests so the flow parameters were not equal between each case therefore no quantitative comparisons were realized so far. The disks were plexiglass cut with a laser cutter. For the first design the disk was cut with teeth at its end. This design was unable to form jet at its exit, the teeth were too short and only a liquid sheet was formed. The second and the third design had grooves on the border of the plate. These grooves were able to correctly guide the flow to coarse jets (1mm) but when the number of jet increased, the jets were merging was formed. The last design is the most promising way because of its ability to generate a large number of jets without slowing down too much the flow.

4. Conclusion

The present work proposed an extension of the existing analytical development on the radial spread of a liquid jet over a horizontal surface to the case of a thin radial flow. When the gap (H) between the jet nozzle and the plate is reduced the discharging area may be smaller than the inlet area leading to an increase of

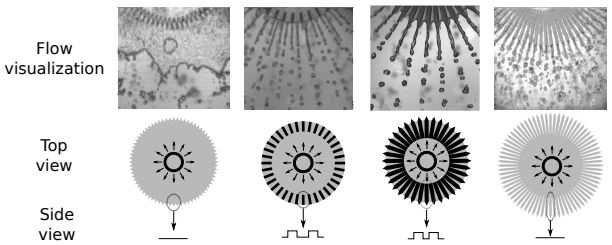

FIGURE 11: Comparison of several plate structures for jet generation. The black areas on the side of the sketch correspond to grooves. The arrows are showing the flow directions on the disk.

the main flow speed downstream of the thin cylindrical opening. This increase of speed, defined here as $\frac{1}{\alpha}$, can be related to the relative gap of the nozzle $\frac{H}{R}$. Numerical computations with a volume of fluid method were realised with for $\frac{H}{R}$ ranging from 0.2 to 3 and with Q of 3 and 6 *l/min*.

The results of these computations allowed to express α in respect of $\frac{H}{R}$. α is increasing with the opening ratio until the asymptotic value of 1 is reached. Taking in account the flow acceleration allowed to extend the set of equation from the jet impacting flow to the thin cylindrical opening flow. The liquid layer thickness and the surface speed differ with a maximum error of 4% between the flow predicted by the model and computations. Mains discrepancies appear in the region close to the nozzle where the analytical model assumption of a constant velocity outside the boundary layer is not valid. However, further downstream the model and the computations are in good agreement.

Références

[1] G. Matthews, Pesticide application methods, John Wiley & Sons, 2008.

[2] P. C. M. W. A. Taylor, A. R. Womac, B. P. Taylor, An attempt to relate drop size to drift risk, in : International Conference on Pesticide Application for Drift Management, 2004.

[3] S. Reichenberger, M. Bach, A. Skitschak, H.-G. Frede, Mitigation strategies to reduce pesticide inputs into ground- and surface water and their effectiveness ; a review, Science of The Total Environment 384 (1–3) (2007) 1 – 35.

[4] M. Massinon, F. Lebeau, Experimental method for the assessment of agricultural spray retention based on high-speed imaging of drop impact on a synthetic superhydrophobic surface, Biosystems Engineering 112 (1) (2012) 56 – 64.

[5] P. Miller, M. B. Ellis, Effects of formulation on spray nozzle performance for applications from ground-based boom sprayers, Crop Protection 19 (8–10) (2000) 609 – 615, {XIVth} International Plant Protection Congress.

[6] M. Ellis, C. Tuck, P. Miller, The effect of some adjuvants on sprays produced by agricultural flat fan nozzles, Crop Protection 16 (1) (1997) 41 – 50.

[7] M. B. Ellis, C. Tuck, P. Miller, How surface tension of surfactant solutions influences the characteristics of sprays produced by hydraulic nozzles used for pesticide application, Colloids and Surfaces A : Physicochemical and Engineering Aspects 180 (3) (2001) 267 – 276.

[8] P. Holloway, M. B. Ellis, D. Webb, N. Western, C. Tuck, A. Hayes, P. Miller, Effects of some agricultural tank-mix adjuvants on the deposition efficiency of aqueous sprays on foliage, Crop Protection 19 (1) (2000) 27 – 37.

[9] D. Nuyttens, K. Baetens, M. D. Schampheleire, B. Sonck, Effect of nozzle type, size and pressure on spray droplet characteristics, Biosystems Engineering 97 (3) (2007) 333 – 345.

[10] A. Hewitt, International standards for drift reduction technology studies, Tech. rep., OECD Workshop (2005).

[11] C. Dumouchel, On the experimental investigation on primary atomization of liquid streams, Experiments in fluids 45 (3) (2008) 371–422.

[12] J. W. Strutt and Lord Rayleigh, On the instability of jets, Proc. London Math. Soc 10 (3) (1878) 4–13.

[13] G. Brenn, U. Lackermeier, Drop formation from a vibrating orifice generator driven by modulated electrical signals, Physics of Fluids (1994-present) 9 (12) (1997) 3658–3669.

[14] S. Ishigai, S. Nakanishi, M. Mizuno, T. Imamura, Heat transfer of the impinging round water jet in the interference zone of film flow along the wall, Bulletin of JSME 20 (139) (1977) 85–92.

[15] X. Liu, J. Lienhard, J. Lombara, Convective heat transfer by impingement of circular liquid jets, Journal of heat transfer 113 (3) (1991) 571–582.

[16] M. L. Hosain, R. B. Fdhila, A. Daneryd, Heat transfer by liquid jets impinging on a hot flat surface, Applied Energy.

[17] A. Marshall, M. Di Marzo, Modelling aspects of sprinkler spray dynamics in fires, Process Safety and Environmental Protection 82 (2) (2004) 97–104.

[18] D. Wu, D. Guillemin, A. W. Marshall, A modeling basis for predicting the initial sprinkler spray, Fire safety journal 42 (4) (2007) 283–294.

[19] H. Aghajani, S. Dembele, J. Wen, Analysis of a semi-empirical sprinkler spray model, Fire Safety Journal 64 (2014) 1–11, cited By 0. doi:10.1016/j.firesaf.2014.01.004.

[20] N. De Cock, M. Massinon, B. Mercatoris, F. Lebeau, Numerical modelling of mirror nozzle flow, Vol. 5, 2014, pp. 3632–3640.

[21] M. P. Fard, D. Levesque, S. Morrison, N. Ashgriz, Characterization of splash-plate atomizers using numerical simulations, Atomization and Sprays 17 (4).

[22] J. M. Gordillo, H. Lhuissier, E. Villermaux, On the cusps bordering liquid sheets, Journal of Fluid Mechanics 754 (2014) R1.

[23] E. J. Watson, The radial spread of a liquid jet over a horizontal plane, Journal of Fluid Mechanics 20 (1964) 481–499.

[24] T. Azuma, T. Hoshino, The radial flow of a thin liquid film : 2nd report, liquid film thickness, Bulletin of JSME 27 (234) (1984) 2747–2754.

[25] T. Azuma, T. Hoshino, The radial flow of a thin liquid film : 3rd report, velocity profile, Bulletin of JSME 27 (234) (1984) 2755–2762.

[26] A. Lichtarowicz, E. Markland, Calculation of potential flow with separation in a right-angled elbow with unequal branches, Journal of Fluid Mechanics 17 (1963) 596–606. doi:10.1017/S0022112063001531.

[27] S. Chu, Separated flow in bends of arbitrary turning angles, using the hodograph method and kirchhoffs free streamline theory, Journal of fluids engineering 125 (3) (2003) 438–442.
[28] Q. Hou, A. Kruisbrink, F. Pearce, A. Tijsseling, T. Yue, Smoothed particle hydrodynamics simulations of flow separation at bends, Computers and Fluids 90 (2014) 138–146.
[29] L. A. S. S. Deshpande, M. F. Trujillo, Evaluating the performance of the two-phase flow solver interfoam., Computational Science and Discovery 5 (1).
[30] R. Mankbadi, S. Zaki, Computations of the contract coefficient of unsymmetrical bends, AIAA journal 24 (8) (1986) 1285–1289.
[31] T. Azuma, T. Hoshino, The radial flow of a thin liquid film : 1st report, laminar-turbulent transition, Bulletin of JSME 27 (234) (1984) 2739–2746.

Experimental study of cavitating flow and fluid hammer in cryogenic conditions

Claudia Esposito

Environmental and Applied Fluid Dynamics Department, von Karman Institute for Fluid Dynamics, Belgium, claudia.esposito@vki.ac.be

Supervisor: Maria Rosaria Vetrano

Associate Professor, Environmental and Applied Fluid Dynamics Department, von Karman Institute for Fluid Dynamics, Belgium, vetrano@vki.ac.be

University Supervisor: Johan Steelant

Associate Professor, Department of Mechanical Engineering, KU Leuven, Belgium, johan.steelant@kuleuven.be

Abstract

Two phase flows appear in spacecraft operations due to low-pressure or vacuum conditions in the propulsion system. When the launch starts the propellant is confined in tanks which are isolated by a set of valves. As the spacecraft is ejected from the launch vehicle the propellant lines are filled and pressurized. This is the so-called priming phase. A bubble flow is produced by the combination of different phenomena such as boiling, due to the chilldown of the propellant line, cavitation, caused by the passage of the fluid through a valve, and fluid hammer. Each of these processes takes place in a highly thermodynamic non-equilibrium environment. The consequence is that validated theoretical models to describe them are not available yet. Further difficulties rise from the experimental point of view. The cryogenic nature of the propellants and the complexity of the multiphase process strongly limits the possible techniques to be used.

The aim of this research project is the characterization of two sub-processes happening during the priming operation: cavitation and fluid hammer. For this purpose an orifice configuration will be used. Orifices are quite common in rocket propulsion systems. Moreover they can easily experience cavitation because of the high velocity reached in the vena contracta. Liquid Nitrogen (LN_2) is the chosen working fluid. Since cryogenic fuels are thermosensitive, their behaviour during cavitation is completely different from that of non-cryogenic fluids. Liquid Nitrogen seems to be the best choice. In fact its properties allow less stringent requirements in terms of temperature respect to other cryogenic fluids. It is an easy handling and low cost cryogen as well.

Determination of the technical requirements of the experimental set-up and working conditions for LN_2 is the first task of this project. Selection of proper measurement techniques is requested as well. The experimental investigation will be carried out by means of pressure, temperature and flow rate sensors. Special attention will be given to optical visualizations. The aim is to retrieve quantitative information about the flow topology during cavitation and fluid hammer. The pressure waves generated by the fluid hammer will be also analyzed, as well as the temperature variations.

In order to accomplish that and to assess performances of the measurement techniques, tests on a simpler and non-cryogenic test bench will be carried out. Results of this experimental campaign will be compared to the physical models available in literature. They will provide a first estimate to decide on working conditions and orifice design.

Finally the results of the experimental campaign will be used to realize a database. It will help to validate numerical codes developed to design valves and pipes against damages due to cavitation or fluid hammer.

Keywords: cavitation, orifice, cryogenic flows, fluid-hammer.

Scaled model of the pollutant dispersion after an explosion in a complex environment

Charline Fouchier

Environmental and Applied Fluid Dynamics Department, von Karman Institute for Fluid Dynamics, Belgium, charline.fouchier@vki.ac.be

Supervisor: Jean-Marie Buchlin

Professor and Head of the department, Environmental and Applied Fluid Dynamics Department, von Karman Institute for Fluid Dynamics, Belgium, buchlin@vki.ac.be

University Supervisor: Alessandro Parente

Professor, Aero-Thermo-Mechanical Department, ULB, Belgium, Alessandro.Parente@ulb.ac.be

Explosion, whether accidental or not, is a major concern in the security and safety fields. Understanding its mechanics and consequences in cities and industries helps to protect goods and people from disasters. Examples of tragedies caused by explosions are numerous and consequences are often catastrophic. Industrials using explosives charges can represent a threat for their environment. They have to foresee the risks implied by their activities and reduce them as much as possible.

Although research on the overpressure propagation following an explosion in an urban environment is well-developed, the knowledge about the dispersion phenomenon due to a chemical explosion is not well acquired. The present research project aims to answer two fundamental questions: when the effect of the atmospheric boundary layer outweighs the effect of the explosion on the chemical dispersion and what is the impact of the environment configuration surrounding the explosion.

The global objective of the research is to study the chemical dispersion following a detonation in a complex environment. A solid explosion with a pollutant source will be experimentally simulated in free field and in different urban and industrial configurations under an atmospheric boundary layer. The chemical dispersion and the overpressures caused by the explosion will be measured for each configuration through a fast response optical measurement technique and fast response pressure sensors.

The project can be structured through four mains stages. Tests will be first conducted without any chemical marker in a low speed wind tunnel to ensure correct pressure measurements in confined area. The second stage is the elaboration of the atmospheric boundary layer in the low speed tunnel of the von Karman institute L1-B. The third stage will be the development and design of the pollutant source and the feasibility study of tests. During this period, selection and insertion of a proper chemical marker (powder or gas) suiting the good visualisation of a fast dispersion will be done. To visualise the propagation of the chemical marker, a fast response optic measurement technique will be developed and tested in L1-B. The fourth stage of the present project is the simulation of a chemical explosion in a complex environment. Tests will be conducted in different configurations.

The main challenge of the project is to adapt existing measurement techniques used for dispersion to be used at very high speed. The experimental data will be post-processed and compared with a numerical model that will be developed in parallel to the project. Particularly, one part of the study will focus on the transition between the predominance of the explosion effect on the dispersion and the predominance of the effect of the winds of the atmospheric boundary layer. The result of the study aims to protect the cities and industries against chemical explosion by understanding the phenomenon and then being able to foresee the threat.

Keywords: blast wave, atmospheric dispersion, explosion, urban configuration

Optical caustics produced by spheroidal droplets in the glory region: experimental observations and numerical simulations

Sara González Ruiz

Department of Environmental and Applied Fluid Dynamics, von Karman Institute for Fluid Dynamics, Belgium, sara.gonzalez.ruiz@vki.ac.be

Supervisor: Jeroen van Beeck

Professor, Department of Environmental and Applied Fluid Dynamics, von Karman Institute for Fluid Dynamics, Belgium, vanbeeck@vki.ac.be

University Supervisor: Steve Vanlanduit

Professor, Department of Mechanical Engineering, Vrij Universiteit Brussel, Belgium, steve.vanlanduit@vub.ac.be

Abstract

The present paper describes the ongoing work for the development of an optical technique for the sizing of water droplets and irregular particles. This technique is based on the interference patterns that appear in the out-of-focus plane when laser light is backscattered by a particle. Two different patterns appear in the backscattering plane; the glory pattern, produced by water droplets, and the speckle pattern, produced by irregular particles. In this paper, the glory pattern produced by slightly non-spherical droplets is studied by means of experimental observations and of a ray tracing algorithm.

Keywords: light scattering, glory, droplets, non sphericity, caustics

1. Introduction

Liquid sprays are widely used in diverse fields such as agriculture, food processing or fire safety industries. In most of the applications, droplet size has great influence on the efficacy of the spray and it is therefore an important characteristic to consider when selecting the optimal properties of a liquid spray. Also in many meteorological and other research studies droplet size is an important factor. Therefore, many techniques exist nowadays to measure the droplet size. Among these, optical techniques are the most common due to their non-intrusive nature. Some examples of optical techniques for droplet size characterization are the rainbow [1], laser diffraction, and ILIDS [2]. All these techniques comprise an emitter (e.g. a laser beam) and an optical receiver located at different scattering angles. In some applications, because of lack of space or unavailability of more than one optical access to the droplets under study, a technique with a more compact configuration is required. The glory technique is ideal for these applications, since both emitting and receiving optics are located in the backscattering region. The inversion algorithm that exists for this technique is valid for spherical droplets in the micrometer range. In most applications, however, droplets are not perfectly spherical, thus in order to measure droplet size in this situation, it is important to understand the influence that non-sphericity has on the glory pattern. In this paper, the glory pattern produced by slightly non-spherical droplets is observed experimentally. Furthermore, a ray tracing algorithm is applied to numerically simulate the optical caustics appearing in the pattern.

2. The glory pattern from spherical droplets

A droplet illuminated with coherent light, e.g. a laser beam, scatters the light in all directions in space. When the focused image of this droplet is observed from a certain direction, several intensity maxima can be seen on its surface. These intensity maxima correspond to the points from which the light rays are scattered towards the observer and they are known as

glare points [3]. In the far field, the light rays scattered by the particle from the glare points interfere with each other, creating different maxima and minima of light intensity. This interference pattern can be observed when imaging the particle out-of-focus, and it depends on several parameters, such as the particle size, the refractive index of the particle and the surrounding medium, etc. When the droplet is observed in-focus at a scattering angle of approximately 180°, the glare points that are seen in the droplet surface correspond to a bright spot in the center of the droplet and a circular ring at the edge of the droplet (Fig. 1). The light scattered by the droplet at this angle interferes in the out-of-focus plane creating concentric rings of maximum and minimum intensity. This interference pattern is known as the glory.

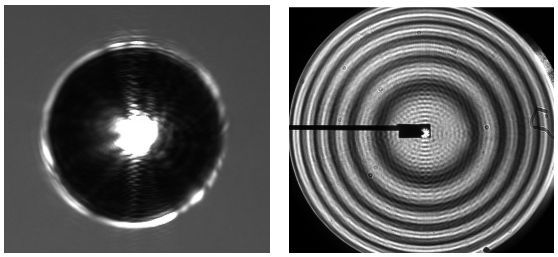

(a) (b)

Figure 1: Glare points (a) and glory pattern (b) observed from a water droplet in the focused and out-of-focus plane respectively.

2.1. Light as an electromagnetic wave

The scattering of light as an electromagnetic wave is mathematically described by the Maxwell equations: a set of partial differential equations that predict the interaction of light with an arbitrary particle. In the case of an homogeneous sphere, the Lorenz-Mie theory provides an exact solution to these equations [4, 5]. According to this solution, the glory intensity in a certain point in space is given by:

$$I = \frac{I_0}{(k_0 r)^2}\left[i_1(d,\theta)\sin^2\varphi + i_2(d,\theta)\cos^2\varphi\right] \quad (1)$$

where i_1 and i_2 are the perpendicular and parallel normalized components of the scattered light intensity, θ is the scattering angle, φ is the polarization angle, I_0 is the incident light intensity, $k_0 = 2\pi/\lambda$ is the wave number, λ is the wavelength of the incident light and r is the distance to the droplet. Fig. 2 shows the normalized far-field intensity of the glory as a function of the scattering angle, for a water droplet with a diameter of $d = 500\mu m$ and a relative refractive index of m = 1.33.

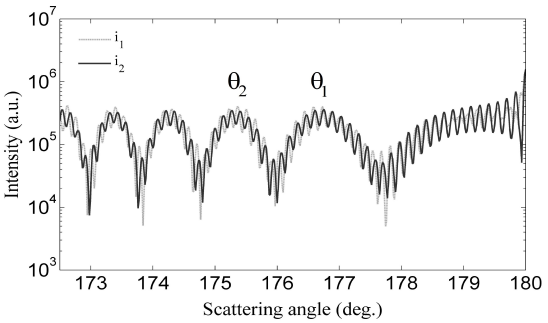

Figure 2: Parallel and perpendicular components of the light intensity at scattering angles between 172.5° and 180° (for a water droplet with $d = 500\mu m$, m = 1.33). θ_1 and θ_2 are two consecutive glory maxima.

2.2. Geometrical optics approximation

The geometrical optics approximation describes the light in terms of rays that follow a rectilinear path while traveling in an homogeneous medium. This approximation can predict the angle, θ, at which the rays are scattered by a droplet by simple geometrical equations [6]. Fig. 3 shows the geometrical light rays that contribute the most to the glory intensity pattern. They are the near-centered rays, which suffer one external reflection (p = 0) and one internal reflection (p = 2). In addition, higher order rays scattered from the edge of the droplet also play an important role in the formation of the glory pattern [7].

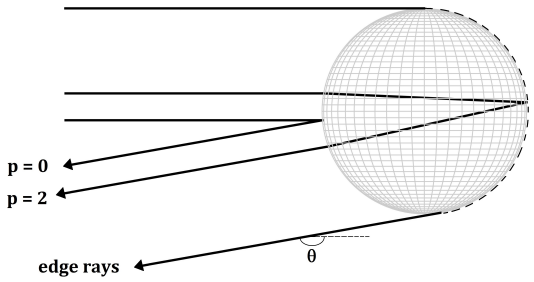

Figure 3: Schematic of geometrical optics rays giving the main contribution to the glory intensity, depicted for $\theta = 170°$.

The contribution of these rays to the glory intensity pattern can be further described by analyzing the angular frequency spectrum of the glory. Fig. 4 shows the angular frequency spectrum of the glory intensity profile produced by a water droplet with a diameter of $d = 500\mu m$ and a relative refractive index of m =

1.33. Three dominant peaks can be noted in the angular frequency spectrum. These peaks are explained by the principle of optical interference at infinity between two parallel rays separated by a distance δ. The frequency of these peaks is then calculated similarly to those of Young's double-slit experiment [6, 8]:

$$F_i = \delta_i/\lambda \tag{2}$$

From eq. 2, it is possible to conclude that the two near-centered rays ($p = 0$ and $p = 2$) are responsible for the low frequency oscillations in the glory pattern, while the higher order rays scattered from the edge of the droplet are responsible for the high frequency oscillations in the glory pattern.

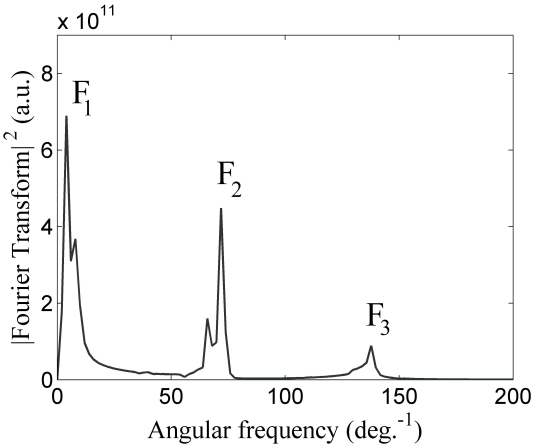

Figure 4: Fourier Transform of the light scattered by a droplet ($d = 500\mu m$, m = 1.33) in the backscattering region.

2.3. Droplet sizing

The angular intensity rings in the glory pattern have been used in other studies to characterize the size of water droplets with diameters between several micrometers up to a few millimeters. For the smaller droplets in this range, the dominant frequency in the glory intensity oscillations is the one corresponding to the interference between rays scattered from the edge of the droplet. In this case, eq. 2 can be directly used to relate the highest frequency in the glory rings to the droplet diameter [9]. For droplet diameters bigger than $200\mu m$, the lowest frequency is dominant in the glory pattern, thus the main intensity peaks in the glory pattern are no longer due to the edge rays, but to the near-centered rays. In this case, a relation can be found between the droplet diameter and the angular position of two consecutive maxima in the glory pattern [10].

3. Experimental observations from spherical and spheroidal droplets

In order to study the glory pattern from spheroidal droplets of different aspect ratios, a water droplet was levitated in the air by means of an ultrasonic acoustic levitator. The acoustic levitator consists of two parts: a transducer, which emits an ultrasonic sound wave, and a reflector, which reflects the emitted sound wave. Between these two elements, the areas of high and low pressure of the reflected sound wave interfere with the high and low pressure areas of the original wave, creating nodes (areas of minimum pressure) and anti-nodes (areas of maximum pressure). The places in between nodes and anti-nodes have a constant upward pressure, that counteract the gravity forces experienced by the droplet, and thus makes it levitate. The droplets levitated in the laboratory had a diameter in the range of $100 - 300\mu m$.

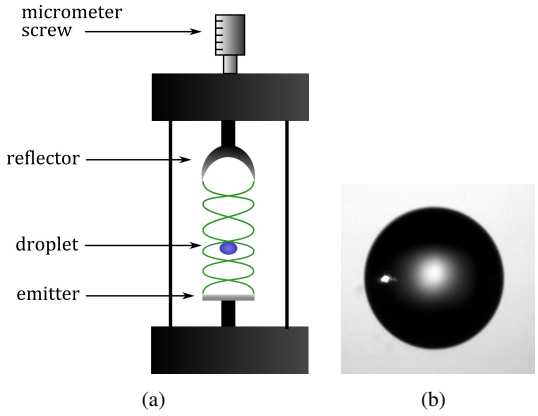

Figure 5: (a) Schematic representation of the acoustic levitator (b) shadowgraph image of a levitated droplet.

The levitated droplet was illuminated by a He-Ne laser which emitted linearly polarized light with a wavelength of 632.8 nm. The light scattered by the droplet in the glory region was recorded by a CCD camera with a resolution of 0.0218 °/pixel and an angular field of view of 20°. The droplet was illuminated at 90° from the incident laser beam with parallel white light, and another CCD camera with a magnification factor of 0.79 μm/pixel was used to record a shadowgraph image of the droplet. Fig. 6 shows the glory pattern recorded from levitated droplets of different aspect ratios.

When the aspect ratio of the levitated droplet was close to 1, a bright astroid curve could be observed in the image, superposed to the glory concentric rings. Since the resolution of the shadowgraph images is not

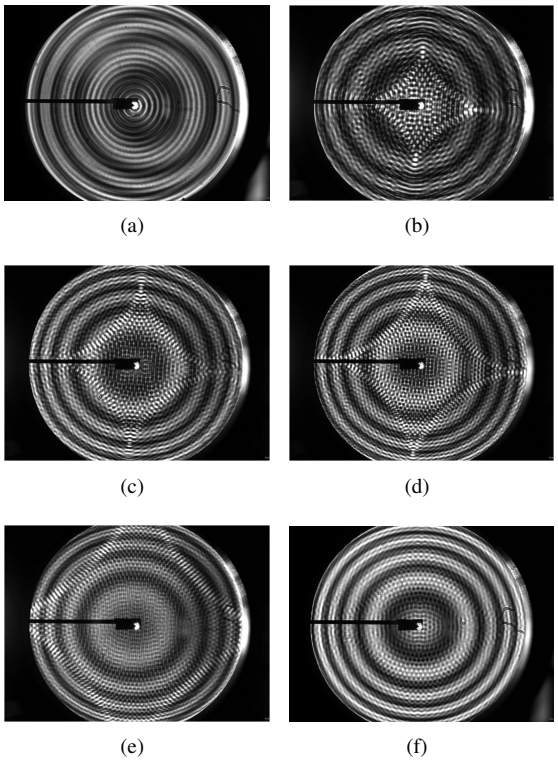

Figure 6: Glory pattern produced by a spheroidal droplet of different aspect ratio.

sufficient to calculate the aspect ratio with enough accuracy, the following conclusions were postulated: *a*) when the droplet is completely spherical, no caustics appear in the image and the glory pattern with low and high frequency rings can be observed (Fig. 6a); *b*) droplets with aspect ratio very close to 1 produce an optical caustics with the shape of an astroid curve, that moves towards lower scattering angles as the aspect ratio of the droplet deviates from 1 (Fig. 6b-e); *c*) for a non-sphericity higher than 0.2%, no caustics were observed in the image but the interference between the caustics and the glory rings is still visible, which indicates that an optical caustic appears at lower scattering angles outside the field of view of the camera (Fig. 6f).

In order to gain more insight into this phenomenon, the optical caustics produced by a spheroidal droplet will be numerically simulated by means of a Ray Tracing algorithm, which will be described in the following section.

4. Numerical simulations of optical caustics in the glory region

The optical caustics can be identified as a large density of light rays at a certain scattering angle.

4.1. Ray Tracing algorithm

In this subsection, the Ray Tracing algorithm, based on the one of Yu [11], is briefly introduced.

A droplet centered in the origin of coordinates is given by the equation:

$$\frac{x^2}{a^2} + \frac{y^2}{b^2} + \frac{z^2}{c^2} = 1 \tag{3}$$

where a, b and c are the semi-axes in the x, y and z directions, respectively. The aspect ratio is defined in this case as the ratio a/c.

The trajectory of a light ray can be defined by a unit vector, $\vec{k}$, and a point in space (x_0,y_0,z_0). An incident light ray travels through the external medium with refractive index m_1 without being deviated from its trajectory. However, when the light ray reaches the droplet, which has a refractive index m_2 which differs from the external medium, the light ray is deviated. This deviation occurs due to the change in refractive index and it is described by the Snell's law:

$$m_1 \sin\theta_1 = m_2 \sin\theta_2. \tag{4}$$

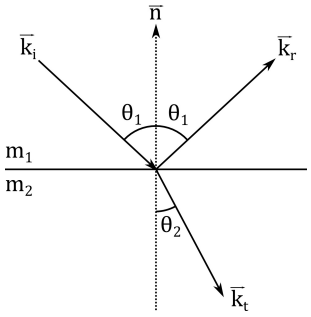

Figure 7: Snell's law.

Applying the Snell's law, the trajectory of the reflected and transmitted light rays can be expressed in their vector form as [11]:

$$\vec{k}_r = \vec{k}_i - 2(\vec{k}_i \cdot \vec{n})\,\vec{n} \tag{5}$$

$$\vec{k}_t = m\left[\vec{k}_i - (\vec{k}_i \cdot \vec{n})\,\vec{n}\right] + \left[1 - m^2 + m^2\left(\vec{k}_i \cdot \vec{n}\right)^2\right]^{1/2}\vec{n} \tag{6}$$

where $m = m_2/m_1$. When the incident angle θ_1 exceeds the critical angle, total reflection occurs, and the square root in eq. 6 is a complex number.

The scattering and polarization angles at which a light ray are scattered by the droplet is defined in Fig. 8.

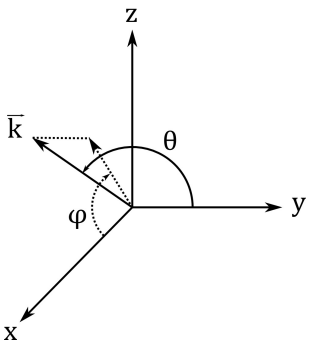

Figure 8: Definition of the scattering and polarization angles at which a light ray are scattered by a droplet.

4.2. Results

Unlike the rays that suffer one external reflection, which are not associated with any optical caustics from spheroidal droplets, the light rays that suffer one internal reflection do result in optical caustics when scattered from spheroidal droplets. However, the optical caustics associated to these rays occur in the rainbow region and are therefore not of interest for the present study. The caustics observed during the experimental investigation are not caused by these rays, but by rays that are internally reflected a higher number of times. Optical caustics were simulated for several rays. The rays that suffer 5 internal reflections (p = 6) were the ones that gave the closest results when compared to the experimental observations. The results obtained for these rays are presented in Fig. 9 for droplets of different aspect ratios.

From the simulations, no caustics were observed from completely spherical droplets. For droplets with an aspect ratio close to 1, an optical caustic with the shape of an astroid curve was obtained. This curve moves toward lower scattering angles as the aspect ratio of the droplet deviates from 1. With this the conclusions postulated previously in section 3 are confirmed.

5. Conclusions

Caustics were experimentally and numerically observed in the glory region when the droplet sphericity is close to one. The caustics take the shape of an astroid curve and simulations have shown that they were caused by rays that are internally reflected five times. The caustics are thus an indication for the non-sphericity of the droplet. However, since the glory pattern can still be observed, it remains possible to use it to determine the droplet size, which makes this a good technique for analyzing the size of non-spherical and spherical droplets.

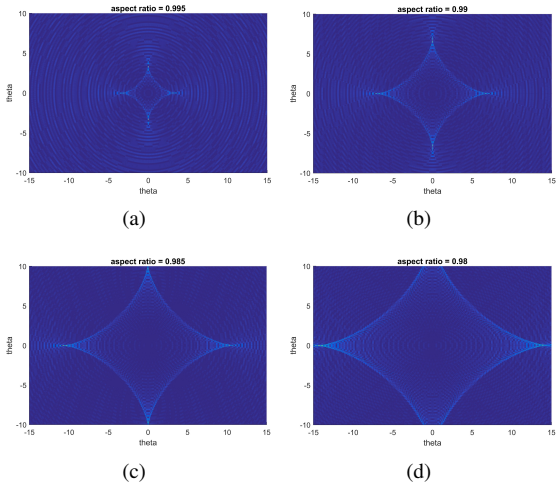

Figure 9: Numerical simulation of a caustic produced by p = 6 from a spheroidal droplet of increasing aspect ratio (a to d).

Acknowledgments

This PhD project is funded by the Agency for Innovation by Science and Technology in Flanders (IWT).

References

[1] J. van Beeck, Rainbow phenomena: development of a laser-based, non-intrusive technique for measuring droplet size, temperature and velocity, Ph.D. thesis, Technische Universiteit Eindhoven (1997).
[2] S. Dehaeck, Development of glare point, shadow and interferometric planar techniques for gas bubble sizing, Ph.D. thesis, Universiteit Gent (2007).
[3] H. van de Hulst, R. Wang, Glare points, Applied Optics 30 (1991) 4755–4763.
[4] H. van de Hulst, Light Scattering by Small Particles, Dover Publications, 1981.
[5] M. Kerker, The scattering of light and other electromagnetic radiation, Academic Press, 1969.
[6] E. Hecht, Optics, Addison Wesley Longman, 2002.
[7] P. Gillis, C. Deleuze, V. Henri, J. Lesceux, Backscattering of light from a water droplet: The glory effect, American Journal of Physics 50 (1982) 416–421.

[8] J. van Beeck, M. Riethmuller, Rainbow phenomena applied to the measurement of droplet size and velocity and to the detection of nonsphericity, Applied Optics 35 (1996) 2259–2266.
[9] M. Vetrano, S. G. Ruiz, J. van Beeck, Single and multiple droplet sizing by backscattering glory in the micrometric range, Optics Communications 341 (2015) 271–275.
[10] S. G. Ruiz, M. Vetrano, J. van Beeck, Feasibility of using glory and speckle patterns for sizing spherical and irregular particles, Applied Optics 53 (21) (2014) 4722–4728.
[11] H. Yu, Laser beam interaction with spheroidal droplets: Computation and measurement, Ph.D. thesis, Technische Universität Darmstadt (2013).

Oscillation of a planar gas jet impinging on a deformable wall

Miguel Alfonso Mendez

Environmental and Applied Fluid Dynamics Department, von Karman Institute for Fluid Dynamics, Belgium, mendez@vki.ac.be

Supervisor: Jean-Marie Buchlin

Professor, Environmental and Applied Fluid Dynamics Department, Belgium, buchlin@vki.ac.be

University Supervisor: Herman Deconinck

Professor, Aeronautics and Aerospace Department, von Karman Institute for Fluid Dynamics, Belgium, deconinck@vki.ac.be
Département d' Aéro-Thermo-Mécanique, Faculté des Sciences Appliquées, Université Libre de Bruxelles, Belgium

Abstract

This paper presents the last research activities in the framework of a PhD project on the dynamics of gas jet impinging on vertical falling liquid films. The configuration is relevant in continuous coating technology, where impinging gas jets are used to control the final coating thickness on a moving substrate. In the previous VKI PhD Symposium, it was shown that the gas jet develops sustained oscillation if the shape of the liquid interface is sufficiently deformed by the impingement. In particular, it was shown that these oscillations are a combination of a harmonic response to the liquid interface motion and a non harmonic response. In this work, we prove that the non harmonic response is due to the shape of the impinged interface and that it is independent of its motion. To this end, the dynamics of the impinged liquid film is reproduced by a deformable wall, with both fixed and time varying shapes. The response of the impinging jet flow is analyzed via flow visualization and Time Resolved Particle Image Velocimetry (TR-PIV), while the interface motion is monitored by a novel dynamic masking algorithm.

Keywords: Impinging Jets, Hydrodynamic Feedback, Time Resolved PIV, Dynamic Masking.

1. Introduction

The impingement of a planar gas jet flow onto a flat surface is one of the most popular flow configuration in fluid dynamics, with a large range of industrial applications. Impinging jets produce high convective heat fluxes, which is employed in drying, heating or cooling applications [1; 2; 3] and high pressure and shear stress gradients, which is employed in film and coating thickness control [4; 5; 6].

The classical configuration, with the flow impingement normal to the wall, this configuration is characterized by a entrainment flow aligned with the jet and a symmetric and orthogonal bifurcation of the streamlines into two wall jets, released from the stagnation point. If either of these two features are hindered, impinging jet flows are prone to develop self-sustained oscillations [7; 8]. When the characteristic Strohual number is low ($St = O(10^{-3})$), these oscillations are sustained by a hydrodynamic feedback, which manifests as large scale recirculations bounding the jet flow. Typical examples are the jet impingement on a V-shape [9], encountered in fluidic devices, or the jet discharge into rectangular cavities [10], encountered, for example, in thin slab casting moulds [11]. Self-sustained oscillation of impinging jets impacts any applications, resulting in oscillatory stagnation regions which can drastically enhance mixing and heat transfer or compromise the stability of film thickness control in coating processes.

The control of the coating thickness on a moving substrate by means of impinging gas jet is known as Jet Wiping, and the stability of this process is the main topic of this PhD thesis. Jet wiping is common in paint, paper and galvanizing industry. With respect to other methods, it is economic, contactless and continuous, but the coating uniformity –thus the product quality– is limited by the undulating patterns. Previous ULB-VKI thesis on the topic [12; 13] have shown

that these undulations are due to sustained oscillations of the impinging jet, and the research conducted in the first two years of this thesis has confirmed that these oscillations are driven by a hydrodynamic feedback as in other well-known configurations featuring oscillating impinging jet flows.

In particular, the gas jet impingement on a vertical falling liquid film has been reproduced on a laboratory model [14; 15] in which the liquid film flow rate was pulsed at controlled frequency and amplitudes. The scope was to investigate if a perturbation on the liquid film, in the form of gravity waves, could promote oscillations in the gas jet. The results have shown that this occurs only if the liquid interface is sufficiently deformed by the impingement, producing an asymmetric shape capable of hindering the flow bifurcation at the impingement.

In this configuration, in which the liquid interface acts as an oscillating V-shape, the gas jet oscillations have been revealed using high speed flow visualization and a dedicated image processing routine, while large recirculation zone were observed via Particle Image Velocimetry (PIV). A typical snapshot is shown in Fig.1, where these two techniques are combined with Level Detection and Recording to monitor the liquid interface [15; 16; 17].

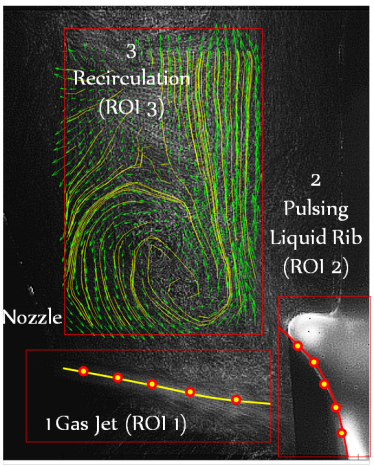

Figure 1: Example snapshot and region of interest (ROI) of the processing techniques used to monitor gas jet oscillation (1), liquid interface (2) and flow field (3).

As a second step, to prove that the role of the liquid interface is purely geometrical, the liquid film has been replaced by a solid surface in a second laboratory model. This model, sketched in Fig.2, consists of a flexible membrane fixed on a plate on one side and on a slider on the other. In this work, the jet flow response has been analyzed in unsteady conditions, with the slider oscillating at prescribed frequencies and in steady condition, with slider holding the membrane in a 2D rib. In both cases, the membrane is sufficiently flexible to follow the slider motion, but not to be deformed by the impinging jet, for which it represents a rigid boundary.

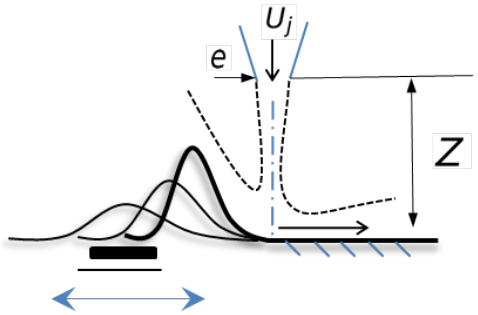

Figure 2: Simplified Laboratory Model: a gas jet impinges on a 2D membrane which reproduces the interface of the liquid coat in jet wiping process.

The experimental set up is described in Section 2. The measurement techniques developed to study the impinging jet response were presented in detail in [18], and are recalled in Section 3. The data processing includes the detection of the jet oscillation frequency, the monitor of the membrane motion, and the tracking of the produced recirculation structures bounding the jet flow. The results are presented in Section 4. Finally, Section 5 closes with the conclusions and a brief description of the ongoing research activities of the PhD project.

2. Experimental Set Up

The experimental setup is sketched in Fig.3. A nozzle (1), supplied by compressed air and seeding particles (primary injection), is installed on a 2D axis support (2). To produce a laser sheet, an optical setup (3) is installed above the nozzle and a secondary injection (4), to seed the entrainment flow, is installed above the jet. The oscillating membrane is installed on an oscillating support (5) driven by an EC motor.

The membrane is a $2mm$ thick sheet of $VitonFKM$, glued to an aluminum plate above the impingement and pinned on a slider below it. The oscillating motion of the slider is driven by a EC motor (MaxonEC-4pole45) through a crank mechanism (Fig.4) which

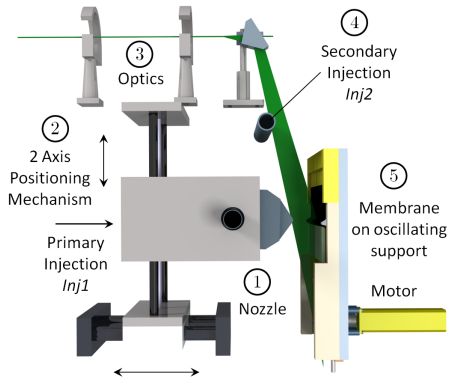

Figure 3: Side view of the experimental set up: a nozzle is installed on a two-axis positioning mechanism and discharges normal to the oscillating membrane

drives the oscillatory motion of the slider in the vertical direction. Figure 5 shows a cross section of the nozzle and its stagnation chamber. Two turbulence grid generators are installed to uniform the turbulence intensity ($TI \approx 2\%$ in the centerline). The chamber is equipped with a pressure tap, connected to a piezoresistive pressure transducer *AMS* 5812. All the experiments were performed with a $P_n = 230 \pm 2\% Pa$, corresponding to an outlet velocity of $U_j = 18 \pm 3\% m/s$, thus a Reynolds number $Re_j \approx 1800$.

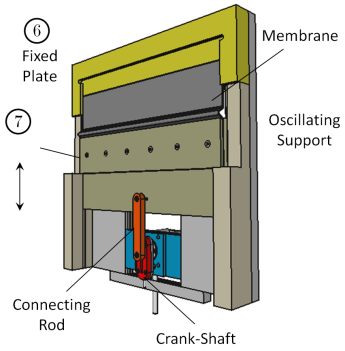

Figure 4: Detail of the oscillating support: the membrane is attached on a fixed plate (6) above the impingement, on a slider (7) below the impingement. The vertical oscillation of the slider is imparted by a crank-shaft mechanism, driven by a EC motor.

This nozzle is supplied by a seeding generator (Laskin Nozzle PIVTEC45-M) operating with a mineral oil (Ondina Shell 917). The seeding generator is

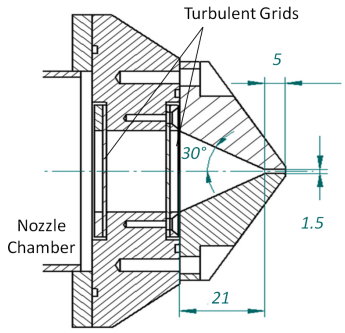

Figure 5: Cross section of the Nozzle facility, with the main quotes.

also connected to the secondary injection (Inj_2), positioned above the jet (Fig.3), to seed the surrounding flow before the PIV experiments.

The light source is a single cavity diode-pumped Nd:YLF laser, from Quantronix Darwin Duo system, framing green laser pulses at a maximum $f = 10kHz$. The optical set up installed above the jet produces a laser sheet of $2mm$ thick, $5cm$ wide in the impingement region. The camera is a CMOS Photron FASTCAM SA1 and it is installed at $30cm$ with a $105mm$ Micro-Nikkor objective, providing a scaling factor of $M = 21.8 \pm 0.2 pixel/mm$. The maximum size of each video sequence is $5.5Gb$, corresponding to $n_t = 21286$ gray scale images with $n_p = 512 \times 512 pixel^2$ resolution.

In the flow visualization (FV) acquisition, the camera acquires at $f_s = 2kHz$ with large exposure ($t_e = 40\mu s$), synchronized with the laser cavity pulsing at $8kHz$. As each frame is exposed to four laser pulses, and the secondary seeding is closed, the jet flow appears as a connected area. An example of a typical FV snapshot is in Fig.6a. Besides allowing for a simple identification of the jet flow, this acquisition has a large observation time ($T_e \approx 10s$), which gives a high frequency resolution in the analysis of the jet oscillation (Sec.3.2). In the particle image velocimetry (PIV) acquisition, laser and camera frame at $f_s = 10kHz$ and the images are acquired in single frame mode with frame exposure defined by the laser pulse width. The secondary injection is open and the entire field of view is seeded. An example of PIV snapshot is in Fig.9.b. This acquisition was used to extract the large scale dynamics of the flow field within the period of a jet oscillation (Sec.3.3). Each test was repeated with both FV and PIV configuration, starting the acquisition $5s$ af-

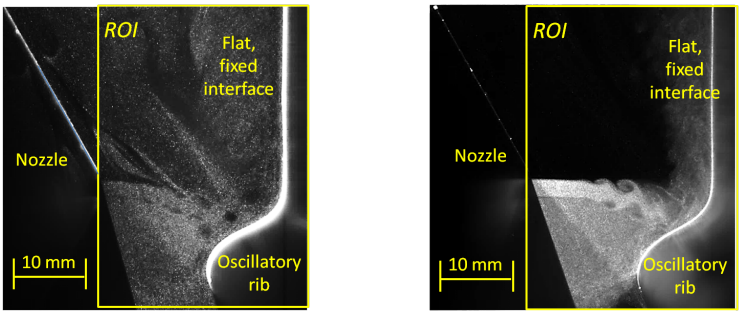

(a) (b)

Figure 6: Example of a) FV and b) PIV acquisition snapshots with Region of Interest (ROI) selected for the image processing. The condensation of the seeding particles on the membrane makes the interface clearly visible.

ter the jet flow is produced. This results in a thin layer of condensed oil on the membrane, which simplifies its detection via image processing (Sec.3.1).

3. Quantitative Flow Visualization

For both FV and PIV acquisitions, the image processing starts by tracking the membrane interface. This allows to compute the phase shift between the videos, by overlapping the temporal evolution of the membrane profiles obtained in each of them. Moreover, in the PIV processing, the membrane profiles are used for the automatic masking of the images. The interface tracking is performed by a dynamic masking routine, developed in *Matlab*, based on the Eigenbackground decomposition, discussed in 3.1. The gas jet tracking and the PIV processing are discussed in Sec.3.2 and Sec.3.3.

3.1. Eigenbackground Decomposition and Masking

Firstly introduced in [19], this method is a popular adaptive background subtraction method to detect moving objects in the video surveillance analysis. The key idea is to reshape the video sequence as a matrix, and to consider its rank-based decomposition via Principal Components Analysis (PCA). Large and bright objects, moving slowly and/or periodically, are described by a low rank approximation of the matrix, contrary to small objects moving quickly and/or randomly. Such low rank approximation of the video sequence is obtained by expressing every image as a linear combination of few basis images referred to as *eigenbackgrounds*. Practically, the method is a Proper Orthogonal Decomposition (POD) of the video sequence, being the eigenbackgrounds the equivalent of the spatial modes (*topomodes*) of velocity snapshot matrix S_U (Sec.3.3).

The algorithm consists of two phases: a *learning phase* and a *testing phase*. The learning phase consists in computing the eigenbackgrounds from a portion of the video, known as training video. The testing phase consists in projecting every image in the space spanned by the eigenbackgrounds. Given the original set of n_t images I_i, sampled at f_s, the training video matrix was constructed selecting a set of $n'_t = n_t/F_{ds}$ images I_j, sampled at $f'_s = f_s/F_{ds}$. A factor of $F_s = 25$ was chosen as a compromise between frequency resolution, statistical independence and video size. Each of these n_t images $I_j \in \mathbb{R}^{n_p}$, with resolution $n_p = n_x \times n_y$, is reshaped into a column vector $I_j \in \mathbb{R}^{n_p \times 1}$ and stacked on a training matrix $A_t \in \mathbb{R}^{n_p \times n_t}$ which has the gray scale domain in the column space and the temporal evolution in its row space. With such construction, the eigenbackgrounds $\Phi = [\phi_1, \phi_2, \dots \phi_{n_t}]$ are defined as the eigenvectors of the zero-mean shifted covariance matrix $\hat{C}$:

$$C\ \Phi = \Lambda\ \Phi;\ C = \hat{A}_t \hat{A}_t^T\ \ with\ \ \hat{A}_t = A_t - \mu\ , \quad (1)$$

where Λ is the diagonal matrix containing the λ_i eigenvalues sorted in descending order and $\mu = \frac{1}{n'_t} \sum_1^{n'_t} I_j$ is the time-averaged image.

Instead of solving eq.1, since $n'_t << n_p$, it is convenient to diagonalize the covariance $\hat{K}$ of the transposed training video matrix:

$$K\ \Psi = \Lambda\ \Psi;\ K = \hat{A}_t^T\ \hat{A}_t\ \ with\ \ \hat{A}_t = A_t - \mu\ , \quad (2)$$

which gives a temporal eigenbasis $[\psi_1, \psi_2, \dots \psi_{n'_t}]$, and compute the eigenbackrounds recalling the relation between Φ, Ψ, Λ, and the Singular Value Decomposition (SVD) of the training video matrix:

$$A_t = \Phi \Sigma \Psi^T = \Phi \Lambda^{1/2} \Psi^T \rightarrow \Phi = A_t \Psi (\Lambda)^{-1/2} \quad (3)$$

In practice, obtaining the eigenbackgrounds Φ solving eq.1 is equivalent to the discrete version of the standard POD, whereas using eq.2 and then eq.3 is equivalent to the snapshot POD method[1] from Sirovinch [21]. The eigenbackground (EIG) method consists in computing, in the spirit of PCA analysis, an adaptive background B_i for every image attribute I_i, as a linear combination of the first $k_c << n_p$ eigenbackgrounds $\Phi_{k_c} = [\phi_1, \phi_2, \ldots \phi_{k_c}]$ and the average image μ:

$$B_i = \Phi_{k_c} \mathbf{b} + \mu \quad where \quad \mathbf{b} = \Phi_k^T (I_i - \mu). \quad (4)$$

Eq.4 is a projection of the attribute vector I_i in the eigenspace spanned by the first k_c eigenbackgrounds, being $\mathbf{b}$ the coefficient vector of the combination. In the basic formulation, the number of eigenbackgrounds retained k_c is chosen by fixing a threshold for the last eigenvalue λ_{k_c} retained. The background obtained B_i are then subtracted to the original image and a moving object is identified as the regions of the images in which $I_i - B_i$ is larger than a given threshold. In this work, the backgrounds are constructed considering only the time varying part, $B_i = \Phi_{k_c} \mathbf{b}$, having rank k_c computed from the distribution of energy (i.e. norm) of the matrix A_t along its single-rank components. At the scope, let δ define the *relative information content*

$$\delta(k) = \frac{\sum_{i=1}^{k} \sqrt{\lambda_i}}{\sum_{i=1}^{n'_t} \sqrt{\lambda_i}}, \quad (5)$$

which is shown in Fig.7 for the FV and PIV video sequences, as a function of $\hat{k} = k/n_t$. The criteria to select the cut-off rank k_c is based on the observation that $\delta(\hat{k})$ tends to be linear as the contributes of each eigenbackgrounds tend to be equal, i.e. for a fairly uncorrelated noise. Fig.8 shows the cut-off rank obtained by imposing a tolerance on the second derivative $d^2\delta/d\hat{k}^2 < 10^{-3}$. For the examples in Fig.6, this criteria gives $k = 23$ for the PIV sequence, $k = 35$ for the FV sequence, showing that the former is more easily compressed than the latter. Fig.8 shows the background images B_i corresponding to these examples. The detection of the membrane interface is then easily completed via image binarization, as described in [17].

[1] This decomposition is equivalent SVD of the snapshot snapshot matrix analyzed. However, the SVD computation generally requires more memory allocation than either eq.1 (if $n'_t >> n_p$) or the eq.s 2-3 (if $n'_t << n_p$). A detailed example of video decomposition via SVD is proposed in [20].

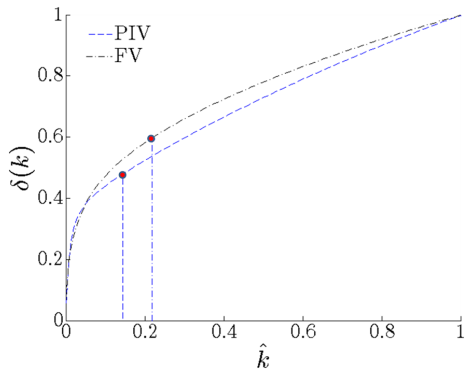

Figure 7: Relative information content (RIC) $\hat{\delta}(\hat{k})$ as a function of the percentage of rank $\hat{k} = k/n'_t$ considered in the FV and the PIV videos.

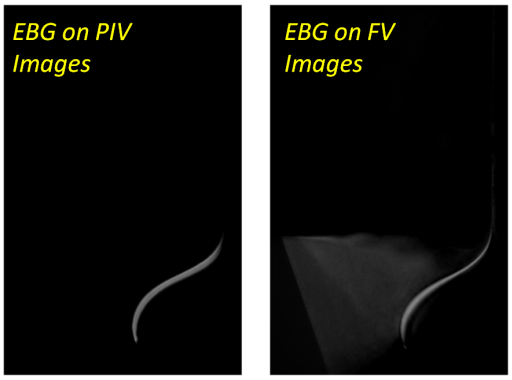

Figure 8: Low rank approximation of the example snapshots in Fig.6, computed with $k_c = 23$ eigenbackgrounds for the PIV images and $k_c = 35$ eigenbackgrounds for the FV images.

3.2. Analysis of the Jet Flow Response

The methodology to track the jet oscillation in FV videos is based on finding the geometrical centerline of the jet in every image as proposed in [14]. First, the images are cropped around the jet as shown in Fig.9a and horizontally recontrasted. Then, to increase differentiability of the gray scale contour, the images are

low-pass filtered using a Gassian kernel and the column gray scale profile is smoothed with a second order Savizty-Sgolay filter (Fig.9b). In each column, the position of the jet centerline is determine as the first peak of the the corresponding gray scale profile. The jet centerline reconstruction (Fig.9a) is further smoothed via Savizty-Sgolay filter.

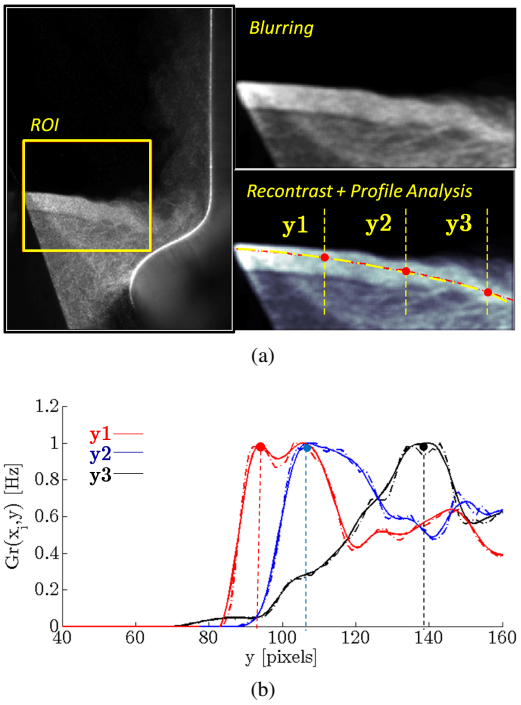

Figure 9: Detection of jet flow geometrical centerline. A ROI is cropped from the FV visualization sequence. After equalization and blurring, the gray scale profile in each column is used to locate the jet centerline.

3.3. Analysis of the Flow Field Response

The particle image velocimetry is performed over the ROI shown in Fig.6a, which varies between $224 \times 512 pixels^2$ to $384 \times 512 pixels^2$ depending on the jet stand-off distance considered. The processing is performed with the PIVlab package [22] using standard iterative multi-step interrogation (three passes from 64×64 to 8×8) with spline window deformation. The sub-pixel interpolation is a 2D Gaussian and the vector validation is carried out with standard median test. Moreover, as the characteristic time scale of the investigated phenomena is two order of magnitude lower than the acquisition frequency, the temporal analysis of the PIV in this work has been carried out on a downsampled data set, in which each flow realization is computed as the average of a moving window of size $F_s = 2K + 1$:

$$\vec{U}_{DS}(x_n, y_n, t_j) = \frac{1}{F_s} \sum_{i=j-K}^{i=j+K} \vec{U}(x_n, y_n, t_i) \ . \qquad (6)$$

where $x_n \in [1, n_x]$, $y_n \in [1, n_y]$ is the spacial grid and $t_n \in [1, n_t']$ is the dowsnampled time vector. This operations corresponds to a linear low-pass filtering in the time domain. The median test is repeated after every time average, and the vector field is smoothed via the fast and robust smoothing spline method proposed in [23]. To analyze the large scale dynamics of the flow field surrounding the jet, a time window size of $F_s = 25$ was selected. This significantly reduces the number of velocity realization and increases the flow coherence, while retaining a sampling frequency of $f_s = 400Hz$, sufficient to capture the hydrodynamic feedback.
Finally, to extract the dominant flow features, the obtained discrete set of velocity fields U_{DS} is decomposed in orthonormal spatial (*topo*-modes, ϕ_i), temporal (*chrono*-modes, ψ_i) and amplitudes σ_i:

$$\vec{U}_{DS}(x_n, y_n, t_n) = \sum_{i=1}^{i=n_t'} \sigma_i \, \phi_i(x_n, y_n) \, \psi_i(t_n) \ . \qquad (7)$$

Which can be rewritten in matrix form as:

$$S_U = \begin{pmatrix} u_1 & u_2 & \cdots & u_{n_t'} \\ \vdots & \vdots & \cdots & \vdots \\ v_1 & u_2 & \cdots & v_{n_t'} \\ \vdots & \vdots & \cdots & \vdots \end{pmatrix} = \Phi \, \Sigma \, \Psi^T \qquad (8)$$

therefore:

$$S_U = \begin{pmatrix} \phi_1 & \cdots & \phi_{n_t} \end{pmatrix} \begin{pmatrix} \sigma_1 & \cdots & 0 \\ 0 & \ddots & 0 \\ 0 & \cdots & \sigma_{n_t} \end{pmatrix} \begin{pmatrix} \psi_1 \\ \psi_2 \\ \vdots \\ \psi_{n_t'} \end{pmatrix}, \qquad (9)$$

where $S_U \in \mathbb{R}^{2 n_x n_y \times n_t}$ is the snapshot velocity matrix, containing in each column the realization of the vector fields $\vec{U}_{DS}(x_n, y_n, t_j) = (u_j(x_n, y_n) v_j(x_n, y_n))$ reshaped as a column. When assembling the matrix S_U, two different approaches were tested to deal with the

points periodically occupied by the membrane. The first approach consisted in placing a random number, the second in extrapolating velocity points from the rest of the domain. The choice only had an effect in the topomodes $\phi_i(x_n, y_n)$, in those regions in which the artificial replacement took place, which is not of interest in the flow analysis. Since $n_x n_y >> n'_t$, the POD decomposition in 7 was computed using Sirovinch's approach [21], i.e. via eq.2 and eq.3, replacing A_t by snapshot velocity matrix S_U. The decomposition was used to construct a low rank representation of the flow field, computing the cut-off rank K_c with the same criteria used for the eigenbackground decomposition in Sec.3.1. Finally, it was of interest to analyze the flow field response in terms of rotation rate and strain rate by computing the second invariant of the velocity gradient tensor $\nabla\vec{U}_{DS}$ in each snapshot $\vec{U}_{DS}(x_n, y_n, t_j)$:

$$Q = \frac{1}{2}\left(\|\Omega\|^2 - \|S\|^2\right) \tag{10}$$

where $S = \frac{1}{2}(\nabla\vec{U}_{DS} + (\nabla\vec{U}_{DS})^T)$ is the rate-of-strain tensor, $\Omega = \frac{1}{2}(\nabla\vec{U}_{DS} - (\nabla\vec{U}_{DS})^T)$ is the vorticity tensor, and $\|X\| = Tr[XX^T]^{1/2}$ is the Frobenious norm of the tensor X. The resulting expression reads:

$$Q = -\frac{1}{2}\left[\left(\frac{\partial v}{\partial y}\right)^2 + 2\,\frac{\partial u}{\partial y}\frac{\partial v}{\partial x} + \left(\frac{\partial u}{\partial x}\right)^2\right], \tag{11}$$

Eq.11 is evaluated using first order finite differences.

4. Results

4.1. Experimental Matrix and Data Parametrization

The test cases considered combine three stand off distances Z and three impingement positions Y, analyzed for two membrane oscillation frequency and in steady condition, with the membrane hold at its maximum deflection. As shown in Fig.10, the frame of reference is positioned at the point below which the membrane is free to move and deform.

To analyze the interaction between membrane motion, jet oscillation and flow field topology, it was of interest to define a 0D time dependent variable representative of each dynamics. For the membrane motion, we consider the horizontal displacement of a point at a fixed distance y^*, namely the one in which the membrane reaches its maximum height ($H_{max} \approx 11mm$) during the oscillatory motion. For the jet oscillation, we consider the vertical displacement of a centerline point at $z^* = Z/2$.

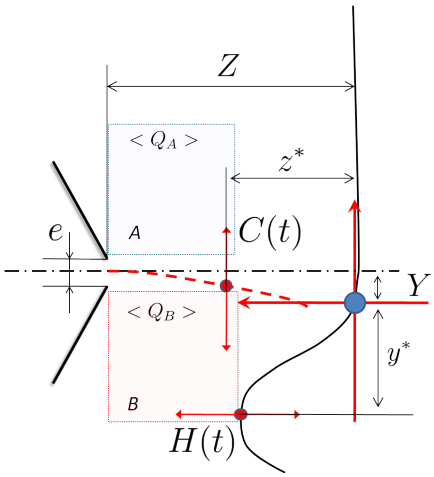

Figure 10: Definition of reference axes and 0D quantities of interest. The distances (Z, Y) are nondimensionalized $(\hat{Z}, \hat{Y})$ with respect to the jet opening e.

For the flow field response, we define an integral quantity representing the unbalance in the Q field between a rectangular region A above the jet and a rectangular region B below the jet (Fig.10). In particular, we consider the spatial average of the $Q(x_n, y_n)$ field, over a domain D containing Np points, including only positive values of Q, defined as:

$$\langle Q_D \rangle = \frac{1}{Np}\sum_{(x_n,y_n)\in D}\sum Q^+(x_n y_n)\,, \tag{12}$$

where $Q^+ = Q : Q > 0$. To measure the asymmetry in the vorticity content between the regions A and B sketched in Fig.10, we define a coefficient $\alpha_q = \langle Q_A \rangle - \langle Q_B \rangle$. In other words, $\alpha_Q < 0$ implies that, in the region below the jet, the vorticity dominates over the strain more than it does above the jet. Finally, to plot $H(t)$, $C(t)$ and $\alpha_q(t)$ in the time scale, each 0D quantity $x(t_n)$, containing n'_t time realizations, in rescaled into $x^*(t) \in [-1, 1]$:

$$x^*(t_n) = \frac{x(t_n) - \mu(x(t_n))}{\|x(t_n) - \mu(x(t_n))\|} \tag{13}$$

being $\mu(x(t_n)) = \frac{1}{n'_t}\sum_0^{n'_t} x(t_n)$ the time average. It is worth recalling that $C^*(t)$ is obtained from the FV acquisition, $\alpha_q^*(t)$ is obtained from the PIV acquisition, and $H^*(t)$ is obtained in both. Therefore, phase shift between C^* and α_q^* is computed, in the unsteady tests, by cross correlating the membrane displacements obtained in the two videos.

4.2. Gas Jet Response in the Frequency Domain

The power spectral densities (PSD) of the gas jet centerline $C^*(t)$ for the tests studied are collected in Fig.11. For plotting purposes, the frequency domain f_j is limited to $f_j = 150Hz$, and the PSD in each graph is normalized with respect to the maximum PSD detected within the three tests.

Regardless of the stand-off distance $\hat{Z} = Z/e$, at $\hat{Y} = 0$ the response of the jet to the membrane motion is the superimposition of a harmonic response f_h and a higher frequency f_f, which is not affected by the membrane motion. Noteworthy, f_f scales with the standoff distance and leads to a constant Strouhal number $St_Z = f_f Z/U_j \approx 0.07$, as commonly encountered in other configuration promoting self sustained oscillation of impinging jets (e.g. in the V-shape case, $St_Z \approx 0.13$ [9]). This oscillation is due a hydrodynamic feedback produced by the asymmetry of the membrane shape and remains unchanged in the oscillatory test. The situation changes when moving the impingement point: at $\hat{Y} = 1$ this oscillation is damped by the motion of the membrane and it completely disappears, in both steady and unsteady tests, at $\hat{Y} = 2$. Remarkably, for an impingement in this position (and above), the steady cases do not display any jet oscillation. To understand what determines the difference in the jet responses, two unsteady configurations are analyzed, namely $(\hat{Z}, \hat{Y}, f) = (10.2, 1, 3Hz)$, corresponding to the 'bimodal response' case, and $(\hat{Z}, \hat{Y}, f) = (10.2, 2, 3Hz)$, corresponding to the 'harmonic response' case.

4.3. Flow field, Jet oscillation and Membrane Motion

Fig.12 plots the temporal evolution of C^*, H^* and α_q^* for the 'bimodal response' test case. It is evident that the jet is stable ($C(t) \approx 0$) when the membrane is below the average position ($H^* < 0$) and this condition is characterized by a balance in the vorticity content above and below the jet ($\alpha_q \approx 0$). When the membrane moves above its mean shape, starting from a deflection of the bottom wall jet of about 40°, an unstable configuration is produced and the jet centerline oscillates around its mean position, downward biased with respect to the average position. During the oscillation, the vorticity content below the jet dominates the one above the jet ($\alpha_q < 0$).

This unbalance in the Q field is not symmetric and oscillates at the frequency of the jet oscillation. Moreover, it is worth noticing that the Q unbalance α_q is delayed from jet oscillation $C^*(t)$, a possible sign that the unbalance of the vorticity content is a result, rather than a cause, of the jet oscillation.

Fig.13 plots the velocity vector field and the Q field for a set of 8 snapshots (4 in the descending phase and 4 in the raising phase of the membrane) indicated in Fig.12. Indeed, a large vortex is trapped between the jet flow, the entrainment flow, and the deflected wall jet and bounds the jet below the centerline. This vortex is unstable and its strength oscillates at the frequency of the jet oscillation, as visible from the oscillation of α_q in Fig.12. These oscillations stop when the membrane interface partially recovers its symmetry, reducing the deflection of the bottom wall jet and releasing the vortex below the jet. The same analysis is repeated in Fig.14 and Fig.15, for the 'harmonic response' case where the impingement is moved at upward.

From the temporal evolutions of C^*, H^* and α_q^*, three key differences with respect to the case in Fig.13 are evident. First, the jet oscillation within a membrane period are strongly damped and the jet periodically bends downward. Second, the non harmonic component f_f disappears from both the jet centerline $C^*(t)$ and the Q unbalance $\alpha_q^*(t)$. Third, the deflection of the jet is gradual and reaches its maximum only in the descending phase of the membrane. As the impinging of the jet is moved upward, the recirculation produced by the confinement grows larger and more stable. The increased stability is evident from the behavior of α_q, which responds harmonically. The increased size is evident from the drop in the second invariant Q.

Nevertheless, a strong link is observed in the periodic, downward, deflection of the jet and the periodic formation of a large scale recirculation below the jet. The phase delay between $\alpha_q^*(t)$ and $C*(t)$ in test at $\hat{Y} = 1$ is reversed with respect to the case at $\hat{Y} = 0$: the peak of vorticity occurs before the jet reaches its maximum deflection.

5. Conclusions and Future Work

The response of the gas jet to the membrane motion, particularly in the 'bimodal response' case in Fig.12 share several similarities with the response of the gas jet on the perturbed liquid film presented in [14]. First, the presence of two different modes, which have been proved in this work to be linked to the motion of the impinged interface (the harmonic response) and to the shape of the interface itself (non harmonic response). Second, Fig.s 12 and 14 finally confirm that the oscillations of the jet are triggered only if the impinged interface is capable of deflecting one of

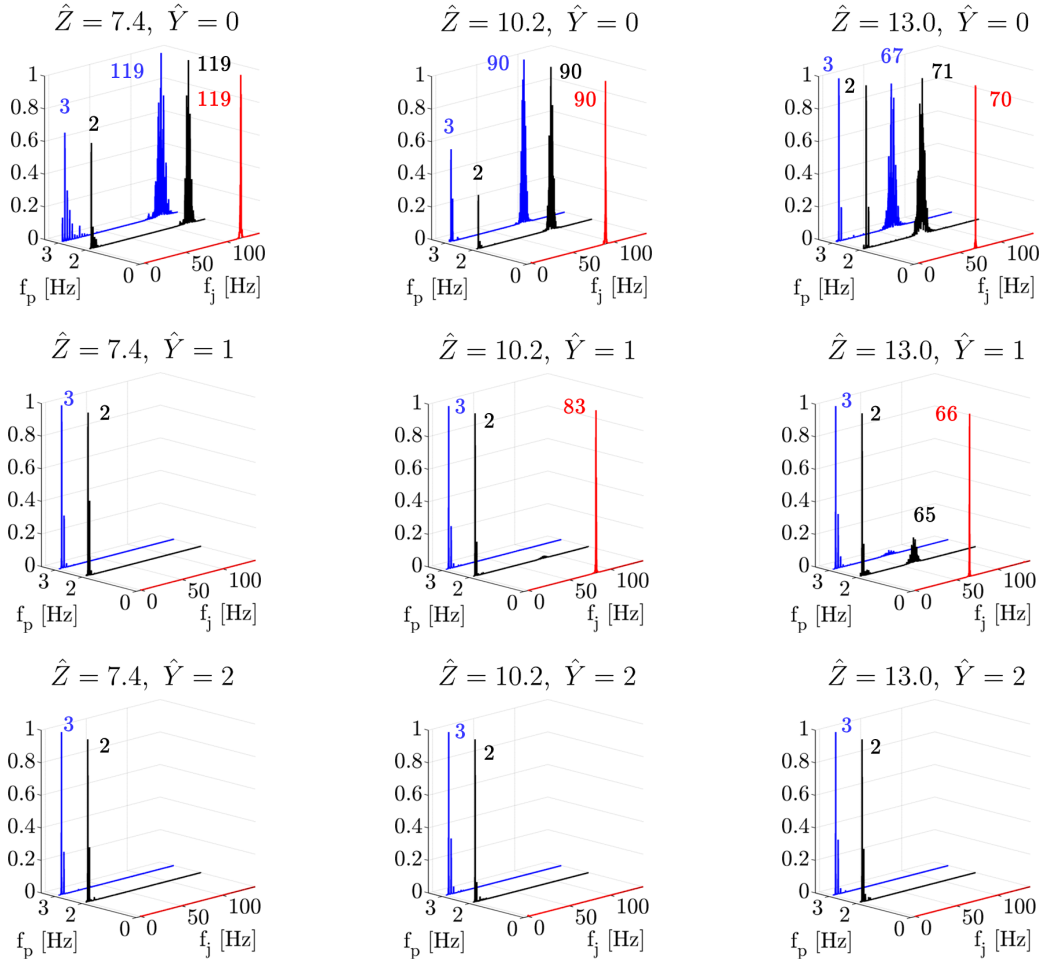

Figure 11: Power Spectral Density of the gas jet oscillation $C^*(t)$ for the steady ($f_p = 0\,Hz$) tests and the unsteady tests ($f_p = 2,3\,Hz$) at three dimensionless stand-off distances $\hat{Z} = Z/e$ and three dimensionless impingement positions $\hat{Y} = Y/e$.

the wall jets above critical angle of about 40°. Third, Fig.s 13 and 15 confirm that the oscillation of the jet is always combined with large scale recirculation produced by the entrainment flow, the deflected wall jet and the impinging jet itself.

Besides corroborating the conclusions in [14], the detailed experimental characterization presented in this work adds two new important elements in the understanding of the dynamics of gas jet impinging on liquid films, and thus the stability of jet wiping processes.

The first element is the introduction of a new variable, thanks to the complete decoupling between the jet flow and the shape of the impinged interface: the vertical distance Y between the impingement point and the point from which the wall jet deflection starts. Contrary to what happens in the simplified configuration presented in [14] and shown in Fig.1, interface disturbances are convected downward by gravity in the jet wiping configuration studied in [12; 13]. This suggests that the impinging flow periodically switches between the 'bimodal response' and the 'harmonic response' observed in Fig.s 12 and 14.
The second element introduced in this work is the phase delay between the occurrence of the large scale recirculation below the jet and the jet deflection, which questions whether the former is the cause or the consequence of the latter. Fig.12 suggests, in fact, that

the destabilizing mechanism attracting the jet down is, at least in its initial stage, promoted by a physical mechanism which is different from the pressure drop produced by the recirculation.

To conclude, this work proves that the role of the liquid film interface in triggering the oscillation of an impinging gas jet is purely geometrical, and opens the path to two new research activities aiming at revealing the physical mechanism behind the phenomenon. First, it is of interest to reproduce the impinging configuration analyzed in this work on a single phase CFD model, which will provide highly resolved spatially information on the coupling between velocity and pressure field. Second, it is of interest to explore new modal decomposition methods to characterize the jet flow response in terms of independent modes, having their own spatial and temporal dynamic. An excellent candidate to the scope is the Dynamic Mode Decomposition (DMD) proposed in [24], and under current investigation.

Acknowledgments

M.A.Mendez is supported by a F.R.S.-FNRS FRIA grant and the research project is funded by ArcelorMittal. The experiments were conducted in collaboration with the Vrije Universiteit Brussel (VUB), at the VUB-MECH laboratories, thanks to the support of Dr. A.Nila, Ing. Alain Wery, and Prof. J. van Beeck. Finally, the author gratefully acknowledges the contribution of I.Scarpeccio, who took part in the development of several *Matlab* routines in the framework of his short training program (STP) at the VKI [25].

References

[1] N.Zuckerman and N.Lior, Jet Impingement Heat Transfer: Physics, Correlations, and Numerical Modeling, Advances in Heat Transfer 39 (2006) 565–631.

[2] J.-M. Buchlin, Convective Heat Transfer in Impinging Gas Jet Arrangements, Journal Of Applied Fluid Mechanics 4 (2) (2011) 137–149.

[3] E. Specht, Impinging jet drying, in: E. Tsotsas, A. S. Mujumdar (Eds.), Modern Drying Technology, Volume 5, Process Intensification, Wiley-VCH, 2014, Ch. 1, pp. 1–26.

[4] C.V., Tum, D.H., Wood, Wall Pressure and Shear Stress Measurement Beneath an Impinging Jet, Experimental Thermal and Fluid Science 13 (1996) 364–373.

[5] A.Gosset,J.-M.Buchlin, Jet Wiping in Hot-Dip Galvanization, Journal of Fluids Engineering 129 (4) (2007) 466–475.

[6] E.A. Elsaadawy, G.S. Hanumanth, A.K.S. Balthazaar,J.R. McDermid,A.N.HryMak, and J.F.Forbes, Coating Weight Model for the Continuous Hot-Dip Galvanizing Process, Metallurgical and Materials Transactions B 38 (3) (2007) 413–424.

[7] D. Rockwell and E. Naudascher, Self-Sustained Oscillations of Impinging Free Shear Layers, Annual Review of Fluid Mechanics 11 (67) (1979) 3643–3651.

[8] D. Rockwell, Oscillation of Impinging Shear Layers, AIAA 21 (1983) 645–663.

[9] C.-K. Lin, F.-B.Hsiao and S.S.,Sheu, Flapping Motion of a Planar Jet Impinging on a V-Shaped Plate, Journal of Aircraft 30 (3) (1993) 320–325.

[10] A. Matoui, R. Schiestel, A. Salem, Study of the Oscillatory Regime of a Turbulent Plane Jet Impinging in a Rectangular Cavity, Applied Mathematical Modelling 27 (2) (2003) 89–114.

[11] N.J. Lawson, M.R. Davidson, Crossflow characteristics of an oscillating jet in a thin slab casting mould, Journal of Fluids Engineering 121 (1999) 588–595.

[12] A.Gosset, Study of the Interaction between a Gas Flow and a Liquid Film Entrained by a Moving Surface, Ph.D. thesis, Universite Libre de Bruxelles (2007).

[13] K.Myrillas, Experimental and Numerical Investigation of Gas and Liquid Film Interaction, Ph.D. thesis, Universite Libre de Bruxelles (2011).

[14] M.A. Mendez, Dynamics of Gas Jet Impingement on Vertical Falling Liquid Films, in: Proceedings of the 6th Symposium of VKI PhD Research, Rhode Saint Genese, BE, 2015.

[15] M.A. Mendez, L. Nemeth, J.-M. Buchlin, Measurement of Liquid Films Thickness via Light Absorption and Laser Tomography, in: Proceedings of the 10th International Conference on Experimental Fluid Mechanics (EFM 2015), Prague, CZ, 2015.

[16] D. Bouchez, L. Zimmer, M.L. Riethmuller , Optical detection and characterization of interfaces, in: 9th Symp. of flow visualization, 2000.

[17] M.A. Mendez, J.-M. Buchlin, A Research Methodology To Study Jet Wiping Processes, in: Proceedings of the 11th European Coating Symposium ECS2015, Eindhoven, NL, 2015.

[18] M.A. Mendez, J.-M. Buchlin, Quantitative Flow Visualization of Confinement-Driven Instabilities of an Impinging Slot Jet, in: Proceedings of the 11th International Symposium on Particle Image Velocimetry (PIV2015), Santa Barbara, California, US, 2015.

[19] N.M. Oliver, B. Rosario , A.P. Pentland, A bayesian computer vision system for modeling human interactions, PAMI 22 (8) (2005) 831–843.

[20] M.A. Mendez, J.-M., Buchlin, Experimental characterization of straw jets via image processing techniques, in: 10th Pacific Symposium on Flow Visualization and Image Processing, Naples, 2015.

[21] L. Sirovich, Turbulence and the dynamics of coherent structures, Quart. Appl. Math. 45 (1987) 561–590.

[22] W. ,Thielicke,E.J. Stamhuis, Pivlab towards userfriendly, affordable and accurate digital particle image velocimetry in matlab, Journal of Open Research Software 2 (1) (2014) e30.

[23] Garcia, D., Robust smoothing of gridded data in one and higher dimensions with missing values, Computational Statistics and Data Analysis 54 (2010) 1167–1178.

[24] O.J., Schmid, Dynamic mode decomposition of numerical and experimental data, J. Fluid Mech. 656 (2010) 5–28.

[25] I.Scarpeccio, Experimental characterization of confinement-driven instabilities of a slot jet impinging on a flexible membrane, Tech. Rep. VKI SR 2015-49, von Karman Institute, Supervisors: M.A.Mendez, J.-M. Buchlin, (2015).

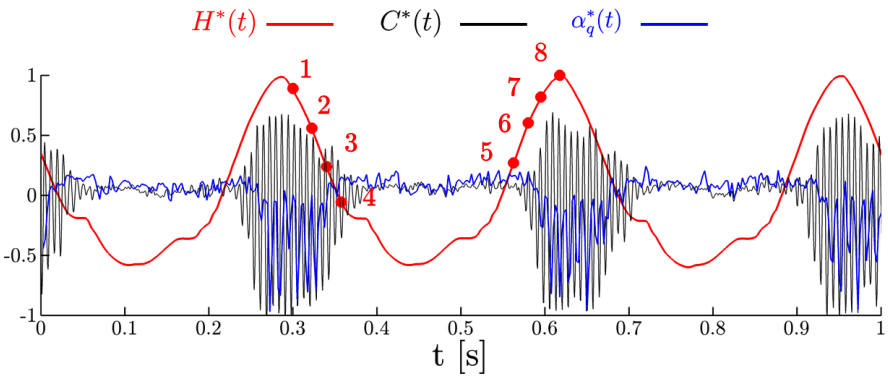

Figure 12: Temporal evolution of dimensionless membrane displacement H^*, jet centerline oscillation C^* and unbalance of the second invariant Q of the vorticity field between a region above and a region below the jet. Test at stand-off distance $\hat{Z} = 10.2$, impingement distance $\hat{Y} = 0$, membrane frequency $f_p = 3\,Hz$.

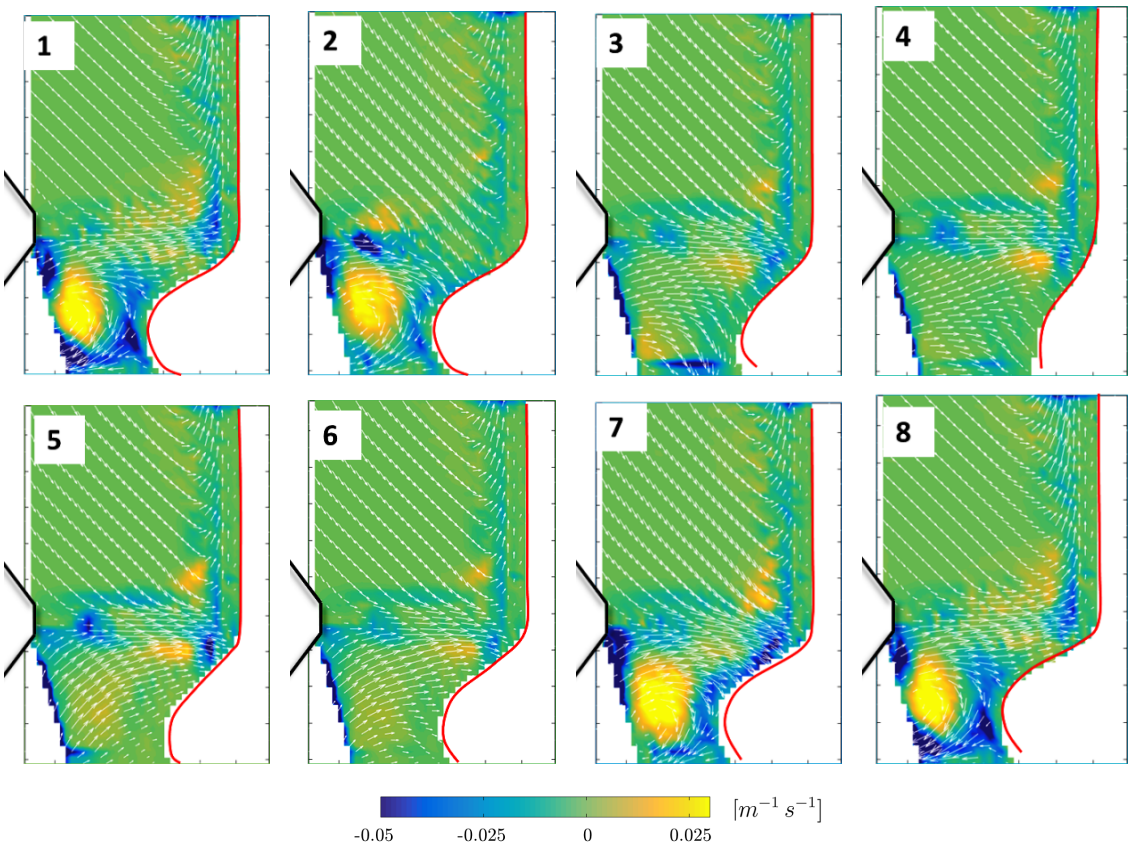

Figure 13: Snapshots of flow field and contour plot of second invariant Q of a low rank approximation of the downsampled data set $\vec{U}_{DS}$. Test at stand-off distance $\hat{Z} = 10.2$, impingement distance $\hat{Y} = 0$, membrane frequency $f_p = 3\,Hz$).The index of each figure corresponds to an instant taken from figure Fig.12.

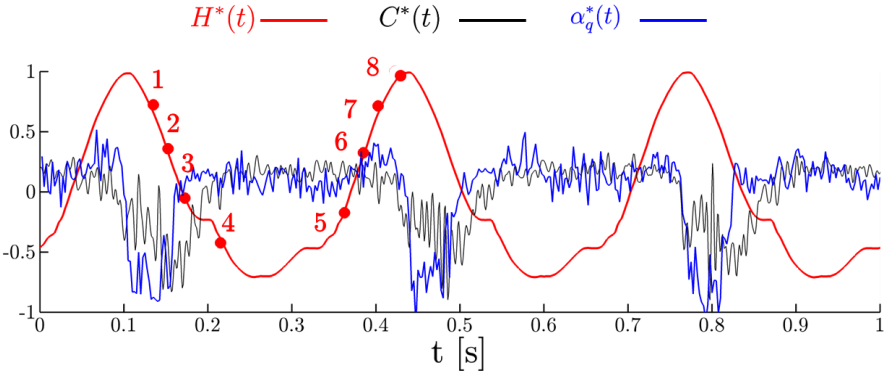

Figure 14: Temporal evolution of dimensionless membrane displacement H^*, jet centerline oscillation C^* and unbalance of the second invariant Q of the vorticity field between a region above and a region below the jet. Test at stand-off distance $\hat{Z} = 10.2$, impingement distance $\hat{Y} = 1$, membrane frequency $f_p = 3\,Hz$.

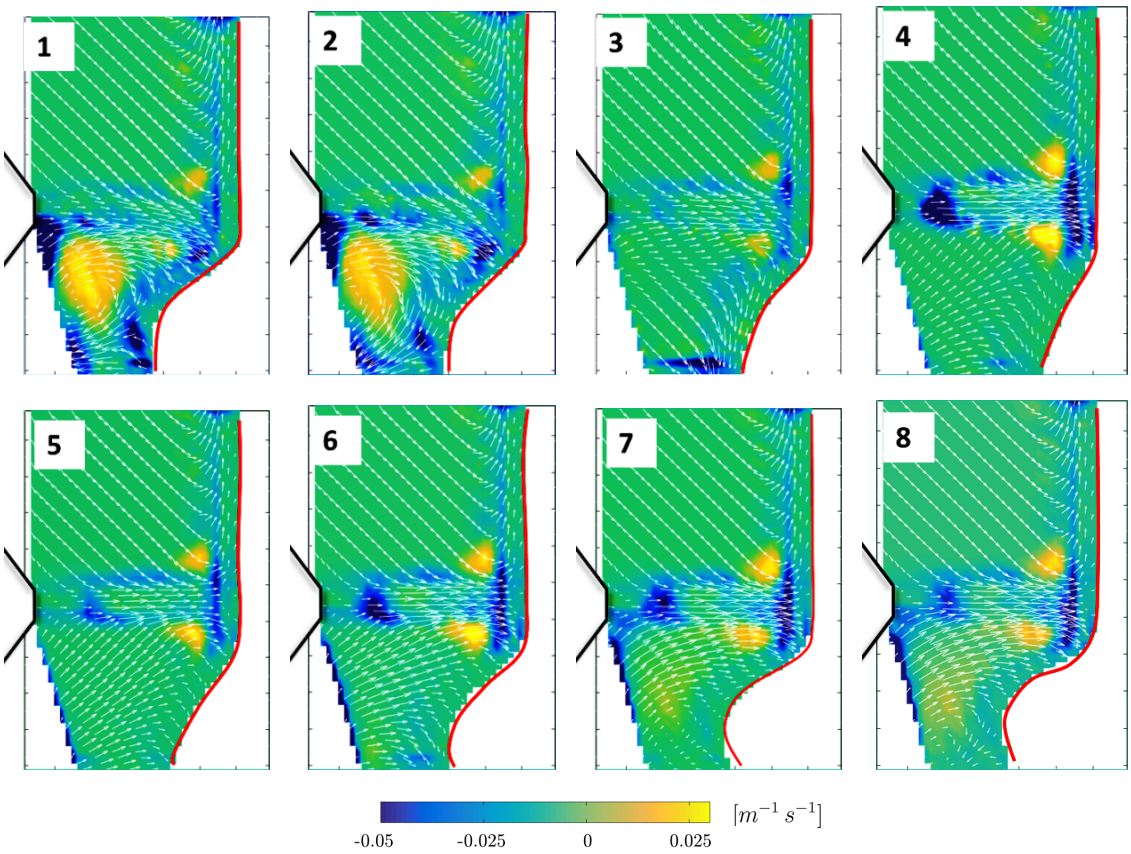

Figure 15: Snapshots of flow field and contour plot of second invariant Q of a low rank approximation of the downsampled data set $\vec{U}_{DS}$. Test at stand-off distance $\hat{Z} = 10.2$, impingement distance $\hat{Y} = 1$, membrane frequency $f_p = 3\,Hz$. The index of each figure corresponds to an instant taken from figure Fig.14.

Cryogenic sloshing dynamics in partially filled cylinder subjected to horizontal sinusoidal excitations

Alessia Simonini

Environmental and Applied Fluid Dynamics Department, von Karman Institute for Fluid Dynamics, Belgium, simonini@vki.ac.be

Supervisor: Maria Rosaria Vetrano

Associate Professor, Environmental and Applied Fluid Dynamics Department, von Karman Institute for Fluid Dynamics, Belgium, vetrano@vki.ac.be

University Supervisor: Pierre Colinet

Professor, Fluid Physics - Transfer Interfaces and Processes Department, Université Libre de Bruxelles, Belgium, pcolinet@ulb.ac.be

Abstract

The motion of a free liquid surface inside its container is called sloshing and it is strongly affected by external excitations applied to the partially filled container. It can refer to embarked containers filled of fluid, motion of cooling liquids in systems subjected to earthquake or motion of propellant inside a tank, which can influence the trajectory of vehicles. The understanding and the prediction of this particular motion is of special importance in space veichles which are powered by cryogenic propellant. This is the case of the cryogenic upper stage where the dynamic response to sloshing can also interfere on the thermodynamics of the stored fuel. The scope of this paper is to investigate cryogenic sloshing by means of non-intrusive optical techniques and to evaluate their performances. Liquid nitrogen is used as substitute fluid of a real cryogenic propellant (LH_2/LO_2). A preliminary study of particle image based technique such as, LeDaR and PIV applied to a container partially filled with liquid nitrogen and subjected to a lateral harmonic excitation are presented, underling the difficulty of such a critical thermodinamic environment.

Keywords: Cryogenic sloshing, PIV, LeDaR, Free Surface

1. Introduction

The motion of a free liquid surface inside its container is called sloshing and it is strongly affected by external excitations applied to the partially filled container. It can refer to embarked containers filled of fluid, motion of cooling liquids in systems subjected to earthquake or motion of propellant inside a tank. One of the important feature of sloshing is the behavior of the liquid-gas interface: in gravity dominated free surface flows, small vibrations can cause uncontrolled liquid motion inside tanks while in microgravity environment, the undetermined position of the free surface can cause problems in the feeding line due to injection of gas at the place of liquid. The understanding and the prediction of this particular motion is of special importance in space veichles which are powered by cryogenic propellant, as in the case of the upper stage of Ariane 5. In a gravity dominated condition, the cryogenic liquid propellant stays on the bottom of the tank while the stratified ullage is above the free surface. If the movement of the fluid is not predicted, the trajectory of the rocket can be comrpomised. Moreover, under impact of sloshing, the thermal equilibrium of the interface is disturbed and the moving fluid can arrive to a critical state for which a sudden depressurization happens in the hydrogen tank. This condition may lead to structural instabilities. Several experiments have been conducted since the 50s, in order to characterize the sloshing behavior under different excitation conditions, during ground tests and in full-scale orbitating vehicles[1; 2; 3; 4; 5]. It is during these years that several experimental works were carried out in

order to validate mathematical models describing liquid sloshing. Abramson reports, in his main work[3], the important role of the experimental research in propellant sloshing especially when quantitative data are obtained since these are the ones necessary for the design of space systems. In the collection of references regarding experiments in sloshing, the main devices used to obtain quantitative information are load cells and strain gages, which give global information on amplitude and frequency response. Other devices used to visualize the free surface behavior are capacitance and resistive probes, which are intrusive measurement techniques. Regarding the understanding of sloshing modes, from a qualitative point of view, again Abramson underlines the convenience to have transparent tanks. In 1966, Dodge studied experimentally sloshing of various liquids by means of a dynamometer and an electromagnetic probe[6]. Nowdays, experiments on fluid sloshing are still mainly performed by means of intrusive probes [7; 8]. In 2010 El-Kamali, in his Ph.D. thesis on the modelization of liquid sloshing, still underlined the difficulties to find quantitative experimental results concerning free surface modes in order to validate numerical codes [9]. In the lasts ten years, a great interests has been given to imagery techniques applied to sloshing[10; 11; 12], but none of them is providing velocity field information and an estimation of the free surface behaviour in a quantitative way. The main goal of this work is to present the possibility to characterize the free surface shape and the velocity field of liquid nitrogen contained in a partially filled transparent vessel. Liquid nitrogen is chosen, because of its reduced hazard, as replacement fluid for liquid hydrogen and liquid oxygen, the most common cryogenic propellants used for space applications. For both kind of measurements, particles are added to liquid nitrogen: in the first case lighter particles are floating at the free surface, giving the possibility to apply Level Detection and Recording (LeDaR)[13]; in the second case, particles which are matching the density of the fluid are inserted in the liquid to perform Particle Image Velocimetry (PIV) in liquid nitrogen.

2. Analysis of the problem

The analythical solution for determining the natural frequencies and the response to various forced excitations are widely known for various container geometries where the liquid has been assumed to be incompressible, non-viscous and in irrotational motion and even considering the effect of capillary-gravity waves.

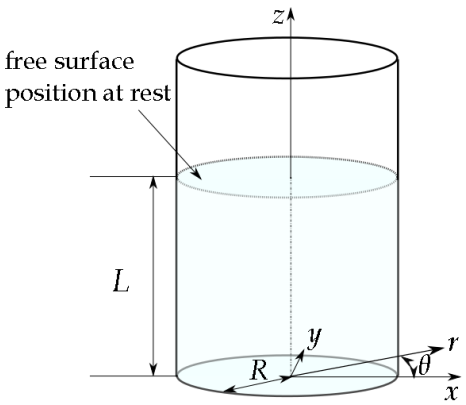

Figure 1: Reference system

For a liquid in an upright circular cylindrical tank, this had the advantage of employing the well-developed potential theory, leading to a first approximation of natural frequencies and in case of external excitation to a first approximated formula for fluid oscillations. Indeed, considering the system composed by an upright cylindrical tank of radius R partially filled with a liquid till a certain level L, as shown in figure 1, considering the effect of capillary-gravity waves, the natural frequencies can be express by:

$$\omega_{mn}^2 = \frac{g\xi_{mn}}{R}\left(1 + \frac{\sigma}{\rho g R^2}\xi_{mn}\right)\tanh\left(\frac{\xi_{mn}L}{R}\right) \qquad (1)$$

where ρ and σ are the density and the surface tension of the fluid, respectively. m refers to the diametral nodes and n to the circumferential nodes for the different kind of vibration[1]; ξ_{mn} are the roots $dJ_1(\xi_{mn}r/R)/dr|_{r=R} = 0$, where J_1 is the Bessel function of first order and first kind[3]. The asymmetric modes are of major concern since they are associated to a horizontal oscillation of the center of mass (fig. 2). Symmetrical modes about the vertical axis are possible but not excited so often[14]. In the case of a lateral excitation, the first asymmetric mode(m=1,n=1) is the predominant[4] and it is related to the lowest natural frequency of the system. For the first mode, m=1, we have a nodal diameter perpendicular to the direction of motion. Frictionless liquid, however, exhibits an oscillatory behavior for any disturbance and shows for a forced excitation at the resonances unbounded levels in the response. Unfortunately, it is exactly in and around these resonances, where we are

[1] The number n is always referred as n-1 circumferential nodes.

mainly interested in the value of the magnification functions of the liquid forces, moments and the free liquid surface displacement. The main sources of viscous damping are[15]:

1. viscous dissipation at the free surface due to the interaction liquid-gas;
2. viscous damping in the interior fluid;
3. viscous dissipation at a rigid boundary of the tank;

In this case, the effect of capillary hysteresis at the contact line has been neglected, considering a tank with a radius much bigger than the capillary length of the fluid. For larger liquid height ratios, $L/R > 1$, the contribution of the container bottom will diminish as the height ratio L/R increases. As may be observed the wave motion penetrates only to about a depth of the order of one wave length, while the lower part of the liquid follows the container motion like a rigid body. The contribution to the damping shall mainly come from the side wall damping and the internal damping of the viscous liquid. Bauer et al.[16] performed a viscous analysis of the problem which shows that the peaks of resonance are now finite and that the liquid is not always oscillating, but shall in some cases just performs an aperiodic motion.

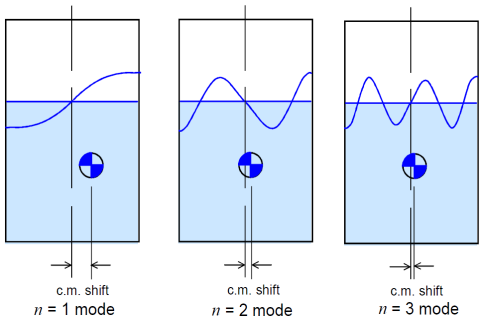

Figure 2: Scheme of first asymmetrical modes[17].

Considering a case for which $L/R > 1$, and making the hypothesis of small oscillations and velocities, Bauer find the dependence of the natural frequencies from two important dimensionless parameters, the Bond number, Bo, and the Ohnesorge number, Oh:

$$\mathrm{Bo} = \frac{\rho g R^2}{\sigma} \tag{2}$$

$$\mathrm{Oh} = \sqrt{\frac{\rho \nu^2}{\sigma R}}, \tag{3}$$

The Bond number is describing the relative importance of gravity forces respect to surface tension forces while the Ohnesorge number measures how easy the free surface breaks, and it is important because it affects the natural frequencies[18]. As reported by Bauer et al.[16], for liquid in containers with $L/R > 1$:

- if L/R increases, the liquid motion has a stronger decays and the natural frequencies are larger.
- The ohnesorge number decrease has the same effect as the increase of L/R. This means that with larger surface tension σ, the motion of the liquid decays faster with increased oscillation frequency. With increasing kinematic viscosity ν, the actual decay magnitude is increased at an increased oscillation frequency.
- The increases of the Bond number exhibits at increased decay, an increased oscillations frequency.
- At very large L/R, for the most important fundamental mode, internal damping and boundary-layer damping are of the same comparable magnitude.

Considering the dimensionless numbers, Bo and Oh, in table 1 are reported the values of a typical aerospace application for liquid hydrogen and oxygen and the value for the experimental test, in case the replacment fluid is liquid nitrogen or water. The latter has been used in a previous experimental campaign.

Table 1: Bond and Ohnesorge numbers

	LH_2	LO_2	LN_2	LH_2O
Bo	$3.6{\cdot}10^{5}$	$8.5{\cdot}10^{5}$	$1.4\cdot10^{3}$	$2.6{\cdot}10^{2}$
Oh	$3.6{\cdot}10^{-5}$	$5.0{\cdot}10^{-5}$	$3.0{\cdot}10^{-4}$	$1.9{\cdot}10^{-4}$

3. Experimental methodology

3.1. Non-intrusive measurement techniques

3.1.1. LeDaR

LeDaR is the acronymous of Level Detection and Recording. This technique has been used for the first time at von Karman Institute[19; 13] in order to characterize water free surface flows. In this technique, the gas/liquid interface is illuminated by a laser sheet along a line. In order to enhance the contrast between the liquid and the air, a fluorescent dye, which absorbs the laser light, is added to water. Images are acquired

and the interface is detected by image processing. The use of a fluorescent dye in order to enhance the gas liquid interface is a fundamental part of this technique. At the best author knowledge, no fluorescent dye exist which is soluble in liquid nitrogen. For this reason, floating particles have been chosen as scattering media in order to detect the free surface. The particles used are 3M K46 glass bubbles (density 0.46 g/cc and peak size [10%, 50%, 90%] = [15, 40, 70] m). Their density is almost half of that one of liquid nitrogen at ambient pressure (807 Kg/m3 at 106 Pa). This allows them to float on the free surface in order to detect the position of the gas/liquid interface. The amount of particles inserted is 10mg/l which gives a volume ratio of 40000. The laser used to illuminate them is a He-Ne laser with power of 30 mW at 633 nm. The laser sheet generated illuminates the section of the cylinder corresponding to the plane of excitation. The amount of particles is such that the technique can be considered non-intrusive, but at the same time, only a part of those particles lyes for each instant on the illuminated part of the free surface. In order to completely characterize the free surface shape at a given phase of the external motion, 200 phase locked images have been acquired with a PCO-pixelfly qe camera with resolution of 1392x1024 pixel^2. The phase locked acquisition is in phase with the motion of the sloshing table and they are performed during the steady state of the fluid motion.

The test matrix for the LeDaR experiment is shown in table 2, where D is the diameter of the cell, f and A are the frequency and amplitude of the excitation applied, respectively, and L is the level of liquid inside the cell.

Table 2: Test conditions matrix

Test	D [mm]	L [mm]	A [mm]	f [Hz]	Phase locked pos. [%]
1	80	$> D$	1.5	2	18.8
2					47.3
3					78.8
4				2.5	21.4
5					47.1
6					75.8

3.1.2. PIV

In literature few works regarding PIV in cryogenics are present[20; 21]. Both of them underline the difficulty to find classic PIV particles which are neutrally buoyant for liquid nitrogen and the difficulty to seed the fluid. Indeed during the seeding procedure humidity could be trapped between particles with a consequent clusterization of the latters due to formation of ice crystals. Commercial particles which respect the density matching of liquid nitrogen are not easily available cause they are normally manufactured to match water density. The only choice has been to use Cospheric hollow glass sphere (density 830 Kg/m^3 and diameter [5-15] μm). Given the available density of the particles, in this case, the working condition has to be set consequently in order to be as close as possible to 830 Kg/m^3, which means a temperature of $\approx$72K (see fig. 3). In this working point, P=0.05 MPa while Bo=1.3$\cdot$10^3 and Oh=3.5$\cdot$10^{-4}. The amount of PIV particles inserted is of the order of 60mg/l.

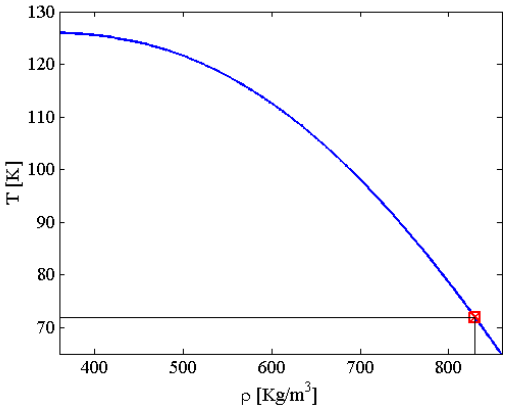

Figure 3: T-ρ diagram for nitrogen.

3.2. Sloshing experimental setup

In order to perform optical techniques during liquid nitrogen sloshing the main three hardware components are:

1. the transparent sloshing cell;
2. the cryostat, a device able to maintain the sloshing cell at cryogenic temperature along time;
3. the sloshing table.

The principal element of the experimental setup consists in a cylindrical cell, so called sloshing cell. This cell is mainly composed by a quartz module. It is made by a square bar of 100 mm^2 and 134 mm of height with a cylindrical hole drilled inside till a depth of 104 mm and a diameter of 80 mm. This design allows to minimized image distortion due to the curved walls by means of refractive index matching

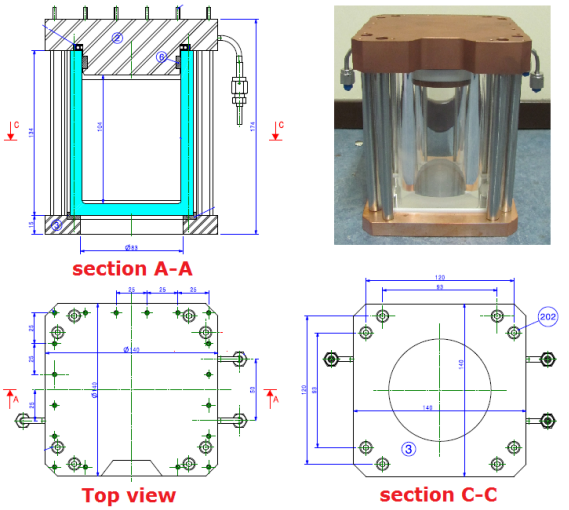

Figure 4: Drawing of the sloshing cell and its picture.

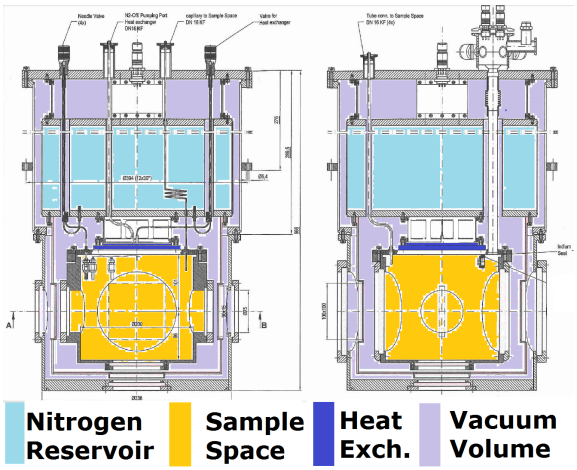

Figure 5: Drawing of the cryostat.

($n_{quartz} = 1.45, n_{LN_2} = 1.205$[21]). Since the cell has to be leak-tight and gas-tight the hole is closed by an upper flange with a cryogenic o-ring as connection. The upper flange is pushed against the o-ring by means of a system of invar bars and a bottom flange. The upper flange is provided by a feeding line and an evacuation line. Between the quartz and the bottom flange a Teflon joint is used to compensate the different thermal contractions of quartz and metallic parts. The assembled cell is shown in figure 4.

The cell is inserted inside the sample area of the cryostat (see fig. 5). The latter is a system constituted by a liquid nitrogen reservoir and a sample space, both surrounded by a volume kept in vacuum ($\approx 10^{-4}$ Pa) in order to minimize heat transfer with the external environment. A supplementary shield is limiting also radiation from the environment. The liquid nitrogen reservoir is used to cool down the sample space by means of a heat exchanger on which liquid nitrogen flows. The heat exchanger is provided by a rtd sensor in order to set the desired temperature. The cell is placed inside the sample space with its upper flange in contact with the heat exchanger. Gas helium is inserted inside the sample space in order to enhance the heat exchange inside the sample space itself. The bottom part of the cryostat is provided with 5 windows in order to optically access the inner part where the cryogenic sloshing cell is placed. The latter is filled with liquid nitrogen coming from the reservoir of the cryostat. The sample space is provided with a cryogenic temperature sensor (RTD) which assesses its temperature. The sloshing cell is considered in thermal equilibrium when temperature variations in time are of the order of one Kelvin per hour.

As above mentioned, the temperature in the sample space can be regulated by the heat exchanger. On the contrary, the cryogenic sloshing cell has no control on pressure with the consequence that the working conditions follow the saturation line of liquid nitrogen, as shown in figure 6.

Finally, the full equipment is mounted on a shaking table where all the PIV equipment can be mounted. The shaking table used for this experiment is Shakespeare (acronymous of SHaking Apparatus for Kinetic Experiments of Sloshing Project with EArthquake REproduction). Shakespeare can provide customized excitations. It is provided by an optical displacement sensor (ODS) to track the history of the motion (Accuracy 1m - 250Hz resolution). The setup to perform both, LeDaR and PIV, it is composed by a CW laser and a camera. Depending on the technique the kind of camera and laser necessary are different.

The sketch of the general experimental setup for non-intrusive measurement technique applied to cryogenic sloshing is shown in 7.

3.3. Experimental procedures

For both, LedaR and PIV, the procedure followed to insert the particles in the cell is:

1. insert the quantity of desired particle inside the cell;
2. insert the cell inside the cryostat
3. mount the cryostat with all the different shields
4. vacuum the cell
5. insert gas nitrogen inside the cell at 0.1 MPa

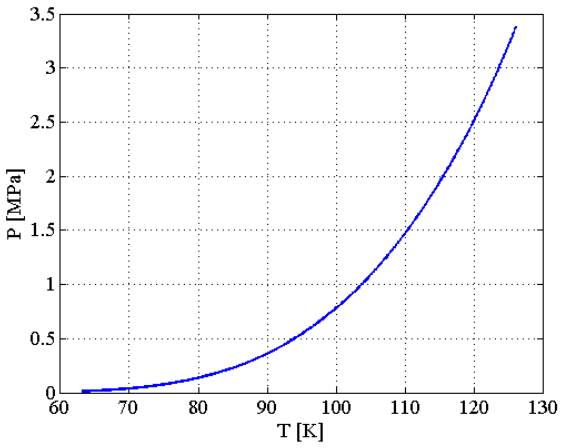

Figure 6: P-T diagram for nitrogen.

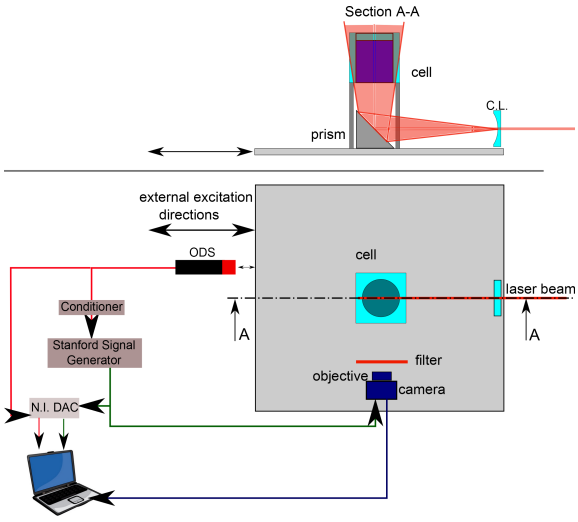

Figure 7: Sketch of the LeDaR and PIV setup.

6. repeat purging cycle 3-4 times in order to remove humidity from the cell and from the particles
7. start the cooling down of the cryostat

Before injecting liquid nitrogen inside the cell, the thermal equilibrium of the sample space for a temperature of 70K is waited. The system is considered at the thermal equilibrium if the variation of temperature read at the rtd inside the sample space is of the order of 1K/h. Then, liquid nitrogen is injecting while the cryostat is shaked with a sinusoidal motion in order to enhance the mixing of the particles and to avoid that they get stucked at the bottom of the cell. The cell is than filled with liquid nitrogen till $L = 2R$.

4. Data processing

4.1. LeDaR data processing

The image post processing used for the LeDaR technique is done with a VKI code and consists in the following steps:

- For each image an intensity filter is applied in order to remove less intense structures which do not belong to the liquid gas interface
- A rough mask is applied to select the ROI in which the liquid/gas interface is present.
- The maxima of each image pixel column are computed and an instantaneous profile of the liquid/gas interface is determined.
- The images corresponding to profiles which differ from each other of maximum +/- 3 px (+/- 0.2 mm with the used calibration) are selected.
- These profiles are averaged.
- The maxima of the average image are computed and the final average liquid/gas interface profile is computed.

The same procedure is also made for the reference liquid/gas interface position, i.e. the position of the interface when the liquid is at rest.

4.2. PIV data processing

The following steps compose the image processing procedure:

- Dynamic masking of the images in order to isolate the Region of Interest (ROI).
- Vector calculation of the PIV images. Different parameters are tested and the cross correlation peak ratio is kept for all cases above a threshold of 2.
- Vector post-processing of the velocity vector field

The dynamic masking of the images is done in order to limit the PIV processing to the ROI. The masking is performed taking advantage of the lighter particles (particle density is not uniform) which are floating on the surface of the liquid/gas interface and that, being illuminated by the laser sheet, generate a quasi-continuous line, which can be found using standard filtering algorithms. An example of PIV image and

relative mask is shown in Figure 8. The Particle Image Velocimetry analysis has been conducted in time series mode, meaning that the image i+1 is cross correlated with the image i giving rise to an instantaneous velocity field.

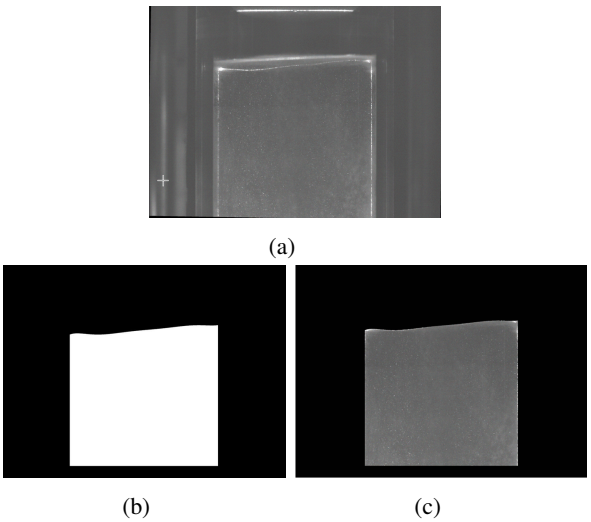

(a) (b) (c)

Figure 8: Example of masking process. (a) Raw image, (b) mask computed by image processing, (c) mask applied to the image.

The PIV processing has been done using the parameter listed in Table 3. Even if a minimal cross-correlation peak of 2 has been set for the vector calculations, in the vicinity of the contact line (between the fluid and the solid reservoir), due to the presence of low signal to noise ratio, in some cases, unphysical values of the velocities are present. The post processing aims to eliminate these values using the following two filters:

- The Allowed vector range filter restricts the vectors to a user specified range in units of particle separation [pixel]
- The median filter computes a median vector from a group of neighboring vectors and compares the middle vector with this median vector ± deviation of the neighboring vectors. The center vector is rejected when it is outside the allowed range of the average vector ± deviation of the neighbor vectors.

The vector eliminated could be replaced by interpolation (median filter) but this has not been done during this post-processing. Therefore, the velocity maps would contain some holes, i.e. zones in which the fluid velocity is not determined. A more aggressive post processing can be done if needed but then precautions should be taken about the results obtained. Another important point to take into account is the use of a mesh composed by rectangular elements in order to compute cross correlation in PIV. This kind of mesh is not adapted to the region in which the liquid/gas interface is curved or oblique due to the inevitable truncation of the squared elements.

Table 3: Vector calculation parameters

Quantity	Value
Iteration type	Sequential cross-correlation
Initial window size	128x128 pixels
Final window size	96x96 pixels
Initial overlap	50%
Final overlap	75%
Number of passes	2
Minimal cross correlation peak ratio	2

4.3. PTV data processing

The PTV method here combines PIV+PTV method. First standard PIV is made to determine a velocity field. The velocity vectors are then used as estimators of the displacement of each particle contained in the related cross-correlation window allowing used to decrease the number of possible particle partners and therefore to reduce the number of false measurements. The detection and tracking of individual particles (PTV) then is performed. The detection of particle is based on intensity threshold and pairing of particles between the frames. The velocity of each particle is then computed from its displacement. The PTV post processing uses a filter which corrects the velocity values using the velocity information in the neighborhood. It first searches all valid vector positions and check for vectors in the neighborhood than, based on the velocity values of these vectors, it interpolates the velocity field. The result of this filter is a smoothed velocity field where spurious vectors have been replaced by the interpolation of the neighboring vectors.

5. Results

5.1. LeDaR

In this section the liquid gas interface measured by LeDaR for the tests Test 4, 5 and 6 are presented. It is

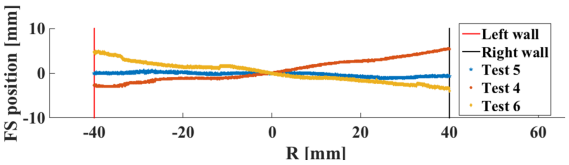

Figure 9: Example of an image of LeDaR in LN_2.

possible to observe that the reconstruction of the liquid/gas interface profiles does not allow to have relevant information about the contact angle. This is de to two main reasons. First the LeDar technique has not a sufficient spatial resolution to be capable to evaluate an apparent contact angle close enough to the solid wall to be representative of the process. Secondly, since particles have been added to the fluid interface, the contact angle is most probably affected and will not represent the one associated to the sloshing phenomenon. A way to overcome these two problems would be to perform LeDaR visualizations zoomed on the contact line position using a different way to optically distinguish between the fluid and the gas phase.

5.2. Fluid velocity

In this section two examples of results are reported. The first one aims to show vector maps, which presents a low number of invalid vectors and the relative effect of post processing. The other one would, on the contrary, show the effect of post processing in presence of a higher number of invalid vectors.

It is possible to notice, referring to Figure 10, that the impact of the post-processing is marginal for both PIV and PTV results. Indeed, for PIV only the vectors in the upper-left corner of the ROI are affected while for PTV, which suffers less of the meshing effect, the post-processing effect is barely visible. When the interface presence affects strongly the image quality (wrong masking, brighter spots, disperse scattered light presence,...), the velocity vectors, especially for PIV, are strongly disturbed and, sometimes, unphysical even after post-processing (see Figure 11). On the contrary, also in this case, PTV results are less affected since the technique is based on the pairing of isolated particles therefore it is less affected by noise present in the images. Therefore, it is possible to conclude, that, for the test cases analyzed in this work, the Particle Tracking Velocimetry seems more adapted to the determination of the velocity field, even in the presence of additional noise generate by the liquid/gas interface itself.

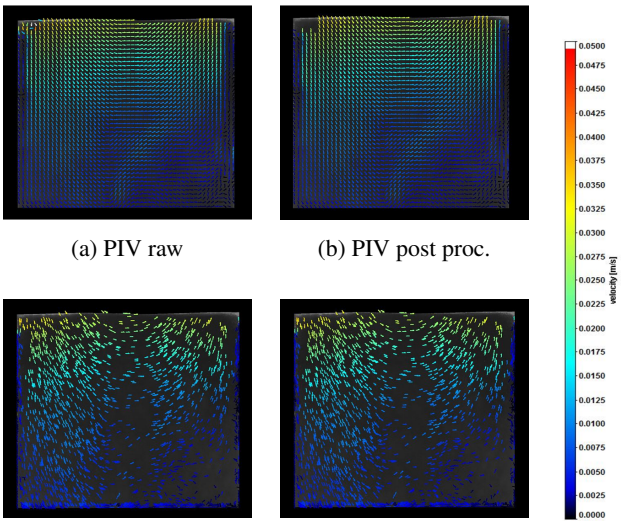

(a) PIV raw (b) PIV post proc.

(c) PTV raw (d) PTV post proc.

Figure 10: Example of PIV and PTV velocity maps and effect of post-processing in case of low number of invalid vectors.

6. Conclusions

In this work, the liquid gas interface profile and the velocity field of LN_2 during sloshing have been determined using two optical measurement techniques. The LeDaR technique, used to determine the 2D position of the liquid/gas interface has given satisfactory results but it fails in the vicinity of the reservoir wall, where the contact line position is perturbed by the presence of the particles used as seeding. The determination of the contact angle would need the use of a different seeding which could keep the contact angle unperturbed. The fluid velocity field has been determined by means of both PIV and PTV. It has been showed that, if the liquid/gas interface is enough flat and horizontal, the number of invalid vector computed by PIV is low and therefore both PIV and PTV can satisfactory determine the velocity field. Contrarily, when the liquid gas interface is not anymore flat and horizontal, the rectangular mesh used for the PIV cross correlations and the presence of additional noise close to the wall perturb strongly the PIV velocity field, while the PTV remains undisturbed. It should be remembered that, the PIV measurement presented here, are all instantaneous flow field, therefore more affected by the noise and the quality of the images.

It is possible therefore to conclude that the use of optical techniques can allow the characterization of the sloshing phenomenon in cryogenic fluids. Never-

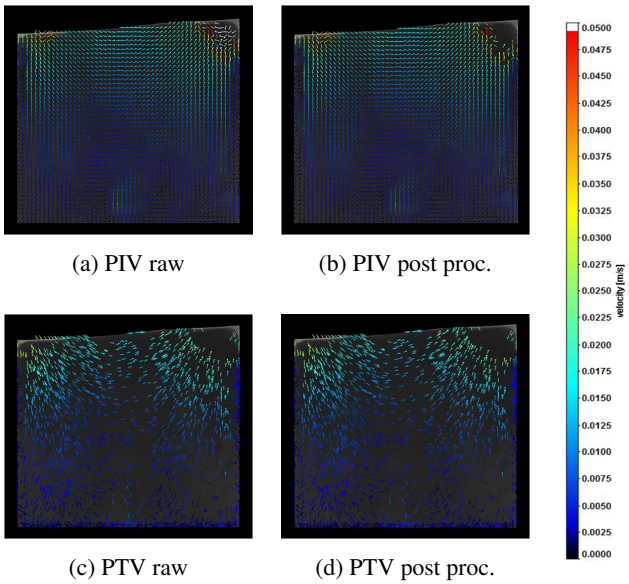

(a) PIV raw (b) PIV post proc.

(c) PTV raw (d) PTV post proc.

Figure 11: Example of PIV and PTV results with the different post-processing where the effect of the post processing is strong.

theless, some improvements are needed and they are part of the future work planned for this research activity. In the case of LeDaR, it is clear that the presence of the particles on the surface disturbs strongly the contact angle, therefore other techniques should be considered. A possibility would be to use techniques based on the deflection of light due to the curvature of the liquid meniscus or to find a luminescent material which can be dissolved in LN_2. As future work the PIV technique will definitely need the development of unstructured meshes which could dynamically be adapted to the liquid/gas interface shape. This development has already started at VKI in collaboration with the University of Bristol.

Acknowledgments

The financial support of the presented work was provided by Fonds de la Recherche Scientifique (FNRS), FRIA fellowship.

References

[1] J. Miles, On the sloshing of liquid in a cylindrical tank., Tech. rep., Ramo-Wooldridge Corporation (1956).

[2] H. Abramson, Application of similitude theory to the problem of fuel sloshing in rigid tanks, Tech. rep., SRI (1958).

[3] H. Abramson, The dynamic behavior of liquids in moving containers, SP 106, NASA (1966).

[4] T. Lance, Analysis of propellant slosh dynamics and generation of an equivalent mechanical model for use in preliminary voyager autopilot design studies., TM 33-306, NASA (1966).

[5] R. Lacovic, Management of cryogenic propellants in a full-scale orbiting space vehicle., TM 33-306, NASA (1966).

[6] F. Dodge, Experimental and theoretical studies of liquid sloshing at simulated low gravities., Tech. rep., SRI (1966).

[7] T. Arndt, M. Dreyer, P. Behruzi, M. Winter, Laterally excited sloshing tests with liquid nitrogen ln2, Reston, Va., 2008.

[8] Lacapere, J., Vieille, B., Legrand, B., Experimental and numerical results of sloshing with cryogenic fluids, in: Array (Ed.), EUCASS Proceedings Series Advances in AeroSpace Sciences, Vol. 1, 2009, pp. 267–278. doi:10.1051/eucass/200901267.
URL http://dx.doi.org/10.1051/eucass/200901267

[9] M. El-Kamali, Sloshing of liquids with surface tension: Static and dynamic studies, Theses, Conservatoire national des arts et metiers - CNAM (2010).

[10] T. Arndt and M. Dreyer, Damping behavior of sloshing liquid in laterally excited cylindrical propellant vessels, Journal of Spacecraft and Rockets 45 (5).

[11] E.J. Hopfinger and V. Baumbach, Liquid sloshing in cylindrical fuel tanks, Progress in Propulsion Physics 1 (2009) 279–292.

[12] N. Kulev, S. Basting, E. Bnsch, M. Dreyer, Interface reorientation of cryogenic liquids under non-isothermal boundary conditions, Cryogenics 62 (2014) 48 – 59.

[13] B. Tóth, Two-phase flow investigation in a cold-gas solid rocket motor model through the study of the slag accumulation process , Ph.D. thesis, Universite Libre de Bruxelles - von Karman Institute (2008).

[14] T. S. C. Institute, Fluid structure interaction effects on and dynamic response of pressure vessels and tanks subjected to dynamic loading, RR 527, HSE-UK (207).

[15] R. Ibrahim, Liquid Sloshing Dynamics: Theory and Applications, Cambridge University Press, Cambridge, 2005.

[16] H.F. Bauer and W.Eidel, Free oscillations and response of viscous liquid in rigid circular cylindrical tank, Aerospace Science and Technology (3) (1999) 495–512.

[17] F. Dodge, The new "dynamic behavior of liquids in moving containers", SP 106, SRI (2000).

[18] A. Royon-Lebeaud, Liquid sloshing in cylindrical reservoirs subjected to an harmonic oscillation: non-linear wave regimes and breaking, Ph.D. thesis, Université Joseph-Fourier - Grenoble I (2005).
URL https://tel.archives-ouvertes.fr/tel-00009117

[19] P.Planquart, M. Riethmuller, A. Joly, J. Detry., Real time optical detection and characterisation of water model free surfaces - application to the study of the mold., no. 4th European Continuous Casting Conference, Birmingham, 2002.

[20] G. Bewley, Using frozen hydrogen particles to observe rotating and quantized flows in liquid helium, Ph.D. thesis (2006).

[21] F. Enrico, Visualization of classical and quantum turbulence in cryogenic fluids, Ph.D. thesis, Università degli studi di Trieste (2012).

Multiscale and multiphysical modeling of the atmospheric boundary layer

Orkun Temel

Environmental and Applied Fluid Dynamics Department, von Karman Institute for Fluid Dynamics, Belgium, orkun.temel@vki.ac.be

Supervisor: Jeroen van Beeck

Professor, Environmental and Applied Fluid Dynamics Department, von Karman Institute for Fluid Dynamics, Belgium, vanbeeck@vki.ac.be

University Supervisor: Laurent Bricteux

Professor, Departement Mecanique, Universite de Mons, Belgium, laurent.bricteux@umons.ac.be

Abstract

Within the field of the environmental fluid dynamics, atmospheric boundary layer is one of the topics studies mostly due to many engineering application including heavy gas dispersion, wind energy assessment and wind comfort studies. This study is devoted to develop a convenient numerical modelling methodology for the computational fluid dynamics simulations sustained by the inflow conditions acquired by the numerical weather prediction simulations.

Keywords: Atmospheric boundary layer, turbulence modelling, mesoscale modelling

1. Introduction

For the modeling of ABL, there are two different numerical approaches which are being called with their associated spatial length scale. One of them, the mesoscale approach is to apply numerical weather prediction (NWP) codes at the regional scale. These NWP models are used for both operational and research purposes. However the spatial resolution reached with mesoscale simulations is limited; therefore the other approach is to apply computational fluid dynamics (CFD) codes at the micro-scale range. Even though it might solve the resolution problem of mesoscale models, the inflow condition problem arises. The inflow conditions of the microscale CFD approach depend on a scale that the CFD codes are not designed to work with due to the limited spatial and temporal range that can be covered with CFD simulations. In addition to the difference between the length scales associated with these two different approaches, important physical processes, which have crucial impact on the turbulence within the atmospheric boundary layer can not be taken into account by using the microscale approach. like radiative heat transfer, water phase change, cloud convection Hence, there is an increasing interest in the usage of mesoscale codes, or generally speaking NWP codes, to provide boundary and initial conditions to microscale simulations. Nevertheless, the results of the mesoscale simulations can not be used directly as inflow conditions for CFD simulations unless the turbulence models coherently developed with the atmospheric physics are employed.

2. Numerical approach

In this present study, Weather Research and Forecasting (WRF) model [2] has been used as mesoscale code and the microscale-CFD simulations have been performed by using OpenFOAM.

2.1. Microscale CFD code: OpenFOAM

Numerical simulations with standard and developed turbulence closures and solvers are performed with the open source C++ CFD toolbox OpenFOAM, which is using finite volume method for the discretization of differential equations. The heat transfer is modelled by using the Bousinessq approximation. It must noted that for the atmospheric studies, the potential temperature, $\theta = T(P_0/P)^{R/C_p}$, is being used instead of static temperature. Energy equation in terms of potential temperature is implemented to a

modified version of "buoyantBousinesqSimpleFoam" solver of OpenFOAM which is a steady state turbulent incompressible solver based on Semi-Implicit Method for Pressure-Linked Equations (SIMPLE) velocity-pressure coupling algorithm [1].

2.2. Mesoscale NWP code: WRF

Mesoscale simulations are performed with Weather Research and Forecasting Model (WRF), an open source next-generation mesoscale numerical weather which is designed to fulfill both, atmospheric research and operational forecasting needs [2]. WRF is, mainly, a Fortran code which resolves the compressible Euler equations by means of the finite difference method. The model uses higher-order schemes for temporal integration and advections schemes like Runge-Kutta 2nd and 3rd order time integration schemes and 2nd to 6th order advection schemes in horizontal and vertical directions. These equations are formulated using a terrain-following hydrostatic-pressure vertical coordinate which gives the flexibility to work on rectangular computational grid. The energy equation is formulated in terms of potential temperature, effect of water vapor is already included, scalar transport equations for water vapor, rain etc. are solved simultaneously.

In addition to terrain-following hydrostatic pressure coordinate in vertical direction, with the stretching option close to the ground, the code uses Arakawa-C grid with uniform grid spacing in horizontal direction. For simulations with "real cases module", WRF uses global re-analysis data to provide initial conditions and lateral boundary conditions. Gravity wave absorbing boundary condition is applied to top boundary and for the bottom boundary, derivatives of variables are defined with surface-layer parametrization schemes. The results of global re-analysis data is being provided by NCAR and NCEP in order to be used for mesoscale simulations.

For weather forecasting or global circulation modeling, uniform grid can be sufficient to resolve synoptic scales and provide efficient forecasting. However for research purposes or engineering applications, high spatial resolution might be needed. For such circumtances, WRF employs nesting technique which introduces "child grids" to computational domain in addition to the largest "parent grid", increasing progressively the spatial resolution of mesh. Initial and boundary conditions for these child grids are sustained from the parent grid which uses global re-analysis data as boundary and initial conditions.

3. Development of RANS closures based on the Monin-Obukhov theory

Monin-Obukhov similarity theory [3] stands as the only universally accepted for the determination of the turbulent fluxes within the surface layer. Theory is based on the Monin-Obukhov stability length which corresponds to the altitude where the shear production of turbulent kinetic energy becomes equal to the buoyancy production of turbulence kinetic energy. Another importance of Monin-Obukhov similarity length is the fact that it refers to the stability class of atmospheric boundary when q is positive and creating production of turbulence with buoyancy, ABL is unstable and when q is negative, the turbulence is being damped by the negative buoyancy and ABL becomes stable.

$$L = -\frac{u_*^3}{\kappa\left(\frac{g}{T_w}\right)\left(\frac{q}{C_p\rho}\right)} \tag{1}$$

where κ is the von Karman constant, u_* friction velocity, g gravity acceleration, T_w surface temperature, q turbulent heat flux, C_p specific heat and ρ is the air density The inflow conditions for atmospheric boundary layer under the assumption of horizontally homogeneity can be acquired from the Monin-Obukhov theory. However, the closure coefficients of RANS closures like standard $k-\epsilon$ [4], RNG $k-\epsilon$ [5] and $k-\omega$ [6] are not derived coherently with the physics of atmospheric boundary layer. It is reported that the usage of standard models cause an over-dissipation of turbulence along the streamwise direction for the homogeneous atmospheric boundary layer simulations [7]. In other words, the standard models are not able to maintain the inflow turbulent conditions and over-dissipate or over-product along the streamwise direction unphysically in the absence of any obstacles or structures that can affect the turbulence. In literature there are $k-\epsilon$ closures developed for non-neutral atmospheric boundary layer [8] and only for neutral cases [9]. However, the previously proposed methodologies in the literature are limited with the standard $k-\epsilon$. Moreover, these models are based on introducing an additional source term but keeping the classical C_1, C_2 and C_3 coefficients [9]. Therefore, by using the inflow conditions acquired from the Monin-Obukhov similarity theory, the closure coefficients of the proposed models are derived from the analytical solutions of simplified turbulent transport equations. Modifications are conducted for three different turbulence models which are standard $k-\epsilon$, $k-\omega$ and Re-Normalisation Group (RNG) $k-\epsilon$. The turbulent in-

flow conditions and velocity and potential temperature gradient according to the Monin-Obukhov theory are:

$$\nu_t = \frac{u_*}{\phi_m}\kappa z \tag{2}$$

$$k = 5.48u_*^2\left[\frac{\phi_e\left(\frac{z}{L}\right)}{\phi_m\left(\frac{z}{L}\right)}\right]^{\frac{1}{2}} \tag{3}$$

$$\epsilon = \frac{u_*^3}{\kappa z}\phi_e\left(\frac{z}{L}\right) \tag{4}$$

$$\frac{\partial u}{\partial z} = \frac{\phi_m u_*}{\kappa z} \tag{5}$$

$$\frac{\partial \theta}{\partial z} = \frac{\phi_e \theta_*}{z} \tag{6}$$

In order to define the velocity and potential temperature profiles within the surface layer, dimensionless stability functions for momentum and heat which are denoted by ϕ_m and ϕ_e are defined as a function of stability length and altitude. Gradients of wind speed and potential temperature are as given with the dimensionless stability functions which are based on full-scale observations from the 1968 KANSAS experiments [10].

$$\phi_m = \left(1 + A\frac{z}{L}\right)^P \tag{7}$$

$$\phi_e = \left(1 + B\frac{z}{L}\right) \tag{8}$$

where A, B and P becomes -16, -0.25, -1 for unstable and 5, 1, 4 for stable conditions. Transport equations for the turbulence kinetic energy and its dissipation are as given below.

$$u_j\frac{\partial k}{\partial x_j} = \frac{\partial}{\partial x_j}\left[\left(\frac{\nu_t}{\sigma_k}\frac{\partial k}{\partial x_j}\right)\right] + P + P_b - \epsilon \tag{9}$$

$$u_j\frac{\partial \epsilon}{\partial x_j} = \frac{\partial}{\partial x_j}\left[\left(\frac{\nu_t}{\sigma_\epsilon}\frac{\partial \epsilon}{\partial x_j}\right)\right] + S_\epsilon \tag{10}$$

$$S_\epsilon = \frac{\epsilon}{k}(C_1 P + C_3 P_b - C_2\epsilon) \tag{11}$$

It must be noted that the main difference between standard and RNG models is the fact that the RNG model uses varying C_1 coefficient instead of utilizing a constant value, C_1 is defined as a function of shear strain, turbulence kinetic energy and dissipation rate of turbulence.

$$C_1 = C_1^0 - R = C_1^0 - \frac{\eta\left(1 - \frac{\eta}{\eta_0}\right)}{1 + \beta\eta^3} \tag{12}$$

where, $\eta = Sk/\epsilon$, $S = (2S_{ij}S_{ij})^{0.5}$ and the coefficients β and η_0 are taken to be 0.12 and 4.38 respectively. Finally, the C_2 and C_3 coefficients have been determined in the following form, respectively for $k-\epsilon$ and RNG $k-\epsilon$.

$$C_2^* = C_1 + \frac{\kappa^2}{\sigma_\epsilon\sqrt{C_\mu}} \tag{13}$$

$$C_2^* = (C_1^0 - R) + \frac{\kappa^2}{\sigma_\epsilon\sqrt{C_\mu}} \tag{14}$$

$$C_3 = \frac{L\phi_m}{\kappa z\phi_\epsilon}\left[C_1(\phi_m - 1) - C_2^*(\phi_\epsilon - 1)\right] \tag{15}$$

$$C_3 = \frac{L\phi_m}{\kappa z\phi_\epsilon}\left[(C_1^0 - R)(\phi_m - 1) - C_2^*(\phi_\epsilon - 1)\right] \tag{16}$$

Transport equations for $k-\omega$ turbulence model are given in Eq.17, Eq.18 and Eq.19.

$$u_j\frac{\partial k}{\partial x_j} = \frac{\partial}{\partial x_j}\left[\left(\alpha_k\nu_t\frac{\partial k}{\partial x_j}\right)\right] + P + P_b - \omega C_\mu k \tag{17}$$

$$u_j\frac{\partial \omega}{\partial x_j} = \frac{\partial}{\partial x_j}\left[\left(\alpha_\omega\nu_t\frac{\partial \omega}{\partial x_j}\right)\right] + S_\omega \tag{18}$$

$$S_\omega = \alpha\frac{\omega}{k}P + C_3\frac{\omega}{k}P_b - \beta C_\mu\omega^2 \tag{19}$$

ω stands for the specific dissipation rate of turbulence kinetic energy and the inflow condition for ω:

$$\omega = \frac{\epsilon}{kC_\mu} = \frac{u_*\sqrt{\phi_\epsilon\phi_m}}{\kappa z\sqrt{C_\mu}} \tag{20}$$

The derived closures constants for $k-\omega$ model are as follows:

$$\beta^* = \alpha + \frac{\alpha_w\kappa^2}{\sqrt{C_\mu}} \tag{21}$$

$$C_3 = \frac{L}{\phi_\epsilon\kappa z}\left(\alpha\left(\phi_m^2 - 1\right) - \beta^*(\phi_\epsilon\phi_m - 1)\right) \tag{22}$$

In order to asses the developed models capability to provide homogeneous atmospheric boundary layer under non-neutral stratification, simulations have been performed by using the Monin-Obukhov inflow conditions for stable and unstable conditions. Simulations have been performed for a full-scale non-neutral atmospheric boundary layer using a 2 dimensional domain of 1 km length and 300 m of height.

The similarity functions of Monin-Obukhov theory (Eq.34 and Eq.33) had been determined by Businger [11] based on the full-scale experiments and it must be noted that these similarity functions are valid within a range of $0 < z/L < 1$ and $-2 < z/L < 0$, under stable

and unstable conditions respectively. Therefore, considering the height of the domain which is 300 m, the Monin-Obukhov length, L, is taken as 250 m and -250 m for stable and unstable cases.

Proposed turbulence closures have been validated by comparing the vertical profiles of velocity, potential temperature, turbulence kinetic energy and its dissipation at the outlet of the computation domain with the theoretical profiles of the Monin-Obukhov theory. Since the theoretical profiles have been used as inflow conditions, this validation procedure exposes the capability of turbulence closures to maintain the horizontal homogeneity by sustaining the balance between terms within the transport equations. As can

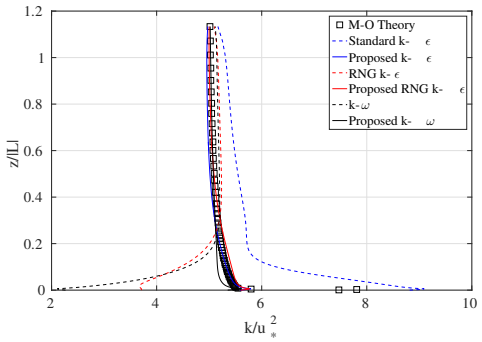

Figure 1: Comparison of the standard and proposed models with the Monin-Obukhov theory under stable stratification: Normalized turbulence kinetic energy

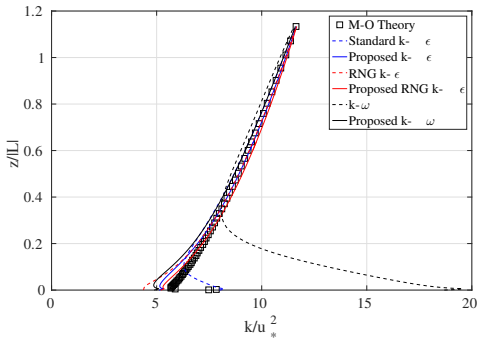

Figure 2: Comparison of the standard and proposed models with the Monin-Obukhov theory under unstable stratification: Normalized turbulence kinetic energy

be seen in Fig.1 and Fig.2, proposed closures provided much better estimations of turbulence kinetic energy with respect to the standard closures. The detailed derivation procedure with the obtained results have been submitted to the Journal of Applied Mathematical Modelling under the title of "Development of two-equation eddy viscosity models based on the Monin-Obukhov similarity theory".

4. Adaptation of mesoscale turbulence parameterization schemes as RANS closures for coupled CFD/NWP simulations

Monin-Obukhov theory is also being used for the parameterization of surface turbulent fluxes by the mesoscale models. However, it must be noted that is only valid within the surface layer, $z < 0.1z_i$ now within the whole boundary layer. Moreover, the applicability of Monin-Obukhov theory for extreme conditions is open to question. Therefore the formulation being applied for the closures based on Monin-Obukhov must be revised coherently with the mesoscale turbulence parameterization schemes which also use this theory as their ground boundary condition. On this framework, eight different first-order and one-and-half order one-dimensional mesoscale turbulence parametrization schemes so called planetary boundary layer (PBL) schemes have been adapted as two-equation Reynolds-averaged Navier-Stokes (RANS) closures for atmospheric boundary layer (ABL) simulations. For the first-order schemes, which employ algebraic relationships to define turbulent viscosity, a new formulation has been proposed for the derivation of turbulent inflow conditions by using the features of one-and-half order schemes which are based on a turbulence kinetic energy closure with an empirically modelled dissipation term. New k-ϵ closures have been developed with closure constants based on Monin-Obukhov similarity theory and formulation based on the Coriolis parameter proposed by Detering and Etling [12]. Finally simulations have been performed for Askervein Hill case with inflow conditions sustained by mesoscale simulations

4.1. Planetary boundary schemes

Turbulent fluxes within the atmospheric boundary layer are modeled by using the following formulation [2].

$$< w'C' >= -K_C \left(\frac{\partial C}{\partial z} - \gamma \right) \tag{23}$$

Here C is a generic variable which can be u, v or and K_C is the eddy diffusivity coefficient for each variable. Additionally, γ_C is the counter gradient term which is related with the contribution of large scale eddies to

the vertical turbulent transport in the atmosphere [13]. The counter gradient term is only applicable for the scalars and it is defined as

$$\gamma_C = b\frac{\overline{(w'C')_0}}{w_* z_i} \tag{24}$$

The main difference between different mesoscale turbulence parameterization schemes so called "planetary boundary layer (PBL) schemes" comes from their degree of complexity to determine the eddy diffusivity coefficients. In this present study, eight different PBL schemes are taken into account, which are Medium Range Forecast (MRF) [14], Yonsei University (YSU) [15], Boulac and Lacarratte (BouLac) [17], Mellor-Yamada-Janjic (MYJ) [16], Mellor-Yamada-Nakanishi-Niino (MYNN) [18], [19], two different versions of Quasi-Normal-Scale-Elimination (QNSE) [20] and University of Washington (UW) [21] schemes. Among them, YSU and MRF schemes are first order schemes which eddy diffusivity coefficients are calculated by using stability functions and bulk parameters.

$$\nu_t = \frac{u_*}{\phi_m}\kappa z\left(1-\frac{z}{z_i}\right)^2 \tag{25}$$

In Eq.25, u_* is the friction velocity which is defined differently for each first-order scheme. In contrast to algebraic first order schemes, an additional transport equation for turbulence kinetic energy is solved for BouLac, MYJ, MYNN, QNSE and UW schemes and the eddy diffusivity coefficients are derived from similarity functions, which differ for each PBL scheme. One-and-half order schemes use a similar approach to RANS models to define eddy diffusivity coefficients.

$$\nu_t = S_m k^{1/2} l \qquad \alpha_t = S_h k^{1/2} l \tag{26}$$

$$\frac{\partial k}{\partial z} = \frac{\partial}{\partial z}\left[l k^{0.5} S_k \frac{\partial k}{\partial z}\right] + P_s + P_b - \epsilon \tag{27}$$

The modeled form shear production, buoyancy production/destruction and dissipation of turbulence kinetic energy are as given:

$$P_s = \nu_t\left[\left(\frac{\partial u}{\partial z}\right)^2 + \left(\frac{\partial v}{\partial z}\right)^2\right] \tag{28}$$

$$P_b = -\beta g \alpha_t \frac{\partial \theta_v}{\partial z} \tag{29}$$

$$\epsilon = \frac{k^{1.5}}{B_1 l} \tag{30}$$

Each one-and-half order scheme has its unique definition for S_m, S_h, B_1. So that the dissipation term ϵ, and the turbulent viscosity ν_t are calculated differently for each scheme.

4.2. Mesoscale simulations

a computational configuration of four nested domains which covers the north hemisphere of the world is being chosen as computational grid. The domains are as shown in Figure.3 and spatial and temporal resolution of computational approach is as given in Table 1. The time period of interest is the TU-03B turbulence run of Askervein Hill full scale experiments, which corresponds to the 03/10/1983 - 14:00-17:00. However the spin-up simulation has been started at 02/10/1983 - 00:00.

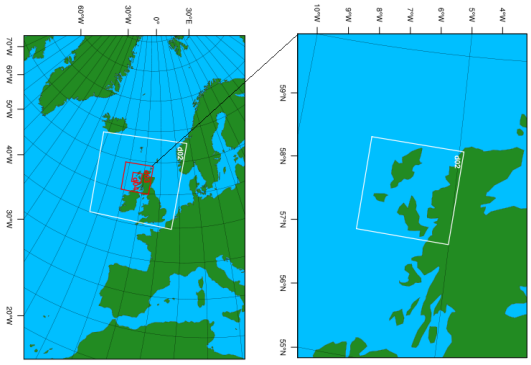

Figure 3: Mesoscale domain setup

Table 1: Configuration of mesoscale domains

Domain	dx km	dy km	dt s	Lx km	Ly km
1	45	45	90	4500	4500
2	15	15	30	1200	1200
3	5	5	10	400	400
4	1.6	1.6	3.33	120	120

In this study, Kain-Fritsch cumulus parameterization [22] is used only for domains D1 and D2 and the Rapid Radiative Transfer Model (RRTM) [23] for longwave and shortwave fluxes. For the microphysics parameterizations, the Thompson scheme [24] and the classical 5 layer land-surface scheme are used [25]. For the validation of mesoscale results, weather baloon measurements have been used. Even though

the sounding data contains a high level of uncertainity due to the uncertainity of the weather baloon's position, it gives essential information about the large scale convective motions. Also in case of having fine vertical resolution below the ABL height, it might also be used to compare different turbulent parameterization schemes and evaluate atmospheric stability classes. However, considering the date of the Askervein Hill experiments, the atmospheric sounding data is quite limited but still we take advantage of validating our model against weather baloon measurements which are performed at three meteorological stations in Britain. These three stations are Valentia Observatory, Camborne and Tornshavn and their locations are as presented in Fig.4 with the velocity vectors are extracted from the mesoscale simulation with performed with YSU scheme at 03/10/1983-12:00 when the weather baloon measurements were being performed in three stations. As can be seen that the Camborne and Tornshavn stations are aligned on the south-west direction which is the main flow direction in the mesoscale results. Hence it is possible to say that if the mesoscale simulations are on agreement with the weather baloon measurements at Camborne and Tornshavn stations, mesoscale model can be accepted as validated in the spatial range which covers the South Uist, Askervein Hill for a time period that the convective cloud at Tornshavn would be convected to Camborne region. Computed and measured wind speed profiles are presented for each station in Fig.5-Fig.7. Considering the mean wind speed above ABL is $40km/h$ and the length between two stations is $400km$, the results of mesoscale simulations can be used as inflow conditions for CFD simulations during the time period 12:00-22:00 which also covers the TU03-B experimental campaign in Askervein Hill.

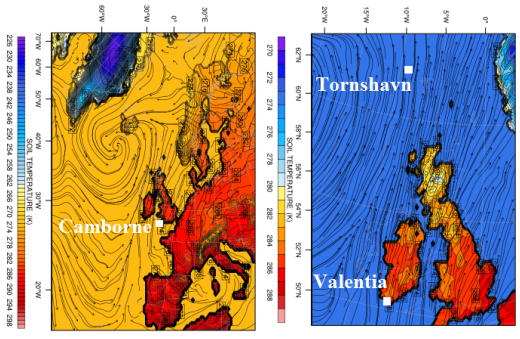

Figure 4: Locations of stations and wind speed vectors at ground level for D1 (a) and D2 (b)

It must be noted that due to the lack of fine resolution measurements within the first kilometer of the atmosphere, it is not possible to evaluate the performances of different PBL schemes based on weather baloon measurements. However, for all stations, the mesoscale results are on a good agreement with the weather baloon measurements. Therefore the results of mesoscale simulations can be used as inflow conditions for microscale-CFD simulation of ABL.

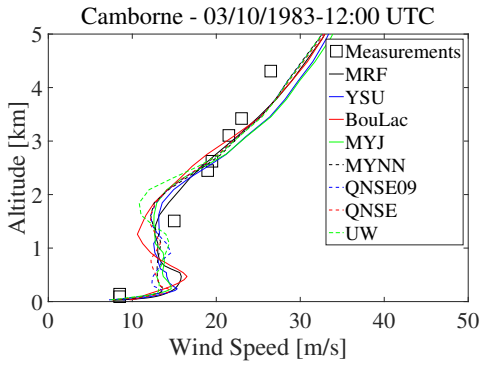

Figure 5: Mesoscale results vs weather baloon measurements: Camborne station

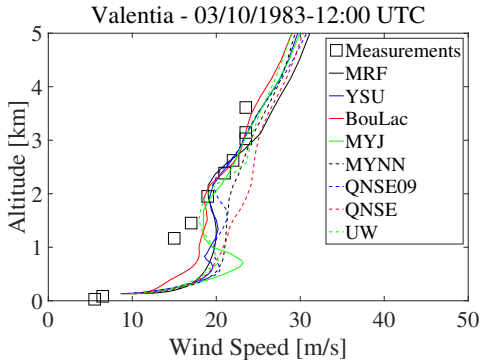

Figure 6: Mesoscale results vs weather baloon measurements: Valentia station

4.3. *Development and application of the new turbulence closures based on the PBL schemes*

The applicability of RANS models based on the Monin-Obukhov theory is limited for the surface layer and valid under the assumptions of horizontal homogeneity. Therefore the developed approach [26] has been extented to work consistently with the mesoscale turbulence parameterization schemes based on the formulation proposed by Detering and Etling [12]. In this part of the study, only the $k-\epsilon$ model has been adapted based on the mesoscale turbulence parameterization

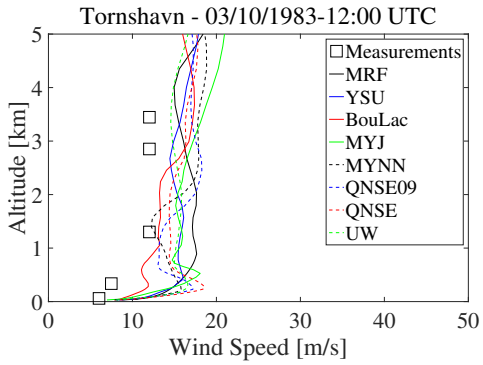

Figure 7: Mesoscale results vs weather baloon measurements: Tornshavn station

schemes by using the following closure constant:

$$C_2 = C_1^0 + C_f Ro^{-1} + \frac{\kappa^2}{\sigma_\epsilon}\sqrt{\frac{B_1}{C_q S_m}} \qquad (31)$$

where C_1^0 equals to 1.44 and C_f is an empirical constant which is set to be 111 for QNSE scheme [20], however in this present study, it is set to be 200.0 for all adapted RANS closures and the Rossby number which is a function of friction velocity, $Ro = u_*/|f|L$, where f is the Coriolis parameter and L is the macroscale. Turbulent length scale, l_t is defined as $C_\mu^{0.75}k^{1.5}/\epsilon$. The turbulent length scale, l_t, can be related with the macroscale proportionally with the velocity scales. As a crude approximation, $u_* \sim 0.1U_\infty$. Therefore the macroscale becomes $L = 10C_\mu^{0.75}k^{1.5}/\epsilon$. In Eq.31, C_q, S_m, B_1 are constants related with the mesoscale turbulence modeling approach and they are as presented in Table.2. The topography of Askervein

Table 2: Summary of closure constants

Scheme	B_1	S_m	C_q	C_μ
MRF	45	45	90	4500
YSU	15	15	30	1200
MYJ	5	5	10	400
BouLac	1.6	1.6	3.33	120
MYNN	5	5	10	400
QNSE	1.6	1.6	3.33	120
QNSE09	1.6	1.6	3.33	120
UW	1.6	1.6	3.33	120

hill is as presented in Fig.8. The mesh, which is based on a previous study [27], contains approximately 330000 hexahedral cells with a low level of skewness, the height of domain is set to be $1km$, and the mesh covers a region of $6x6km^2$. Symmetry boundary condition has been applied to lateral and top boundaries. Under non-neutral conditions the applicability of symmetry boundary condition to the top boundary is open to question due to the updraught-downdraught convective movement, however for neutral ABL, symmetry boundary condition can be applied. The inflow conditions for velocity and turbulence kinetic energy are acquired from mesoscale simulations. As a result of different C_μ constants and length scale definitions being applied by the turbulence parameterization schemes, the turbulence kinetic energy inflow conditions acquired by the mesoscale simulations are quite different for each scheme. Similarly, the velocity shear on the ground is also estimated differently for each scheme as well. Even though the effect of geostrophic wind is not present within the surface layer, different estimations of friction velocity and turbulence kinetic energy lead to the conclusion that the large-scale motions which can be modeled only by mesoscale simulations have an important impact on the prediction of momentum transport within the surface-layer.

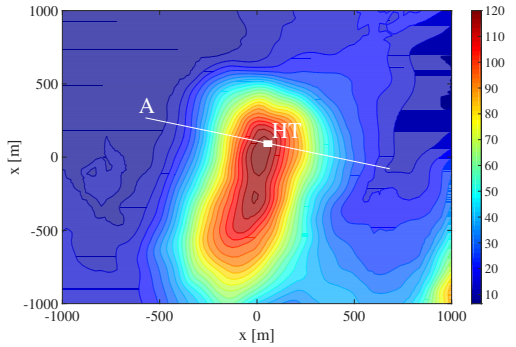

Figure 8: Askervein hill topography and measurement locations

The comparison for simulated and measured velocity components along the horizontal measurement line A is presented in Fig.9 and Fig.10. For the estimation of vertical velocity, all adapted $k-\epsilon$ closures have performed similarly except the BouLac scheme which overestimated the vertical velocity peak at the top of the hill and provided a less accurate estimation of vertical velocity within the re-circulation region after the hill. In contrary to BouLac and the other one-and-half order schemes, the first order schemes, YSU and MRF, estimated a stagnation point after $350m$ in the downstream of the hill. Among the first order schemes, it is likely to state that the MYJ and UW schemes are found out to be performing best for the

estimation of vertical velocity.

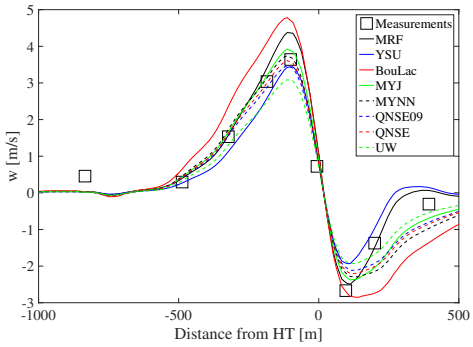

Figure 9: Comparison of vertical velocity along the streamwise measurement line (lineA)

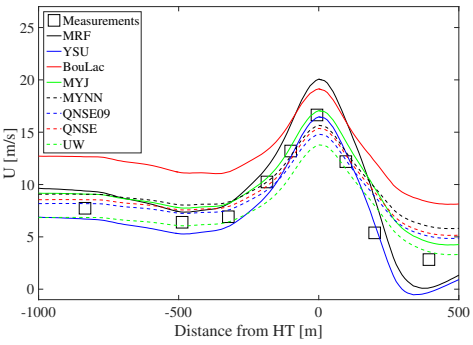

Figure 10: Comparison of horizontal velocity along the streamwise measurement line (lineA)

The same conclusion can be drawn for BouLac scheme in terms of the horizontal velocity estimation. Even in the upstream of the hill, the wind speed is overestimated by the BouLac scheme. All other schemes managed to determine velocity accurately in the upstream of the hill. Coherently with the vertical velocity estimations, by MRF and YSU schemes a stagnation point is also determined in the downstream of the hill. In comparison to the measurements, it might be possible to claim that the effect of the hill on the downstream is overestimated by the first order schemes.

Evolution of turbulence kinetic energy on the line-A in comparison the measurements are as given in Fig.11. All adapted $k-\epsilon$ closures, expect BouLac which exposed to an unphysically decrease of turbulence kinetic energy, managed to provide a developed flow in the upstream of the hill. The failure of the BouLac scheme to ensure developed conditions

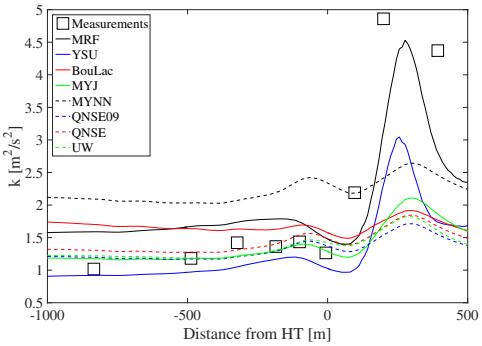

Figure 11: Comparison of turbulence kinetic energy along the streamwise measurement line (lineA)

in the upstream region However, only MYJ, QNSE, QNSE09 and UW closures determined accurately the turbulence kinetic energy in the upstream region. Despite the fact that YSU is found out to be better than MRF, MYNN and BouLac schemes, the turbulence kinetic energy is slightly underestimated. Even though, the effect of the hill on the downstream region in terms of velocity have been concluded to be overestimated by the first order schemes, YSU and MRF schemes provided performed better within the wake region.

At the hill top, the measured and computed vertical profiles of wind speed and turbulence kinetic energy are as presented in Fig.12 and Fig.13.

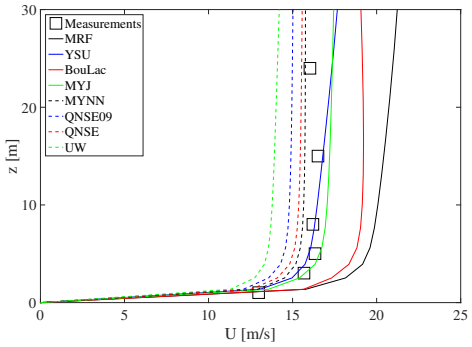

Figure 12: Comparison of vertical profile of wind speed at the hill top (HT)

As seen in Fig.12, YSU $k-\epsilon$ and also the two other $k-\epsilon$ closures based one-and-half order schemes, MYJ and MYNN, are found out to be performing well. However in terms of the shear within the first 10 meters of the surface layer, MYJ and YSU performed much better than all other closures. Finally,

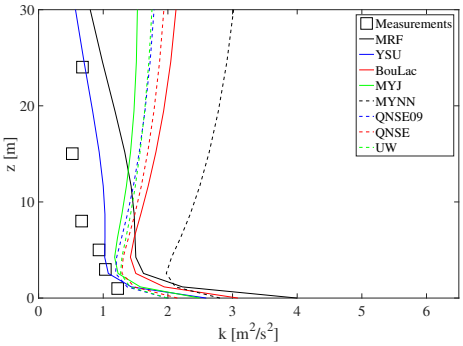

Figure 13: Comparison of vertical profile of turbulence kinetic energy at the hill top (HT)

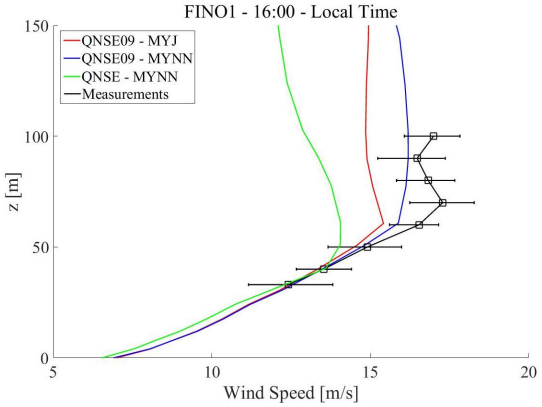

Figure 14: Evaluation of the updated QNSE scheme

it can be concluded that among all models, YSU performed best and MYJ is the best-performing model among the one-and-half order models. This part of this study is submitted to the Journal of Turbulence and also the preliminary results regarding the turbulence modeling methodology for coupled CFD/NWP simulations is accepted to be presented in the 1st International Winercost Conference, Ankara-Turkey.

5. Improved mesoscale turbulence parameterization schemes

Mesoscale turbulence parameterization schemes have huge impact on the inflow conditions of microscale CFD simulations. Therefore, any possible improvement on their performances is essential for CFD/NWP coupling.

5.1. Updated QNSE scheme

Quasi-normal scale elimnation scheme (QNSE) is developed especially for the stable atmospheric boundary layer which is quite important for the wind energy assessment studies. Its formulation is based on the utilization of MYJ scheme for unstable conditions and reverts to its original formulation which is based on a new spectral theory of turbulence. MYNN scheme is the improved version of MYN scheme, QNSE scheme is also updated with the MYNN formulation and different versions of model have been compared for an observed low-level jet over the North Sea, the results have been compared with the field measurements as presented in Fig.14. Results have been presented in BERAWIND Wind Energy PhD Symposium [29].

5.2. Improved BouLac scheme

According to the Monin-Obukhov theory and full scale experiments, within the surface layer, the production of turbulence kinetic energy should be equal to its dissipation under neutral conditions. In order to solve this inconsistency, B_1 coefficient which is the dissipation tuning coefficient is defined as a function of similarity functions which define velocity and temperature gradients.

$$B_1 = \frac{1}{C_\mu^{0.75}\phi_m^{0.25}\phi_e^{0.75}} \tag{32}$$

Similarity functions, ϕ_m and ϕ_e are defined based on the experimental fittings [11].

$$\phi_m = \left(1 + A\frac{z}{L}\right)^P \tag{33}$$

$$\phi_e = \left(1 + B\frac{z}{L}\right) \tag{34}$$

where A, B and P becomes -16, -0.25, -1 for unstable and 5, 1, 4 for stable conditions. New approach has been implemented into WRF and simulations are still being performed for different reference cases.

6. Conclusion and future work

In this present study which is mainly devoted to the development of turbulence models for coupled CFD/NWP simulations, firstly three different RANS models have been modified based on the Monin-Obukhov similarity theory. However, the Monin-Obukhov theory is only applicable for the surface layer, therefore in order to provide a numerical methodology that can be applied for the full boundary

layer, mesoscale turbulence parameterization schemes have been adapted as RANS closures. Developed models have been validated for the Askervein Hill case by the CFD simulations sustained by the inflow conditions acquired by mesoscale simulations. In addition to the improvements in RANS modeling for microscale approach, modified versions of QNSE and BouLac scheme have been proposed and some further validation studies for these new models are still ongoing. The current results have shown the potential of CFD/NWP coupling for the wind energy assessment studies and the same methodology will also be applied to Oklahoma City case for the heavy gas dispersion study. Different RANS closures, not only standard $k-\epsilon$ will also be adapted with the mesoscale turbulence parameterization schemes and their performances will be evaluated. Another possible future work can be the application of non-linear eddy viscosity models for CFD/NWP coupling.

Acknowledgments

This study has been supported and funded by the Fonds de la Recherche Scientifique de Belgique (FRS-FNRS).

References

[1] Karki, K. C. and Patankar, S. V. (1989). Pressure based calculation procedure for viscous flows at all speeds in arbitrary configurations, AIAA journal, 27(9), 1167-1174.

[2] W.C. Skamarock et al., *A Description of the Advanced Research WRF Version 3*, National Centre for Atmospheric Research (2008).

[3] Foken, T., et al., *50 years of the MoninObukhov similarity theory.*, Boundary-Layer Meteorology, 119(3), 431–447.

[4] Jones, W.P., Launder, B.E., *The Prediction of Laminarization with a Two-Equation Model of Turbulence*, International Journal of Heat and Mass Transfer, Vol. 15, pp. 301-314, (1972).

[5] Speziale, C. G. and Thangam, S. (1992). *Analysis of an RNG based turbulence model for separated flows*, International Journal of Engineering Science, 30(10), 1379-IN4.

[6] Wilcox, D.C. (1988), *Re-assessment of the scale-determining equation for advanced turbulence models*, AIAA Journal, vol. 26, no. 11, pp. 1299-1310.

[7] Pontiggia, M., Derudi, M., Busini, V. and Rota, R, *Hazardous gas dispersion: a CFD model accounting for atmospheric stability classes*, Journal of Hazardous Materials, 171:739-747, 2009

[8] C. Alinot and C. Masson, *Aerodynamic simulations of wind turbines operating in atmospheric boundary layer with various thermal stratifications*, In 50th AIAA Aerospace Meeting, Nashville, Tennessee, January 2002, AIAA.

[9] A. Parente et Al., *A Comprehensive Modelling Approach for the Neutral Atmospheric Boundary Layer: Consistent Inflow Conditions,Wall Function and Turbulence Model*, Boundary-Layer Meteorology,

[10] Kaimal, J. C. and Wyngaard, J. C., (1990), The kansas and minnesota experiments, Boundary-Layer Meteorology, 50(1-4), 31-47.

[11] Businger, J. A., Wyngaard, J. C., Izumi, Y. and Bradley, E. F., (1971), *Flux-profile relationships in the atmospheric surface layer*, Journal of the atmospheric Sciences, 28(2), 181-189.

[12] Detering, H., and Etling, D., *Application of the E - ϵ Model to the Atmospheric Boundary Layer*, 1985: Boundary-Layer Meteorol. 33, 113133.

[13] I. Troen and L. Mahrt, *A simple model of the atmospheric boundary layer: Sensivity to surface evaporation*, Boundary-Layer Meteorology, 37:453–478, 1986.

[14] S.Y. Hong and H.L. Pan, *Nonlocal boundary layer vertical diffusion in a medium-range forecast model*, Monthly Weather Review. 124:2322–2339, 1195.

[15] S.-Y. Hong, Y. Noh, J. Dudhia, *A new vertical diffusion package with an explicit treatment of entrainment processes*, Monthly Weather Review. 134:2318–2341, 2005.

[16] T. Yamada and G. Mellor, *Development of a turbulent closure model for geophysical fluid problems*, Reviews of Geophysics and Space Physics. 40,41:851–875, 1982.

[17] P. Bougeault and P. Lacarrere, *Parameterization of orography-induced turbulence in a mesobeta-scale model*, Monthly Weather Review. 117:1872–1890, 1989.

[18] Nakanishi, M., and H. Niino, *An improved MellorYamada level 3 model: its numerical stability and application to a regional prediction of advecting fog.*, 2006: Bound. Layer Meteor. 119, 397407..

[19] Nakanishi, M., and H. Niino, *Development of an improved turbulence closure model for the atmospheric boundary layer.*, 2009: J. Meteor. Soc. Japan, 87, 895912.

[20] Sukoriansky, S., B. Galperin, and V. Perov., *Application of a new spectral model of stratified turbulence to the atmospheric boundary layer over sea ice.*, 2005: Bound.Layer Meteor., 117, 231257.

[21] Bretherton, Christopher S., and Sungsu Park, *A new moist turbulence parameterization in the Community Atmosphere Model.*, 2009: J. Climate, 22, 34223448.

[22] J.M. Fritsch and J.S. Kain, *Convective parameterization for mesoscale models: the Kain-Fritcsh scheme, representation of cumulus convection in numerical models*, Americal Meteorological Society, page 246, 1993.

[23] E.J. et Al. Mlawer, *Radiative transfer for inhomogeneous atmosphere: RRTM, a validated correlated-k model for the longwave*, Journal of Geophysical Research, 102:166–316, 1997.

[24] Thompson et al., *Explicit forecasts of winter precipitation using an improved bulk microphysics scheme. Part II: Implementation of a New Snow Parameterization* , Journal of Geophysical Research, 136–12:5095–5115, 2008.

[25] Dudhia Jimy , *A multi-layer soil temperature model for MM5*, the Sixth PSU/NCAR Mesoscale Model Users' Workshop, 1996.

[26] Temel O., van Beeck J., (2016), *Two equation eddy-viscosity models based on the Monin-Obukhov theory*, submitted to Journal of Applied Mathematical Modeling

[27] Balogh, M., Parente, A., Benocci, C. (2007), *RANS simulation of ABL flow over complex terrains applying an enhanced k- model and wall function formulation: Implementation and comparison for Fluent and OpenFOAM*, 2007: Journal of wind engineering and industrial aerodynamics, 104, 360-368.

[28] Temel O., van Beeck J., (2016), *Adaptation of mesoscale turbulence parameterization schemes as RANS closures for ABL simulations*, submitted to Journal of Turbulence.

[29] Temel O., van Beeck J., (2015), *An improved mesoscale tur-*

bulence parameterization scheme for very stable ABL, poster presented in PhD Seminar on Wind Energy, Brussels, 10th of December

[30] Temel O., van Beeck J., (2015), *Turbulence modelling for coupled CFD/NWP atmospheric boundary layer simulations*, accepted to be presented in 1st WINERCOST Conference, Ankara, Turkey, 21st of April

Turbulent heat transfer at different Prandtl number fluids in natural convection boundary layer on a vertical plate

Agustín Villa Ortiz

Environmental and Applied Fluid Dynamics Department, von Karman Institute for Fluid Dynamics, Belgium, villaortiz@vki.ac.be

Supervisor: Jean Marie Buchlin

Professor, Environmental and Applied Fluid Dynamics Department, von Karman Institute for Fluid Dynamics, Belgium, buchlin@vki.ac.be

University Supervisor: Tony Arts

Professor, Institute of Mechanics, Materials and Civil Engineering, Université Catholique de Louvain, Belgium, arts@vki.ac.be

Abstract

In the context of the Generation IV of nuclear power reactors, liquid metals ($Pr \ll 1$) are proposed as coolant agents. The thermal design of those depends on the proper thermohydraulic characterization. However, the actual thermal turbulence models are not able to reproduce accurately the thermal field of this sort of fluids, specially in natural convection flows.

The present paper focuses on the thermal turbulence models currently used in forced convection ($Re \approx 13000$ – 24000),who are tested in natural convection at different Prandtl numbers. Two configurations are considered: a Rayleigh Benard cell and a natural convection boundary layer around a cylinder. No relevant differences are found between the proposed approaches, due to the low turbulence in the investigated test case. The relevance of using 3D geometries for natural convection cases is shown, specially when $Pr \neq 1$. Buoyancy effects in momentum turbulence models as turbulence production is studied. Predictions improve when the buoyancy production term is included in case of high Reynolds turbulence models, i.e. when coarse meshes are used. However, in case of finer meshes, where low Reynolds models are needed, have shown the inclusion of the buoyancy term has negative effects.

Keywords: turbulence, heat transfer, turbulence modelling, RANS, LES, OpenFOAM, low Prandtl number, natural convection, Rayleigh Benard cell, boundary layer

1. Introduction

1.1. Context of the project

The MYRRHA reactor (Multi-purpose hYbrid Research Reactor for High-tech Applications) is a fast reactor under design in Belgium by SCK•CEN, which can operate in critical and subcritical modes [**?**]. It contains a proton accelerator of 600 MeV, a spallation target and a multiplying medium with MOX fuel, cooled by an eutectic of lead and bismuth (LBE).

MYRRHA is piloted by an ADS (accelerator driven system), which provides the high energy protons that are used in the spallation target to produce neutrons which feed the core. Neutrons impact in fuel atoms, producing new atoms, neutrons and energy (heat). In function of the operating model (critical or subcritical) the production of neutrons varies, which they initialize a new series of fission reactions.

In the context of the MYRRHA project, the understanding of natural convection in LBE has an important role in the safety and design of the reactor. In same accident or maintenance scenarios, where high temperature differences appear, natural convection is the dominant flow phenomenon and therefore are critical during the design phase. The understanding of the natural convection flow at low Prandtl numbers is mandatory to simulate the scenarios at the design phase.

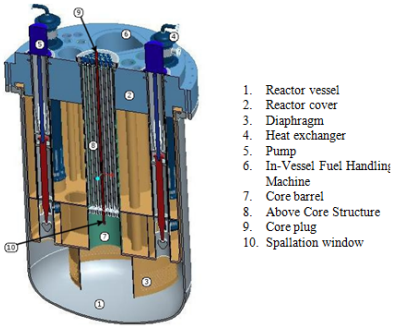

Figure 1: MYRRHA reactor cross section

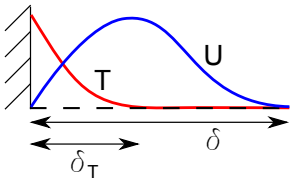

(a) $Pr > 1$

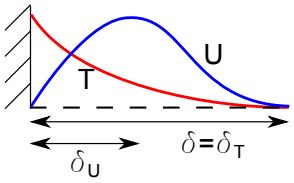

(b) $Pr < 1$

Figure 2: Velocity and temperature boundary layers in natural convection in function of the Prandtl number.

1.2. Natural convection

Natural convection flows are driven by buoyancy forces. Those forces are originated by the gravitational acceleration and density variations (due to changes in the temperature field). The Prandtl number Pr is characteristic of non isothermal flows.It relates the kinematic viscosity (ν) and the thermal diffusivity (α), whose expression is $Pr = \nu/\alpha$. The influence of the Prandtl number in natural convection flows is shown in Fig. 2.

In case of high Prandtl number (Fig. 2a), the kinematic viscosity is larger than the thermal diffusivity. Viscous forces balance the buoyancy forces, but out of the thermal boundary layer, there is no buoyancy. Then the viscous forces are balanced with the inertial ones. Since the thermal boundary layer is very thin, this balance is present in most of the momentum boundary layer.

In case of low Prandtl number (Fig. 2b), the thermal diffusivity is larger than the kinematic viscosity. It results in a larger thermal boundary layer thickness in comparison with the previous case. The buoyancy forces are balanced with the inertial forces. Viscous forces are negligible in this case, and this is why the momentum boundary layer ends with the thermal one. Only in the closest region to the wall the viscous forces are significant, where the velocity reach its maximum velocity.

1.3. Flow simulation tools

Numerical tools to simulate fluid flows are classified based by the level of modelization and the computational cost.

In the industrial environment, Reynolds Averaging Navier Stokes (RANS) simulations are the most popular. The computational cost is low even in relatively complex problems. The Reynolds averaging introduces new unknowns that are provided by turbulence models. It means the turbulence is completely modelled, so the reliability of these simulations lies in the accuracy of the turbulence models.

The increase of computational power has allowed to perform Large Eddy Simulations (LES) in simple industrial cases. They resolve the big scales of motion, but the smallest scales are modelled. The accuracy of the results is more reliable than the RANS simulations, but the computational cost is significantly higher.

The highest accuracy is given by Direct Numerical Simulations (DNS). All the motion scales are resolved, resulting in large meshes and computational cost. It is widely used in academic cases, in order to understand the physics of the phenomenon, and to provide information for developing new RANS turbulence models.

1.4. Objectives

The current research project aims to contribute to the state of the art of thermal turbulence modelling in low Prandtl numbers in natural convection flows. The understanding of the physics beyond these phenomena is required. Simulations will be performed to study the effect of the Prandtl number in natural convection, and to test the available turbulence modelling possibilities.

1.5. Summary

In the current paper, an introduction to RANS simulations and thermal turbulence modelling is present in Sections 2.1 and 2.2. The investigated test cases

are explained in Section 2.3, and the obtained results are studied in Section 3.

The conclusions of these simulations and the future work is detailled in Section 4.

2. Methodology

2.1. RANS equations

RANS equations are used to simulate the flow inside the MYRRHA reactor. Different configurations, such as forced convection, conjugate heat transfer or particle tracking can be performed on it by using this numerical approach. However, turbulence models are needed to provide valid results. It is important to understand how these simulations work in order to select the best configuration for each application.

Navier Stokes equations can be rewritten by using the Reynolds Averaging as

$$\sum_j \frac{\partial \overline{U_j}}{\partial x_j} = 0 \tag{1a}$$

$$\sum_j \frac{\partial \left(\overline{U_i}\,\overline{U_j}\right)}{\partial x_j} = -\frac{1}{\rho}\frac{\partial \overline{p}}{\partial x_i} + \sum_j \frac{\partial}{\partial x_j}\left(\nu \frac{\partial \overline{U_i}}{\partial x_j} - \overline{u_i' u_j'}\right) + \overline{f_{b,i}} \tag{1b}$$

$$\sum_j \frac{\partial \left(\overline{U_j}\,\overline{T}\right)}{\partial x_j} = \sum_j \frac{\partial}{\partial x_j}\left(\alpha \frac{\partial \overline{T}}{\partial x_j} - \overline{u_j' T'}\right) + \overline{Q} \tag{1c}$$

where the mean velocity $\overline{U}$ and $\overline{T}$ are the unkowns of this system of equations, and the subindex denote the spatial coordinates. However, due to the averaging, new terms are derived. The terms $-\overline{u_i' u_j'}$ and $-\overline{u_j' T'}$ are composed by the fluctuations of velocity and temperature are taken, and they become new unknowns in the system of equations. They are provided by the called turbulence models.

The momentum turbulence models, like $k-\varepsilon$, $k-\omega$ or Reynolds Stresses models provide the $-\overline{u_i' u_j'}$ term, the Reynolds Stress tensor. They have been widely studied and tested in the past by comparing with experimental and numerical data.

In case of the turbulent heat flux vector $-\overline{u_j' T'}$, analogies and transport equations models are used, but there is still a huge distance in terms of maturity between the development of momentum and thermal models. It yields sometimes in an inaccurate prediction of the thermal field, that could carry drastic consequences if the thermal models are not used properly, when the flow configuration has not been deeply studied before.

2.1.1. Buoyancy forces in RANS equations

The most popular approach to simulate incompressible flows where temperature differences result in density changes is the Boussinesq approximation.All the fluid properties are assumed to be constant except the density in the gravity term to take into account buoyancy. Eq. (1b) is transformed into

$$\sum_j \frac{\partial \left(\overline{U_i}\,\overline{U_j}\right)}{\partial x_j} = -\frac{1}{\rho_0}\frac{\partial \overline{p}}{\partial x_i} + \sum_j \frac{\partial}{\partial x_j}\left(\nu \frac{\partial \overline{U_i}}{\partial x_j} - \overline{u_i' u_j'}\right) + \frac{\overline{\rho}}{\rho_0} g_i \tag{2}$$

where g_i is the component of the gravity in the direction i and the $\overline{\rho}/\rho_0$ can be expressed in function of the thermal expansion coefficient β

$$\frac{\overline{\rho}}{\rho_0} = 1 - \beta(T - T_0) \tag{3}$$

The resulting momentum equation is:

$$\sum_j \frac{\partial \left(\overline{U_i}\,\overline{U_j}\right)}{\partial x_j} = -\frac{1}{\rho_0}\frac{\partial \overline{p}}{\partial x_i} + \sum_j \frac{\partial}{\partial x_j}\left(\nu \frac{\partial \overline{U_i}}{\partial x_j} - \overline{u_i' u_j'}\right) + g_i\left(1 - \beta(T - T_0)\right) \tag{4}$$

2.2. Thermal turbulence models

Two main approaches are proposed in order to study the turbulent heat transfer.

1. First orders models
   This is the simplest approach, where the Boussinesq hypothesis is used to model the turbulent heat flux, which will be function of the gradient of temperature and the turbulent thermal diffusivity α_t:
   $$-\overline{u_j' T'} = \alpha_t \frac{\partial \overline{T}}{\partial x_j} \tag{5}$$
   where α_t is the only unknown, instead of the three components of the turbulent heat flux.
   An analogy between the turbulent viscosity ν_t (obtained by the momentum turbulence models) and the turbulent thermal diffusivity α_t by means of a turbulent Prandtl number Pr_t:
   $$Pr_t = \frac{\nu_t}{\alpha_t} \tag{6}$$
   Studies approximated this number to different values [1], but the most extended assumptions for it is the Reynolds analogy, where a value of 0.85 – 0.9 is used. By means of this analogy,

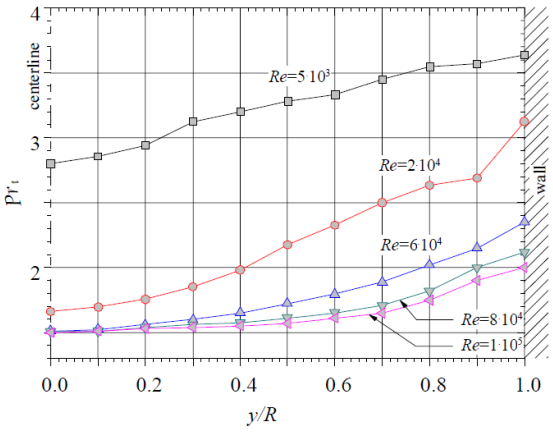

(a) Pr_t as a function of the distance with the wall and Reynolds number

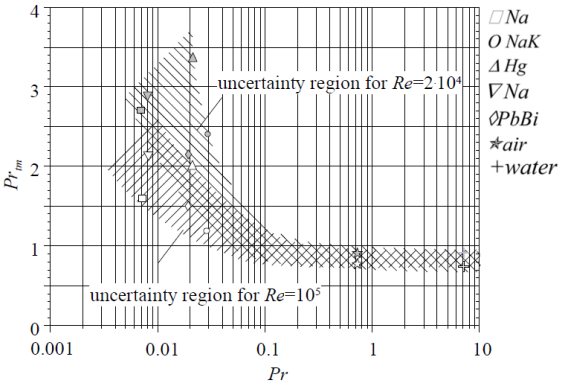

(b) Pr_t as a function of Prandtl number

Figure 3: Measured turbulent Prandtl number in function of the distance with the wall, Reynolds number and Prandtl number in a fully developed turbulent circular duct flow with a constant wall heat flux. [1]

only the additional momentum turbulence equations are solved.

Posterior works proved that this default value is too low for low Prandtl number fluids. For this reason, in literature the use of a value of $Pr_t = 2$ is recommended. Moreover, measurements and DNS simulations showed that he turbulent Prandtl number varies as a function of the flow regime and the geometry, as it is shown in Fig. 3. As one can see, the Reynolds analogy is fairly used in forced convection cases where $Pr \approx 1$, but not in case of low Prandtl numbers, where the turbulent Prandtl number value is larger.

Yakhot obtained an analytical expression, where Pr_t is formulated as a function of the turbulent Peclet number. Kays developed posteriorly a correlation that fits the Yakhot expression in an acceptable range for low Peclet numbers [2], i.e. the range of low Prandtl number flows.

The use of transport equations became popular when the additional computational cost was affordable. The fluctuations of the temperature to the square k_θ and its dissipation rate ε_θ are computed similarly to the turbulent kinetic energy and the turbulent kinetic energy dissipation rate [3; 4; 5]. Manservisi and Menghini [6] developed a $k_\theta - \varepsilon_\theta$ model, which has been tested in different channel flows at $Pr = 0.025$.

2. Second order models

   In these models, the Boussinesq hypotesis is not used. The turbulent heat flux is computed explicitly or by using transport equations. In case of anisotropic flows, these models can provide more accurate results than the first order approaches. Shams *et al.* [7] have tested an AHFM where the effect of low Prandtl number and buoyancy forces are taken into account.

The previous models have been tested in forced convection at high and low Prandtl numbers. They have been correctly set in order to obtain a good agreement with different test cases.

In the case of natural convection flows, the state of the art of the thermal turbulence models is not as developed as in forced convection. In most of the cases, RANS models are assessed [8; 9] with experimental data [10; 11] of natural convection boundary layers. Low Reynolds $k - \varepsilon$ and Reynolds stress models are tested by using the Reynolds analogy. It is shown that a good heat transfer predictions needs a low Reynolds model, but due to its isotropic formulation, the turbulent transport normal to the mean gradient is under predicted. Despite this fact, the mean flow properties do not suffer from these problems. In case of the Reynolds stress model, it is able to reproduce the turbulent diffusion, but a fully differential stress model is needed to predict the turbulence structures. Hence, the improvement of the turbulence model results passes through the use of more complex momentum and thermal turbulence models.

2.3. Test cases

The turbulence thermal models

- Constant turbulent Prandtl number [1]
- Kays correlation [2]

- Manservisi and Menghini $k_\theta - \varepsilon_\theta$ [6]

have been implemented in OpenFOAM 2.3.1, in an exclusive library. It allows to select independently momentum and thermal turbulence models. A thermal material transport library has been developed to a better integration of the thermal modelling in any solver. These models have been validated previously in forced convection [12]. LES/DNS databases were considered, where detailed flow and turbulence data are available. In this paper, the focus is given to natural convection.

In the case of LES and DNS, most of the natural convection simulations are limited to confined flows, such as Rayleigh Benard cells [13] or vertical channels [14]. The effect of the Prandtl number is studied in Rayleigh Benard cells, and standard models are investigated. Their deficiencies are shown, and a new model is proposed under this flow configuration. In the case of vertical channels, it is shown that the near wall flow regime is dependent on buoyant effects away from the wall.

A few works are related with unconfined flows. In the case of Yan *et al.*[15], LES have been performed in a spatial developing boundary layer, and good agreements were obtained. In case of [16; 17], temporal developing DNS was performed. In this technique, periodic boundary conditions are imposed in the streamwise direction. A correlation is established between time and space, which allows the technique to reduce the computational cost. However, issues are found when the time developing technique is used. The absence of entrainment to the boundary layer provokes the underestimation of the Reynolds stresses and turbulent heat flux.

2.3.1. Rayleigh Benard cell

The Rayleigh Benard cell is a natural convection case, where two horizontal plates are at different temperatures. The bottom plate has a higher temperature than the top one. The flow is driven by the temperature differences, appearing rotating cells as it is shown in Fig. 4. A Rayleigh Benard cell is defined by the Rayleigh and Prandtl numbers

$$Ra = \frac{g\beta\Delta T D^3}{\alpha\nu} \tag{7}$$

$$Pr = \frac{\nu}{\alpha} \tag{8}$$

$$\Gamma = \frac{H}{D} \tag{9}$$

where g is the gravitational acceleration, β is the thermal expansion coefficient of the fluid, $\Delta T = T_h - T_c$ is the difference of temperature between the plates, D the separation between the plates and α is the thermal diffusivity. Both numbers are related by the Grashof number

$$Gr = \frac{Ra}{Pr} \tag{10}$$

The wall-normal distance, the velocity and the temperature are expressed in a non-dimensional form as

$$\frac{y}{D} \tag{11}$$

$$\frac{u}{u_0} \tag{12}$$

$$\frac{T - Tc}{\Delta T} \tag{13}$$

where $u_0 = \sqrt{g\beta\Delta T D}$.

The results of Otic *et al.*[13] and Li *et al.* [18] are proposed as test cases for this geometry. The test cases of Otic, whose results are available in the KIT DNS databse [19], offer different Prandtl numbers, but the Grashof number of those simulations is not large enough to ensure a turbulent regime. Periodic boundary conditions are proposed in the spanwise and streamwise directions.

In the case of the database of Li, the Grashof number is higher than in the previous database, but only one Prandtl number is considered. Velocity and temperature data is provided close to the cold plate. This test case has no periodic boundary conditions, but walls are limiting the domain. The proposed configurations are shown in Table 1.

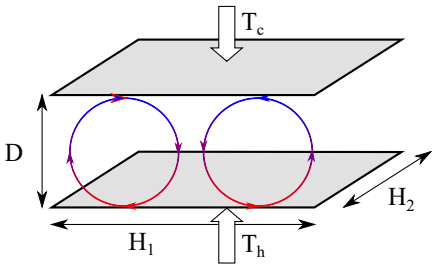

Figure 4: Rayleigh Benard sketch.

Author	Ra	Pr	Gr	Γ
Otic *et al.*	$6.3 \cdot 10^5$	0.71	$8.9 \cdot 10^5$	7.92
Otic *et al.*	$5 \cdot 10^4$	0.025	$2 \cdot 10^6$	8
Li *et al.*	$2.88 \cdot 10^{10}$	0.7	$4.1 \cdot 10^{10}$	1

Table 1: Flow properties of the simulated Rayleigh Benard cells

2.3.2. Cylinder

The natural convection boundary layer of Barhaghi *et al*. [20] is simulated in order to validate the numerical set-up, extensible to other vertical boundary layer cases. The maximum Grashof number is $Gr_x = 5{\cdot}10^{11}$, and the Prandtl number is $Pr = 0.7$. The computational domain is the shown in Fig. 5. The represented geometry reproduces their experimental facility, where the fluid is warmed by a vertical internal cylinder. The hot fluid goes out of the facility through a concentric annulus. In order to avoid stratification in the region between the external and the top walls, a cold inflow is imposed at the bottom of the cylinder. The inflow velocity is low enough to ensure the natural convection as the dominant phenomenon.

In a boundary layer, the friction velocity u_τ is defined as:

$$u_\tau = \sqrt{\frac{\tau_w}{\rho}} \tag{14}$$

where τ_w is the wall shear stress $\tau_w = \mu \frac{\partial U}{\partial n}$. This friction velocity is used to express in a non-dimensional form the velocity and the distance to the wall:

$$u^+ = \frac{u}{u_\tau} \tag{15}$$

$$y^+ = \frac{y\, u_\tau}{\nu} \tag{16}$$

The thermal field is characterized by the friction temperature and the non dimensional temperature:

$$T_\tau = \frac{q_w}{\rho\, c_p\, u_\tau} \tag{17}$$

$$T^+ = \frac{T_h - T}{T_\tau} \tag{18}$$

The proposed configuration is shown in Table 2.

Ra	Pr	Gr
$3.5 \cdot 10^{11}$	0.7	$5 \cdot 10^{11}$

Table 2: Flow properties of the simulated vertical cylinder

3. Turbulence thermal model assessment

3.1. Rayleigh Benard cell

The effect of the Prandtl number has been tested by the Otic test cases [13]. Two different Prandtl

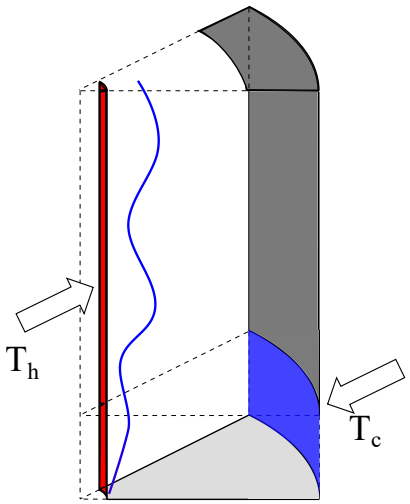

Figure 5: Cylinder sketch.

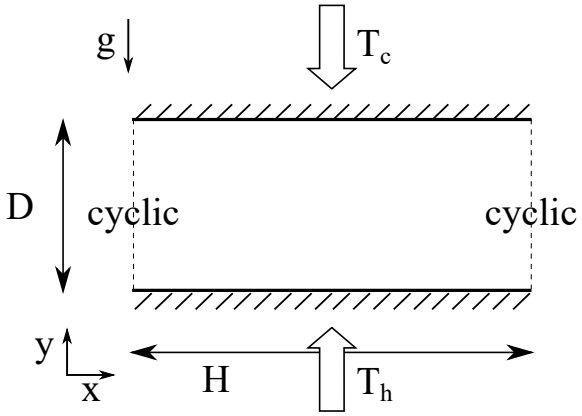

Figure 6: Schematic of simulated Rayleigh Benard cell.

numbers are used: $Pr = 0.71$, representing air, and $Pr = 0.025$, representing LBE. Since the Manservisi $k_\theta - \varepsilon_\theta$ turbulence model is a low Reynolds turbulence model, resolved meshes will be used to compare the different turbulence models. As equal as in the test case, Boussinesq approximation for incompressible, buoyant flows has been taken into account. A schematic of the test case is shown in Fig. 6. 2D and 3D meshes are considered. The corresponding 2D grid resolution is $n_x \times n_y = 200 \times 120$, and the 3D one is $n_x \times n_y \times n_z = 200 \times 120 \times 200$.

The proposed boundary conditions in these simulations are

- At the walls

  $\vec{U} = [0\ 0\ 0] \qquad T|_{y=0} = T_h \qquad T|_{y=D} = T_c$

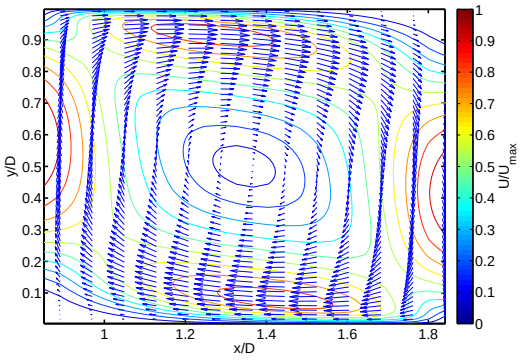

Figure 7: Contour of the mean velocity field and velocity vectors for $Ra = 6.3 \cdot 10^5$, $Pr = 0.71$, from $x/D = 0.851$ to 1.841 ($U_{max} = 0.357 m/s$).

- Low Reynolds approximations for k and ε
- Periodic boundary conditions between the laterals for all the variables

3.1.1. Ra=630000, Pr=0.71

The 2D results for $Pr = 0.71$ simulation are shown in Figs. 7 to 9. The velocity vectors of one cell is shown in Fig. 8. As one can see, maximum velocities are reached close to the horizontal walls and close to the adyacent cells. The velocity reaches there a maximum value of $|U| = 0.357\ m/s$. As one can see in Fig. 8, the temperature remains practically constant inside the recirculation cell. Both warm and cold boundary layers are completely developed, and the stratification is observed between them. Only far from the centre of the cell the temperature tends to the minimum and maximum values, where the flow reaches the maximum velocity.

A comparison between the different thermal turbulence models is shown in Fig. 9. The temperature field is averaged inside the cells and compared with the DNS data. A good agreement between the simulations and the reference data is evident. All the proposed turbulence models provide similar results. This behaviour leads to a simulation without turbulence models. The similar results concludes that the turbulence model selection has no effect in this simulations since the turbulence level is not high enough.

A 3D simulation has been performed in laminar regime. A comparison between the 2D and 3D results is shown in Fig. 10. An averaging in the homogeneous directions has been performed in the 3D simulation to retrieve the shown temperature profile. The 3D simulation provides a better approximation. The boundary

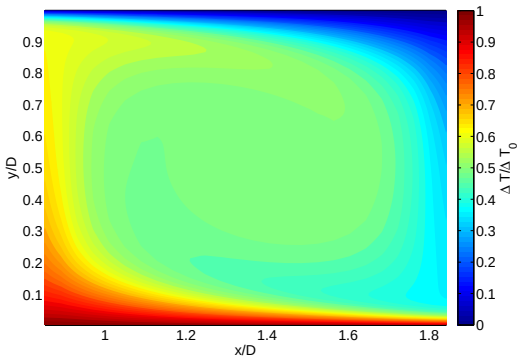

Figure 8: Contour of the non dimensional mean temperature field for $Ra = 6.3 \cdot 10^5$, $Pr = 0.71$, from $x/D = 0.851$ to 1.841.

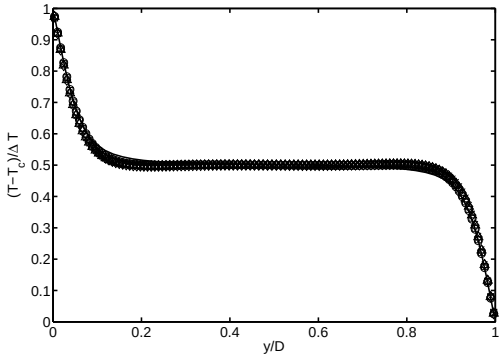

Figure 9: Non dimensional temperature profiles for $Ra = 6.3 \cdot 10^5$, $Pr = 0.71$, with Reynolds analogy ($\circ$), $Pr_t = 2$ ($\times$), Kays correlation ($\square$) Manservisi $k_\theta - \varepsilon_\theta$ model ($\triangle$) and no turbulence model ($\diamond$), compared agains DNS data (-) [19].

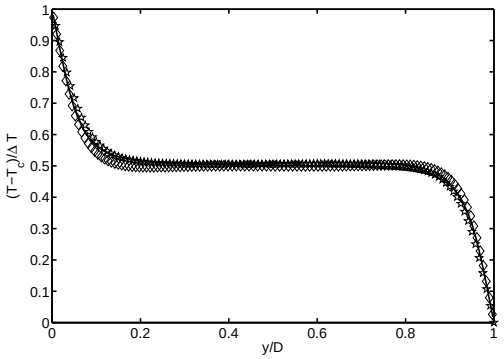

Figure 10: Non dimensional temperature profiles for $Ra = 6.3 \cdot 10^5$, $Pr = 0.71$, for the 2D ($\diamond$) and 3D ($\star$) simulations without turbulence model, compared against DNS data (-) [19].

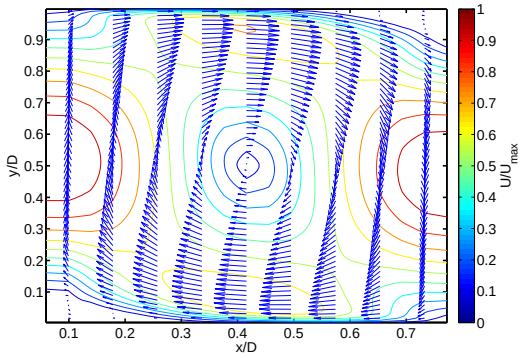

Figure 11: Contour of the mean velocity field and velocity vectors for $Ra = 5 \cdot 10^4$, $Pr = 0.025$, from $x/D = 0.594$ to 0.772 ($U_{max} = 1.026 m/s$).

layer obtained through the 2D simulation is thinner than the one given by the 3D simulation.

3.1.2. Ra=50000*, Pr*=0.025

The 2D simulations results are shown in Figs. 11 to 13. For $Pr = 0.025$, the maximum velocity is $|U| = 1.026\ m/s$, as it is shown in Fig. 11. In Fig. 12 one appreciates that, due to the large thermal diffusivity, both thermal boundary layers (the warm and cold ones) are much thicker than in the case of $Pr = 0.71$, and there is no stratification.

This fact is more clear in Fig. 13, where the DNS profile shows no complete boundary layers. However, the simulations do not agree that well with the reference data. The thickness of both boundary layers is thinner than the DNS ones, which provokes to reach

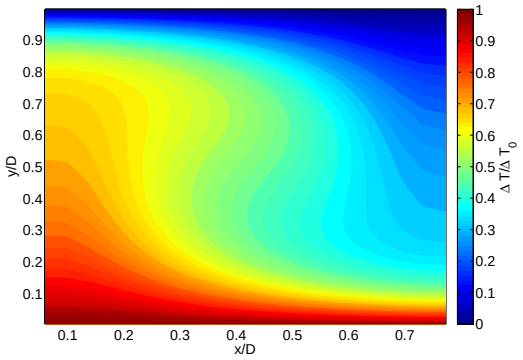

Figure 12: Contour of the non dimensional mean temperature field for $Ra = 5 \cdot 10^4$, $Pr = 0.025$, from $x/D = 0.594$ to 0.772.

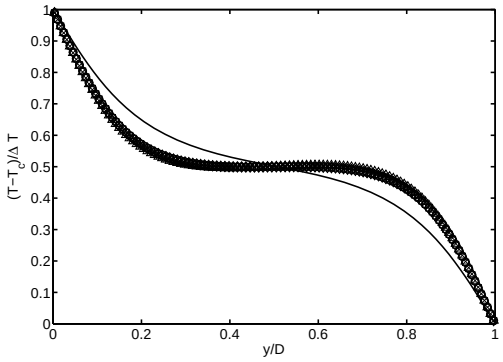

Figure 13: Non dimensional temperature profiles for $Ra = 5 \cdot 10^4$, $Pr = 0.025$, with Reynolds analogy ($\circ$), $Pr_t = 2$ ($\times$), Kays correlation ($\square$), Manservisi $k_\theta - \varepsilon_\theta$ model ($\triangle$) and no turbulence model ($\diamond$), compared against DNS data (-) [19].

the bulk temperature sooner than expected. Even the low Prandtl turbulence models are not capable to reproduce the temperature field significantly better than the Reynolds analogy, thought they were more suitable in forced convection cases [12].

A comparison between the 2D and 3D simulation is shown in Fig. 14. As one can see, the 3D simulation predicts accurately the temperature profile. Indeed, the 2D profile has a much thinner boundary layer, if it is compared with the 3D and the reference profiles. The same phenomenon was observed in the previous case in Fig. 10 at $Pr = 0.71$, where both simulations (2D and 3D) results were closer. This fact can be related to the Prandtl number effect. For low Prandtl numbers, the high thermal diffusivity leads to a thicker

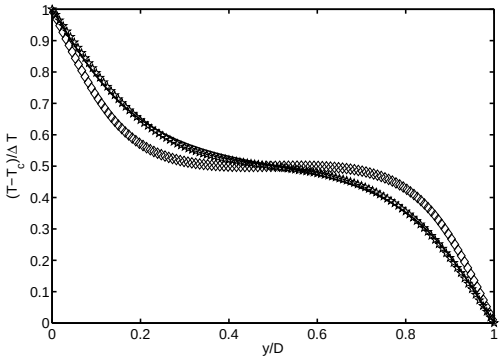

Figure 14: Non dimensional temperature profiles for $Ra = 5 \cdot 10^4$, $Pr = 0.025$, for the 2D ($\diamond$) and 3D ($\star$) simulations without turbulence model, compared against DNS data (-) [19].

boundary layer. But, due to the effect of the two dimensions domain, simulations are not capable to reproduce properly the diffusion of the temperature in both cases ($Pr = 0.71$ and 0.025). Buoyancy forces are volumetric forces, so the use of 2D meshes is contradictory, specially when low Prandtl numbers are used as it has been shown.

3.1.3. Ra=2.88 · 10^{10}, Pr=0.7

The previous test cases have a Grashof number below 10^9, so turbulence effects are not important. Industrial cases are mostly turbulent flows, and the mesh size is important in order to reduce the computational cost and to obtain accurate results. Wall functions are then needed in order to obtain a balance between these two objectives. Therefore, the test case of Li *et al.*[18], whose Grashof number is $Ra = 2.88 \cdot 10^{10}$ and $Pr = 0.7$ will be used to study the grid resolution.

Velocity and temperature boundary layers in the cold plate are provided on their database. Two momentum turbulence models have been used, in order to be coherent with the used mesh. The Launder and Sharma low Reynolds $k - \varepsilon$ and the standard $k - \varepsilon$ are analysed. In the first one, no wall functions are needed, but the standard $k-\varepsilon$ has to be used with them to ensure a good prediction in the region close to the wall. An usual correction in turbulence models is the use of the production of turbulent kinetic energy due to buoyancy forces G_b, which is expressed as:

$$G_b = \beta \vec{g} \overrightarrow{\overline{u'T'}} = \beta \vec{g} \left(\alpha_t \nabla T \right) \qquad (19)$$

which is used as a production term in the k equation and can be used as well as a source term in the ε equation.

The chosen thermal turbulence model for these simulations is the Reynolds analogy, since it has been used in previous works at this Prandtl number [8; 9].

The grid resolution for the simulations has been selected in function of the non dimensional wall distance. First grid point is located at $y/D = 0.01$ when the standard $k - \varepsilon$ is used, and $y/D = 0.0001$ when the low Reynolds model is applied. The corresponding 2D grid resolution for the Launder and Sharma model is $n_x \times n_y = 120 \times 120$. In case of the standard $k - \varepsilon$, the 2D grid resolution is $n_x \times n_y = 80 \times 80$ and the 3D one is $n_x \times n_y \times n_z = 80 \times 80 \times 80$. The standard models in OpenFOAM have been extended with the buoyancy term, in order to compare the influence of this term. The boundary conditions are the same than in the previous case for the Launder Sharma model, and ν_t, k and ε wall functions are used for the standard $k - \varepsilon$ model. The scheme of these simulations is similar to Fig. 6, but there are walls instead of cyclic boundary conditions.

The velocity profiles are shown in Fig. 15. In the case of the standard $k-\varepsilon$ model, differences are found between the 2D and 3D results. The velocity in the 2D case is higher than in the 3D case. Differences in the profile are found on their shape: the 2D simulation collapses close to the centre of the cell, however the 3D case differs from the rest of the simulations. When the buoyancy production is included in the turbulence model, in the 2D simulation the thickness of the boundary layer is thicker than the no-buoyant case. The 3D buoyant case provides a better prediction than its no-buoyant case.

If one compares with the 2D ANSYS Fluent simulation (which includes by default the buoyant term in the turbulence model), similar results are obtained with the 2D OpenFOAM simulations.

When the temperature predictions for these two turbulence models are compared in Fig. 16, one can see, as in the previous test cases, that buoyant 2D simulations do not predict accurately the temperature profile. The use of the buoyant production term improves the thermal prediction. When the 3D buoyant $k - \varepsilon$ simulation in OpenFOAM is compared with the 2D one in Fluent, similar results are obtained.

In the case of the Launder and Sharma model, the addition of the buoyant term is not recommended. The velocity profile is over-predicted close to the wall, but it follows the same tendency than the high Reynolds model once the velocity peak is reached. The inner thermal boundary layer is overpredicted too, and the

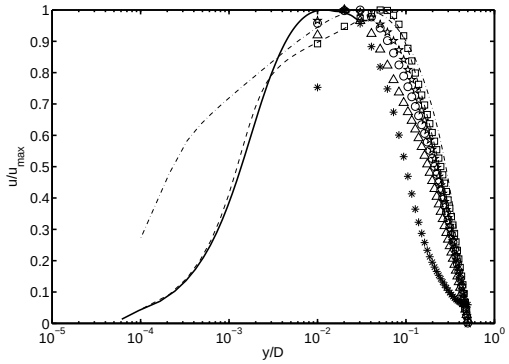

Figure 15: Non dimensional velocity profiles for $Ra = 2.88 \cdot 10^{10}$, $Pr = 0.7$, for $k-\varepsilon$ 2D (∘) and 3D (*) simulations in OpenFOAM and 2D (☆) in ANSYS Fluent, buoyant $k-\varepsilon$ 2D (□) and 3D (△) simulations, Launder and Sharma (−−) and buoyant Launder and Sharma (− · −), compared against DNS data (-) [18].

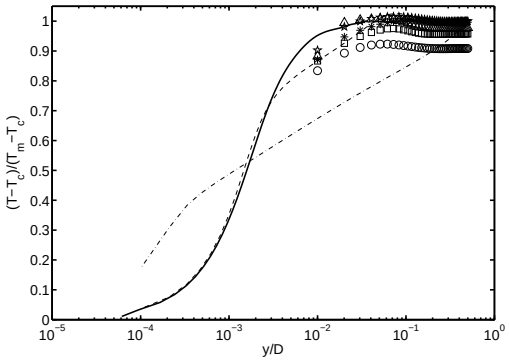

Figure 16: Non dimensional temperature profiles for $Ra = 2.88 \cdot 10^{10}$, $Pr = 0.7$, for $k-\varepsilon$ 2D (∘) and 3D (*) simulations in OpenFOAM and 2D (☆) in ANSYS Fluent, buoyant $k-\varepsilon$ 2D (□) and 3D (△) simulations, Launder and Sharma (−−) and buoyant Launder and Sharma (− · −), compared against DNS data (-) [18], where $T_m = (T_h + T_c)/2$.

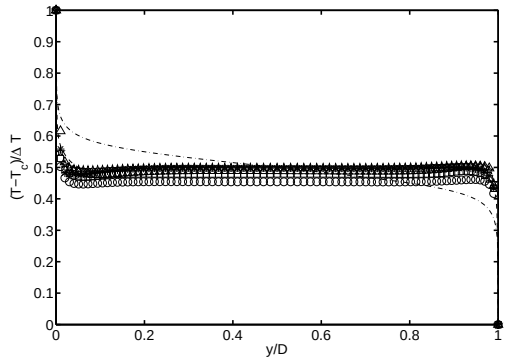

Figure 17: Non dimensional temperature profiles for $Ra = 2.88 \cdot 10^{10}$, $Pr = 0.7$, for $k-\varepsilon$ 2D (∘) and 3D (*) simulations in OpenFOAM and 2D (☆) in ANSYS Fluent, buoyant $k-\varepsilon$ 2D (□) and 3D (△) simulations, Launder and Sharma (−−) and buoyant Launder and Sharma (− · −) models.

rest of the boundary layer do not follow the reference profile or the other results profiles. On the other hand, if buoyancy effects are not taken into account, velocity and temperature inner boundary layers are well captured, and its outer layer follows the same tendency than the buoyant high Reynolds model.

A comparison between the different simulations along a vertical profile of the cell is shown in Fig. 17, where $\Delta T = T_h - T_c$. As one can see, the buoyant $k-\varepsilon$ model reaches a higher bulk temperature than its standard version, but it is not enough to reach the average value between the cold and hot plates. The use of 3D grids improves the prediction along the domain. The Launder and Sharma $k-\varepsilon$ model is able to reach the mean value in the centre of the cell, but if the buoyancy is taken into account in the momentum turbulence model, an extra diffusivity is introduced. Since there is no DNS data for this profile, it is not possible to estimate the accuracy of the results. In any case, the Launder and Sharma turbulence model is able to capture the velocity and temperature gradients of the boundary layer, that allows to reproduce the rest of the flow accurately.

3.2. Cylinder

A 2D simulation of the test case of Barhaghi [20] has been performed. No axisymmetry axis is applied, therefore a simple natural boundary layer is studied. The expected maximum Grashof number is $Gr_x = 5 \cdot 10^{11}$, and $Pr = 0.7$. As in the reference work,

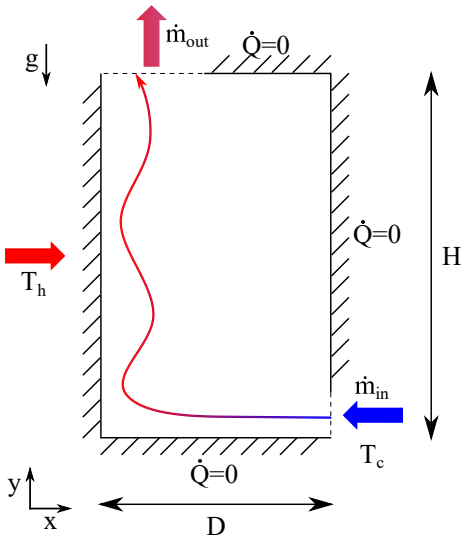

Figure 18: Schematic of simulated natural boundary layer.

Boussinesq approximation for incompressible, buoyant flows has been taken into account. The Launder and Sharma $k-\varepsilon$ model with Reynolds analogy have been applied as turbulence models. The schematic of the test case is shown in Fig. 18. The corresponding grid resolution is $n_x \times n_y = 210 \times 400$.

The bottom and the wall opposite to the heated wall are considered adiabatic, while the heated wall has a temperature $T_h = 353\ K$. The incoming flow has a temperature $T_c = 298\ K$, and a developed laminar profile, whose bulk velocity is 0.6 m/s. The boundary conditions for k and ε are the same as the proposed ones in the previous case of Section 3.1.

As one can see in the obtained results of Fig. 19, there are recirculations in the corner between the heated and the bottom walls, focused in Fig. 20. It is due to the effect of buoyancy when the inflow approaches to the heated wall. The incoming fluid is suctioned by the vertical boundary layer, and it ascends to follow it. Since the wall is heating from the bottom, a natural boundary layers is growing at $y = 0\ m$. These two flows meet at $y/D \approx 0.04$. The recirculations appears as a consequence of the viscous forces in that region, where the thermal boundary layer is not developed at all, and the detachment of the flow who comes from the inlet.

The low velocities in the right side of the domain in comparison with the boundary layer velocity, specially in the upper part, are linked to the temperature stratification shown in Fig. 21. The warmed fluid who

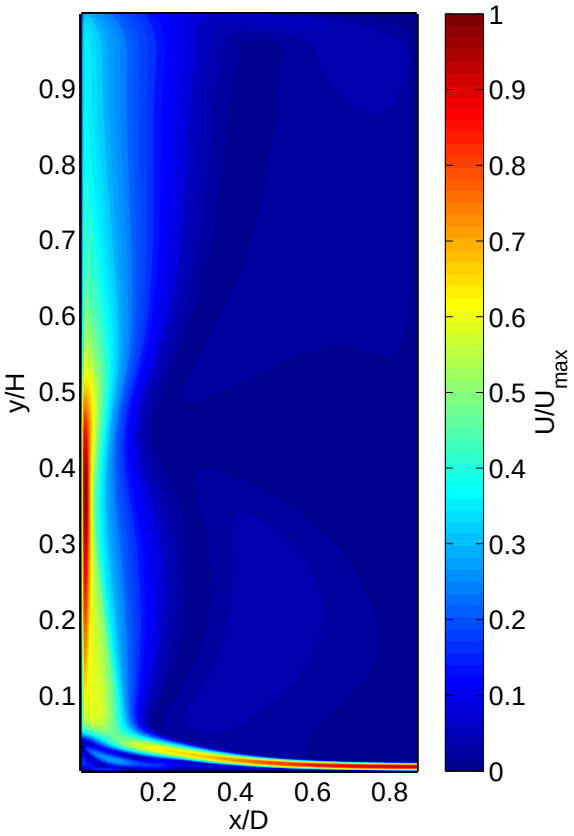

Figure 19: Mean velocity field of 2D natural boundary layer.

does not pass through the outlet orifice is recirculated to the boundary layer due to the viscous forces. Finally, the heat is transported by diffusion. Due to this stratification, the velocity along the boundary layer decreases. A high temperature region is observed in where the recirculations are found, as it is found in Fig. 22. The recirculated flow is continuously heated, and the temperature is higher in the stagnation point between the two incident flows. The recirculation provoked by the inflow transports the thermal energy around the bottom wall.

The stratification effects are visible in Fig. 23, where the velocity prediction does not reach the reference value. The stratification is also visible in Fig. 24, where the temperature far from the wall tends to a constant temperature. However, in this case a fair agreement with LES is found.

The decreasing velocity along the heated wall is

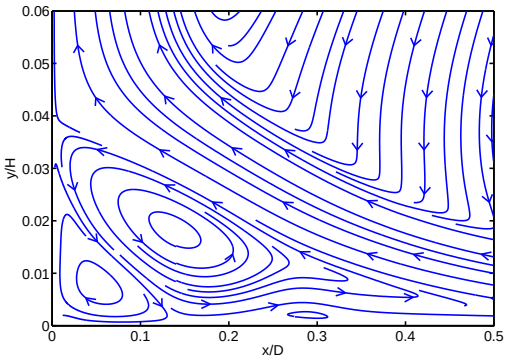

Figure 20: Streamlines at the recirculation zone between the heated and the bottom walls.

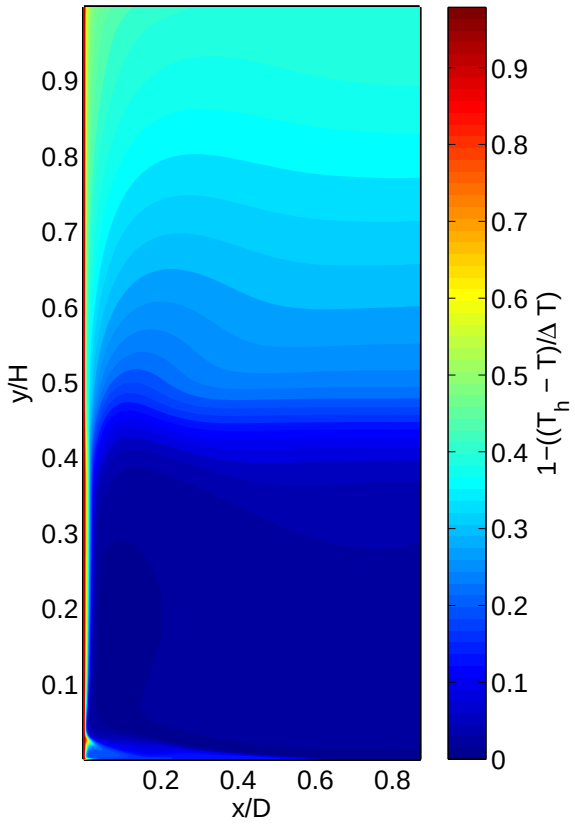

Figure 21: Mean temperature field of 2D natural boundary layer.

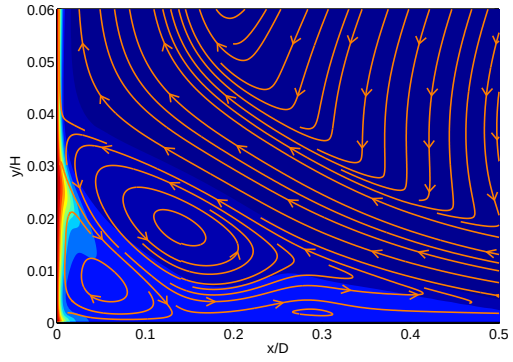

Figure 22: Streamlines and temperature field comparison at the recirculation zone between the heated and the bottom walls.

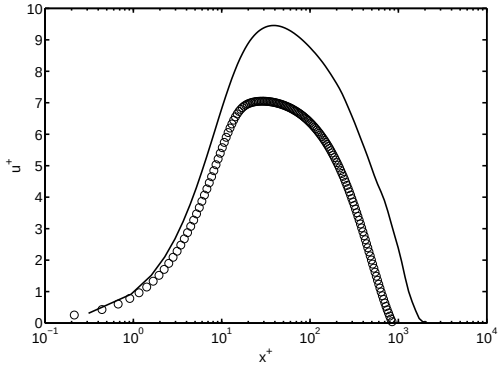

Figure 23: Dimensionless velocity profile for $Gr_y = 1.8 \cdot 10^{11}$ (∘) compared against LES data (-) [20].

the responsible of the underprediction of the velocity. This phenomena seems to be related with the temperature stratification. It provokes a limitation of the buoyancy forces, and the viscous forces becomes important, reducing the velocity of the fluidwhen it ascends.

In order to deal with the stratification, it is proposed:

- a 3D simulation of the test case would lead to a better prediction of the phenomenon.
- in addition, the velocity inlet in the bottom of the cylinder should be adjusted in order to increase the velocity and reduce the stratification, but then the natural convection phenomenon would be compromised. A trade between reducing the stratification and conservating the natural convection mechanism is needed.

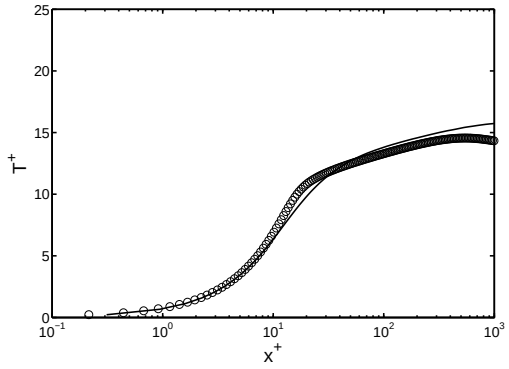

Figure 24: Dimensionless temperature profile for $Gr_y = 1.8 \cdot 10^{11}$ (∘) compared against LES data (-) [20].

4. Conclusions

The state of the art of natural convection flows has been reviewed. The complexity of turbulence modelling in this kind of flows has been tested in a 2D and 3D Rayleigh Benard cells. No differences between the different thermal turbulence models have been found during the 2D simulations, even in the case of $Pr = 0.025$, where all the thermal models offer different results in forced convection. It is related with the low turbulence level of the available data at different Prandlt number. It has been shown that 3D simulations are more accurate than the 2D ones, since the buoyancy forces cannot be appropriately estimated with 2D meshes. Differences between 2D and 3D results become important when the Prandtl number is low.

A second simulation has been performed at a higher Rayleigh number, where the effect of the momentum turbulence boundary has been studied. In case of coarse meshes, when high Reynolds turbulence models are used, the buoyancy production in the turbulent kinetic energy provides a better agreement between than the case where this term is not taken into account. The benefits of using a 3D mesh are more visible in the temperature field. On the other hand, for low Reynolds models the use of buoyancy corrections is counterproductive. It does not capture the gradient at the wall as its standard version, which provokes a bad prediction of velocity and temperature profiles.

A natural convection boundary layer through a vertical hot cylinder has also been simulated. The results shown temperature stratification in the top of the domain. In the light of the previous simulations, a 3D computation would lead to better results. In the other hand, increasing the inlet velocity is proposed to avoid stratification. Preliminary RANS simulations will be performed, in order to set appropriate boundary conditions, and hybrid LES/DNS simulations will be performed with this purpose.

Different Prandtl numbers below the unity(0.025, 0.2 and 0.71) will be investigated for this flow configuration. To validate the obtained results, a comparison with relevant velocity and temperature statistics, obtained by experimental measurements (for Prandtl 0.2 and 0.71), will be done.

These results will be used to assess RANS thermal turbulence models for low Prandtl numbers. If it is necessary, an optimization of the model constants will be performed, in order to reproduce the main patterns of the flow. Since these turbulence models are going to be used in industrial applications, they must be adapted to the constraints proposed on each of them. They must be extended in order to be used with wall functions, widely employed in the industry. The final configuration of the thermal turbulence models will be compiled in strategies to simulate natural convection flow at low Prandtl numbers.

Acknowledgments

To Ivan Otic, author of the Rayleigh Benard cell database [13; 19] for his advices when running those RANS simulations.

References

[1] OECD Nuclear Energy Agency. Nuclear Science Committee, Handbook on Lead-bismuth Eutectic Alloy and Lead Properties, Materials Compatibility, Thermal-hydraulics and Technologies, OECD Nuclear Energy Agency, 2007.

[2] W. M. Kays, Turbulent prandtl number. where are we?, ASME Transactions Journal of Heat Transfer 116 (1994) 284–295.

[3] Y. Nagano, M. Shimada, Development of a two-equation heat transfer model based on direct simulations of turbulent flows with different prandtl numbers, Physics of Fluids 8 (12) (1996) 3379–3402.

[4] C. B. Hwang, C. A. Lin, A low Reynolds number two-equation kt-et model to predict thermal field, International Journal of Heat and Mass Transfer 42.

[5] B. Deng, W. Wu, S. Xi, A near-wall two-equation heat transfer model for wall turbulent flows, International Journal of Heat and Mass Transfer 44 (4) (2001) 691 – 698.

[6] S. Manservisi, F. Menghini, Triangular rod bundle simulations of a {CFD} $k - \varepsilon - k_\theta - \varepsilon_\theta$ heat transfer turbulence model for heavy liquid metals, Nuclear Engineering and Design 273 (0) (2014) 251 – 270.

[7] A. Shams, F. Roelofs, E. Baglietto, S. Lardeau, S. Kenjeres, Assessment and calibration of an algebraic turbulent heat flux model for low-prandtl fluids, International Journal of Heat and Mass Transfer 79 (2014) 589 – 601.

[8] R. Henkes, C. Hoogendoorn, Comparison of turbulence models for the natural convection boundary layer along a heated vertical plate, International journal of heat and mass transfer 32 (1) (1989) 157–169.

[9] T. Peeters, R. Henkes, The reynolds-stress model of turbulence applied to the natural-convection boundary layer along a heated vertical plate, International Journal of Heat and Mass Transfer 35 (2) (1992) 403–420.

[10] K. Kitamura, M. Koike, I. Fukuoka, T. Saito, Large eddy structure and heat transfer of turbulent natural convection along a vertical flat plate, International journal of heat and mass transfer 28 (4) (1985) 837–850.

[11] T. Tsuji, Y. Nagano, Characteristics of a turbulent natural convection boundary layer along a vertical flat plate, International Journal of Heat and Mass Transfer 31 (8) (1988) 1723–1734.

[12] A. Villa Ortiz, Implementation in OpenFOAM of a heat transfer turbulence model for low Prandlt number fluids, von Karman Institute for Fluid Dynamics, Rhode-St-Genese, Belgium, June 2014.

[13] I. Otic, G. Grötzbach, M. Wörner, Analysis and modelling of the temperature variance equation in turbulent natural convection for low-prandtl-number fluids, Journal of Fluid Mechanics 525 (2005) 237–261.

[14] C. Ng, A. Chung, D an.d Ooi, Direct numerical simulation of natural convection in a vertical channel.

[15] Z. Yan, E. Nilsson, Large eddy simulation of natural convection along a vertical isothermal surface, Heat and Mass Transfer 41 (11) (2005) 1004–1013.

[16] M. Z. Abedin, T. Tsuji, Y. Hattori, Direct numerical simulation for a time-developing natural-convection boundary layer along a vertical flat plate, International Journal of Heat and Mass Transfer 52 (19) (2009) 4525–4534.

[17] A. G. Abramov, E. M. Smirnov, V. D. Goryachev, Temporal direct numerical simulation of transitional natural-convection boundary layer under conditions of considerable external turbulence effects, Fluid Dynamics Research 46 (4) (2014) 041408.

[18] L. Li, C. Resagk, R. du Puits, Viscous boundary layers in turbulent rayleigh-bnard convection, Journal of Physics: Conference Series 318 (8) (2011) 082004.
URL `http://stacks.iop.org/1742-6596/318/i=8/a=082004`

[19] Karlsruher Institut für Technologie, DNS Database of Turbulent Natural Convection in Horizontal Fluid Layers, `http://iketwww1.fzk.de/iket/turbit/` (1998).

[20] D. G. Barhaghi, L. Davidson, R. Karlsson, Large-eddy simulation of natural convection boundary layer on a vertical cylinder, International journal of heat and fluid flow 27 (5) (2006) 811–820.

DEVELOPMENT OF
ADVANCED CFD AND OPTIMIZATION

Acceleration of turbomachinery steady simulations on GPU

Mohamed Hassanine Aissa

Turbomachinery and Propulsion Department, Von Karman Institute for Fluid Dynamics, Belgium, aissa@vki.ac.be

Supervisor: Tom Verstraete

Assistant Professor, Turbomachinery and Propulsion Department, Von Karman Institute for Fluid Dynamics, Belgium, tom.verstraete@vki.ac.be.

University Supervisor: C. Vuik

Professor, applied mathematical Institute , TU Delft, the Netherlands, vuik@tudelft.nl

Abstract

Steady state CFD simulations, which rely on implicit time integration, are not experiencing great accelerations on GPUs. Moreover, most of the reported acceleration effort concerns solving the linear system of equations while neglecting the acceleration potential of running the system assembly also on the GPU. In this paper, we present the software implementation of an implicit RANS CFD solver, which is fully running on GPU. We use the flexible GMRES implementation of the Paralution package for the linear system solve along with the incomplete LU factorization for the preconditioning. We propose also a control mechanism capable of accelerating the system solve without altering the flow convergence by reducing the number of times an incomplete LU factorization is performed. Speedups of 9.2x compared to a 1xcore CPU and 3.5x compared to a 4xcores CPU were measured for 3D flow predictions in turbine applications.

Keywords: steady CFD, linear systems, GPU, ILU, Krylov subspace, GMRES

1. Introduction

Turbomachinery components are nowadays quite often designed by using optimization algorithms, which scan the design space guided by CFD simulations [1]. The algorithm requires therefore a large number of simulations making any time gain on the CFD level very beneficial for the overall optimization procedure. These steady CFD simulations advance an initial flow solution based on an explicit or implicit numerical time integration scheme. Implicit schemes are known to be more stable and faster to converge than explicit ones because these schemes advance the flow solution with a large time step in every flow iteration, which is not possible for explicit solvers due to stability limitations. This property comes however at a high cost, since at every flow iteration a linear system of equations $Ax = b$ has to be assembled and solved. The system assembly comprises the computation of the system matrix A and the right-hand side b. The system solve, due to the sparsity character, uses an iterative solver such as the Generalized Minimal Residual Algorithm for Solving Non-symmetric Linear Systems [2], which reduces the residual $r = Ax - b$ iteratively.

For CFD problems in turbomachinery dealing with high-resolution meshes, this system of equations is large but sparse. With the growth of the problem size and complexity, the use of High Performance Computing (HPC) becomes inevitable and in this field Graphics Processing Units (GPUs) are gaining in importance through the reported speedup of many CFD applications [3; 4]. While dense matrix vector operations are very efficient on GPUs [5], solving a sparse linear system of equations is more challenging, since there is less independent operations for the large GPU computational power. Moreover, most linear systems require a preconditioner to converge, which enhances the serial aspect of the algorithm and reduces drastically the GPU performance gain.

In some GPU-accelerated applications [6; 7], in

which the linear solver takes most of the execution time, the CPU is used for the calculation of the right-hand side and the system matrix. In this case the high porting effort of the system assembly is not worth the performance gain. Considering the system solve, generally a linear solver is implemented on a GPU using a low-level programming language. The flexibility of the low-level approach makes it possible to adapt the data storage and the algorithm to the sparsity pattern (non-zero elements distribution) of the system matrix in order to enhance the performance. In this context the effort is concentrated on accelerating the sparse matrix-vector product (SpMV), which constitutes the core of many linear solvers. Bell [7] examined the optimization possibilities for SpMV on GPU without reordering the system matrix. He identified the diagonal format (DIA) as suitable for structured meshes and the Hybrid matrix format (HYB) for unstructured ones. The optimization is part of the CUSP library. Cecka [8] did similar work for FEM problems examining the effect of the memory optimization on the overall performance comparing local, global and shared memory. Istvan [9] reviewed relevant research for SpMV on GPU and concentrated on GPU tuning of SpMV operations for the Compressed Sparse Row (CSR) matrix format making use of the L1-cache locality, shared memory, and thread cooperation. The author presented a speedup of 1.4x over cuSparse and suggested that, cache hit maximization was the key method behind the observed performance gain. The SpMV method was used for a relatively simple Poisson problem which is not representative for global performance gain in realistic FEM or CFD problems. It is also heavily based on the Fermi architecture with the hardware characteristic hard-coded in the performance fine tuning algorithm.

GPU iterative solver performance has been gradually increasing but the bottleneck remains the inherently serial preconditioner such as e.g. the Incomplete LU (ILU) factorization. These functions have been the subject of extended research [10]. In order to improve the performance by extracting more fine-grained parallelism, the tuning of GPU hardware features is not sufficient anymore, the system matrix has to be reordered to provide the GPU with more independent instructions. Level-scheduling is one established alternative to elevate the parallelism of the factorization, where independent rows of the system matrix are implicitly grouped in the same level. Graph-coloring is an other method where an explicit reordering is performed giving independent matrix elements the same color, then every color is thread-safe for a massively parallel solve. Naumov [11] shows a parallel graph coloring method reaching a higher parallelism than in level scheduling. His work is included in the cuSparse Nvidia library. Work of Dutto [12] examined the effect of many reordering techniques on the GMRES solver convergence behavior. Another method [13] to extract more parallelism is to transform the ILU factorization in a minimization problem of a set of equations that could be computed in groups independently. Groups can be so small to contain only one equation making it possible for every non-zero element of the incomplete L and U matrices to be computed asynchronously and in parallel. This ILU version can be found in ViennaCL [14].

In this work the reference CFD simulation is performed on CPU using PETSc [15] and 70% of the execution time is spend on the system assembly, while the rest is for the system solve. The same balance is also found in some FEM applications, e.g. Darve [16] ported a CPU application based on PETSc with 80% of execution time for the system assembly. This observation motivated us to port the assembly part to the GPU to enhance the speedup by avoiding any data transfer to the CPU during the simulation. For the system solve we use the preconditioned flexible GMRES solver of the Paralution library [17], which is build on the efficient cuSparse library. This library has been reported [18] to allow a speedup of factor 5x for a neutron diffusion problem. Paralution performs however the assembly of the system matrix on the host, which implies a data transfer from GPU to the host CPU. To address this issue we developed an interface to connect the system of equations, which is assembled on the GPU, to the linear solver. We use a library linear solver instead of a self-implementation because the scope is not to design a fast linear solver but to optimize the frequent use of linear solvers in steady simulations. For this purpose we present an *on-demand* LU factorization capable of reducing the number of times an ILU preconditioner matrix is built for the system solve without altering the flow accuracy. This new technique enables the linear solver to use previously computed LU matrix as preconditioner instead of computing a new one every iteration. We combine this technique with standard ILU to deliver the best speedups for coarse and fine meshes.

Our contributions are:

- A GPU-CPU communication free solver based

on implicit time stepping.

- An *on-demand* ILU preconditioner build to reduce the computational time.
- Analysis of the advantages and drawbacks of the GPU for implicit solvers
- An interface to Paralution and ViennaCL linear solvers
- A sorting algorithm to transform matrix with double entries to COO then CSR

2. Description of the Flow Solver

The flow solver uses a cell-centered finite volume discretization on multiblock structured grids. It solves the Reynolds-Averaged Navier Stokes (RANS) equations in time-dependent integral form:

$$\frac{\partial}{\partial t}\int_{\Omega}\vec{W}d\Omega + \oint_{\partial\Omega}(\vec{F_c}-\vec{F_v})dS = \int_{\Omega}\vec{Q}d\Omega\,, \quad (1)$$

with $\vec{W} = \{\rho, u, v, w, p\}$ the vector of primitive variables , Ω the cell volume and S the cell surface. The convective fluxes $\vec{F_c}$ are computed using a Roe upwind approximation of a Riemann Solver while second order accuracy is achieved through the MUSCL approach (Monotone Upstream-Centered Schemes for Conservation Law). The viscous fluxes $\vec{F_v}$ are approximated using a central discretization scheme. The source term $\vec{Q}$ contains contributions from the Spalart-Allmaras (SA) one-equation turbulence model.

The time integration scheme for cell I follows the equation below [19, p. 192]:

$$\frac{(\Omega\bar{M})_I}{\Delta t_I}\Delta\vec{W}_I^n = -\beta\vec{R}_I^{(n+1)} - (1-\beta)\vec{R}_I^n\,, \quad (2)$$

with $\vec{R}$ the residual,$\Delta\vec{W} = \vec{W}^{n+1} - \vec{W}^n$ the solution change and $\bar{M}$ the mass matrix. For explicit time stepping $\beta = 0$ and $\Delta\vec{W}$ depends only on the available residual at time point t^n. For implicit time stepping $\beta \neq 0$ (e.g. $\beta = 1$) the right-hand side contains the residual $\vec{R}^{n+1}$, which depends on the non available solution $\vec{W}^{n+1}$. A linearization of the residual is used:

$$\vec{R}_I^{n+1} \approx \vec{R}_I^n + \left(\frac{\delta\vec{R}}{\delta\vec{W}}\right)_I \Delta\vec{W}^n\,, \quad (3)$$

where $\frac{\delta\vec{R}}{\delta\vec{W}}$ an approximate *Jacobian* matrix. Substituting the linearization into the initial equation gives:

$$\left[\frac{(\Omega\bar{M})_I}{\Delta t_I} + \left(\frac{\delta\vec{R}}{\delta\vec{W}}\right)\right]\Delta\vec{W}^n = -\vec{R}_I^n\,. \quad (4)$$

When this equation is applied to the entire mesh the full linear system appears with the form $Ax = b$. Residuals and Jacobian are first evaluated on cell surfaces and then summed in a local assembly procedure (see equation 1). The global assembly concatenates the local items to a large global matrix and right-hand side containing all the problem unknowns. A multistage time stepping method such as implicit Runge-Kutta [20] solves multiple successive linear systems for every flow iteration, in which only the right-hand side is updated then multiplied by a different stage coefficient α:

$$\begin{aligned}
\vec{W}^{(0)} &= \vec{W}^n \\
A^{(0)}[\vec{W}^{(1)} - \vec{W}^{(0)}] &= -\alpha_1\vec{R}(\vec{W}^{(0)}) \\
A^{(0)}[\vec{W}^{(2)} - \vec{W}^{(0)}] &= -\alpha_2\vec{R}(\vec{W}^{(1)}) \\
&\vdots \\
A^{(0)}[\vec{W}^{(m)} - \vec{W}^{(0)}] &= -\alpha_m\vec{R}(\vec{W}^{(m-1)}) \\
\vec{W}^{n+1} &= \vec{W}^{(0)} + [\vec{W}^{(m)} - \vec{W}^{(0)}].
\end{aligned} \quad (5)$$

The nature of the flow solved in this work and the mesh complexity leads to a stiff system matrix that requires further treatment, e.g. preconditioning, to enhance the linear system convergence. A preconditioner is any form of modification to the original linear system, which makes it easier to solve by a given iterative method [21]. The linear system of equations is modified as follow:

$$M^{-1}Ax = M^{-1}b\,, \quad (6)$$

with M the preconditioning matrix. M can be filled by an incomplete factorization of the original system matrix: $A = LU - R$, where L and U are upper and lower matrix respectively while R is the residual of the factorization. The general algorithm of the incomplete LU factorization can be found in [21]. This factorization - involving a Gaussian elimination process - is inherently serial with recursive computations, in which every value of the L and U matrices depends on the computation of several values of previous rows and columns. This dependency makes any parallelization difficult.

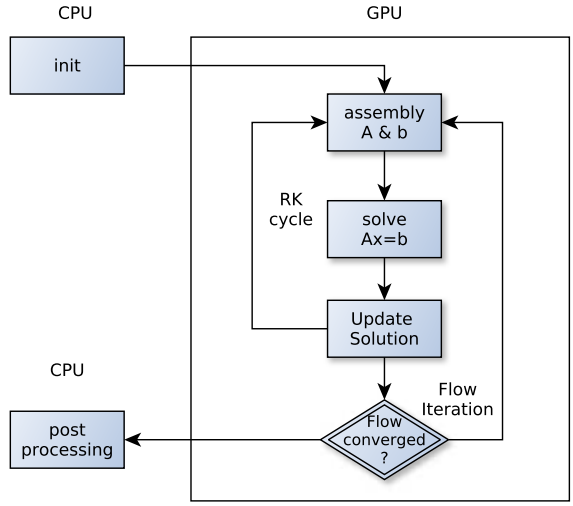

Figure 1: Flow solver algorithm with an outer loop for the flow iteration: $\vec{W}^{n+1} = \vec{W}^n + \Delta\vec{W}$, and an inner loop of Runge-Kutta cycles for the computation of $\Delta\vec{W}$

3. Flow Solver Implementation

The reference CPU-based implicit solver, written in C++, solves the linear system of equations using the PETSc package. The residual and flux Jacobians are computed serially in a loop over all mesh faces. Profiling has revealed that the ILU preconditioner is not the bottleneck in the CPU implementation taking a small portion of the execution time. Three libraries have been considered for solving the linear system of equations on GPU: PETSc (GPU version), viennaCL and Paralution. While PETSc requires only a small change on the data type of the system matrix and right-hand side to run the linear solver on GPU, the library does not provide GPU implementation of incomplete LU factorization and moreover can not accept external data computed on GPU. As a result only the system solve can be offloaded to the GPU, which minimizes the expected speedup. A second alternative is to use ViennaCL. While this OpenCL-based library can process data residing on the GPU, it performs a costly data copy from CUDA type of data to OpenCL. The third alternative is Paralution, which can process data residing on the GPU and is at the same time based on CUDA cuSparse library. The latter library has been chosen for the linear system solve. To describe the flow solver implementation, we first introduce briefly some GPU computing techniques used in this work before we present the two main parts of the GPU flow solver (see figure 1) namely system assembly and system solve.

3.1. GPU Computing

The GPU is a co-processor featuring a large number of cores organized in streaming multiprocessors, which access directly a global memory. Every multiprocessor is a set of scalar processors with access to a shared memory local to the multiprocessor. Each of these processors has its own local and register memory. Programs running on GPU are called kernels. When calling a kernel the GPU starts a large number of threads (unit of execution) grouped in blocks of threads. Threads among the same block are grouped in warps of 32 threads with consecutive thread ID that execute the same instructions. When threads of the same warp have different operations, they are executed serially and this performance decreasing situation is called *thread divergence*. The GPU acceleration is based on hiding the memory latency with computations, which means if a warp is blocked waiting for data (latency) the GPU schedules another warp to take over with no overhead for the scheduling. This technique is more effective if a kernel with a large number of blocks is executed, because more warps are likely to be available for the scheduler. For this reason the first place to optimize a GPU code is through increasing the number of active wraps, which can run simultaneously (occupancy). In the second place, the algorithm should ensure that neighboring threads, which run together in one warp, access memory positions located very near to each other in order to avoid long wait times for variables load. This approach is called a 'coalesced access'.

type of access to GPU global memory

```
a= array[idx];      -> coalesced access
a= array[n x idx]; -> a striped access
a= array[random];  -> non-coalesced acces
```

The number of active warps defining the occupancy is proportional to the number of started threads and the memory consumption per thread in terms of registers and shared-memory. The variables declared in a kernel are locally saved in fast access registers until there are no registers anymore and the rest of the data is stored in global memory. Since all threads share a certain amount of registers the kernel consumption on registers limits the number of blocks of threads that could run simultaneously. In case the kernel needs to start few threads, a technique called multi-streaming can be used to increase the number of active warps by starting multiple independent kernels at the same

time. Every kernel contributes to the occupancy by providing active warps. This is different from the standard one-stream approach, in which kernels are executed one after the other.

3.2. System Assembly

The global system matrix is a concatenation of local block matrices, which are divided in diagonal and off-diagonal blocks. The dominance of the diagonal blocks, which contain the inverse of the time step, improves the convergence of the linear solver. Therefore, when small time steps are used FGMRES converges with fast Jacobi preconditioner without the need for factorization. However, large time steps decrease the diagonal dominance and require thus the incomplete LU factorization. The off-diagonal blocks contain mainly the flux Jacobians defining the bandwidth of the matrix, which is the number of rows separating the non-zero elements from the matrix diagonal.

For the CFD application, the global assembly of the linear system is made by looping over the cell faces in the mesh. On every cell face a contribution to the cell local system matrix is computed along with a residual. Since for each cell six faces contribute to the same system matrix, a risk for *race condition* is eminent, in which up to six threads simultaneously update the system matrix of the same cell. To avoid race conditions *atomic add* or *graph-coloring* are generally used.

In this work an other alternative that conserves the data coalescence has been chosen, in which the contributions are stored along with their positions in the system matrix (row, column). The face contribution belonging to two neighbor-cells is stored twice with the belonging cell index and sign. Computing and storing all face contributions leads to three large arrays: two for indices (column array, row array) and a third array for the contribution's value. Contributions belonging to the same cell are identified over identical index in column and row arrays then summed up using *sort* and *reduce* capabilities of the `THRUST` library. This library generates 3 arrays free of repetition hosting the position and value of all non-zero elements (*nnz*) of the system matrix. This data arrangement is known under Coordinate format (COO). The COO format stores *nnz* values in double precision and $2*nnz$ integers. To reduce the storage size while keeping the same information content, the row array can be transformed in row offset array, in which the column offset of the first non-zero element in every row is stored. This operation is performed by the CUSP library, which provides the CSR arrays that constitute the input for the iterative solver of Paralution. A similar but less complicated algorithm allows to sort and scan the right-hand side for duplicated entries.

Kernels in this work are based on the same global memory access pattern. The data such as the residual is organized in a 1D array of $N_{cells} * N_{variables}$ double precision values. The index function is as follow:

```
index= var*ncells+ i+iMax*(j+jMax*k).
```

We assure the coalesced access by mapping the CUDA thread index (`threadIdx.x`) to i. A mapping to j would lead to a striped access with a stripe of $iMax$ elements.

3.3. System Solve

The flow solver has a modular design with an interface to PETSc, Paralution and ViennaCL libraries. We use the FGMRES linear solver of Paralution library along with the incomplete LU preconditioner (ILU). To accelerate the linear system solve while preserving the accuracy of the solution, the LU matrix should be provided for a lower cost. As reported by many authors [13; 21], the accuracy of the ILU affects the conditioning of the system leading to a larger number of linear system iterations to convergence. Since iterations of the linear solver are faster than the LU factorization on GPU, the additional inner iterations are generally less expensive than the saved time in the LU factorization. The accuracy of the factorization is here traded against performance.

To decrease the time spent in the factorization the linear solver uses the LU matrix of previous outer iterations. As a result the linear solver skips the factorization for some flow iterations. The factorization is performed only *on-demand* when the LU quality is so decreased that the linear solver needs more iterations to converge than a user defined threshold:

Pseudo-code of on-demand LU factorization

```
if (itr> MAX_ITR ) M <-LU_Factorization (A)
(x, itr) <- FGMRES (A,M,b)
```

The *on-demand* factorization changes only the values of L and U matrices not the ordering of the non-zero elements, which does not affect the flow solver converge and accuracy.

4. Results

The numerical results were obtained using a Tesla K40 GPU (Kepler architecture) with a theoretical

Table 1: Characteristics of used meshes and underlying linear systems

Mesh	N_{Cells}	N_{Rows}	nnz	nnz/row
Coarse	40k	200k	5.7M	[20 .. 30]
Fine	300k	1500k	52.6M	[20 .. 35]

peak performance of 1,682 Gflops in double precision and 12 GB of global memory. The GPU implementation is realized with CUDA 7.0. The host CPU is an Intel(R) Xeon(R) CPU E5-2640 with a clock rate of 2.50GHz and the CPU parallelization uses openMPI.

The test case is a transonic flow over the LS89 inlet guide vane cascade [22], which experiences a turning of 74 degree through the NGV geometry and a passage shock with a peak Mach number of 1.3. The validation of the flow solver against experimental data can be found in [23]. The stopping criterion for the linear solver is for the relative Residual to reach values below 10^{-6} and the flow solvers stops when the minimization of the L_2norm of the residual reaches 10^{-6}. The 2-stages Runge-kutta (RK) time stepping method has been chosen for the benchmark, since the RK methods with more stages presented no convergence acceleration in the treated CFD case while costing extra execution-time. We treat two types of meshes to explore the GPU potential: a coarse and a fine one (see table 4).

4.1. Assembly Acceleration

The assembly phase on the GPU experiences a 7x acceleration for the coarse mesh compared to a 1xCore CPU and 12x acceleration for the fine one (see figures 2 and 3). The multi-streaming contributed to the speedup by 10% improve of the performance compared to the one-stream GPU version for the coarse Mesh. The coalesced memory access has more impact on the performance with an improve of 23% compared to a striped access for the same coarse mesh.

A multiblock mesh layout originates, in general, from the mesh generator designed to improve the mesh quality towards accurate CFD results. For complicated geometries it leads to multi-block meshes presenting blocks of different sizes and many interfaces between the mesh blocks. We propose an analysis of the achieved acceleration by addressing possibilities for further improvements considering first large then small mesh blocks and finally the interface

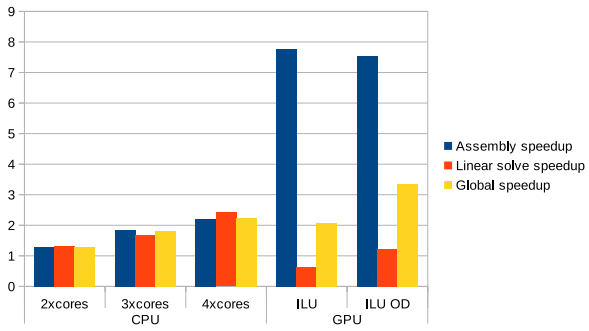

Figure 2: Speedups of the flow solver on the coarse mesh with GPU ILU and *on-demand* ILU compared to a 1xcore to 4xcores CPU

update between all kind of blocks. Large blocks provide the GPU kernels with a high amount of independent operations for processing at the same time, which maximizes the number of active threads. The limiting factor in this case is the register usage. Since the kernels are starting large number of threads and computing complicated algorithms, the total number of used registers is very high. The register consumption limits the achieved occupancy (see section 3.1). A way to improve the occupancy for memory-demanding kernels is to divide when possible the kernels in small, less memory demanding, sub-kernels.

Blocks with few cells on the other hand, are in fact not limited by register usage but by the small number of started threads. The GPU is not provided with enough active threads to hide the memory latency. In this case, the multi-streams technique (see section 3.1) can improve the occupancy by starting more than one kernel at the same time.

The interfaces require a cell update between blocks and this procedure involves few cells proportional to the *surface to volume* ratio ($r_{StoV} * N_{Cells}$). A solution is to use a mesh generator that takes into account the reduction of the number of blocks and neighboring blocks along with the increase of block size in terms of cells (e.g. `hMETIS` [24]).

The higher speedup of the assembly phase on GPU for the fine mesh is then, due to the larger blocks and lower *surface to volume* ratio.

4.2. Linear Solve Acceleration

The linear solve operation on the coarse mesh is 40% slower than on the 1xCore CPU. This is mainly caused by: (1) the ILU preconditioner, (2) the total number of performed linear solves and (3) the size of the system matrix. The ILU preconditioner contains low fine-grained parallelism and is more efficient on

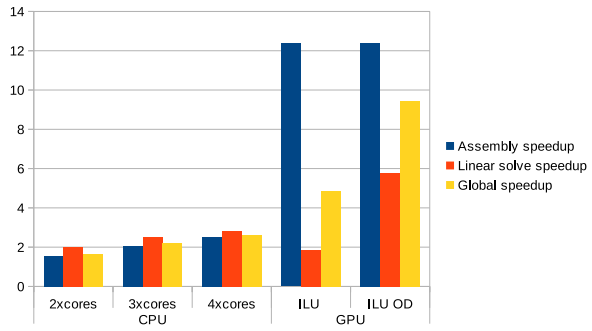

Figure 3: Speedups of the flow solver on the fine mesh with GPU ILU and *on-demand* ILU compared to a 1xCore to 4xCores CPU

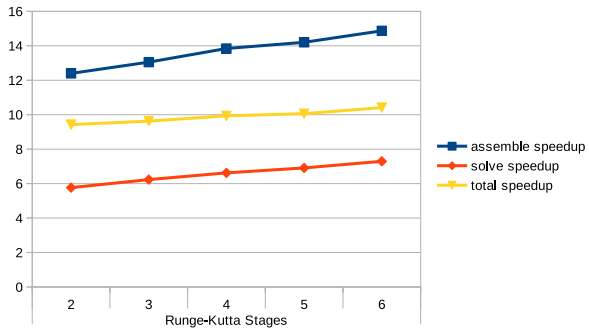

Figure 4: Speedups on the fine mesh with ILU-OD for different RK stage numbers

CPU. Moreover, the CPU implementation of ILU factorization has a set of techniques to improve the linear solve convergence, which decreases dramatically the GPU performance once ported to the GPU. This results on the flow solver using GPU ILU to perform 32 % more linear solve operations. The flow convergence is on the other hand exactly the same for CPU and GPU implementation in terms of number of flow iterations, this for the sake of a fair comparison.

For 2-stages RK, the flow requires 827 flow iterations to converge. The standard ILU performs one factorization per flow iteration , while the *on-demand* ILU (ILU-OD) reduces the total number of factorization to only 113. This corresponds to a 86% decrease, which explains the improved speedup for the linear solver when ILU-OD is used. The *on-demand* ILU is only as fast as a 2xcores CPU, because the size of the system matrix is not enough to observe the advantage of GPUs for sparse matrix-vector products (SpMV). The fine mesh presents on the other hand, a larger system matrix with more non-zero elements. While the standard ILU implementation is 1.8x faster than the 1xCore ILU, the ILU-OD is 5.5x faster than 1xCore ILU and 2.05x faster than a 4xCores CPU. The *on-demand* mechanism decreased here also the number of factorization by 86%. In addition to that the size of the matrix showed the advantage of GPU on SpMV.

4.3. Global Acceleration of the Flow Solver

The global speedup on the coarse mesh is 2.07x and 3.35x for ILU and ILU-OD respectively compared to a 1xCore CPU. This correspond to a speedup of 1.15x and 1.5x compared to a 4xCores CPU. The larger contribution of the speedup is done in the assembly phase. For the fine mesh the GPU performance is improved to reach a speedup of 4.8 and 9.43 for the flow solver using ILU and ILU-OD respectively compared to a 1xCore CPU. ILU and ILU-OD are 1.8x and 3.4x faster than 4xCores CPU. The RK methods with more stages have not shown a convergence acceleration in terms of number of flow iterations in the treated case, but can be used to demonstrate an improvement of the speedups with the increase of the number of stages (see figure 4). The more stages we have the more residuals are computed which gives more room for the GPU to excel in the assembly. In addition to that the system solve is repeated with the same ILU which advantages again the GPU. Assembly acceleration of 14x is reached for 6-stages RK and a global speedup of 10x is achieved for the same RK scheme.

5. Conclusion

In this paper, we presented a flow solver with one order of magnitude acceleration on GPU compared to an optimized serial CPU version. We demonstrated that implicit time stepping in CFD applications can profit from the GPU computational power, provided an appropriate GPU occupancy is reached and a good mesh in terms of surface to volume ratio is used. As the bottleneck of the GPU flow solver is the incomplete LU factorization used as preconditioner, on-demand ILU factorization presented in this work improved the overall speedup by 60 to 80%. The on-demand ILU can be applied as well on CPU's but will have a very limited effect there. This once again shows that acceleration techniques can be very different on various architectures.

Acknowledgments

This research activity is funded by the European unions Framework 7 research program (Project No.

316394). We are also grateful to NVIDIA for the hardware donation.

References

[1] S. Shahpar, S. Caloni, Aerodynamic optimization of high-pressure turbines for lean-burn combustion system, Journal of Engineering for Gas Turbines and Power 135 (5) (2013) 055001.

[2] Y. Saad, M. H. Schultz, Gmres: A generalized minimal residual algorithm for solving nonsymmetric linear systems, SIAM Journal on scientific and statistical computing 7 (3) (1986) 856–869.

[3] Brandvik, Tobias and Pullan, Graham , An Accelerated 3D NavierStokes Solver for Flows in Turbomachines, Journal of Turbomachinery 133 (2).

[4] L. Fu, Z. Gao, K. Xu, F. Xu, A multi-block viscous flow solver based on gpu parallel methodology, Computers & Fluids 95 (2014) 19–39.

[5] S. Barrachina, M. Castillo, F. D. Igual, R. Mayo, E. S. Quintana-Ortí, Solving dense linear systems on graphics processors, in: Euro-Par 2008–Parallel Processing, Springer, 2008, pp. 739–748.

[6] S. Georgescu, P. Chow, H. Okuda, Gpu acceleration for fem-based structural analysis, Archives of Computational Methods in Engineering 20 (2) (2013) 111–121.

[7] N. Bell, M. Garland, Implementing sparse matrix-vector multiplication on throughput-oriented processors, in: Proceedings of the Conference on High Performance Computing Networking, Storage and Analysis, ACM, 2009, p. 18.

[8] C. Cecka, A. J. Lew, E. Darve, Assembly of finite element methods on graphics processors, International journal for numerical methods in engineering 85 (5) (2011) 640–669.

[9] I. Reguly, M. Giles, Efficient sparse matrix-vector multiplication on cache-based gpus, in: Innovative Parallel Computing (InPar), 2012, IEEE, 2012, pp. 1–12.

[10] Y. Saad, H. A. Van Der Vorst, Iterative solution of linear systems in the 20th century, Journal of Computational and Applied Mathematics 123 (1) (2000) 1–33.

[11] M. Naumov, P. Castonguay, J. Cohen, Parallel graph coloring with applications to the incomplete-lu factorization on the gpu, Tech. rep., Nvidia Technical Report NVR-2015-001, Nvidia Corp., Santa Clara, CA (2015).

[12] L. C. Dutto, The effect of ordering on preconditioned gmres algorithm, for solving the compressible navier-stokes equations, International Journal for Numerical Methods in Engineering 36 (3) (1993) 457–497.

[13] E. Chow, A. Patel, Fine-grained parallel incomplete lu factorization, SIAM Journal on Scientific Computing 37 (2) (2015) C169–C193.

[14] K. Rupp, et al., Viennacl, Web Page: http://viennacl. sourceforge. net.

[15] S. Balay, S. Abhyankar, M. Adams, J. Brown, P. Brune, K. Buschelman, V. Eijkhout, W. Gropp, D. Kaushik, M. Knepley, et al., Petsc users manual revision 3.5, Tech. rep., Technical report, Argonne National Laboratory (ANL) (2014).

[16] J. Wong, E. Kuhl, E. Darve, A new sparse matrix vector multiplication graphics processing unit algorithm designed for finite element problems, International Journal for Numerical Methods in Engineering 102 (12) (2015) 1784–1814.

[17] D. Lukarski, N. Trost, Paralution project, URL http://www. paralution. com. Accessed: January.

[18] N. Trost, J. Jiménez, D. Lukarski, V. Sanchez, Accelerating cobaya3 on multi-core cpu and gpu systems using paralution, Annals of Nuclear Energy 82 (2015) 252–259.

[19] J. Blazek, Computational Fluid Dynamics:Principles and Applications, Elsevier, 2001.

[20] S. Xu, D. Radford, M. Meyer, J.-D. Müller, Stabilisation of discrete steady adjoint solvers, Journal of Computational Physics 299 (2015) 175–195.

[21] Y. Saad, Iterative methods for sparse linear systems, Siam, 2003.

[22] T. Arts, M. Lambert de Rouvroit and A.W. Rutherford, Aero-thermal Investigation of a highly loaded transonic linear Turbine Guide Vane Cascade, TN 174, von Karman Institute for Fluid Dynamics (1990).

[23] T. V. Aissa, Mohamed Hassanine, C. Vuik, A gpu-accelerated navier-stokes solver for steady turbomachinery simulations.

[24] G. Karypis, V. Kumar, hmetis 1.5: A hypergraph partitioning package, Tech. rep., Technical report, Department of Computer Science, University of Minnesota, 1998. Available on the WWW at URL http://www. cs. umn. edu/metis (1998).

Adjoint surface optimization for internal and external aerodynamics applications by means of OpenFOAM

Giacomo Alessi

Environmental and Applied Fluid Dynamics Department, von Karman Institute for Fluid Dynamics, Belgium, giacomo.alessi@vki.ac.be

Supervisor: Jeroen van Beeck

Professor, Environmental and Applied Fluid Dynamics Department, von Karman Institute for Fluid Dynamics, Belgium, vanbeeck@vki.ac.be

Supervisor: Tom Verstraete

Associate Professor, Turbomachinery and Propulsion Department, von Karman Institute for Fluid Dynamics, Belgium, verstraete@vki.ac.be

University Supervisor: Bert Blocken

Professor, Civil Engineering, Leuven university, Belgium, Bert.Blocken@bwk.kuleuven.be

Abstract

The interest in the optimization field applied to fluid dynamics is rapidly increasing and more and more applications can be found in various research and industrial fields, e.g.: aerospace, turbomachinery, automotive, energy, sport competitions, etc... The adjoint optimization method is particularly interesting in this respect, for its computational cost independent from the number of design variables, opening a vast design freedom. However, whereas the adjoint-based shape optimization is well-known in the aeronautical industry, it does not have the same degree of maturity and robustness in any other fields. Therefore, it is the subject of ongoing innovative research collaborations between academia and industry.

The adjoint optimization will be applied to three different test cases: a U-bend duct, an idealized application (Ahmed body) and a real application (E-Car333 vehicle). The chosen test cases involve turbomachinery and automotive industrial applications with the aim to reduce the pressure loss and the drag, respectively. The optimization tool to develop is based on the evaluation of a surface sensitivity map that indicates the shape modifications to perform. Grounded on the information given by the sensitivity maps, different techniques (CAD-based and node-based shape modification techniques) will be applied to obtain the final body shape and their performance compared. Geometrical and aerodynamic constraints will be added to avoid not feasible final shapes and to limit the regions to which the body movement will be applied. The modelling of turbulence could highly influence the optimization results but previous studies have not been found in literature. Therefore, different approaches, Reynolds Averaged Navier-Stokes (RANS) and Large Eddy Simulation (LES), will be studied and compared, giving hints on their use and on their advantages and limits for the studied cases. Once that the best approach to be used has been identified, it can be used to optimize the real application case (E-Car333 vehicle). The CFD opensource software OpenFOAM will be used for the fluid dynamics evaluations and the implementation of the optimization tools.

The results of the numerical simulations will be validated against experiments on the original and optimized shapes to evaluate the reliability of the optimization process. The parameters of interest, i.e. pressure loss and drag, and the flow field characteristics will be validated through quantitative and qualitative comparison. In particular, pressure measurements will be performed to measure the obtained pressure loss reduction while Particle Image Velocimetry (PIV) measurements will be used to understand and validate the flow field evolution inside the U-bend duct. Concernig the Ahmed body, drag and lift measurements will be performed for a quantitative validation while smoke visualizations will be carried out for a qualitative comparison of the flow field characteristics.

The achievement of a reliable routine would considerably speed up the design process, not only of the chosen test cases but of any application related to internal and external aerodynamics. In fact, in spite of the test cases chosen, the optimization tools that will be implemented can be extended to any application that aim to obtain a pressure loss and drag reduction.

Keywords: adjoint surface optimization, pressure loss and drag reduction, tubulence approaches

Towards flutter analysis of composite aero-engine fan blades

Christopher Chahine

Turbomachinery and Propulsion Department, von Karman Institute for Fluid Dynamics, Belgium, christopher.chahine@vki.ac.be

Supervisor: Tom Verstraete

Adjunct Professor, Turbomachinery and Propulsion Department, von Karman Institute for Fluid Dynamics, Belgium, tom.verstraete@vki.ac.be

University Supervisor: Li He

Professor, Department of Engineering Science, University of Oxford, United Kingdom, li.he@eng.ox.ac.uk

Abstract

Composite fan blades are today increasingly used in high bypass ratio aero-engines due to their inherent weight advantage over metallic blades. However, decreased out-of-plane stiffness and reduced mass density increase their susceptibility to flutter. An accurate prediction of this aeroelastic instability therefore becomes a prime consideration in the design process. The classical energy method, which is based on the assumption of small aeroelastic coupling, is today the most widely applied flutter prediction technique. For composite fan blades the strength of aeroelastic coupling is uncertain and so is the applicability of the energy method. This paper presents an attempt to predict the aeroelastic coupling effects of a typical composite fan blade via the shift of the resonant frequency caused by the unsteady aerodynamic forces. To allow an assessment of the material impact on the frequency shift, the computations are performed with both, a full titanium and a composite blade. The results show that a significant amount of aeroelastic coupling is present for the titanium blade which is further increased by introducing a composite material. Values of the predicted frequency shift indicate that the energy method is likely to produce misleading results if applied for large aero-engine fan blades.

Keywords: flutter, decoupled, composite fan blade, energy method, aeroelastic coupling

1. Introduction

Aero-engine manufacturers are increasingly introducing fan blades made of composite materials, notably carbon fiber reinforced plastics, to substitute their metallic counterparts for reduced engine weight and improved overall fuel efficiency. It is well known that fan blades of high bypass ratio aero-engines are prone to flutter due to geometrical features such as lean, sweep and low hub-to-tip radius ratios. With the introduction of composite materials the susceptibility to flutter compared to metallic blades is generally further increased due to a lower blade density (lower mass ratios) and decreased out-of-plane stiffness compared to metallic alloys. The onset of flutter can rapidly lead to harmful high amplitude vibrations with the potential result of complete component failure. It is therefore imperative that the flutter stability is accounted for during the design process. In the past decades various computational methods have been developed for the prediction of flutter in turbomachinery applications. Reviews of these developments can be found in [1], [2] and more recently [3] and [4]. A more specific overview on computational aeroelasticity methods for aero-engine fan blade assemblies is presented by Wu et al. (2004) [5]. The method that is by far the most frequently applied for turbomachinery flutter predictions today is the energy method proposed by Carta (1967) [6]. In this method the structure and the fluid are essentially treated in a decoupled manner, based on the assumption of negligible aeroelastic coupling which implies that the unsteady flow has no significant impact on the eigenmodes and eigenfrequencies of the blade. Thus, the unsteady flow field is computed with

a prescribed vibratory blade motion, which is typically obtained from a modal analysis of the blade either in vacuum or with the steady state aerodynamic forces included, and the flutter stability is inferred from the work that the aerodynamic forces perform on the blade during one period of the forced oscillation. It is generally accepted that the assumption of small aeroelastic coupling is valid for the majority of turbomachinery cases, as most applications have high stiffness and exhibit sufficiently high structural to fluid mass ratios with the result that the unsteady aerodynamic forces induced by the blade vibration are negligible with respect to the blades inertia and stiffness forces. However, it is questionable whether these assumptions still hold true for large aero-engine fan blades made of carbon fiber reinforced plastics. An indication of the problem is given by Sadeghi & Liu (2005) [7], who predicted the flutter stability of a two dimensional cascade with different mass ratios using both the decoupled energy method and a fully coupled aeroelastic code. Their results show that the energy method fails to correctly predict the onset of flutter if the mass ratios are small. The purpose of this paper is to attempt a more specific assessment of the validity of the energy method for a composite fan blade representative for a typical modern high-bypass ratio turbofan engine.

2. Case study

The case study in this work is a transonic fan blade designed for a large high-bypass ratio turbofan engine. The blade is a wide-chord, low aspect ratio design which closely resembles a modern fan blade used in todays engines. However, no three-dimensional features (i.e. lean and sweep) were applied. An overview over some of the key design quantities of the blade is given in Table 1. The bypass splitter was included in the design process in order to match the engine cycle design requirements for bypass and core flows. For computational efficiency, this part was removed from the fluid domain for the computations performed in this work.

3. Fluid analysis

The unsteady flow field resulting from the forced motion of the blade is computed using the commercial CFD code Numeca FINE/Turbo¢. The non-linear harmonic method introduced by [8] and [9] is applied with an extension for moving meshes in Cartesian coordinates as reported in [10]. Only the fundamental flow harmonic is considered in the computations, assuming that higher harmonics do not significantly contribute to the net energy transfer between the blade and the flow. A multi block structured mesh with an O4H topology consisting of about 1.2 million points is used to discretize the fluid domain. The eddy viscosity is computed using the one equation turbulence model of Spalart & Allmaras [11]. An overview of the discretized fluid domain along with the solid mesh is given in Fig. 1.

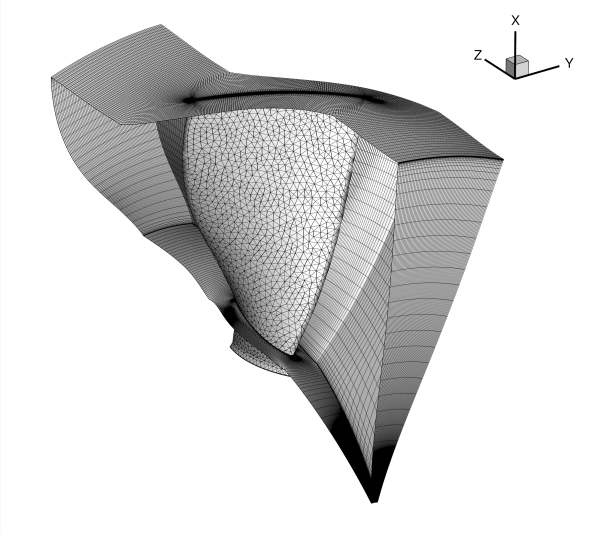

Figure 1: **Overview of fluid and solid meshes used for the flutter analyses.**

4. Structural model

The structural modelling of composite blades is distinctly more complicated than modelling blades made of metallic alloys. One reason for this lies in the anisotropy of the properties of composite materials,

Table 1: **Fan blade design parameters**

Hub-to-tip radius ratio	0.35
Aspect ratio (height/mid-height chord	1.7
Bypass ratio @ cruise	8.5
Number of blades	19
Tip relative inlet Mach number @ cruise	1.3
Tip diameter (m)	3.26

which is at the same time one of their biggest advantages over isotropic metals. In theory composite material properties can be tailored by adapting fiber angles, ply stacking sequences and ply thicknesses to give optimal support of a structure for a given loading condition. However, for design, analysis and manufacturing reasons, todays practical laminated fan blades exhibit quasi-isotropic material properties, meaning that the individual plies are stacked in such a fashion that the resulting laminate has globally isotropic in-plane properties. Although this approach clearly does not take full advantage of the capabilities of composite materials, the resulting laminate has usually still better specific strength and stiffness than a comparable metallic alloy, which is one of the driving factors behind the application of composites in aerospace applications. The usage of quasi-isotropic laminates has another advantage, in that it does enable the generation of a computational model with material characteristics that closely resemble those of a real composite blade.

In this work the fan blade is discretized with quadratic tetrahedral elements, cf. Fig. 1, and the material properties of a quasi-isotropic laminate made of a representative carbon fiber reinforced plastic (CFRP) are applied, as reported in [12]. The blade is modelled as a full composite blade without a honeycomb or foam core or any grid-stiffening features. The material properties used are summarized in Table 2. For each mesh element a local material coordinate system is defined, such that the out-of-plane component z is locally perpendicular to the closest point of the curved mid-surface of the blade. A finite element solver [13] is used for the computation of the blades modeshapes and eigenfrequencies. Centrifugal stiffening of the blade is taken into account by means of a non-linear geometric static analysis preceding the modal analysis. Due to the discrepancy between the meshes used for the structural and CFD analyses an interpolation is required to transfer the modeshapes obtained from the structural analysis onto the CFD mesh in order to perform the computations with the blade vibration imposed. In this work a thin plate spline (TPS) radial basis function is applied for this purpose.

5. Evaluation of aeroelastic coupling

The aeroelastic system comprising the blade and the surrounding air flow is governed by the equation of motion

$$M\ddot{u} + C\dot{u} + Ku = D, \tag{1}$$

where M is the mass matrix, C is the damping matrix, K is the stiffness matrix and D represents the external aerodynamic forcing. With the modeshapes $\Phi = [\phi_1, \phi_2, , \phi_N]$ known from the finite element computations, the problem can be considerably simplified by transforming the set of N coupled equations of motion in physical coordinates given by Eq. (1) to a set of N decoupled equations in modal coordinates, hence allowing each equation to be solved independently. Such a transformation is possible by making use of the orthogonality of the modeshapes with respect to the mass and stiffness matrices. By defining a modal mass $m = \Phi^T M \Phi$ and a modal stiffness $k = \Phi^T K \Phi$, and decomposing the physical displacements as $u = \Phi q$, where q is the modal coordinate of the modeshape under consideration (only one in case of decoupled flutter analysis), the modal equation becomes

$$m\ddot{q} + c\dot{q} + kq = d, \tag{2}$$

representing a single degree of freedom system for the unknown q. As the modeshapes are dimensionless, they are typically scaled for unity modal mass $m = 1$ and modal stiffness $k = \omega_n^2$ which further simplifies the solution process. Because the modeshapes are not naturally orthogonal to the damping matrix, a modal damping is usually defined as

$$c = 2\xi\omega_n m \tag{3}$$

where ξ is the damping ratio for the current mode.

Forces are transformed from physical to modal space by pre-multiplication with the transpose of the modeshape, hence the modal damping force is given by

$$d = \Phi^T D. \tag{4}$$

One of the basic assumptions of the energy method is a fixed predetermined resonant frequency, i.e. that flutter occurs at one of the natural frequencies and

Table 2: **Quasi-isotropic CFRP laminate properties**

E_x (GPa)	38.994
E_z (GPa)	11.793
G_{xz} (GPa)	3.2086
ν_{xy} (GPa)	0.33375
ν_{xz} (GPa)	0.30052
ρ (kg/m^3)	1594.3

eigenmodes of the blade. This assumption can be validated by investigating the amount of aeroelastic coupling in the system and more specifically the shift of the aeroelastic resonant frequency with respect to the natural frequency of the blade in the chosen eigenmode. If the frequency shift is small, say less than 1 %, the decoupled energy method might well be used to predict flutter with an acceptable accuracy. In the energy method a harmonic motion of the blade in one of its eigenmodes ϕ, with an arbitrarily defined modal amplitude $\hat{q}_{CFD}$ (for instance 0.5 % of chord, assuming the aerodynamic damping forces to depend linearly on the modal amplitude) and its associated eigenfrequency ω_n are imposed in the unsteady CFD computation for the determination of the modal aerodynamic damping forces $d(q)$. The work that the fluid does to the blade in one vibration period can then be determined by

$$W_A = \pi \sum_{j=1}^{N} [\hat{d}\hat{q} sin(\Psi)]_j, \tag{5}$$

where N is the total number of blade surface cells of the fluid mesh and Ψ is the phase shift between the modal damping force amplitude and the movement of the mesh cell. The aerodynamic damping is commonly defined as

$$D_A = -W_A, \tag{6}$$

such that negative values of aerodynamic damping indicate an unstable situation where the fluid performs work to the blade. An equivalent viscous damping coefficient can be obtained by considering the work per period of a viscous damping force $\zeta_A \dot{q}$ which is given by $\pi\zeta_A 2\pi\omega\hat{q}_{CFD}$. Equating this expression with the aerodynamic damping yields

$$\zeta_A = \frac{D_A}{2\omega\pi^2\hat{q}_{CFD}}. \tag{7}$$

In coupled flutter prediction methods the modal equation, Eq. (2), and the fluid equations are solved simultaneously to obtain the modal displacements q and the unsteady aerodynamic forces f. Since the bidirectional interaction between fluid and structure is accounted for, the aeroelastic resonant frequency and the associated vibration mode are a direct result of the computation. However, in this paper a different approach is followed, which can be easily implemented also if no coupled solver is available. The method is based on an approximation of the frequency shift using a decoupled method. Similar approaches were reported by Marshall [14], who used a harmonic balance method to derive an expression for the frequency shift based on the energy method, and later by Moffat & He [15], who derived the frequency shift for forced response and flutter computations based on an emulation of a fully coupled method. Both methods were compared to results of fully coupled calculations and an acceptable agreement was found. The approach used in this paper is based on the latter method and will be further explained in the following.

Assuming a harmonic blade motion, $q = \hat{q}e^{i\omega t}$, and a harmonic damping force at the same frequency, $d = \hat{d}e^{i\omega t}$, with $\hat{q} \in \mathbb{R}$ and $\hat{d} \in \mathbb{C}$, the forces in the modal equation, Eq. (2), can be represented as vectors and plotted in the Argand diagram as shown in Fig. 2. Note that the modal blade displacement $\hat{q}$ is in phase with the inertial force amplitude $m\omega^2\hat{q}$. It is well known that only the component of the complex damping force that is out of phase with the blade displacement, $Im\{\hat{d}\}$, is able to do

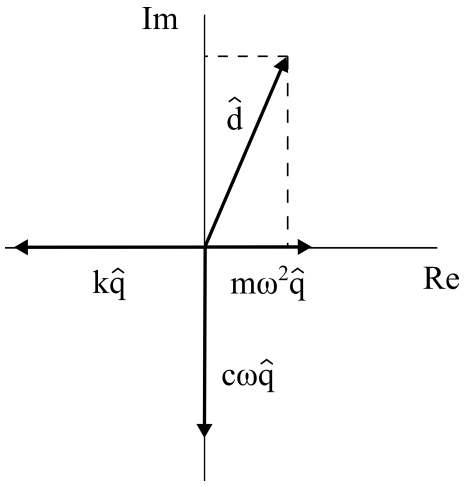

Figure 2: **Argand diagram of the forces in the aeroelastic system.**

work to the system and thus contribute to the aerodynamic damping. In contrast the damping force component that is in phase with the blade displacement, Red , is also in phase with the inertial and stiffness forces and therefore acts like an added mass in the aeroelastic system, which in turn affects the systems resonant frequency. As the energy method is based solely on the computation of the aerodynamic damping, the in phase component of the damping force is neglected, thus the method inherently assumes that resonance occurs at the blade natural frequency.

By applying Newtons second law to the real components of the forces we obtain

$$-k\hat{q} + Re\{\hat{d}\} + m\omega^2\hat{q} = 0. \quad (8)$$

An approximation of the resonant frequency of the system with the contribution of the added mass due to the damping forces included can thus be given as

$$\omega_{dyn} = \sqrt{\frac{k - Re\{\hat{d}\}/\hat{q}}{m}} \quad (9)$$

with $k = \omega_n^2$ and $m = 1$, as mentioned above. The amplitude of the complex modal damping force is obtained from the unsteady CFD computations as

$$\hat{d} = \frac{\hat{q}}{\hat{q}_{CFD}} \sum_{j=1}^{n} [\Phi_j (D_j^{Real} + iD_j^{Imag})] \quad (10)$$

where D_j^{Real} and D_j^{Imag} are the real and imaginary components of the physical complex damping forces.

6. Results and discussion

The operating point chosen for the evaluation of the frequency shift is 70 percent speed, near stall at sea level conditions with the fan blade vibrating in its first bending mode (1F). This is a condition where stall flutter typically occurs for fan blades, cf. [16], [17]. Contour plots of this vibration mode for the composite fan blade and a geometrically identical reference blade modelled with material properties of Ti-6Al-4V alloy are shown in Fig.3.

Frequency shift computations were performed for interblade phase angles (IBPAs) 0, -180, 180, -90 and 90 degrees according to the travelling wave assumption of Lane (1956). The results are summarized in Fig. 4, which depicts the frequency shift in percent plotted versus the IBPA. A negative frequency shift is obtained for all computations, indicating a reduction

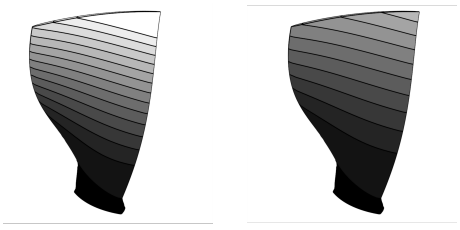

Figure 3: **Contour plots of the mass normalized first bending mode if the composite blade (left) and the titanium blade (right) at 70 percent speed.**

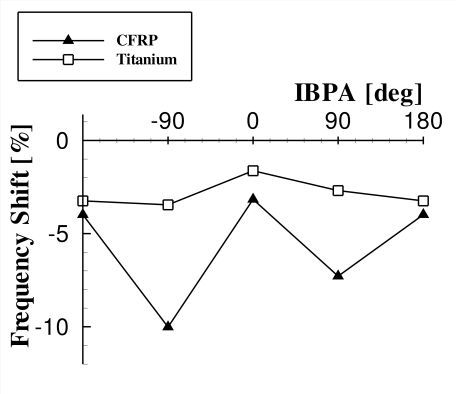

Figure 4: **Frequency shift plotted versus the interblade phase angle.**

of the aeroelastic resonant frequency with respect to the blades natural frequency due to the added mass effect. The values of frequency shift are overall significant for both materials under consideration. Values for the titanium blade range from -1.62 % at IBPA 0 to -3.45 % at IBPA -90. These are, already without the consideration of a composite material, values which point to a non-negligible impact of the unsteady aerodynamic forces on the aeroelastic response of the fan blade. Although a fixed rule for the applicability of the energy method depending on the frequency shift does not exist to the best knowledge of the authors, it is widely accepted that it needs to be applied with care for a frequency shift bigger than one percent, see e.g. [14].

The substitution of the titanium alloy with a composite material leads to an overall increased magnitude of frequency shift, as initially expected at the outset of this work. The calculated ratios of the frequency shift of the composite blade over its corresponding value of the titanium blade listed in Table 3 show that the impact of the material substitution is highest at IBPAs of -90 and 90 degrees, where the frequency shift is almost tripled by the composite material. At this IBPAs also the highest magnitude of frequency shift is observed for the composite blade reaching a value of -7.3 % at IBPA 90 and -10.0 % at IBPA -90. The strong dependency of the frequency shift on the IBPA appears to be a reasonable result, as the effect of added mass originates from the phase shift between the unsteady aerodynamic damping forces and the blade motion, which can also be seen in Fig. 2. To explain this further, the complex modal damping forces for all computed IBPAs of the composite blade are plot-

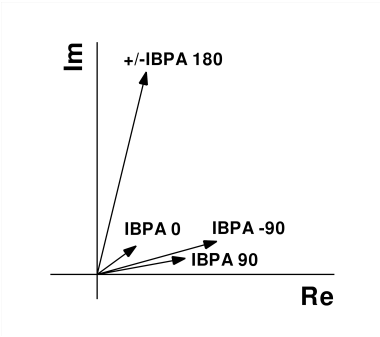

Figure 5: **Argand diagram of complex modal damping forces at different IBPAs for the composite blade.**

ted in the Argand diagram shown in Fig. 5. As can be seen, the modal damping force amplitude increases from 0 to 180 degrees IBPA while its phase angle with the blade displacement (real component only) first decreases towards 90 degrees IBPA and then increases again towards 180 degrees IBPA. This rather high phase angle is the reason why the real component of the modal damping force at 180 degrees IBPA is close to the value of 0 degrees IBPA, leading to comparable values of frequency shift despite the considerable difference in force magnitude between the two cases. For IBPAs of 90 and -90 degrees the modal damping force is dominated by its real component leading to the highest observed values of frequency shift as shown in Fig. 4.

7. Conclusions

In this paper a method for the computation of the aeroelastic resonant frequency of a fan blade and the associated shift with respect to the blades eigenfrequency is presented and applied to a composite fan blade typical for a modern high bypass ratio turbofan engine. The obtained frequency shift is used as an indicator to assess the validity of the invariant vibration frequency assumption made in flutter predictions based on the energy method. A titanium blade of identical geometry is used as a reference case to enable an assessment of the material impact on the frequency shift. Although the method applied is itself based on a decoupled approach, giving only an approximation of the frequency shift of the real aeroelastic system, the values obtained give rise to considerable doubt as to whether the energy method is an appropriate tool for the flutter prediction of large fan blades. Frequency shifts obtained for the titanium blade range from -1.62 % to -3.45 %, indicating an already significant amount of aeroelastic coupling at which the energy method should be applied with great care. Values of frequency shift are observed to globally increase over the entire range of interblade phase angles when the titanium material is substituted with a quasi-isotropic carbon-fiber reinforced-plastic. The predicted frequency shift for the composite blade ranges from -3.16 % to -10.0 %, giving a strong indication that the assumptions of the energy method are not valid anymore.

Table 3: **Impact of blade material on the frequency shift**

IBPA (deg)	$\Delta f_{comp}/\Delta f_{ti}$
−180	1.23
−90	2.90
0	1.95
90	2.71
180	1.23

Acknowledgments

The research leading to these results has received funding from the European Union Seventh Framework Programme (FP7/2007-2013) under grant agreement no [316394] and the EPSRC.

References

[1] O. O. Bendiksen, Aeroelastic Problems in Turbomachines, in: AIAA paper 90-1157-CP, 1990.

[2] J. Marshall, M. Imregun, A REVIEW OF AEROELASTICITY METHODS WITH EMPHASIS ON TURBOMACHINERY APPLICATIONS, Journal of Fluids and Structures 10 (3) (1996) 237–267.

[3] R. E. Bartels, a. I. Sayma, Computational aeroelastic modelling of airframes and turbomachinery: progress and challenges., Philosophical transactions. Series A, Mathematical, physical, and engineering sciences 365 (1859) (2007) 2469–2499. doi:10.1098/rsta.2007.2018.

[4] A. Datta, W. Johnson, An Assessment of the State-of-the-art in Multidisciplinary Aeromechanical Analyses, in: AHS Specialist's Conference on Aeromechancs, San Francisco, CA, 2008.

[5] X. Wu, A. I. Sayma, W. Vahdati, M. Imregun, Computational Techniques for Aeroelasticity and Aero-Acoustic Analyses of Aero-Engine Fan Assemblies, in: International Conference on Fans, London, 2004.

[6] F. O. Carta, Coupled Blade-Disk-Shroud Flutter Instabilities in Turbojet Engine Rotors, Journal of Engineering for Power 89 (3) (1967) 419–426. doi:10.1115/1.3616708.

[7] M. Sadeghi, F. Liu, Computation of cascade flutter by uncoupled and coupled methods, International Journal of

Computational Fluid Dynamics 19 (8) (2005) 559–569. doi:10.1080/10618560500508367.

[8] L. He, W. Ning, Efficient Approach for Analysis of Unsteady Viscous Flows in Turbomachines, AIAA Journal 36 (11) (1998) 2005–2012.

[9] W. Ning, L. He, Computation of Unsteady Flows Around Oscillating Blades Using Linear and Nonlinear Harmonic Euler Methods, ASME Journal of Turbomachinery 120 (3) (1998) 508–514.

[10] F. Debrabandere, B. Tartinville, C. Hirsch, G. Coussement, Extension of the Non-Linear Harmonic Method to Flow Computations Around Moving and Deforming Structures, in: IFASD 2013 – 16th International Forum on Aeroelasticity and Structural Dynamics, 2013.

[11] P. R. Spalart, S. R. Allmaras, A One-Equation Turbulence Model for Aerodynamic Flows, Recherche Aerospatiale (1) (1994) 5–21.

[12] R. Akkerman, On the properties of quasi-isotropic laminates, Composites Part B:Engineering 33 (2) (2002) 133–140. doi:10.1016/S1359-8368(02)00002-1.

[13] G. Dhondt, CalculiX CrunchiX USER' S MANUAL version 2.5 (2012).

[14] J. Marshall, Prediction of turbomachinery aeroelasticity effects using a 3D non-linear integrated method, Phd dissertation, Imperial College of Science, Technology and Medicine (1996).

[15] S. Moffatt, L. He, On decoupled and fully-coupled methods for blade forced response prediction, Journal of Fluids and Structures 20 (2) (2005) 217–234. doi:10.1016/j.jfluidstructs.2004.10.012.
URL http://linkinghub.elsevier.com/retrieve/pii/S0889974604001446

[16] M. Vahdati, A. I. Sayma, J. G. Marshall, M. Imregun, Mechanisms and Prediction Methods for Fan Blade Stall Flutter, Journal of Propulsion and Power 17 (5) (2001) 1100–1108.

[17] M. Vahdati, G. Simpson, M. Imregun, Mechanisms for Wide-Chord Fan Blade Flutter, Journal of Turbomachinery 133 (4).

Quantifying inflow uncertainties for CFD simulations of dispersion in the atmospheric boundary layer

Clara García Sánchez

Environmental and Applied Fluid Dynamics Department, von Karman Institute for Fluid Dynamics, Belgium, clara.garciasanchez@vki.ac.be

Supervisors: Catherine Gorlé and Jeroen van Beeck

Assistant Professor, Department of Civil Engineering and Engineering Mechanics, Columbia University, New York, USA, catherine.gorle@columbia.edu

Professor, Environmental and Applied Fluid Dynamics Department, von Karman Institute for Fluid Dynamics, Belgium, vanbeeck@vki.ac.be

University Supervisor: Gustaaf van Tendeloo

Professor, EMAT, Department of Physics, University of Antwerp, Belgium, staf.vantendeloo@uantwerpen.be

Abstract

Pollutant dispersion within urban environments is a major concern given the growing number of street level pollutant sources. However the uncertainties present in simulations of full-scale atmospheric boundary layer flows make the accurate prediction of pollutant levels a challenging task. The present article describes a step towards developing a methodology that can predict pollutant concentrations with quantified confidence intervals, based on the natural variability in the inflow boundary conditions for Reynolds-averaged Navier-Stokes simulations. The objective is to predict dispersion in urban environments using an uncertainty quantification framework that represents the natural variability in the ABL inflow conditions.

Keywords: dispersion, atmospheric boundary layer, uncertainty quantification, inflow conditions, Reynolds-averaged Navier-Stokes.

1. Introduction

The fast expansion of urban environments combined with the population growth is leading to an increased number of pollutant sources, and a risen exposure to these pollutants inside urban canopies. Consequently, in order to develop sustainable cities, there is a need to accurately predict in which locations pollutant concentration pose a threat to human health, and how we can mitigate these effects by designing efficient urban layouts. In the last decades, computational fluid dynamics (CFD) simulations have been widely used to predict dispersion in urban environments [1; 2; 3]. However the accurate prediction (and validation) of pollutant concentration poses a considerable challenge for wind engineers, due to the geometrical complexity of urban environments, and the turbulent nature of the atmospheric boundary layer (ABL) [4]. In addition, the variability of the atmospheric conditions at scales larger than the microscale significantly influences dispersion. Traditional boundary conditions used for Reynolds-averaged Navier-Stokes (RANS) simulations of the urban boundary layer impose a steady-state inflow condition, which does not represent this intrinsic variability in atmospheric conditions. It has been shown [5] that accounting for wind-direction fluctuations improves the prediction of pollutant dispersion in the ABL over flat terrain. It can therefore be expected that including a more realistic representation of the large scale variability will also improve the predictive capabilities of traditional RANS simulations for pollutant dispersion within a complex urban canopy. The research presented here focuses on using an Uncertainty Quantification (UQ) framework to include the natural atmospheric variability in the inflow conditions for RANS simulations. Validation with field measurements is performed to

evaluate the predictive capabilities of the framework in a realistic full-scale scenario. We consider the Joint Urban 2003 (JU2003) field experiment, and model one Intense Observation Period (IOP) during which concentration measurements for a continuous tracer release were performed. Three uncertain variables are defined in the inflow definition for the neutral ABL: wind magnitude and direction, and roughness length. The ranges of these variables are based on the most upstream available field measurement. The uncertainty in the inflow variables is propagated through the simulations to obtain statistics, i.e. expectation, variance and 95% confidence intervals for the outcome quantity of interest. In the following we present a summary of the experimental campaign in section 2, a description of the baseline simulation in section 3, and the uncertainty quantification methodology applied in section 4. Section 5 presents the results and comparison with the measurements. Finally section 6 includes the conclusion from the results and the possible future research guidelines.

2. Experimental Campaign: Joint Urban 2003

The JU2003 field campaign in Oklahoma City [6] was performed to provide experimental data for validation of dispersion models aimed at predicting accurate pollution levels inside the urban canopy. During the real scale measurement campaign several types of measurement techniques were employed, and a vast number of experimental stations were set up within the city and in the surroundings. Figure 1 presents the locations map from the different sensors described in the following subsections.

2.1. Velocity Measurements

Two sets of velocity measurements are considered within this work. These velocity measurements were performed by Dugway Proving Ground [7] with two different types of sonic anemometers: Portable Weather Display System (PWIDS), which have a sampling frequency of 1 second, averaging every 10 seconds, providing wind magnitude and direction; and the Super Portable Weather Display System (SPWIDS), which have a sampling frequency of 10Hz, and provide three velocity components.

2.2. Tracer Measurements

Tracer concentrations were recorded during several Intense Observation Periods (IOP). In this study we selected IOP9 as the period of interest. This IOP corresponds to the morning of the 27th of July. We focus on the first continuous release during that morning which took place between 04:00 and 04:30 am (UTC). This IOP was selected due to the high concentration of measurement locations downtown, and due to the neutrally-stable stratification characteristics of this period. The tracer concentration measurements were recorded by ten FRD-built mobile, real-time analyzer. Each of these analyzers consisted of a TGA4000 (Trace Gas Analyzer), which is a fast response instrument with a response time less than 1 second. The analyzer is designed to specifically measure the concentration of SF_6 in ambient air [8; 9].

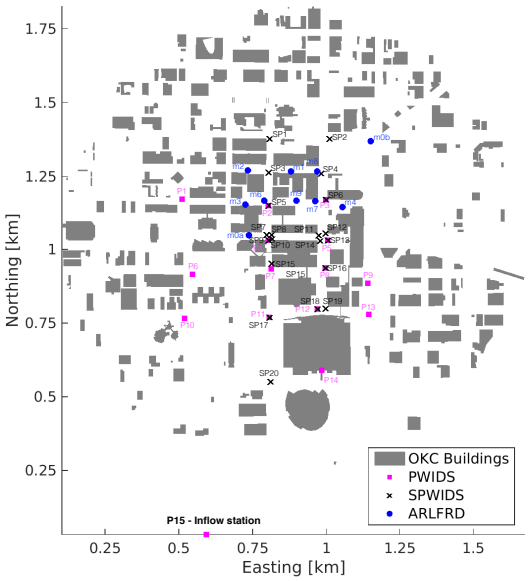

Figure 1: PWIDS, SPWIDS and ARLFRD mobile locations.

3. Numerical domain and simulation set up

Prior applying the uncertainty quantification methodology, a preliminary analysis based on three deterministic simulations was performed to evaluate the simulation set-up and obtain an initial estimate of the concentration field. The set of three baseline simulations considers the mean and extreme wind direction conditions for the UQ study.

3.1. Governing Equations

The governing equations for a neutral atmospheric boundary layer flow are the incompressible Reynolds-averaged Navier-Stokes equations for continuity and

momentum:

$$\frac{\partial \overline{u_j}}{\partial x_j} = 0 \tag{1}$$

$$\overline{u_j}\frac{\partial \overline{u_i}}{\partial x_j} = -\frac{1}{\rho}\frac{\partial \overline{p}}{\partial x_i} + \nu\frac{\partial^2 \overline{u_i}}{\partial x_j \partial x_j} - \frac{1}{\rho}\frac{\overline{\partial u_i' u_j'}}{\partial x_j} \tag{2}$$

where $\overline{u_i}$ are the time-averaged velocity components, ρ is the density, p the pressure, ν the kinematic viscosity and $\overline{u_i u_j}$ is the specific Reynolds stress tensor. In the work presented here $\overline{u_i u_j}$ is modeled using the standard k-ε model, which computes the specific Reynolds stress tensor based on the linear eddy viscosity hypothesis [10]:

$$\overline{\partial u_i' u_j'} = \frac{2}{3}k\delta_{ij} - 2\nu_t S_{ij} \tag{3}$$

where k is the turbulence kinetic energy, δ_{ij} is the Kronecker delta, ν_t the turbulent viscosity and S_{ij} the rate of strain tensor. The turbulent viscosity is computed as a function of k and ε, the dissipation rate, as follows:

$$\nu_t = C_\mu \frac{k^2}{\varepsilon} \tag{4}$$

with C_μ a turbulence model constant equal to 0.09. k and ε are obtained from their respective transport equations:

$$u_j\frac{\partial k}{\partial x_j} = \frac{\partial}{\partial x_j}\left[\left(\nu + \frac{\nu}{\sigma_k}\right)\frac{\partial k}{\partial x_j}\right] + P_k - \varepsilon \tag{5}$$

$$u_j\frac{\partial \varepsilon}{\partial x_j} = \frac{\partial}{\partial x_j}\left[\left(\nu + \frac{\nu}{\sigma_\varepsilon}\right)\frac{\partial \varepsilon}{\partial x_j}\right] + C_{\varepsilon 1}\frac{\varepsilon}{k}P_k - C_{\varepsilon 2}\frac{\varepsilon^2}{k} \tag{6}$$

with P_k the turbulent production term and σ_k, σ_ε, $C_{\varepsilon 1}$ and $C_{\varepsilon 2}$ model constants with the respective values: 1, 1.3, 1.44, 1.92. Dispersion is modeled using an Eulerian approach [11], solving the advection-diffusion equation for a passive scalar:

$$\overline{u_j}\frac{\partial \overline{C}}{\partial x_j} - D_C\frac{\partial^2 \overline{C}}{\partial x_j^2} = Q_S \tag{7}$$

In equation 7, C is the passive scalar concentration, D_C the diffusion coefficient and Q_S is the release amount corresponding to the first continuous release carried out during IOP9. Turbulent dispersion is represented using a standard gradient diffusion model, which is defined as the ratio of turbulent viscosity and the turbulent Schmidt number (0.7). The tracer is introduced in the!computational cell corresponding to the release location presented in figure 1 at the start of the RANS simulation. The open source finite volume code OpenFOAM is used to perform the simulations.The equations are discretized using a second order scheme for velocity and concentration. The simpleFoam steady-state incompressible solver is used to perform the coupling between pressure and velocity. The simulations are run for 3000 iterations, reaching converged residuals below $\sim 10^{-6}$ for velocity, turbulence quantities and concentration.

3.2. Boundary Conditions

It is well known that the boundary conditions are of paramount importance for the results of a CFD simulation [12]. When performing validation with field measurements the significant variability in the real scale ABL flows presents a challenge for the definition of the boundary conditions. In the present study, the formulation for the inflow conditions is given by the exact solution of the governing equations for a neutrally stratified horizontally homogeneous turbulent boundary layer, but the friction velocity u_* and the roughness length z_0 are varied to represent the uncertainty in the inflow conditions. The profiles for velocity and turbulent variables are given by:

$$U = \frac{u_*}{\kappa}ln\left(\frac{z+z_0}{z_0}\right) \qquad k = \frac{u_*^2}{\sqrt{C_\mu}} \qquad \varepsilon = \frac{u_*^3}{\kappa(z+z_0)} \tag{8}$$

where κ, is the von Karman constant equal to 0.41, u_* is the friction velocity and z_0 is the roughness length[13; 14; 15]. For the top and outlet boundaries, zero gradient boundary conditions are applied for velocity and turbulence quantities, while a fixed atmospheric pressure is used at the outlet. A no-slip boundary condition is applied at the ground and the buildings patches, and different wall functions are used. For the ground a modified wall function using the ABL roughness length is applied [16; 17; 18], while a standard smooth wall function is applied on the buildings. In addition to the roughness length and the friction velocity, which is determined by the velocity magnitude at a reference height, the wind direction is the third uncertain parameter in the boundary conditions. To represent the variability in the wind direction, different inlet and outlet boundaries are defined for each case. A more detailed explanation of the methodology is included in section 4.

3.3. Computational model and mesh design

The domain size is designed to minimize the computational time and resources necessary to perform the

UQ study, while respecting the best practice guidelines for wind engineering simulations introduced by COST 732. The domain size is shown in figure 2. Considering the height of the highest building in the geometry (H), the inflow boundary is placed at distance larger than 5H from the most upstream building, and the top boundary is further than 5H from the tallest building. Additionally, the outflow boundary is placed at least 5H downstream the last building.

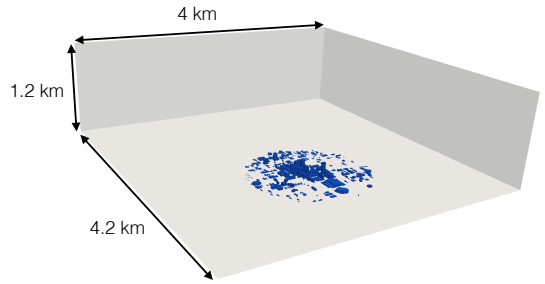

Figure 2: Computational domain size.

SnappyHexMesh is used to design the mesh over the city. This tool creates hex dominant meshes in very complex geometries with minimal user interaction, providing a flexible approach to mesh different complex city geometries. The mesh is constructed in three steps: castellated mesh construction, snapping and layers addition. The mesh is kept constant for all the simulations included in the UQ study, having a total of ~7.4 million cells, with higher vertical resolution where the tracer release takes place.

4. Uncertainty Quantification methodology

Generally, two different kinds of uncertainties can be identified: uncertainty due to the physical variability of the system (aleatory uncertainty) and uncertainty due to a lack of knowledge (epistemic uncertainty). Epistemic uncertainty is reducible by using or developing more sophisticated models, but aleatory uncertainty is intrinsic of the system being modeled, and therefore, irreducible. To improve the predictive capabilities of the simulations, the representation of the aleatory uncertainty in the system of!interest is essential. The number of uncertainties encountered in wind engineering flows is large, and the development of a method that can progressively account for different uncertainties could significantly impact the way computational tools are used in the wind engineering design practice. In this paper, we take a first step towards that goal by accounting for the aleatory uncertainty in the inflow boundary conditions for simulations of pollutant dispersion in downtown Oklahoma City. The inflow uncertainty is expected to be of primary importance because the inflow largely determines flow and dispersion patterns within the urban canopy, and is directly related to the irreducible atmospheric variability. The UQ process used to quantify the inflow uncertainty consists of three steps presented in the following sections: 1) defining the probability density functions (PDF) of the uncertain input quantities; 2) propagating these uncertainties through the simulations to obtain statistics of the outcome of interest; 3) evaluating the result [19].

4.1. Uncertain inflow quantities

Three uncertain variables are chosen: inflow velocity direction, θ, inflow velocity magnitude at a reference height, U, and ABL roughness length, z_0. These three parameters are selected because they define a range of inflow profiles, as specified using equations included in 8. In order to define the ranges of interest and the probability distributions for the uncertain wind speed and direction, a 30 minute measurement time series recorded at PWIDS 15 during the period of the continuous tracer release is analyzed, and the minimum and maximum from the time series defines the ranges. PWIDS 15 was selected to define the inflow because it is the most upstream measurement station considering the dominant south wind direction during the measurement.

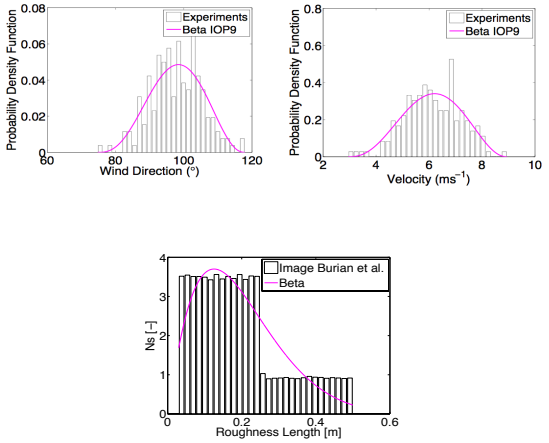

Figure 3: Probability density functions for velocity magnitude and direction during IOP9 and for roughness length.

Figure 3 presents the resulting probability distributions for the velocity magnitude and direction. The probability distribution for the roughness length was

obtained based on a roughness map of Oklahoma city in 2003 [20].

Considering that the wind direction is an uncertain variable, the lateral boundaries of the computational domain define two inlets and two outlets, which are assigned depending on the inflow direction of the case as presented in figure 4. The selection of the flow boundaries, and the definition of the values for the other uncertain inflow variables values is done through a fully automated shell scripting process.

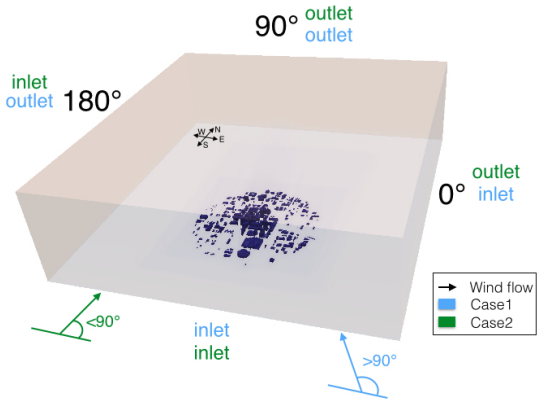

Figure 4: Automatic process to select the case type depending on direction configuration.

4.2. Propagation Algorithm

A non-intrusive polynomial chaos expansion (PCE) method is used to propagate the inflow uncertainties, similar to the one described by [21]. The response metrics of interest are represented by calculating the chaos expansion coefficients for known orthogonal polynomial basis functions from a set of response evaluations. The non-intrusive code RAY, developed at Stanford UQ lab, is used first to define the collocation points through a Clenshaw-Curtis quadrature on an isotropic tensor grid, defining 9 different values for each of the uncertain variables leading to 729 simulations in total [22]. The code is used to automatically run and queue the OpenFOAM simulations, and post-process the results in a parallel Linux environment .

In the following part we briefly describe the process to construct the polynomial chaos expansion for each quantity of interest, and their statistics (e.g. mean and 95% confidence interval) using the set of 729 RANS simulation results. The quantities of interest, q^k, are the velocity magnitude and direction, and concentration at the different measurement locations in the downtown area. Each q^k depends on the values adopted for the three uncertainty variables,ξ_j, i. e. the velocity magnitude and direction measured at the inflow boundary and the roughness length:

$$q^k = q^k(\xi_1, \xi_2, \xi_3) \qquad with\ k = 1, ..., n \tag{9}$$

Each variable ξ_j is defined on a corresponding interval, Ξ_j, and together they compose the hypercube, $\Xi = \Xi_1 x \Xi_2 x \Xi_3$. A probabilistic characterization of the quantities of interest can be obtained through the construction of the PCE:

$$q^k = \sum_{i=0}^{\infty} q_i^k \psi_i(\xi_1, \xi_2, \xi_3) \approx \sum_{i=0}^{P} q_i^k \psi_i(\xi_1, \xi_2, \xi_3) \tag{10}$$

where P is the order of the truncation of the series, and ψ_i are orthogonal Legendre polynomials with a maximum order of 3 in this case. The coefficients q_i^k are evaluated using Galerkin projection with the integrals computed using Clenshaw-Curtis quadrature on an isotropic tensor grid:

$$q_i^k = \frac{\int_\Xi q^k \psi_i d\xi_1 d\xi_2 d\xi_3}{\int_\Xi \psi_i \psi_i d\xi_1 d\xi_2 d\xi_3} \tag{11}$$

$$q_i^k = \frac{\sum_{l=0}^{N} q^k\left(\xi_1^l, \xi_2^l, \xi_3^l\right) \psi_i\left(\xi_1^l, \xi_2^l, \xi_3^l\right) w^l}{\sum_{l=0}^{N} \psi_i\left(\xi_1^l, \xi_2^l, \xi_3^l\right) \psi_i\left(\xi_1^l, \xi_2^l, \xi_3^l\right) w^l} \tag{12}$$

where $\left(\xi_1^l, \xi_2^l, \xi_3^l\right)$ is point 1 of the isotropic tensor grid (abscissa) (9 for each of the variables, 729 points in 3D), while w^l are the integration weights.

Once the coefficients are evaluated we can compute statistic quantities of q^k given the input distributions for the uncertain parameters, ξ_j, without rebuilding the PCE representation, since these are simply integrals over Ξ for which the same Clenshaw- Curtis quadrature rules as for equation 9 can be used. For example, the mean value can be calculated as follows:

$$E\left[q^k\right] = \int_\Xi q^k d\xi_1 d\xi_2 d\xi_3 \approx \sum_{i=0}^{P} q_i^k \left(\int_\Xi \psi_i d\xi_1 d\xi_2 d\xi_3\right) \tag{13}$$

In addition, the PCE response surfaces can be reconstructed and used to compute probability density functions for the quantities of interest by sampling the surfaces according to the beta distributions included in figure 4. In this case 10.000 samples were generated in the uncertain inflow space, and the corresponding values of the PCE response surface were

calculated for each quantity of interest, i.e. the velocity and concentration at the different measurement locations. These values define the probability density functions that are used to compute the mean and 95% confidence intervals as presented in the next section. Additionally, other statistics of interest could be obtained from the probability distributions such as the variance, and third and fourth order moments, skewness and kurtosis [23; 24].

5. Results

5.1. Wind Speed and Direction

The results for wind speed and direction are presented in figure 5, where the arrows represent the mean from the measurement period of interest (black) and from the CFD UQ study (magenta). The arcs represent the 95% confidence interval from the experiments (black) and from the UQ CFD study (magenta). The analysis presented below focuses on determining whether the mean from the experimental data lies within the confidence interval defined by the CFD UQ study, which is quantified in table 5.1. In the table, a ✓ mark means that the mean from the experimental data is within the 95% confidence interval predicted by the UQ study, while a ✗ mark indicates that it falls outside of that range. For the stations where the experimental mean is not within the confidence interval from the UQ study, the table reports two additional values: ΔU, which is the percent difference between the mean measurement and the closest bound of the 95% confidence interval, and $\Delta\theta$, which is the absolute difference in degrees between the experimental mean flow direction and the closest UQ bound. When considering all 34 (PWIDS and SPWIDS) measurement stations, the confidence interval from the CFD UQ study encompasses the mean of the measurement in 27 stations for the velocity magnitude and in 21 stations for the velocity direction.

The fact that the mean from the field measurement is not within the predicted range at all measurement stations can be explained by a number of additional uncertainties that are not accounted for in the simulations, e.g. uncertainties introduced by the use of the k-ε turbulence model [23], or by geometrical uncertainties. Despite these limitations, the results of the study provide valuable information concerning locations in the downtown area where the wind prediction is highly sensitive to uncertainty in the inflow boundary conditions. For example near station P3 or P12 the flow direction can change completely, while in other

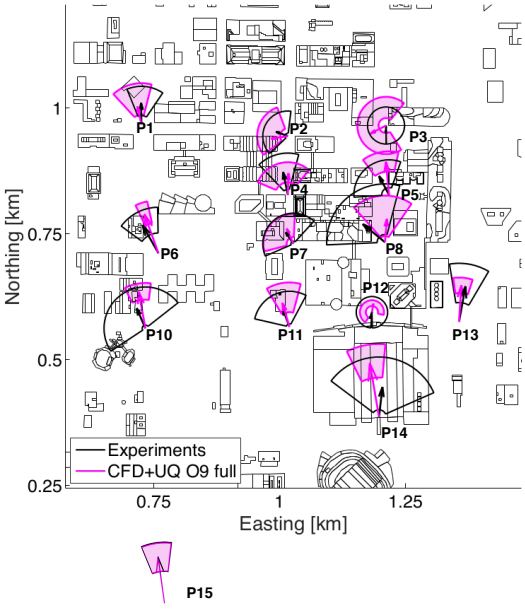

Figure 5: Wind fields comparison between experiments and uncertainty quantification outcome.

locations, such as P2 or P11 the confidence interval is much smaller.

5.2. Concentration fields

Considering the dispersion measurements, 8 fixed measurement stations provided readable concentration values during IOP9. The values obtained at these locations will be compared in non-dimensional form:

$$K = \frac{C}{C_S}\frac{U_{ref}H^2\rho}{Q_S} \tag{14}$$

where C is the local concentration, C_S the concentration at the source location, U_{ref} the reference velocity at PWIDS 15, H is a characteristic building height, ρ is the air density and Q_S is the volumetric concentration at the source. Figure 6 presents the comparison between the results from the UQ study and the measurements for the period of interest. As for the wind magnitude and direction, 95% confidence intervals were calculated based on 10000 samples from the PCE response surface. In 7 out of 8 stations the measured mean concentration was found to be within the 95% confidence interval obtained from the CFD UQ study as it can be observed from the figure. Table 5.2 presents a summary of the results, including the mean from the experiments and the UQ study. The only station where the 95% criteria agreement is not obtained

Table 1: Velocity magnitude and direction comparison between experiments and UQ results

PWIDS	$\Delta U[\%]$	Validated	$\Delta\theta[^\circ]$	Validated
1	-	✓	-	✓
2	-	✓	-	✓
3	1.32	✗	-	✓
4	-	✓	-	✓
5	10.24	✗	-	✓
6	-	✓	4.13	✗
7	-	✓	-	✓
8	-	✓	9.07	✗
10	30.72	✗	-	✓
11	-	✓	-	✓
12	-	✓	15.73	✗
13	-	✓	-	✓
14	30.86	✗	1.6	✗
15	-	✓	-	✓

over predicts the lover 95% confidence bound compared to the experimental mean value by a difference of 32.33%.

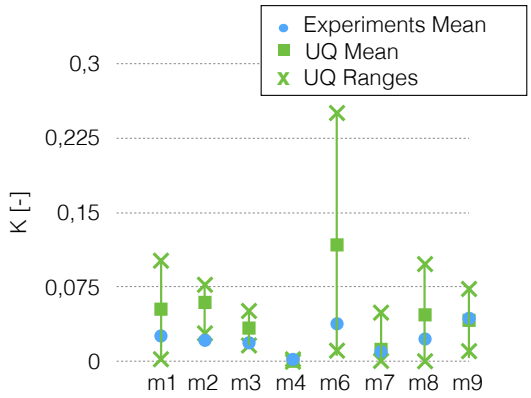

Figure 6: Concentration fields comparison between experiments and uncertainty quantification outcome.

6. Conclusion

When performing simulations of atmospheric boundary layer flows to predict full-scale flow properties the number of uncertainties is large. Some of these uncertainties are intrinsic to the system being modeled, and therefore irreducible. Consequently, if we want to understand the predictive capabilities of

Table 2: Concentration comparison between experiments and UQ results.

m	Experiments Mean	UQ Mean	ΔK [%]	Validated
1	0.0259	0.0528	-	✓
2	0.0215	0.0596	32.33	✗
3	0.0190	0.0338	-	✓
4	0.0023	0.0005	-	✓
6	0.0381	0.1174	-	✓
7	0.0101	0.0127	-	✓
8	0.0228	0.0471	-	✓
9	0.0436	0.0416	-	✓

current CFD simulations for wind engineering applications, it is necessary to quantify the effect of these uncertainties. The work presented here is a first step towards defining a methodology that can predict dispersion with quantified uncertainty margins, by accounting for the irreducible natural variability in the inflow boundary conditions for RANS simulations. In this study, 729 RANS simulations of flow and dispersion in downtown Oklahoma City were performed and post-processed with a non-intrusive polynomial chaos method to compute mean values and 95% confidence intervals of the velocity and concentration field for comparison with the field measurement data obtained during the Joint Urban 2003 campaign. Three uncertain variables, i.e. velocity magnitude and direction, and roughness length, were defined to represent the uncertainty in the inflow profiles for the simulations. Considering the predictions for velocity magnitude and direction, the experimental mean was within the 95% confidence interval obtained from the UQ study in 27 out of 34 and 21 out 34 stations for the velocity magnitude and direction, respectively. The results indicate the areas in the city where the wind prediction is highly sensitive to the inflow boundary conditions, which implies that results of a single deterministic simulation would have limited predictive value in these locations. Considering the concentration fields, it was shown that in 7 out of the 8 available measurement stations the experimental mean is within the 95% confidence interval obtained from the CFD UQ study. As for the velocity field, the UQ approach allows to identify areas that are particularly sensitive to the inflow boundary conditions. Future work will further investigate the accuracy of the PCE approach presented here for predicting the mean and 95% confidence intervals presented in this study. The response

of the local tracer concentration to changes in the inflow variables, in particular the wind direction, can be relatively sharp. Such sudden changes can occur when the flow changes from going into one specific street canyon to another, and the use of a single polynomial chaos expansion representation approach for quantities with a sharp response surface can lead to the appearance of the Gibbs phenomena. In summary, the approach presented in this work aims to quantify inflow uncertainty in RANS simulations of flow and dispersion within urban canopies in an efficient and practical manner such that a more realistic prediction that accounts for the intrinsic variability in the flow conditions can be obtained. The computational time and resources required by the proposed method remain reasonable, since PCE response surfaces can be constructed from a pre-determined set of RANS simulations at the collocation points. The method can be applied to predict mean values and 95% confidence intervals, and evaluation of the variance throughout the flow field enables identifying locations that are particularly sensitive to the inflow conditions.

Acknowledgments

The first author's contribution was supported by the Agency for Innovation by Science and Technology in Flanders (IWT). The authors acknowledge the computing resources provided by the Centre for Turbulence Research at Stanford University for performing the UQ study and the additional resources provided by the Department of Civil Engineering and Engineering Mechanics at Columbia University and the von Karman Institute for Fluid Dynamics.

References

[1] Schatzmann, M. et al., Cost732 model evaluation case studies: Approach and results., Tech. rep., COST Office (2010).

[2] Cheng, Y. et al., A comparison of large eddy simulations with a standard k-ε reynolds-averaged navier-stokes model for the prediction of a fully developed turbulent flow over a matrix of cubes., Journal of Wind Engineering and Industrail Aerodynamics 91 (2003) 1301–1328.

[3] Klein, P. et al., Flow variability in a north american downstown street canyon., Journal of Applied Meteorology and Climatology 46 (851-877).

[4] R. B. Stull, An Introduction to Boundary Layer Meteorology, Atmospheric Science Library, 1988.

[5] Vervecken, L. et al., Accounting for wind-direction fluctuations in reynolds-averaged simulation of near-range atmospherics dispersion, Atmospheric Environment 72 (142-150).

[6] Allwine, K.J., et al., Joint urban 2003: Study overview and instrument locations, Tech. rep., PNNL (2006).

[7] Storwold, D., Meteorology division cste-dtc-dp-wd-me-m, UT 84022-5000, Building 4034/Room 111 Dugway (2003).

[8] Clawson, K. L., et al., Joint urban 2003 vertical sf_6 real-time analyzer and time-integrated sampler data characteristics, Tech. rep., Air Resources Laboratory Field Research Division National Oceanic and Atmospheric Administration (2003).

[9] Air Pollution Line Source, Encyclopedia of Earth, 2011.

[10] D. C. Wilcox, Turbulence Modeling for CFD, La Cañada: DCW Industries, 1993.

[11] e. a. Gorlé, C., Dispersion in the wake of a rectangular building: Validation of two reynolds-averaged navier-stokes modeling approaches, Boundary Layer Meteorology 137 (1) (2010) 115–133.

[12] Franke, J., et al., Best practice guideline for the cfd simulation of flows in the urban environment, Tech. rep., COST 732 (2007).

[13] Launder, B. E., et al., The numerical computation of turbulent flows, Computer Methods in Applied Mechanics and Engineering 3 (269-289).

[14] Norris, S. E., et al., Appropriate boundary conditions for computational wind engineering models revisited, in: The Fifth International Symposium on Computational Wind Engineering (CWE2010), 2010.

[15] Richards, P.J. et al., Appropriate boundary conditions for computational wind engineering models using the k-ε turbulence model, Journal of Wind Engineering and Industrail Aerodynamics 46/47 (145-153).

[16] Parente, A. et al., Improved k-ε model and wall function formulation for the rans simulation of abl flows., Journal of Wind Engineering and Industrail Aerodynamics 99 (267-278).

[17] Parente, A. et al., A comprehensive modelling approach for the neutral atmospheric boundary layer: consistent inflow conditions, wall function and turbulence model closure., Boundary Layer Meteorology 140 (3) (2011) 411–428.

[18] Gorlé, C., et al., Cfd modeling of small particle dispersion: The influence of the turbulence kinetic energy in the atmospheric boundary layer, Atmospheric Environment 43 (673-681).

[19] Iaccarino, G., Introduction to uncertainty representation and propagation, Tech. rep., Neuilly-sur-Seine, France: NATO Research and Technology Organization (2009).

[20] Burian, S.J. et al., Morphological analyses using 3d building databases: Oklahoma city, oklahoma, Tech. rep., Los Alamos National Laboratory (2003).

[21] García-Sánchez, C. et al., Quantifying inflow uncertainties for cfd simulations of the flow in downtown oklahoma city, Building and Environment 78 (118-129).

[22] Iaccarino, G., Introduction to uncertainty representation and propagation, Tech. rep., AVT- 193 short course on uncertainty quantification (2011).

[23] Gorlé, C., et al., Quantifying turbulence model form and inflow uncertainties in wind engineering flows, Journal of Wind Engineering and Industrail Aerodynamics special issue CWE 2014.

[24] Eldred, M., et al., Comparison of non-intrusive polynomial chaos and stochastic collocation methods for uncertainty quantification, in: AIAA Paper, no. 0976, 2009.

[25] Chantrasmi, T., Padé-legendre method for uncertainty quantification with fluid dynamic applications, Ph.D. thesis, Stanford University (2011).

Experimentally and numerically driven optimization of high performance instrumentation for real engine testing

Aude Lahalle

Turbomachinery and Propulsion Department, von Karman Institute for Fluid Dynamics, Belgium, aude.lahalle@vki.ac.be

Supervisor: Fabrizio Fontaneto

Assistant Professor, Turbomachinery and Propulsion Department, von Karman Institute for Fluid Dynamics, Belgium, fontaneto@vki.ac.be

Co-Supervisor: Tony Arts

Professor, Head of Departement, Turbomachinery and Propulsion Department, arts@vki.ac.be

Abstract

During the development phase of an engine, extensive testing is performed. The measurements provide benchmark data for the design and contribute to the certification of the engine. Therefore, the quality of the instrumentation employed is crucial and must undergo a careful calibration process. The output is a performance evaluation in terms of Recovery Factor (RF), defined as: RF = X_{meas}/X_{real} (with X being pressure/temperature). State of the art instrumentation exhibits RF as high as 99,80%, exceeding certification limits, and therefore requiring calibrations. As modern engines are heavily instrumented, the calibration budgets are substantial.

This PhD aims at providing to provide a design methodology to precisely control and enhance the RF. The project is structured such that the three main activities (experiments, numerical simulations and optimization) are tightly linked and complement each other. In the present paper, an overview of the experimental work realized is given, as well as a preliminary analysis of the physical phenomena affecting the RF.

Keywords: Turbomachinery, instrumentation, total pressure and temperature probe, optimization

Nomenclature

CADO	[-]	Computer Assisted Design Optimization
CFD	[-]	Computational Fluid Dynamics
H	[-]	Number of heads
L	[m]	Distance between two extreme heads
P	[Pa]	Static pressure
RF	[-]	Recovery Factor
T	[K]	Static temperature
y^+	[-]	Wall distance in wall coordinates

Greek

ΔT	[K]	$T_{Nozzle} - T_{Probe}$
η	[-]	Recovery Factor

Subscripts

0	Total value
meas	Measured quantity
real	Real quantity

1. Introduction

On the 20th of November 2015, CFM's latest engine, LEAP 1A, achieved joint FAA/EASA certification, thereby concluding a process which began in 2005 with the announcement of the CFM/LEAP family. The certification is the final phase of the development of an engine and is the starting point of its mass production and commercialization. The certification is the result of extensive internal testing performed throughout the development phase of an engine: each particular component as well as the full

engine are tested in both ground and flight conditions. The measurements, issuing from several specific tests (such as fan blade out, bird ingestion, triple red-line endurance test, etc) provide benchmark data for the design, but also contribute to verifying that the certification requirements are met prior to official certification tests. For each test, the quality of the instrumentation employed is fundamental as artifacts might cause an incorrect interpretation of the experimental data which could lead to the uncertification of the engine. Therefore, it is absolutely necessary to submit the instrumentation to a careful calibration process.

A calibration can be realized for different flow conditions (e.g. Mach number, flow angles), statically or dynamically. The output is an evaluation of the performance of the measurement chain to retrieve the real quantities of the flow field such as total pressure, total temperature or flow angles. This performance is expressed in terms of Recovery Factor (RF), and is defined as follows:

$$RF = \frac{X_{meas}}{X_{real}} \tag{1}$$

Typically, total temperature and/or total pressure rakes are employed in engine testing, providing RFs as high as 99,80%. In other words, when only considering the measured data, i.e. not recovered, the margins tolerated by the certification limits are exceeded as nowadays engines need to be certified on a basis of some hundredth of a percent for the efficiency. Therefore, considerable resources are devoted to these very costly and time-consuming calibrations, which can account significantly for the instrumentation's cost and production time. Moreover, as modern engines are heavily instrumented, the instrumentation expenses represent a substantial item in the budget development of a new engine.

2. Motivation and target

Hypothetically, by introducing a RF as high as 99,98%, the correction introduced by the RF would be negligible in comparison with the standards required by industrials, i.e. the certification limitations, therefore allowing the calibration process to be drastically reduced in terms of costs as well as time.

Therefore, the present PhD project focuses on the development of highly reliable design procedures in order to provide a methodology which delivers probes with a high RF. The project aims to present a design strategy able to precisely control and enhance the RF.

3. Methodology

Over the past year, the von Karman Institute (VKI) has developed a calibration methodology which proves to be robust and reliable enough to meet industrial requirements in terms of facility repeatability and measurement uncertainty as described in [1]. Through these different experiences, an experimental database has been built, pointing out the differences in terms of RF according to the shape of the probe and the nature of its sensors.

In a second step, the operating conditions (total pressure, total temperature, static pressure and flow angle) of the facility are used as overall boundary conditions for numerical simulations by means of the open-source Computational Fluid Dynamics (CFD) software OpenFOAM. The target of these simulations is to provide a full understanding of the flow physics taking place inside and around the different probes which have been experimentally calibrated and obtain their validation through a thorough comparison with experiments. Aerodynamic simulations are realized using a steady configuration, which will then be extended to an unsteady configuration in order to describe the transient aero-thermal phenomena taking place. These numerical simulations aim to highlight the geometrical parameters affecting the RF.

Finally, by means of the in-house VKI optimizer, CADO (Computer - Assisted - Design - Optimization), the geometrical parameters identified in the previous step will be iteratively modified, targeting an enhancement of the RF by means of user-defined constraints. The most promising designs generated by the optimizer can then be experimentally tested and used for high-fidelity simulations.

The project is structured in such a way that the three main activities (experiments, numerical simulations and optimization) are tightly linked and complement each other.

4. Experimental Setup

The experiments conducted at VKI permit the continuous development of a database gathering the performance of the different probes. According to Eq. (1), these performances have been concerning pressure Recovery Factor (η_P) and temperature Recovery Factor (η_T), which are defined respectively by Eq. (2) and Eq. (3), and result from a calibration process for different Mach numbers and flow angles.

$$\eta_P = \frac{P_{0,meas}}{P_{0,real}} = \frac{P_{0,probe}}{P_{0,nozzle}} \quad (2)$$

$$\eta_T = \frac{T_{0,meas}}{T_{0,real}} = \frac{T_{0,probe}}{T_{0,nozzle}} \quad (3)$$

4.1. Experimental facility

The measurements were performed in VKI's high speed calibration facility, C4, a highly versatile atmospheric discharge calibration nozzle. A 73m^3 high pressure reservoir, filled by a compressor, supplies C4 in air at a controlled total pressure and temperature (Fig. 1).

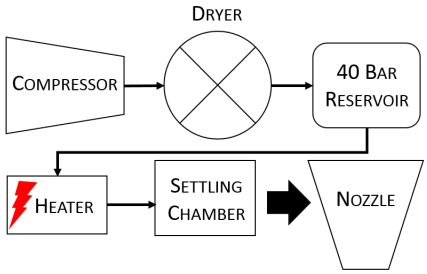

Figure 1: Complete operation line of the C4 facility

The air fed to the reservoir is beforehand passing through a dryer to minimize the presence of humidity in the flow. In addition, an in-line heater is installed downstream of the reservoir, enabling the setting of a large range of temperatures. The temperature is maintained through a feedback Proportional-Integral-Derivative (PID) loop, by means of a sensor placed at the inlet of the nozzle. The calibration nozzle (Fig. 2) is directly connected to a settling chamber, placed upstream of the nozzle. This settling chamber consists of multiple mesh-wires which aim to homogenize the incoming flow in terms of pressure, temperature and turbulence.

The calibration nozzle itself consists of a circular convergent nozzle, characterized by a contraction ratio of 14.75 and an outlet diameter if 50mm. The discharge Mach number at the nozzle exit, which can vary between 0.1 up to sonic conditions, is regulated by means of a needle valve allowing the operator to control the total pressure upstream the nozzle. The outlet static pressure is fixed by the atmospheric conditions.

4.2. Instrumentation and measurement chain

C4 is equipped with total temperature and pressure instrumentation at 6 measurement positions which are

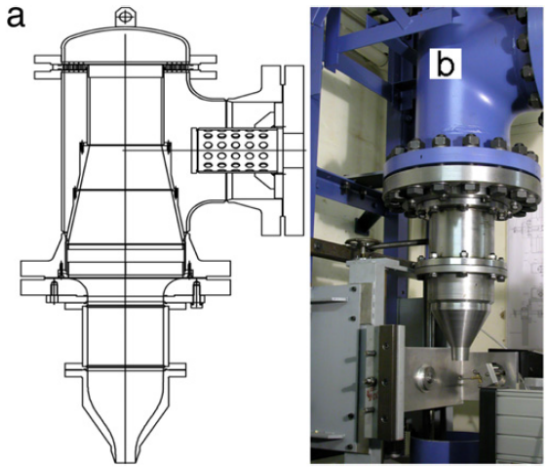

Figure 2: VKI's calibration facility, C4 - (a) and (b)

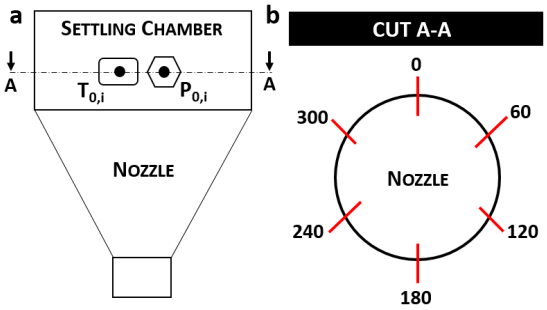

Figure 3: Nozzle measurement location, side view (a) and top view (b)

located in the settling chamber behind the mesh-wires screens and distributed circumferentially every 60° (Fig. 3).

The nozzle inlet total pressure, $P_{0,Nozzle}$, results from the pneumatic average of 6 total pressure probes connected to a DP15 Validyne differential pressure transducer, referenced to atmospheric conditions. The total pressure measured by the probe, $P_{0,Probe}$, is connected to a DP45 Validyne referenced to the nozzle inlet conditions. Both signals are then connected to a CD15 Validyne sine wave demodulator.

The mean nozzle inlet total temperature, $T_{0,Nozzle}$, is acquired using 4 Platinum Resistance Thermometers (RTDs - PT100) and located at 60, 120, 180 and 240° (Fig. 3). The PT100 sensors are connected to a Seneca PT100 K109pt measurement bridge. $T_{0,Nozzle}$ is obtained by performing an average on the 4 values read by the PT100, which is reasonable, as the biggest scatter between the 4 PT100s (0.15K) is lower than the uncertainty on $T_{0,Nozzle}$ (0.19K).

The total temperature acquired by the probe,

$T_{0,Probe}$, is obtained by measuring in differential with respect to $T_{0,Nozzle}$. For that matter, a reference thermocouple is placed inside the nozzle at 300°. This strategy is based on the laws of thermo-electricity which state that connecting in series two thermocouples of the same type will display a voltage difference directly proportional to the temperature difference at the junction. However, the voltage difference is very low, a few μV, which required the use of an Agilent precision nano-voltmeter.

Finally the last position, 0°, is dedicated to the sensor required by the heater to control the temperature of the incoming flow.

The PT100 and Validyne signals are connected to a National Instrument acquisition board (Fig. 4). In addition, a traversing system allowing the displacement in terms of yaw and pitch angles is connected through the last channel of the acquisition board in order to record the angular positions. A dedicated computer is the final device of the measurement chain, and records the acquired signals, the voltage difference obtained by the nano-voltmeter and also the traversing system's output.

In order to synchronize all the instruments, an acquisition routine has been developed using LabView.

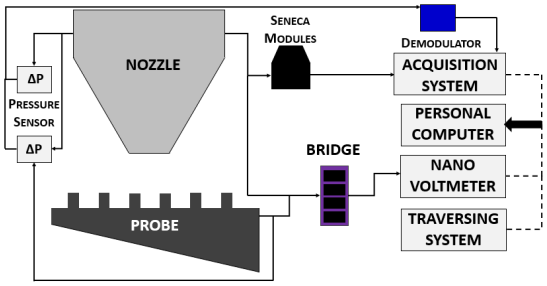

Figure 4: Measurement chain for probe calibration

4.3. *Uncertainty computation*

For each measurement of pressure and temperature, a type B uncertainty computation of the static calibration against national standards taking into account the measurement chain has been performed [1]. The error was then propagated on the pressure and temperature RFs.

The following paragraphs focus on the experiments performed in C4. For a better readability, the plots do not contain the computed uncertainties. However, as an example, typical uncertainty values retrieved for a calibration can be observed in Fig. 6 and Fig. 7

4.4. *Results*

In the last 18 months, multiple probes have been calibrated in terms of Mach numbers (Fig. 6 and Fig. 7), yaw or pitch angles. Among the calibrated probes, various designs have been encountered ranging from single sensor probes (pressure or temperature sensors) to dually instrumented (thermocouple and pressure tap) rakes. Several head geometries have been experienced (Fig. 5):
- cylindrical (A,B, C) or elliptical (D,E,F) geometries,
- heads equipped with 0 (C,F), 2 (D,E) or 4 (A,B) ventilation holes,
- heads which have ventilation holes aligned (A,D) or inclined (B,E) with respect to the stem axis of the probe.

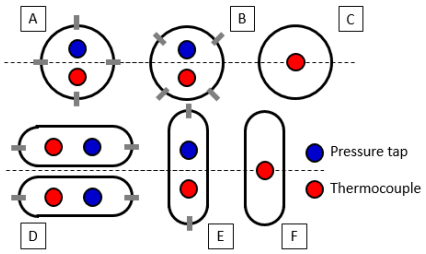

Figure 5: Summary of the different geometric configurations

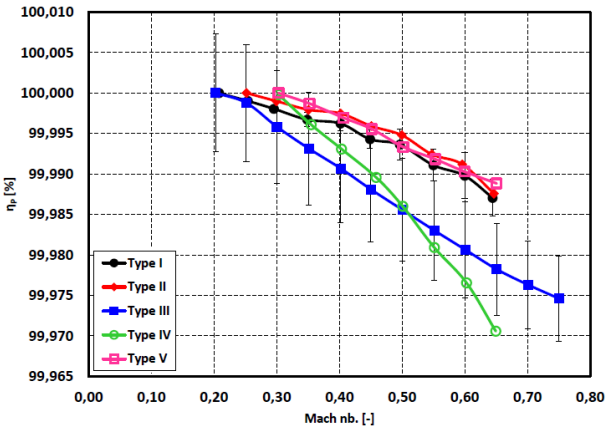

Figure 6: Pressure Recovery Factor as a function of Mach Number for different types of sensors

As a result, a considerable database in terms of pressure and temperature recovery coefficients has been constituted. However, it is still unclear which are the parameters affecting the RF. Since the beginning of the partnership with industry, the experimental set-up has been kept identical, conforming to the requirements of the industrial quality system. Additionally,

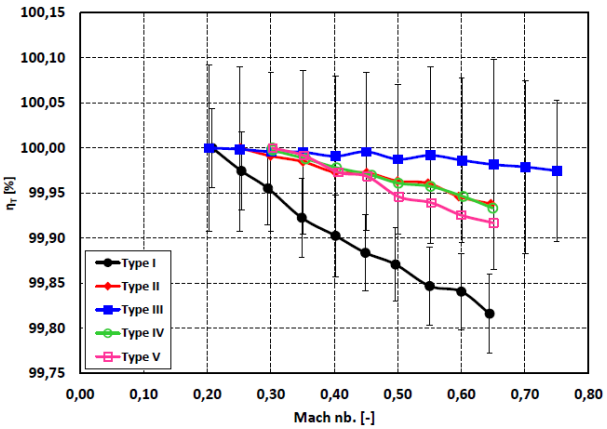

Figure 7: Temperature Recovery Factor as a function of Mach Number for different types of sensors

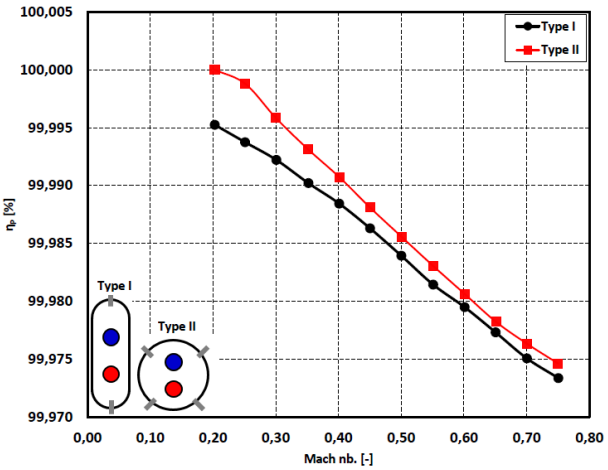

Figure 8: Pressure Recovery Factor as a function of Mach Number - Comparison

the procedures followed during the calibrations have also been kept identical, which guarantees the repeatability and confidence in the measurements. Therefore, the differences which have been noticed between the different calibrations should only be linked with the characteristics of the probe itself. The following paragraph gives an outlook of a parameter which could result in those variations.

The nomenclature employed for the comparison is the following:

Case	Head Geometry	Sensor Type
Type I	E	K
Type II	B	K
Type III	F	E
Type IV	C	K

Table 1: Nomenclature employed for the comparison

Fig. 8 (respectively Fig. 9) shows the comparison of the pressure (resp. temperature) RF for two probes with identical thermocouple types (type K) but different head geometries. The RFs have been normalized by the maximum pressure (resp. temperature) RF.

As highlighted in Fig. 8, the cylindrical heads exhibit a slightly better performance than the elliptical heads. However as the Mach number increases, from M = 0,40 and up, the difference between both heads becomes constant ($\Delta\eta_P$ = 0,0015 %).

The instrumentation (i.e. the pressure sensor and thermocouple) is identical for both geometries, which leaves as possible explanation that only the geometry of the head contributes to the RFs difference. In the case of the cylindrical head, the blockage effect of the instrumentation on the flow field might be less important than for the elliptical head. The ratio between the frontal area of the instrumentation with respect to the head area is lower in the elliptical head, which could result in a higher drop for the pressure recovery factor. However, this hypothesis does not hold for the temperature RFs. Fig. 9 displays a clear influence of the head geometry on the evolution of the RF, but the physical explanations remain unknown. To better understand the flow field, numerical simulations are required, in particular inside the heads.

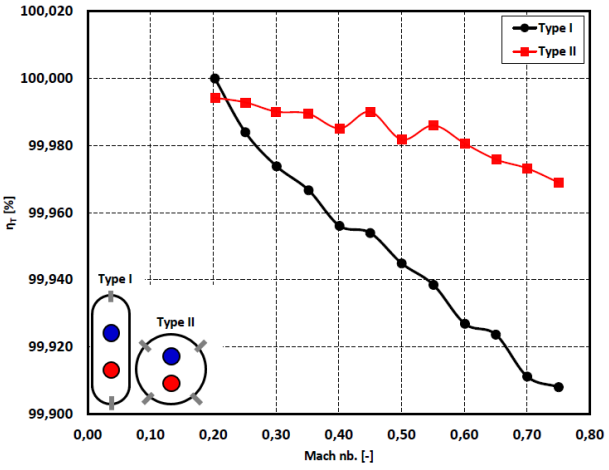

Figure 9: Temperature Recovery Factor as a function of Mach Number - Comparison

5. Numerical Simulations

The previous paragraphs have highlighted the differences which exist between different probe geometries. However it is still difficult to explain the cause of these differences, mainly due to the lack of information of the flow field topology inside the heads.

Nowadays numerical simulations have become a key tool in the prediction and understanding of flow field phenomena. In particular, the influence of multihole pressure probes on the flow field has been investigated numerically, Malviya et al. [2] have focused on conical and hemispherical heads of pneumatic probes, highlighting that conical probes are worse in comparison with hemispherical heads in complex flows. Coldrick, Ivey and Wells [3] used CFD calculations to assess the feasibility of realizing a pneumatic probe with specific industrial requirements. As in [4] their study focused on a Cobra probe, and investigated its influence on the flow field. They compared simulations performed with and without the presence of a probe, which causes a substantial blockage and reads erroneous pressure values. Nevertheless, the authors suggested that a displacement of the probe away from the center of the passage could probably solve the issue.

In a similar framework as the present project, Aschenbruck, Hauptmann and Seume [5] and Herbst et al. [6] have investigated the influence of a multihole pressure probe on the flow field in axial-turbines. Experimentally obtained pressure measurements were conducted and compared with CFD simulations. As in [3], simulations with and without probe displayed good agreement with flow areas with low gradients. Based on the results, the authors concluded that when encountering differences between probe measurements and numerical results, they were caused by the potential effect of the probe.

In addition, CFD can also be used to calibrate probes as has been demonstrated by Guzman, Fletcher and Hooper [4]. They have investigated numerically, using an in-house CFD code, the flow field behavior around a four-hole Cobra probe. Numerical results have been compared with experimental results and have shown good agreement quantitatively and qualitatively. This investigation has demonstrated the effectiveness of using numerical analysis to provide information for engineering design purposes.

However, few investigations have been performed on the blockage effect of the probe itself on the flow field, and on the flow topology inside the heads of the probes. Moreover few studies have focused on the design of pressure and/or temperature probes with an effective performance combining experimental data and numerical simulations.

Based on the experimental data available at VKI, this project intends to understand the physics occurring inside and around the probe in order to control, and potentially increase, its performance in terms of RF. As a first step, numerical simulations were performed on a representation of the experimental set-up, investigating the aerodynamics taking place. In a further step, this investigation will include the thermal effects described by [7] and reported by [8]: conduction, convection and radiation.

5.1. Numerical setup

5.1.1. Geometrical model

The simulated probe (Fig. 10) is modeled based on the different probe geometries which have been experimentally calibrated at VKI. The probe is composed of three heads mounted on a stem with its support. Each head is instrumented with total quantities sensors: a thermocouple and a pressure tap, respectively acquiring total temperature and total pressure. The particularity of this prototype is the inclination of each head with respect to the others.

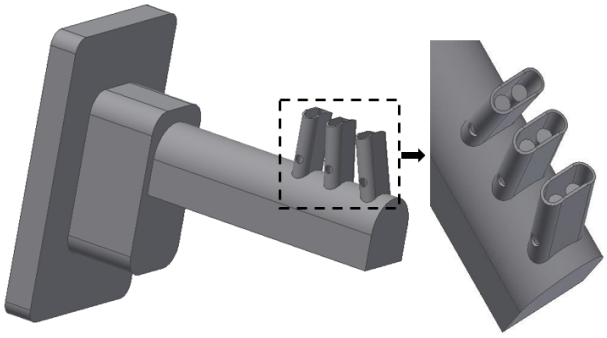

Figure 10: Geometrical model of the probe simulated

For simplicity, and as a first step, the dimensions of the thermocouple and pressure sensor have been assumed to be identical which allowed to halve the numerical domain (Fig. 11) using a symmetry plane.

5.1.2. Mesh

The unstructured mesh contains 8,8 million hexahedral cells. The quality of the mesh has been secured by respecting a maximum skewness of 0.7, a maximum expansion rate of 2 and a maximum aspect ratio of 4000. The first cell size has been imposed such

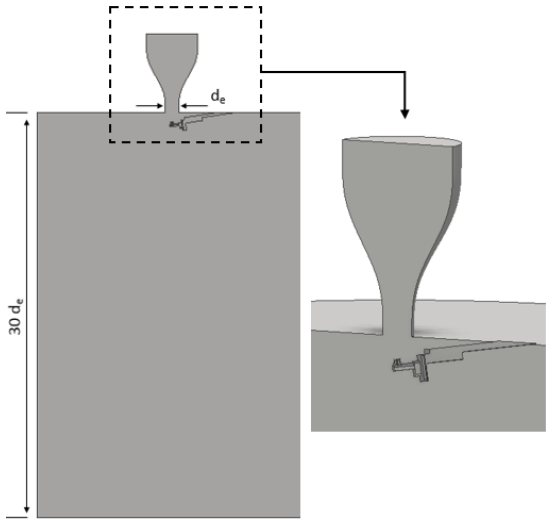

Figure 11: Numerical domain for simulations

that a criterion of $y^+ \leq 30$ is respected. Particular attention has been given to the mesh refinement around the heads, in order to ensure a sufficient number of cells inside each head and between the different sensors: 0,1 mm (resp. 0,05mm) in Zone 1 (in Zone 2) as shown in Fig. 12 .

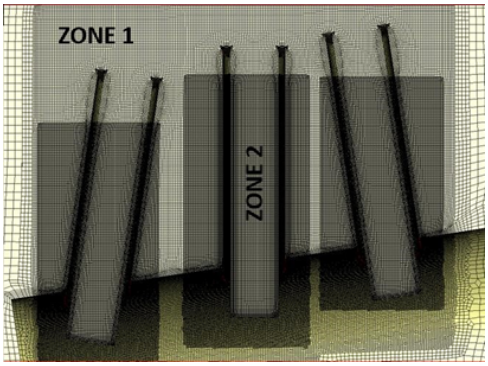

Figure 12: Mesh refinement over the heads

5.1.3. Boundary conditions

As mentioned in 4.1 the experimental conditions are the ones wished to be reproduced during the simulations, as one objective of the numerical simulations is to compare the results with the experimental data. The boundary conditions are summarized in Fig. 13.

Since the simulations are purely aerodynamic, no heat transfer is considered so far. Heat transfer issues will be introduced at a later stage.

[1]	Inlet	Total pressure, P_0 Total temperature T_0 Velocity directions
[2]	Nozzle and probe walls	Adiabatic
[3]	Cylinder contours	Atmospheric pressure

Table 2: Boundary conditions for numerical simulations

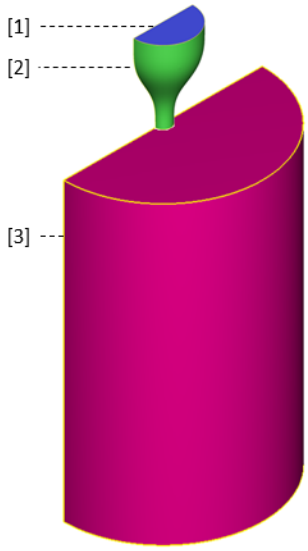

Figure 13: Boundary conditions for the numerical simulation

5.2. Preliminary results

Simulations have been done using two Computational Fluid Dynamics (CFD) codes: OpenFOAM and Numeca FINEOpen. As an initial goal, the simulations were run in order to obtain the flow field topology in and around the probe (Fig. 14).

For all cases, the same mesh was used as well as the same boundary conditions. On the other hand, the solvers and the discretization schemes are not identical for the two CFD codes.

As a first step, simulations were run for boundary conditions corresponding to M = 0,30. Total temperature and pressure, as well as velocity directions were imposed at the inlet, and the atmospheric pressure was assumed at a far-field distance from the jet. When using OpenFOAM, the unsteady solver *rhoPimpleFoam* was used with large time steps, the discretization scheme was 1st order and the k-ω SST turbulence model was used. Regarding FineOpen, the same boundary conditions were imposed as for OpenFOAM, while the discretization scheme was 2nd order.

The simulations offer a detailed view of the flow

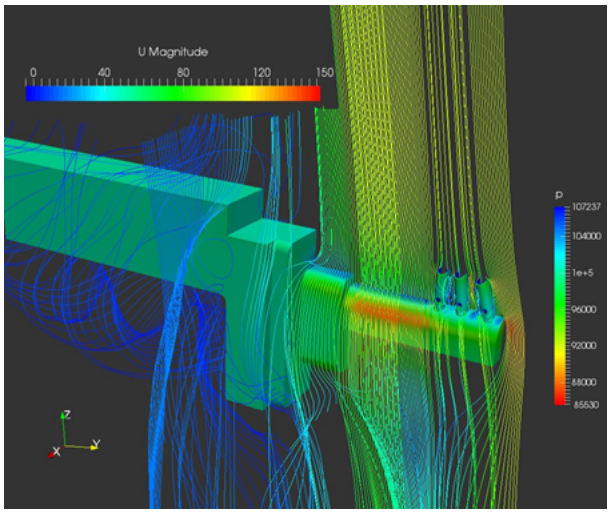

Figure 14: Flow field in and around the probe at M = 0,30 - OpenFOAM

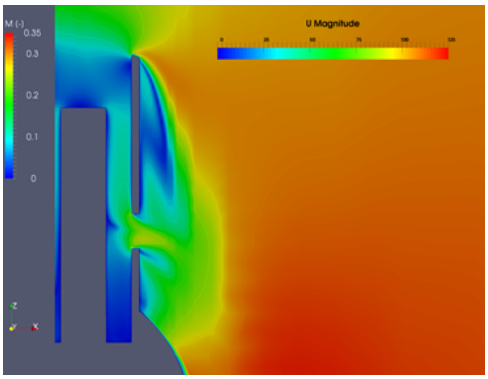

Figure 15: Velocity distribution for M = 0.30 - OpenFOAM

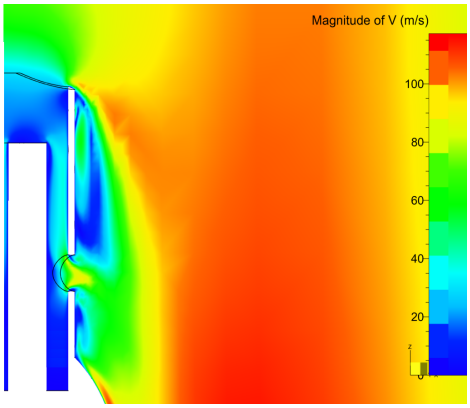

Figure 16: Velocity distribution for M = 0.30 - FineOpen

topology occurring in and around the heads of the probe. In particular, recirculation areas are visible at the the edge of the head, which then mixes with the exiting flow through the ventilation holes. Fig. 15 and Fig. 16 also highlight the presence of a recirculation zone inside the head.

Moreover, these simulations also provide information on the pressure distribution, which can be used to compute a numerical pressure RF. However, unlike the probes which have been calibrated in the C4 facility, these pressure sensors have been slightly modified due to to mesh restrictions. In fact, the pressure taps of the heads are entirely full, i.e. no pneumatic tube. The assumed to be measured total pressure, $P_{0,probe}$, is computed as a surface average on the cylinder top surface of the sensor.

6. Conclusions and Future Work

As mentioned in the introduction, one of the targets of the numerical simulations is to compare the experimental calibration performed in the C4 facility with numerically computed pressure RFs. Different sets of numerical boundary conditions should be tested in order to establish a comparison between experiments and numerical simulations. Furthermore, the pressure sensor has been modeled as a solid tube, which is not the case experimentally. An investigation is currently focusing on the effect of the presence of a pressure tube on the pressure RF.

The present results focus only on the aerodynamic aspect of the problem, however probes are also calibrated in terms of temperature RF. The next milestone is set to include the challenging thermal aspects (Fig. 17), and mostly their modeling.

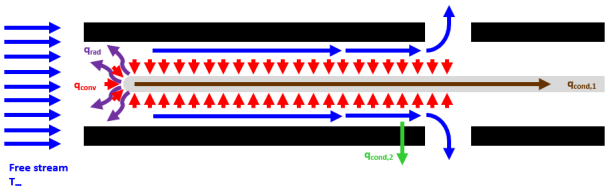

Figure 17: Illustration of the different thermal effects to consider

Several investigations have been carried out on the possible influence of convection, conduction and radiation on the temperature RF. Bonham et al. [7] have studied the thermal effects on the calibration of a total temperature probe, and have developed a design for highly performing probe. This strategy will also be extended in the present work: an extensive and thorough investigation of the flow field in and around the probe combined with an optimization process will

provide a methodology to control and possibly increase the RF based on user-defined specifications.

References

[1] C. F. de Metrologie, 27 exemples d'evaluation d'incertitudes d'etalonnages - Les guides techniques du College Francais de Metrologie, Lexitis Editions, France, 2013.

[2] Malviya, Vihar, Mishra, Rakesh, Palmer, Edward and Majumdar, Bireswar, CFD based analysisof multi-hole pressure probe geometry on flow field interference, Fluid mechanics and fluid power (2007) 113–122.

[3] S. Coldrick, P. Ivey and R. Wells, Considerations for using 3D pneumatic probes in high speed axial compressors, no. Proceedings of ASME Turbo Expo, Amsterdam, The Netherlands, 2002.

[4] M.M. de Guzman, C.A.J. Fletcher and J;J; Hooper, Computational investigation of cobra probe operation, Int. J. Num. Meth. Heat Fluid Flow 4 (4) (1994) 425–4445.

[5] J. Aschenbruck, T. Hauptmann and J.R. Seume, Influence of a multi-hole pressure probe on the flow field in axial-turbines, no. European Turbomachinery Conference, Madrid, Spain, 2015.

[6] F. Herbst, S. Bluemel, E. Fakiolas and J.R. Seume, Numerical investigation of the interaction between probe, flow and blading in an axial-turbine, no. International Gas Turbine Congress, Osaka, Japan, 2011.

[7] C. Bonham, S.J. Thorpe, M.N. Erlund and R.D. Stevenson, Stagnation temperature measurements using thin-film platinum resistance sensors, Measurement Science and Technology 25 (1) (2013) 493–499.

[8] R. Moffat, Gas Temperature Measurement, Michigan: General Motors Research Laboratories.

Adjoint-based design optimization of a turbocharger radial turbine

Lasse Mueller

Turbomachinery and Propulsion Department, von Karman Institute for Fluid Dynamics, Belgium, lasse.mueller@vki.ac.be

Supervisor: Tom Verstraete

Adjunct Professor, Turbomachinery and Propulsion Department, von Karman Institute for Fluid Dynamics, Belgium, tom.verstraete@vki.ac.be

Promoter: Herman Deconinck

Professor, Univ. Libre de Bruxelles (ULB), Aero-Thermo-Mechanics Department, Belgium, hdeconink@ulb.ac.be

Abstract

The aim of this Phd project is to develop an adjoint-based optimization methodology for turbomachinery applications. This paper describes the optimization system which makes use of 3D multiblock structured Navier-Stokes solver, a discrete adjoint solver and a sequential quadratic programming optimization algorithm. The accuracy of the discrete adjoint solver is verified by comparing adjoint-based gradients with central finite differences.

A dedicated CAD-based parametrization of the radial turbine is detailed which inherently satisfies a geometric constraint of radial fibred blades that is imposed to the design due to mechanical restrictions.

Keywords: Turbocharger radial turbine, Adjoint-Based optimization, CFD

1. Introduction

High fidelity computational fluid dynamics (CFD) and numerical optimization methods have made significant contributions to the recent advances in the design of turbomachinery. Current optimization techniques may be classified into gradient-free and gradient-based methods [1].

Gradient-free optimization techniques like genetic algorithm or evolutionary methods have proven to be well suited for complex design applications and have been successfully applied to three-dimensional design optimization [2; 3; 4]. They are robust and easy to implement, but become computationally too expensive for industrial design applications with many design parameters and tight convergence tolerances. In contrast, gradient-based methods are computationally more efficient for high dimensional design problems and require less iterations to converge [5]. However, the performance and accuracy of the gradient-based algorithm is significantly determined by the gradient computation.

The adjoint method [6] to calculate cost function gradients is widely used in aerodynamic shape optimization and has been applied extensively to external flow problems [7; 8; 9; 10; 11], but more recently, it has also been applied to the aerodynamic design of turbomachinery blades [12; 13; 14; 15]. The adjoint method is nowadays the preferred choice for sensitivity analysis and design optimization for large scale design problems due to its low computational cost virtually independent of the number of design parameters.

Even though the adjoint method has gained much attention in recent years for the aerodynamic design of turbomachinery blades, it has been mainly applied only to axial machines, such as axial turbines and axial compressors, but not to radial turbines. This is partly due to the complexity of the geometry partly due to the flow in radial turbines which is inherently three di-

mensional with strong secondary flow motion, tip leakage flow and separation at various operating conditions.

The aim of this study is to show that adjoint-based optimization can be used for the design of radial turbines. For this purpose a dedicated CAD-based parametrization is proposed that allows the imposition of geometric constraints which are necessary due to mechanical and manufacturing restrictions. Further to improve the robustness of the CFD and adjoint solver for such a flow, a recently proposed method [16] to stabilize discrete adjoint solvers has been implemented and is applied in this study.

The remainder of the paper is organized as follows: Section 2 introduces the baseline turbine wheel which is the datum geometry of this study. Next, the developed gradient-based optimization system is presented (Sec. 3) including the parametrization (Sec. 4) and the numerical model (Sec. 5). In Sec. 6, the objective and constraints of this optimization will be presented before discussing the results in Sec. 7.

2. Baseline Turbine Wheel

The baseline turbine wheel is presented in Fig. 1. It is a radial inflow design with 10 radially stacked blades, a wheel diameter of $d_{wheel} = 50\ mm$ and axial length of $l_{wheel} = 25\ mm$. Due to external constraints the number of blades, the diameter and the axial length of the wheel are fixed in this optimization. The tip clearance is kept constant to $\Delta h_{tip} = 0.3\ mm$ which is a state-of-the-art value for impellers of this small size [17]. Table 1 summarizes the geometrical data and performance characteristics at design point.

The turbine output power is 10 kW at a total-to-total pressure ratio of $\pi_{TT} = 1.6$ and mass flow of $\dot{m} = 89.4\ g/s$. At design operating conditions, the flow is entirely subsonic with separation at the tip due to incidence and almost zero exit-swirl. The computed total-to-static isentropic efficiency of $\eta_{TS} = 89.7\ \%$ is already close to the achievable limit for impellers of this size which motivates the use of a gradient-based optimizer to find the necessary design modifications in order to improve further the aerodynamic performance.

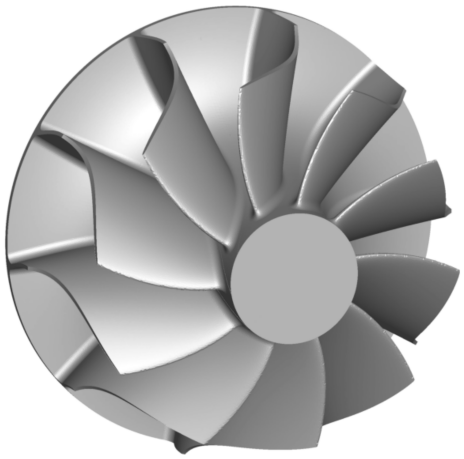

Figure 1: **Baseline turbine wheel.**

3. Optimization Algorithm

A schematic of the optimization algorithm is illustrated in Fig. 2. The system makes use of a gradient-based optimization algorithm, a newly developed 3D multiblock structured Navier-Stokes solver and the corresponding discrete adjoint solver to evaluate cost function sensitivities. Both The optimization package SNOPT [18] is integrated into the framework. It is a general-purpose optimization software for large-scale constrained optimization and uses a sequential quadratic programming (SQP) algorithm (cf. [19] for more details).

In each iteration, a sequence of operations are performed (Fig. 2) to evaluate the cost function J and its sensitivities with respect to the design variables $dJ/d\boldsymbol{\alpha}$ which are then used by the gradient-based optimizer to determine the search

Table 1: **Geometrical and performance data of the baseline wheel at design point**

Blade count	N	10
Wheel diameter	d_{wheel}	50 mm
Wheel length	l_{wheel}	25 mm
Area ratio	A_{in}/A_{out}	0.704
Tip clearance	Δh_{tip}	0.3 mm
Rotational speed	RPM	140,000
Power	P	10 kW
Mass flow	$\dot{m}$	89.4 g/s
Pressure ratio	π_{TT}	1.6
Isentropic efficiency	η_{TS}	0.897

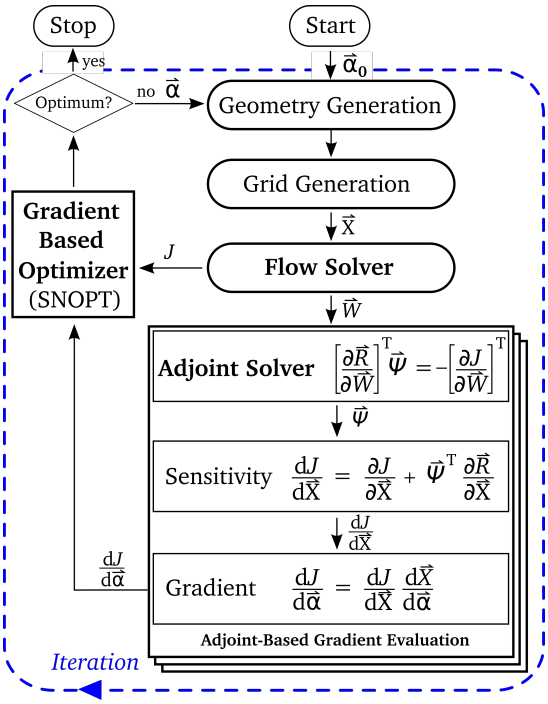

Figure 2: **Schematic of the gradient-based optimization algorithm (Adapted from [20]).**

direction suitable to optimize the design problem.

The geometry generation of the radial turbine uses a dedicated parametrization (Sec. 4) based on Bézier and B-spline curves and surfaces that allows to incorporate geometric constraints while guaranteeing smooth shape variations. The Navier-Stokes solver (Sec. 5.1) evaluates the aerodynamic performance and provides both the converged flow solution $\overline{W}$ to the adjoint solver and the objective value J to the gradient-based optimizer. The adjoint-based gradient evaluation chain (Sec. 5.3) computes the function gradient vector $dJ/d\boldsymbol{\alpha}$ at a computational cost roughly twice as much as the non-linear flow solver. This process is repeated until no further improvement can be found by the optimization algorithm.

4. Parametrization and Design Variables

The parametrization is one of the crucial steps in every optimization. On the one hand the design space should be diverse and large enough in order to include optimal designs, on the other hand geometrical restrictions are invariably imposed due to mechanical and manufacturing constraints. In particular, turbocharger radial turbines have to

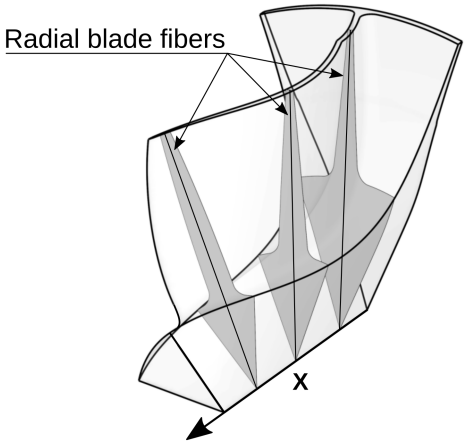

Figure 3: **Radial fibered blade sections of the baseline turbine wheel.**

withstand the harsh environment of high mechanical stresses and high temperatures. As a result, radial turbines are commonly designed with radial blading, composed of radial blade fibers as illustrated in Fig. 3, in order to avoid bending stresses within the blades due to centrifugal forces.

In present study, this geometrical constraint is inherently satisfied by the parametrization of the radial turbine. It is based on Bézier and B-spline curves and surfaces and is defined by:

1. the meridional flow path,
2. the camber line surface defined by a blade angle distribution,
3. the blade thickness distribution which is added normal to the camber line surface, and
4. the number of blades.

Figure 4 shows the parametrization of the meridional flow path which is subdivided into three patches: an inlet patch ①, an intermediate patch ② where the blade is located, and an outlet patch ③. Each patch is defined by a B-spline at hub and shroud with an underlying set of control points. The coordinates of the control points are the geometrical parameters which can be modified by the optimization program and the possible variation in axial and radial direction is indicated by arrows in Fig. 4. The inlet width of the meridional flow path remains unaltered in order to avoid a redesign of the junction to the scroll. However, the outlet width of the turbine wheel is a free design parameter which is controlled by the last control point of the outlet patch and a series of dependent parameters at

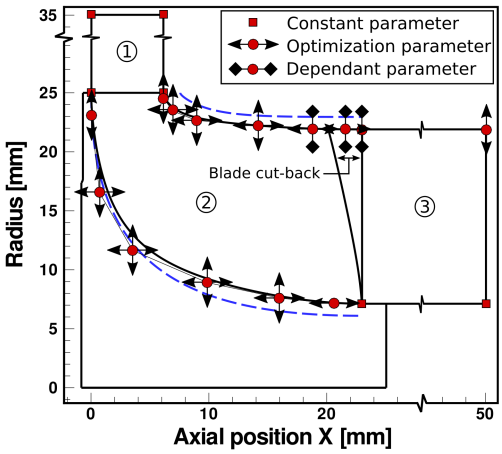

Figure 4: **Parametrization of the meridional flow path with three patches ①-③. Dashed lines at hub and shroud represent constant curves where the blade thickness is specified.**

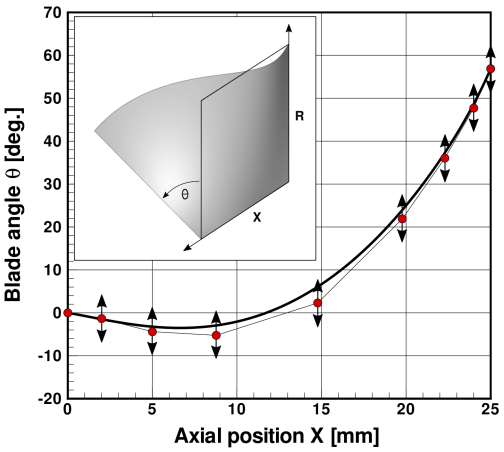

Figure 5: **Blade angle θ parametrization.**

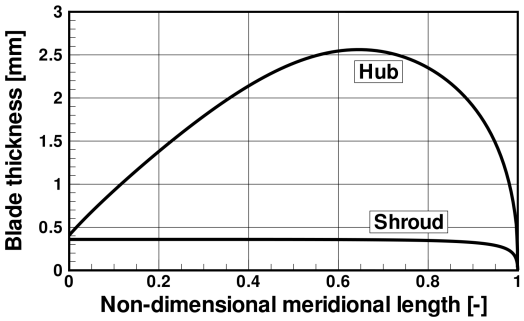

Figure 6: **Blade thickness at hub and shroud curve illustrated in Fig. 4.**

the shroud (indicated by diamond shaped arrows in Fig. 4). The position of the blade in the meridional plane is decoupled from the flow path and kept constant within this design study.

The camber line surface of the radial blading is defined by a blade angle θ-distribution with respect to the meridional plane along the machine axis (Fig. 5). Eight degrees of freedom are used for the blade angle distribution which allows a large shape variation, while guaranteeing the geometric constraint of radial blade fibers.

Next, the pressure side and suction side surfaces of the blade are constructed by adding a thickness distribution (Fig. 6) normal to the camber line surface and intersecting both blade sides with the hub and shroud curves of the meridional flow path. The span-wise thickness distribution of the blade is linearly interpolated in between two constant curves at hub an shroud where the thickness distribution is specified (dashed lines in Fig. 4). The cut-back of the blade at the trailing edge is one additional design parameter which enables to reduce mechanical stresses close to the hub within the blade at the trailing edge. However, it is not used as free parameter in present optimization and kept constant to its original value which is illustrated in Fig. 4.

In total, 28 design variables have been selected for this optimization: 20 parameters for the hub and shroud curves of the meridional flow path and eight degrees of freedom for the blade angle θ-distribution. Each parameter can be modified within a given range by the optimization program. The blade thickness distribution, as well as turbine wheel diameter, its axial length and the number of blades have been kept constant.

5. Numerical Model

5.1. Flow Analysis

The flow solver, which has been developed in this PhD project, employs a cell-centered finite volume discretization on multiblock structured grids. The three dimensional compressible Reynolds-Averaged Navier-Stokes (RANS) equations are solved with an implicit time integration scheme accelerated by local time-stepping and multigrid. The fluid is considered as a calorically perfect gas and the eddy-viscosity hypothesis is

used to account for the effect of turbulence. Convective fluxes are computed using Roe's approximate Riemann solver [21] with a MUSCL-type reconstruction [22] of primitive variables to attain second order accuracy. Oscillations near shocks are suppressed by a van-Albada type limiter [23]. The numerical dissipation of the scheme is controlled by the entropy correction of Harten [24] for both linear and non-linear eigenvalues. Viscous fluxes are calculated with a central discretization scheme, while the negative Spalart-Allmaras turbulence model [25] is used for the turbulence closure problem assuming fully turbulent flow from the inlet ($Re_{inlet} \approx 300,000$ based on turbine wheel diameter). Boundary conditions are imposed weakly by utilizing the dummy cell concept [26].

Strong secondary flow motion, which are inevitable in radial turbines at various operating conditions, may prevent the flow solver to converge to a fully steady-state solution. Since this is an essential requirement for an adjoint-based optimization, the flow solver uses a method proposed in [16] that combines Runge-Kutta time-stepping and Krylov methods as smoother inside FAS multigrid. As illustrated in [16] the proposed algorithm (1) enables fully converged flow solutions for some cases where conventional algorithms would fail or (2) offers improved efficiency when applied to stable cases. For a generic m Runge-Kutta stage time stepping method the algorithm reads as

$$\begin{aligned}
\boldsymbol{W}_c^{(0)} &= \boldsymbol{W}_c^{(n)} \\
\boldsymbol{P}^{-1}[\boldsymbol{W}_c^{(1)} - \boldsymbol{W}_c^{(0)}] &= -\alpha_1 \boldsymbol{R}(\boldsymbol{W}_c^{(0)}) \\
\boldsymbol{P}^{-1}[\boldsymbol{W}_c^{(2)} - \boldsymbol{W}_c^{(0)}] &= -\alpha_2 \boldsymbol{R}(\boldsymbol{W}_c^{(1)}) \qquad (1) \\
&\vdots \\
\boldsymbol{P}^{-1} \underbrace{[\boldsymbol{W}_c^{(m)} - \boldsymbol{W}_c^{(0)}]}_{\Delta \boldsymbol{W}_c^{(m)}} &= -\alpha_m \boldsymbol{R}(\boldsymbol{W}_c^{(m-1)}) \\
\boldsymbol{W}_c^{(n+1)} &= \boldsymbol{W}_c^{(n)} + \Delta \boldsymbol{W}_c^{(m)}
\end{aligned}$$

where α_m is the stage coefficient and $\boldsymbol{W}_c$ the vector of conservative variables. The non-linear residual $\boldsymbol{R}$ contains the spatial discretization of convective and viscous fluxes, the source term due to centrifugal forces and Coriolis effects, and all boundary conditions. The system matrix $\boldsymbol{P}^{-1}$ in Eqn. 1 is defined as

$$\boldsymbol{P}^{-1} = \frac{\Omega}{\Delta \mathrm{t}} \boldsymbol{I} + \frac{\partial \widetilde{\boldsymbol{R}}}{\partial \boldsymbol{W}_c} \qquad (2)$$

containing a 1st-order approximate jacobian of the non-linear residual ($\partial \widetilde{\boldsymbol{R}} / \partial \boldsymbol{W}_c$) and a time term in order to improve the diagonal dominance of the matrix. For computational efficiency, the system matrix is only computed in the first Runge-Kutta stage and reused subsequently. However, the linear system of equations in every Runge-Kutta stage is solved with an ILU(0)-preconditioned GMRES solver of the publicly available PETSc library [27]. Mean-flow and the turbulence model equations are loosely coupled. Equation 1 is applied to the mean-flow equations as smoother inside FAS-cycle multigrid, whereas the turbulent model is updated only on the finest grid level with a backward Euler method.

5.2. Discretization and Boundary Conditions

Figure 7 shows a slice of the computational grid of the radial turbine with a close-up of the blunt leading edge. In total, 96 layers of cells are used in span-wise direction, including 20 cells to model the tip clearance. Special care was given to grid independence of the flow solution to avoid any scatter of the results due to grid dependence. In order to meet common grid quality requirements the average wall-spacing is $y^+ \approx 1$ and the maximum cell expansion ratio is limited to 1.2 for 20 cells in blade normal direction. The computational cost has been reduced by modeling only one blade pitch and using periodic boundary conditions in circumferential direction. At the radial

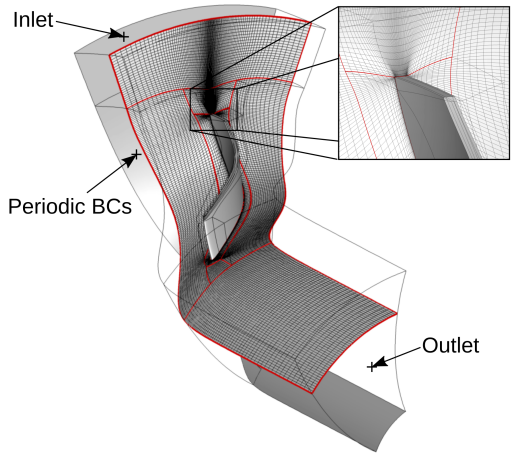

Figure 7: **Computational grid with a close-up of the blunt leading edge and trailing edge.**

inlet of the domain a uniform total pressure, total temperature, and flow angles are prescribed, while at the outlet the radial-equilibrium pressure distribution is used by imposing the static pressure at a reference radius. The solid surfaces (blade surfaces and endwalls) are considered adiabatic with the no-slip velocity condition.

5.3. Adjoint-Based Sensitivity Analysis

In the present work, the adjoint technique [28] is used to compute the sensitivities of the objective function with respect to the design parameters ($dJ/d\boldsymbol{\alpha}$), where $\boldsymbol{\alpha}$ is the set of design variables introduced in Sec. 4. The objective function, e.g. the aerodynamic performance of the machine, is a function of the flow solution $\boldsymbol{W}_c$ and of the computational grid $\boldsymbol{X}(\boldsymbol{\alpha})$, which is defined by the design variables $\boldsymbol{\alpha}$:

$$J = J(\boldsymbol{W}_c(\boldsymbol{X}(\boldsymbol{\alpha})), \boldsymbol{X}(\boldsymbol{\alpha})). \tag{3}$$

As indicated in Eqn. 3, the flow solution itself also depends on the design variables through the coordinates of the computational grid. This relation is determined by the nonlinear flow solver, when the converged flow solution satisfies the flow equations and all boundary conditions

$$\boldsymbol{R}(\boldsymbol{W}_c(\boldsymbol{X}(\boldsymbol{\alpha})), \boldsymbol{X}(\boldsymbol{\alpha})) = 0. \tag{4}$$

Therefore, the design variable sensitivity can be computed by applying the chain rule as

$$\frac{dJ}{d\boldsymbol{\alpha}} = \underbrace{\left[\frac{\partial J}{\partial \boldsymbol{X}} + \boldsymbol{\psi}^T \frac{\partial \boldsymbol{R}}{\partial \boldsymbol{X}}\right]}_{\frac{dJ}{d\boldsymbol{X}}} \frac{d\boldsymbol{X}}{d\boldsymbol{\alpha}} \tag{5}$$

where $\boldsymbol{\psi}$ is the adjoint or co-state vector that satisfies the adjoint equations

$$\left[\frac{\partial \boldsymbol{R}}{\partial \boldsymbol{W}_c}\right]^T \boldsymbol{\psi} = -\left[\frac{\partial J}{\partial \mathbf{W}_c}\right]^T. \tag{6}$$

Equation 6 is a linear system which defines the discrete adjoint equations of the optimization problem. It depends on the function of interest J and is solved next to the flow equations using the converged flow solution of the primal flow solver. Thus, each objective and constraint function requires a separate adjoint calculation.

The computational cost to compute the design variable sensitivities ($dJ/d\boldsymbol{\alpha}$) by Eqn. 5 depends on the number of design parameters through the sensitivity of the grid coordinates w.r.t. the design variables ($d\boldsymbol{X}/d\boldsymbol{\alpha}$), which represents the differentiation of the geometry and grid generation and is currently approximated by central finite differences.

In practice, the adjoint equations (Eqn. 6) are not solved with a direct solver due to memory limitations for large three-dimensional cases. Instead, the discrete adjoint solver uses the same time marching method as the primal flow solver

$$\begin{aligned}
\boldsymbol{\psi}^{(0)} &= \boldsymbol{\psi}^{(n)} \\
\boldsymbol{P}^{-T}[\boldsymbol{\psi}^{(1)} - \boldsymbol{\psi}^{(0)}] &= -\alpha_1 \boldsymbol{R}_\psi(\boldsymbol{W}_c, \boldsymbol{\psi}^{(0)}) \\
\boldsymbol{P}^{-T}[\boldsymbol{\psi}^{(2)} - \boldsymbol{\psi}^{(0)}] &= -\alpha_2 \boldsymbol{R}_\psi(\boldsymbol{W}_c, \boldsymbol{\psi}^{(1)}) \\
&\vdots \\
\boldsymbol{P}^{-T} \underbrace{[\boldsymbol{\psi}^{(m)} - \boldsymbol{\psi}^{(0)}]}_{\Delta\boldsymbol{\psi}^{(m)}} &= -\alpha_m \boldsymbol{R}_\psi(\boldsymbol{W}_c, \boldsymbol{\psi}^{(m-1)}) \\
\boldsymbol{\psi}^{(n+1)} &= \boldsymbol{\psi}^{(n)} + \Delta\boldsymbol{\psi}^{(m)}
\end{aligned} \tag{7}$$

where $\boldsymbol{P}^{-T}$ represents the transposed system matrix of the primal flow solver (Eqn. 2) and $\boldsymbol{R}_\psi$ the adjoint residual defined as:

$$\boldsymbol{R}_\psi = \left[\frac{\partial J}{\partial \boldsymbol{W}_c}\right]^T + \left[\frac{\partial \boldsymbol{R}}{\partial \boldsymbol{W}_c}\right]^T \boldsymbol{\psi}. \tag{8}$$

With this approach, the differentiated nonlinear residual ($\partial \boldsymbol{R}/\partial \boldsymbol{W}_c$), which is a large and sparse matrix, is computed on-the-fly and directly multiplied by the adjoint vector $\boldsymbol{\psi}$ in Eqn. 8. This reduces the memory consumption since no matrix has to be stored. Moreover, convergence of the adjoint solver is guaranteed provided the primal flow solver converges asymptotically [29; 30; 16].

This is illustrated in Fig. 8 which shows the convergence history of the normalized primal and adjoint density residual of a radial turbine simulation using Eqns. 1 and 7 with three Runge-Kutta stages on three multigrid levels. As can be seen, both residuals have the same rate of convergence after the coarse grid initialization with a residual reduction of about 14 orders of magnitude until the simulations were terminated. For computational efficiency, it is sufficient to run less iterations to obtain an accurate gradient which is shown in Fig. 8 by the evolution of entropy gradient with respect to the 4th design variable ($dJ/d\alpha_4$). As can be seen, after approximately 300 multigrid-cycles the entropy gradient does not change significantly and it is therefore considered sufficiently accurate.

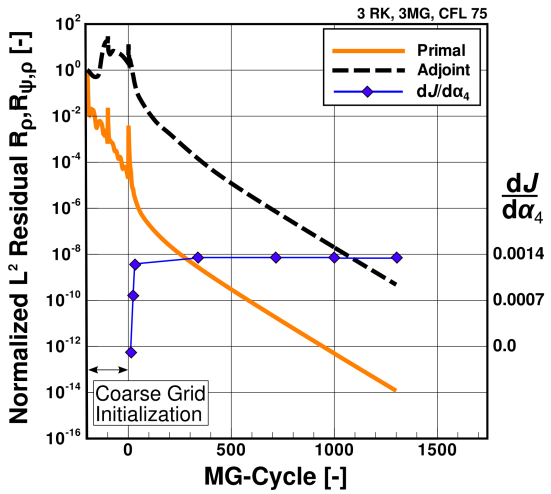

Figure 8: **Convergence plot of normalized $\mathbf{L^2}$ primal residual $\overline{\boldsymbol{R}}_\rho$ and adjoint residual $\overline{\boldsymbol{R}}_{\psi,\rho}$ of the continuity equation and evolution of entropy gradient with respect to the 4th design variable ($dJ/d\alpha_4$).**

The differentiation of non-linear residual ($\partial \boldsymbol{R}/\partial \boldsymbol{W}_c$) is the most time consuming part of the development of an adjoint solver. In this work, it is partly hand coded partly computed by algorithmic differentiation. In particular, the Jacobians due to Roe's approximate Riemann solver are differentiated using TAPENADE [31] in forward mode. Moreover, to simplify the development of the discrete adjoint solver the turbulence model is not differentiated and the constant eddy viscosity (CEV) assumption is applied. Although it is a rather crude approximation and may cause inaccurate gradients in the design of transonic blades with strong shocks [32], studies have shown that although gradients may differ the CEV assumption is a valid approach in engineering applications as the optimization convergences to nearly identical solutions [32; 20].

6. Objectives and Constraints

The present optimization is aiming at improving the aerodynamic performance of the radial turbine at design conditions by minimizing the mass-flow averaged entropy generation rate between inlet and outlet of the domain

$$Obj: \quad \Delta s = \frac{s_{out} - s_{in}}{s_{ref}}, \quad s = \frac{P}{\rho^\gamma} \tag{9}$$

where the reference entropy s_{ref} is computed with the constant total inlet conditions. The objective is subject to two constraints to retain the design operating conditions of mass flow and total pressure ratio. This can be formulated as follows

$$Constr1: \quad 1 - \frac{\dot{m}}{\dot{m}_{ref}} \leq 0 \tag{10}$$

$$Constr2: \quad 1 - \frac{\pi_{TT}}{\pi_{TT,ref}} \leq 0 \tag{11}$$

with the reference mass flow and total pressure ratio of the baseline design.

7. Results and Discussion

7.1. Gradient Verification

The adjoint-based gradients ($dJ/d\boldsymbol{\alpha}$) have been compared with central finite differences which is illustrated in Fig. 9 for both the objective function gradients (top) and constraint function gradients of mass flow (middle) and pressure ratio (bottom). In total, 56 CFD simulations were necessary to compute the gradient vectors using central finite-differences while only four simulations (1 CFD + 3 Adjoint) were required to get the corresponding adjoint-based gradient vectors.

Overall, the adjoint-based gradients and the finite-difference gradients agree well, keeping in mind that finite difference gradients are itself prone to errors by truncation and subtraction errors depending on the chosen step size. In particular the errors introduced due to finite differences for the geometry and grid generation are rather large for certain design parameters. Therefore, a next step in this PhD project is to replace the grid generation, which is currently done by a commercial software, by an in-house developed code. This would allow to differentiate the code using algorithmic differentiation which would improve the quality of the gradients and eliminates the dependence on the step size.

8. Conclusions

This paper describes an adjoint-based aerodynamic design optimization of a turbocharger radial turbine aiming at improving the aerodynamic performance at design operating conditions while constraining mass flow and pressure ratio of the

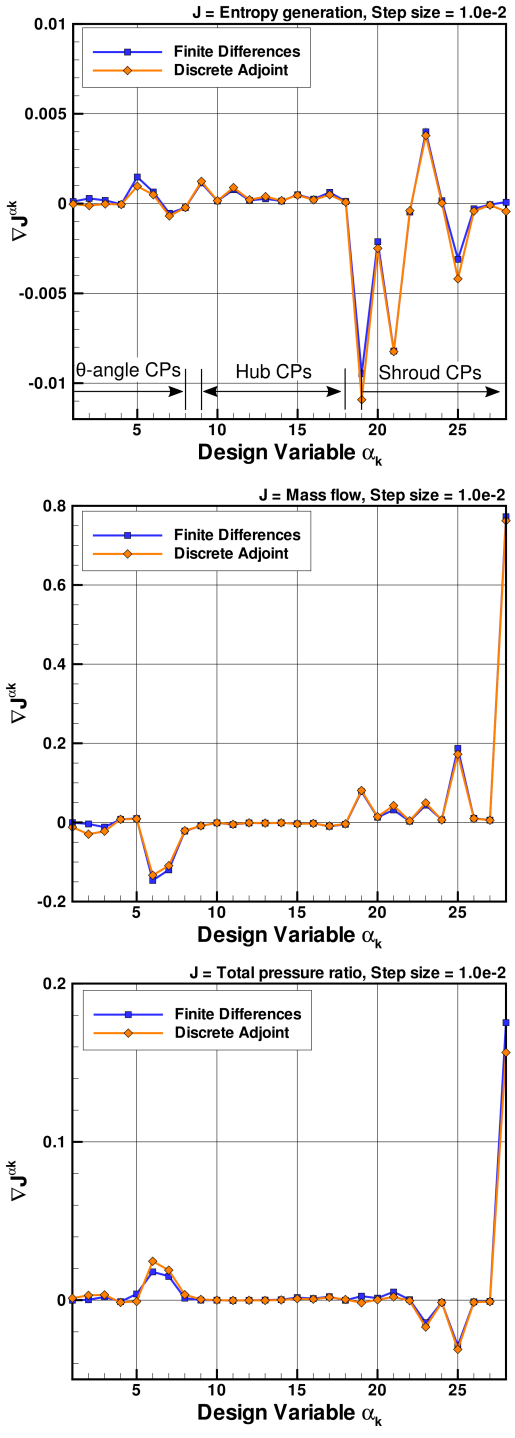

Figure 9: **Comparison of adjoint-based gradients (Adjoint) and gradients computed by central finite differences (FD) for entropy generation (top), mass flow (middle), total pressure ratio (bottom).**

machine. The core components of the optimization system are a newly developed 3D multiblock structured Navier-Stokes solver, the corresponding discrete adjoint solver and a sequential quadratic programming optimization algorithm.

A dedicated CAD-based parametrization has been proposed which inherently satisfies a geometric constraint of radial fibred blades that is imposed to the design due to mechanical restrictions. In addition, it allows to incorporate other constraints such as minimal thickness of the blade and axial length of the machine.

The adjoint-based gradients have been verified and are in fair agreement with finite difference gradients. However, to further improve the quality of the adjoint-based gradients, a next step in this PhD project is to replace the grid generation, which is currently done by a commercial software, by an in-house developed code. This would allow to differentiate the code using algorithmic differentiation which would improve the quality of the gradients and eliminate the errors due to finite difference approximations and the dependence on the step size.

References

[1] Vanderplaats G.N., Numerical Optimization Techniques for Engineering Design, Vanderplaats Research and Development, Inc, 2001.

[2] Mueller L.; Alsalihi Z.; Verstraete T., Multidisciplinary Optimization of a Turbocharger Radial Turbine, J. Turbomach. 135 (2) (2013) 9 pages.

[3] Shahpar S.; Caloni S., Aerodynamic Optimization of High-Pressure Turbines for Lean-Burn Combustion System, J. Eng. Gas Turbines Power 135 (5).

[4] Joly M.; Verstaete T.; Paniagua G., Multidisciplinary Design Optimization of a Compact Highly Loaded Fan, Structural and Multidisciplinary Optimization 49 (3) (2014) 471–483.

[5] Zingg D.W.; Nemec M.; Pulliam T.H., A Comparative Evaluation of Genetic and Gradient-Based Algorithms Applied to Aerodynamic Optimization, European Journal of Computational Mechanics 17 (1-2) (2008) 103–126.

[6] Pironneau O., On optimum design in fluid mechanics, Journal of Fluid Mechanics 64 (1974) 97–110.

[7] Jameson A., Aerodynamic Design Via Control Theory, Journal of Scientific Computing 3 (3) (1988) 233–260.

[8] Jameson A., Optimum Aerodynamic Design using CFD and Control Theory, AIAA-95-1729-CP (1995).

[9] Jameson A., VKI Lecture Series on Aerodynamic Drag Prediction and Reduction, von Karman Institute for Fluid Dynamics, 2003, Ch. Aerodynamic Shape Optimization Using the Adjoint Method.

[10] Giles M.; Pierce N.A., Adjoint Equations in CFD: Duality, Boundary Conditions and Solution Behaviour, AIAA Journal.
[11] Palacios F.; Economon T.D.; Wendorff A.D.; Alonso J.J., Large-scale aircraft design using SU2, AIAA SciTech (2015).
[12] Duta M.C.; Shahpar S.; Giles M.B., Turbomachinery Design Optimisation using Automatic Differentiated Adjoint Code, in: Proceedings of GT2007, no. GT2007-28329.
[13] Wang D.X.; He L., Adjoint Aerodynamic Design Optimization for Blades in Multi-Stage Turbomachines: Part I - Methodology and Verification, Journal of Turbomachinery 132 (2) (2010) 14 pages.
[14] Walther B.; Nadarajah S., Constrained Adjoint-Based Aerodynamic Shape Optimization of a Single-Stage Transonic Compressor, Journal of Turbomachinery 135.
[15] Shahpar S.; Caloni S., Adjoint Optimisation of a High Pressure Turbine Stage for Lean-Burn Combustion System, 10th European Conference on Turbomachinery, Fluid Dynamics and Thermodynamics, 15-19 April 2013, Lappeenranta, Finland. (2013).
[16] Xu S.; Radford D.; Meyer M.; Müller J.-D., Stabilisation of Discrete Steady Adjoint Solvers, Journal of Computational Physics 299 (2015) 175–196.
[17] J. Kammeyer, C. Natkaniec, J. Seume, Tip Leakage in Small Radial Turbines – Optimum Tip-Gap and Efficiency Loss Correlations, in: ASME Turbo Expo 2010, no. GT2010-22680.
[18] Gill P.E., Murray W., Saunders M.A., User's Guide for SNOPT Version 7: Software for Large-Scale Nonlinear Programming (2008).
[19] Gill P.E., Murray W., Saunders M.A., An SQP algorithm for Large-Scale Constrained Optimization, SIAM J. Optim. 12 (2002) 979–1006.
[20] Marta A.C.; Shankaran S., On the Handling of Turbulence Equations in RANS Adjoint Solvers, Computer & Fluids 74 (2013) 102–113.
[21] Roe P.L., Approximate Riemann Solvers, Parameter Vectors, and Difference Schemes, Journal of Computational Physics 43 (1981) 357–372.
[22] van Leer B., Towards the Ultimate Conservative Difference Scheme, V. A Second Order Sequel to Godunov's Method, Journal of Computational Physics 32 (1) (1979) 101–136.
[23] Venkatakrishnan V., On the Accuracy of Limiters and Convergence to Steady State Solutions, in: AIAA Conference, no. 93-0880, 1993.
[24] Harten A.; Hyman J.M., Self-Adjusting Grid Methods for One-Dimensional Hyperbolic Conservation Laws, Journal of Computational Physiscs 50 (2) (1983) 235–269.
[25] Allmaras S.R.; Johnson F.T.; Spalart P.R., Modifications and Clarifications for the Imlementation of the Spalart-Allmaras Turbulence Model, in: ICCFD7-1902, 7th International Conference on Computational Fluid Dynamics, 2012.
[26] Blazek J., Computational Fluid Dynamics: Principles and Applications, 2nd Edition, Elsevier Science Ltd, Amsterdam, 2001.
[27] S. Balay, S. Abhyankar, M. F. Adams, J. Brown, P. Brune, K. Buschelman, V. Eijkhout, W. D. Gropp, D. Kaushik, M. G. Knepley, L. C. McInnes, K. Rupp, B. F. Smith, H. Zhang, PETSc Web page, http://www.mcs.anl.gov/petsc (2014).
URL `http://www.mcs.anl.gov/petsc`
[28] Giles M.B.; Pierce N.A., An Introduction to the Adjoint Approach to Design, Flow,Turbulence and Combustion 65 (2000) 393–415.
[29] Nielsen E.J.; Lu J.; Park M.A.; Darmofal, D.L., An implicit, exact dual adjoint solution method for turbulent flows on unstructured grids, Computer & Fluids 33 (2004) 1131–1155.
[30] Dwight R.; Brezillon J.; Vollmer D., Efficient algorithms for solution of the adjoint compressible Navier-Stokes equations with applications, in: Proceedings of the ONERA-DLR Aerospace Symposium (ODAS), 2006.
[31] L. Hascoët, V. Pascual, The Tapenade Automatic Differentiation tool: Principles, Model, and Specification, ACM Transactions On Mathematical Software 39 (3).
URL `http://dx.doi.org/10.1145/2450153.2450158`
[32] Kim C.S.; Kim C.; Rho O.H., Feasibility Study of Constant Eddy-Viscosity Assumption in Gradient-Based Design Optimization, Journal of Aircraft 40 (6) (2003) 1168–1176.

9. Nomenclature

Latin

$\overline{\boldsymbol{I}}$	Identity matrix
J	Function of interest, Cost-Function
P	Static pressure
$\boldsymbol{R}$	Residual vector
S	Meridional length
$\boldsymbol{W}_c$	Vector of conservative variables
$\boldsymbol{X}$	Vector of grid coordinates

Greek

$\boldsymbol{\alpha}$	Vector of design variables
Δ	Delta/difference
Δt	Time step
ρ	Density
$\boldsymbol{\psi}$	Adjoint vector/co-state vector

Subscripts and Superscripts

$1, 2$	Inlet,outlet
ref	Reference

AD	Algorithmic Differentiation
CAD	Computer Aided Design
CFD	Computational Fluid Dynamics
CEV	Constant Eddy Viscosity
CP	Control Point
Constr	Constraint
Obj	Objective
MUSCL	Monotonic Upstream-Centered

	Scheme for Conservation Laws
PETSc	Portable, Extensible Toolkit for Scientific Computation
RANS	Reynolds-Averaged Navier-Stokes
SNOPT	Sparse Nonlinear OPTimizer
SQP	Sequential Quadratic Programming

CAD based adjoint optimization of turbomachinery components using automatic differentiation

Ismael Sànchez Torreguitart

Turbomachinery and Propulsion Department, von Karman Institute for Fluid Dynamics, Belgium, ismael.sanchez.torreguitart@vki.ac.be

Supervisor: Tom Verstraete

Associate Professor, Turbomachinery and Propulsion Department, von Karman Institute for Fluid Dynamics, Belgium, tom.verstraete@vki.ac.be
Visiting Professor, School of Engineering and Material Science, Queen Mary University Of London, UK, t.verstraete@qmul.ac.uk

Abstract

Adjoint based optimization methods have been introduced for more than 2 decades and have witnessed a tremendous improvement over time. Although they have numerous advantages such as efficient computation of the gradient, large number of design variables, and mathematical convergence towards the (local) optimum, the methods are not yet picked up largely by industry. One major bottleneck herein is that adjoint methods mainly work on deforming the CFD grid and as such loose the connection to CAD, the industry adopted standard for the design of components. After the optimization a step is required which transforms the optimal shape, defined by grid points, back to a smooth CAD shape. This step is complicated, not easily automated and invariably impairs optimality of the shape as CAD systems will only approximate the optimal shape.
This work aims to alleviate this problem by expressing the optimization problem through NURBS [1] parameters, which are commonly used in CAD, rather than working directly on the CFD grid. It means that the optimal shape remains defined within the CAD tool. It also means that grid sensitivities will need to be propagated to the CAD-based parameters, requiring the CAD kernel and the grid generation tool to be differentiated. The differentiation is going to be done using ADOL-C [2], which is an Automatic Differentiation (AD) tool written in C/C++ that uses overloaded operators and functions. One distinguishes between the forward and reverse mode of AD depending on whether the starting point of the differentiation process occurs at the beginning or the end of the design chain. Both modes allows to accurately computing the exact sensitivities with the best possible machine accuracy. In the forward mode the computational time and storage cost is proportional to the number of design variables, whereas in reverse mode the computational speed is not proportional to the number of design variables but to the number of output (dependent) parameters instead. The ultimate aim is to do the differentiation in reverse mode (adjoint) as this approach is very attractive for the freedom to have an unlimited number of design variables in a CFD optimization algorithm. However, a forward differentiation framework will be developed first in order to validate the sensitivities obtained in reverse mode. Once the AD sensitivities are obtained in forward mode, they will be compared against Finite Differences (FD) second order central derivatives by tuning the step size. After obtaining a reasonable agreement between the FD and AD sensitivities for an appropriate step size, the AD differentiated CAD kernel and grid generation tool will be integrated in a real CFD adjoint based optimization algorithm. The VKI LS89 axial turbine aerofoil [3; 4; 5] is selected to test the methodology on a 2D case as a first demonstrator but extensions to more complex 3D industrial turbomachinery shapes are going to be tested next.

Keywords: CAD kernel, grid generation, Automatic Differentiation, adjoint optimization, sensitivities

References

[1] L. Piegl, W. Tiller, The NURBS book, Springer Science & Business Media, 2012.

[2] A. Walther, A. Griewank, A package for the automatic differentiation of algorithms written in c/c+, URL https://projects. coin-or. org/ADOL-C.

[3] R. Van den Braembussche, O. Léonard, L. Nekmouche, Sub-

sonic and transonic blade design by means of analysis codes, Computational Methods for Aerodynamic Design (Inverse) and Optimization, AGARD CP 463.

[4] T. Arts, M. L. De Rouvroit, Aero-thermal performance of a two dimensional highly loaded transonic turbine nozzle guide vane: A test case for inviscid and viscous flow computations, in: ASME 1990 International Gas Turbine and Aeroengine Congress and Exposition, American Society of Mechanical Engineers, 1990, pp. V001T01A106–V001T01A106.

[5] T. Arts, M. Lambertderouvroit, A. Rutherford, Aero-thermal investigation of a highly loaded transonic linear turbine guide vane cascade. a test case for inviscid and viscous flow computations, NASA STI/Recon Technical Report N 91 (1990) 23437.

Adjoint optimization of turbomachinery components under mechanical constraints

Marc Schwalbach

Turbomachinery and Propulsion Department, von Karman Institute for Fluid Dynamics, Belgium, marc.schwalbach@vki.ac.be

Supervisor: Tom Verstraete

Associate Professor, Turbomachinery and Propulsion Department, von Karman Institute for Fluid Dynamics, Belgium, tom.verstraete@vki.ac.be
Visiting Professor, School of Engineering and Material Science, Queen Mary University Of London, UK, t.verstraete@qmul.ac.uk

University Supervisor: Nicolas R. Gauger

Professor, Chair for Scientific Computing, Head of Computing Center (RHRK), TU Kaiserslautern, Germany, nicolas.gauger@scicomp.uni-kl.de

Abstract

In the present day, multidisciplinary optimizations using gradient-free methods are widely used in academia and industry. However, the limitations of these methods are becoming apparent due to the curse of dimensionality. Gradient-based optimization methods using adjoints offer an efficient alternative with a computational cost independent on the size of the design space. In the field of turbomachinery, most gradient-based multidisciplinary optimizations are currently based solely on aerodynamic cost functions and constraints. A structural stress analysis is usually performed after the aerodynamic shape optimization to verify the structural feasibility of the optimized shape. As a result, the optimized shape may be aerodynamically optimal, but structurally unfeasible. This could lead to costly trial-and-error iterations in the design process, which can be avoided if the structural constraints are taken into account during the optimization procedure.

In order to include structural constraints in the optimization process, gradient-based optimization methods require the sensitivities of structural quantities of interest with respect to the design variables. However, the computation of these gradients comes at a high computational cost using approximation methods such as finite differences. The same gradients can be computed at a significantly lower computational cost, and with a higher accuracy, using the *adjoint* method. One way of obtaining the adjoints is by using the so-called discrete approach, for which the structural solver has to be differentiated using *algorithmic differentiation* (AD; also known as *automatic differentiation* or *computational differentiation*). Particularly in turbomachinery, an additional complexity known as the *cold-to-hot* transformation has to be taken into account. Components, such as e.g. turbine blades, deform due to the pressure and centrifugal forces during running conditions. As a result, the running *hot* shape differs from the manufactured *cold* shape. This deformation leads to an untwisting of the blades and a reduction of clearance space, which can have a substantial effect on the performance.

Typically, the optimization procedure is performed using a master geometry in the *hot* state and the transformation to the *cold* state is computed a posteriori using a *hot-to-cold* transformation. However, this does not take into account different design points, each with different loads and thus, a different deformation. In this PhD thesis, an approach will be developed which parametrizes the *cold* state and deforms to the *hot* shape within the optimization loop. This will allow the optimization of the *cold* state design parameters directly, rather than a posteriori, for arbitrary design points. To this end, a structural solver combined with a cold-to-hot transformation has to be differentiated. Preliminary results show the successful implementation of an adjoint cold-to-hot CAD transformation tool. This tool allows the transformation of the CAD geometry based on FEM displacements, as well as the computation of the CAD control point sensitivities with respect to FEM displacements using adjoint AD.

Keywords: adjoints, optimization, algorithmic differentiation, C++, turbomachinery, CAD

Full rotor CFD simulations of two wind turbines in a row using RANS

Nikolaos Stergiannis*

Environmental and Applied Fluid Dynamics, von Karman Institute for Fluid Dynamics, Belgium, nstergiannis@gmail.com

Jeroen van Beeck

Professor, Environmental and Applied Fluid Dynamics, von Karman Institute for Fluid Dynamics, Belgium, vanbeeck@vki.ac.be

Chris Lacor

Professor, Department of Mechanical Engineering, Fluid Dynamics and Thermodynamics Research Group, Vrije Universiteit Brussel, Belgium

Rory Donnelly

Industrial Supervisor, 3E S.A., iLab Department, Belgium

Abstract

Numerical simulations of two wind turbine generators including the exact geometry of their blades and hub are compared against a simplified actuator disk model (ADM). The wake expansion of the upstream rotor is investigated and compared with measurements. Computational Fluid Dynamics (CFD) simulations have been performed using the open-source platform OpenFOAM [1]. The multiple rotating frame (MRF) approach used to model the inner rotating reference frames in a stationary computational mesh and outer reference frame. The standard $k-\omega$ turbulence closure scheme has been used to solve the steady state, three dimensional Reynolds Averaged Navier-Stokes (RANS) equations for the full rotor CFD simulations. For the case of ADM, $k-\varepsilon$ performed better against other turbulent models and was used in a fine computational mesh. Results of near and far wake downstream are compared with wind tunnel measurements along two horizontal lines downstream. Full rotor simulations showed good agreement against the experimental data and amplifying the differences between the simplified models.

Keywords: CFD, OpenFOAM, RANS, MRF, ADM, wind turbine, wake effects.

1. Introduction

1.1. Wind energy and CFD

Wind energy is one of the first renewable energies that humans used over the years. The great potential of using that energy source was recognized early by extracting the power of wind in order to sail.

Nowadays, following the increasing demand of the world for more clean energy, humans harvest the wind in order to produce electricity. In line with the climate change and the new worldwide horizons for more environmental friendly energy sources, wind energy has become one of the fastest growing industries. Wind turbines are growing continuously in size and are clustered in wind farms in order to produce more electricity.

As this rapid development is reaching the design limits of the available materials, the critical optimization process is on the Operational and Capital Expenses (OPEX & CAPEX) and on the total power production. Apart from the complex terrain effects, the uncertainties of the wind flow variables and the instabilities of the Atmospheric Boundary Layer, the wind turbines that operate in a wind farm will also deal with wake effects and their interaction. Part of the wind power is extracted from a wind turbine and as a result a velocity deficit with increased levels of turbulence is developing downstream.

*Corresponding author. Tel:+32 484.55.28.10

Email address: nikolaos.stergiannis@vki.ac.be, nstergiannis@gmail.com (Nikolaos Stergiannis)

The so called wake effects are of great importance in wind farms since they can cause total power losses up to 30% [2; 3; 4]. The clustered wind turbines that are in a row will be affected from the upstream flow of a wake, causing power losses and unexpected loads from the turbulence fluctuations . To optimize the wind farms and reach the maximum potential production of installed wind turbines within a limited sized area, we have to understand the physics involved at the process and be able to predict in advance the wake expansion. In addition, early estimation of the wake characteristics can optimize the wind farm layout and so the downstream wind turbines can work in better conditions reducing the number of failures and as a sequence the OPEX.

Several linear mathematical models have been developed in order to predict such flows. Yet, all the models include assumptions and simplifications following experimental observations. Computational Fluid Dynamics (CFD), instead, provide more sophisticated methods, such as the Reynolds Averaged Navier Stokes (RANS) equations, that can resolve the wind flow more accurately [5],. Following the trend of technological growth, the computational cost will continue to decrease on the years to come. Hence, the usage of CFD will be economically affordable for optimizing industrial applications. Over the last decades the CFD scientific community is growing and so on the ongoing research on turbulence modeling, numerical schemes, numerical methods and models, time and spatial filtering of fluid dynamics equations.

CFD simulations can be performed on both steady and unsteady state problems. It is common and acceptable, within limitations, the assumption of using a steady state approach to resolve a time-varying (unsteady state) problem when someone is interesting in the mean values of the flow that are statistically observed in time. RANS equations can then be used in order to extract such information for a simulated flow. The main mathematical challenge of the turbulence closure problem can be resolved by modeling all the turbulence length scales of a flow with a turbulence model [6; 7]. More advanced methods can either model only part of the turbulence length scales using Detached Eddy Simulation (DES), Large Eddy Simulation (LES) or resolve all of them using Direct Numerical Simulation (DNS). Unfortunately, less modeling assumptions increase the computational cost. The majority of the industrial applications includes turbulence flows of high Reynolds number, making the use of DNS impossible with the existing computers.

1.2. The 4th blind test experiment

The 4th Blind Test (BT4) experiment (Figure 1) was organized by NOWITECH and NORCOWE in 2015. The total power output from two in-line turbines was investigated under the influence of different inlet conditions and turbine separation distance. [8].

The axial separation distance between the turbines was set to $x/D = 2.77$, $x/D = 5.18$ and $x/D = 9.00$, where the diameter $D = 0.894m$. Furthermore, three different inflow conditions at the inlet of the test section were tested:

- Low turbulence uniform inflow: No grid at the inlet to the test section. At the position of the upstream turbine the turbulence intensity measured is $TI = 0.23\,\%$. The mean wind speed is uniform across the test section, apart from small wall boundary layer effects.
- High turbulence uniform inflow: An evenly spaced turbulence gird at the tunnel inlet generates a higher turbulence intensity level of $TI = 10.0\,\%$ at the location of the upstream turbine. The mean wind speed is uniform across the test section.
- High turbulence shear inflow: A turbulence grid with increasing vertical distance between the horizontal bars is installed at the inlet of the test section. This is creating a non-uniform shear flow with a mean turbulence intensity of $TI = 10\,\%$ over the rotor swept area of the upstream turbine.

The high Turbulence Intensity (TI) CASE-B was tested on three different downstream axial separation distances of $x/D = 2.77$, $x/D = 5.18$ and $x/D = 9$, where the diameter $D = 0.894\,m$. In our study, CASE-B3 of high TI and $x/D = 9$ axial separation distance was chosen to eliminate the impact of the second wind turbine at the single wake expansion of the first and because more measured data were available downstream. A uniform velocity profile of $11.5\,m/s$ similar to the experiment for the CASE-B3 was considered. The two wind turbines are constructed with the same aluminum blades, using the NREL S826 airfoil section from root to tip.

2. Mathematical model

2.1. Statement of the problem

The physical problem under investigation is the flow over two identical wind turbines in a row under

controlled conditions of a wind tunnel. The current study is focusing on the wake expansion and prediction by different CFD approaches.

2.2. Governing equations

The governing equations solved of the flow field are the continuity and conservation of momentum equations:

$$\frac{\partial \rho}{\partial t} + \nabla \cdot (\rho \vec{u}) = 0 \tag{1}$$

$$\frac{\partial (\rho \vec{u})}{\partial t} + u \cdot \nabla (\rho \vec{u}) = -\nabla p + \nabla \cdot \tau + S_M \tag{2}$$

Where ρ is the air density, $\vec{u}$ is the fluid velocity vector, p the pressure, τ the shear stress tensor and S_M a momentum source term. The stress tensor, is related to the strain rate as:

$$\tau = \mu \left[\nabla \vec{u} + (\nabla \vec{u})^{\tau} - \frac{2}{3} \cdot \delta \cdot \nabla \vec{u} \right] = 0 \tag{3}$$

where δ is Kronecker's delta and μ is the dynamic viscosity of the fluid.

2.3. The Multiple Rotating Frame (MRF) formulation

The multiple rotating frame (MRF) approach was used to model the inner rotating reference frame in a stationary outer computational mesh and reference frame.

A position vector $\vec{r}$ can be expressed by the acceleration term for a rotating frame Ω as:

$$\left[\frac{d\vec{r}}{dt} \right]_{inertial} = \left[\frac{d\vec{r}}{dt} \right]_{rotating} + \vec{\Omega} \times \vec{A} \tag{4}$$

The absolute velocity of the inertial frame, using the notation i for inertial and r for rotating, can be expressed as:

$$\vec{u}_i = \vec{u}_r + \vec{\Omega} \times \vec{r} \tag{5}$$

Following the same notation, the incompressible Navier-Stokes equations for steady flow in multiple frames of reference can be written in terms of absolute velocity at the inertial frame of reference:

$$\nabla \vec{u}_i = 0 \tag{6}$$

$$\nabla \cdot (\vec{u}_i \otimes \vec{u}_i) = -\nabla \left(\frac{p}{\rho} \right) + \nu \nabla \cdot \nabla (\vec{u}_i) \tag{7}$$

and at the rotating frame of reference:

$$\nabla \vec{u}_i = 0 \tag{8}$$

$$\nabla \cdot (\vec{u}_r \otimes \vec{u}_i) + \vec{\Omega} \times \vec{u}_r = -\nabla \left(\frac{p}{\rho} \right) + \nu \nabla \cdot \nabla (\vec{u}_i) \tag{9}$$

2.4. Turbulence modeling

To model turbulence, several two-equation turbulence closure schemes were utilized. Those linear eddy viscosity models are using the Boussinesq assumption (Equation 10) for the Reynolds stresses:

$$\tau_{ij} = 2\mu_t \left(S_{ij} - \frac{1}{3} \frac{\partial u_k}{\partial x_k} \delta_{ij} \right) - \frac{2}{3} \rho k \delta_{ij} \tag{10}$$

where

$$S_{ij} = \frac{1}{2} \left(\frac{\partial u_i}{\partial x_j} + \frac{\partial u_j}{\partial x_i} \right) \tag{11}$$

- *$k - \varepsilon$ turbulence model*

The standard $k - \varepsilon$ model [9] despite is not a general neither a very accurate model but may sometimes lack accuracy it is one of the models most commonly used by the wind energy industry mainly because it has been widely tested over the years. It is based on model transport equations for the turbulence kinetic energy, k and its dissipation rate, ε. At high Reynolds numbers, the model uses the following transport equations:

$$\frac{Dk}{Dt} = \frac{1}{\rho} \frac{\partial}{\partial x_k} \left[\frac{\mu_t}{\sigma_k} \frac{\partial k}{\partial x_k} \right] + \frac{\mu_t}{\rho} \left(\frac{\partial U_i}{\partial x_k} + \frac{\partial U_k}{\partial x_i} \right) \frac{\partial U_i}{\partial x_k} - \varepsilon \tag{12}$$

$$\frac{D\varepsilon}{Dt} = \frac{1}{\rho} \frac{\partial}{\partial x_k} \left[\frac{\mu_t}{\sigma_\varepsilon} \frac{\partial \varepsilon}{\partial x_k} \right] + \frac{C_1 \mu_t}{\rho} \frac{\varepsilon}{k} \left(\frac{\partial U_i}{\partial x_k} + \frac{\partial U_k}{\partial x_i} \right) \frac{\partial U_i}{\partial x_k} - C_2 \frac{\varepsilon^2}{k} \tag{13}$$

The turbulent viscosity μ_t is calculated from equation 14 below:

$$\mu_t = \rho C_\mu \frac{k^2}{\varepsilon} \tag{14}$$

According to the recommendations of Launder et al [10] the standard constants of the $k-\varepsilon$ model are given in Table 1.

- *$k - \omega$ turbulence model*

The basic transport equations for this two-equation model [7; 11] are:

$$\frac{Dk}{Dt} = P - \beta^* \rho \omega k + \frac{\partial}{\partial x_j}\left[\left(\mu + \sigma_k \frac{\rho k}{\omega}\right)\frac{\partial k}{\partial x_j}\right] \quad (15)$$

$$\frac{D\omega}{Dt} = \frac{\gamma \omega}{k} P - \beta \rho \omega^2 + \frac{\partial}{\partial x_j}\left[\left(\mu + \sigma_\omega \frac{\rho k}{\omega}\right)\frac{\partial \omega}{\partial x_j}\right] \quad (16)$$

where

$$P = \tau_{ij} \frac{\partial u_i}{\partial x_j} \quad (17)$$

and τ_{ij} derived from Equations 10 and 11.

The turbulent viscosity μ_t is computed from the following expression:

$$\mu_t = \frac{\rho k}{\omega} \quad (18)$$

The default model constants for the $k-\omega$ turbulence model correspond to the values of Table 2.

The γ coefficient was chosen in order to yield an appropriate value for the von Karman constant ($\kappa \approx 0.41$), via the expression 19:

$$\gamma = \frac{\beta}{\beta^*} - \frac{\sigma_\omega \kappa^2}{\sqrt{\beta^*}} \quad (19)$$

- *$k - \omega$ SST turbulence model*

The expression for turbulence transport equation k, is identical to the standard Menter baseline two-equation model [12]. The model [13; 14] (written in conservation form) is given by the following two equations:

$$\frac{Dk}{Dt} = P - \beta^* \rho \omega k + \frac{\partial}{\partial x_j}\left[(\mu + \sigma_k \mu_t)\frac{\partial k}{\partial x_j}\right] \quad (20)$$

$$\frac{D\omega}{Dt} = \frac{\gamma}{\nu_t} P - \beta \rho \omega^2 + \frac{\partial}{\partial x_j}\left[(\mu + \sigma_\omega \mu_t)\frac{\partial \omega}{\partial x_j}\right] + 2(1 - F_1)\frac{\rho \sigma_{\omega 2}}{\omega}\frac{\partial k}{\partial x_j}\frac{\partial \omega}{\partial x_j} \quad (21)$$

Table 1: Constants of $k - \varepsilon$ turbulence model

C_μ	C_1	C_2	σ_k	σ_ε
0.09	1.44	1.92	1.0	1.3

Table 2: Constants of $k - \omega$ turbulence model

C_μ	σ_k	σ_ω	β^*	β	γ
0.09	0.5	0.5	0.09	0.072	0.52

where

$$F_1 = \tanh(arg_1^4) \quad (22)$$

$$arg_1 = \min\left[\max\left(\frac{\sqrt{k}}{\beta^* \omega d}, \frac{500\nu}{d^2 \omega}\right), \frac{4\rho\sigma_{\omega 2} k}{CD_{k\omega} d^2}\right] \quad (23)$$

$$CD_{k\omega} = \max\left(2\rho\sigma_{\omega 2}\frac{1}{\omega}\frac{\partial k}{\partial x_j}\frac{\partial \omega}{\partial x_j}, 10^{-20}\right) \quad (24)$$

with ρ the density, $\nu_t = \mu_t/\rho$ the turbulent kinematic viscosity, μ the molecular dynamic viscosity, d the distance from the field point to the nearest wall and P similar to Equation 17.

At the standard version of $k-\omega$ SST, the definition of eddy viscosity was given by the vorticity magnitude, following the expression:

$$\mu_t = \frac{\rho a_1 k}{\max(a_1 \omega, \Omega F_2)} \quad (25)$$

where the vorticity is given by:

$$\Omega = \sqrt{2 W_{ij} W_{ij}} \quad (26)$$

with

$$W_{ij} = \frac{1}{2}\left(\frac{\partial u_i}{\partial x_j} - \frac{\partial u_j}{\partial x_i}\right) \quad (27)$$

At the updated model of 2003 which was also used in the current paper, the eddy viscosity is derived from the strain invariant, such as:

$$\mu_t = \frac{\rho a_1 k}{\max(a_1 \omega, S F_2)} \quad (28)$$

where the strain invariant:

$$S = \sqrt{2 S_{ij} S_{ij}} \quad (29)$$

with S_{ij} given by Equation 11.

At the latest version, the production limiter that is used for both k and ω equations is replaced by:

$$\min(P, 10\beta^* \rho \omega \kappa) \quad (30)$$

and the definition of $CD_{k\omega}$ uses 10^{-10} at the second term:

$$CD_{k\omega} = \max\left(2\rho\sigma_{\omega 2}\frac{1}{\omega}\frac{\partial k}{\partial x_j}\frac{\partial \omega}{\partial x_j}, 10^{-10}\right) \quad (31)$$

Table 3: Constants of $k-\omega\ SST$ turbulence model

σ_{k1}	σ_{k2}	$\sigma_{\omega1}$	$\sigma_{\omega2}$	β^*
0.85	1.0	0.5	0.856	0.09
β_1	β_2	γ_1	γ_2	α_1
0.075	0.0828	5/9	0.44	0.31

The constants of the $k-\omega\ SST$ turbulence model that are given in Table 3, are from the updated model of 2003.

2.5. Wind turbine modeling

For the cases of actuator disk models, the wind turbine rotors are approximated as momentum sinks to represent the axial thrust force T, associated with a constant uniform thrust coefficient C_T over the rotor area:

$$T = 0.5\rho A C_T U_{ref}^2 \tag{32}$$

where A is the surface area of the rotor-disk, ρ the air density, U_{ref} the undisturbed (from the rotor under investigation) reference free-stream velocity and C_T the thrust coefficient of the rotor.

Once the U_ref is known, the C_T can be estimated through the thrust curve of the wind turbine generator considered as uniform over the rotor area [2]. However, in operating conditions, the flow across the rotor is very complex with varying span-wise properties mainly because of the blade characteristics, rotational velocity, turbulence, finite number of blades but as well as other flow characteristics related to non-uniform inflow conditions, atmospheric boundary layer shear and so on.

To overcome the limitations of the standard actuator disk model, several more advanced models like the generalized actuator disk, actuator line model, actuator surface, have been proposed [15].

The drawback of the advanced models is mainly that they need several input variables such as airfoil data, detailed blade geometry which most of the times are not available or confidential for industrial applications. Finally, most of the advance models require time resolved CFD simulations which increase the final computational cost [16]. In line with this, a new developed actuator ring model proposed by the author, will use the advantages of a coupled Blade Element Method (BEM) and actuator disk theory with steady state CFD simulations [17]. Therefore, it is expected to help wind industry to optimize the wind farm design, production and power prediction.

The standard actuator disk model that was used in this study is implemented in OpenFOAM based on the induction factor α:

$$\alpha = 1 - \frac{C_P}{C_T} \tag{33}$$

where C_P the pressure coefficient.

The thrust force is then given by Equation 34:

$$T = 2\rho A\alpha(1-\alpha)U_{ref}^2 \tag{34}$$

In all the cases under investigation a constant uniform reference wind speed of $11.5\,m/s$ have been used. The coefficients C_P and C_T have been provided from the wind tunnel measurements and were used as inputs to the simplified models for a straightforward comparison of their performance at the wake expansion.

3. Full rotor CFD simulations

To address the question of how much information is lost with the simplified models, results are compared with more advanced CFD simulations that include the full geometry of both wind turbine rotors, including their hubs.

3.1. Computational domain

The computational domains were designed to match the exact wind tunnel dimensions to represent the experimental setup and account for possible blockage effects (Fig. 1, Fig.2). Particularly for the CASE-B3, the domain have been extended by $3.7\,m$ in length (30 % of total) to avoid any numerical oscillations from the outlet at the far wake measurements downstream.

The *blockMesh* utility of OpenFOAM platform with in-house code was used to generate a multi-block hexahedral computational mesh of $670k$ cells. That mesh was further modified and refined in regions of interest with the more advanced *snappyHexMesh* utility. It was also used as a coarse mesh for the test of different turbulence models with the actuator disk models.

For the full rotor cases, before the snapping of the mesh at the imported surfaces several local surface

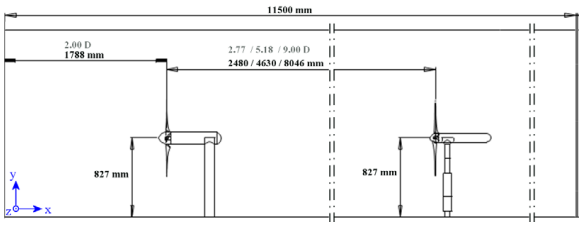

Figure 1: Turbine positions in the wind tunnel and reference coordinate system

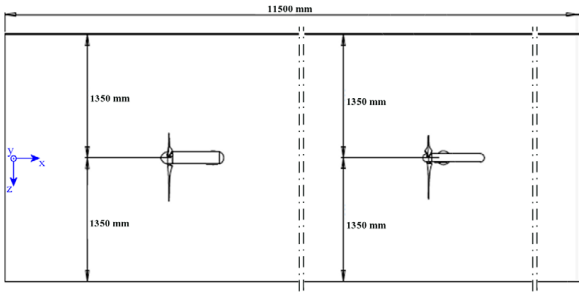

Figure 2: Wind tunnel test section from above and reference coordinate system

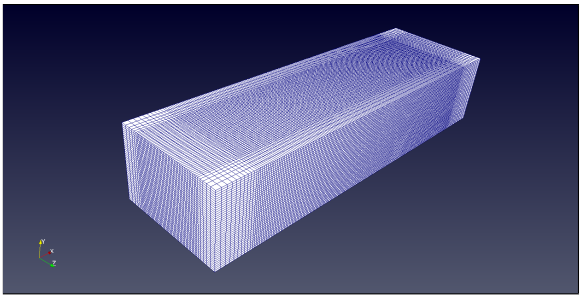

Figure 3: 3D view of the multi-block mesh that was generated with *blockMesh* utility.

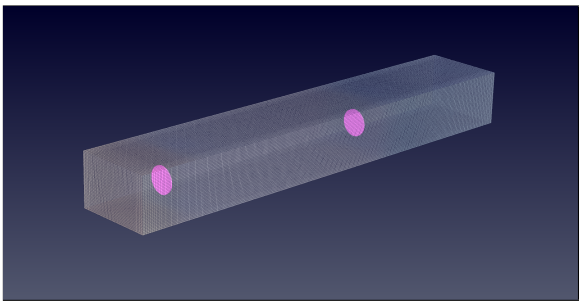

Figure 4: Positioning of the two actuator disk models for the CASE-B3.

refinements have been done at the blades, hubs, nacelles and the two towers of the wind turbines. Five cell-layers were added normal to the surfaces of the geometries with an expansion ratio of 1.5.

The global cell size at the centered block of the mesh is $0.0675^3\,m^3$. According to each region, those cells have been refined down to $0.003375^3\,m^3$ and $0.016875^3\,m^3$, whereas the cells close to the geometries had a global size of $0.00105^3\,m^3$ and $0.0007^3\,m^3$ at the surface.

The final fine computational mesh size was 30Mi cells for the full rotor CFD simulations and 14Mi cells for the ADM case.

At the design condition for a Tip Speed Ratio (TSR) $\lambda = \Omega R\,/\,U_{ref} = 6$, the Reynolds number at the tip is $Re_c = \lambda U c_{tip}\,/\,\nu \approx 10^5$. Therefore the above cell sizes ensure that high-Reynolds wall functions can be applied at the first cell to the walls.

3.2. *Solution methodology and boundary conditions*

All the simulations have been performed in the open-source CFD platform OpenFOAM, using the steady state incompressible solver *simpleFoam* which is based on the Semi-Implicit Method for Pressure-Linked Equations (SIMPLE) algorithm.

Initial values and inlet values for the turbulence characteristics were estimated by using the experimental measured TI and the turbulent length scales ℓ of each case with the following expressions:

$$k = \frac{3}{2}\left(\overline{U}TI\right)^2 \tag{35}$$

$$\varepsilon = C_\mu^{0.75}\frac{k^{1.5}}{\ell} \tag{36}$$

$$\omega = C_\mu^{0.75}\frac{\sqrt{k}}{\ell} \tag{37}$$

where $\overline{U} = U_{ref} = 11.5\,m/s$ and density of air $\rho = 1.25\,kg/m^3$.
The boundary conditions that were used are summarized in Tables 4 and 5.

4. Results and discussion

For the cases under investigation, qualitative and quantitative results of the wake expansion are given below.

Three turbulence models have been tested in advance, on a coarse computational domain of 670k cells

Table 4: Inflow and outflow boundary conditions

	Dirchlet Fixed value	Neumann Zero gradient
Inlet	$\vec{U}, k, \varepsilon, \omega$	p
Outlet	$p = 0$	$\vec{U}, k, \varepsilon, \omega$

Table 5: Other boundary conditions

Sides, top and bottom	Slip condition
Blades, hubs, nacelles, towers	Wall functions
Actuator Discs	Momentum sinks
Rotating Frame WT1	TSR: $\lambda = 6$
Rotating Frame WT2	TSR: $\lambda = 4 - 5$

with actuator disk models which consist of 312 cells each. Results showed different wake expansion for each turbulence model (Fig. 6). In Fig. 5 the performance of each model is compared against wake measurements along a horizontal line at hub height $h_{hub} = 0.827m$. The $k - \varepsilon$ turbulence model had a better agreement with the experimental measurements and therefore it was chosen for the case of actuator disk models at the fine computational mesh that was described in subsection 3.1.

4.1. Qualitative results

The differences between the simplified ADM and the full rotor CFD simulations can be also observed qualitative by comparing the horizontal slices at hub height of velocity magnitude (Figure 7) and of the calculated vorticity magnitude (Figure 8). Further details on the wake development downstream are given with the slices of the velocity magnitude (Figures 9, 10) at several positions downstream of the first wind turbine rotor. Those figures present the calculated flow field downstream for both the actuator disk model and the full rotor CFD simulations. The sides of the rectangular white box in the center are equal to the diameter of the wind turbine rotor.

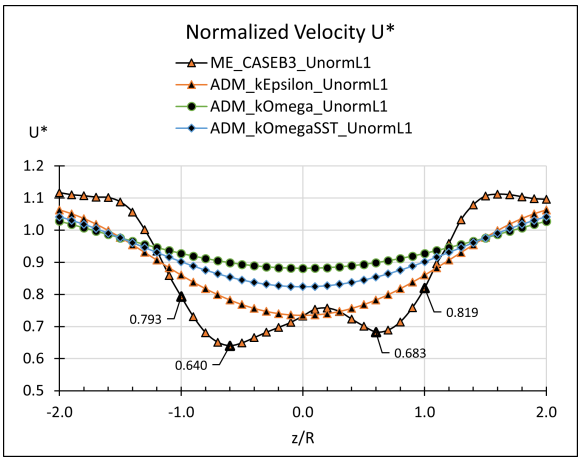

Figure 5: Velocity deficit of $k - \varepsilon$, $k - \omega$ and $k - \omega SST$ turbulence models with ADM against measurements along a horizontal line at h_{hub}

4.2. Quantitative results

To compare the performance of the different approaches, a quantitative comparison against the experimental measurements was done. Wake profiles along two horizontal lines behind the upstream wind turbine rotor and at the elevation of the center of the turbine hub ($h_{hub} = 0.827m$) were extracted covering an horizontal span width from $z = -944mm$ to $z = +944mm$. The two horizontal lines L1, L2 are located $2.77D$ and $5.18D$ downstream the first wind turbine rotor respectively.

Calculated values of the normalized mean velocity $U^* = U_{wake}/U_{ref}$ are compared against the BT4 measurements for the cases of standard actuator disk model using the $k - \varepsilon$ turbulence model (Figure 12, left side) and for the full rotor CFD simulations using the $k - \omega$ turbulence model (Figure 12, right side).

5. Conclusions

The single wake expansion of an upstream wind turbine was investigated for the case of two opera-

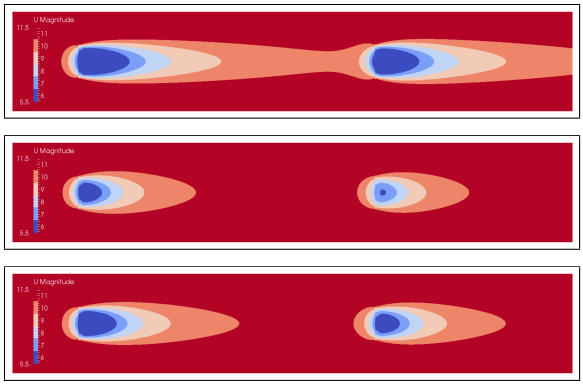

Figure 6: Velocity magnitude at hub height predicted with different turbulence models and actuator disks on a coarse computational mesh; From top to bottom: $k-\varepsilon$, $k-\omega$ and $k-\omega SST$ turbulence models.

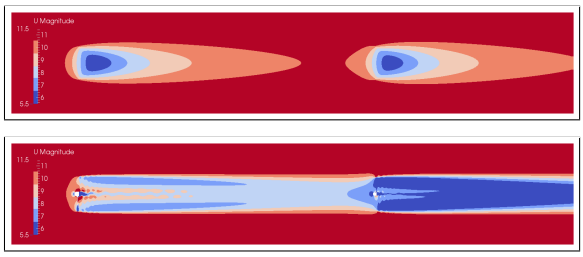

Figure 7: Velocity magnitude at hub height on a fine computational mesh; Actuator disk models using $k=\varepsilon$ (top) and full rotor CFD simulations using $k-\omega$ (bottom).

tional wind turbines in a row under the controlled conditions of a wind tunnel. OpenFOAM open-source platform was used, using the multiple rotating frames (MRF) utility and the incompressible solver simpleFOAM.

Two different numerical approaches have been tested. The full rotor CFD simulations including the exact wind turbine geometries with their hubs and simulations with simplified actuator disk models that represented the wind turbines in the flow field as momentum sinks. Both cases were investigated qualitative and compared against experimental measurements in two downstream positions over horizontal lines at hub height.

For the case of full rotor CFD simulations the $k-\omega$ turbulence model was utilized while for the case of ADM a further study on different turbulence models showed better performance of the $k-\varepsilon$ turbulence model. The standard two equation $k-\varepsilon$ turbulence model predicted more accurately the velocity deficit

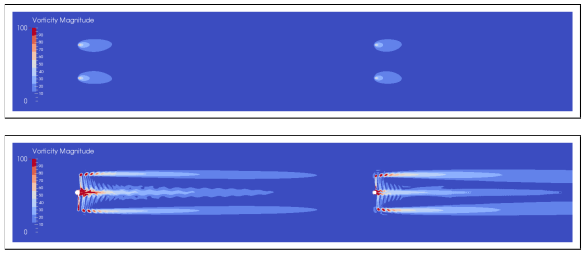

Figure 8: Vorticity magnitude at hub height; Actuator disk models (top) and full rotor CFD simulations (bottom)

at the two downstream positions, while the $k-\omega SST$ was slightly better than the standard $k-\omega$.

The full rotor CFD simulations showed good agreement with the measurements at both downstream positions of the near ($2.77D$) and far ($5.18D$) wake. The U-shape of the horizontal velocity profile at the far wake was not observed at the full rotor CFD simulations. The justification of that can be derived from the absence of nacelles and towers. Instead of a U-shape, two local minimum values of $U^*=0.651$ and $U^*=0.652$ were observed against the one local minimum value of $U^*=0.697$ from the measurements. Although the difference is small, better agreement of the far wake is expected if the tower and nacelle are also included [18; 5]. In addition, the presence of the tower would amplify the wake at the core (center of the rotor) and would increase the TKE downstream [19; 20; 16]. As a result, we could expect a local minimum value at the center of the wake similar to what it was observed in the experiment. Finally, the asymmetry of the near wake at the measurements could also be related to a wake meandering downstream due to the blade-tower interaction and from enhanced vortex shedding of the cylindrical tower at certain Reynolds numbers.

In all cases, the ADM under-predicted the wake effects downstream, a behavior that was observed also by other studies [2; 16; 17; 21; 3]. Especially for the downstream distance of five diameters, which is of high interest since it is commonly used by industry as a separation distance in wind farms, results showed that there is a lack of capturing accurately the velocity deficit with the standard actuator disk models. Results of ADM, as it can be seen on Figure 5, are also very sensitive to the chosen turbulence model.

The present study address the question of how much information of the wake is lost when we move to a simplified model. Wind energy industry needs more advanced and accurate models to estimate better the

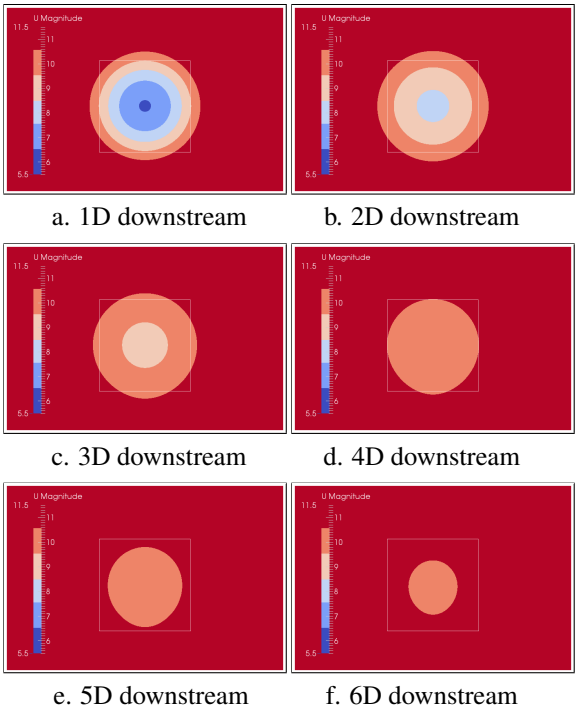

a. 1D downstream b. 2D downstream

c. 3D downstream d. 4D downstream

e. 5D downstream f. 6D downstream

Figure 9: From a to h: vertical slices of the velocity magnitude with ADM at several positions downstream the first wind turbine.

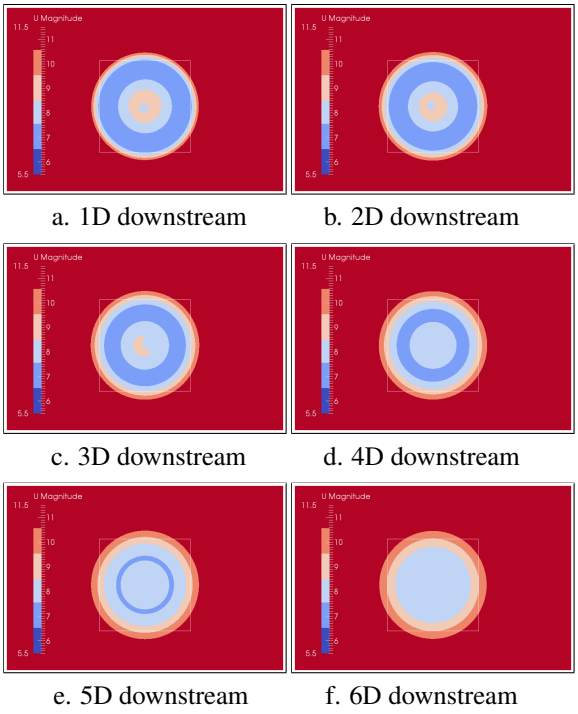

a. 1D downstream b. 2D downstream

c. 3D downstream d. 4D downstream

e. 5D downstream f. 6D downstream

Figure 10: From a to h: vertical slices of the velocity magnitude with full rotor CFD simulations at several positions downstream the first wind turbine.

wake losses and limit the risks of new potential wind projects as well as optimizing and operating more efficiently the existing ones. In line with the above, the research group of the authors are investigated a new actuator ring model that can be used with steady state simulations and wind farm optimization [17].

Acknowledgments

This work has been funded by INNOVIRIS, formerly known as the ISRIB (Institute for the encouragement of Scientific Research and Innovation in Brussels), the Brussels Institute for the promotion of scientific research and innovation, in the framework of the DOCTIRIS program and under the research project:

"Non-deterministic advanced CFD modeling of wind turbine wakes and their interaction with applications to wind farms including complex terrain effects".

The authors acknowledge the Norwegian Technical National University (NTNU) for providing the experimental data of Blind Test 4 and professors Lars Roar Stran and Per-ge Krogstad for their support.

References

[1] OpenFOAM 2016 openfoam.org URL `www.openfoam.org`

[2] Rados K, Mosfilis S, Stergiannis N, Tourlidakis A, Caralis G and Zervos A 2012 Cfd modeling approaches of wind turbine single and multiple wakes *European Wind Energy Conference and Exhibition 2012, EWEC 2012* vol 3 pp 1842–1849 ISBN 9781627482912

[3] Prospathopoulos J, Politis E, Rados K and Chaviaropoulos P 2011 *Wind Energy* **14** 285–300

[4] Barthelmie R J, Rathmann O, Frandsen S T, Hansen K S, Politis E, Prospathopoulos J, Rados K, Cabezón D, Schlez W, Phillips J, Neubert A, Schepers J G and van der Pijl S P 2007 *Journal of Physics: Conference Series* **75** 012049 ISSN 1742-6596

[5] Bazilevs Y, Hsu M, Kiendl J, Wüchner R and Bletzinger K 2011 *International Journal for Numerical Methods in Fluids* **65** 236–253

[6] Markatos N C 1986 *Applied Mathematical Modelling* **10** 190–220

[7] Wilcox D 1993 *Turbulence modeling for CFD* second edi ed vol 93 (DCW Industries) ISBN 0963605100

[8] S"æ"tran L and Bartl J 2015 *Invitation to the 2015 Blind test 4 Workshop Combined power output of two in-line turbines at different inflow conditions*

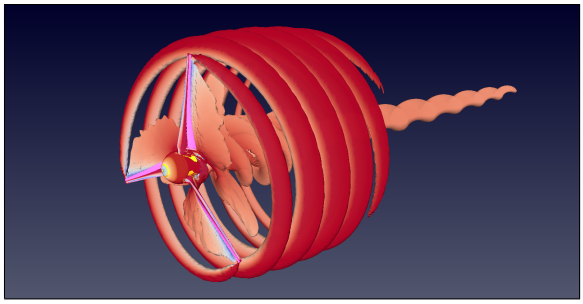

Figure 11: Representation of wind turbine vortexes using the Q criterion for the full rotor CFD simulations.

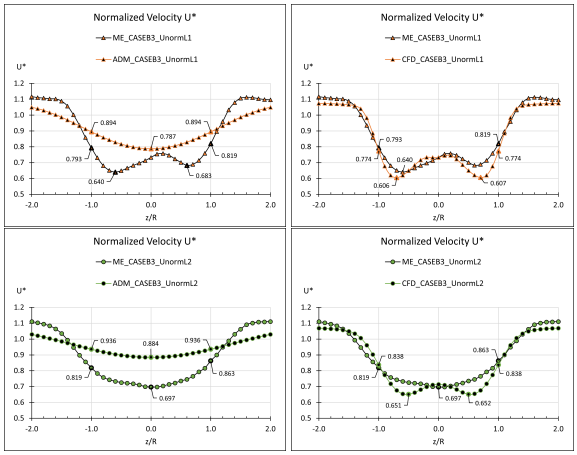

Figure 12: Normalized velocity U^* against measurements along two horizontal lines at the wake of the upstream wind turbine rotor. Results of ADM (left) and full rotor CFD simulations (right).

[9] Launder B E and Spalding D B 1974 *Computer Methods in Applied Mechanics and Engineering* **3** 269–289 ISSN 00457825

[10] Launder B E, Morse A, Rodi W and Spalding D B 1973 Prediction of free shear flows: A comparison of the performance of six turbulence models *NASA. Langley Res. Center Free Turbulent Shear Flows* vol 1 pp 361–426

[11] Wilcox D C 2008 *AIAA Journal* **46** 2823–2838 ISSN 0001-1452

[12] Menter F R 1994 *AIAA* **32** 1598–1605

[13] Menter F R, Kuntz M and Langtry R 2003 *Turbulence Heat and Mass Transfer 4* **4** 625–632

[14] Hellsten A 1998 *29th AIAA, Fluid Dynamics Conference* 1–11

[15] Mikkelsen R 2003 *Actuator disc methods applied to wind turbines* Ph.d thesis Technical University of Denmark

[16] Sanderse B, Pijl S and Koren B 2011 *Wind Energy* **14** 799–819 ISSN 10954244

[17] Vafiadis K, Stergiannis N, Tourlidakis A and Rados K 2013 Computational investigation of horizontal axis wind turbine wake *European Wind Energy Conference and Exhibition, EWEC 2013* vol 3 pp 1692–1700 ISBN 9781632663146

[18] Bazilevs Y, Hsu M C, Akkerman I, Henicke B, Spielman T and E Tezduyar T 2011 *International Journal for Numerical Methods in Fluids* **65** 207–235

[19] Troldborg N, Sorensen J N and Mikkelsen R 2010 *Wind Energy* **13** 86–99 ISSN 10954244

[20] Vermeer L J, S"ø"rensen J N and Crespo A 2003 *Progress in Aerospace Sciences* **39** 467–510 ISSN 03760421

[21] Crasto G, Gravdahl a R, Castellani F and Piccioni E 2012 *Energy Procedia* **24** 385–392 ISSN 18766102

AERO-THERMAL INVESTIGATIONS IN TURBOMACHINERY

Active tip leakage flow control in high pressure turbines

Bogdan Cezar Cernat

Turbomachinery and Propulsion Department, von Karman Institute for Fluid Dynamics, Belgium, cernat@vki.ac.be

Supervisor: Sergio Lavagnoli

Associate Professor, Turbomachinery and Propulsion Department, von Karman Institute for Fluid Dynamics, Belgium, lavagnoli@vki.ac.be

University Supervisor: Tony Arts

Professor, Universite catholique de Louvain / von Karman Institute for Fluid Dynamics, Belgium, arts@vki.ac.be

Abstract

Current research in modern gas turbine engines aims at maximizing the propulsion efficiency, power output and components lifetime, while reducing the engine weight, fuel consumption, maintenance costs and environmental impact. The high pressure (HP) turbine, located downstream of the combustor, represents one of the most critical parts of the propulsion system. Being exposed to very high gas temperatures and mechanical loads, it requires a complex balance between aerodynamics, heat transfer and mechanical durability.

The physical gap between the rotor airfoil tip and the stationary casing in unshrouded turbines generates non-uniform, unsteady hot gas path flows responsible for severe problems affecting the aero-thermal performance of the rotor blade. The leakage of high-momentum fluid over the tip reduces the amount of turbine work extracted, as it crosses the blade gap without any turning. The injection of these transonic, hot flows (1700 K) into the main working fluid generates mixing phenomena and secondary flows contributing up to one third of the turbine aerodynamic losses. The periodic disruption of the casing boundary layer by the rotating blades, combined with the generation of shock structures in the tip gap and the periodic ingestion of stator wakes, gives rise to fierce unsteady variations in heat transfer and aerodynamic loads onto the turbine casing, accompanied by intense thermal stresses inside the solid blade. The main purpose of this research is the conceptual study and development of a novel active control strategy for the aerothermal management of rotor tip leakage flows and enhancement of the blade cooling.

1. Introduction

Recent developments in flow control research will be considered to design an effective mitigation solution, based on the emission of coolant jets from the stationary outer casing towards the moving airfoil tip. The actuation principle will be designed to provide a fast-response flow regulation of the steady or pulsating coolant streams for a wide range of mass-flow rates. Piezoelectric or fluidic actuators could be employed in order to generate a fluid pulsation matching the required intensity and frequency levels (1-10 kHz). A reduced order model representative of the system thermodynamics will be developed to simulate the overall engine energy balance, considering the actuation power consumption, the necessary coolant mass flow and the perspective tip leakage loss reduction. This analysis will set the target performance for the flow control system to reach a significant net efficiency gain.

Steady-state and unsteady RANS CFD computations will be used to simulate the fluid dynamics of a state-of-art unshrouded turbine rotor with active tip flow control, operated at engine representative conditions. A portion of the high momentum flow is expected to contribute to the tip leakage reduction, while the other to be entrained by the vortical structures of the airfoil secondary flows. The numerical calculations will predict the unsteady interaction between the coolant jet injections from the casing and the unsteady, three-dimensional tip gap flow. A multi-objective parametric study will employ CFD simulations to investigate different flow control solutions.

The experimental campaign will first comprise the

characterization of the active flow control apparatus in a dedicated test bench to determine the injection waveform, duty cycle, turbulence intensity and mass flow rate. This detailed investigation will define the actual performance of the injection system with respect to the design requirements. The AFC actuator will then be integrated in the VKI transonic turbine test rig, and tested in full aero-thermal engine similarity. The measurement campaign will allow to model the complex tip region flow physics, originating from the interaction between the low temperature jets and the hot transonic leakage flow. The impact of the AFC system on the stage aero-thermodynamics will be assessed by time-averaged and time-resolved measurements. Ultimately this research project will provide a unique data-set of aero-thermal measurements defining the aerodynamic and thermal effectiveness of the apparatus operated at engine representative conditions. The final output of this project will advance the understanding of turbine tip flows and define essential design guidelines for future active flow control solutions in high speed rotating machinery.

Analysis and consequences of the separation/transition mechanisms of the flow on a modern low-pressure gas turbine airfoil

Julien Clinckemaillie

Turbomachinery and Propulsion Department, von Karman Institute for Fluid Dynamics, Belgium, julien.clinckemaillie@vki.ac.be

Supervisor: Tony Arts

Professor and Head of Department, Turbomachinery and Propulsion Department, von Karman Institute for Fluid Dynamics, Belgium, tony.arts@vki.ac.be

University Supervisor: Hervé Jeanmart

Professor, Institute of Mechanics, Materials and Civil Engineering, Université Catholique de Louvain, Belgium, herve.jeanmart@uclouvain.be

Abstract

The present study focuses on the results of the experimental investigation of the separated flow mode of transtition along the suction side of a very-high-lift, mid-loaded low-pressure turbine airfoil (T106C). A rigorous analysis of the effect of the Reynolds number on the overall aerodynamic performance of the airfoil is presented for uniform inflow conditions. The separation bubble topology is presented in terms of correlations based on the characteristic points of the boundary layer separation, and a comparison with other prediction models is also shown at the end of this paper. Furthermore, a detailed analysis of the effect of incoming periodic wakes on the aerodynamic performance of the airfoil is presented, where some features of the multi-mode transition germane to unsteady wake-boundary layer interactions in a low-pressure turbine environment are discussed for specific cases.. This experimental study was performed on a large scale linear cascade in the S-1/C transonic wind tunnel, operating at a fixed exit isentropic Mach number equal to 0.65, covering a range of exit isentropic Reynolds numbers (90,000 – 200,000 based on chord length) and at low inlet free-stream turbulence intensity (0.8%). The simulation of incoming periodic wakes was realized by means of a disc equipped with bars rotating at high speed upstream of the leading edge plane, allowing an engine representative simulation of the operating conditions (flow coefficient, reduced frequency, wake width and depth) encountered in low-pressure turbines of modern aero-engines.

Keywords: Turbomachinery, low-pressure turbine, transition, multi-mode transition, separation, bursting, unsteady wake-boundary layer interaction, blade-row interference

Nomenclature

c	Chord
E	Hot-film voltage
f	Frequency
FSTI	Free-stream turbulence intensity
g	Pitch
h	Span
K	Acceleration parameter
LE	Leading edge
LPT	Low-pressure turbine
M	Mach number
P	Pressure
PS	Pressure side
PSDI	Power spectral density integral
Re	Reynolds number
s	Curvilinear coordinate
SS	Suction side
t	Time

TE	Trailing edge
U	Peripheral speed
V	Velocity
x	Axial coordinate
y	Pitch-wise coordinate

Greek symbols

β	Flow angle
γ	Intermittency
	Heat capacity ratio
ϕ	Flow coefficient
τ	Pseudo-wall shear stress
ζ	Kinetic energy loss coefficient

Subscripts

0	Reference length
	Total condition
	Zero-flow condition
1	Upstream condition
2	Downstream condition
ax	Axial
bar	Referring to the bars
is	Isentropic
L	Laminar
m	Mid-span
MD	Maximum displacement
r	Reduced
R	Reattachment
S	Separation
T	Turbulent
w	Wall
∞	Free-stream

1. Introduction

The actual design trend for modern state-of-the-art commercial aero-engines is characterized by an ever-increasing bypass ratio. This, in turn, requires the low pressure turbine (LPT) to provide an increasingly higher power output in order to drive the large fan, without any efficiency penalty. At the same time, the current need to save weight and to reduce production and maintenance costs translates itself into a reduction of the blade count per row and thus increased pitch-to-chord ratios. The combined effect of those design requirements on the low-pressure turbine implies an increased aerodynamic loading per blade, and has led to the development of very-high-lift and even ultra-high-lift airfoils. They are characterized by an increased velocity peak level on the suction side, followed by a significant diffusion of the flow along the rear part of the suction side until the trailing edge. The resulting strong adverse pressure gradient can lead to a separation of the boundary layer, particularly under the low Reynolds number conditions which are germane to low pressure turbines of commercial jet engines operating at cruising altitude. These separation bubbles cause a significant degradation of the engine efficiency, particularly open separation bubbles that fail to reattach, resulting in a major loss in aerodynamic efficiency, thrust and flow turning [1]. For large commercial aero-engines, a component efficiency drop of 2 percent can occur between sea-level take-off conditions, where the Reynolds number is of the order of 5 10^5, and high-altitude cruising conditions where the Reynolds number drops by a factor of 3 to 4 [2; 3]. This drop in efficiency can even become as large as 7 percent for smaller engines operating at even higher cruising altitudes (e.g. Unmanned Aerial Vehicles [3]). Due to the low Reynolds numbers typical of high-altitude cruising conditions, a large part of the boundary layer developing on the suction surface of a very-high-lift LPT blade may still be laminar until past the velocity peak, even with significant background free-stream turbulence intensity levels. If the subsequent diffusion is strong enough, the boundary layer is not able to withstand the adverse pressure gradient and separates from the surface. If transition from laminar to turbulent occurs soon enough in the separated free shear layer, the flow will reattach to the surface and a separation bubble is formed. The separation and transition of the boundary layer are thus closely linked, and the accurate prediction of transition onset and development under relevant conditions is essential to the design of efficient LPT airfoils.

A considerable wealth of information on transition can be found in the literature. Mayle [1] discerned three modes of transition and considered that none of them is more crucial to low-pressure turbines than the separated-flow transition mode. A classification of the separated-flow transition based on the type of separation bubble, long or short, and its effect on the overall pressure distribution along the suction surface was also proposed. Short bubbles have only a local displacement effect, with the pressure distribution before and after the bubble remaining very close to that of the flow without separation, whereas long bubbles interact with the outer flow to such an extent that the overall pressure distribution is extremely modified, a phenomenon typically associated with drastically increased losses and significantly reduced outlet flow

angle. The change from a short bubble type to a long one is called bursting, and can be triggered by small changes in either Reynolds number or angle of attack. Mayle's study has since then been critically discussed, reviewed and extended by other research groups such as Volino et al. [2], Walker [4] and most notably Hatman & Wang [5] who further classified the type of separation bubble by the location where transition onset takes place, as the separation can either be laminar or already transitional. The transition processes described here above can also be strongly affected by the periodic unsteady nature of the flow in gas turbines. Although the periodic unsteadiness can take multiple forms, the present paper focuses entirely on the unsteady blade-wake interactions, as discussed by Halstead et al. [6] and Mayle [1].

A great amount of state-of-the-art studies concerning the aerodynamic performance of very-high-lift low-pressure turbine airfoils under uniform and periodic inflow conditions can be found in the literature. However, most studies have been performed in low-speed wind tunnels [2; 7; 8] or in high-speed wind tunnels with an unrealistically high flow coefficient [9]. The aim of the present praper is to contribute to the available literature by discussing the aerodynamic performance of a very-high-lift mid-loaded low-pressure turbine airfoil (T106C) under engine representative conditions in terms of exit Mach and Reynolds number, and including the effects of unsteady blade row interference phenomena on the behavior of the boundary layer along the suction surface of the airfoil providing a realistic reduced frequency and flow coefficient. The background free-stream turbulence intensity was kept at a low level (0.8%) in order to better highlight the effects of the periodic unsteady blade-wake interactions.

2. Experimental Setup

2.1. Experimental facility

The measurement campaign was performed in the high speed S-1/C wind tunnel of the von Karman Institute (Fig. 1). This continuous closed-loop wind tunnel is driven by a 615 kW axial flow compressor. A cooler maintains the temperature close to atmospheric conditions (~290 K) and dry air is maintained at all conditions. The mass flow can further be regulated with a by-pass valve, while the absolute pressure level inside the test section can be lowered down to ~10,000 Pa by means of a vacuum pump. This implies that the flow through a linear cascade of two-dimensional LPT airfoils can be aerodynamically investigated over a large range of independently adjusted exit isentropic Mach ($M_{2,is}$ = 0.5 - 0.8) and Reynolds numbers ($Re_{2,is}$ = 2 10^4 – 3 10^5 based on a chord c ranging between 0.02 and 0.10 m), allowing to cover a wide range of engine representative operating conditions.

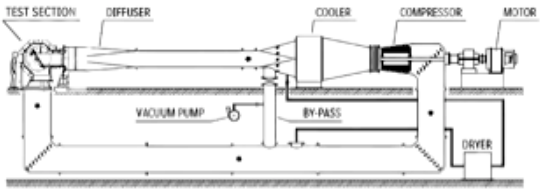

Figure 1: The S-1/C high speed, variable density wind tunnel

The test section consists of a linear cascade of six up-scaled T106C high-lift, mid-loaded low-pressure turbine blades and two end-blocks (effectively forming 7 blade passages) with a span of 225 mm. This guarantees a sufficiently high aspect ratio (above 2.30) and therewith limits the impact of the end-wall boundary layers at mid-span of the inlet duct. The main characteristics of the test cascade are listed in Tab. 1 [10]. Located in a plane 0.67 x/c_{ax} upstream of the cascade, a spoke-wheel type wake generator equipped with bars and driven by a 30 kW electric motor generates periodically incoming wakes in order to simulate unsteady blade row interference effects. The wake generator consists of a solid brass disk with a diameter of 625 mm on which 32 equally spaced cylindrical molybdenum bars with a diameter of 2 mm and a length of 215 mm are mounted. The rotating bars are only parallel to the blade leading edge when passing in front of the central instrumented blade, extending over the entire blade span except for a clearance of 30 mm for safety reasons. The rotational speed of the disk (adjustable by means of a variable frequency controller) as well as the amount of bars were carefully determined in order to match conditions representative of a modern commercial aero-engine in terms of reduced frequency and flow coefficient. For this experimental campaign, a rotational speed of 2,665 RPM was chosen. In this configuration, a flow coefficient $\phi = V_{1,ax}/U_m$ of 0.75 and a reduced frequency $f_r = (f_{bar}c)/V_{2,is}$ of 0.62 were achieved. In the following presentation of the results, both cases – uniform (without periodic incoming wakes) and periodic inflow conditions – will be discussed.

Table 1: T106C cascade characteristics

Chord	c	mm	93.01
Pitch-to-chord ratio	g/c	-	0.95
Aspect ratio	h/c	-	2.4:1
Blade stagger angle	ϕ	deg	30.7
Inlet flow angle	β_1	deg	32.7

2.2. Instrumentation

The third airfoil from the top of the cascade can be alternatively replaced by an instrumented blade with pneumatic wall static pressure taps or with wall hot-film gauges (for pseudo-wall shear stress measurements). In both cases, the sensors are located at blade mid-span and deployed along the suction side length, with a higher concentration of sensors in the region where the boundary layer is expected to separate at low Reynolds numbers. A fixed Pitot probe allows measuring the total pressure upstream of the cascade, while the upstream total temperature is quantified by means of a bare type-K thermocouple (without flow velocity correction since the thermocouple is located in a stagnation region). The inlet (P_{01}, T_{01} and β_1) and outlet (P_2) boundary conditions are accurately quantified in measurement planes located at an axial distance of 0.67 x/c_{ax} upstream of the LE and 0.55 x/c_{ax} downstream of the TE respectively. In the presence of the wake generator used to simulate the periodic inflow conditions, the upstream boundary conditions P_{01} and β_1 cannot be measured but are determined using hot-wire data previously obtained in identical flow conditions [11] and based on the total pressure measured by a Pitot probe located upstream of the wake generator. The pitch-wise distributions of flow angle and total pressure upstream and downstream of the cascade were quantified by means of wall static pressure taps, a 3-hole and a 5-hole probe respectively. A Pitot probe with a flattened head was also traversed upstream of the cascade in the spanwise direction in order to characterize the inlet end-wall boundary layer. The latter was quantified as fully turbulent (shape factor = 1.4) with a boundary layer thickness equal to 13% of the inlet duct width and a displacement thickness ranging between 3 and 5 mm for the Reynolds numbers investigated. All pneumatic measurements were sampled at 400 Hz before being subsequently time-averaged, with the exception of the continuous probe traverses which were sampled at 1 kHz with a sufficiently slow carriage speed in order to take into account their relatively low time response. Since a quantitative calibration of the hot-films array is not possible, the raw output signal of the hot-film gauges was processed in a semi-quantitative manner [12] using Eq. 1, where the value of the pseudo-wall shear stress is proportional to the associated bridge voltage reading E during the experiment, and the voltage reading E_0 under zero-flow conditions. The hot-film signals were sampled at 60 kHz and low-pass filtered at 25 kHz. The (measured) frequency response of the hot-film gauges was ~10 kHz.

$$\tau_w = \left(\frac{E^2 - E_0^2}{E_0^2} \right)^3 \quad (1)$$

2.3. Uncertainty

The reader should realize that the tests were performed at very low absolute pressure (~10,000 Pa), and that the ambient pressure was used as the main reference pressure for all pneumatic measurements. The application of a rigorous error propagation will therefore lead to higher uncertainties, especially at the lowest Reynolds numbers. However, the obtained results proved to be very repeatable, not only during the measurement campaign, but also when compared to previous measurement campaigns performed in similar flow conditions [10; 11]. The following uncertainty values were estimated for the lowest Reynolds number, the most critical one for the uncertainty estimation. The relative uncertainties on isentropic Mach and Reynolds number are 2.2% and 2.5% respectively, while the absolute uncertainty for the kinetic energy losses and exit flow angle are 0.034 and 1.5 deg respectively.

3. Results and Discussion

3.1. Time-averaged pneumatic results

Fig. 2 shows the blade velocity evolution (isentropic Mach number evolution) along the suction side of the T106C blade for four exit isentropic Reynolds numbers (90,000 – 200,000), at nominal exit isentropic Mach number (0.65), at low free-stream turbulence intensity (FSTI = 0.8%) and with uniform inflow conditions. The fully turbulent 2D Navier-Stokes numerical computation TRAF2D (using the algebraic Baldwin-Lomax turbulence model, and with uniform inflow boundary conditions) is used as a reference velocity distribution, characterized by a fully attached boundary layer along the entire surface of the airfoil. The reader is referred to Arnone [13] for more information on the numerical code.

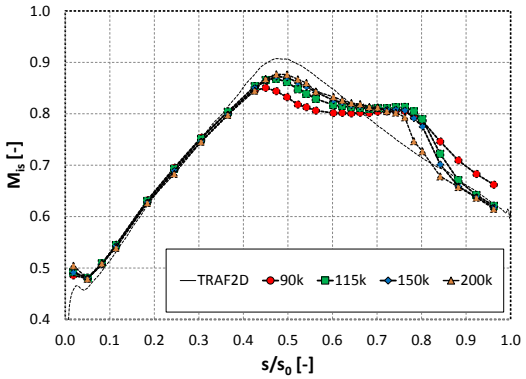

Figure 2: Isentropic Mach number evolution along the suction side of the T106C blade for four different Reynolds numbers; uniform inflow conditions

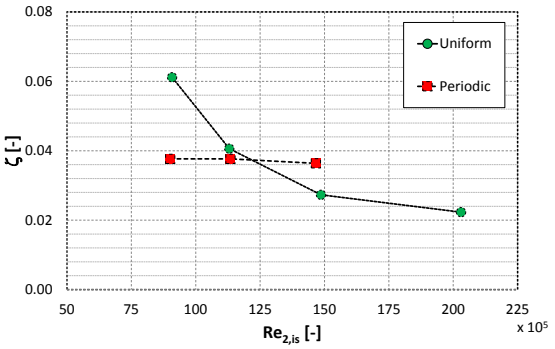

Figure 3: Mass-averaged kinetic energy losses as a function of $Re_{2,is}$; comparison between uniform and periodic inflow conditions

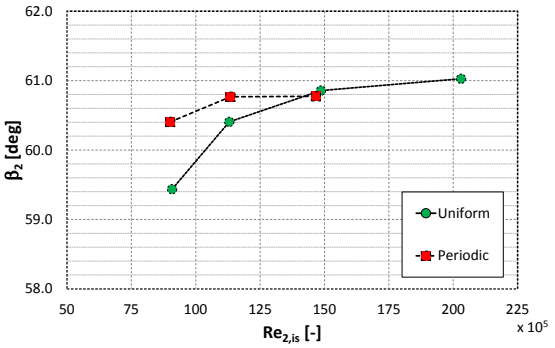

Figure 4: Mass-averaged outlet flow angle β_2 as a function of $Re_{2,is}$; comparison between uniform and periodic inflow conditions

For all the investigated cases, the results show a significant deviation from the numerical prediction due to the presence of a separation bubble along the diffusing part of the suction side downstream of the velocity peak. For the highest Reynolds number ($Re_{2,is} = 200,000$), the separated shear layer is reattaching to the blade surface before the trailing edge, resulting only in a locally perturbed aerodynamic loading of the blade in the region of the separation bubble, caused by the displacement effect of the latter. However, the velocity distribution is significantly altered for the lowest Reynolds number ($Re_{2,is} = 90,000$) as the separated shear layer is unable to reattach before the trailing edge, resulting in an open separation bubble. Between these two extreme cases, the bursting of the separation bubble from a short type ($Re_{2,is} = 150,000$) to a long type ($Re_{2,is} = 115,000$) takes place, corroborating the results obtained by Michálek et al. [10] which identified a critical Reynolds number of 140,000 at which bubble-bursting takes place.

The mass-averaged kinetic energy losses (Eq. 2) and exit flow angle are presented in Fig. 3 and 4 respectively, showing the progressive augmentation of losses as well as the reduction in turning angle as the exit isentropic Reynolds number is lowered, culminating in a significant deterioration of the aerodynamic performances for the lowest Reynolds number investigated.

$$\zeta = 1 - \frac{1 - (\overline{P_2}/\overline{P_{02}})^{\gamma-1/\gamma}}{1 - (\overline{P_2}/\overline{P_{01}})^{\gamma-1/\gamma}} \qquad (2)$$

In the presence of periodic incoming wakes generated upstream of the cascade, several conclusions can be drawn from the time-averaged blade velocity distribution alone (Fig. 5) when compared to the steady state results for the lowest Reynolds numbers (90,000 and 115,000). The most striking difference compared to the steady state case is the significant decrease of the separation bubble size even for the lowest Reynolds number. This is due to the reenergizing effect that the convected turbulent wake has on the unstable boundary layer downstream of the velocity peak. A time-averaged reduction of the aerodynamic loading on the front part of the suction surface is also observed, due to the periodically altered inlet velocity triangle in the presence of a wake, resulting therefore in periodic pressure disturbances on the blade surface [14].

Fig. 6 and 7 present the downstream pitchwise traverses through the wake for uniform and periodic inflow conditions respectively. From the uniform case, it is clearly visible that the main source of losses emanates from the suction side of the airfoil since that part of the wake grows wider and deeper with decreasing Reynolds number. Under periodic inflow conditions however, the wake profiles, where P_{01} is an accurate estimation of the inlet total pressure downstream of the wake generator based on previously obtained data [11], remain nominally unaltered for different

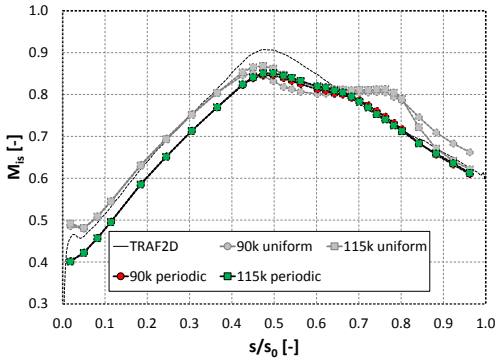

Figure 5: Isentropic Mach number evolution along the suction side of the T106C blade for two different Reynolds numbers; comparison between uniform and periodic inflow conditions

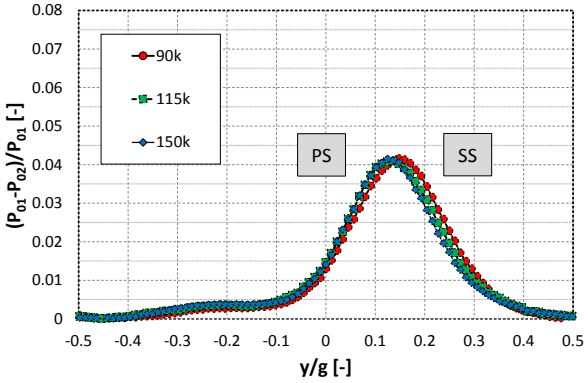

Figure 7: Pitchwise wake profiles for three different Reynolds numbers with periodic inflow conditions

Reynolds numbers, a conclusion that is supported by the relatively constant kinetic energy losses with respect to $Re_{2,is}$ (Fig. 3). Interestingly, for Reynolds numbers bigger than 125,000, the losses in the periodic case are greater than in the uniform case, an observation that can be attributed to a bigger surface being covered by turbulent flow in the periodic case, thereby increasing the profile losses [3].

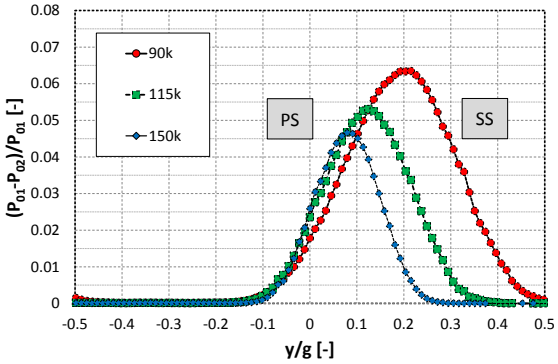

Figure 6: Pitchwise wake profiles for three different Reynolds numbers with uniform inflow conditions

3.2. *Time-resolved hot-films anemometry results*

The status of the boundary layer developing on the suction surface of the airfoil can further be investigated using the output signals of hot-film gauges, albeit qualitatively rather than quantitatively (Eq. 1). Fig. 8 presents the evolution of the mean pseudo-wall shear stress, the rms normalized by the local mean value and the local intermittency factor for one Reynolds number ($Re_{2,is} = 115,000$) with uniform inflow conditions. The local intermittency factor is computed following Eq. 3 [15] and is based on the progressively increasing power spectral density integral ($PSDI$) throughout the transition process as the boundary layer goes from laminar ($PSDI_L$, $\gamma_{PSDI} = 0$) to turbulent ($PSDI_T$, $\gamma_{PSDI} = 1$).

$$\gamma_{PSDI(s)} = \frac{PSDI(s) - PSDI_L}{PSDI_T - PSDI_L} \tag{3}$$

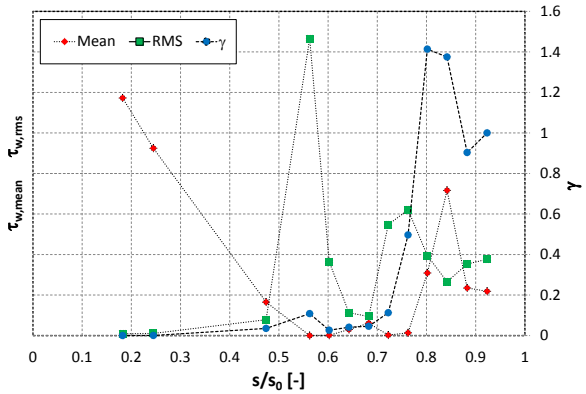

Figure 8: Mean pseudo-wall shear stress, rms and intermittency factor evolution along the suction side; $Re_{2,is} = 115,000$; uniform inflow conditions

Upstream of the velocity peak ($s/s_0 < 0.5$), the pseudo time-averaged wall shear stress values are all above zero with low rms values and a low energy content (Fig. 9), as expected for an accelerating laminar boundary layer. The spectral peak at ~170 Hz and its first harmonic are believed to be linked to large periodic flow structures generated upstream of the cascade [10]. The separation point ($s/s_0 = 0.56$) is characterized by a zero value for the wall shear stress and a first peak in the rms value as well as a global increase of the energy content, especially in the lower frequency range (1,000 – 2,000 Hz). An explanation for the first peak in rms was proposed by Michálek et al. [10]

who linked it with the periodic ejection of flow from the near-wall region into the shear layer, as described by Hatman and Wang [5]. The high value of the first rms peak can also partly stem from the near-zero mean value of the pseudo-wall shear stress with which the rms is normalized.

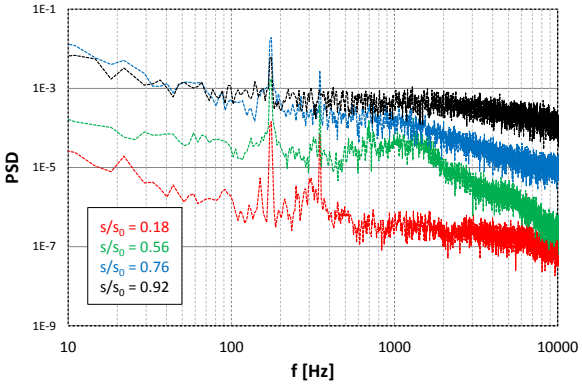

Figure 9: Power spectral density of four hot-film sensors along the suction side; $Re_{2,is} = 115,000$; uniform inflow conditions

In the separation region ($s/s_0 = 0.64 - 0.68$), a slight increase of the wall shear stress can be observed, suggesting the back flow caused by the vortical structure inside the bubble. The transition onset takes place between $s/s_0 = 0.72$ and 0.76, marked by the increase of both the rms and the local intermittency and roughly corresponding to the maximum displacement point, as described by Hatman & Wang. The second peak in rms (between $s/s_0 = 0.76$ and 0.80) corresponds to the mid-transition point with the largest velocity fluctuations taking place. Finally, the end of transition takes place between $s/s_0 = 0.84$ and 0.88 (roughly at the reattachment point), aft of which a fully turbulent boundary layer develops until the trailing edge. The above desciption of the separation bubble topology and transition evolution corresponds to a laminar separation/long bubble type as described by Hatman & Wang.

Fig. 10 and 11 present the space-time diagrams of the phase-locked averaged pseudo-wall shear stress and its rms respectively normalized by the maximum value at the same sensor location, thus emphasizing the periodic fluctuation of the signal at the expense of its absolute value, for one Reynolds number ($Re_{2,is} = 115,000$) and with periodic inflow conditions. Three wake passing events are shown in order to provide a better interpretation of the results. The following discussion concentrates mainly on the diffusing region of the blade ($s/s_0 > 0.5$), where the unsteady wake-boundary layer interaction effects are the most critical.

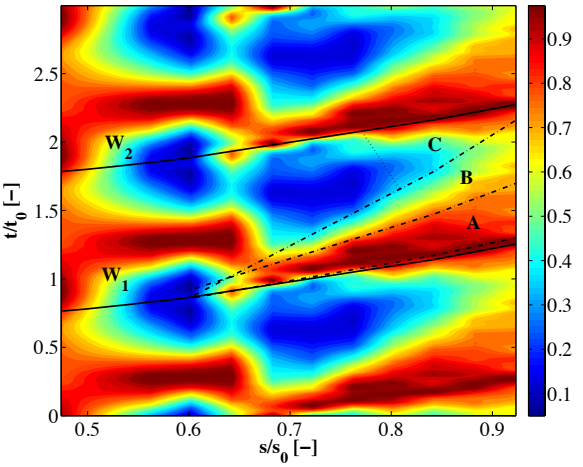

Figure 10: Space-time diagram of the phase-locked averaged mean pseudo-wall shear stress for $Re_{2,is} = 115,000$ with periodic inflow conditions

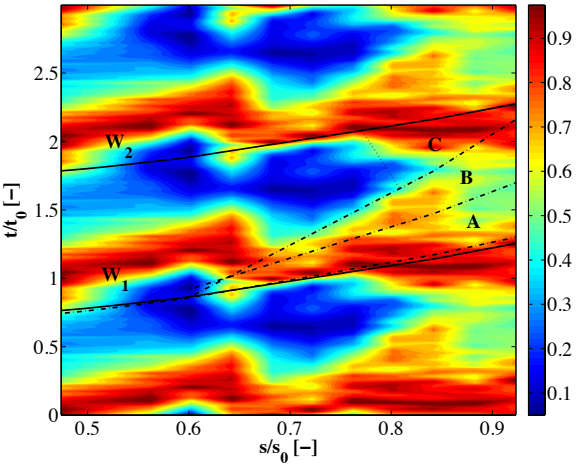

Figure 11: Space-time diagram of the phase-locked averaged pseudo-wall shear stress rms for $Re_{2,is} = 115,000$ with periodic inflow conditions

As described by Halstead et al. [6], the unsteady boundary layers are developing along two separate but coupled paths: the wake-induced path (lying under the wake trajectory, or lagging slightly behind the latter) and the path between two consecutive wakes. The first path W_1 induced by the presence of the wake can be clearly observed in the obtained results, with the typical wedge-shaped wake-induced transitional strip (zone A) and the associated calmed region (zone B) starting at the location $s/s_0 = 0.62$, well into the diffusing part of the blade. The shape of the wedge is related to the different convection velocities of the leading and trailing edges of turbulent spots (0.5 V_{is}

and 0.88 V_{is} respectively) as well as the convection velocity of the calmed region (0.3 V_{is}). This transitional region is characterized by an abrupt increase of the wall shear stress coupled with high rms values, followed by a gradual decay of both in the calmed region, an observation that was confirmed by analyzing the hot-film time traces (not shown). In the path between two consecutive wakes, a region of attached (non-zero wall shear stress) transitional (high rms) flow can be observed where the calmed region becomes weaker (zone C), eventually merging with the following wake-induced transitional strip W_2 until the trailing edge. Finally, after analyzing the signal of the most aft hot film sensor, the calmed region could not be discerned anymore, thus assuming that the boundary layer is fully turbulent and attached when reaching the trailing edge of the blade. This is a typical case of multi-mode transition where, at a fixed moment in time, transition can take place at different locations on the blade and be triggered by different mechanisms. As a final remark, it should be noted that separation, characterized by near-zero wall shear stress and rms values, only seems to take place intermittently between two consecutive wake passing events, an observation that was confirmed after analyzing the time traces of the processed hot-film signals. This demonstrates the overall suppressing effect that incoming wakes have on the separation bubble. The earliest point of separation ($s/s_0 = 0.56$) also coincides with the separation location under uniform inflow conditions (Fig. 8).

4. Correlations of the characteristic points for the uniform inflow conditions: prediction model

From the detailed analysis of the time-averaged and time-resolved measurements, the characteristic points (i.e. separation, maximum displacement, reattachment and transition onset) can be determined and allow the construction of a prediction model for the separated fow transition mode with uniform inflow conditions. The aim of the prediction model is to provide the main separation bubble features (such as the acceleration parameter K and the local Reynolds number) at the location of the characteristic points. The constructed prediction model is then compared with the prediction model proposed by Hatman & Wang [5] which is based on flat plate, low speed measurements at low turbulence intensity (FSTI = 0.3 - 0.6 %) and the prediction models proposed by Michalek et al. [10] and Houtermans et al. [16]. The authors express the position of those characteristic points based on a local Reynolds number (Eq. 4) instead of a Reynolds number based on the displacement or momentum thickness (which can not be measured in the current configuration), as they report a better data correlation by using this definition.

$$Re_s = \frac{sV_{\infty,s}}{\nu_s} \tag{4}$$

The location of the separation, maximum displacement and reattachment points was determined by using the same procedure as described by Houtermans et al. [16] using the time-averaged velocity distribution V_∞ and its gradient $\frac{dV_\infty}{ds}$.

4.1. Separation point

The onset of separation was determined as the location where the time-averaged wall-shear stress value goes to zero and this location was further cross-checked with the procedure described hereabove using the velocity distribution due to the coarser spatial resolution of the hot-film sensors. The local Reynolds number $Re_{s,S}$ is represented as a function of the local acceleration parameter $K_{s,S}$ (Eq. 5) at the separation location (Fig. 12). The obtained correlation (Eq. 6) shows a good agreement with the correlations of Hatman & Wang and Michalek et al.

$$K_{s,S} = \frac{\nu}{V_\infty^2}\frac{dV_\infty}{ds} \tag{5}$$

The investigated flow regimes (with uniform inflow conditions) presented in the first part of this paper covered the open separation and the laminar separation with short as well as long bubble (bursting occurs at around $Re_{2,is} = 140,000$).

$$Re_{s,S} = 30920 - \frac{124990}{K_s \cdot 10^6} + \frac{26180}{(K_s \cdot 10^6)^2} \tag{6}$$

The bursting from a short to a long bubble type occurred between $K_{s,S} = -1.3 \cdot 10^{-6}$ (laminar separation/short bubble) and $-2.0 \cdot 10^{-6}$ (laminar separation/long bubble), corroborating the data from Hatman & Wang and Michalek et al. who found a value of $K_{s,S} = -1.3 \cdot 10^{-6}$ and $-1.7 \cdot 10^{-6}$ respectively.

4.2. Maximum displacement point

The maximum displacement point location was determined from the velocity distribution as being the point where a rapid change in slope occurs and the flow diffusion continues further downstream, corresponding to a pressure increase up to the reattachment

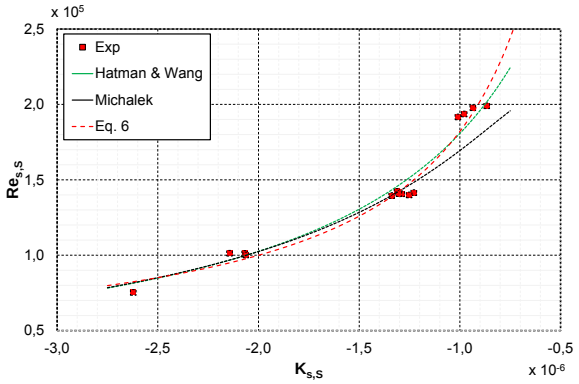

Figure 12: Correlation between separation Reynolds number and acceleration parameter at separation

point. For this reason, the maximum displacement is also called pressure recovery point (Houtermans et al., [16]). The maximum displacement location is correlated to the separation point location (Eq. 7), and this relation remains valid for both short and long bubbles.

$$Re_{s,MD} = 30,089 + 1.0203 \cdot Re_{s,S} \quad (7)$$

The obtained relation is compared with the correlations provided by Hatman & Wang, Michalek et al. and Houtermans et al. [16] as plotted in Fig. 13.

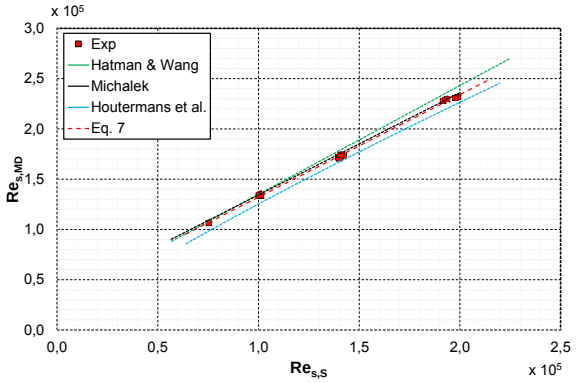

Figure 13: Correlation for the maximum displacement Reynolds number

4.3. Reattachment point

The bubble topology characterization is finalized with the reattachment point location correlation (Eq. 8), which is also compared with the correlations of Hatman & Wang, Michalek et al. and Houtermans et al. (Fig. 14).

$$Re_{s,R} = 29,475 + 1.0633 \cdot Re_{s,S} \quad (8)$$

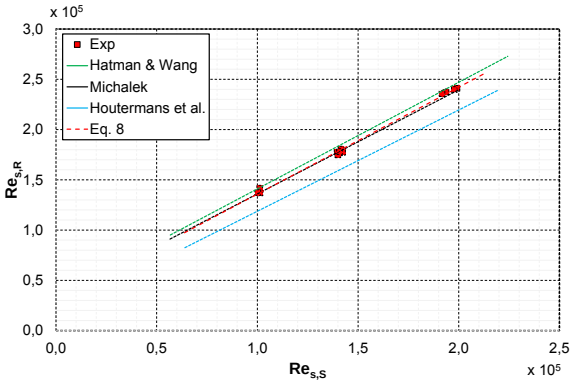

Figure 14: Correlation for the reattachment Reynolds number

5. Conclusions and future work

A rigorous investigation of the aerodynamic performance of the very-high-lift mid-loaded T106C LPT blade was performed at high isentropic exit Mach number (0.65) and for a range of engine representative isentropic exit Reynolds numbers (90,000 – 200,000), covering the bursting of the separation bubble from a short type to a long or even fully open one.

In the case of uniform inflow conditions, the Reynolds number has a significant influence on the physical size of the separation bubble, and therefore on the aerodynamic losses and loading of the airfoil. A significant deterioration of the aerodynamic performance was observed as the Reynolds number decreases, culminating in a fully open separation bubble at the lowest Reynolds number investigated. A prediction model for the separated-flow mode of transition has been proposed and compared with good agreement with prediction correlations available in the literature.

In the case of periodic inflow conditions, a beneficial effect of the unsteady wake-boundary layer interactions was observed at the lower Reynolds numbers (90,000 – 115,000), as the impinging turbulent wakes are periodically suppressing the separation bubble. An analysis of the boundary layer evolution along the diffusing part of the suction surface showed that its development occurs along two distinct paths for one wake-passing event: the wake-induced transitional strip, characterized by its wedge shape and the calmed region, and the path between two consecutive wakes, characterized by attached transitional flow. Furthermore, at higher Reynolds numbers ($Re_{2,is} > 125,000$), an inversion of the loss evolution occurs: the aerodynamic losses under periodic inflow conditions become more significant than under uniform inflow conditions

due to an increased surface being covered by turbulent flow, therefore increasing the profile losses.

The aerodynamic performance of low-pressure turbine airfoils in the S-1/C wind tunnel has so far mainly been analyzed based on time-averaged data acquired by means of pneumatic probes with a (very) low frequency response. However, in order to obtain more information and physical insight into the inherently unsteady nature of the separation/transition process, time-resolved data are obviously required. To this end, a calibration methodology for constant temperature hot-wire anemometry in a compressible non-isothermal low-density flow (such as in the S-1/C wind tunnel) will be applied in order to perform accurate time-resolved velocity measurements in the wake region directly downstream of the trailing edge. The obtained data will also be invaluable for the validation of models dealing with boundary layer separation/transition in a low-pressure turbine environment.

Finally, as described in the introduction of this paper, reducing the weight of the low-pressure turbine is one of the main current trends in aeroengine design. Recent developments in material technology allow the use of lighter materials in parallel with the common practice of reducing the blade count per row. However, the manufacturing process of the blade using these lighter materials can result in a rougher finish of the blade surface. An experimental measurement campaign is in the process of being concluded, and a thorough analysis of the processed data is under way.

6. Acknowledgments

The funding of this work by the Fonds pour la Formation à la Recherche dans l'Industrie et dans l'Agriculture (FRIA - FNRS) is gratefully acknowledged by the first author. The author also wishes to acknowledge the permission to have access to previous experimental results obtained within the framework of the European research projects UTAT (GRD1-2001-40192) and TATMo (AST5-2006-030939) performed at the von Karman Institute.

References

[1] Mayle, R. E., The role of laminar-turbulent transition in gas turbine engines, Journal of Turbomachinery 113 (1991) 509–537.

[2] Volino, R. J. and Hultgren, L. S., Measurements in separated and transitional boundary layers under low-pressure turbine airfoil conditions, Journal of Turbomachinery 123 (2001) 189–197.

[3] Hodson, H. P. and Howell, R. J., The role of transition in high-lift low-pressure turbines for aeroengines, Progress in Aerospace Sciences 41 (2005) 419–454.

[4] Walker, G. J., The role of laminar-turbulent transition in gas turbine engines: a discussion, Journal of Turbomachinery 115 (1993) 207–217.

[5] Hatman, A. and Wang, T., A prediction model for separated-flow transition, Journal of Turbomachinery 121 (1999) 594–602.

[6] Halstead, D. E., Wisler, D. C., Okiishi, T. H., Walker, G. J., Hodson, H. P. and Shin, H.-W., Boundary layer development in axial compressors and turbines: part 1 of 4 - Composite picture, Journal of Turbomachinery 119 (1997) 114–127.

[7] Schobeiri, M. T. and Ozturk, B., Experimental study of the effect of periodic unsteady wake flow on boundary layer development, separation, and re-attachment along the surface of a low pressure turbine blade, in: ASME Turbo Expo 2004: Power for Land, Sea and Air, no. GT2004-53929, Vienna, Austria, 2004.

[8] Stieger, R., Hollis, D. and Hodson, H., Unsteady surface pressures due to wake induced transition in a laminar separation bubble on a LP turbine cascade, in: ASME Turbo Expo 2003: Power for Land, Sea and Air, no. GT2003-38303, Atlanta, USA, 2003.

[9] R. Ciorciari, Kirik, I. and Niehuis, R., Effects of Unsteady Wakes on the Secondary Flows in the Linear T106 Turbine Cascade, Journal of Turbomachinery 136 (2014) 0910101–1 – 11.

[10] Michael, J., Monaldi, M. and Arts, T., Aerodynamic performance of a very high lift low pressure turbine airfoil (T106C) at low Reynolds and high Mach number with effect of free stream turbulence intensity, in: ASME Turbo Expo 2010: Power for Land, Sea and Air, no. GT2010-22884, Glasgow, UK, 2010.

[11] T. Arts, Aerodynamic performance of two very high lift low pressure turbine airfoils (T106C - T2) at low Reynolds and high Mach numbers, in: 5th European Conference for Aerospace Sciences, Munich, Germany, 2013.

[12] Hodson, H. P., Detection of boundary layer transition and separation in high speed turbine cascades, in: Measurement Techniques for Transonic and Supersonic Flow - Proc. 7th Symposium, Aachen, Germany, 1983.

[13] A. Arnone, Viscous Analysis of a Three-Dimensional Rotor Flow Using a Multigrid Method, Journal of Turbomachinery 116 (1994) 435–445.

[14] Dietz, A. J. and Ainsworth, R. W., Unsteady Pressure Measurements on the Rotor of a Model Turbine Stage in a Transient Flow Facility, in: International Gas Turbine and Aeroengine Congress and Exposition, no. ASME-92-GT-156, Cologne, Germany, 1992.

[15] Coton, T., Arts, T., Lefebvre, M. and Liamis, N., Unsteady and calming effects investigation on a very high-lift LP turbine blade - Part I: experimental analysis, Journal of Turbomachinery 125 (2003) 281–289.

[16] Houtermans, R., Coton, T. and Arts, T., Aerodynamic performance of a very high lift low pressure turbine blade with emphasis on separation prediction, Journal of Turbomachinery 126 (2004) 406–413.

Experimental characterization of unsteady flows in a high speed axial compressor

Giulia Dell'Era

Turbomachinery and Propulsion Department, von Karman Institute for Fluid Dynamics, Belgium, dellera@vki.ac.be

Supervisor: Fabrizio Fontaneto

Assistant Professor, Turbomachinery and Propulsion Department, von Karman Institute for Fluid Dynamics, Belgium, fabrizio.fontaneto@vki.ac.be

University Supervisor: Tony Arts, Philippe Chatelain

Professor, Turbomachinery and Propulsion Department, Head of the Department, von Karman Institute of Fluid Dynamics, Belgium, arts@vki.ac.be
Professor, Université Catholique de Louvain, Institute of Mechanics, Materials and Civil Engineering, Belgium, philippe.chatelain@uclouvain.be

Abstract

In the frame of the design of new aircraft engines, the definition of the operating range of the compressor is an issue of paramount importance as influences the performance of the whole engine. The surge line indeed limits the operating range while creating unsteady phenomena such as rotating stall and surge. The formation of these instabilities therefore has to be defined. A state-of-the-art booster has been tested at VKI and characterized regarding stall inception patterns, which are different in all the speed lines investigated, but all of them seem to be triggered by a low frequency component. The investigation of the stall inception origin is presented in this article, and seems to be linked to the instability of the entire system.

Keywords: Axial compressor, rotating stall, surge

1. Introduction

The operating range of a compressor is limited at low mass-flow rates by the presence of unstable phenomena such as rotating stall and surge. I.J. Day [1] observed that in multistage compressors part-span stall appears in the low speed range in the front stages, while the increase of rotational speed drives the machine in full span rotating stall and then surge, and moving the origin of the instability from the front to the rear stages. This finding is illustrated in the performance map shown in Fig. 1.

Rotating stall and surge will not only degrade the aerodynamic performance of the machine by creating a pressure ratio and efficiency drop, but will also affect the design of a new machine on the structural point of view. As shown in E. Poursaeidi [2], rotating stall may create fatigue cracks, which cause the rupture of blades and the consequent breakdown of the engine. Stall phenomena may also create blade vibration and casing deformation, and therefore have to be taken into account in the structural design. As a consequence the aerodynamic design results to be the tradeoff between aerodynamic and structural constraints.
As the unstable range is dominated by strongly machine dependent phenomena, the functioning of a specific compressor may not fall in the general classification proposed by I.J. Day [1]. For example T. Pan et al. [3], [4], show a case of rotating stall initiated by a low frequency component linked to mild surge even at low rotational speed. It is also well known that every compressor may exhibit a different behavior regarding the stall inception patterns: some follow the 'classical' models proposed by I.J. Day [5] and present the cases of spikes (e.g. N. Courtiade, X. Ottavy [6]), or modal waves (e.g. R. Mailach, K. Vogeler[7]), while some others do not. An example is provided by M.

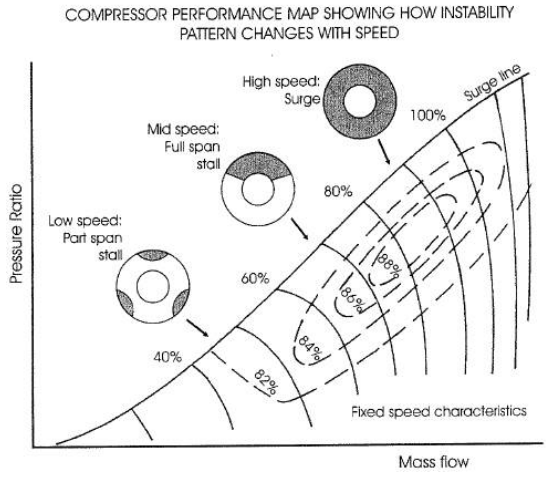

Figure 1: Performance map of a typical multistage compressor, I.J. Day [1]

Inoue et al. [8], which shows a rotor stalling at first with spikes, then, while closing the throttling valve, presents a modal activity.
There is another difficulty encountered by compressor designers: CFD simulations are not able to provide a sufficiently accurate prediction of the unstable regime. N. Gourdain [9] shows indeed that neither the stall inception patterns nor the stall cell size are correctly represented by unsteady simulations. Therefore the CFD validation and improvement, together with a good design practice, can only be derived from an appropriate experimentation.
The first stage of a state-of-the-art booster has been tested in order to be characterized in its unstable regime, and particularly to have a better understanding regarding the stall inception. This article aims the definition of the origin of the stall inception on this machine.
In the first part of the article the experimental set-up and the instrumentation are presented, together with the aerodynamic design of the stage. The different stall inception patterns are then described and are followed by the frequency analysis and the analysis of the time-resolved pressure signals.

2. Aerodynamic design of the stage

In an engine, the fan supplies the core with a pressure ratio distribution skewed towards the hub. The booster has the function to counterbalance this effect, while not yielding a high pressure ratio. The new design technologies tend to increase the aerodynamic load, imposing high diffusion factors in the low radius region thus making hub critical stages.
The present booster is the first stage of the core and has been scaled to be adapted to the test section of the facility employed for the experimental campaign. A fixed stagger inlet guide vane row (IGV) is placed to simulate the spanwise flow distribution provided by the fan root. The rotor blades are characterized by a 0.84 hub/tip ratio and an inlet relative Mach number at the tip of approximately 0.8. The nominal rotational speed is 8750 rpm (100% Nn).

3. Facility and instrumentation

3.1. VKI-R4 facility

The tests are performed in the VKI-R4 compressor rig, shown in Figures 2 and 3. It is a closed-loop configuration used for investigating high speed axial and radial compressors. A throttle valve allows the regulation of the mass flow while the inlet total temperature is maintained using water heat exchangers and the inlet total pressure is regulated by means of a control system connected to pressure and vacuum reservoirs. The shaft with a maximum rotational speed of 9000 rpm is driven by a 450 kW DC motor, via a 1:12 gearbox. The test section, designed to represent the first

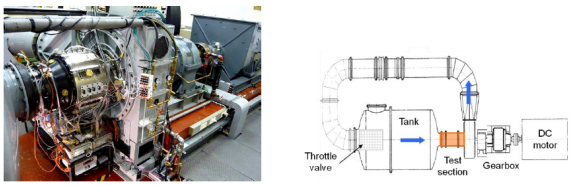

Figure 2: Photo and layout of the VKI-R4 compressor rig test section.

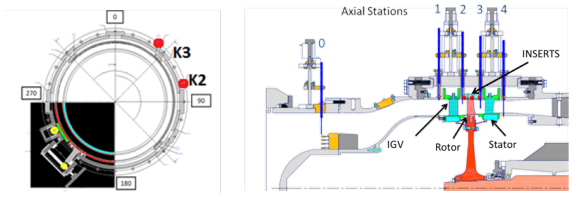

Figure 3: Circumferential and axial cross-section of the VKI-R4 compressor rig.

LP stage of a high bypass ratio turbofan engine consists of an IGV row with 100 blades simulating the effects of a fan, a rotor row with 76 blades followed by a stator row of 100 vanes. The signal from an optical once-per-revolution sensor mounted on the shaft

is recorded to be used in phase-locked and ensemble averages.

3.2. *Instrumentation, data acquisition and uncertainty*

Five axial locations, presented in Figure 3, allow acquisitions along radial traverses: far upstream the IGV (plane 0), at the IGV inlet (plane 1), at the rotor inlet (plane 2), at the rotor outlet (plane 3) and at the stator outlet (plane 4). Probe traverses are available at four circumferential positions (0 deg, 90 deg, 180 deg, 270 deg, Figure 3).
The focus of this study is the understanding of the stall phenomena appearing in the compressor stage considered, therefore both the global performance and the detailed topology of the flow are investigated. Rakes and static pressure taps located in plane 0 and plane 4 provide time averaged measurements of global quantities such as pressure ratio, mass flow and efficiency. Time resolved pressure measurements describe the topology of the flow field on the rotor casing, at the rotor outlet and at the stator outlet. The fast response probe utilized is located at the rotor outlet at midspan at 90 deg (see Figure 4).

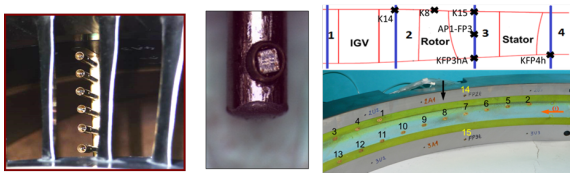

Figure 4: rakes, AP1-FP3 fast-response total pressure probe head and inserts in the casing

3.2.1. *Steady instrumentation*

The steady measurements are sampled continuously in real-time during the experiments at 2 Hz allowing the monitoring of the machine and the evaluation of the global performance.
Each of the four rakes located in plane 0 and in plane 4 consists of six small Kiel heads each one containing a total pressure tap and a T-type thermocouple junction. The corresponding axial position is equipped also with static pressure taps at the hub and in the casing.
The uncertainty associated to the measurements is calculated with the ASME method (proposed by Dieck [10]) and the values are presented for a 95% confidence interval. The uncertainty values retrieved are 0.5 mbar and 0.7 K which result in a 0.00053 uncertainty on the pressure ratio.

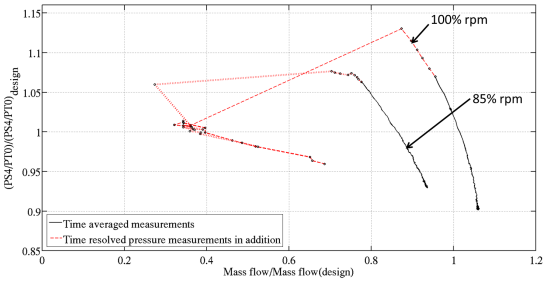

Figure 5: Speed lines 100% Nn and 85% Nn on the static-to-total performance map

3.2.2. *Unsteady instrumentation*

Fifteen piezo-resistive pressure transducers (see Figure 4) monitor the static pressure at the rotor casing by means of time-resolved measurements. These differential sensors have a range of 15 psi and a resonance frequency higher than 200 kHz. They are contained in a metallic insert and protected by a cavity which is limiting the bandwidth to 60 kHz.
The determination of the time resolved pressure levels in both the axial and the circumferential directions is fundamental for the detection of the stall cell(s). The sensors cover an arc of 42 deg (K2 and K3 represent the two extremes and are located respectively at 38 and 80 deg) and are equally spaced by one rotor pitch. The sensors are axially displaced between plane 2 and plane 3 as shown in Figure 4. The static pressure at the hub is retrieved in plane 3 and plane 4 by means of sensors located at 66 deg. The sensors are calibrated in situ by pressurizing the loop.
They are characterized by an uncertainty of 1.2 mbar, computed with the ASME method as for the steady instrumentation.

A fast response aerodynamic pressure probe (AP1-FP3, see Figure 4) is located at midspan at the rotor outlet at 90 deg. This is used together with the static pressure taps at the hub and in the casing to determine the size of the stall cell(s). The probe has an output voltage Vp proportional to the measured pressure and an output voltage Vs proportional to the measured temperature. The probe is characterized by a 3 mm diameter stem and a flush mounted 25 psi absolute sensor which has a resonance frequency of around 300 kHz.
The probe presents a calibration uncertainty of 1.8 mbar.
All the acquisitions of the time resolved data are performed with a 16 bit data acquisition system for 10 s

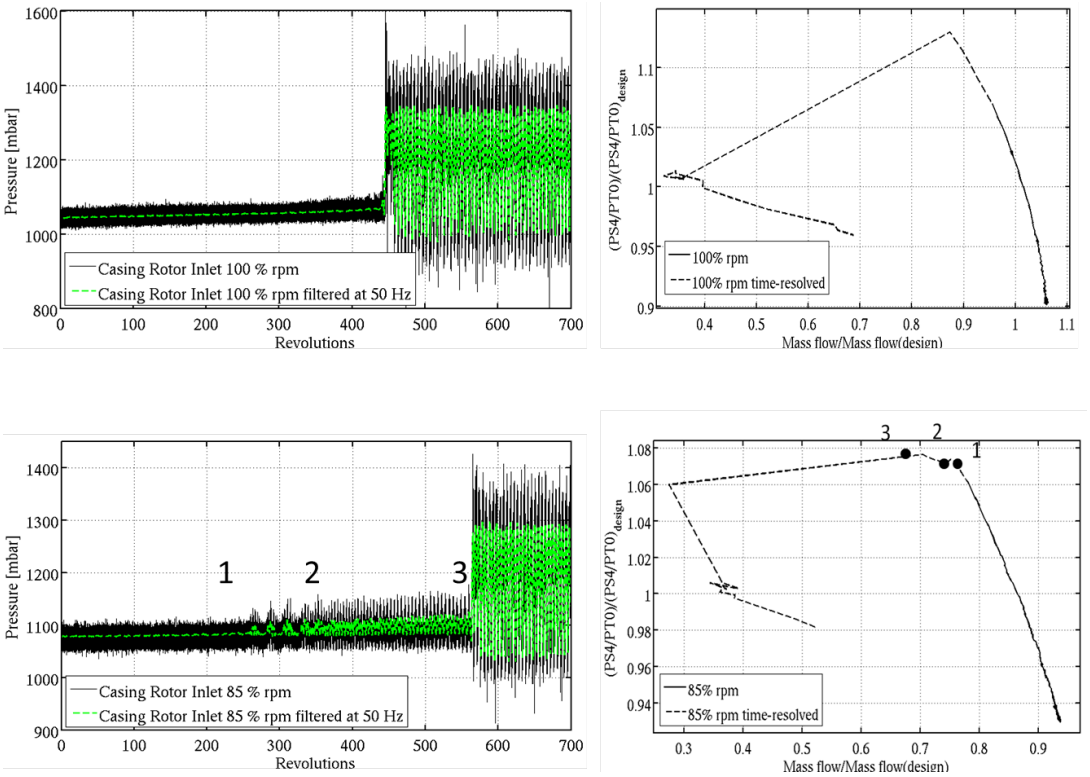

Figure 6: Time resolved pressure signal for the speed lines 100% Nn and 85% Nn and the corresponding static-to-total performance map

with a sampling frequency of 1MHz.

4. Rotating stall inception

This axial compressor stage has been tested in five speed lines, each one is showing a different stall inception pattern. As their characterization have already been presented ([11]), the focus on the current study is on two speed lines: 100% Nn and 85% Nn.
The performance map, Fig. 5, presents a sudden drop in the pressure rise for the case 100% Nn, which corresponds to an abrupt stall inception, while for the case 85% Nn the pressure ratio increases before the flow breakdown.
The corresponding time-resolved pressure signals describe the stall inception patterns in details. The one retrieved with the sensor located at the casing rotor inlet is shown as an example (Fig. 6), but similar patterns are visible for all the sensors. The case 100% Nn is characterized by a sudden presence of high amplitude fluctuations, which correspond to the flow breakdown. In the case 85% Nn instabilities appear before the flow breakdown, at first they are modulated by a lower frequency component (between points 1 and 2 in Fig. 6) and then become continuous (between points 2 and 3 in Fig. 6).

5. Frequency analysis

In order to have a better understanding on the various stall inception patterns a frequency analysis has been applied using as a technique the wavelet transformation. This methodology is suitable for the description of the frequency content of a signal during a transient as it can follow its evolution. The details of the wavelets employed can be found in Ref.[11] and are applied to the signals which have been low pass filtered at 50 Hz, in order to focus on the rotating stall cell.

Figure 7 shows the case 100%Nn with the signal retrieved at the casing rotor inlet and the corresponding wavelet transformation. In the bottom graph it is possible to visualize a frequency component related to the rotating stall cell ($\approx$ 30Hz), which remains constant during the transient. This is representative of the fact that the number of cells does not vary during the transient. In this case there is only one cell occupying approximately 50% of the annulus

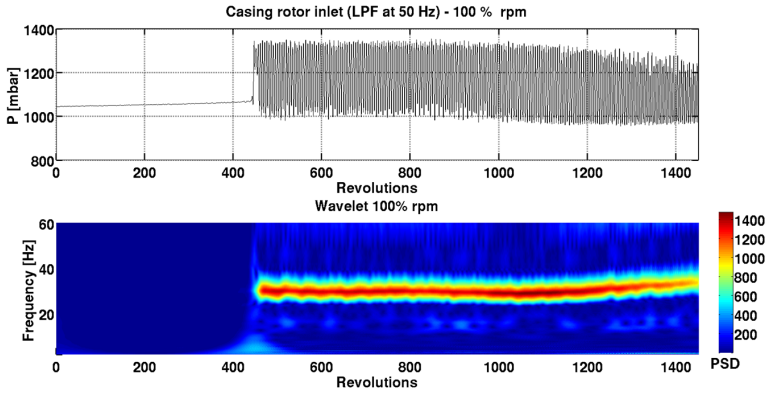

Figure 7: Time resolved pressure signal for the speed line 100% Nn and corresponding wavelet transformation

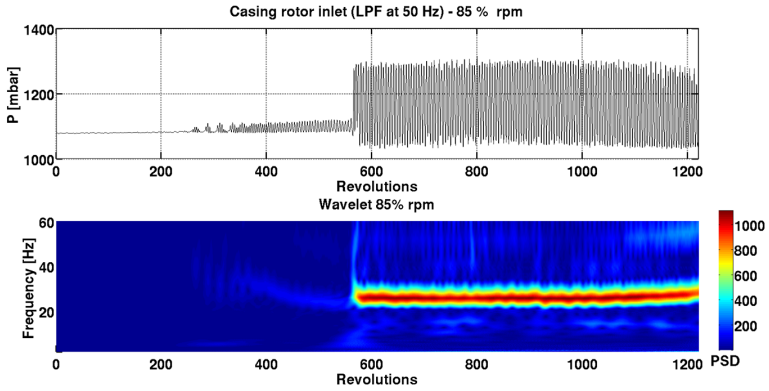

Figure 8: Time resolved pressure signal for the speed line 85% Nn and corresponding wavelet transformation

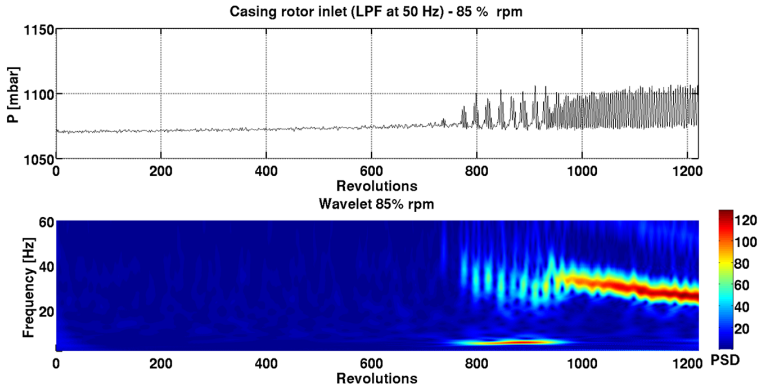

Figure 9: Time resolved pressure signal for the speed line 85% Nn and corresponding wavelet transformation (first part of the transient)

and rotating at 20% of the rotor frequency for all the speed lines investigated ([11]). There is also a low frequency component appearing before the formation of the rotating stall cell.

The case 85% Nn (Fig. 8) presents similar patterns with respect to the case 100% Nn. The low frequency component though appears also in the part of the transient when the instabilities arise. This is visible in

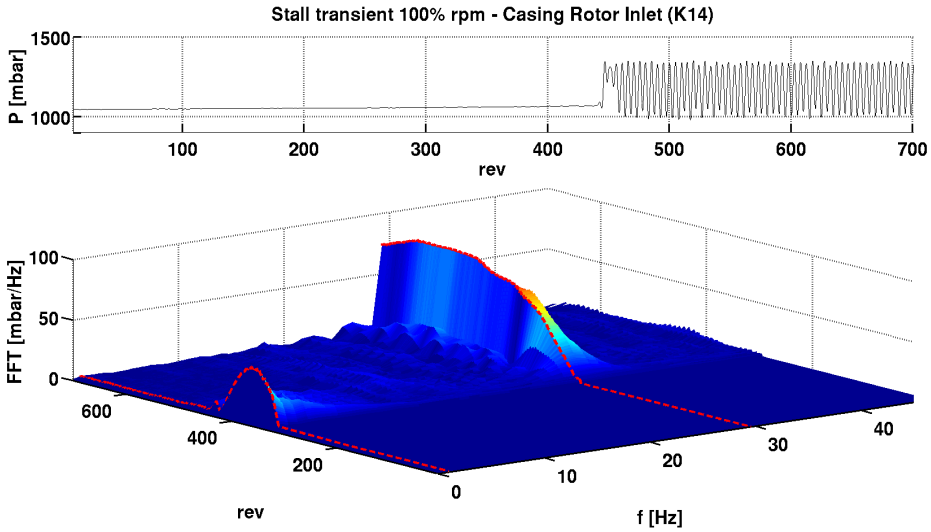

Figure 10: Time resolved pressure signal for the speed line 100% Nn retrieved at the casing rotor inlet and corresponding Window Fourier Transformation

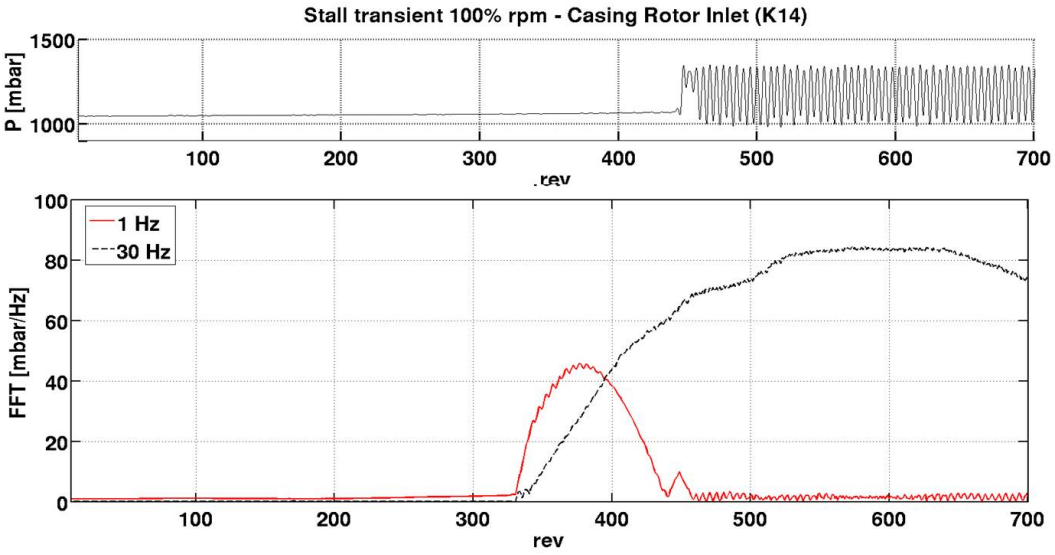

Figure 11: Time resolved pressure signal for the speed line 100% Nn retrieved at the casing rotor inlet and corresponding frequency components extracted from the Window Fourier Transformation

Fig. 9, which shows the first part of the transient.

The low frequency component seems to cause both the flow breakdown and the presence of the instabilities for all the speed lines investigated, therefore the understanding of its origin is crucial for the complete description of the stall inception. In the wavelet transformations the low frequency component appears to be $\approx 5Hz$ which corresponds to the facility Helmholtz frequency. It is thus hypothesized that an acoustic resonance might be the cause of the flow breakdown.

The wavelet transformations though are not able to locate the origin of the low frequency component in the machine, nor to identify it in a precise time during the transient. A Window Fourier Transformation (WFT) is therefore applied.

A WFT consists of an FFT applied to a window of the time-resolved pressure signal which is sliding along the transient. In the present case the window consists of 112 revolutions and is applied every revolution.

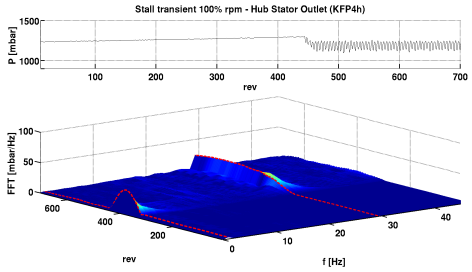

Figure 12: Time resolved pressure signal for the speed line 100% Nn retrieved at the hub stator outlet and corresponding Window Fourier Transformation

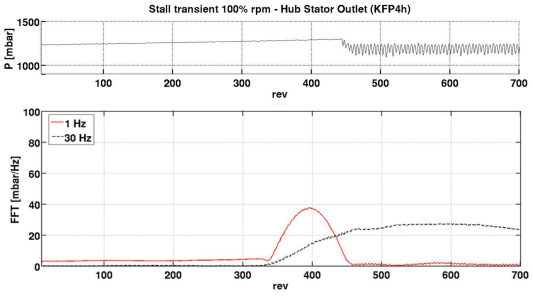

Figure 13: Time resolved pressure signal for the speed line 100% Nn retrieved at the hub stator outlet and corresponding frequency components extracted from the Window Fourier Transformation

This has been chosen in order to insure both an accurate frequency resolution in the spectrum and in the transient. The result obtained is a three-dimensional graph such as the one reported in Fig. 10, where it is possible to visualize the spectrum evolution along the transient.
This procedure is presented at first for the signal retrieved with the sensor at the casing rotor inlet. For the case 100% the three-dimensional plot shows the presence of a low frequency component quite spread in the spectrum, appearing before the sharp continu-

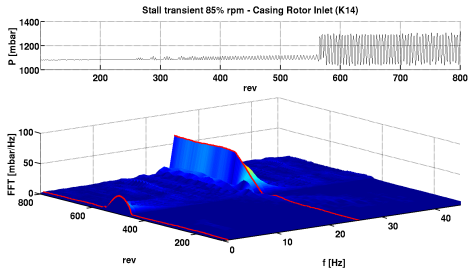

Figure 14: Time resolved pressure signal for the speed line 85% Nn retrieved at the casing rotor inlet and corresponding Window Fourier Transformation

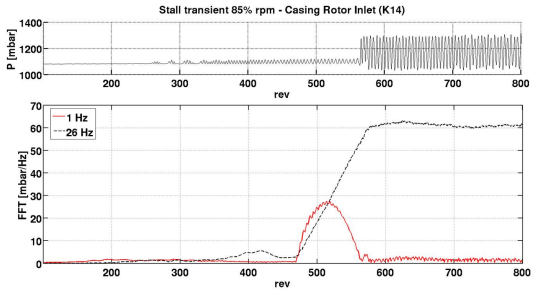

Figure 15: Time resolved pressure signal for the speed line 100% Nn retrieved at the casing rotor inlet and corresponding frequency components extracted from the Window Fourier Transformation

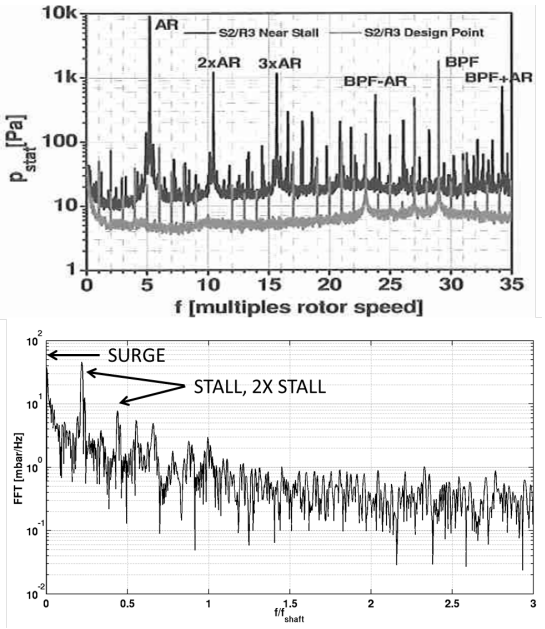

Figure 16: Typical spectrum retrieved in the presence of acoustic resonance [12], spectrum retrieved on the stage at the casing rotor inlet at rev. 376 in the case 100% Nn

ous peak related to the rotating stall cell. Considering only these two peaks in a 2D graph (Fig. 11), it is possible to point out that the low frequency component triggering the flow breakdown is $\approx 1Hz$, and that its peak corresponds to a part of the transient where in the time-resolved signal there is still no precursors of the flow breakdown (see Fig. 11).
This procedure has then been applied to several sensors in different axial, radial and circumferential locations. The presence of the low frequency peak is evident at all the various locations and therefore suggests the relation of this component to the whole system and not to a specific location of the stage. As an example is reported the case of the sensor positioned at the hub

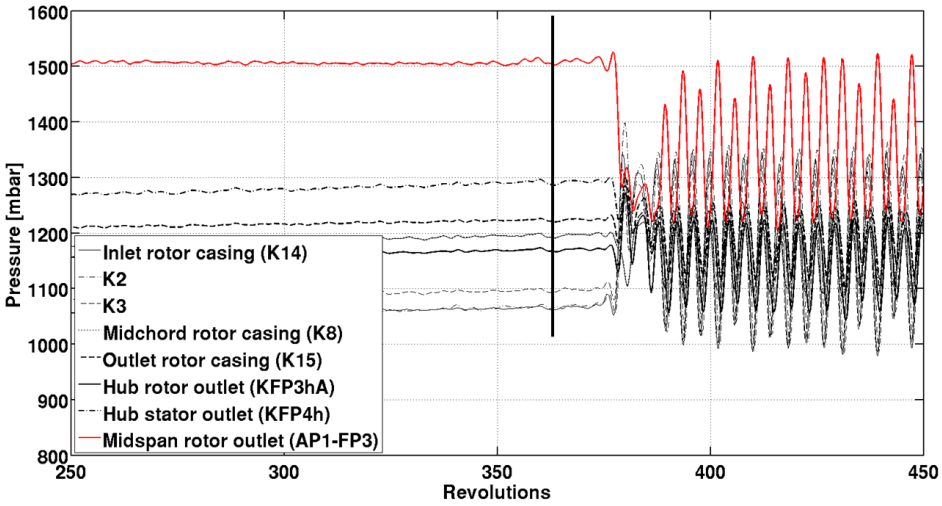

Figure 17: Time resolved pressure signal for the speed line 100% Nn retrieved at different machine locations

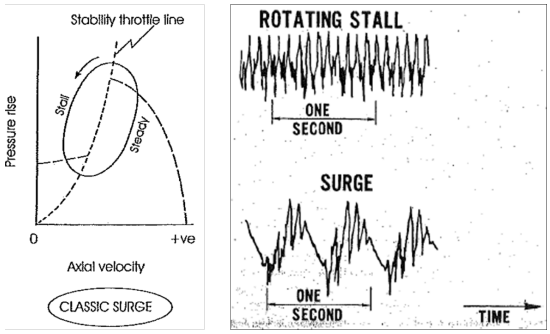

Figure 18: Surge cycle on the characteristic curve [13] and typical surge and stall signals [14]

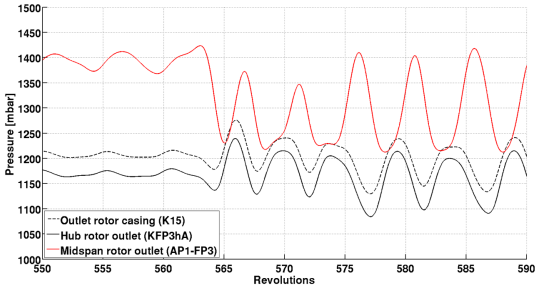

Figure 19: Time resolved pressure signal for the speed line 85% Nn retrieved at different machine locations at the flow breakdown

stator outlet in Fig. 12 and 13.
The case 85% Nn is presented in Fig. 14 and 15 showing as an example the procedure applied to the signal retrieved with the sensor at the inlet rotor casing. The stage appears to behave similarly in both cases (85% and 100% rpm): the low frequency peak rises before the flow breakdown at all the locations. The peak rises also in the part of the transient preceding the instabilities.
The WFT discards the hypothesis of acoustic resonance, as the peak is proven to be spread between 1 and 5 Hz and higher at 1 Hz. Therefore would not match with the Helmholtz resonance frequency of the facility. Moreover, as pointed out by B. Hellmich [12], [15] and retrieved also by N. Courtiade and X. Ottavy [6], an acoustic resonance always appears as a sharp peak in the spectrum appearing with its harmonics, wheras in the current case the low frequency component is spread and does not exhibit any modulation. This is shown in Fig. 16 where is presented a typical spectrum retrieved in case of acoustic resonance, such as in the case studied by Seume [12], and the WTF retrieved at the highest peak of the low frequency component.
A low frequency component evident in the whole the system can therefore be linked to the hysteresis cycle of the system. As a further proof the time resolved pressure measurements are analyzed.

6. Time resolved pressure signal and discussion on the nature of the low frequency component

For this analysis all the signals are low pass filtered at 50 Hz in order to focus on the low frequency range. Figure 17 represents the time-resolved pressure signal retrieved with various sensors at 100% Nn. At all

the locations of the machine exists a precursor to the flow breakdown (which in the Figure 17 corresponds to the black line ($\approx$ *rev*360)). This precursor fluctuation appears in the part of the transient where the 1 Hz component shows the peak and is simultaneous in the axial and radial direction.

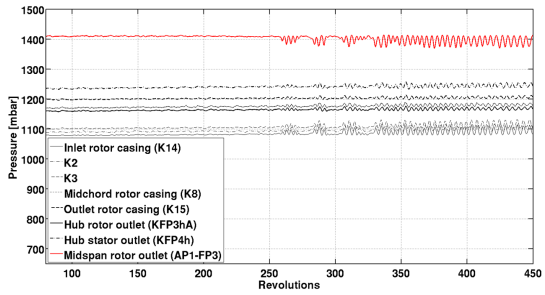

Figure 20: Time resolved pressure signal for the speed line 85% Nn retrieved at different machine locations when the instabilities arise

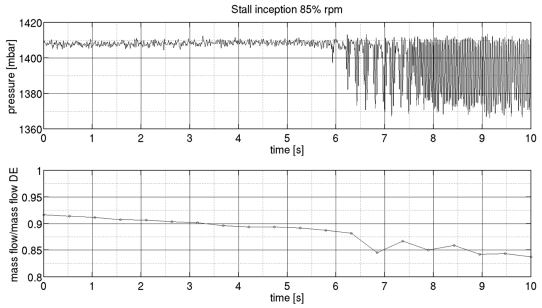

Figure 21: Time resolved pressure signal for the speed line 85% Nn retrieved with the fast response pressure probe and corresponding mass flow evolution

Such a low frequency component triggering the presence of precursor fluctuations and the flow breakdown in the whole system may be linked to surge or, at least, to the hysteresis cycle of the compressor. Surge indeed is an instability of the entire system which creates an axial pulsation and therefore a hysteresis cycle on the characteristic curve. A typical signal retrieved during surge is presented in Figure 18 [14]. The figure points out that the machine is periodically entering and exiting stall condition and that this phenomenon is characterized by a much lower frequency than the one of the rotating stall cell (Figure 18, right).

As the machine oscillates between stalled and unstalled condition mass flow fluctuations will occur. This is visible in Fig. 18 (left) which represents the theoretical characteristic curve retrieved by Greitzer [13].

The case 85% Nn seems to verify all the features presented in a typical hysteresis cycle. The explanation is provided in the following paragraphs.

Figure 19 presents the pressure signals at midspan, casing and hub at the rotor outlet. At the flow breakdown (rev 565) the total pressure level reaches the static pressure one. This means that the mass flow is approximately zero or slightly negative.
The figure presenting the various signals at the instabilities arise (Fig. 20) show that they all appear at the same time in the axial and radial direction. The phenomenon is thus system related. The time shift existing in the circumferential direction is due to the presence of the rotating stall cell.

The time-resolved signal retrieved by the probe (Fig. 21) at the instabilities arise shows a similar pattern with respect to the one of a typical surge signal (Figure **??**): there is a single precursor fluctuation, followed by oscillations between stalled and unstalled condition.
Furthermore the mass flow evolution along the transient presents a fluctuation corresponding to the part of the transient when the signal oscillates between stalled and unstalled condition (see Fig. 21).
The mass flow evolution though, being sampled at 2 Hz, requires a further proof to confirm the actual presence of its fluctuations. The compressor stage characteristic therefore will be modeled employing the equations proposed by Moore and Greitzer [16], in order to compare the result with the experimental data. The hypothesis that the low frequency component is linked to the system hysteresis cycle therefore seems to be the most probable.

7. Conclusions

A state-of-the-art booster stage has been tested in the unstable regime in order to investigate on the stall inception patterns.
The experimental campaign allowed to understand the mechanisms appearing in the machine at the stability limit. The high speed range is characterized by abrupt stall inception, while the low speed range presents instabilities before the flow breakdown. In both cases it is triggered by a low frequency component.
The low frequency component seems to be linked to the surge cycle, as it is associated to mass flow fluctuations. This will be proved by the comparison with a software which models the compressor characteristic curve employing a 2-D model.
These measurements can be used to improve the de-

sign of the future boosters and to ameliorate the design practice of this kind of machines.

List of Symbols

IGV Inlet Guide Vane
Nn shaft speed [% with respect to design speed]
WFT Window Fourier Transform

References

[1] I.J. Day, C. Freeman, The unstable behavior of low and high-speed compressors, Journal of Turbomachinery 116 (2) (1994) 194–201.

[2] E. Poursaeidi, M.R. Mohammadi Arhani, S. Hosseini, M. Darayi, M. Arablu, Partial stall effects on the failure of an axial compressor blade, Journal of Engineering for Gas Turbine and Power 137 (12) (2015) 122602.

[3] Q. Li, T. Pan, Z. Li, T. Sun, Y. Gong, Experimental study of compressor instability inception in a transonic axial flow compressor, no. ASME Turbo Expo 2014, Disseldorf, Germany, 2014.

[4] T. Pan, Q. Li, T. Sun, Z. Li, Y. Gong, Effect of radial loading distribution on partial surge initiated instability in a transonic axial flow compressor, no. ASME Turbo Expo 2015, Montreal, Canada, 2015.

[5] T.R. Camp, I.J. Day, A study of spike and modal stall phenomena in a low speed axial compressor, Journal of Turbomachinery 120 (3) (1998) 393–401.

[6] N. Courtiade, X. Ottavy, Experimental study of surge precursors in a high speed multistage compressor, Journal of Turbomachinery 135 (6) (2013) 061018.

[7] R. Mailach, K. Vogeler, Unsteady aerodynamic blade excitation at the stability limit and during rotating stall in an axial compressor, Journal of Turbomachinery 129 (3) (2007) 503–511.

[8] M. Inoue, M. Kuroumaru, T. Tanino, M. Furukawa, Propagation of multiple short-length-scale stall cells in an axial compressor rotor, Journal of Turbomachinery 122 (1) (2000) 45–54.

[9] N. Gourdain, Simulation Numerique des Phenomenes de Decollement Tournant dans les Compresseurs Axiaux, Ph.D. thesis, Ecole Centrale de Lyon (2005).

[10] R. H. Dieck, Measurement uncertainties methods and applications, ISA, Research Triangle Park, 2007.

[11] G. Dell'Era, N. Habotte, J. Desset, J.-F. Brouckaert, S. Hiernaux, Experimental characterization of stall phenomena in a single-stage low-pressure axial compressor, Journal of Engineering for Gas Turbine and Power 229 (5) (2015) 549–559.

[12] B. Hellmich, J.R. Seume, Causes of acoustic resonance in a high speed axial compressor, Journal of Turbomachinery 130 (6) (2008) 031003.

[13] E.M. Greitzer, Surge and rotating stall in axial flow compressors. Part I: Theoretical compression system model, Journal of Engineering for Power 98 (2) (1976) 190–198.

[14] E.M. Greitzer, Surge and rotating stall in axial flow compressors. Part II: Experimental results and comparison with theory, Journal of Engineering for Power 98 (2) (1976) 199–211.

[15] B. Hellmich, Acoustic resonance in a high-speed axial compressor, Ph.D. thesis, Gottfried Wilhelm Leibniz Universitat Hannover (2008).

[16] F. K. Moore, E.M. Greitzer, A theory of post-stall transients in axial compression systems: Part I - Development of equations, Journal of Engineering for Gas turbines and Power 108 (1) (1986) 68–76.

Performance robustness of turbine squealer tip designs due to manufacturing and engine operation

Cis De Maesschalck*

Turbomachinery and Propulsion, von Karman Institute for Fluid Dynamics, Belgium, cis.demaesschalck@vki.ac.be

Guillermo Paniagua

Adjunct Professor, Aeronautics and Aerospace Department, von Karman Institute for Fluid Dynamics, Belgium, gpaniagua@me.com

Associate Professor, Department of Mechanical Engineering, Purdue University, United States

University Supervisor: Chris Lacor

Professor, Faculty of Applied Sciences, Department of Mechanical Engineering, Vrije Universiteit Brussel, chris.lacor@vub.ac.be

Abstract

In unshrouded turbines profuse rotor blade tip design strategies have been proposed towards improved aerothermal performance. However, the actual geometry during the engine operation differs from the envisioned design geometry. Manufacturing inaccuracies, combined with the harsh turbine environment can lead to relevant geometrical variations. Hence, the future optimization of the tip designs requires estimation of the uncertainties on the aerothermal performance due to the geometrical variability.

The objective of the current manuscript is to quantify the influence of the manufacturing tolerances and profile degradation during engine operation in the blade tip region on the overall turbine performance. An extensive numerical study was conducted on a modern high pressure turbine rotor, operating at a high Reynolds and high subsonic outlet conditions. The Stochastic Collocation Method was used to investigate the effects of the geometrical variability of a single squealer tip design. The variation of three geometrical characteristics was investigated: the tip clearance size, squealer depth and rim corner radius. Three-dimensional Reynolds-Averaged Navier-Stokes simulations were performed, adopting the Spalart Allmaras model for the turbulence closure, to examine the aerodynamic and heat transfer characteristics.

The results highlight the influence of the combined geometrical variability on the overtip flow structures, detailed heat transfer signatures, loss development and downstream flow characteristics. This study yields a deeper insight into the robustness of turbine squealer tip geometries and highlights the importance of taking the consequences of these unavoidable geometrical changes into account from an early stage in the turbine design optimization.

Keywords: High Pressure Turbine, Tip Leakage Flow, Uncertainty Quantification, Stochastic Collocation

Nomenclature

CFD	Computational Fluid Dynamics
d	Cavity depth [% of span]
h	Clearance height [% of span]
L	Lagrangian
M	Mach number [-]
N	Amount of performed simulations
Q	Heat transfer [W] or Heat Flux [W/m^2]
$\overline{Q}$	Heat transfer, normalized by the Baseline case
R	Corner radius [% of rim thickness]
SCM	Stochastic Collocation Method
SST	Shear Stress Transport
TLV	Tip Leakage Vortex
w	Quadrature weights

*This paper was presented during the 22nd International Symposium on Air Breathing Engines in Phoenix, AZ (USA), Oct. 25-30, 2015 (Paper Nb. ISABE2015-20205)

y Stochastic response

Greek Symbols

η Efficiency
ξ Standardized input value
μ Mean level
σ Standard deviation

Subscripts

abs Absolute quantity
rel Relative quantity
tot Total quantity
w wall

1. Introduction

The tip region is a prime component defining the durability of the gas turbine engine and the periodic overhaul [1]. Hence, numerous rotor blade tip shapes have been proposed and extensively investigated in recent years. Numerical and experimental campaigns were performed on diverse topologies, comprising simple flat tip designs [2], carved profiles [3], winglet shapes [4] and squealer tips [5]. The present investigation addresses a single squealer design, a prevalent tip shaping strategy in current engines. This design has a central cavity defined by an upstanding rim all around the pressure and suction side. This geometry has been widely studied both numerically [6,7] as well as experimentally in low [8,9] and high speed environments [10]. However, the profile in operation may differ significantly from the optimal designed geometry. Indeed, manufacturing tolerances as well as the unavoidable distortion during operation (e.g. erosion, oxidation, creep, rubbing, foreign object damage, etc...) can lead to considerable shape alterations [1]. To realize a proper assessment of the turbine aerodynamics, thermal loads and consequent component durability, we ought to estimate the uncertainties related to the geometrical variability. In this view, Bunker and Bailey [11] studied the effect of the squealer cavity depth and oxidation on turbine blade tip heat transfer and observed an increase in the cavity heat flux as the rim material is removed.

Recently, non-intrusive probabilistic uncertainty methodologies such as polynomial chaos expansion and stochastic collocation methods [12] have received an increasing interest [13]. These methods allow to propagate large uncertainties through complex models while requiring considerably less simulations compared to conventional Monte Carlo methods. Considering the relatively high computational cost of turbomachinery computational fluid dynamics (CFD), these efficient techniques offer opportunities to include a-priori known uncertainties already from an early design phase or test a-posteriori the robustness of the design outcome [14]. Such assessment, indispensable for a proper reliability evaluation [15, 16], could additionally be used to justify discrepancies between numerical predictions and experimental data [17,18]. Nevertheless, these methods are not widely adopted (yet) in the gas turbine community [19], except for rare examples [20]. Moreover, to the best of the authors knowledge, no rigorous study on the combined geometrical effects of a squealer tip has been conducted using such non-intrusive uncertainty quantification methodology.

The current paper presents the results of an extensive numerical study, investigating the robustness of a squealer tip design to manufacturing tolerances and operational degradation, adopting the stochastic collocation method. This work gives a deeper insight into the distinct geometrical influences on the aerothermal characteristics of the turbine rotor and quantifies confidence intervals for the heat transfer signatures and aerodynamic flow properties.

2. Numerical Methodology

The simulated blade row subject of this paper is part of a state-of-the-art high pressure turbine stage. The rotor is characterized by a Reynolds number of $2.4\text{x}10^5$ and an exit relative Mach Number ($M_{rel,exit}$) of 0.73. The most important specifications are presented in Table 1.

Table 1: Turbine specifications

Parameter		
Reynolds number	-	$2.4x10^5$
Exit Relative Mach number	-	0.73
Blade count	-	48
Non Dimensional Speed	-	281
Tip gap - Design	% span	1.38%
Rotor pressure ratio	-	2.2
$T_{tot,a,gas}/T_w$	-	1.47
$T_{tot,r,gas}/T_w$	-	1.33

Only one periodic section of the turbine rotor has been modeled and the computational domain is split in two distinct subdomains (Fig. 1): one 'downblock' which remains the same for every evaluated geometry

and an 'upperblock' that is altered, depending on the particular tip design considered.

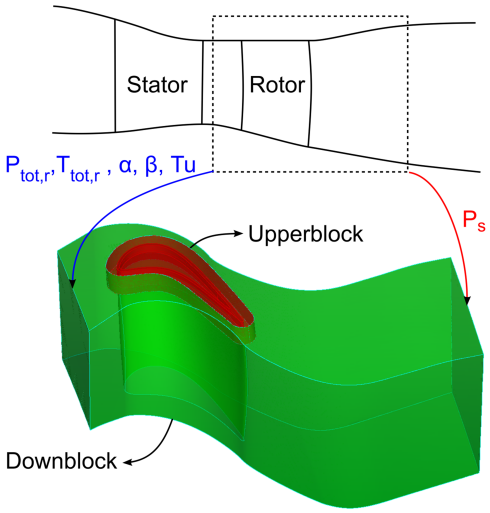

Figure 1: Computational domain

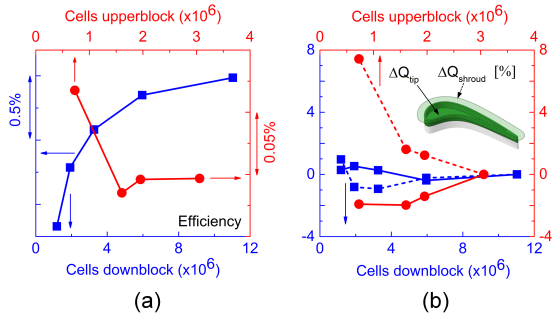

Figure 2: Mesh sensitivity analysis: a) effect on rotor efficiency, b) effect on tip and shroud heat transfer

A fully hexahedral mesh is generated through Numeca Hexpress®, separately for both subdomains. In order to ensure the grid independency of the simulations, a mesh sensitivity analysis was conducted, summarized in Fig. 2. The computations were performed by increasing the mesh resolution isotropically for one domain while maintaining the mesh density for the other domain. For this study, a general squealer design with sharp rim edges was used. Fig. 2a presents the effect on the rotor efficiency while Fig. 2b shows the variability in the heat transfer onto the tip (solid lines) and the overtip casing (dashed lines) compared to the finest grid solution. In both graphs, the lower and left axis refer to the influence of the down-block refinement (blue curves with square labels) and the upper and right axis to the upperblock resolution (red curves with round markers). In Fig. 2a we observe a negligible effect on the efficiency when refining the upperblock domain beyond 2 million cells. Hence, the same efficiency offset associated with the downblock grid will equally affect each tip configuration, ensuring a valid comparison among different profiles. The influence of the downblock resolution on the tip and shroud heat transfer is limited: less than 0.4% between the two finest grids. The influence of the upperblock is more pronounced but still limited to 1.5% between the two finest grids.

Based on the latter analysis, the main mesh settings of the 2nd finest grid were adopted for all simulations during this investigation. Additionally, extra refinements were included to capture accurately the rim corner radii, resulting in an average total mesh size of the upperblock around 5 to 6 million. The downblock mesh contains about 6 million cells and divides the blade span of the main passage into about 140 radial divisions. The tip gap has around 40 cells and the first cell size was fixed such that the y^+ values remain below 0.2 along all solid surfaces to accurately resolve the complete aerothermal boundary layer. These mesh settings are comparable to the densities adopted in previous numerical studies where a sufficient resolution of the overtip leakage flow was achieved [6,21]. A view of the final mesh for the baseline squealer design and a zoom into the overtip region can be seen in Fig. 3.

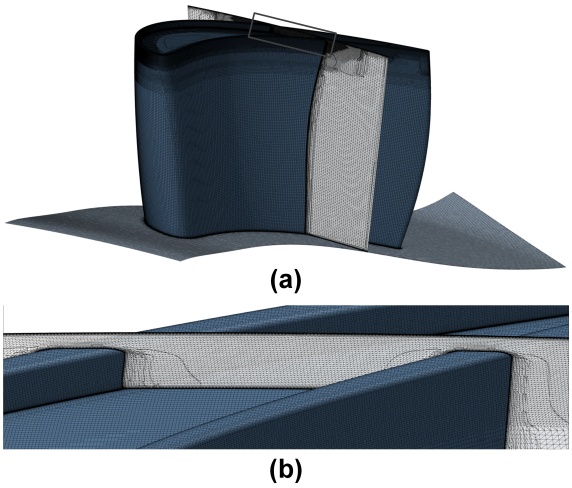

Figure 3: Full rotor mesh (a) and zoom of the tip gap region (b)

The simulations were performed with Numeca FINE/Open®, adopting the Spalart Allmaras model for the turbulence closure. This model has been proven suitable for high fidelity aerothermal simula-

tions of the overtip gap flowfield and heat transfer in a transonic environment. The experimental validation of the adopted solver can be found in [3], performed on a similar transonic high pressure turbine. At the rotor inlet (Fig. 1), pitchwise averaged radial profiles of relative total pressure, temperature, flow angle and turbulent quantities were imposed. At the downstream end of the computational domain, a static pressure was fixed, satisfying the radial equilibrium condition. The imposed quantities give rise to a total to static pressure ratio across the rotor of 2.2 and an engine representative gas to wall temperature ratio of about 1.5.

3. Robustness Assessment

3.1. Geometrical variability

Fig. 4a shows the investigated squealer tip geometry, widely used in the industry, consisting of an upstanding rim all along the pressure and suction side which creates a central cavity. Ideally, the turbine operates at a predefined design clearance (i.e. the distance between the rotating blade and the stationary shroud) and the top edges of the squealer rims are sharp. However, these rim edges are prone to wear due to the extremely harsh pressure and temperature-operating conditions, which results in the radiusing of the top rims during engine service [24,25]. Moreover, unintentional rubbing of the blade tip against the non-rotating casing may cause scraping of the squealer rim and consequently cause a reduction of the cavity depth. Lastly, during engine transients, the tip clearance undergoes large variations induced by the different thermal dilatation rates of the rotating and stationary frames.

The three distinct features of the squealer tip geometry (radius 'R', cavity depth 'd' and clearance height 'h') are presented in Fig. 4b. The baseline squealer tip geometry adopts a design clearance of 1.38% of the blade span. The cavity depth to rim thickness ratio is 2 and are respectively 1.23 and 2.5 times the design clearance (i.e. about 1.7% and 3.4% of the blade span). The baseline radius is 25% of the rim thickness. The parameter variabilities considered representative of engine operation and typical manufacturing errors are summarized in Table 2, reported as percentage of blade span or rim thickness. All uncertainties are assumed to have a normal distribution.

3.2. Stochastic collocation

In this work, the Stochastic Collocation Method (SCM) has been used to assess the eventual uncertainty on an output quantity y(x,ξ) due to a set of

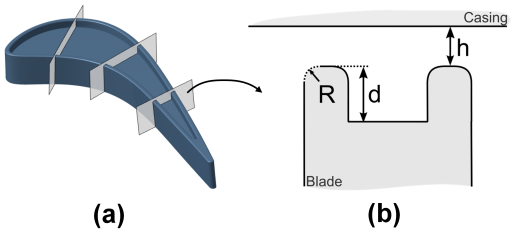

Figure 4: Squealer design (a) and applied variability (b)

Table 2: Adopted variabilities

Parameter	**[%]**	**Baseline (μ)**	$\sigma_{op.}$	$\sigma_{man.}$
Tip Clearance **'h'**	span	**1.38**	0.45	0.17
Cavity depth **'d'**	span	**3.4**	1.19	0.08
Corner radius **'R'**	rim th.	**25**	10	-

known geometrical input variabilities. **y** depends on the position **x** inside the domain and the standardized input variable ξ. In this case, the output quantity of interest (**y**) could be the heat flux at a certain axial location (**x**) where the behavior of the (independent) input random variables can be defined through normal probabilistic density functions $X = \mu + \sigma\xi$ with $\xi \sim N(0, 1)$.

The SCM [12] describes the stochastic response y(**x**,ξ) by adopting a polynomial expansion based on the Lagrangian interpolation of the Np samples at the Gaussian quadrature points:

$$y(x, \xi) \approx \sum_{j=1}^{N_p} y_j(\mathbf{x}) L_j(\xi) \tag{1}$$

Where the coefficients $y_j(x)$ are the simulation results at the collocation points ξ_j and the Lagrangian polynomials $L_j(\xi)$ are defined as:

$$L_j(\xi) = \prod_{\substack{i=1 \\ i \neq j}}^{N_p} \frac{\xi - \xi_i}{\xi_j - \xi_i} \tag{2}$$

In this case, combined effects of the multiple geometrical effects are considered and the consequent multi-dimensional interpolation is performed based on a tensor product approach, adopting all Nt samples. In order to maximize the performance, the collocation points defined from the optimal orthogonal polynomials should be used. In the case of a normal input distribution, the collocation points for a Lagrange interpolation of order p are essentially the roots of the Hermite polynomial of order p+1 [22].

For the SCM, the first two statistical moments of the output variable, i.e. mean μ_y and variance σ_y^2 are analytically available in a closed form:

$$\mu_y = \sum_{j=1}^{N_t} y_j(\mathbf{x}) w_j(\xi) \tag{3}$$

$$\sigma_y^2 = \sum_{j=1}^{N_t} y_j^2(\mathbf{x}) w_j(\xi) - \mu_y^2 \tag{4}$$

where w_j are the quadrature weights corresponding to a certain collocation point. For the data-processing of the eventual robustness intervals based on the simulations output, the open-source toolkit DAKOTA from the Sandia National Labs has been used [23].

3.3. Investigated cases

The simulated tip designs are summarized in Fig. 5. The three axes show the three different geometrical effects: the clearance gap, the cavity depth and the corner radius. The Baseline case is centered at the origin, further denoted as 'BL'. In order to evaluate the influence of the operational variabilities, 6 cases were computed, each located at the roots of a 3rd order Hermite polynomial ($\mu \pm \sigma_{op.}\sqrt{3}$, blue labels, simulations h^+/h^-, d^+/d^- and R^+/R^-). Additionally, the combined effect of a change in tip clearance and cavity depth was investigated (red labels, simulations 1-4). The influence of the manufacturing tolerances was only assessed for the combined change of the clearance and cavity depth (green labels, a-h).

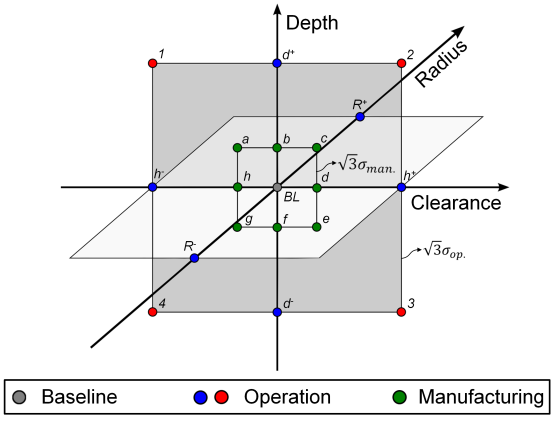

Figure 5: Overview of the evaluated cases

The investigated levels of tip clearance, cavity depth and rim corner radius are summarized in Table 3.

Table 3: Characteristics of the simulated designs

Par.	$\mu - \sigma_{op.}\sqrt{3}$	$\mu - \sigma_{man.}\sqrt{3}$	μ	$\mu + \sigma_{man.}\sqrt{3}$	$\mu + \sigma_{op.}\sqrt{3}$
h	0.6	1.09	1.38	1.67	2.16
d	1.33	3.24	3.4	3.54	5.44
R	7.68	-	25	-	42.32

* the same percentage conventions were adopted as in Table 2

4. Results

First, the influence of the corner radius will be discussed. Then the rotor global performance, heat transfer and the loss production will be analyzed more in detail, focusing on the combined effect of clearance and cavity depth variations.

4.1. Influence of the corner radius

Fig. 6a presents the influence of the corner radius on four turbine performance indicators: the turbine efficiency and the heat fluxes onto the blade tip, overtip shroud and upper 50% of the suction side. Each quantity is compared to the baseline case ('BL'). Larger radii of curvature lead to a decrease in size of the separation bubble created at the pressure side of the rim, where the leakage flow enters the overtip cavity. Hence more leakage gas flows into this overtip region [25], which enhances the development of the tip leakage vortex (TLV). As a consequence, the rotor efficiency reduces almost linearly with the rim corner radius, roughly by 0.15% per 20% of corner radius increase. Both the tip as well as the suction side heat transfer intensifies with the corner radius, while the shroud thermal flux declines.

Fig. 6b presents the tip heat flux for the baseline case as well as the results of the simulations performed with a smaller (R^-) and a larger (R^+) radius. We notice that the increase of total tip heat transfer is associated to the stronger vortical structure impinging on the tip cavity bath in the aft part of the blade (Fig. 6b, 'A'), overcompensating the slight decrease in the strength of the hot spot near the leading edge. The decrease in shroud heat transfer is mainly located at the PS entrance in the downstream half of the turbine rotor.

Even though extreme cases for the corner radius were investigated (ranging from ~8% up to ~42% of the rim thickness), its influence remains relatively limited (in particular concerning the heat transfer) compared to the other two geometrical effects: variations in clearance and cavity depth. For this reason, only the

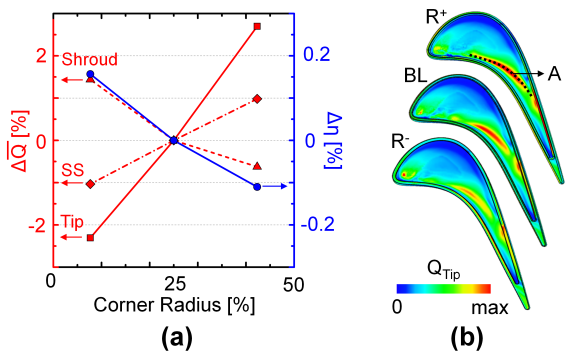

Figure 6: Influence of the corner radius on global performance (a) and tip heat flux (b)

combined effect of the latter two parameters was simulated and taken into account for the total robustness quantification. However, where relevant, the influence of corner radius will be indicated.

4.2. *Global performance and overtip flow*

Fig.7 shows the influence of the gap size and cavity depth on the rotor performance, through four contour plots, relative to the *BL* case: efficiency and heat transfer onto the tip, suction side and overtip shroud. The simulated cases for the operational and the manufacturing variabilities are also depicted in the figure (already shown in Fig. 5). A cubic interpolation was used to generate the contours. This approach reveals the general trends associated to tip clearance and cavity depth variations over a wide range.

The efficiency is primarily dominated by the clearance change and increases almost linearly, about 2% per 1% of gap size reduction, in accordance with previous studies [26]. On the heat transfer side, tight clearances are generally associated with lower thermal loads. The cavity depth has a higher impact on the rotor heat transfer levels than on the rotor efficiency. On the tip, the surface averaged heat flux shows to be the highest for the baseline cavity depth, and the baseline case offers a reduction in heat load up to 10% for a fixed gap size. For tighter clearances, larger depths are generally favorable. On the contrary, a cavity depth of 3.4% of the blade span promises optimal performances for the shroud thermal load. However, considering a fixed clearance, only a potential improvement of 2-4% is possible through cavity depth variations. Eventually, the suction side heat transfer is primarily governed by the gap size, favoring higher depths at high clearances.

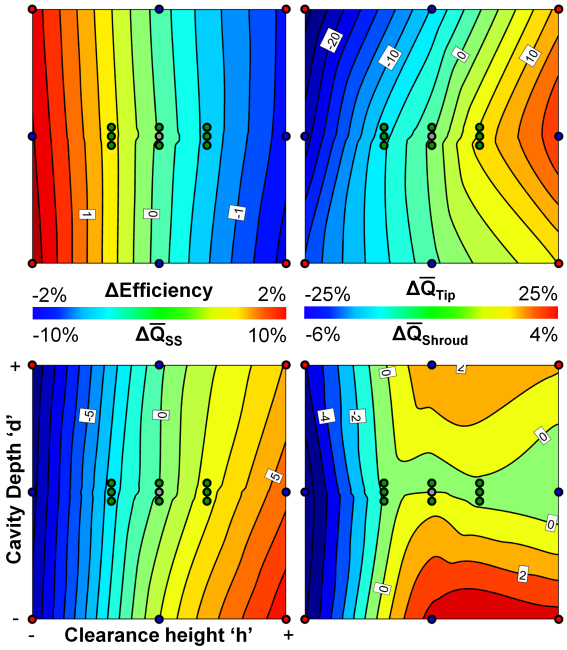

Figure 7: Global performance for clearance and cavity depth variations

Fig. 8 illustrates the overtip flow topology for the baseline case (*BL*). The solid walls are colored by the heat transfer levels while the relative Mach number distributions with streamlines are displayed on several cutting planes along the rotor camberline. Due to the size of the incoming boundary layer carrying low momentum fluid and the relative casing movement, flow enters the blade tip channel both at the pressure side (blue streamlines) as well as at the suction side (red streamlines). The flow crossing the suction side rim rolls up in a large vortex which creates a considerable zone of low heat transfer in the front section of the blade. This fluid turns along the blade camberline, gets pushed towards the shroud and exit the overtip region by crossing the suction side squealer (region 'A'), contributing to the formation and energization of the TLV. The initiation point of the TLV (indicated with 'B') and the point where all of the SS fluid exits the overtip region ('C') will determine the suction side heat transfer. The flow entering through the pressure side rim in the blades front part, rolls up into a vortex, remains entrained close to the pressure side squealer and leaves the gap region in the aft section of the blade. In region 'D' (right downstream the switch-point 'C'), the fluid coming from the PS does not enter the cavity anymore but gets directly accelerated and ejected towards the suction side into the TLV which

gathers strength as it progresses downstream towards the rotor outlet.

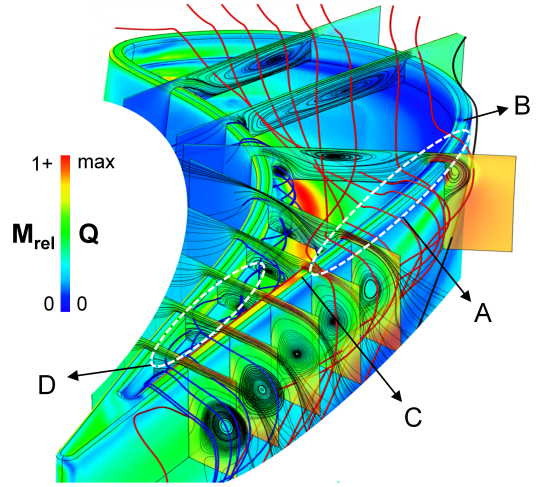

Figure 8: Flow topology for the baseline case with blade heat transfer and overtip Mrel contours

Fig. 9 illustrates the relative Mach number distribution at mid-height for all investigated cases. In the front part, the overtip Mach number tends to increase at larger cavity depths (in particular near the SS) while a slight drop can be noticed when increasing the clearance level. In the aft part, enlarged gap sizes induce higher overtip velocities. Interestingly, a trend of equal magnitude can be observed when considering the cavity depth variations. The signature of the exit jet shows the propagation of the TLV into the main passage (tracked by line 'A') and is mainly dominated by the gap size. The circles depict the regions with a drop in Mach number, precisely where almost all the fluid that entered the overtip region from the SS, has exited the gap (cfr. Fig. 8, point 'C'). This is particularly visible for the cases where a significant amount of fluid is entrained within the overtip region, i.e. at large clearances and cavity depths.

4.3. Heat transfer analysis

Tip. Fig. 10 presents the surface averaged tip heat transfer along the machine axis normalized by the heat flux of the *BL* case. To highlight the influences of the distinct geometrical variabilities, the simulations altering only one type of (operational) geometrical characteristic have been included, i.e. clearance size (h^-/h^+), cavity depth (d^-/d^+) and corner radius (R^-/R^+). Additionally, the $\pm 2\sigma$ uncertainty bands have been colored in light/dark grey for both the operational and manufacturing variabilities. In order to

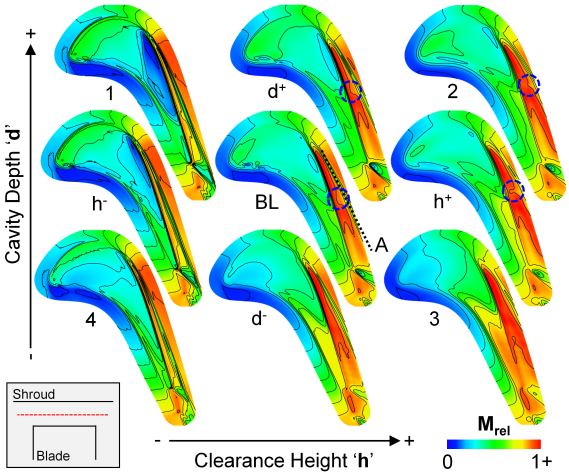

Figure 9: Mid-gap relative Mach number in the overtip region

explain the observed differences and trends more in detail, Fig. 11 depicts the tip heat transfer for all 9 cases with operational geometry changes.

The general trend on Fig. 10 reveals an initial decrease and subsequent increase of the tip heat transfer along the rotor chord. Near the LE, the flow travels over the first part of the SS tip rim and impinges immediately onto the cavity floor (Fig. 11, 'A'). This results in an enhanced heat transfer in the blade front part. Downstream the separation line with the flow coming from the pressure side (Fig. 11, 'B'), the overall surface heat flux decreases due to the large (slow) recirculation zone (cfr. Fig. 8). Eventually, the flow accelerates inside the cavity and a significant part of the heat transfer can be attributed to the impingement line of the pressure side vortex (Fig. 11, 'C'). Fig. 10 indicates the major contributor to the variations are clearance changes, giving rise to modifications as high as ±25%. The changes due to the cavity depth are mainly located in the very front part (caused by the impingement strength of the vortex near the LE) and in the aft part. In the rear half of the blade chord, a decrease in depth lowers the absolute magnitudes of the heat transfer (e.g. Fig. 11, case d^- and 3), the reduced surface area brings it back to a similar level as the *BL* (Fig. 10). Increasing the depth similarly lowers the peaks by 10% the aft part. Lastly, as indicated in Fig. 6, the overall sensitivity to the radius variations remains limited. However, in the central part of the blade, the effect of the corner radius is of a similar order of magnitude as the depth variations.

Shroud. Fig. 12 shows the casing heat transfer from 20% C_{ax} upstream of the rotor LE up to 20% C_{ax}

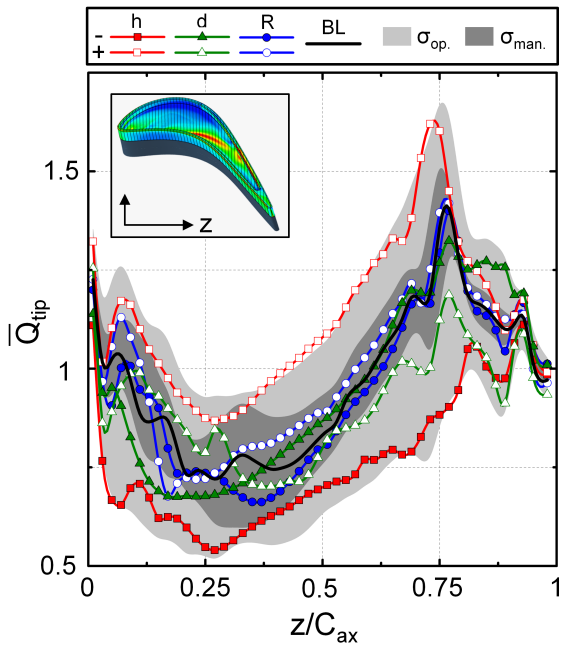

Figure 10: Tip heat transfer along machine axis

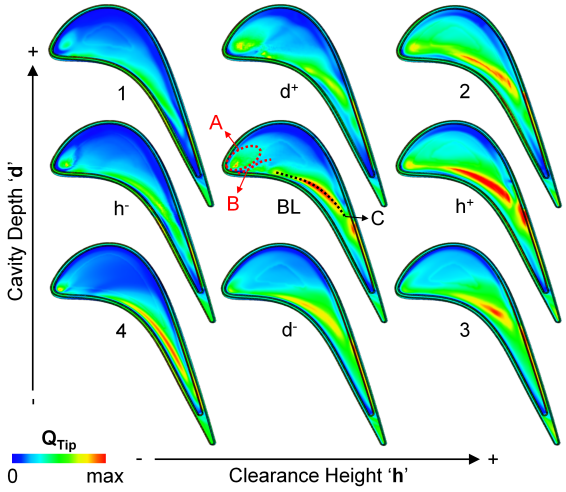

Figure 11: Tip heat transfer contours for clearance and cavity depth variations

downstream of the blade TE. For consistency, the same labels and color codes have been adopted as in Fig. 10. In the first 70% of the blade, the thermal load variations remain limited to less than ±10%, mainly due to modifications of the heat flux levels right above the squealer rim surfaces. However, in the blade aft part and further along the machine axis, the shroud heat transfer is very sensitive to tip geometry variations. In particular, one can observe a considerably different signature for the tight clearance compared to the baseline and large clearance levels.

In this view, Fig. 13a illustrates the overtip shroud heat transfer for the large cavity depth at small (Case 1), baseline (Case d^+) and large (Case 2) clearances. For the tightest clearance there is only one line of high heat transfer near the SS. However, for the two other clearances, two parallel stripes of large heat transfer immerge, aligned with the SS edge. Fig. 13b shows a detailed view of the overtip shroud heat transfer, together with several cuts of the flows relative Mach number, visualizing the TLV location and strength. In the case of the smaller clearance (Case 1), the TLV size is rather small and its core remains close to the SS surface. Consequently, the flow leaving the overtip region across the SS rim bends downwards immediately and rolls up into the leakage vortex. For larger clearances, the vortex size is considerably more voluminous and its center is located further away from the SS. Therefore, the flow gets contracted a first time when crossing the SS rim (first line of high heat transfer, 'A'), remains close to the shroud surface, and then gets accelerated a second time ('B') when passing the vortex centerline before rolling up into the TLV.

Suction side. Fig. 14a shows the surface averaged heat load onto the suction side for the upper 25% of the blade span (relative to the mean value of the BL case). The presented cases and adopted symbols are identical to Fig. 10 and Fig. 12. The overall trend shows a drop in the thermal loads after the leading edge and an increase in the aft part (z/C_{ax} ¿50-65%). Interestingly it is not only the second half of the profile (where the heat transfer signature is fully determined by the TLV development), but also the front part (z/C_{ax}¡40%) which are be heavily affected by the geometrical variations (heat transfer variations up to ±20%).

Fig. 14b presents the detailed heat transfer signature in the upper half of the blade suction side for the simulated case at a smaller clearance (h^-), the baseline case (BL) and a large clearance (h^+). The dashed line indicates the separation line between the immerging vortex structures and the main passage flow. These vortex structures include the upper passage vortex and the tip leakage vortex. The upper zone is divided into two parts, separated by another region of low heat transfer (dashed-dot line). At the tip, the latter line coincides with the initiation point of the tip leakage vortex (i.e. point 'B' in Fig. 8). Conse-

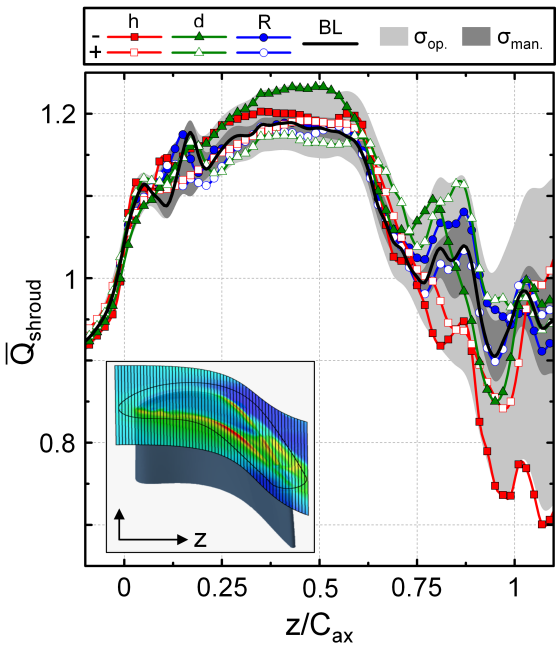

Figure 12: Shroud heat transfer along machine axis

quently the upstream region (labeled '1') is characterized by flow entering the cavity from the SS while the downstream zones (marked '2' and '3') are characterized by fluid streams that exit the overtip region. The enhanced heat transfer in region 1 is the result of the 'scraping' of the boundary layer through the relative movement of the casing. Fluid near the stationary shroud which is not entering the overtip gap gets pushed downwards, rolls up and merges eventually with the upper passage vortex. In the back part, the heat transfer signature is determined by the TLV. A first region (2) can be identified, characterized by the initial development of the leakage vortex. A second region (3) starting at about 80% Cax shows a considerably enhanced heat transfer. This is due to the large overtip velocities reached by the flow that enters the PS and is immediately accelerated towards the SS (Fig. 8, region 'D'). This leads to a sudden increase of the vortex size and strength and consequent large thermal load on the suction side surface. Generally, the main driving parameter for the SS heat transfer is the clearance, the tighter the better.

4.4. Loss development and downstream flow field

In order to quantify the loss development throughout the turbine, Fig. 15 presents the vorticity and relative total pressure drop along the rotor axial direction

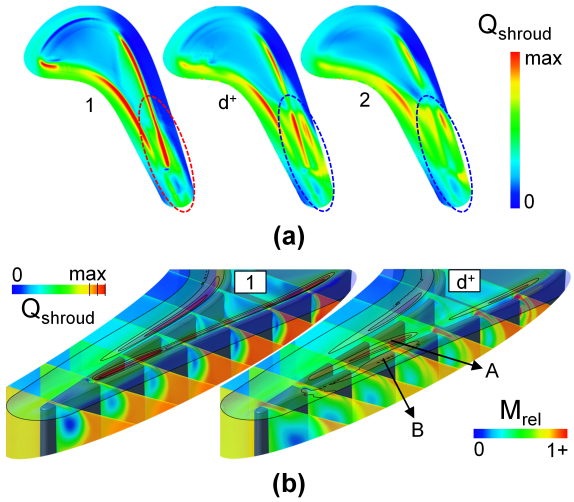

Figure 13: Overtip shroud heat flux for clearance variations (a) and driving vortex structures (b)

(compared to the inlet and normalized by the downstream dynamic pressure in the *BL* case). Only the two cases with clearance variations were included besides the *BL* simulation for clarity, the other ones showed to be very close to the BL case. The $\Delta P_{tot,r}$ gives a direct indication of the loss generation across the stage. In the first half of the blade, one can see that the tighter clearance gives a slightly increased pressure drop. However, in the aft part, the larger TLV (cfr. also the enhanced vorticity) and especially the downstream mixing overcompensates the initial trend, and results in about 5% additional pressure losses compared to the baseline.

To investigate the effect of the tip geometry on the quality of the flow received by a downstream stator, Fig. 16a shows the $\Delta P_{tot,r}$ and the absolute flow angle deviation at 50% C_{ax} behind the rotor TE. Both clearance as well as cavity changes are included. The predictions indicate that the influence of tip clearance and cavity depth remains limited to the upper 50% of the blade span. Gap size variations can lead up to a 40 deg. difference with the *BL* simulation. Interestingly, while the tip leakage loss core shows a higher pressure loss with clearance, the opposite trend can be observed when considering the center of the upper passage vortex. This effect on the UPV and the major influence on the TLV size and strength is illustrated in Fig. 16b where the downstream relative pressure is presented and the isolines indicate the vortex size.

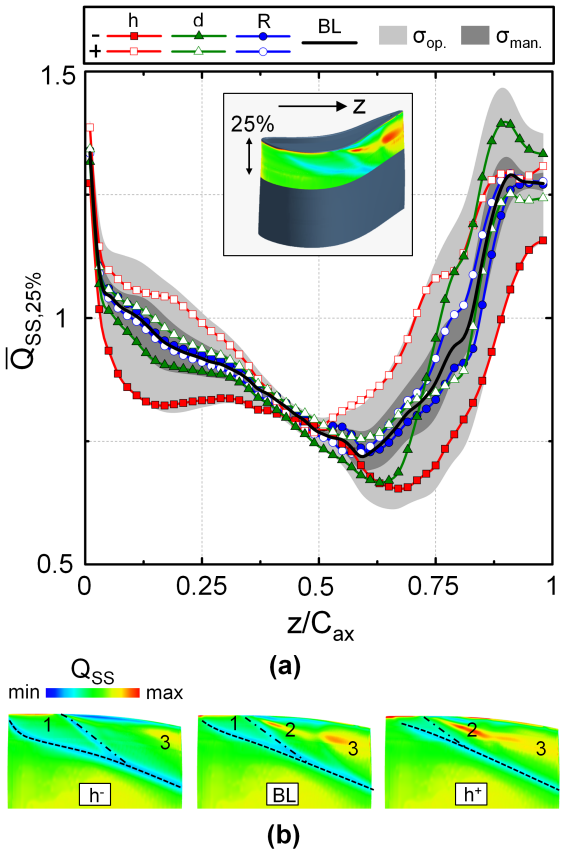

Figure 14: Suction side heat transfer along Cax

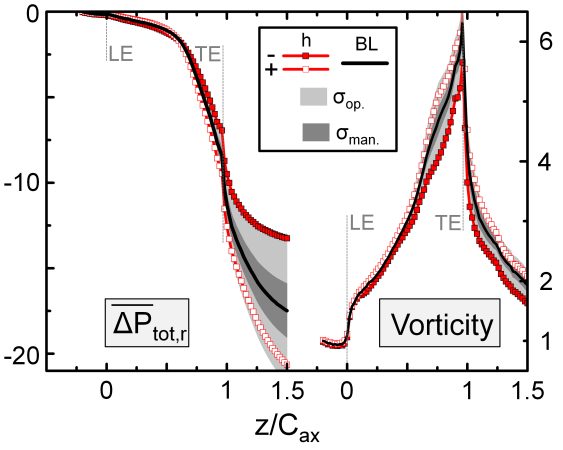

Figure 15:

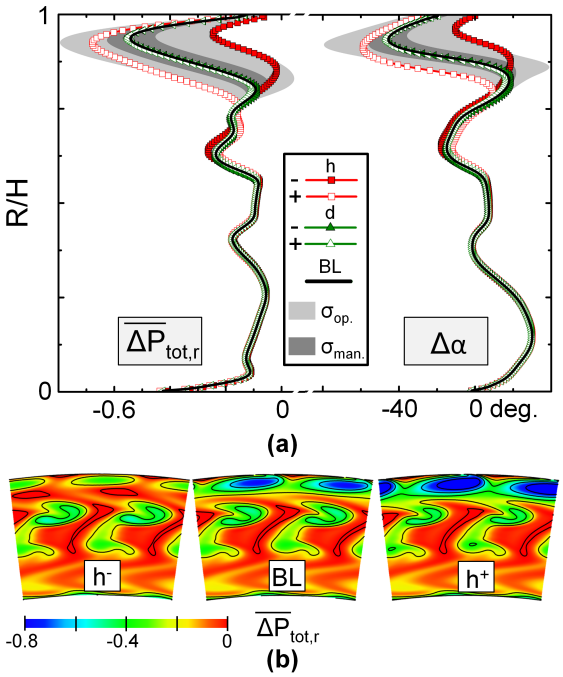

Figure 16: Ptot,r loss and absolute flow angle deviation 50% Cax downstream of the rotor TE (a), Ptot,r loss for clearance variations (b).

5. Conclusions

This numerical study focused the precise quantification of the effects associated to manufacturing/operational tolerances/variability on the aerothermal performance of high pressure turbines. The stochastic collocation method was used to assess the robustness of a squealer tip design in terms of rim corner radius, cavity depth and tip clearance variations.

The corner radius has the smallest effect, affecting the heat transfer 2% and efficiency ±0.15%. The efficiency is primarily driven by the clearance, 1% variation in the tip gap results in 2% variation in the aerodynamic efficiency. At design and larger clearances, the mean cavity depth induced the largest tip heat transfer. Varying the cavity depth may reduce the tip heat flux with 10% while increasing the shroud heat flux by 2-4%.

The predicted flow topology revealed that a portion of the leakage flow enters the overtip region from the suction side, generating a large recirculation zone of low heat transfer in the front part of the blade. Additionally, 3 distinct regions could be identified along the suction side: a first zone acts as an inlet whereas the two downstream zones let fluid leave the gap region. Moreover, a distinct drop in jet exit Mach number was observed in between the two aft regions.

The tip heat transfer shows fluctuations as high as ±25%, mainly governed by the clearance alterations. Cavity depth changes affect the front and rear parts caused by the impingement of the vortex near the LE. The shroud thermal load variations induce considerable variations in the last 30% of the rotor blade. Due to an important change in flow regime occurring at larger clearances, an additional acceleration of the tip leakage jet is provoked which generates a double line of high heat transfer. Remarkably, also the front part of the suction side is significantly altered by the geometrical changes and the 3 distinct flow regions can be clearly recognized.

The downstream field is generally altered in the upper 50% of the blade height, giving rise up to 40 deg. angle deviations. Interestingly, low clearances slightly increase the upper passage vortex strength.

The present study yields insight into the robustness of squealer tip designs and points out the importance of integrating the effects of these unavoidable geometry changes within the optimization strategies of future turbines.

6. Acknowledgements

The authors would like to acknowledge the Agency for Innovation by Science and Technology (IWT) in Belgium for the PhD fellowship (Nb. 121270) of Mr. De Maesschalck. Likewise the authors wish to thank Clara García Sánchez for her valuable suggestions concerning the uncertainty quantification methodology.
This paper was presented during the 22nd International Symposium on Air Breathing engines in Phoenix, AZ (USA), Oct. 25-30, 2015 (Paper Nb. ISABE2015-20205).

7. References

[1] Bunker, R. S., 2006, "Axial Turbine Blade Tips: Function, Design, and Durability," *J. Propul. Power*, **22**(2), pp. 271-285.
[2] Bunker, R. S., 2001, "A Review of Turbine Blade Tip Heat Transfer in Gas Turbine Systems," *Ann. N.Y. Acad. Sci.*, 934, pp. 64-79.
[3] De Maesschalck, C., Lavagnoli, S., Paniagua, G., 2014, Blade Tip Carving Effects on the Aerothermal Performance of a Transonic Turbine, ASME. J. Turbomach. 137(2): 021005-021005-10.
[4] ODowd, D. O., Zhang, Q., He, L., Oldfield, M. L. G., Ligrani, P. M., Cheong, B. C. Y., and Tibbott, I., 2011, Aerothermal Performance of a Winglet at Engine Representative Mach and Reynolds Numbers, ASME J. Turbomach., 133(4), p. 041026.
[5] De Maesschalck, C., Lavagnoli, S., Paniagua, G., Verstraete, T., Olive, R., Picot, P., 2015, Heterogeneous Optimization Strategies for Carved and Squealer-like Turbine Blade Tips, ASME Paper No. GT2015-42983.
[6] Krishnababu, S. K., Newton, P. J., Dawes, W. N., Lock, G. D., Hodson, H. P., Hannis, J., and Whitney, C., 2009, Aerothermal Investigations of Tip Leakage Flow in Axial Flow TurbinesPart I: Effect of Tip Geometry and Tip Clearance Gap, ASME J. Turbomach., 131(1), p. 011006.
[7] Mischo, B., Behr, T., and Abhari, R. S., 2008, Flow Physics and Profiling of Recessed Blade Tips: Impact on Performance and Heat Load, J. Turbomach., 130, 021008
[8] Camci, C., Dey, D., and Kavurmacioglu, L., 2005, Aerodynamics of Tip Leakage Flows Near Partial Squealer Rims in an Axial Flow Turbine Stage, J. Turbomach., 127, pp. 1424.
[9] Nasir, H., Ekkad, S. V., Kontrovitz, D. M., Bunker, R. S., and Prakash, C., 2004, Effect of Tip Gap and

Squealer Geometry on Detailed Heat Transfer Measurements Over a High Pressure Turbine Rotor Blade Tip, J. Turbomach., 126, pp. 221-228.
[10] Key, N. L., and Arts, T., 2006, Comparison of Turbine Tip Leakage Flow for Flat Tip and Squealer Tip Geometries at High-Speed Conditions, J. Turbomach., 128, pp. 213-220.
[11] Bunker, R. S., Bailey, J. C., 2001, Effect of Squealer Cavity Depth and Oxidation on Turbine Blade Tip Heat Transfer, ASME Paper No. GT2001-0155.
[12] Eldred M.S., 2009, Recent Advances in Non-Intrusive Polynomial Chaos and Stochastic Collocation Methods for Uncertainty Analysis and Design, AIAA Paper No. 2009-2274
[13] Najm, H. N., 2009, Uncertainty Quantification and Polynomial Chaos Techniques in Computational Fluid Dynamics, Annual Review of Fluid Mechanics, Vol. 41: 35-52
[14] Lange, A., Voigt, M., Vogeler, K., Schrapp, H., Johann E., Gmmer, V., 2012, Impact of Manufacturing Variability on Multistage High-Pressure Compressor Performance, ASME. J. Eng. Gas Turbines Power, 134(11):112601-112601-8
[15] Bunker, R. S., 2009, The Effects of Manufacturing Tolerances on Gas Turbine Cooling, J. Turbomach 131(4), 041018.
[16] Fadlun, E. A., Michelizzi, I., De Iaco, M., 2008, Measurement Error Influence on Gas Turbine Operability for Condition-Based Maintenance and Reliability/Availability Improvement, ASME Paper No. GT2008-50749
[17] Spieler, S., Staudacher, S., Fiola, R., Sahm, P., Weischuh, M., 2008, Probabilistic Engine Performance Scatter and Deterioration Modeling, ASME J. Eng. Gas Turbines Power, 130, p. 042507.
[18] Seshadri, P., Parks, G. T., Shahpar, S., 2014, Leakage Uncertainties in Compressors: The Case of Rotor 37, Journal of Propulsion and Power, Vol. 31, No. 1, pp. 456-466.
[19] Montomoli, F., Carnevale, M., D'Ammaro, A., Massini, M., Salvadori, S., 2015, Uncertainty Quantification in Computational Fluid Dynamics and Aircraft Engines, SpringerBriefs in Applied Sciences and Technology, ISBN: 978-3-319-14680-5
[20] Montomoli, F., DAmmaro, A., Uchida, S., 2013, Uncertainty Quantification and Conjugate Heat Transfer: A Stochastic Analysis, J. Turbomach 135(3), 031014.
[21] Wheeler, A. P. S., Atkins, N. R., and He, L., 2011, Turbine Blade Tip Heat Transfer In Low Speed And High Speed Flows, ASME J. Turbomach., 133(4), p. 041025.
[22] Xiu, D., 2010, Numerical Methods for Stochastic Computations: A Spectral Method Approach, Princeton University Press
[23] Adams, B.M., Ebeida, M. S., Eldred, M. S., Jakeman, J. D., Swiler, L. P., Stephens, J. A., Vigil, D. M., Wildey, T. M., Bohnhoff, W. J., Dalbey, K. R., Eddy, J. P., Hu, K. T., Bauman, L. E., Hough, P. D., Dakota, A Multilevel Parallel Object-Oriented Framework for Design Optimization, Parameter Estimation, Uncertainty Quantification, and Sensitivity Analysis: Version 6.2 User's Manual," Sandia Technical Report SAND2014-4633, July 2014, Updated May 8, 2015.
[24] Ameri, A., Bunker, R.S., 2000, Heat transfer and flow on the first-stage blade tip of a power generation gas turbine. Part 2: Simulation results, J. Turbomach 122(2), 272-277
[25] Montomoli, F., Massini, M., Salvadori, S., 2011, "Geometrical uncertainty in turbomachinery: Tip gap and fillet radius," Computers and Fluids, Volume 46, Issue 1, July 2011, Pages 362-368.
[26] Yoon, S., Curtis, E., Denton, J., and Longley, J., 2010, "The Effect of Clearance on Shrouded and Unshrouded Turbines at Two Levels of Reaction," ASME paper No. GT2010-22541

Determination and modeling of the aero-thermal behaviour of a cooling channel

Gian Luca Gori

Turbomachinery and Propulsion Department, von Karman Institute for Fluid Dynamics, Belgium, gian.luca.gori@vki.ac.be

Supervisor: Tony Arts

Professor, Turbomachinery and Propulsion Department, von Karman Institute for Fluid Dynamics, Belgium, mysupervisormail@vki.ac.be

Abstract

Internal Cooling technology for Gas Turbines, although supported by wide literature, still present possible important improvements. The classical CFD codes, based on constant Pr_t and isotropic turbulence, present a limited fidelity for the convective heat transfer prediction (at best 10-15%). A direct contribution to the causes of the low liability will be given by high detailed and high quality experimental data.

Keywords: turbomachinery, convective heat transfer, internal cooling

1. Introduction

The present research on cooling channels focuses on an aeronautical application (gas turbine), but is of definite interest to many other fields of engineering (oil industry, automotive, nuclear environments). The performance, in terms of thermal efficiency and specific power of a gas turbine cycle, increases with the TIT (Turbine Inlet Temperature). The limits are set by the blades and endwalls material resistance against thermal and mechanical loads. The life time of these components will increase by using efficient cooling techniques, cutting down the high costs for parts replacements. A major contribution to the heat extraction is given by forced convection in internal passages (Fig. 1).

The main objective of internal cooling channels is to maximize the wall heat transfer while keeping the channel pressure drop as low as possible. Initially designed with smooth walls, their surface has rapidly been equipped with various obstacles to increase the thermal exchange area and the local mixing. The resulting flow field is strongly 3D and unsteady; it becomes even more heterogeneous when the channel is put into rotation (rotor blades application). The strong assumptions of isotropic turbulence and constant Pr_t limit the accuracy of the heat transfer prediction (at best 10-15%) by CFD. The lack of experimental data due to the complexity and the availability of representative facilities, certainly, does not help for numerical improvements. The present research wants to contribute at providing high quality and high resolution experimental data acting directly on the causes of the CFD low fidelity.

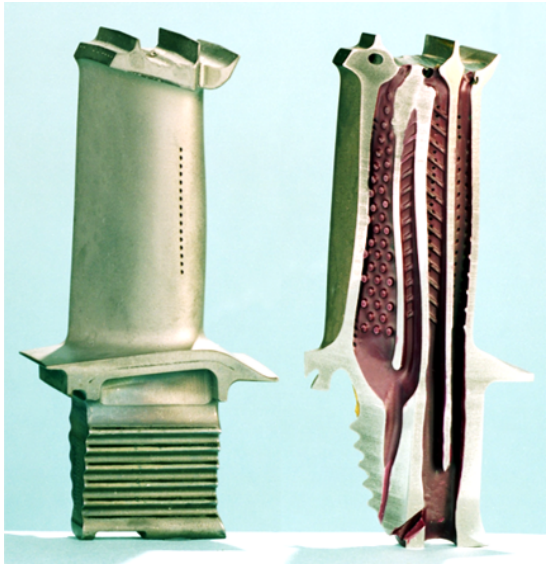

Figure 1: An air-cooled HP turbine blade and its cross-section.

Unlike most of the investigations available in lit-

erature, not only the wall heat transfer and velocity fields, but also the flow temperature distribution will be object of this experimental study. Although for velocity and surface heat transfer measurements, Particle Image Velocimetry (PIV) and Liquid Crystal Thermography (LCT) are already consolidated and largely used techniques, a few Cold Wire measurements show to affect the flow field [1]. Therefore, Laser-Induced Fluorescence (LIF) has been selected for two dimensional temperature measurements, as it is a non-intrusive optical approach. The technique is a spectroscopic method based on the spontaneous emission of molecules after excitation by a laser pulse. Never applied yet for internal cooling research so far, it will need to be developed for this specific application.

Neglecting the fluorescence re-absorption and the Beer's attenuation, a simplified expression of the signal intensity I_f in function of the emitted wavelength λ and absolute temperature T is given by Eq. 1 [2] :

$$I_f(\lambda) = K_{opt}(\lambda)K_{spec}(\lambda)V_c I_1 C e^{\beta(\lambda)/T} \quad (1)$$

where K_{opt} is an optical constant, V_c the measuring volume, I_1 the incident laser intensity, C the molecular concentration of the fluorescent tracer, K_{spec} and β constants related to the spectroscopic and physical properties of the target molecule. More details on the different contributions and parameters dependencies are presented in Ref. [3]. The final output, registered by a detector, is an image with a signal given by the integral of the expression in Eq. 1 all over the spectra.

The signal obtained by a single camera, therefore, does not depend only on temperature but also on the intensity of the laser pulse and the concentration of the tracer. Information of the local temperature might be retrieved by the so called single-line approach. A calibration is needed to know the constants. However, problems occur when concentration and/or laser intensity vary in space and/or in time. The latter issues disappear when two or more ground states are taken into account. The method is called multi-line approach. It requires two or more excitations and/or two or more detection systems. A double detection and single excitation is normally a good compromise for keeping the set-up as simple as possible. Multiline approaches, indeed, are usually considered worthless [3]. By the two-line approach, the dependence on the concentration of the dye is cancelled in the expression of the ratio between the two different ground states. Further, if the excited state is the same in the two cases the latter becomes independent also of the laser intensity. Finally, if temperature dependence of the overlap coefficient and laser energy fluctuations are neglected the intensity ratio R_f is represented by Eq. 2.

$$R_f(T) = \frac{I_{f,1}}{I_{f,2}} = \frac{K_{opt,1}}{K_{opt,2}} exp\left(\frac{\beta_1 - \beta_2}{T}\right) \quad (2)$$

The $I_{f,1}$ and $I_{f,2}$ are the intensity of the light seen by the two cameras provided by the two coloured filters. The calibration is still required for determining the constant $K_{opt,1}/K_{opt,2}$. The technique takes into account two different spectral bands of the emitted fluorescence for the two cameras, taking the name of two-color LIF. The selection of these two spectral bands defines the parameters β_1 and β_2. They represent the single temperature sensitivities of the two different spectral bands 1 and 2. Therefore, as discussed in [4], to obtain a high temperature dependence of R_f is obtained with $(\beta_1 - \beta_2)$ as large as possible. Compared to dual-excitation (e.g. [5]) the method required only one laser source and two cameras[6].

If the flow under investigation does not contain fluorescent molecules, a fluorescent dye must be added to the main flow. The objective is to create a well-mixed flow which allows the measurements without modifying the physics. For heat transfer and temperature determination both *Re* and *Pr* numbers of the experiments should match the real operating ones. Although *Re* can be adjusted by modifying the flow velocity, *Pr* is a property of the working fluid that needs to be carefully taken into account. Therefore, it is important to point out that for the specific application of air-cooled HP turbine blades the working fluid is represented by part of air bled from the compressor. Although liquid-phase PLIF is more developed than gas-phase PLIF, the latter is preferable in order to represent correctly the same physics. Therefore, it has been chosen to use a mixture of air and a selected tracer for the current measurements.

The choice of the latter influences the accessible temperature range as well as the evaluation procedure. Several temperature measurements have been performed using atomic, diatomic (e.g. OH, NO, O2, iodine, CH, C2) and organic molecules (e.g. ketones, toluene)[3]. Mono- and diatomic molecules provide spectra in absorption and fluorescence emission both in the UV range whereas in lager molecules the absorption and emission bandwidth are generally more continuous. The original application of organic molecules is the study of the mixing process between fuel and air in combustion systems. However, the temperature dependence allows the evaluation of the gas

temperature and even simultaneous measurements of temperature and fuel concentration. Toluene and acetone are the most used tracers for gas-phase LIF thermography (e.g. [7][8][9][10]). Acetone started to be used for its high signal, low toxicity and low cost [11]. The absorption (between 200 and 350 nm) was measured in 1992 by Lozano [12] and in 1996 again by Thurber [5]. The emission, instead, occurs between 300 and 550 nm [13]. The air-acetone vapor mixture Pr has been investigated numerically by the NASA CEA algorithm [14] based on equilibrium and assuming frozen reaction. With a maximum tracer concentration of 15% in volume the computed Pr varies less than 5% to the one of air at ambient condition. Toluene have been characterized in [15] [16]with his absorption (240-290 nm) and the emission (250-350 nm) as well as the quenching due to oxygen. In this case the concentration needs to keep lower than 1% in volume in order to limit the variations of Pr. The red shift of toluene made this tracer suitable for two-color thermography. For both acetone and toluene, the time required for the vapor sublimation is relative short which makes the seeding procedure simple [17] [18]. In particular, the discussion of the preliminary results will analyse pro and cons of acetone and toluene. Details of the characteristics of fluorescent tracers used for gas-phase thermography are referred to Ref. [19].

Acetone vapor mixed with air was selected as the working fluid for the preliminary study for simplicity as well as the aforementioned advantages. Toluene present possible re-absorption of the emitted light, quenching by oxygen and deeper UV fluorescence spectra. However, the discussion of the preliminary results will show the low relevance of this drawbacks compared to the possible improvements.

2. Preliminary study

As a first step, static measurements were performed in a cell in order to be able to investigate the behaviour of different fluorescent tracers as well as to evaluate the performance of specific coloured filters for two-color measurements. The objective is to obtain the intensity ratio in function of the assumed uniform temperature inside the cell, which defines the sensitivity of the measurements. According to some available data of the emission spectra of acetone and toluene two-color acetone LIF thermography have been performed. A preliminary analysis was performed to select the proper filters to place in front of the two cameras of the experimental set-up in Fig. 4. As already mentioned, high sensitivity is obtained when $(\beta_1 - \beta_2)$ is maximized. Thus, the two spectral bands should be selected with high and low dependence respectively [4], or even better with opposite sensitivity with temperature (one camera with positive dependence and the other one with negative dependence). Different possible couples of filters have been first evaluated numerically and finally the SHX350 and the XUL0385 (Asahi Spectra) were used.

2.1. Experimental set-up

The test section is a $50x50mm^2$, $90mm$ height aluminum cell (Fig. 2). The structure is composed by two main parts in order to have a complete access inside (manly for the calibration and cleaning). In the bottom part a small tap allows to introduce the tracer with a syringe. On top of that a fan take place in order to mix properly the air with the vaporized tracer. The pressure was monitored by a water manometer to estimate the vapor concentration inside the cell. Four thermocouples probes, previously calibrated, were installed to monitor the temperature at the same high of the laser beam. The top part is composed by five aluminum walls. Four of them have a quartz window for the laser and the cameras optical accesses, each of them sealed with two o-rings and a thin screwed plate. The 2 parts were fixed by a clamp in order to press the lateral walls on the seal gum placed in the groove of the bottom part. Then, all the external walls were thermally insulated by a 15 mm thickness foam.

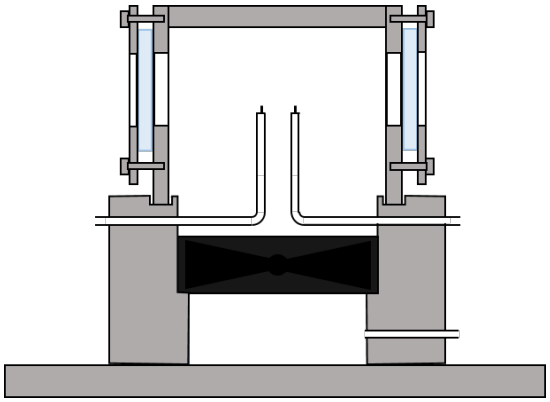

Figure 2: Sketch of the measurement cell.

As already mentioned the two-color technique requires mainly two detectors (Lavision Imager Intense) and one excitation source. The latter was provided by a Nd:Yag laser (Quantel Big Sky Laser) with 266 nm wavelength pulses of 33 mJ and 532 nm wavelength pulses of 180 mJ. Downstream the laser beam

two dichroic mirrors at 45° allow to decrease the green laser power. The fluorescent dye does not have absorption at 532 nm but it is also important to cut down, as much as possible, reflections scattered inside the cell. After the dichroic mirrors the beam passes through a fused-silica spherical lens in order to focus the beam in the middle of the cell.

The main issue of the set-up is represented by the location of the two cameras. It is important, indeed, that they should observe as better as possible the same area with the same magnification. This is not a big issue for these uniform static measurements but it will be really important for the 2D temperature distribution. In order to decrease the number of degrees of freedom and use only one camera lens the set-up is the one shown in Fig. 3 and sketched in Fig. 4. The light path coming from the investigated area is focused by an UV 100 mm camera lens and divided by a ND filter positioned at 45°. The two band-pass filters are mounted directly in front of the 2 sensors. Camera 2 is also provided by a stopband filter (500-600 nm) in order to cut down the green laser reflected light. A bellow mounted between the splitter cage and the Camera 1, has the purpose to allow the focusing with both detectors at the same time. The cameras were provided by the coloured filters selected and discussed previously.

A series of 400 pictures were taken at 3 Hz repetition rate of the laser for every different temperature inside the cell. Binning of 8 by 8 pixels was used to maximize the signal. Temperature was increased by heating up manually the aluminum bottom wall by a heat gun. During the measurements an acquisition system store the signal of the four thermocouples triggered by the first flash lamp of the laser with a frequency of 300 Hz. The required data was derive, finally, through the processing of the images and the thermocouple signals.

2.2. *Methodology*

The image processing is always more relevant in optical techniques for high quality data. Therefore, it is really important to use a proper method to derive the required information. The fist operation was the background subtraction where background images were taken with no acetone inside the cell. The laser, at the same power of the measurement, was present to take into account internal reflections. However, possible scattering of acetone vapor was not taken into account. After that, the calibration was applied thanks to the pictures taken previously with a millimetre paper in the same position of the laser beam. Translation, rotation and magnification were used to match exactly the two field of view. In order to have the pixels in the same location, a linear interpolation was applied to all the images. It have been seen that, in these measurements, the more accurate the calibration is, the more uniform R_f gets in the field of view. If there is not exact matching of the two pictures the calibration formula for the determination of the temperature in function of R_f must change within the region of interest. A secondary effect is represented by the real spatial resolution of the measurements which increases with higher mismatch. After this operation, the intensity ratio was computed in every location of the laser beam. In this point the mean and the standard deviation were obtained both for spatial and time dimensions.

Mean and standard deviation of the thermocouples were also computed in order to assess the spatial uni-

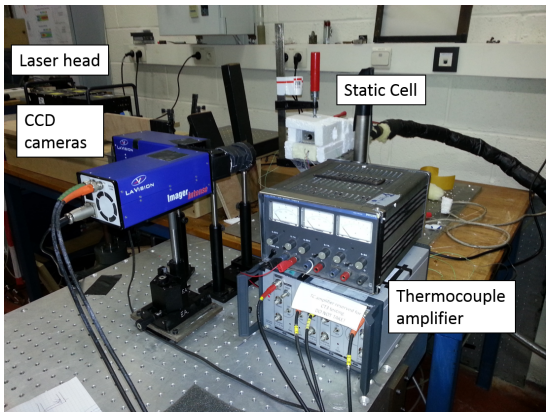

Figure 3: Experimental set-up used for two-color acetone PLIF for uniform temperature measurements.

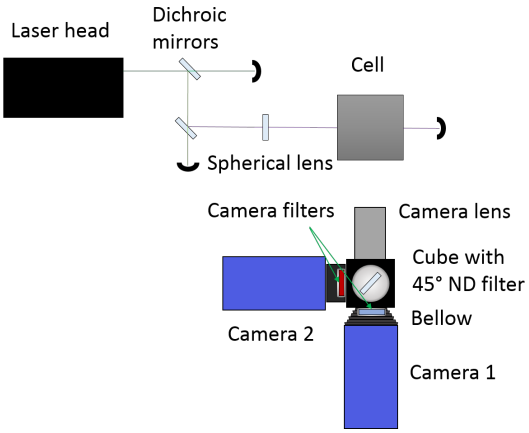

Figure 4: Set-up sketch.

formity and the variation of temperature during the single experiments. The methodology have been designed to evaluate the performance of the measurement technique described in the following section.

2.3. Results

The results of the experimental campaign can be summarized by Fig. 5. The ratio between the two camera intensities is represented for a specific position in function of the mean temperature inside the cell during the specific experiment. The location have been chosen to be in the middle of the laser beam where the fluorescence intensity is higher and the data are more reliable. A strong dependence with temperature can be seen between the six experiments.

The uncertainty on the ratio was computed by the standard deviation recorded by the 400 images taken for each experiment. The results is of the order of 7.3% of the intensity ratio for a confidence level of 95%. It turns that, for the determination of the temperature, the latter may be determined within a range of $\pm 8C$ since the ratio varies of 46% in $50°C$ variation. This value of uncertainty needs to be compared with the measurement range in a specific application. The bigger range the smaller the effect of uncertainty on the measurements. It means that for a measured range of $100°C$ the uncertainty will count 8%. The main contribution on the camera noise is given by the so called shot noise. Its effect on the measurements can be limited only by increasing the signal itself. The energy fluctuations of the laser pulses were not quantified, however, the method is theoretically not affected by these variations.

During the experiments the recorded measurements from the thermocouples have shown variations between $1°C$ and $1.8°C$, whereas dis-uniformity in the spatial dimension are at maximum $0.8°C$.

The results obtained are encouraging and opened a discussion for important improvements required for fulfil the project goals.

2.4. Discussion and Conclusions

The presented results represents a starting point for the final objectives of this research project. Thanks to a wide bibliography research an the preliminary assessment allowed a first measurement set-up has been built for two-color acetone LIF. The presence of an important temperature dependence of the intensity ratio is, indeed, encouraging for detecting the thermal boundary layer in internal flow applications. Furthermore, the experiments put in evidence some aspects which needs to be discussed:

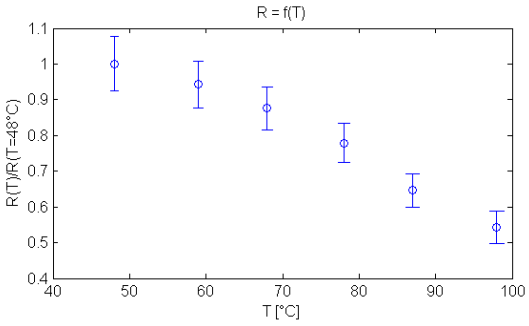

Figure 5: Normalized Intensity Ratio in function of the operating temperature inside the cell.

- the signal is very low (order of 200/4065) and, therefore, the noise acts an important role for the determination of the measurement uncertainty;
- there is not scientific evidence about the dependence with temperature discovered. The filters applied for these measurements were expected to provide a maximum variation of 10% of the signal within $100°C$ variation. The data present in literature of acetone do not show different shape of the spectral emission at different temperatures. In addition, the experiments executed at VKI showed exactly collapsed emission curves at different temperatures after normalization. Further investigations are, therefore, required to give an explanation to the phenomenon encountered.

These considerations are relevant for the interpretation of the results and the determination of the future work. In particular, the method could be test in a continuous flow application. A calibration in situ, required for accurate measurements, may reveal the feasibility of the latter in a real application of an internal flow. As discussed previously, toluene represent the alternative tracer in order to achieve the goals of the project. Although some issues need to be taken into account, two-color measurements have been already performed in literature.

For what concern the low signal, the cameras will be provided by two intensifiers. Although the *shotnoise* will be amplified together with the signal, the read out will account less to the measurement uncertainty. Especially in the case of toluene the CCD cameras, alone, will not be able to detect the deep UV emission for the really low quantum efficiency in that range.

The next step will be to apply the methodology to a simple configuration. The investigation will be car-

ried out in a fully developed 2D internal flow. The design of the set-up is already done and it will be shown in the following section. The goal is to determine the temperature profiles by this technique. As already mentioned, the working set-up will be, further in the future, embedded with the PIV one in order to measure the turbulent heat transport term $\overline{v'T'}$ and, therefore, the *turbulent Prandtl number* Pr_t. Eventually the study of an innovated configuration will take place with the possibility to run some test in rotation.

3. Facility

According to the conclusions of the preliminary study a more complex set-up was required to test the technique in a continuous flow. The global work of the design is represented by the 3D view of the facility in Fig 6.

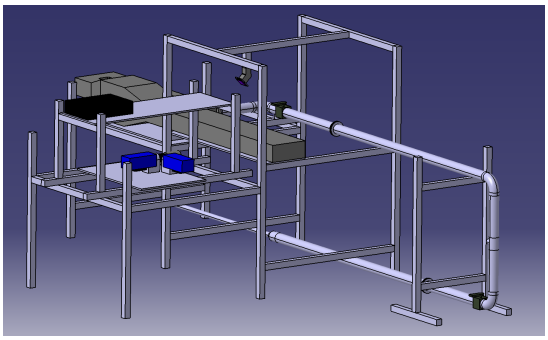

Figure 6: PLIF facility.

The purpose is to perform experiments in an internal 2D flow. The test rig is an already existing model which presents a cross section of $240x40mm^2$. Figure 7 shows it combined with some additional ducts, the settling chamber and the contraction designed at VKI for the RC-1 facility. The channel, as all the structure of the wind tunnel, is made in aluminum. Four optical windows allow the accesses of the light source and the camera. The decision of the streamwise location of them was taken in order to characterize both the inlet and the fully developed region. Originally made in plexiglass, they have been replaced with quartz plates for the UV components of the laser light and the emitted fluorescence. The bottom wall will be heated up with some thin resistances. The goal is to obtain the temperature profiles in order to compare the data with DNS available in literature and some cold wire measurements. In order to match the *Reynolds number* based on the *momentum thickness* of the DNS data ($Re_\theta = 400$), the obtained bulk velocity is 2.63 m/s leading to a mass-flow about 1.8 kg/min. It is, therefore, required to generate the flow inside the test section including the selected fluorescent dye.

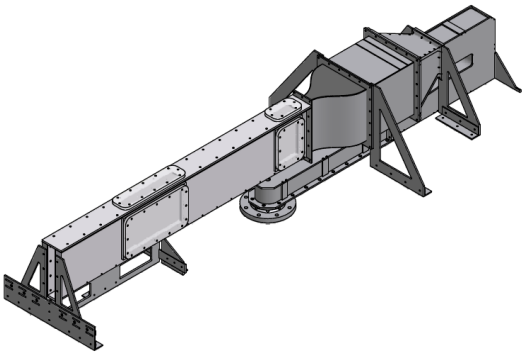

Figure 7: Wind tunnel.

As discussed in the introduction it is also important to monitor the concentration of the tracer in order to keep the *Prandtl number* as close as possible to the real case. Thus, two mass-flow meters will be required to control both the mass-flow and the dye concentration. The LIF flow generator is sketch in Fig. 8. The air is taken from the 7 bar compressed line of the VKI. The flow splits in two branches. One of those pass through the seeder and the other one has the purpose to dilute the mixture. They merge and are connected to the inlet of the wind tunnel. The pipes are made in PE100 Black, resistant to pressurized air up to 16 bars and able to withstand both acetone and toluene vapors. The internal diameter is a DN50 mm. The length of the pipes is determined by the upstream and downstream constraints for the mass-flow meters given by the British Standards [20]. In order to measure such low mass-flow, orifice plates with a diameter ratio of 0.6 have been selected [21]. The latter will produce pressure drops of the order of 100 mbar which will be easy to measure.

The supports hold both pipes, test section and the required equipment for the measurements. The latter is the same presented in the preliminary results. However, as already mentioned, the idea is to provide the cameras with image intensifiers. Considering the high cost of the image intensifiers it would be possible to split the camera sensor of an ICCD to provide the two path with the LIF filters. The laser is mounded on a plate supported by posts fixed to the camera structure. The advantage is, once the set-up is aligned, the illumination will move horizontally with the field of view of the detectors. On the laser support the required optics will be placed and the laser beam will be projected

vertically by a UV enhanced mirror hanged on a horizontal support. In addition, the laser sheet optics may be mounted directly on the top of the channel optical access.

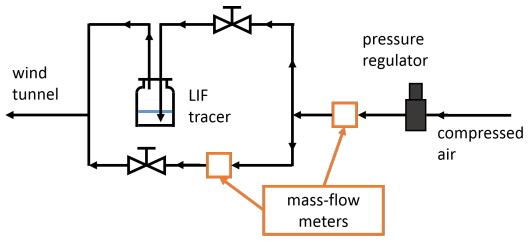

Figure 8: Flow sketch.

4. Conclusion

Evidence of the importance of flow temperature measurements in cooling technology have been discussed. Two-color LIF will be introduced being 2D and non intrusive measurement technique. Some preliminary results, in a static and uniform temperature cell, showed the feasibility the method. Remarks and possible improvements of the measurements were largely treated in the present documents. Constraints and difficulties of the application have been discussed identifying suitable alternatives for the next step. The investigation of the thermal boundary layer for a 2D internal flow needs to be carried out at the moment. A facility have been designed completely for the purpose. Soon after, the set-up will be embedded with the PIV equipment in order to obtain the turbulent heat transport term $\overline{v'T'}$, required for the determination of Pr_t. In summary, the present investigation will cope with the issues on heat transfer prediction by looking directly at the major causes of the numerical and experimental data discrepancies. The aerodynamic and thermal analysis will provide a physical explanation of the complex phenomena of forced convection. The innovative, high quality and high resolution data of the present research will represent a suitable tool for CFD codes validation and modeling improvements.

Acknowledgments

The funding of this PhD research project through a FRIA grant, delivered by the Fonds de la Recherche Scientifique (FNRS), is gratefully acknowledged.

References

[1] T. Arts, M. T. Abad-Lozano, Y. Kinoue and S. Pierret, The Unsteady Temperature Field in a Turbine Blade Cooling Channel, no. RTO Symposium, Advanced Flow Managment, Loen, Norway, 2001.

[2] F. Lemoine, Y. Antoine, M. Wolff and M. Lebouch, Simultaneous temperature and 2D velocity measurements in a turbulent heated jet using combined laser-induced fluorescence and LDA, Experiments in Fluids 26 (1999) 315–323.

[3] A. Y. C. Tropea, J. Foss, Handbook of Experimental Fluid Mechanics, Springer, 2007.

[4] P. Lavieille, F. Lemoine, G. Lavergne and M. Lebouch, Evaporating and combusting droplet temperature measurements using two-color laser-induced fluorescence, Experiments in Fluids 31 (2001) 45–55.

[5] M. C. Thurber, F. Grisch and R. K. Hanson, Temperature imaging with single- and dual-wavelength acetone planar laser-induced fluorescence, Optics Letters 22 (4) (1996) 251–253.

[6] M. Luong, W. Koban and C. Schulz, Novel strategies for imaging temperature distribution using Toluene LIF, Journal of Physics: Conference Series 45 (2006) 133–139.

[7] S. P. Kearney and F. V. Reyes, Quantitative temperature imaging in gas-phase turbulent thermal convection by laser-induced fluorescence of acetone, Experiments in Fluids 34 (2003) 87–97.

[8] Lei Shi, Xiaoan Mao and Artur J Jaworski, Application of planar laser-induced fluorescence measurement techniques to study the heat transfer characteristics of parallel-plate heat exchangers in thermoacoustic devices, Measurement Science and Technology 21 (2010) 116.

[9] V. A. Miller , M. Gamba, M. G. Mungal and R. K. Hanson, Single- and dual-band collection toluene PLIF thermometry in supersonic flows, Experiments in Fluids 54 (2013) 1539–1551.

[10] C. Gessenhardt, C. Schulz and S.A. Kaiser, Endoscopic temperature imaging in a four-cylinder IC engine via two-color toluene fluorescence, Proceedings of the Combustion Institute 35 (2014) 36973705.

[11] M. C. Thurber, F. Grisch, B. J. Kirby and M. Votsmeier, Measurements and modeling of acetone laser induced fluorescence with implication for temperature imaging diagnostics, Applied Optics 37 (21) (1998) 4963–4978.

[12] A. Lozano, Laser-excited luminescent tracers for planar concentration measurements in gaseous jets, Ph.D. thesis, Stanford University (1992).

[13] R. A. Bryant, J. M. Donbar and J. F. Driscoll, Acetone laser induced fluorescence for low pressure/low temperature flow visualization, Experiments in Fluids 28 (2000) 471–476.

[14] S. G., B. J. McBride, Computer Program for Calculation of Complex Chemical Equilibrium Compositions and Applications, Nasa Reference Pubblication 1311, NASA (1994).

[15] W. Koban, J. D. Koch, R. K. Hanson and C. Schulz, Absorption and fluorescence of toluene vapor at elevated temperatures, Phys. Chem. Chem. Phys 6 (2004) 2940–2945.

[16] W. Koban, J. D. Koch, R. K. Hanson and C. Schulz, Oxygen quenching of toluene fluorescence at elevated temperatures, Applied Physics B 80 (2005) 777–784.

[17] M. C. Thurber, Acetone Laser-Induced Fluorescence for temperature and multiparameter imaging in gaseous flows, Ph.D. thesis, Stanford University (1999).

[18] V. A. Miller, M. Gamba, M. G. Mungal and R. K. Hanson, Two-Camera Dual-Band Collecton Toluene PLIF Thermom-

etry in Supersonic Flows, no. 16th Symp on Applications of Laser Techniques to Fluid Mechanics, Lisbon, Portugal, 2012.
[19] S. Faust, M. Goschütz, S. A. Kaiser, T. Dreier, C. Schulz, A comparison of selected organic tracers for quantitative scalar imaging in the gas phase via laser-induced fluorescence, Applied Physics B 117 (2013) 183–194.
[20] B. Standards, Measurements of fluid flow by means of pressure differential devices inserted in circular cross-section conduits running full - Part 1: General principles and requirements, Standard BS EN ISO 5167-1:2003, European Committee for Standardization (2003).
[21] B. Standards, Measurements of fluid flow by means of pressure differential devices inserted in circular cross-section conduits running full - Part 1: Orifice plates, Standard BS EN ISO 5167-2:2003, European Committee for Standardization (2003).

Flow field and heat transfer in a rotating cooling channel

Ignacio Mayo Yague

Turbomachinery and Propulsion Department, von Karman Institute for Fluid Dynamics, Belgium, ignacio.mayo.yaguel@vki.ac.be

Supervisor: Tony Arts

Professor and Head of the Turbomachinery and Propulsion Department, von Karman Institute for Fluid Dynamics, Belgium, arts@vki.ac.be

University Supervisor: Laurent Y. M. Gicquel

CERFACS, Computational Fluid Dynamics Team, Institut National Polytechnique de Toulouse, France, laurent.gicquel@cerfacs.fr

Abstract

The detailed flow field and heat transfer in a rotating rib-roughened cooling channel at engine-like operating conditions is analyzed in the present paper. The first part of the work consists of the experimental investigation in a novel setup by means of 2D Particle Image Velocimetry (PIV) and Liquid Crystal Thermography (LCT). The second part of the work shows Large Eddy Simulations (LES) validated with the previous experimental data, and provides the detailed three-dimensional velocity field in the domain between two consecutive ribs.

Keywords: Channel flow, Heat transfer, Coriolis, PIV, LCT, LES, OpenFOAM

1. Introduction

In order to increase the efficiency of gas turbines, the Turbine Inlet Temperature (TIT) must be as high as possible. An effective technique to increase the TIT is to introduce cooling channels in the blade that allow to keep the temperature below the limits of the construction materials. Gladden and Simoneau **?** show a schematic of the typical cooling technology implemented in a gas turbine blade (Fig. 1). A wide review of the background and advances on this topic is presented by Han et. al **?**. The recent review of Ligrani **?** shows in detail the latest aero-thermal research developments in the field of internal cooling channels, object of the present work. Due to the complexity of the required experimental setup, the details and accuracy of the velocity and heat transfer distributions are limited. Because of these difficulties, the number of works on turbine internal cooling in rotation is considerably lower than in static conditions. Most often, the investigations under rotating conditions are limited to point-wise heat transfer and pressure drop measurements. Moreover, the combination of the velocity field and heat transfer in experimental facilities is hardly ever reported in the same model and at the same experimental conditions. In the present work, a novel experimental facility that allows detailed velocity and heat transfer measurements over a large operating range is introduced. The model selected for the present investigation is a simplification of the geometry implemented in modern gas turbines. Nevertheless, it represents the major features of the

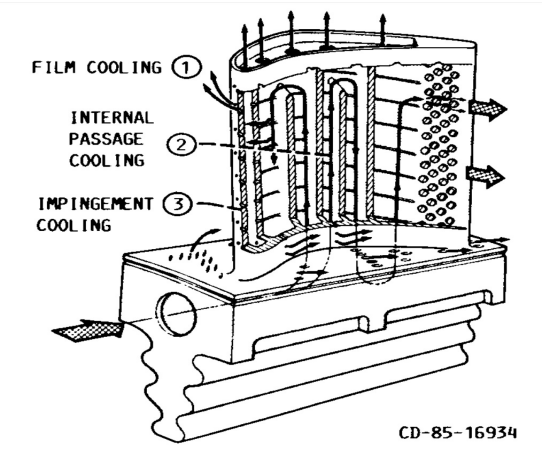

Figure 1: Typical cooled aircraft gas turbine blade (from Gladden and Simoneau **?**)

aero-thermodynamics that take place in such systems, while allowing the comparison with the limited data provided in the literature.

In rotating channels, the additional effects induced by Coriolis and centrifugal buoyancy forces modify significantly the flow field and heat transfer with respect to stationary conditions. The analysis of the continuity, momentum and energy equations of the flow in a rotating frame fixed to the channel, shows that the dimensionless velocity field and the Nusselt number, Nu:

$$Nu = \frac{hD_H}{k_f} \tag{1}$$

are determined by the Reynolds (Re), Rotation (Ro), Buoyancy (Bo), and Prandtl (Pr) numbers:

$$Re = \frac{U_b D_H}{\nu} \tag{2}$$

$$Ro = \frac{\Omega D_H}{U_b} \tag{3}$$

$$Bo = \frac{\Delta\rho}{\rho_0} Ro^2 \frac{r}{D_H} \tag{4}$$

$$Pr = \frac{\mu c_p}{k_f} \tag{5}$$

where h is the heat transfer coefficient, D_H the channel hydraulic diameter, k_f is the fluid thermal conductivity, U_b is the channel bulk velocity, ν the kinematic viscosity, Ω the angular speed, ρ_0 the reference density, $\Delta\rho$ the density variations, r the distance to the axis of rotation, μ the molecular viscosity and c_p the fluid specific heat capacity at constant pressure. In particular, Re addresses the importance of the inertia forces with respect to the viscous forces, Ro accounts for the ratio between the Coriolis forces to the inertia of the fluid, and Bo represents the ratio of the centrifugal-buoyancy force with and the inertia of the fluid.

Coletti et al. **?** and **?** investigated applied the flow field in a rotating channel with a ribbed wall by means of Particle Image Velocimetry (PIV) at a Re of 15000 and a maximum Ro of 0.38. A picture of the main features of the resulting flow field is reproduced in Fig. 2. In the particular case of the figure, the Leading Side (LS) corresponds to the upper wall, guiding the motion of the channel. On the other hand, the lower wall (ribbed wall) acts as Trailing Side (TS). In the case of rotation in the opposite direction, the upper wall would act as Trailing Side and the lower wall as Leading Side. As discussed by Johnston **?** and Coletti et al. **?** the Coriolis-induced secondary flows consist on the fluid motion from the TS to the LS on the area close to the lateral walls perpendicular to the main flow direction, to move back towards the trailing side over a location distant from the lateral walls. In the investigation presented in Ref. **?**, the motion from the LS to the TS caused the skew of the velocity profiles and therefore higher velocities close to the TS in the symmetry plane. Moreover, the turbulence generated in the shear layer behind the rib is enhanced on the TS and reduced on the LS. On the other hand, Fransen et al. **?** performed LES simulations in the same geomtry and at the same conditions as in Ref. **?**, showing an excellent agreement for the static case and on the LS, but with some differences on the TS. At higher rotation rates, Abdel-Wahab and Tafti **?** and Sewall **?** showed by means of Large Eddy Simulations (LES) that the number of secondary flow cells is likely to increase. Nevertheless, the later numerical investigations were not supported by detailed experimental data. Recently, Borello et al. **?**, performed LES in a section of the channel investigated in Ref. **?** by reducing the domain to one rib pitch and applying periodic boundary conditions. The latter simulations showed an excellent agreement with the experimental data, but they were limited to Re=15000 and a maximum Ro of 0.3.

The first objective of the present study is to introduce a new facility set-up to perform PIV measurements in a channel with the same geometry as in Refs. **??** at higher Reynolds, Rotation and Buoyancy numbers. Here, PIV measurements were carried out at a Re equal to 15000 and a Ro=0, 0.38 and 0.77. The effects of the high rotation on the velocity and turbulence fields and on the secondary flows will be discussed in the following sections. Also, the experimental results are compared with those given by Ref. **?**. Secondly, Liquid Crystal Thermography (LCT) is employed in order to provide the heat transfer on the ribbed wall at the same conditions as the PIV measurements. Moreover, additional LCT measurements are supplied at Reynolds numbers of 30000 and 55000, with maximum Rotation numbers of 0.47 and 0.20, respectively. The overall values of the heat transfer are compared with the data given in Refs. **???**. Finally, Large Eddy Simulations (LES) are performed by means of the OpenFOAM open source toolbox **?**. To the author's best knowledge, the suitability of the OpenFOAM LES toolbox to rotating channels is addressed for the first time in the present work. The simulations are carried out at the same conditions as the PIV measurements. In particular, the simulations al-

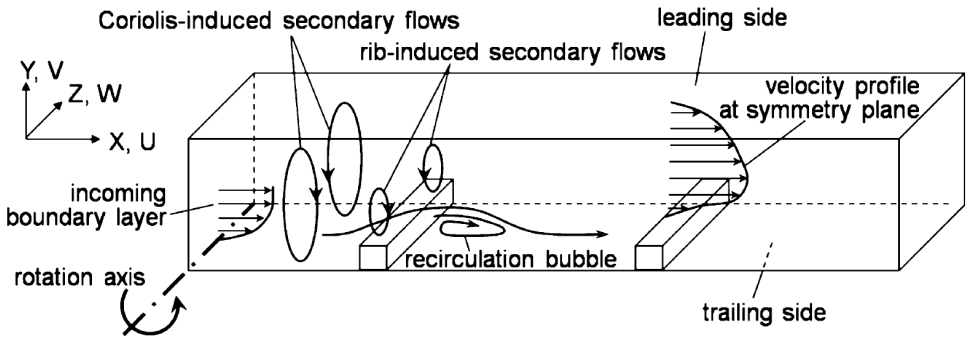

Figure 2: Schematic view of the secondary flows system in the rotating ribbed duct (from Coletti et al. **?**)

low to provide information of the entire flow field in the domain between two consecutive ribs, which is not given by the experimental data.

2. Experimental setup

The rotating RC-1 facility, was employed in the experimental campaign. It is composed of a 2.5m diameter wooden disk on which the test section is mounted together with the required instrumentation. In consequence, this set-up benefits from the same spatial accuracy as a non-rotating experimental set-up. A sketch of the test section and the main instrumentation employed in the PIV measurements is depicted in Fig. 3.

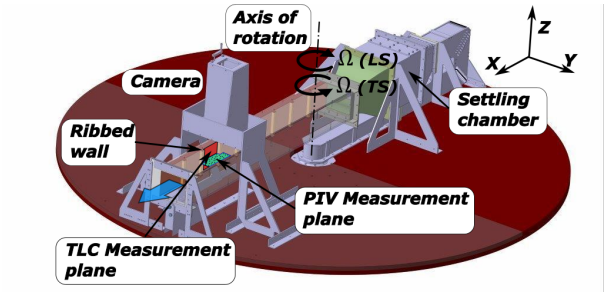

Figure 3: Experimental facility

The working fluid is air, taken from the room at ambient conditions. A centifugal blower provides the required mass flow, which is measured by means of a Venturi nozzle. The flow then passes through a rotary seal, entering the rotating set-up in the center of the disk. The air is then dispatched through a 90 elbow, thentrough a U-shaped pipe before reaching the settling chamber, which contains honeycombs and fine wire screens to minimize secondary flows and large fluid structures. Following the settling chamber, a convergent with an area ratio of 2.7 brings the air finally to the inlet of the test section which is radially outward directed. The rotating frame is driven by a DC motor (which can turn up to 100 RPM) in both clockwise and counterclockwise directions.

The channel geometry is similar to the one investigated in Ref. **?**. The channel has a section of 138×153 mm^2, and a length of 1390 mm. Eight ribs have been placed perpendicularly to the main flow field direction and parallel to the axis of rotation. Each rib has a square cross section and a rib height (H) of 15 mm. The pitch between two consecutive ribs (P) is 150 mm. As a result, the pitch-to-height ratio is 10, while the blockage ratio (H/D_H) is 0.1. The ribbed wall acts as Trailing Side when the angular velocity vector presents the same direction as the Z-axis in Fig. 3. If the angular velocity vector has the opposite direction, the ribbed wall acts as Leading Side. The other three walls are built in Plexiglas, providing the optical access to the measurement plane.

2.1. Velocity measurements

All the instrumentation required for the PIV measurements is mounted on the disk, allowing the same resolution and accuracy as in a non-rotating rig. The power supply and electric signals necessary for the operation are supplied through a slip-ring located in the rotating shaft. A continuous laser AMTRON LS453 JO75-CPXF-2Pi of 808 nm wavelength and 75 W maximum power is employed to illuminate the investigated planes. A 400 μm core diameter optical fiber directs the laser beam to an optical module that produces a laser sheet that covers the symmetry plane of the test section between the 6th and 7th ribs. The flow is seeded with oil particles, injected in the main flow just upstream of the rotary seal. A Phantom v7.1 High Speed Camera, is employed to record the images of the tracer particles in four partially overlapping planes

of 56×42 mm^2 covering the region of interest. The resulting magnification factor is 0.30, that is, about 0.07 mm/pixel. With the selected resolution, the camera is able to store up to 1450 pictures (i.e. 725 PIV realizations) in its 1Gb internal memory. A built-in memory controller is connected to the camera to register statistically independent PIV realizations. The latter device discards a certain number of images before storing each couple of snapshots. More details about the PIV setup can be found in Ref. **?**. The experimental conditions for the PIV experiments are shown in Table 1.

Table 1: Test matrix for the PIV experiments (Re=15000)

Case	Ro	Ribbed wall
1	0.77	Trailing Side (TS)
2	0.38	Trailing Side (TS)
3	0	- (static)
4	0.38	Leading Side (LS)
5	0.77	Leading Side (LS)

2.2. Heat transfer measurements

A 20 μm thick stainless Inconel sheet is glued on the ribbed wall by means of an acrylic adhesive. A uniform layer of matt black paint is applied on the Inconel foil, covered in turn by liquid crystals with a range of active temperature between 35°C and 55°C. An electrical current is applied through a slip-ring located in the rotating shaft in order to heat up the Inconel sheet. The resulting thermal boundary condition is an almost uniform heat flux. The measurements are focused between the 6th and 7th ribs, indicated as the investigated area.

The model is built entirely in Plexiglas (PMMA) as in the PIV setup, and the heated wall is thickened to incorporate an expanded polystyrene (XPS) layer of 30 mm height. The use of XPS in the wall reduces drastically the heat losses and the measurement uncertainty. Furthermore, additional polystyrene has been added on both sides of the investigated area to minimize lateral conduction losses.

A Nikon D300S RGB camera was mounted on a structure placed perpendicularly to the channel, and on the rotating frame.The camera is overseeing the investigated area with a 45° angle in order to minimize the TLCs response with the viewing angle **?**. The illumination source is composed of two 18 W fluorescent tubes, which are also fixed on the rotating disk, parallel to the investigated wall. Two thermocouples are positioned at the inlet and the outlet of the channel acquiring the temperature of the flow in the center of these cross sections, which is then used to compute the bulk temperature in the investigated area. Finally, five thermocouples have been embedded in the external face of the polysterene wall. The resulting temperatures are used to estimate the conduction losses. Each signal of the thermocouple is amplified, and the amplification device is also mounted on the rotating disk. The amplified signals are then recorded via the slip-ring by a stationary acquisition system. More details on the TLC experimental setup and data reduction can be found in Ref. **?**. In the case of the TLC experiments, the channel has been tested at different *Re-Ro* combinations. Table 2 shows the final test matrix for the heat transfer measurements.

The heat transfer results are given in the present work in terms of the heat transfer Enhancement Factor, EF, defined as:

$$EF = Nu/Nu_0 \tag{6}$$

where Nu_0 is the Nusselt number given by the Dittus-Boelter correlation, corresponding to a heated smooth circular channel at the same Reynolds and Prandtl numbers as in the experiments:

$$Nu_0 = 0.023 Re^{0.8} Pr^{0.4} \tag{7}$$

3. Computational details

The design of the test section was conceived to find fully established flow at the measurement location. According to Ref. **?**, this condition is practically achieved after the 6th rib of the channel. Therefore, the domain of the simulations can be reduced to a portion of the channel with a length equal to the rib pitch, as long as periodic boundary conditions are applied at the inlet and outlet sections of the domain. In this fashion, the results obtained in the simulations can be compared with the experimental data obtained between the 6th and 7th ribs. The computational domain selected in this investigation is shown in Fig. 4. The X and Z axes represents the stream-wise and span-wise directions. Also, the Z axis is parallel to the axis of rotation and to the main axis of the rib. Finally, the Y axis is perpendicular to the former. The stream-wise extension of the domain is equal to the rib pitch of the present experimental setup, that is, 150 mm. Figure 4 shows the dimensionless frame of reference, with

Table 2: Test matrix for the TLC experiments. The investigated *Re-Ro* combinations are colored

	Ro									
	0	0.06	0.12	0.20	0.30	0.38	0.47	0.69	0.84	1.00
Re=15000										
Re=30000										
Re=55000										

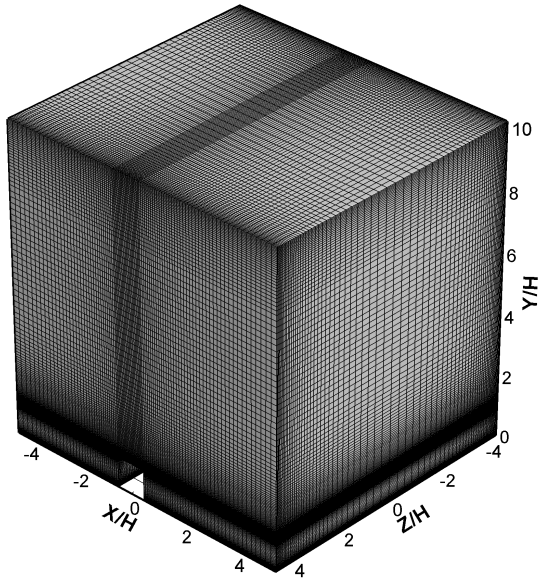

Figure 4: Computational domain and mesh

origin at the intersection of the trailing side of the rib with the lower wall, at the midspan of the channel.

Periodic boundary conditions have been applied at the inlet and outlet planes, X/H=-5 and X/H= 5, respectively. The non-slip boundary condition is applied in the rest of boundary surfaces. The mesh is composed by about 960000 structured hexahedral cells, also shown in Fig. 4. The mesh is refined not only close to the walls and the rib but also in the region of the shear layer generated by the rib, that is, Y/H <3. The resulting mean y^+ is 1.8, whereas the maximum value is 7.3. Five simulations were performed at the same conditions as the PIV experiments, corresponding to the test matrix presented in Table 1.

The present LES simulations were carried out employing the large time-step transient solver integrated in openFOAM **?** for incompressible flow in a single rotating frame $SRFpimpleFOAM$ using the PIMPLE algorithm. During the simulation, the time step was continuously adapted in order to have a maximum CFL number of 0.5. The selected turbulence model corresponds to the local dynamic model based on the subgrid-scale kinetic energy equation proposed by Kim and Menon **?**. The statistical quantities are collected after the stabilization of the simulated flow, and averaged over more than 15 large-eddy turn over times, D_H/U_b.

4. Results

The flow field obtained by means of the PIV experiments is represented in Fig. 5 in each of the cases given in Table 1. In the static case, the flow is accelerated in the area over the rib, where the cross-sectional area of the channel is minimum. Due to the sharp increase of cross-sectional area, the flow separates downstream of the obstacle. In this fashion, a large recirculation bubble with an extension of about $3.8H$ is located downstream of the rib. A second recirculation bubble of reduced size and opposite swirling motion is located in the corner constituted by the rib's trailing edge and the wall. Finally, a third small vortical structure is found just upstream of the rib.

Figure 6 shows the combination of heat transfer Enhancement Factor obtained by means of LCT and the in-plane turbulent kinetic energy obtained from the PIV experiments. In the static case (Fig. 6(c)), there is a region of low EF downstream of the rib, corresponding to the recirculation bubble. The EF shows a maximum in the region of the reattachment point, and then continuously decreases towards the following rib. Just upstream of the rib, where the limited recirculation bubble is located, the EF is low. On the other hand, two regions close to the lateral walls (Z/H = ±4.6) show the maximum EF. This can be due to the combined effect of the shear layer reattachment and the rib-induced secondary flows (depicted in Fig. 2).

When Ro=0.38 and the ribbed wall corresponds to the TS (Fig. 5(b)), the velocity modulus is moderately increased. As discussed in Ref. **?**, the Coriolis-induced secondary flows move fluid away from the LS

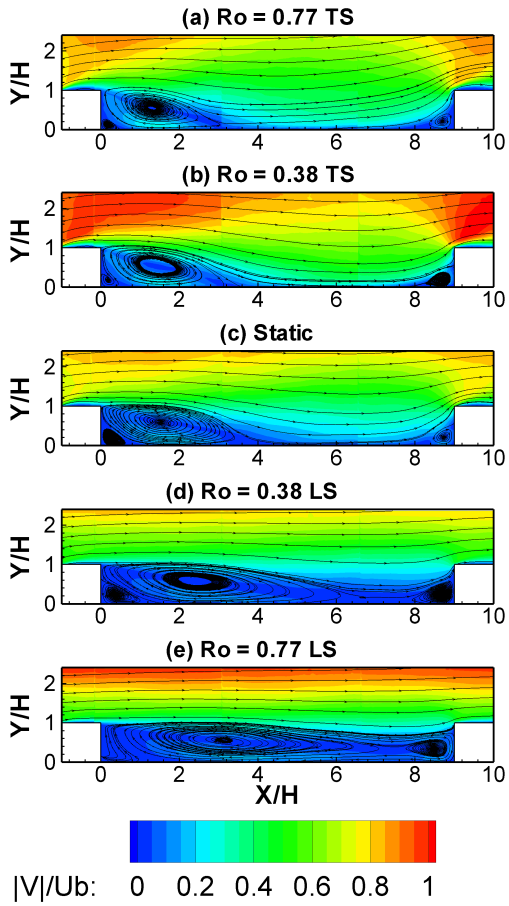

Figure 5: In-plane mean velocity modulus and streamlines for different rotation cases (PIV measurements)

towards the TS in the midspan region, where the measurement plane is located. Therefore, the momentum close to the TS is expected to increase with respect to the static case. Moreover, the size of the recirculation bubble downstream of the rib is slightly reduced to a length of about $3.4H$. Also, in Ref. **?**, it is shown that the Coriolis force induces an increase of the turbulence in the shear layer generated by the rib. This local increase of turbulence can also be due to the vortex stretching generated by the secondary flows. As a result of the high turbulence, the interchange of fluid between the recirculation bubble and the main flow is enhanced, reducing the length of the separated flow. In Fig. 6 it can be seen that the overall turbulent kinetic energy and Enhancement Factor are higher than in the static case. In the particular case of the heat transfer, the footprint of the rib-induced secondary flows is not found on the EF contour over the wall. This is likely due to the Coriolis-induced secondary flows that induce the motion of fluid towards the wall in the mid-span area, increasing locally the heat transfer and reducing the span-wise gradients.

When Ro increases from 0.38 to 0.77 on the TS, the momentum in the PIV measurement plane is reduced, suggesting a change of the secondary flow pattern. As mentioned by Abdel-Wahab and Tafti **?**, the number of secondary flow cells can vary as the Rotation number increases. The secondary flows would still move fluid from the TS to the LS over the lateral walls. However, the fluid would go back to the TS not at the mid-span, but closer to the lateral walls. Another two stream-wise counter-rotating vortices would appear in the mid-span region, inducing a fluid motion away from the TS in the symmetry plane. In this fashion, the momentum close to the TS at high Rotation is reduced. In Fig.6(a), it can be observed that the turbulent kinetic energy is higher than in the static conditions on the top of the rib, and at the same level as at Ro=0.38. However, as the fluid moves downstream, the turbulent kinetic energy is lower than at Ro=0.38 and becomes even lower than in static conditions just upstream of the rib. Therefore, at Ro=0.77, the reattachment area shows a high EF, but then is reduced dramatically towards the following rib. In addition, two spots of very high EF appear close to the lateral walls, at $Z/H \sim \pm$ 3 - 3.5. These spots could be directly related to the locations where the new secondary flows induce a local fluid motion towards the wall.

On the LS, the situation is completely different. At Ro=0.38, Fig.5(d), the separation bubble is enlarged due to the stabilization of the shear layer by the rotation and the consequent reduction of the turbulent kinetic energy. In the present experiments, the flow is not able to reattach to the wall in the space between the obstacles, and the streamline curvature is considerably reduced. In turn, the acceleration of the flow on the top of the ribs is also reduced. In Fig. 6(d), the reduction of the turbulent kinetic energy is evident, driving to a low value of the Enhancement Factor on the wall. Moreover, the variations of the EF in the stream-wise direction are lower than in the precedent cases. On the other hand, two regions of high EF are found in the region next to the lateral walls due to Coriolis-induced secondary flows that move fluid from the TS to the LS in this area. When the rotation rate is augmented on the LS to Ro=0.77, the recirculation bubble also covers the region between the ribs. In this case, the height of the bubble is almost constant and equal to the rib height, leading to the lack of

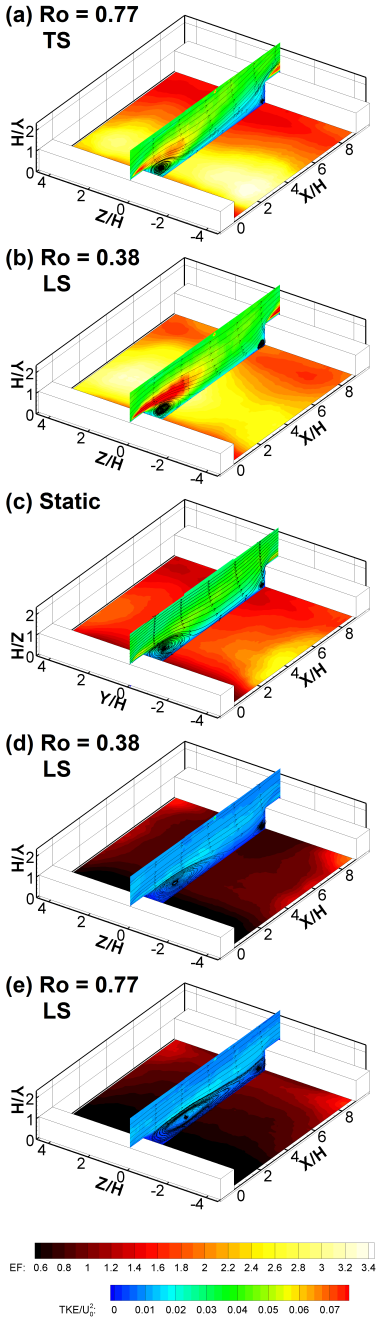

Figure 6: Combination of the flow field and heat transfer at different conditions

streamline curvature in the main flow. Also,the limited recirculation bubble in the corner of the rib's leading side is not present in this case. On the other hand, the momentum is slightly higher than in the previous situations, likely due to a variation in the secondary flow pattern. Concerning the turbulent kinetic energy (Fig.6(e)), there is not a significant variation with respect to the LS at Ro=0.38. Therefore, the turbulent kinetic energy seems to not vary when the rotation rate is high enough. The EF follows the same behavior, that is, the change with respect to the situation at Ro=0.38 is minor. The overall EF is slightly lower than at Ro=0.38, while the areas of high EF close to the lateral walls have disappear.

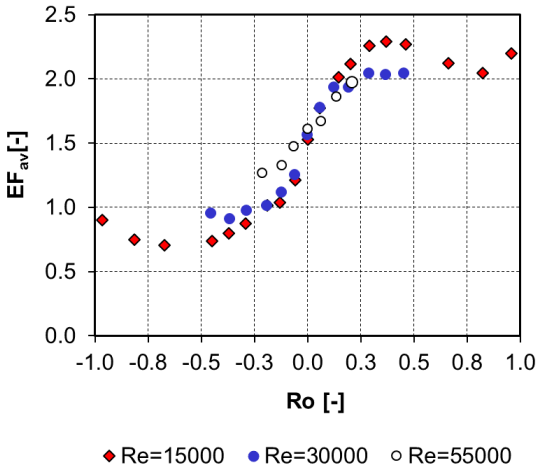

Figure 7: Area averaged Enhancement Factor as a function of the Rotation number for different Reynolds numbers

Figure 7 represents the value of the EF averaged over the area between two ribs, at different Reynolds and Rotation numbers. In this figure, positive values of Ro stand for Trailing Side, and negative Ro for Leading Side. For Re=15000, the behavior of EF is almost linear with Ro in the range $|Ro|$ <0.2. After this point the sensitivity of the overall Enhancement Factor with the Rotation number decreases. This the result of the changing behavior of the turbulence and secondary flows commented previously. For $|Ro|$ >0.3 the variations of the EF are below ± 0.15. It is interesting to note that the sensitivity of the overall EF with respect to Ro decreases as Re increases.

In order to support the present heat transfer data, the ratio of the overall EF at a given Ro to the overall EF in static conditions is compared in Fig. 8 with the numerical data provided by Abdel-Wahab and Tafti **?**, and the experimental data by Johnson et al. **?** and by Kim et al. **?**. The channels investigated in these references present similar aspect ratios similar to the one in the present investigation, but the number of ribbed walls and the rib shape differ. However, the

good agreement between the data present in literature is evident, even if the results correspond to different geometries at slightly different Reynolds numbers. In this Reynolds number range (10000< Re <20000) the EF does not vary for $|Ro|$ >0.3. In the case of the TS, the EF is about 50% higher than in static conditions at Ro >0.3. On the LS, the EF is reduced 50% for $|Ro|$ >0.3.

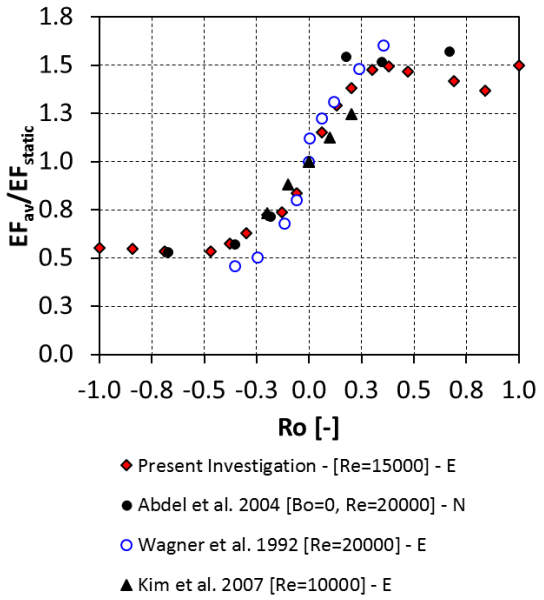

Figure 8: Ratio of the Enhancement Factor in rotating conditions to the Enhancement Factor in static conditions as a function of the Rotation number compared with literature

LES were employed to understand the complex three-dimensional flow under the different rotating conditions. Firstly, the numerical results in the symmetry plane are compared with the PIV data in Figs.9 and 10. The overall agreement in the mean stream-wise velocity profiles is positive, especially in the static case and on the TS. The largest errors are found on the rib and in the recirculation bubble. In particular, the LES reveal a limited recirculation bubble on the top of the rib, leading to a deficit in momentum in this region. Note that the experimental profiles at X/H=0 and 10 are not exactly the same, with a larger difference close to the rib. Indeed the velocity profile provided by the LES are closer to the experimental data at X/H=10. It can be inferred that the flow is not fully established in the test section. Nevertheless, the experimental and numerical velocity profiles are very similar from a distance of 4H downstream of the rib. On the LS, Figs. 9(c) and 10(c), the difference in the velocity profile is larger. The LES provide a large recirculation region covering the area between the obstacles, were the velocity profiles are very similar. Outside the recirculation bubble, the difference in the velocity profiles is large. This can be due also to the fact that the flow is not established in the test section. In particular, the flow is stabilized by rotation on the LS, leading to low turbulence levels and hence less mixing. As a result, it is likely that the length necessary to obtain fully established conditions is larger when the ribbed wall acts as LS. In fact, the difference in the velocity profiles between the numerical and experimental data is reduced at X/H=10. On the other hand, the turbulence profiles are very similar, even in the case of the Leading Side. The turbulence augmentation/reduction driven by rotation is predicted reasonably well by the numerical simulations. The comparison between the LES and the PIV data suggests that the degree of development of the turbulent field is reached in a shorter distance than the main velocity field.

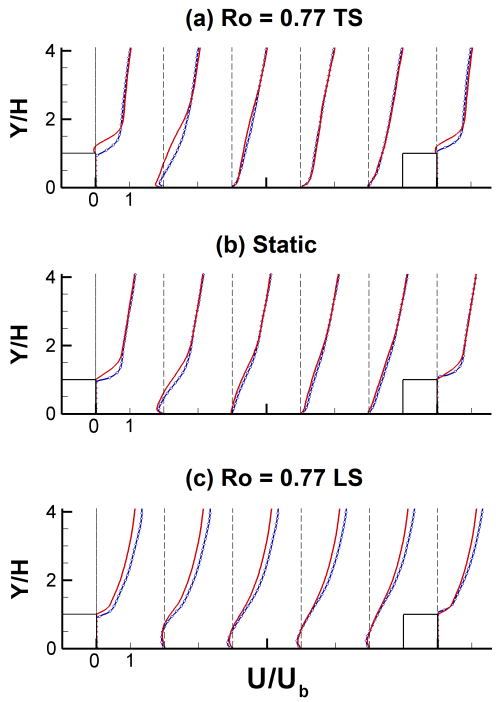

Figure 9: Comparison of the stream-wise mean velocity profiles given by LES (red) and PIV (blue)

Figure 11 represents the three-dimensional behavior of the flow field obtained by means of the LES at

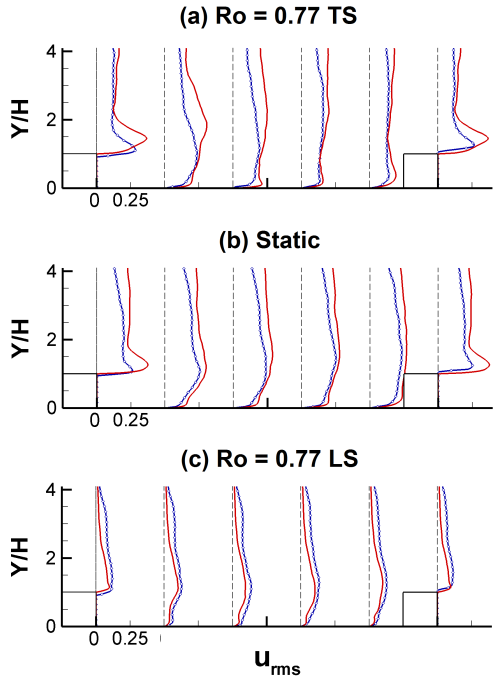

Figure 10: Comparison of the stream-wise turbulent velocity profiles given by LES (red) and PIV (blue)

the conditions of Table 1. In the figure, the contours of the mean stream-wise velocity in the planes X/H=-4.5, 0 and 4.5 are represented. The in-plane mean streamlines (corresponding to the secondary flows) are superimposed to the contours. In static conditions, Fig. 11(a), two large counter-rotating stream-wise vortices are present in the top-half area of the channel. These vortices were identified by Casarsa and Arts **?** as rib-induced secondary flows in high blockage ratio stationary channels, caused by the unbalance between the pressure gradient and the local centrifugal force due to the streamline curvature. In the present simulations, two additional vortices are identified in the top corners, with a swirling motion opposite to the mean rib-induced secondary flows.

When the ribbed wall acts as Trailing Side at Ro=0.38 (Fig. 11(b)), the rib-induced secondary flows and the Coriolis induced secondary flows have the same direction. In this case, the secondary flows move fluid from the TS to the LS close to the lateral walls, to go back to the TS in the midspan region. In addition, the limited corner vortices observed in the top corners in static conditions have disappeared, due to the effect of the Coriolis-induced secondary flows. When Ro is increased to 0.77 (Fig. 11(c)), the secondary flow pattern is quite different. Still there exists a fluid motion from the TS to the LS over the lateral walls. However, the fluid does not go back to the TS in the midspan region, but in the region $Z/H = \pm 3$. This is in excellent agreement with the TLC data, were high heat transfer spots were found in this location. On the other hand, two additional counter-rotating vortices are found in the central region of the channel. These two vortices present a swirling motion that expel fluid from the TS in the midspan region. This is again in good concordance with the experimental data shown in Figs. 5(a)-(b). These counter-rotating vortices in the midspan region of the TS explain the momentum reduction in the symmetry plane. Moreover, Fig. 11(c) suggests that the secondary flows reduce the gradients of the velocity in the Z direction with respect to the static case and the TS at Ro=0.38. Besides, the increase of the rotational speed enhances the motion in the Y direction close to the lateral walls, providing high momentum to the top corners.

When the ribbed wall acts as LS at Ro=0.38 (Fig. 11(d)), the gradients of the stream-wise velocity in the Z direction are reduced. Due to the stabilization of the flow close to the LS, the gradients in the Y direction are smaller than in the previous cases. On the other hand, the flow is destabilized on the TS, increasing the gradients in the Y direction. Again, the Coriolis force induces the secondary motion towards the LS close to the lateral walls. In this instance, additional stream-wise vortices are found in the vicinity of the TS (top wall in Fig. 11(c)). These stream-wise vortices might have a Taylor-Görtler nature, similar to the ones found in rotating high aspect ratio channels by Johnston et al. **?** and Kristoffersen and Andersson **?**. In this case, the vortices induce a fluid motion away from the wall in the midspan area close to the top wall, which acts as Trailing Side under these conditions. When the rotation rate is augmented to Ro=0.77 (Fig. 11(e)), the secondary flow pattern changes again close to the top wall, where the fluid is directed to in the midspan region. In this case, the number of secondary flow cells would have been augmented, as observed by Kristoffersen and Andersson **?** as the Rotation number was increased. In the present simulations, two counter rotating vortices have been observed in the region Y/H >8, $0 < Z/H < 3$. In the region -3< Z/H <0, only one vortex is found. This fact can be due to the low intensity of the vortices and the local grid resolution. In this case, the simulations are able to capture the overall motion of both vortices.

5. Conclusions

PIV and LCT experiments were firstly carried out to understand the physical phenomena in the rotating cooling channels present in turbine rotor blades, and to provide detailed data for CFD validation. Since the experimental data is limited to the velocity field in the channel's symmetry plane and to the heat transfer on the ribbed wall, LES were performed to obtain the flow field main characteristics in the entire domain. Results have revealed a large impact of the rotational forces in the mean and turbulence fields, and in the heat transfer.

When the ribbed wall acts as Trailing Side (TS) at Ro=0.38, the Coriolis forces induce the destabilization of the shear layer generated by the rib and originates two large counter-rotating stream-wise vortices that modify the secondary flow field in the channel. The fluid from the Trailing Side is swept towards the Leading Side (LS) close to the lateral walls, going back to the Trailing Side in the midspan region of the channel. As a result, the momentum in the symmetry plane close to the TS is enhanced, and the recirculation bubble downstream of the rib is reduced. In this case, the heat transfer is enhanced with respect to the static case. When the rotation rate is increased to Ro=0.77, the secondary flow pattern changes, showing two lateral cells with high aspect ratio and two central cells with limited height. In this case, the overall heat transfer does not change much from the situation at Ro=0.38.

When the ribbed wall acts as Leading Side (LS) at Ro=0.38, the shear layer generated by the rib is stabilized, leading to low turbulence levels and avoiding the complete reattachment of the flow. Subsequently, the wall is isolated from the main flow and then the heat transfer is reduced. The secondary flow cells under these conditions are the high aspect ratio cells that drive fluid from the TS to the LS close to the lateral walls, and two low aspect ratio counter-rotating cells on the TS. At Ro=0.77 the recirculation bubble also is present over the whole inter-rib area, driving to a similar heat transfer than in the previous case. On the TS, the stream-wise vortices present a different configuration due to the high rotation rate.

On the other hand, the overall heat transfer values given by the TLC experiments show an excellent agreement with the data present in literature at different rotation numbers, even if the geometries are not exactly the same. In addition, TLC measurements were carried out a different Reynolds numbers. According to the experimental results, the heat transfer Enhancement Factor is more sensitive to rotation a the Reynolds number decreases.

Acknowledgments

The author would like to acknowledge the effort of Gian L. Gori and Aude Lahalle during the experimental campaign, the work of Julien Desset and Gerard Goossens in the design of the experimental facility and the support Jean C. Desilve in the laboratory.

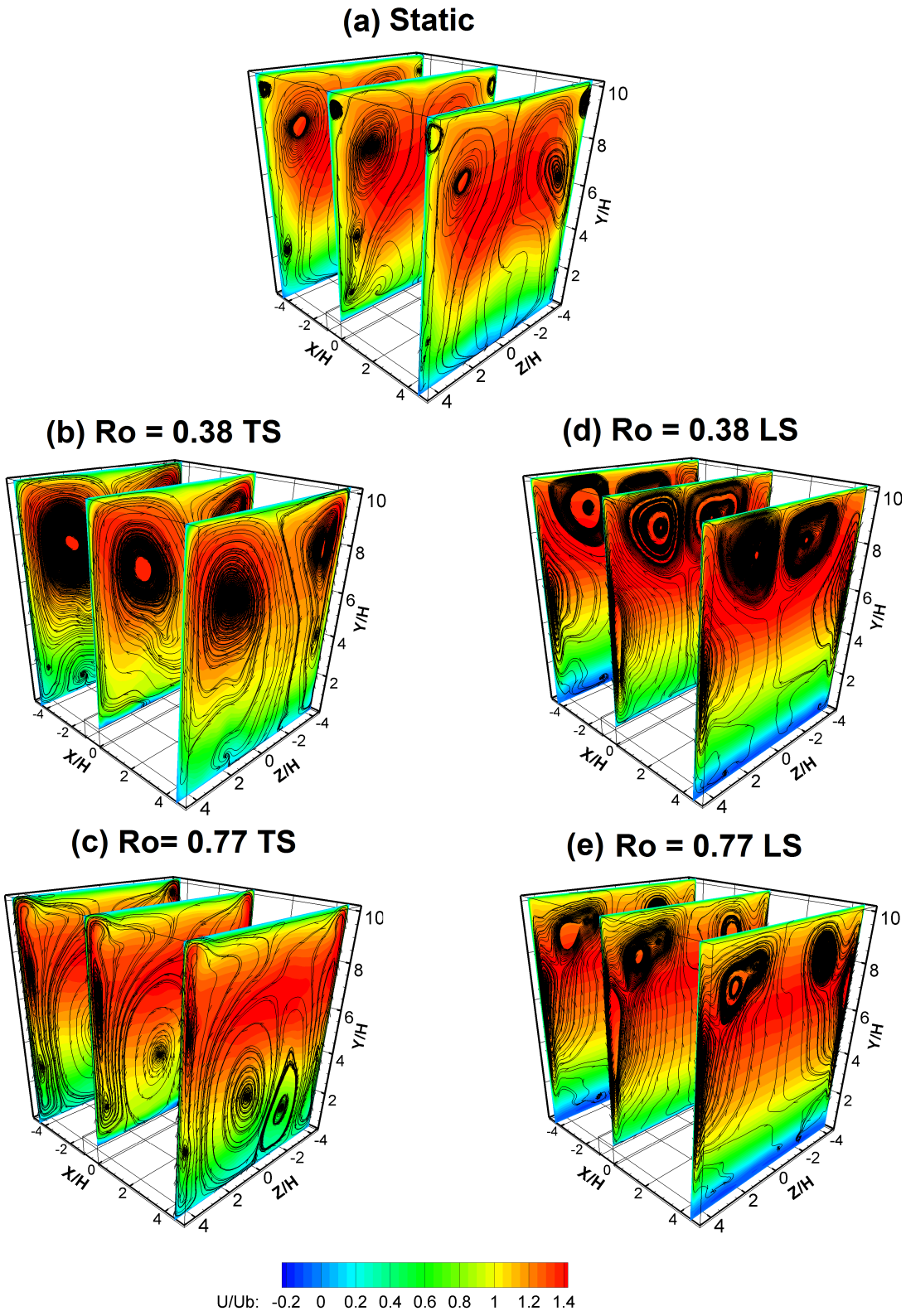

Figure 11: Mean stream-wise velocity and in-plane streamlines in the planes X/H=-4.5, 0 and 4.5 in the LES domain

Blade tip timing and blade tip clearance measurement system based on magnetoresistive sensors

Roberto Tomassini

Turbomachinery and Propulsion Department, von Karman Institute for Fluid Dynamics, Belgium, roberto.tomassini@vki.ac.be

Supervisor: Tony Arts

Full Professor, Turbomachinery and Propulsion Department, von Karman Institute of Fluid Dynamics, Belgium, arts @vki.ac.be

University Supervisor: Gianluca Rossi

Full professor, Mechanical Engineering Department, University of Perugia, Italy, gianluca.rossi@unipg.it

Abstract

A simultaneous Blade Tip Timing (BTT) and Blade Tip Clearance (BTC) measurement system enables the determination of turbomachinery blade vibrations and ensures the monitoring of the existing running gaps between the blade tip and the casing. This contactless instrumentation presents several advantages compared to the well-known telemetry system with strain gauges, at the cost of a more complex data processing procedure. BTT and BTC probes can be optical, capacitive, eddy current as well as microwaves, everyone with its dedicated electronics and many existing different signal processing algorithms. Every company working in this field has developed its own processing method and sensor technology. Hence, repeating the same test with different instrumentations, the answer is often different. Moreover, rarely it is possible to achieve reliability for in-service measurements. Developments are focused on innovative instrumentations and a common standard.

This paper focuses on the results achieved using a novel magnetoresistive sensor for simultaneous BTT and BTC measurements. The sensor measurement principle is described. The sensitivity to gap variation is investigated. In terms of measurement of vibrations, experimental investigations were performed at ITWL (Warsaw - Poland) in a real aeroengine and in the VKI R2 compressor rig. The advantages and limitations of the magnetoresistive probe for turbomachinery testing are highlighted.

Keywords: tip timing, tip clearance, non-contact measurement system, magnetoresistive sensor

1. Introduction

All turbomachinery blades and components experience vibrations during operation due to several sources such as: unbalance, pressure distortions, flutter, stall and surge, mistuning [1]. Unfortunately this undesirable structural motion affects fatigue life, performance and integrity. For more than half a century, vibration measurements have been performed by installing strain gauges on the blades and using telemetry to transmit their signals. Nowadays, the so-called Blade Tip Timing (BTT) technique, is adopted by all manufacturers as a replacement for the classical strain gauge technique because of its non-intrusive character. The main concept behind a BTT system is the determination of the time of arrival (TOA) of the blade tips. Contactless sensors mounted in the casing generate a signal pulse at the blade passage. In absence of any vibration, the TOA of the blade tip depends on the rotational speed only. Nevertheless, when the blade vibrates, blade arrival times will depend on amplitude, frequency and phase of the vibration. Therefore, the blade motion can be measured from time variations.

Another fundamental parameter influencing the machine efficiency is the blade tip clearance. During operation the tip gap changes due to mechanical loads and varying temperature and pressure conditions inside the turbomachine. To prevent a fatal damage,

an accurate monitoring system is mandatory for optimized and safe operations. The so-called blade tip clearance (BTC) measurement systems are based on non-contact probes sensitive to the distance between the passing blade tip and the casing.

The contactless probes adopted in BTT and BTC systems can be of various types: optical, eddy current, microwave, capacitive, etc.. As briefly introduced by Chana [2]. The most used are optical ones, because of the fast rise time, the reliability and the repeatability. However, they suffer from low tolerance to debris which makes their application difficult outside of laboratory conditions [3].

Whatever the technology is, the instrumentation consists of several sensors mounted at fixed angular positions in the casing of a turbomachine, without contact with the blades. To monitor the machine health, the vibrations of the blades are excited with different techniques. Magnetic exciters were used at NASA [4] and at MTU [5]. A jet impinging on the blade tip was proposed by Sonnichsen et al [6], as well as inlet flow distortions by Meyer et al [7]. Nevertheless, tip-timing systems are tested before the real application by means of simulated data. For instance, a numerical calibrator, the UTTC, was realized at Siemens by Uwe and Zidorn [8]. Hardware components were used to generate TTL pulses according to simulated tip timing signals and to directly inject them into commercially available BTT systems. A numerical simulator was developed also by Health and Imregun [9] while developing a new post-processing method, as well as in the work of Gallego Garrido et al [10].

This paper focuses on a novel BTT and BTC probe based on magnetoresistive elements [11]. The sensor measurement principle is described. This technology is already used in commercial displacement sensors, but it is new for turbomachinery applications. A preliminary characterization showed the main advantages: cheap technology, small size, fast response [12]. This paper reports measurements of blade tip clearance and blade vibrations. An innovative testing approach suggested by Rossi and Brouckaert [13], based on the blade motion decomposition, was adopted to realize an innovative calibration bench [14]. In this case the vibration is imposed to the probe, while non-vibrating blades are kept in rotation. A large part of the developments were performed in the innovative bench. Advantages and limitations are reported. Finally, a validation test of the whole instrumentation chain was performed in a real engine at ITWL (Warsaw - Poland). The improved measurement system was then installed in the VKI R2 compressor. The paper ends with the current and future developments.

2. The magnetoresistive sensor

Magnetoresistivity is the ability of a material, like a Permalloy thin film, to change resistance under the influence of a magnetic field [11]. In particular, a change of direction (θ) of the magnetic field, results in a variation of the output DC voltage. By placing a magnetoresistive element beside a permanent magnet, a system sensitive to the variation of magnetic field is created. Hence, if a ferromagnetic object (like a blade) passes in front of it (Figure 1), there will be a distortion of the magnetic field, therefore a variation in the output signal. During the design and development of the novel probe, different configurations of the two components (sensing element-magnet) were investigated. For the same $\Delta\theta$, the output signal amplitude changes with the magnet position, shape and strength. In order to maximize the Signal to Noise Ratio (SNR), a preliminary optimization of the sensor components layout was performed experimentally and numerically [15]. The first sensor prototype manufactured is shown in Figure 2. It is made of a cylindrical permanent magnet placed beside the magnetoresistive thin film. The casing is a 8 mm outer diameter Brass pipe, with the sensing element placed at the top. A length of 40 mm was the best compromise for the tests reported. Smaller probes can be realized, up to 30 mm length. A characterization of the sensor and a comparison with other types of probes, is reported in [14]. Interesting results were pointed out: fast rise time (about 20 ns), high signal repeatability and uncertainty of ± 22 μm (20:1) in clearance measurements.

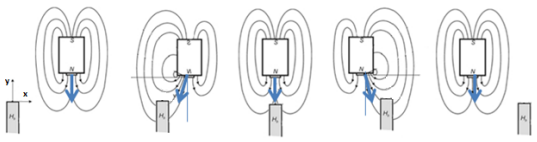

Figure 1: the sensor measurement principle

3. Clearance measurements

This paragraph focuses on the experimental investigations of clearance measurements. Every time a

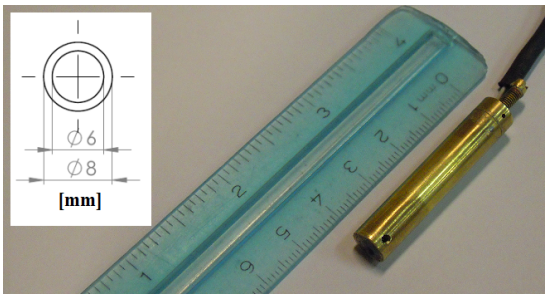

Figure 2: the magnetoresistive sensor

blade is passing in front of the sensor, a pulse is generated. Tests have shown that the amplitude of the output signal is sensitive to variations of the gap between a passing blade tip and the sensor head.

3.1. Test setup and methodology

The passage of a blade in front of the sensor at different gaps was studied in a static test bench. As shown in Figure 3, a blade was mounted in a rotary slider with a resolution of 1°, facing the magnetoresistive sensor installed in a linear slider with a resolution of 10 μm. The sensor axis was aligned with the blade axis at 0° on the rotary slider. The blade passage was discretized and studied in the angular range [-20 + 20]° with an angular step of 2°. The measurements were repeated for different gaps (sensor head-blade tip): [0.5 1 1.5] mm. At every fixed position, the output DC signal was acquired and represents one point of the resulting fitting curves of Figure 4.

3.2. Results

Figure 4 shows the typical pulses observed at the blade passage at different gaps. The variation of the clearance results in a signal amplitude variation: the bigger the gap, the smaller the signal amplitude. An interesting aspect to point out is that, whatever the clearance is, all signals pass through a common point at 0 Volt. This behavior is of fundamental importance for tip timing measurements because the zero volt crossing time does not depend on the clearance. The clearance between a passing blade tip and the new sensor head can be monitored by the maximum peak value or the peak to peak value of the blade pulse. As recently shown by Tomassini et al [14], clearance measurements are possible with an uncertainty of ± 22 μm (20:1).

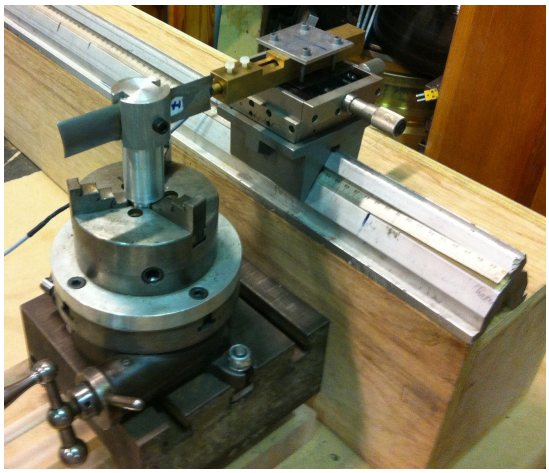

Figure 3: the clearance test bench

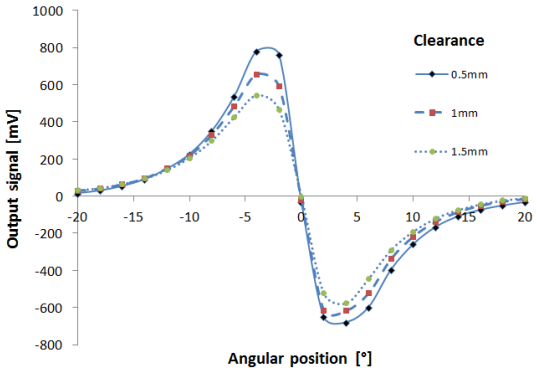

Figure 4: blade passage pulse at different clearances

4. Vibration measurements

The components of the measurement system (sensors, electronics and software) were realized during the on-going collaboration between VKI and the Italian Universities of Perugia and Padova. A large part of the development process was performed in an innovative calibration bench: according to the idea of the blade motion decomposition [13], the new bench was realized and recently presented by Tomassini et al [14]. Instead of having fixed casing sensors and vibrating blades, the innovative approach consist in letting the sensor vibrate while non-vibrating blades are kept in rotation. The biggest advantages of this system are the possibility to know the expected measured vibrations and the flexibility in changing the test conditions. Recently, the whole measurement system (software included) was improved and validated during two external collaborations at Fogale Nanotec (Nimes, France) and at ITWL (Warsaw, Poland) in a

real military engine (Figure 5).
This paragraph reports the validation test in Poland and a vibration test performed in the VKI R2 compressor rig (Figure 6) with the improved instrumentation.

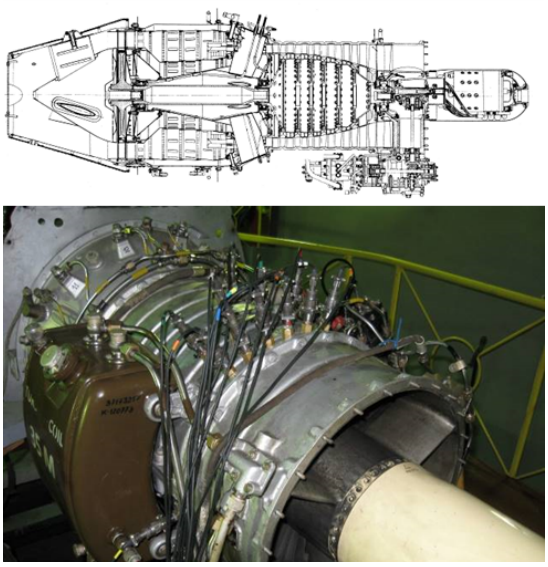

Figure 5: the SO-3 turbojet engine

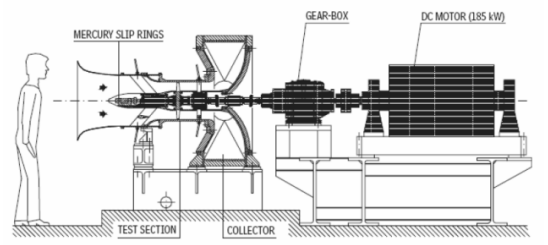

Figure 6: the VKI R2 compressor rig

4.1. Vibration testing: analysis of BTT data

From the acquired signals along a speed transient, a BTT data processing algorithm provides the measured blade tip displacement samples. The basic concept behind a tip-timing system is to calculate the blade vibrations from the time variations. Indeed, if there is a vibration, the arrival time of the blade tip will be delayed (with a positive or negative sign) with respect to the undisturbed rotation. Therefore, at every revolution, for every blade, the tip velocity is estimated from the successive passages of the blades and the variation of the tip arrival time, due to the vibrations, is calculated (ΔTOA). Finally, the blade displacement samples are obtained as follows:

$$S_{ir} = V_{tip} * \Delta TOA \quad (1)$$

Where:
S_{ir} = the measured displacement sample of the blade i (i = 1...24), at the revolution r;
V_{tip} = the blade tip velocity;
ΔTOA = the measured variation of the time of arrival of the blade pulse;

The measured displacements of all the blades are plotted together in the so-called waterfall graph. Displacement amplitudes are plotted against the rotor speed and shifted along the y axis, according to the blade number, in order to have an ensemble plot. From one sensor, it is possible to calculate one sample per blade per revolution. When a blade is vibrating, it has a frequency higher than the revolution frequency, therefore the measurement of the frequency of the vibration of the blade with only one sensor is affected by aliasing. To avoid this, usually 6 to 8 sensors are mounted together in the commercial BTT systems. Nevertheless, what is more important is the calculation of the amplitudes of displacement, which is not affected by aliasing. The algorithm developed in this work processes data from only one sensor therefore the results are correct in terms of amplitudes and aliased in frequency.

4.2. The SO-3 turbojet engine: test setup and methodology

The magnetoresistive sensors were mounted in the military SO-3 turbojet engine of Figure 5. Four sensors were installed in slots prepared in the upper compressor casing in the plane of the second rotor stage of the compressor. The rotor has 41 blades and a tip radius of 207 mm. Tip-timing data were acquired during a speed transient up to 16000 rpm. An inlet obstruction object, namely a piece of felt, was attached to the IGVs to excite the blade resonances. Previous tests performed at ITWL showed two blade resonances around 8000 rpm and 12000 rpm. The objective of the test was to repeat the experiment to validate the diagnostic system based on magnetoresistive elements.

4.3. Results

The magnetoresistive signals were recorded and processed by the ITWL Tip-Timing software. Figures

7 and 8 display the waterfalls of the measured displacements of the first 15 blades. The graph of Figure 7 is related to the test with the ITWL instrumentation, the one of Figure 8 is related to the magnetoresistive probes. Both waterfalls show two resonances around 8000 rpm and 12000 rpm. Some blades were excited at a slightly different speed, which can be due to mistuning. The measured displacements obtained with the magnetoresistive sensors show a drift. There might be several reasons and further investigations on the single components of the measurement chain are on-going.

From the FEM analysis performed at ITWL on the blade geometry, the two measured resonances correspond to the excitation of the first bending mode calculated at about 500Hz. The data must be processed further to have an estimate of the measured vibration frequency. Nevertheless, it is possible to compare the results in a qualitative way. Figure 9 focuses on the measured displacements around 12000 rpm. The peaks of the resonances of the blades in the two tests are in strong agreement, both in amplitude and with respect to the speed. The expected resonances were measured correctly and this confirm the possibility of performing tip-timing measurements with the novel magnetoresistive probes. Moreover, the whole instrumentation chain was successfully working in a real engine for the first time. The VKI sensors were compatible with the ITWL acquisition system and processing software. No damage was reported. Finally, the dedicated electronics developed at VKI was successfully working up to 11KHz blade passing frequency and no particular noise problems were observed.

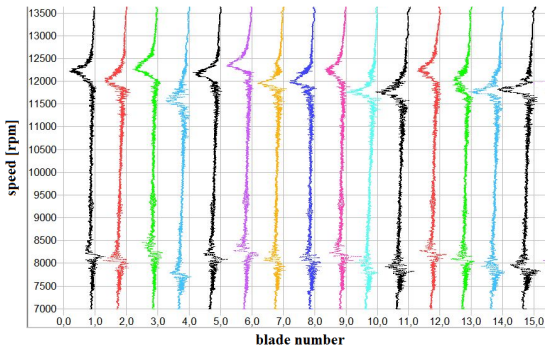

Figure 7: The waterfall of the measured displacements of the first 15 blades - ITWL sensors

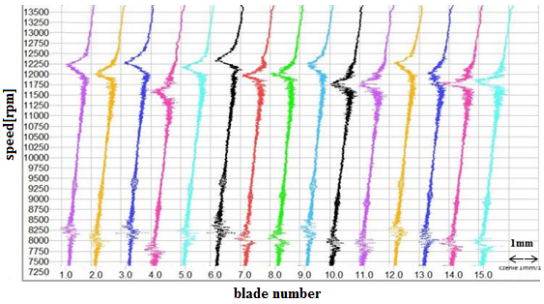

Figure 8: The waterfall of the measured displacements of the first 15 blades - Magnetoresistive sensors

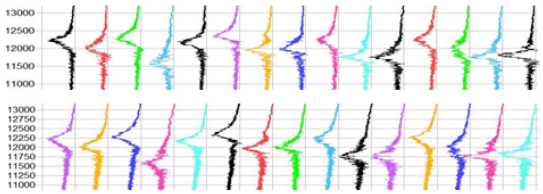

Figure 9: Comparison of the measured displacements around 12000 rpm

4.4. The VKI R2 compressor: test setup and methodology

The validated and improved instrumentation was installed in the VKI R2 compressor. It is a high speed compressor driven by a 185kW DC motor. The rotational speed can vary up to 6000 rpm. It is a single stage axial compressor with a 400 mm tip diameter test section. The rotor is composed of 24 subsonic blades of the NACA 65 family; the hub radius is 100 mm. The stator is composed of 30 blades. The probes can be inserted at four circumferential locations, every 90°. Three sensors were mounted in the casing at [0 90 180]° . Tip-timing signals were acquired along a speed transient from 2000 rpm up to 5500 rpm, with a sampling frequency of 1 MHz per channel. No information was available regarding the expected blade vibration modes and frequencies. For this reason, a hammer test with an accelerometer was performed on the blades to have an estimate of the first bending frequency. It was assessed to be around 480Hz. Considering this and the speed range of the test, it is possible to get the Campbell diagram of figure 10. The red line represents the first bending frequency of the blades. It should account for the contribution of the centrifugal force at different rpm, which increases the blade resonance frequency with the speed, but it could not be estimated at this stage. The Engine Order lines (EO) indicate the multiple integers of the rotor rotational fre-

quency. For instance, the 2EO is the line fitting all the points equal to 2 times the rotational frequency. When a line representing a blade vibration mode crosses an EO line, a synchronous resonance can be excited at the crossing speed. Therefore, during this test, synchronous blade resonances may appear around 2800, 3200, 3600, 4200, 4800 rpm. To let the compressor works in off-design condition, a distortion grid was mounted at the rotor inlet (Figure 11). Moreover, an air injection system at the blade tip was installed to excite asynchronous resonances. Four bent pipes were installed in the casing, two at 0° and two at 180° (figure 11). They blow compressed air at 5 bar against the blade tips during the rotation at about 3500 and 5400 rpm. The air injection was controlled manually by means of a pneumatic valve. It was connected to a collector that sent air to the two couples of casing pipes, as in figure 12.

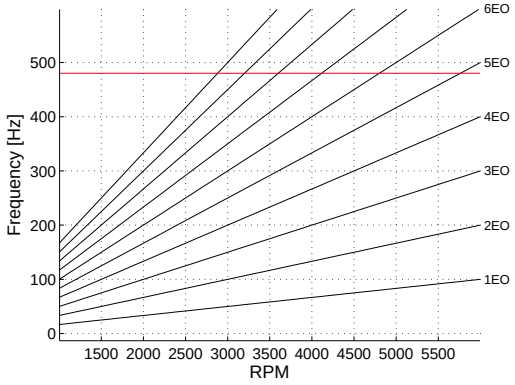

Figure 10: the VKI R2 Campbell diagram

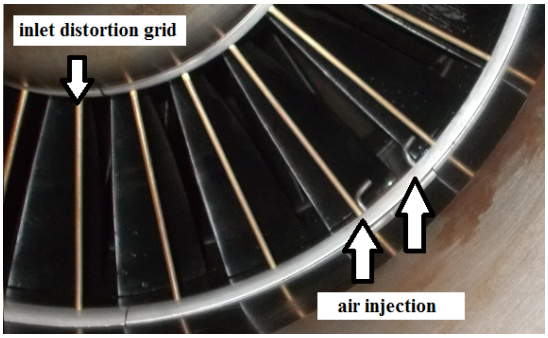

Figure 11: the VKI R2 compressor inlet

4.5. Results

Figure 13 shows the waterfall of the measured displacements of the first 4 blades. The measured displacements of blade 2, 3 and 4 were shifted (by adding a DC constant value) to have the waterfall of all the samples on the same graph.

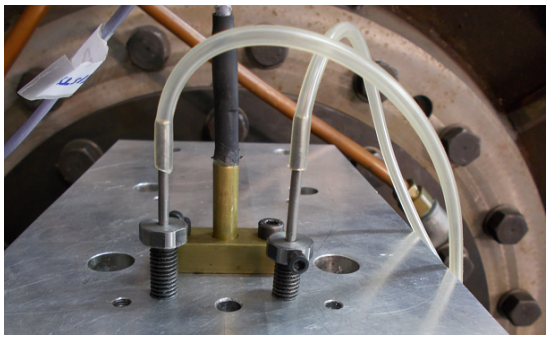

Figure 12: one sensor and the air pipes mounted in the compressor casing

The synchronous blade resonances appear in the waterfall as a change in the DC component of the measured displacement and the maximum peak value is representative of the vibration amplitude. The asynchronous blade resonances appear as an increase of frequency with respect to the base noise of the system and the maximum peak value is representative of the vibration amplitude.

As shown in Figure 14, a synchronous resonance was measured around 3650 rpm and an asynchronous resonance around 3450 rpm, as expected. Nevertheless, the measured amplitudes are moderate. More evident is the synchronous resonance measured around 4900 rpm (Figure 15). The latter was expected to be around 4800 rpm, but the effect of the centrifugal force was not considered. Finally, the asynchronous resonance around 5400 rpm is also present.

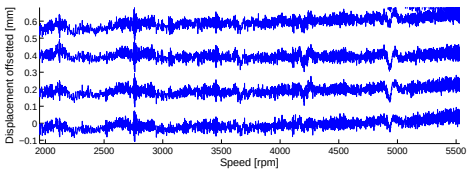

Figure 13: the waterfall of the measured displacements of the first 4 blades

5. Developments

In the last part of this research project attention is given to three major developments:

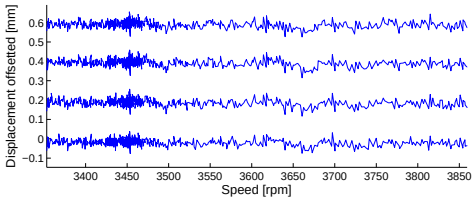

Figure 14: A detail of the measured displacements around 3500 and 3600 rpm

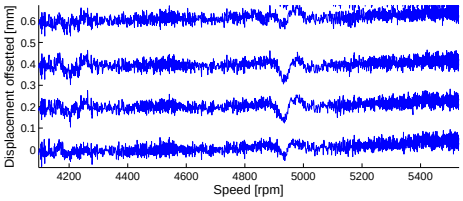

Figure 15: A detail of the measured displacements around 4200 and 4800 rpm

- Investigations on the possibilities to measure through materials
- New sensor configurations
- An algorithm to further analyze the aliased frequencies

Concerning the first point, an experimental campaign was conducted on the different possibilities to detect and to measure the position and the displacement of an object (like a blade), through different shielding materials (like Aluminium), without making holes on them. This is possible thanks to the different magnetic permeabilities of different materials. For instance, the magnetoresistive probes can detect the blade passage through an Aluminium layer, up to 10 mm thickness with a SNR reduction of about 50%. This aspect still requires further studies because of great interest whether in turbomachines and in industrial applications in general.

Regarding the second point, developments are focused on improving the repeatability when using different materials and in extending the maximum temperature range of the probe. On one hand, passages of blades of different ferromagnetic materials at the same distance sensor-blade tip, often results in different maximum voltage levels because of different polarization. This aspect needs a normalization, then the calibration curve can be calculated. To avoid this, studies with different sensor configurations are on-going. On the other hand, current efforts focus also in improving the temperature range of the sensor. In hot environments (like turbine stages) where is needed to cool down the probe, one solution can be to use ceramic shielding materials in front of the sensor head. This configuration works, but not so good for long testing sessions. Another way is the forced cooling around the sensing element, for instance with air or water cooling recirculation system, but this introduces too many connections, which can be not convenient from the logistic and financial point of view. The above mentioned studies are carried out experimentally and numerically. For instance, electromagnets were tested as alternative to permanent magnets. In fact, the former provides more flexibility due to the possibility of magnetic field intensity modulation. Moreover, an electromagnet is useful where there can be accumulation of ferromagnetic material in the sensor head, by designing a cleaning procedure. Numerically, a mathematical model to simulate the blade passage was built (as in Figure 16). The characteristics of the magnet were taken from its datasheet. The blade geometry was repeated in the mesh at different angular positions. Hence, the blade passage can be simulated by the superposition of the results of simulations at different blade angular position. The model was validated with experimental data, as in Figure 17, comparing the magnetic field variation measured and computed at the blade passage. Currently the numerical model is used to investigate new sensor configurations and the effect of the presence of shielding materials.

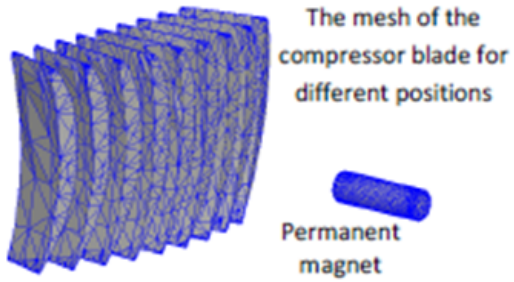

Figure 16: A detail of the mesh

Finally, the last on-going development regards improvements on the processing algorithm of BTT data, to better analyze folded frequencies. Figure 18 shows the measured displacements of the blade 1 of the SO-3 jet-engine calculated with the algorithm developed in the frame of this project. By computing successive FFTs with a window of 200 samples, it is possible

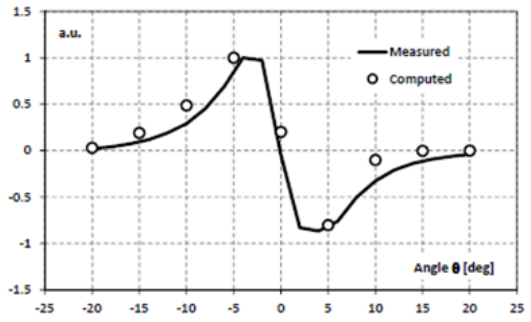

Figure 17: Comparison of magnetic field variations measured and simulated

to have the so-called Z-Plot of Figure 19. The blade resonance around 9000 rpm appears in red. Moreover, there is a zig-zag patch that represents a blade vibration mode presents up to about 12000 rpm. Its frequency is unknown because BTT data is usually aliased due to the fact that it is possible to record only few blade vibration samples per revolution and the nyquist theorem is not satisfied. This results in zig-zag patch like in the Zplot of Figure 19. One way to avoid the aliasing is to use several BTT sensors, which make the measurement chain expensive and complex. A better way can be implemented by considering the multiples of the folded frequencies. An algorithm under development calculates the first N multiples of the folded frequency (Figure 20) and selects among them the most probable true real frequency of vibration. The selection procedure is a combination of methods. A preliminary result on the data from the SO-3 Jet-Engine shows (Figure 21) that the real frequency of the vibration mode measured is around 550 Hz which is in good agreement with FEM Analysis of the Polish Institute.

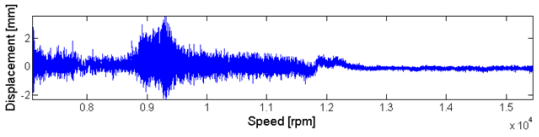

Figure 18: Measured blade1 displacements on the SO3 Jet-engine

6. Conclusions

A magnetoresistive probe for simultaneous Tip-Timing and Tip-Clearance measurements was realized and tested. The blade tip gap can be monitored by means of the maximum signal amplitude or the

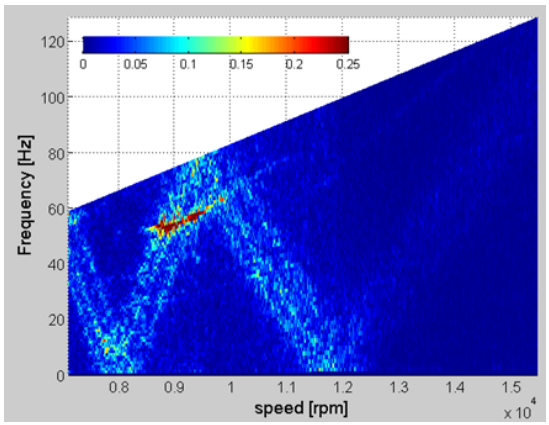

Figure 19: The Zplot of the measured blade1 displacements

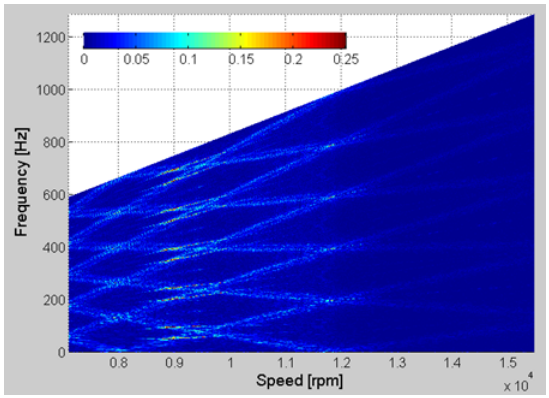

Figure 20: The Zplot of the measured blade1 displacements with multiples of the aliased frequency

peak to peak value. Blade vibration measurements were performed in a real engine at ITWL Poland, and in the VKI R2 compressor. An innovative approach for the testing and the characterization of Tip Timing systems was introduced with the calibration bench. Imposing the vibration to the sensor ensures the advantages of knowing the expected results and having more flexibility in the simulation of different vibration cases. Further developments can significantly help in the non-trivial uncertainty analysis of tip-timing data. Regarding the application of the magnetoresistive technology in turbomachinery testing, the main advantages reported are a performance in line with the existing sensors but at lower costs, small sizes and tolerance to debris. Limitations may occur in applications at high temperature (such as turbines), which should be investigated and with non-ferromagnetic blades, which require special expedients.

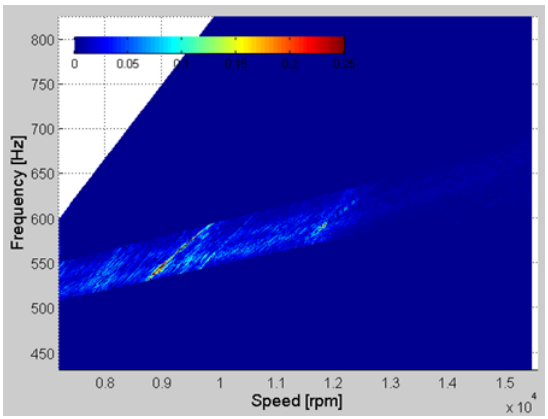

Figure 21: The Zplot of the measured blade1 displacements with the corrected frequency

Acknowledgments

The author would like to acknowledge the professors and technicians of the von Karman Institute, the University of Padova CISAS G. Colombo and the Engineering Department of the University of Perugia. Finally, thanks goes to ITWL (Warsaw - Poland) and Dr. Radoslaw Przysowa for collaborating in this work. The validation test was financed by the Polish National Science Centre (NCN) under the decision DEC-2011/01/D/ST8/07612.

References

[1] J.-F. Brouckaert, Tip timing and tip clearance problems in turbomachinery, Lecture Series VKI-LS-2007, von Karman Institute for Fluid Dynamics (2007).

[2] K. Chana, Fundamentals of tip timing and tip clearance sensors, in Tip timing and tip clearance problems in turbomachinery, Lecture Series VKI-LS-2007, von Karman Institute for Fluid Dynamics (2007).

[3] G. Husler, P. Ettl, M. Schenk, G. Bohn, I. Laszlo, Limits of optical range sensors and how to exploit them, International Trends in Optics and Photonics 74 (1999) 328–342.

[4] J. Dexter, G.V. Brown and O. Mehmed, A magnetic suspension and excitation system for spin vibration testing of turbomachinery blades, National Aeronautics and Space Administration, Lewis Research Center, 1998.

[5] M. Zielinski, Non-contact blade vibration and tip clearance measurements on aero engine compressors with BSSM, in Tip timing and tip clearance problems in turbomachinery, Lecture Series VKI-LS-2007, von Karman Institute for Fluid Dynamics (2007).

[6] H. E. Sonnichsen, P. H. Wawrzonek, R. B. Connell, B. D. Milatovic, Blade vibration test apparatus and method, uS Patent 6,679,121 (Jan. 20 2004).

[7] A. Meyer, H. F. Calvert, C. R. Morse, Effects of obstructions in compressor inlet on blade vibration in 10-stage axial-flow compressor, Tech. Rep. NACA-RM-E9L05, NASA Center (1950).

[8] U. Pfeifer, M. Zidorn, Tip timing measurement chain validation with the universal tip timing calibrator uttc, approach and experience, in: 10th International conference on vibration measurements by laser and noncontact techniques AIVELA 2012, Vol. 1457, AIP Publishing, 2012, pp. 43–51.

[9] S. Heath, M. Imregun, An improved single-parameter tip-timing method for turbomachinery blade vibration measurements using optical laser probes, International journal of mechanical sciences 38 (10) (1996) 1047–1058.

[10] J. Gallego-Garrido, G. Dimitriadis, J. R. Wright, Development of a multiple modes simulator of rotating bladed assemblies for blade tip-timing data analysis, in: 2002 International Conference on Noise and Vibration Engineering, Katholieke Universiteit Leuven, 2002, pp. 1437–1446.

[11] P. Holman, Magnetoresistance (mr) transducers and how to use them as sensors, Honeywell International. July.

[12] J.-F. Brouckaert, R. Marsili, G. Rossi, R. Tomassini, Development and experimental characterization of a new non contact sensor for blade tip timing, in: 10th International conference on vibration measurements by laser and noncontact techniques AIVELA 2012, Vol. 1457, AIP Publishing, 2012, pp. 61–68.

[13] R. G, B. JF, Design of blade tip timing measurements systems based on uncertainty analysis, ISA 58th International Instrumentation Symposium, San Diego, USA.

[14] R. Tomassini, G. Rossi, J. Brouckaert, On the development of a magnetoresistive sensor for blade tip timing and blade tip clearance measurement systems, in: 11th International conference on vibration measurements by laser and noncontact techniques AIVELA 2014: Advances and Applications, Vol. 1600, AIP Publishing, 2014, pp. 65–73.

[15] E. Cardelli, A. Faba, R. Marsili, G. Rossi, R. Tomassini, Magnetic nondestructive testing of rotor blade tips, Journal of Applied Physics 117 (17) (2015) 17A705.

Advanced experimental aero-thermal investigations of wall-bounded swirling flows in three-dimensional ribbed tubes.

Marco Virgilio

Turbomachinery and Propulsion Department, von Karman Institute for Fluid Dynamics, Belgium, marco.virgilio@vki.ac.be

Supervisor: Tony Arts

Professor and Head of Department, Turbomachinery and Propulsion Department, von Karman Institute for Fluid Dynamics, Belgium, tony.arts@vki.ac.be

University Supervisor: Kevin Van Geem

Associate Professor, Laboratory for Chemical Technology, Universiteit Gent, Belgium, Kevin.VanGeem@UGent.be

Abstract

For quite some time now, there is a major need in increasing the gas turbine efficiency by means of increasing the flow temperature. To maintain the blade integrity, at least, internal cooling is needed. To improve the cooling of the blade walls, the internal channels need to be ribbed in order to enhance the heat transfer.

In petroleum refinery and particularly in thermal cracking of hydrocarbons for the production of ethylene, the reactors expect short residence time for endothermic reactions, so a high rate of heat transfer is required. Similarly as in turbomachinery, local obstacles help to enhance the heat transfer in the reactor tubes. The knowledge gained from turbomachinery will be useful in this environment.

Although it has been demonstrated by several authors that the increase of the Nu number is at least about twice the one seen in a smooth tube at the same Reynolds number, the ribbing technique is limited by the rise in the friction losses. Therefore, a multi-objective optimization design is a reasonable method which can find out the best solution to the problem stated before. Anyway, the so considered best geometries need to be tested experimentally to validate the performance provided by the numerical predictions. The knowledge of the turbulent swirling flows dynamics is needed to carry on optimizing techniques for the design of chemical reactors, turbines internal cooling channels or heat exchangers in a more general sense.

The ambition of this Ph.D. research is to measure the aerothermal characteristics and to understand and model the complexity of wall-bounded turbulent swirling flows. The investigation will be done experimentally with Stereo-Particle Image Velocimetry to measure the flow field and with Thermochromic Liquid Crystals to quantify the heat transfer. An important focus will be put on the definition of particular wall obstacles and their optimization in order to provide high local heat transfer.

Keywords: Stereo PIV, Thermochromic Liquid Crystals, Ribbed Channel, Turbulent Flows, Heat Tranfer, Multi-Objective Optimization

NOISE AND AEROACOUSTICS

Prediction of low-speed fan trailing-edge noise based on RANS and on scale resolved simulations

Gabriele Grasso

Environmental and Applied Fluid Dynamics Department, von Karman Institute for Fluid Dynamics, Belgium, gabriele.grasso@vki.ac.be

Supervisor: Christophe Schram

Associate Professor, Aeronautics and Aerospace Department & Environmental and Applied Fluid Dynamics Department, von Karman Institute for Fluid Dynamics, Belgium, christophe.schram@vki.ac.be

University Supervisor: Stéphane Moreau

Professeur titulaire, Département de génie mécanique, Université de Sherbrooke, QC, Canada, Stephane.Moreau@USherbrooke.ca

Abstract

This work compares the prediction of the broadband trailing-edge noise emitted by a four-bladed low-speed ventilation fan obtained with different computational approaches. The objective of each approach is to compute the spectrum of the wall pressure fluctuations close to the trailing-edge, which is an input to Amiet's theory for the computation of the far-field noise spectrum. The wall pressure spectrum can be computed by applying Panton and Linebarger's theory to boundary layer data extracted from a time-averaged simulation, or it can be obtained directly by frequency analysis of a scale resolved simulation. The results of both kinds of computation are compared with the measurements taken on the same fan. A better correspondence with the experimental data has been obtained by using a Scale Adaptive Simulation (SAS) rather than a RANS flow solution.

Keywords: Aeroacoustics, fan noise, hybrid method.

1. Introduction

The trailing-edge noise is the minimum broadband sound that a lifting surface would produce in absence of other sound mechanisms as turbulence interaction at the leading-edge or tip-vortex interaction. This source of sound, caused by the scattering of the boundary-layer disturbances into acoustic waves, as illustrated in Fig. 1, remains the only broadband noise contributor for subsonic fans operating in homogeneous stationary flows, in absence of any upstream, downstream and tip interaction. The present study aims at predicting the trailing-edge noise of a four-bladed low-speed axial fan on which an experimental campaign[1] has been conducted at CETIAT. The available experimental database is shared in a collaborative project including VKI, CETIAT[2] and CETIM[3], aimed at the development and validation of numerical flow and noise prediction methods. In an earlier stage of this research [4], the flow and acoustic prediction have been based on a method using stationary flow computation and semi-analytical Amiet's theory [5]. The flow was first solved using OpenFOAM®, whereby a 3D steady RANS computation was performed using a Multiple Reference Frame method. The wall-pressure spectrum upstream the trailing-edge required in the trailing-edge noise theory was then obtained from a wall-pressure reconstruction model of Panton and Linebarger[6] using boundary-layer information. Furthermore, the statistical reconstruction of the wall-pressure spectrum and the noise computation have been validated with respect to experimental data on a flat plate boundary layer and on a controlled diffusion airfoil[7]. Finally, the far-field sound pressure spectrum was computed by means of Amiet's theory. This method keeps balance between cost and accuracy and for this reason it has already been implemented in an optimization procedure [8].

The purpose of this study is to perform a Scale

Adaptive Simulation (SAS) of the ventilator in order to compute directly the trailing-edge wall-pressure spectrum from the time-resolved CFD data. The SAS model is based on unsteady RANS but it can resolve turbulence structures with LES quality, providing a steady solution in stable flow regions while resolving turbulence in transient instabilities[9]. The results thereby obtained are compared with those previously obtained from RANS data for what concerns the boundary layer characteristics, the wall pressure spectrum and the predicted radiated noise. Furthermore, a comparison of the last two with experimental data is included for validation of both the CFD approaches.

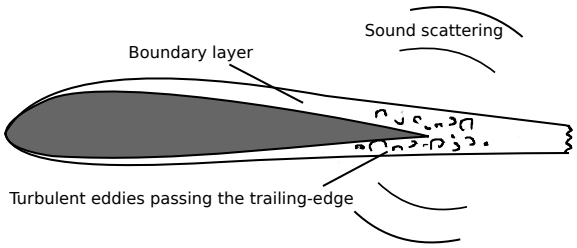

Figure 1: Trailing-edge noise generation mechanism.

2. Methodology for noise prediction

The broadband trailing-edge noise of a stationary airfoil can be computed using Amiet's theory [5]. It assumes the airfoil to be infinitively thin, without camber or angle of attack, and in uniform flow conditions. Under such assumptions, the airfoil is approximated by a flat plate for the analytical derivation of the aeroacoustic transfer function. The main trailing-edge scattering obtained by Amiet [5] has been corrected by a leading-edge back-scattering contribution which accounts for the finite chord length [10]. The radiated sound field is calculated by integrating the induced surface sources on the actual chord length, c and the airfoil span, d, assuming convection of frozen turbulent boundary-layer eddies past the trailing-edge. In the following formulas, the subscripts 1, 2 and 3 indicate the stream-wise, cross-wise and span-wise directions, respectively. For large aspect ratio (d/c), the power spectral density of the sound pressure in the far field is obtained using:

$$S_{pp}(\mathbf{x},\omega) = \left(\frac{\omega c x_3}{2\pi c_0 S_0^2}\right)^2 \frac{d}{2}\left|\mathcal{L}\left(\frac{\omega}{U_c}\frac{\bar{k}x_2}{S_0}\right)\right|^2 \Phi_{pp}(\omega) l_y(\omega), \quad (1)$$

where ω is the angular frequency, $\mathbf{x}$ is the position of the listener, S_0 is the distance from the source, $\mathcal{L} = \mathcal{L}_1 + \mathcal{L}_2$ is the aeroacoustic transfer function, with $\mathcal{L}_1$ the main contributing term from the trailing-edge and $\mathcal{L}_2$ the back-scattering term from the leading-edge. Equation (1) derives from the assumption of large-span airfoils[11], implying that for each listener position there will be only one radiating span-wise aerodynamic wave number k_y. $\Phi_{pp}(\omega)$ is the wall-pressure spectrum upstream the trailing-edge while $l_y(\omega)$ is the corresponding span-wise correlation length. This quantity is modelled in this work by using Corcos' formula[12],

$$l_y(\omega) = \frac{\omega/(bU_c)}{k_y^2 + (\omega/(bU_c))^2} \quad (2)$$

where b is a model constant and U_c is the convective velocity of turbulent structures at the trailing-edge.

$\Phi_{pp}(\omega)$ is the main input to Amiet's theory and can be obtained either directly from a scale resolved simulation or from RANS with a reconstruction model. In the second case, using the model developed by Panton and Linebarger[6], Remmler *et al.* [7] implemented the following expression for the wall-pressure spectrum

$$\Phi_{pp}(\omega) = 8\rho_0^2 \iiint_0^\infty \frac{k_1(\omega)^2}{k(\omega)^2} \exp^{-k(\omega)(x_2+\hat{x}_2)} S_{22}(x_2,\hat{x}_2,\omega) \frac{\partial U_1}{\partial x_2}\frac{\partial U_1}{\partial \hat{x}_2}\, dx_2\, d\hat{x}_2 dk_3 \quad (3)$$

where ρ_0 is the reference density and x_2 is the wall normal distance. The energy spectrum of the vertical velocity fluctuations, S_{22}, is expressed as:

$$S_{22}(x_2,\hat{x}_2,\omega) = \frac{\bar{u_2'}(x_2)\,\bar{u_2'}(\hat{x}_2)}{\pi^2}\Lambda^2 \iint_0^\infty R_{22}\cos(\alpha\,\tilde{k}_1(\omega)\,\tilde{r}_1)\,\cos(\tilde{k}_3\,\tilde{r}_3)\,d\tilde{r}_1\,d\tilde{r}_3 \quad (4)$$

The integration coordinates and the wave numbers were non-dimensionalized with the turbulence integral length scale, Λ. The model therefore uses the stream-wise mean velocity profile $U_1(x_2)$ and the cross-wise velocity fluctuation profile $u_2'(x_2)$. Both velocities and the turbulence integral length scale Λ are calculated from the RANS result. The velocity correlation coefficient R_{22} and the scale anisotropy factor α need to be modelled. In particular, the cross-wise velocity correlation coefficient is modelled according to Panton and Linebarger as

$$R_{22} = \left[1 - \frac{\tilde{r}^2}{2\sqrt{\tilde{r}^2+\tilde{y}^2}}\right] e^{-\sqrt{\tilde{r}^2+\tilde{y}^2}} \quad (5)$$

where $\tilde{r} = \tilde{r_1} + \tilde{r_3}$ and $\tilde{y} = (x_2 - \hat{x}_2)/\Lambda$. This is a symmetric function, thereby implying local homogeneity of turbulence.

No quadratures are used to calculate the quintuple integral in Eq. (3) as they would require prohibitive memory. The integration is performed with a Monte Carlo method using importance sampling to enhance convergence.

In case of rotation, the far-field noise PSD of a low solidity fan with B independent blades is given by an integration over all possible azimuthal positions, ψ, of the stationary airfoil formulation:[13]

$$S_{pp}(\mathbf{X}, \omega) = \frac{B}{2\pi} \int_0^{2\pi} \frac{\omega_e(\Psi)}{\omega} S^{\Psi}_{pp}(\mathbf{x}, \omega_e) d\Psi \quad (6)$$

where X is the position of the listener in the absolute frame of reference and x is its position in the rotating frame attached to the airfoil trailing-edge. The factor $\omega_e(\Psi)/\omega$ accounts for Doppler effects due to the rotation, being ω_e the emitted frequency and ω the observed frequency.

In order to take into account the variation of the flow along the airfoil span, a strip theory is used, splitting the blade in a given number of segments. A local Cartesian frame of reference is defined for each strip close to the trailing-edge, as represented in Fig. 2(a), and boundary layer informations are extracted along the axis normal to the airfoil surface. Then, each strip is approximated by a flat rectangular surface (Fig. 2(b)) in order to comply with the hypothesis of Amiet's theory. A certain overlap can be observed between the surfaces approximating the lowest blade strip and the above strip respectively. This is due to the fact that these surfaces follow the shape of the trailing-edge of the blade which becomes more concave close to the hub. Finally, the total radiated sound is the summation of sound emitted by each rectangular surface. In the present case, the blade is split in 5 strips.

3. Test case: four-bladed low-speed ventilation fan

3.1. Experimental set-up

The ventilator, shown in Fig. 3, has 0.8 m diameter and hub ratio of 0.34. It has four equally spaced blades, two of which are equipped with unsteady pressure sensors in order to measure the wall-pressure spectrum, $\Phi_{pp}(\omega)$, the span-wise correlation length spectrum, $l_y(\omega)$ and the convective velocity of turbulent eddies U_c. The chord at tip is of 0.135 m and the blade's maximum thickness is 4 mm, while the mean tip gap is 5 mm. The shroud trailing-edge is aligned with that of the blade when the stagger angle of the blade is set to 30°. The shroud is mounted on the wall of the reverberant chamber, which is upstream of the ventilator. A rotating microphone performs the acoustic measurements in the reverberant chamber, while three fixed microphones are placed downstream of the ventilator, allowing to make a spatial average of the acoustic data. [1]

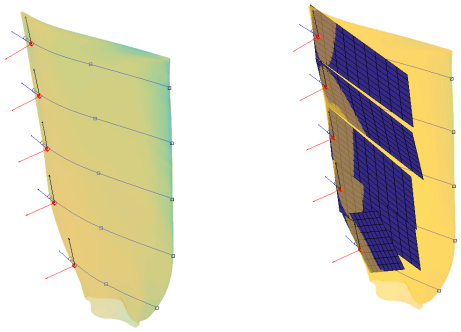

(a) (b)

Figure 2: Division of the blade surface in 5 radial strips: (a) definition of the local frame of reference for the extraction of boundary layer data; (b) definition of planes for the computation of radiated noise by means of Amiet's theory.

3.2. Numerical set-up

3.2.1. RANS computation

A three-dimensional steady RANS computation of the flow around the low-speed ventilation fan has been performed by means of OpenFOAM® 2.3. The flow has been solved in the best efficiency condition for 600 RPM rotational speed. Since the relative Mach number at tip is approximately equal to 0.3, the incompressible solver *simpleFoam* has been selected[14].

Figure 4 depicts the computational domain with the related boundary conditions. The computational domain is divided in three main regions: a stationary region upstream of the ventilator, containing the inlet boundary, a moving reference frame (MRF) region surrounding the ventilator and, finally, another stationary region downstream of the ventilator, containing the outlet boundary. Non-conformal interfaces (defined as *cyclicAMI* in OpenFOAM®) link the MRF with the stationary regions. Periodic boundary conditions have been applied to the lateral patches



Figure 3: View of the ventilator from the aspiration. The unsteady pressure sensors at mid-span and close to the tip are visible on the lower and upper blade, respectively. (Courtesy of CETIAT).

of the domain, allowing to simulate only one quarter of the fan geometry.

The volumetric flow rate ($3.5\,\mathrm{m^3 s^{-1}}$) has been imposed at the inlet a 1% turbulence intensity and 0.01 m turbulent length scale, while a fixed pressure has been imposed at the outlet. The selected turbulence model is $k-\omega$ SST[15] with enhanced wall treatment. Finally, the stationary walls upstream and downstream of the ventilation fan, the hub, the blade surface and the shroud have been defined as no-slip wall. Inside the moving frame of reference, the hub and the blade are defined as stationary walls, while the shroud is counter-rotating with the speed of -600 RPM.

The computational grid has been produced by means of the open source tool snappyHexMesh, which can generate three-dimensional meshes containing hexahedra and split-hexahedra automatically from triangulated surface geometries. SnappyHexMesh also allows to add a boundary layer mesh corresponding to selected surfaces, an option that has been applied to the blade/hub wall and to the shroud for the meshes used in the present study. A grid independence study has been performed in a previous work[4] by producing four different meshes having 1.5, 3.4, 7.2 and 13.9 millions of cells. As can be seen in Fig. 5a, the grid of 7.2 M cells is refined enough

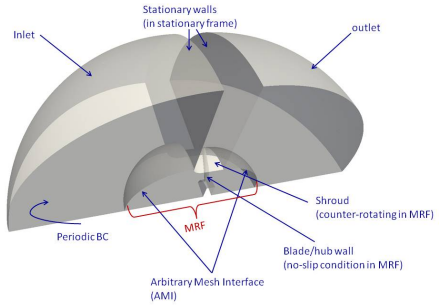

Figure 4: Computational domain with boundary conditions.

to have the non-dimensional wall distance $y+ < 1$ at the first cell on the blade surface. Figure 5b, on the other hand, shows that a smoother pressure coefficient profile can be obtained with the 13.9 M cells mesh. For these reasons, the results presented hereafter are obtained from the most refined mesh.

3.2.2. Scale Adaptive Simulation

The SAS method is a hybrid RANS-LES approach which has been developed by Menter *et al*[16]. It is based on the $k-\omega$ SST turbulence model with the addition of a production term in the ω equation which increases when the flow solution starts to go unsteady. The SAS production term is based on the ratio of the modelled RANS turbulent length scale

$$L = C_\mu^{-1/4}\frac{k^{1/2}}{\omega}, \quad C_\mu = 0.09 \tag{7}$$

and the von Kármán length scale, which is in turn proportional to the ratio of first and second flow velocity gradients. The classical boundary layer formulation of the von Kármán length scale

$$L_{vK,1D} = \kappa\left|\frac{\partial U/\partial y}{\partial U^2/\partial y^2}\right| \tag{8}$$

is generalized for three-dimensional flows as

$$L_{vK,3D} = \kappa\left|\frac{U'}{U''}\right|. \tag{9}$$

Since $L_{vK,3D}$ is smaller in unsteady flow region, when the flow equations resolve unsteadiness the SAS term is activated and increases the production of ω. This causes a decrease of the turbulent viscosity, in which expression ω appears in the denominator, and an increase in the magnitude of the destruction term in the modelled turbulent kinetic energy equation. For this

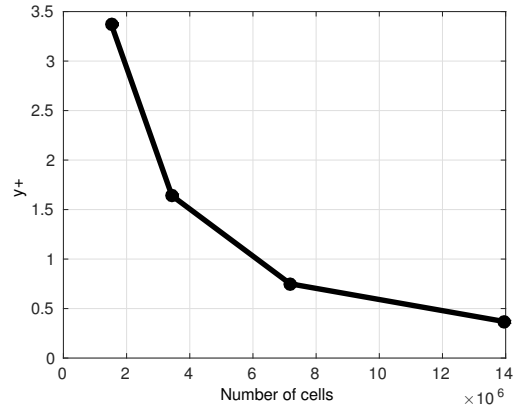

(a) *y+ values vs. number of grid cells*

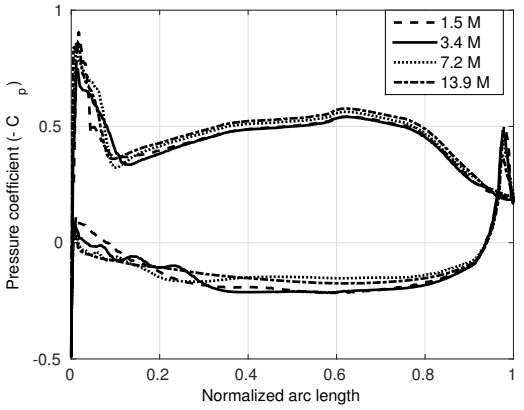

(b) *Pressure coefficient for different grids at mid-span*

Figure 5: Assessment of the grid independence[4].

reason, the solver switches to LES mode in transient unsteadiness.

This approach is implemented in OpenFOAM® in the *kOmegaSSTSAS* LES turbulence model. Since the MRF method adopted in the previous RANS simulation is not suitable for time dependent cases, for the SAS simulation all the computational domain is included in a single rotating frame of reference (SRF). Consequently, the *SRFPimpleFoam* incompressible transient solver (operating in PISO mode) has been used.

In order to ensure the stability of the numerical solution, the time step has been allowed to vary with the constraint of keeping the maximum CFL number below 1. The overall simulation time was of 0.12 s, being 0.1 s the duration of one blade rotation. The transient part of the simulation lasted approximately 0.029 s, after which the wall pressure has been sampled at a frequency of 57 kHz, collecting 5200 samples in total. The SAS data have been averaged in time over a period of 0.005 s. This averaging window corresponds to the time it takes for a fluid parcel to travel along the chord of the blade, from leading to trailing-edge. Finally, this computation has been performed on a cluster of 128 processors for approximately 240 hours.

3.2.3. Flow field comparison

Figure 6 represents the relative velocity field at three equally spaced radial sections close to the hub (6(a), 6(b)), at mid-span (6(c), 6(d)) and in the vicinity of the tip (6(e), 6(f)). This figure compares the RANS results, on the left column, with SAS results, on the right column.

A separation zone on the pressure side of the blade at the lower radius can be seen in both Figs. 6(a) and 6(b), which is the effect of the small axial extent of the hub. The relative velocity contours of Figs. 6(e), 6(f) suggest that SAS predicts earlier, with respect to RANS, the separation of the flow towards the trailing-edge on the suction side of the tip section. Also the separation bubble appearing upstream, close to the leading-edge, is more important in the SAS prediction than in the RANS.

Figures 7(a) and 7(b) depict the trend of the wall pressure coefficient ($-C_p$) at the same radial positions as in Figs. 6(c), 6(d) and Figs. 6(e), 6(f), respectively. While at mid-span (7(a)), the onset of an adverse pressure gradient on the suction side is predicted at approximately 60% of the arc length by both methods, the prediction is rather different towards the tip (7(b)). While the RANS simulation exhibits a favourable pressure gradient on the blade surface from 10% to 80% of the arc length, followed by a steep adverse pressure gradient unto the trailing-edge, the SAS simulation predicts a continuous decay of the pressure coefficient on all the suction side. This explains the bigger extension of the separated flow areas close to both the leading and the trailing-edge seen in Fig. 6(f).

Finally, it is necessary to remind that the tip region is place of considerable three-dimensional effect related to the formation of a tip-clearance vortex and to its interaction with the blade and with the shroud's termination, which are arguably better detected by the SAS simulation.

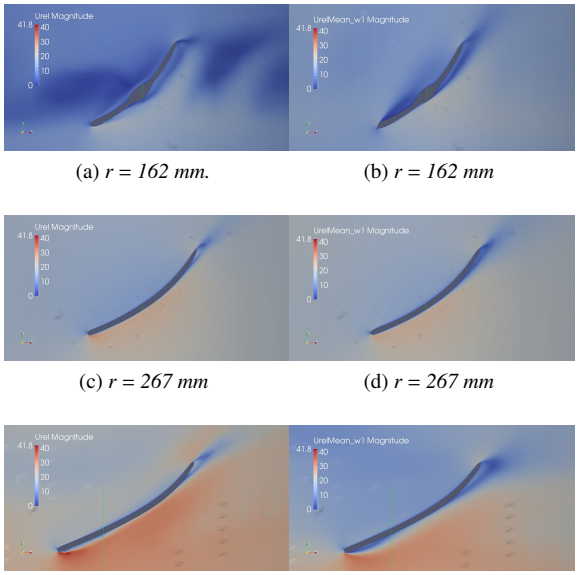

(a) $r = 162$ *mm.* (b) $r = 162$ *mm*

(c) $r = 267$ *mm* (d) $r = 267$ *mm*

(e) $r = 372$ *mm* (f) $r = 372$ *mm*

Figure 6: Relative velocity magnitude visualization at three equally spaced iso-radius planes. Left column: RANS computation. Right column: time averaged SAS computation.

4. Comparison of boundary layer characteristics extracted from RANS and time averaged SAS

As explained in Sec. 2, boundary layer data are extracted, for each blade strip, on a line normal to the blade surface close to the trailing-edge in order to reconstruct the wall pressure spectrum by means of Panton and Linebarger's model.

In summary, the three inputs to the model that are extracted from CFD are:

- the mean stream-wise velocity, $U_1(x_2)$;
- the averaged cross-wise velocity fluctuation, $\bar{u_2'}(x_2)$;
- the turbulent length scale, Λ.

In this section, the boundary layer data extracted from the RANS solution will be compared with those extracted from the time averaged SAS computation. This comparison is done at two radial positions, namely 270 mm and 357 mm, which correspond to the pressure sensors visible in Fig. 3.

4.1. Mean stream-wise velocity

The stream-wise mean velocity profile depicted in Fig. 8 provides the boundary layer thickness, δ, and the undisturbed external velocity, U_e. According to the values reported in Table 1, RANS underestimates δ with respect to SAS. At the mid-span section, U_e is captured with little difference by the two methods, while close to the tip the external velocity predicted by SAS is significantly smaller, due to the complexity of the three-dimensional flow in that region. The presence of a recirculation zone at both radii is revealed by the plots of Fig. 8. While at mid-span the thickness of the recirculating flow region is predicted with a small discrepancy by the two methods, at tip the extension and entity of the recirculation are bigger in the SAS simulation. As in Eq. (3), the trailing-edge wall pressure spectrum depends on the derivative of the mean stream-wise velocity, which is visibly different in the two simulations. This accounts partially for the difference of the corresponding modelled wall pressure spectra, presented in Sec. 5.

	r = 270 mm		r = 357 mm	
	SAS	RANS	SAS	RANS
$\delta\ [m]$	0.018	0.010	0.029	0.027
$U_e\ [ms^{-1}]$	18.56	19.77	21.49	24.96

Table 1: Boundary layer thickness, δ, and external flow velocity, U_e.

4.2. Averaged cross-wise velocity fluctuation

Φ_{pp} is also a function of the energy spectrum of the cross-wise velocity fluctuations S_{22}, defined in Eq. (4), which is in its turn function of the distribution of averaged cross-wise velocity fluctuation, $\bar{u_2'}(x_2)$. This quantity is not provided in the RANS simulation by the $k-\omega$ SST turbulence model, which computes instead the turbulent kinetic energy $k = 0.5\sum \bar{u_i'}^2$. On the contrary, from a time averaged SAS computation it is possible to extract all the components of the Reynolds stress tensor, whose trace is proportional to the turbulent kinetic energy. In order to compute $\bar{u_2'}(x_2)$ from the RANS results, the turbulent kinetic energy is multiplied by an anisotropy factor defined as $\beta_2 = \bar{u_2'}^2/(2k)$ and dependent on the distance from the wall. The β_2 factors used in this work were calculated by Remmler *et al*[7] from a RANS computation of a flat plate boundary layer, using a Reynolds stress transport turbulence model (RSTM).

First, a comparison can be made regarding the distribution of k in the cross-wise direction: as can be

seen in Figs. 9(a) and 9(b), the values predicted in the RANS simulation are one order of magnitude smaller that those predicted by the SAS method. Then, a comparison is made in Figs. 9(c) and 9(d) between the flat plate vertical anisotropy factor with the one computed directly from the Reynolds stress tensor given by the averaged SAS solution. In the boundary layer on the fan blade's suction side the turbulence is more anisotropic than in a zero pressure gradient boundary layer, as it was assumed in first approximation. Even though the β_2 factor used in the post-processing of the RANS data is overestimated, the resulting $\overline{u_2'}(x_2)$ is smaller than the corresponding value given directly by the SAS computation due to the different order of magnitude of the turbulent kinetic energy.

4.3. Turbulent length scale

The third quantity that is extracted from CFD simulations and given as an input to Panton and Linebarger's model is the turbulence integral length scale Λ. When RANS inputs are used, this is simply considered proportional to the turbulent length scale defined in Eq. (7). When, on the other hand, averaged SAS inputs are used, following Panton and Linebarger Λ could be considered proportional to Prandtl's mixing length, l_m, and computed directly with the expression

$$\Lambda = 1.5\, l_m = 1.5\, \sqrt{\frac{-\langle u_1' u_2' \rangle}{|\partial\langle U_1\rangle/\partial x_2|(\partial\langle U_1\rangle/\partial x_2)}}. \quad (10)$$

However, Eq. (10) does not hold in presence of flow recirculation, which is found in this application. For this reason, it was decided to follow in first approximation Prandtl's simple rule for which

$$l_m = \begin{cases} \kappa\, x_2, & \text{for } x_2 < 0.22\,\delta, \\ 0.09\,\delta, & \text{for } x_2 > 0.22\,\delta. \end{cases} \quad (11)$$

even though it is known to represent poorly boundary layers different from zero pressure gradient.

5. Trailing-edge wall pressure spectra and far-field noise results

The trailing-edge wall pressure spectrum has been computed, at two points on the blade surface corresponding to the position of the pressure sensors in the experimental set-up, by using different data sources. The Φ_{pp} reconstruction method described in Sec. 2 has been applied to the boundary layer data, extracted from the RANS and averaged SAS simulation, presented in the preceding section. Furthermore, Φ_{pp} has been computed directly by frequency analysis of the SAS data.

As it can be seen from Figs. 10(a) and 10(b), the RANS based reconstruction fails to match the experimental curve by 20 to 40 dB, which is due to the underestimation of the turbulent kinetic energy in the boundary layer. On the contrary, the SAS averaged data produce a spectrum that has a good match with the experiments up to 1.2 kHz, but then decreases at higher frequencies. The reason for this decrease is still under investigation, but it can be reminded that the higher frequencies of the spectrum produced by Panton and Linebarger's method are influenced by the part of the boundary layer profile close to the wall. In this case, it is possible that the high frequency behaviour of the spectrum depends on the negative $\partial\langle U_1\rangle/\partial x_2$ values computed in the recirculating flow area close to the blade surface.

The wall pressure spectra have been also computed by extracting the pressure fluctuations at the same location on the blade surface than where the boundary layer has been extracted. The power spectral density curves presented in Figs. 10(a) and 10(b) are obtained with Welch's averaging technique, dividing the sampled data in four non-overlapping segments and applying a Hanning window to each segment.In both plots Φ_{pp} is overestimated at low frequencies and underestimated above 500-600 Hz. The accuracy of the prediction at low frequency can improve by adopting a longer sampling time.

Finally, the experimental far-field sound power level (SWL) can be compared with the results obtained by applying Amiet's theory (Eqs. (1) and (6)), in Fig. 11. In order to compute the spectrum of the span-wise correlation length of the pressure fluctuations, $l_y(\omega)$, with Corcos' model (Eq. (2)), it is necessary to provide the value of the convective velocity of turbulent structures, U_c, and of the constant b at each radius. For this, we used the results of the experimental campaign conducted by Rozenberg[17] on an experimental set-up made of the two blades equipped with pressure sensors, but without shroud. The ratio between the external and the convective velocity, α, with the coefficient b computed by Rozenberg are reported in Table 2.

It is notable that the experimental wall pressure spectrum used in Amiet's theory produces a noise spectrum that corresponds to the experimental result only below 400 Hz, while above it decreases significantly. For this reason, we are led to assume the ef-

fect of other noise sources at high frequency, due for instance to the tip-clearance vortex. As for the results obtained with the data directly extracted from the SAS computation, the tendency to overestimation of the wall pressure spectrum below 500 Hz and to underestimation above, seen in the previous plots, is reflected in the noise computation. The best correspondence to the experimental data at low frequency is given by the Φ_{pp} computed from averaged SAS results. Not surprisingly, the noise prediction based on RANS results is far below the experimental curve, since it is directly linked to the corresponding wall pressure spectra.

	$\alpha = U_e/U_c$	b
r = 270 mm	1.34	1.56
r = 357 mm	0.93	0.90

Table 2: Parameters used in wall pressure spectra and noise computation: ratio between the external and the turbulent convection velocity, α, and Corcos' model constant, b.

6. Conclusions and future work

The Scale Adaptive Simulation performed in this study has helped understanding the causes of the offset found between the experimental wall pressure and noise spectra and the prediction based on a RANS simulation of the flow field in the ventilation fan. In fact, the latter was not able to capture the magnitude of the turbulent kinetic energy in the boundary layer on the suction side of the blade, thus leading to an underestimation of the wall-normal velocity fluctuations. Furthermore, the statistical model for the reconstruction of Φ_{pp} was developed for the case of attached boundary layers and has proved its effectiveness, for instance, when applied to a controlled diffusion airfoil[7]. However the related hypothesis are weak in the case of separated boundary layers, which are often found on ventilation fan blades. For this reason they will be reconsidered in order to better extend the wall pressure model to this kind of applications.

So far only the wall pressure spectrum has been extracted from the time resolved SAS results. The convective velocity of turbulent structures and the spanwise correlation length could also be extracted by cross-correlating the pressure signals taken at different points of the blade surface. However, this would have required a much longer sampling period, thus increasing considerably the computational effort. Anyway, the computation of these data will be attempted in the successive stage of this work, which also involves a better understanding of the interaction of the tip-clearance vortex with the blade as a noise generating mechanism.

Acknowledgments

The Authors gratefully acknowledge the support of the EC under the project FlowAirS (Grant Agreement no 289352) and Alain Guédel and Mirela Robitu of CETIAT, Lyon, for providing the geometry of the four-bladed ventilator with the measured wall-pressure and noise spectra.

References

[1] A. Guédel, M. Robitu, C. Dhaussy, Prévision du bruit de bord de fuite d'un ventilateur hélicoïde à quatre pales, Tech. rep., CETIAT (2010).

[2] A. Guédel, M. Robitu, Prediction of the broadband noise of a low-speed axial fan by cfd simulations, international Conference on Fan Noise, Technology and Numerical Methods, Lyon, France, 15-17 April 2015.

[3] M. Legros, Y. Goth, A. Guédel, Fan noise prediction from local experimental source term and numerical sound propagation, international Conference on Fan Noise, Technology and Numerical Methods, Lyon, France, 15-17 April 2015.

[4] G. Grasso, J. Christophe, C. Schram, Broadband trailing-edge noise prediction of a four-bladed axial fan using a semi-analytical method, international Conference on Fan Noise, Technology and Numerical Methods, Lyon, France, 15-17 April 2015.

[5] R. K. Amiet, Noise due to Turbulent Flow past a Trailing Edge, Journal of Sound and Vibration 47 (3) (1976) 387–393.

[6] R. L. Panton, J. H. Linebarger, Wall Pressure Spectra Calculations for Equilibrium Boundary Layers, J. Fluid Mech. 65 (02) (1974) 261–287.

[7] S. Remmler, J. Christophe, J. Anthoine, S. Moreau, Computation of Wall-Pressure Spectra from Steady Flow Data for Noise Prediction, AIAA Journal 48 (9) (2010) 1997–2007.

[8] G. Grasso, J. Christophe, C. Schram, T. Verstraete, Influence of the noise prediction model on the aeroacoustic optimization of a contra-rotating fan, in: 20th AIAA/CEAS Aeroacoustics Conference, 2014.

[9] L. Davidson, Evaluation of the sst-sas model: channel flow, axysimmetric diffuser and axisymmetric hill, in: European Conference on Computational Fluid Dynamics - ECCOMAS CFD 2006, TU Delft, The Netherlands.

[10] M. Roger, S. Moreau, Back-Scattering Correction and Further Extensions of Amiet's Trailing-Edge Noise Model. Part 1: Theory, Journal of Sound and Vibration 286 (2005) 477–506.

[11] J. Christophe, Application of hybrid methods to high frequency aeroacoustics, Ph.D. thesis, Université Libre de Bruxelles - von Karman Institute for Fluid Dynamics (2011).

[12] G. M. Corcos, The structure of the turbulent pressure field in boundary-layer flows, Journal of Fluid Mechanics 18 (1964) 353–379.
[13] J. Christophe, M. Sanjosé, S. Moreau, Uncertainty quantification of low-speed axial fan self noise, in: 14th International Symposium on Transport Phenomena and Dynamics of Rotating Machinery, 2012.
[14] OpenFOAM Foundation, OpenFOAM - The open source CFD toolbox. User Guide, version 2.3.1 Edition (December 2014).
[15] F. R. Menter, Two-equation eddy-viscosity turbulence models for engineering applications, AIAA Journal 32 (8) (1994) 1598–1605.
[16] F. R. Menter, Y. Egorov, The scale-adaptive simulation method for unsteady turbulent flow predictions. part 1: theory and model description, Flow, Turbulence and Combustion (85).
[17] Y. Rozenberg, Modélisation analytique du bruit aérodynamique à large bande des machines tournantes: utilisation de calculs moyennés de mécanique des fluides, Ph.D. thesis, École Centrale de Lyon (2007).

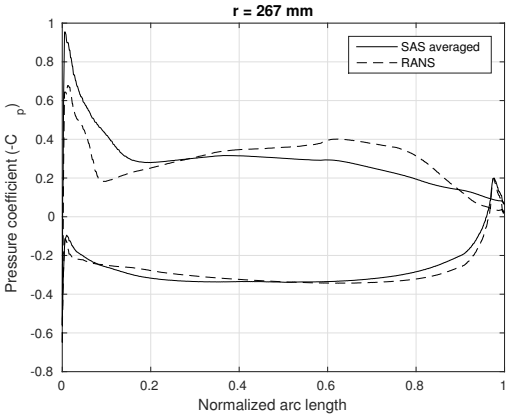

(a)

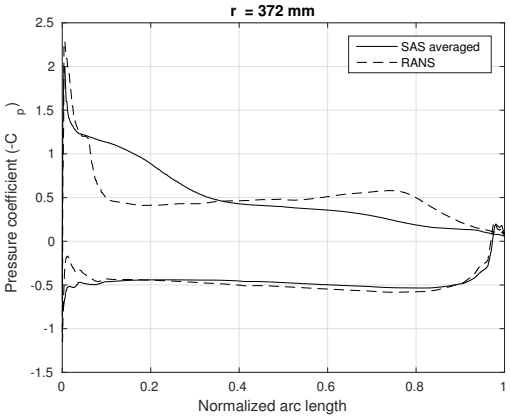

(b)

Figure 7: Pressure coefficient ($-C_p$) over the blade sections corresponding to Figs. 6(c), 6(d) and Figs. 6(e), 6(f), respectively. The arc length is normalized with respect to the chord-wise coordinate. In the scale of the abscissa, 0 represents the leading-edge and 1 represents the trailing-edge.

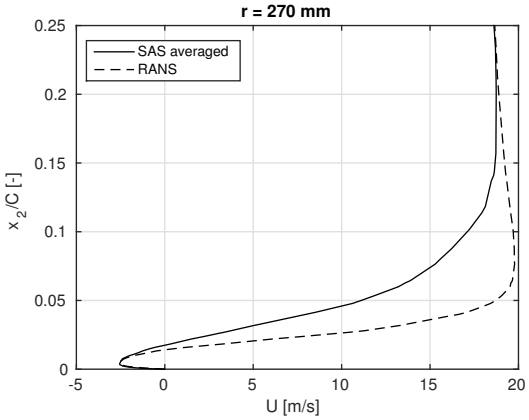

(a)

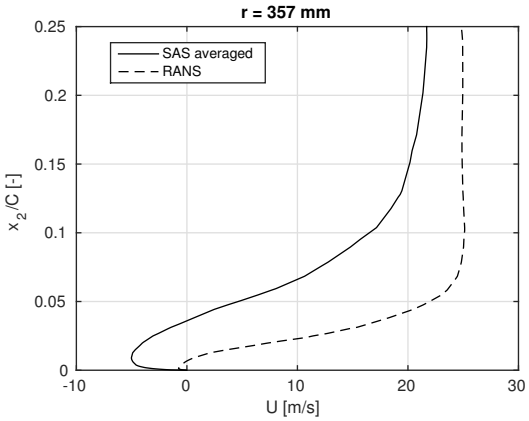

(b)

Figure 8: Comparison of the stream-wise velocity profile extracted from RANS and time averaged SAS computations at the positions of the experimental pressure sensors.

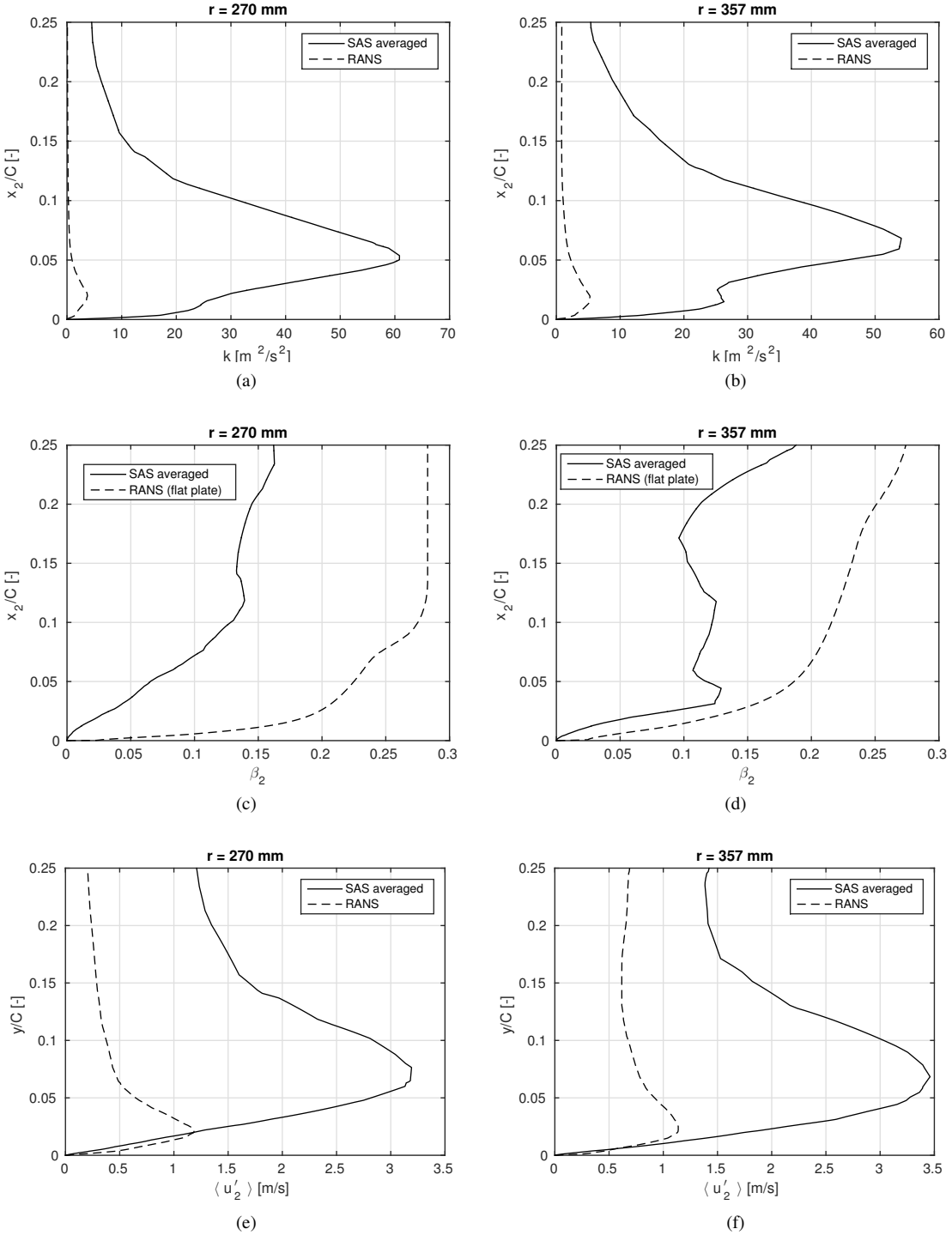

Figure 9: Comparison of the turbulent kinetic energy *(a,b)*, of the β_2 factors *(c,d)* and of the cross-wise average velocity fluctuation *(e,f)* extracted from RANS and time averaged SAS computations at the positions of the experimental pressure sensors.

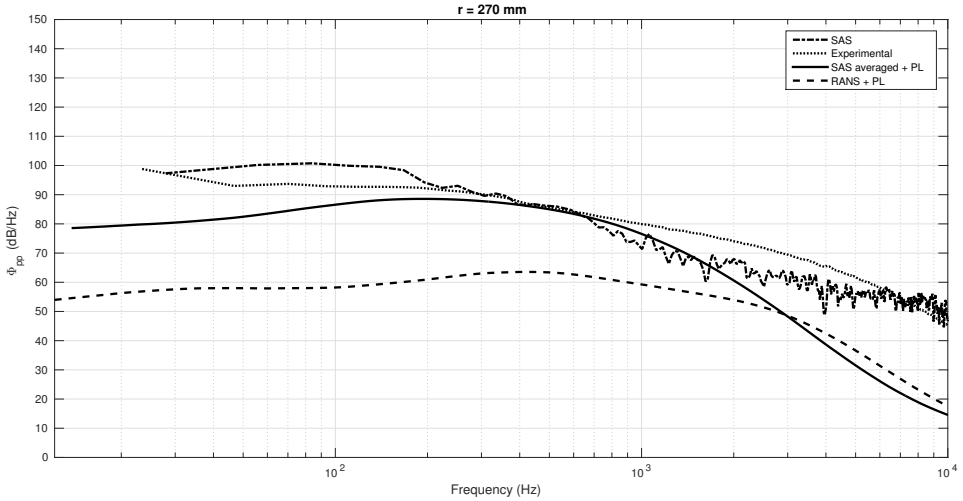

(a)

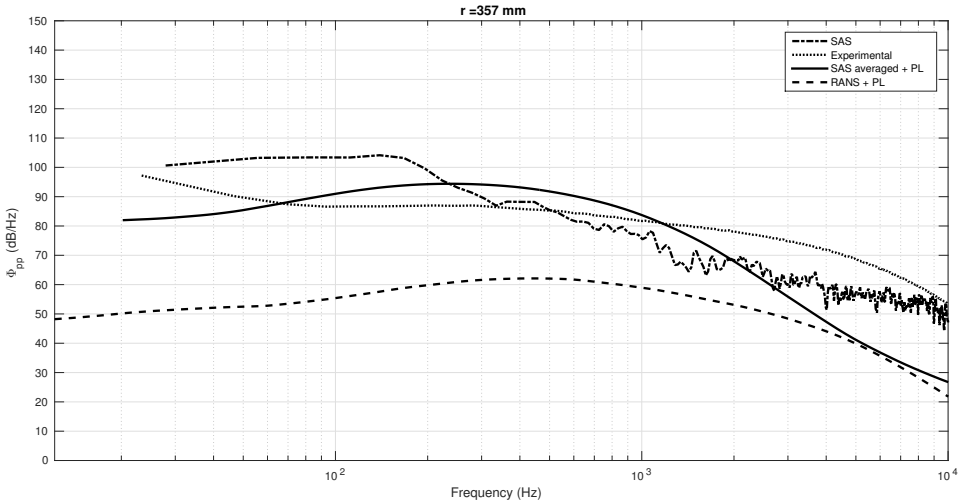

(b)

Figure 10: Trailing-edge wall pressure spectra computed at mid-span and tip.

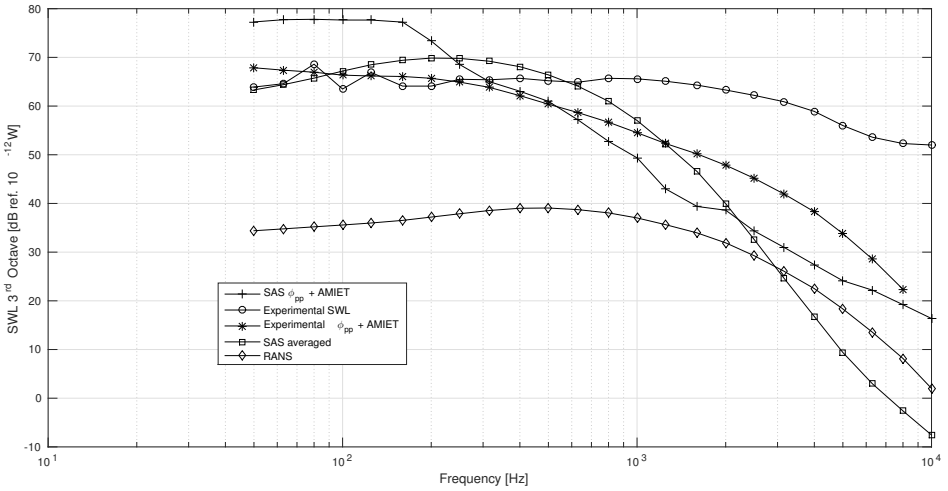

Figure 11: Far-field sound power level spectra, third octave average.

Facility design and shock-cell noise investigation on a supersonic coaxial jet

Daniel Guariglia

Aeronautics and Aerospace Department, von Karman Institute for Fluid Dynamics, Belgium, daniel.guariglia@vki.ac.be

Supervisor: Christophe Schram

Associate Professor, Aeronautics and Aerospace Department & Environmental and Applied Fluid Dynamics Department, von Karman Institute for Fluid Dynamics, Belgium, christophe.schram@vki.ac.be

University Supervisor: Fulvio Stella

Associate Professor, Mechanical and Aerospace Engineering Department, Università degli Studi di Roma "La Sapienza", Italy, fulvio.stella@dima.uniroma1.it

Abstract

The shock-cell noise is a phenomenon that occurs in aeronautic engines when the nozzle is not adapted to the atmospheric pressure. In civil aircraft at cruise it happens that the secondary flow is supersonic, thus the onset of a shock-cells system and broadband noise. This paper aims to describe the design of the new facility FAST (Free jet AeroacouSTic laboratory), completed in 2015, with the aim to investigate experimentally the shock-cell noise phenomenon on a dual stream jet. The rig consists of a coaxial open jet with supersonic capability for both primary and secondary flow. A coaxial silencer is used to remove the spurious noise coming from the feeding lines. The design has been validated by the use of CFD simulations. A preliminary experimental test campaign with the single supersonic jet is presented. Fine scale PIV coupled with a microphone array in the far field enlighten the screech symmetric and antisymmetric modes.

Keywords: Aeroacoustics, shock-cell noise, coaxial jet, supersonic, under-expanded, design, PIV.

1. Introduction

This work is aimed at the experimental investigation of shock-cell noise, being nowadays an important component of the total noise emitted by aeroengines, particularly affecting cabin noise in cruise conditions. In this paper the design and commissioning of a new supersonic coaxial jet rig are discussed, with a specific focus on the design choices that have been made to obtain good flow quality, low background noise and the possibility to perform a variety of flow and acoustic measurements. The target maximum Mach number at the outlet of the primary (central) and secondary (annular) nozzles is equal to 2.2, with a baseline operating point being $M_p = 0.71, M_s = 1.36$ for the primary and secondary flow respectively, as already investigated by Miller and Morris [1]. Many studies are present in the literature on the shock-associated noise [2-9] . These models have been applied with fair success, mostly to single stream supersonic jets, and the objective of this facility is progress further in complexity with a coaxial jet with subsonic primary and supersonic secondary flows. It should be stressed at this stage that the primary flow is unheated, leading to a reversed velocity profile to yield the desired Mach numbers in each stream. Nevertheless it is still a valuable benchmark for physical understanding and the validation of theoretical or numerical models because of the annular shock-cell pattern confined between two shear layers.

2. Aims of the project

In the framework of the AeroTraNet2 project, our main goal is to characterize a coaxial subsonic/supersonic jet with flowfield and acoustic measurements, in different test conditions. The database acquired will be used by partners for data post-processing and for the validation of aeroacoustic models based on CFD. Measurements using microphones, Schlieren,

Background-Oriented Schlieren (BOS), and Stereoscopic Particle Image Velocimetry (SPIV) are considered to provide a comprehensive experimental database. In order to extract useful information on the shock-cell noise generation mechanisms, post-processing techniques such as wavelets, proper orthogonal decomposition, causality correlations and conditional techniques will be used..

Secondary but still scientifically challenging goals are:

– understanding of the sound generation and propagation of sound in the different regions of the jet;
– recreation of acoustic far-field using acoustic analogies;
– research of the shock leakage experimental evidence;

The design of the entire facility and of the coaxial silencer constituted also a challenging engineering goal, which have been completed in 2015.

3. Conceptual design

For the test cases, we selected the operative points of major industrial interest for a future high by-pass aeronautic engines in function of the Core Nozzle Pressure Ratio (CNPR) and Fan Nozzle Pressure Ratio (FNPR) (Fig. 1). The maximum mass flow of $\dot{m} = 1.10$ kg/s has been considered to be compatible with the von Karman Institute (VKI) 40 bar pressure pipeline and compressor station capabilities, allowing in theory continuous operation. In order to further stabilize the air supply, several pressure regulators

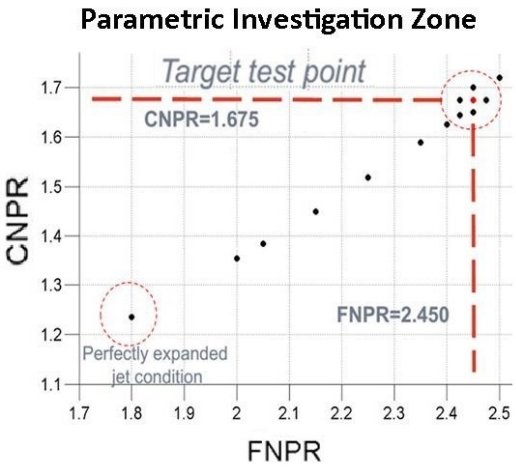

Figure 1: Test matrix chosen for FAST.

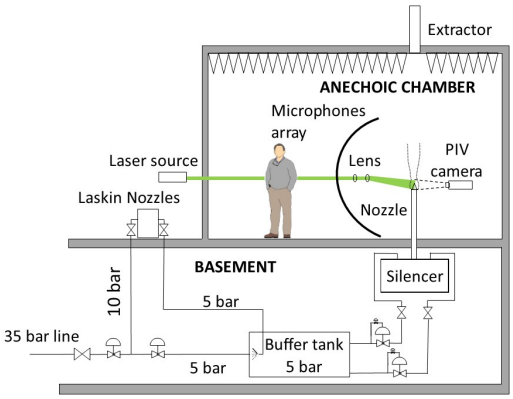

Figure 2: Sketch of the FAST final configuration.

and a buffer tank are implemented. The buffer tank is also used to inject the seeding particles for the LDV and PIV measurements, to ensure a good mixing of that seeding. Since discharging high-speed flow across valves and pressure regulators generates a considerable broadband noise in the system, a significant effort has been invested in the design and manufacturing of an acoustic silencer, with low pressure drop and compatible with the passage of liquid seeding particles. The purpose of the silencer is dual:

1. to reduce the amount of noise form the air supply system that would otherwise degrade the signal-to-noise ratio in the anechoic room, and
2. to prevent a spurious, uncontrolled acoustic excitation of the jet instability. In that respect, the silencer should also provide good anechoic upstream termination of the nozzles, by preventing acoustic standing modes.

The design of the silencer is one of the main subjects discussed below.

4. Detailed design

Fig. 2 shows the final configuration of the facility. The maximum operative pressure is p_{max}=11 bar (except for the seeding generator, which is limited to 5 bar gage pressure). This would consent us to produce a jet theoretically at Mach 2.2, keeping always into account the mass flow rate limitations. An electric valve opens the pressurized circuit, and it closes itself automatically in case of emergency or power cut thanks to a safety battery.

The pressure is first lowered from 40 to 10 bar with the use of two pressure regulators, installed in parallel to ensure a sufficient mass flow. The pressure is further reduced from 10 to 5 bar by

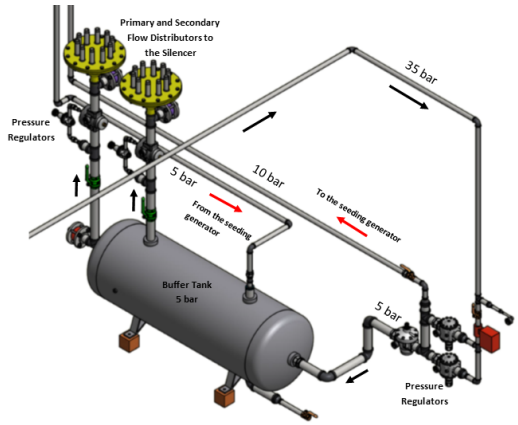

Figure 3: CAD drawing of the air supply system following the sketch in Fig.2.

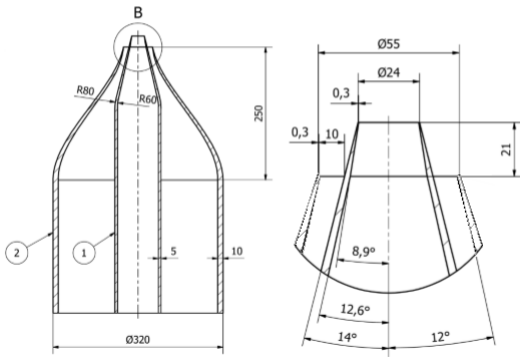

Figure 4: Sketch of the coaxial nozzles: overall (left) and detail (right) view.

a pilot-controlled pressure regulator, before it enters the buffer tank. To facilitate operation of the rig with LDV and PIV, the seeding generator is located on the ground floor, near the computer station. So, part of the flow at 10 bar is diverted to the seeding generator (described in section 4.2). The particles are then injected in the buffer tank, at a pressure of 5 bar, before it enters the two main flow lines.

The mass flow rate of the secondary flow is obtained from isentropic relations, based on the stagnation pressure and temperature in the pipe segment upstream of the nozzle. The mass flow rate of the primary flow is measured by a conditioned orifice mass flow meter (described in section 4.3) placed at the outlet of the buffer tank on that line. The reason for not using the stagnation pressure in the pipe upstream of the primary nozzle is the unknown static pressure at the nozzle outlet, depending on the secondary flow shock-cell structure. The pressure for both primary and secondary circuits is adjusted with two precise pressure regulators, which control two volume boosters.

After the regulators, and before entering in the coaxial silencer, each flow is split in ten flexible tubes of equal length. This detailed design of the coaxial silencer is described in section 5. After the coaxial silencer, the last segment is a vertical straight coaxial duct equipped with honeycomb and three screens to damp out the turbulence developed in the silencer. The ducts internal diameters are $\varnothing_p = 80$ mm and $\varnothing_s = 300$ mm for the primary and secondary flows respectively. Figs. 3 and 5 show the 3D layout of the air supply system and of the section of the silencer and ducts.

4.1. Nozzle design

The designed coaxial nozzle is representative of next generation aeroengine nozzle. The nozzles outlet diameters are $D_p = 18.7$ mm and $D_s = 44$ mm for the primary and secondary jets, respectively. The primary outlet plane is 16.8 mm downstream of the plane of the secondary outlet and so $A_s/A_p = 3.35$. The secondary jet area contraction ratio is about 44, and the primary jet contraction ratio is 12. The primary nozzle has a simple conical shape, with the semi-aperture angle $\alpha = 14°$. The secondary nozzle profile follows a 3rd order polynomial function, modified in the last part to have the throat at the exit. The final shape, validated through CFD, is shown in Fig. 4.

4.2. Seeding Generator

The seeding generator has been selected taking into account the quality requirements in terms of particles density and size. Because of the presence of shock-waves, the inertia of the particles must be small enough to follow the strong decelerations across the shocks. The motion of the particle in a fluid has been studied by Oseen [10] and Tchen [11] who derived the fundamental equations. Jeronimo [12] computed the time response for different sizes of vegetable oil particles in an open jet at Mach $M = 4$. She concluded that particles of the size $\varnothing = 1$ μm, or smaller, are required. The PivPart-45M by PIVTEC Gmbh can provide particles of 1 μm size with adequate density, and can hold 5 bar gage pressure at its outlet port.

4.3. Conditioning Orifice Flow Meter

To measure the mass flow rate of the primary flow, it was necessary to install an orifice plate. A four holes conditioning orifice plate (Fig. 6) is used as its constraints are less severe in terms up upstream and downstream pipe length than for a

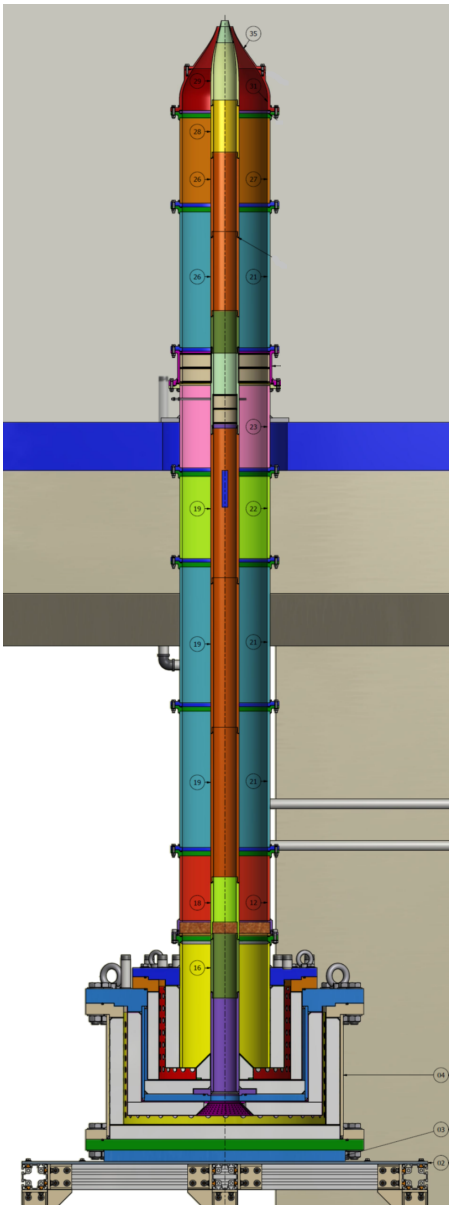

Figure 5: Section of the silencer and main conduits.

single aperture orifice plate[13]. It has been tested extensively with good results and it necessitate of only two diameters of clean section before and after the plate [14].

5. Silencer

The concept that is followed in the design of the silencer is a coaxial, U-turning flow in annular sections, in order to maximize the area of damping material exposed to the incident acoustic field, while minimizing the flow velocity and associated pressure losses (Fig.7). The air enters the circuit from the top plate, through ten equally-spaced inlets. The colored zones represent the

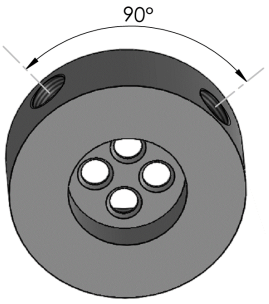

Figure 6: Conditioning orifice plate with four holes.

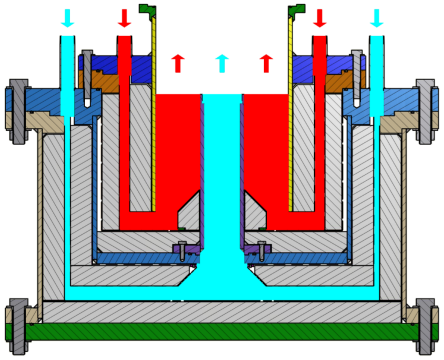

Figure 7: Section of the coaxial silencer. The clean passage areas for the primary and secondary flow are colored in cyan and red respectively. The gray zones represents the phono-adsorbent material.

clean passage areas, while the gray dashed zones are the acoustic absorbing material. Due to space constraints, it has been decided to use a fixed thickness for all the absorbing layers, equal to $d_{abs} = 50$ mm. The clean passage areas have been sized in order to not exceed 10 m/s and reduce both pressure losses and extra noise production. The chosen absorbing material is composed by very fine stainless steel wool (type #000). The relevant dimensions are summarized in Tab.1.

The acoustic performances of the silencer have been numerically verified with COMSOL Multiphysics® 5.0, a commercial FEM solver.

$\varnothing_{max}$	0.98 m	A_p	$2.39{\cdot}10^{-2}$ m^2
h_{max}	0.76 m	A_s	$2.90{\cdot}10^{-2}$ m^2
m_{dry}	~1200 kg	$\varnothing_{p,eq}$	0.192 m
p_{max}	11 bar	$\varnothing_{s,eq}$	0.174 m

Table 1: Silencer maximum dimensions and clean passage area for primary and secondary flow. $\varnothing_{max}$ and h_{max} are the main diameter and height respectively, m_{dry} is the weight without the foam, p_{max} is the max operative pressure, A_p and $\varnothing_{p,eq}$ are the clean passage area and the equivalent diameter for the primary circuit, A_s and $\varnothing_{s,eq}$ are the clean passage area and the equivalent diameter for the secondary circuit.

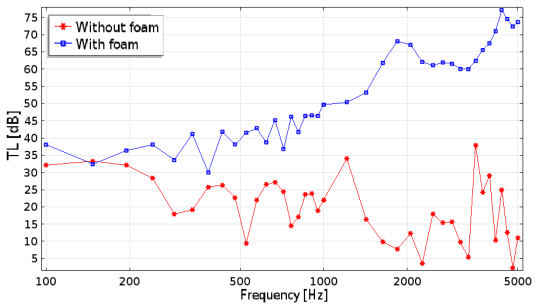

Figure 8: Transmission Loss of the silencer for the primary flow.

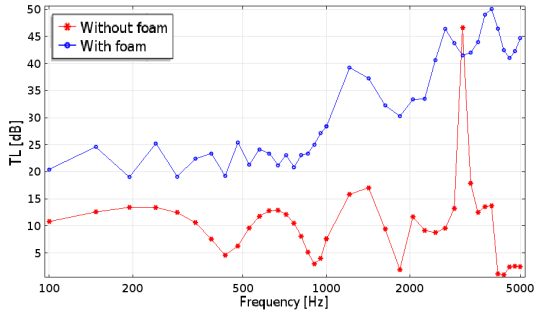

Figure 9: Transmission Loss of the silencer for the secondary flow.

The acoustic module of the software has been used to compute the transmission loss between the ten inlets and the silencer outlet, including the effects of the phono-absorbing material and the grids that hold it in position. Results presented in [15] and re-proposed in Figs. 8 and 9 an effective damping in terms of transmission loss already in the low frequency range, thus confirming the design choice.

6. Installation

The installation phase began in July 2015, when the silencer has been delivered. The metallic foam has been positioned inside cylindrical filters that have been manufactured at VKI (Fig 10). They have been realized starting from perforated metal plate with the same characteristics used for the acoustic simulations: σ=0.4 is the area porosity (the hole's fraction of the boundary surface area, a dimensionless number between 0 and 1), t_p=1.5 mm is the plate thickness, d_h=4 mm is the holes diameter. After having preliminary assembled the filters with the silencer components, they have been transported into the basement of the S1 wind tunnel for the final assemblage. This has also been evaluated in advance, considering the impossibility to use powered lifters (due to space constraints), and thus the installation followed a specific sequence in order to minimize risks for the operators, each component weighting more than 200 kg. After the silencer was in position (Fig **??**), it began the installation of the piping system, ducts and nozzles, being completed in September 2015 (Figs. 11 and 12)

6.1. Instrumentation

The facility is equipped with four brand-new OMEGA pressure sensors. Two model PXM419 are used to measure the pressure in the ducts before the nozzle. Being the area ratio equal to $AR_p = 11$ and $AR_s = 75$ for the primary and secondary circuit respectively, we could assume these as stagnation pressure conditions. The pressure range of the sensors is from 0 till 3.5 bar to cover all the designed working points of the facility.
The pressure taps have been placed immediately after the turbulent grids, in order to measure the correct total pressure. In particular, the duct sections holding the grids has been designed to have the pressure tap of the primary flow under the grids of the secondary flow. In this way, the eventual vortex shedding generated by the connecting pipe is dumped by the secondary flow grids, decreasing the risk of noise pollution (Fig. 13).

One pressure sensor model PXM319 from 0 to 10 bar is used to measure the pressure inside the tank, and one differential PXM419 from 0 to 350 mbar is used with the conditioned orifice plate. A thermocouple K is immersed into the flow after the mass flow meter in order to measure the flow temperature. These three last measures are required in order to compute the mass flow rate following the norm ISO 5167. Inside the anechoic room is also present a thermocouple K to measure the temperature inside the room. Ambient pressure is read from the VKI pressure server. NationalInstrument™LabVIEW is used to moni-

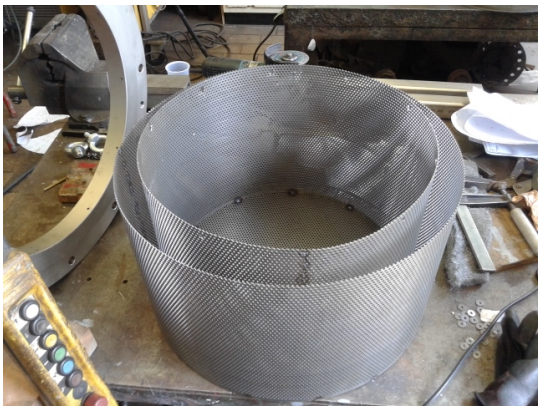

Figure 10: Metallic perforated filters to hold in place the phonoadsorbent material in the silencer.



Figure 11: FAST facility lower part assembled.



Figure 12: FAST facility upper part assembled.

tor and to acquire data from sensors and microphones.

7. Commissioning

7.1. Subsonic regime

The commissioning phase started in October 2015 until December of the same year. Two teams of Research Master students performed experiments in subsonic regime with the aim to validate verify the acoustic performance of the coaxial jet and to make comparison with the literature [16][17]. In particular, a comparison with Kuznetsov and Munin sound predictive theory

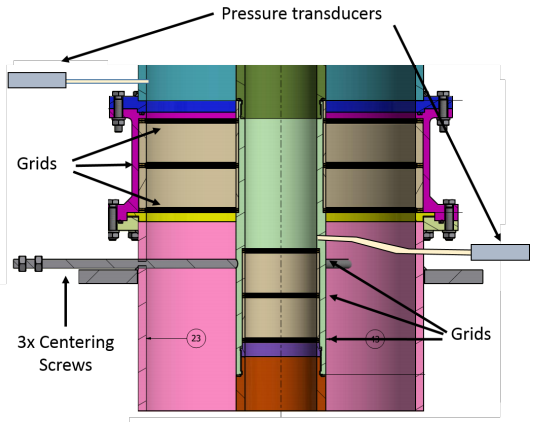

Figure 13: Detail of the ducts. The pressure tap of the primary flow is located below the grids of the secondary one, thus decreasing the risk of introducing vortex shedding noise.

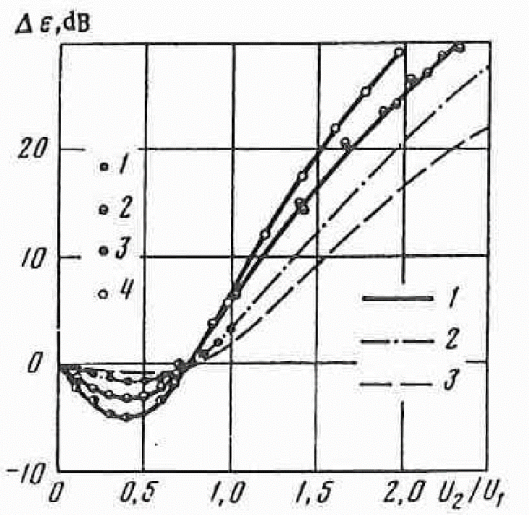

Figure 14: Difference in the acoustic power levels of coaxial jets and a circular jet corresponding to the inner duct, vs flow-velocity ratio. Calculated curves: 1) $\bar{D}$ = 2.0; 2) 1.5; 3) 1.2; experimental points $\bar{D}$ = 1.5; 2) 2.0; 3) 2.7; 4) submerjet jet with $\bar{D}$ = 2.0 where $\bar{D}$ is the diameter ratio. [18]

[18] has been done. This theory approaches analytically the problem of the different acoustic power level between a coaxial jet and a single stream jet, superimposing the effects of an annular jet with a single jet. Their main results, supported by experiments is the curve shown in Fig.

7.1.1. Experimental setup

Four Bruel and Kjaer microphones type 2670 have been used to measure sound with a sampling frequency of f_s = 51200 Hz. Preliminary studies have been done in order to determine the best way to fix the microphones to the structure in order to avoid spurious contamination due to reflections and vibrations. The best results were obtained hanging the microphones to the structures

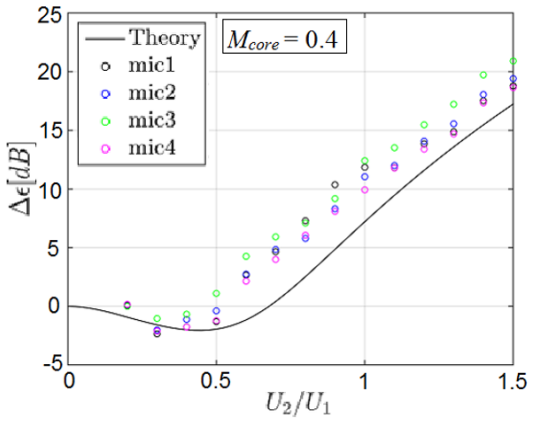

Figure 15: Difference in the acoustic power levels of coaxial jets and a circular jet corresponding to the inner duct, vs flow-velocity ratio. Comparison between experiments and theory [16].

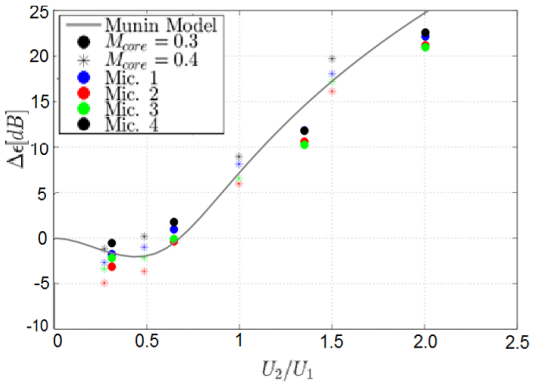

Figure 16: Difference in the acoustic power levels of coaxial jets and a circular jet corresponding to the inner duct, vs flow-velocity ratio. Comparison between experiments and theory [17].

at different distances from the jet axis ($d \approx 20$ $\emptyset_s$).

7.1.2. Results

The results of this campaign showed the facility runs smooth and stable, and test conditions are reproducible with good accuracy. In Figs 15 and 16 are shown the output plots for the two groups, where experiments follow sufficiently good the theoretical curve.

7.2. Supersonic regime

Tests in supersonic regime have been conducted to verify the capability to reach the targeted test conditions. First, the single stream jet supersonic capability has been assessed, reaching CNPR = 3.67 ($M = 1.5$) and maintaining it stable for 20 minutes. Finally, dual flow supersonic conditions have been tried. This check was unfortunately negative, due to the huge pressure drops in the VKI high pressure lines at the required mass flow rate. It has been assessed that the main reason of these pressure drop is the small pipe diameter (24.5 mm)compared to the total pipe length (~ 40 m). Increasing the pressure in the secondary circuit it is possible to assist to a fast decrease of the static pressure in the pipe just before the main electric valve (read with a pressure gauge), until pressure drops below 5 bar (minimum operative point for the buffer tank) and successively it goes below 3 bar and the line is chocked.

A posteriori, this effect it is perfectly explainable thanks to the Fanno flow theory (compressible flow with friction)[19]. In Fanno theory, the most important factor is the non-dimensional parameter $4fL/D$, where f is the Fanning coefficient, L is pipe length and D is the pipe diameter. With this number it is possible to enter into the Fanno tables and retrieve the maximum possible Mach number at the pipe inlet, for which the pipe outlet is chocked. Further increases of the mass flow rate are forbidden, and thus this is a limit condition.
The Mach number at the pipe inlet for our target mass flow rate has been computed at the beginning of the design phase, being $M \approx 0.16$ ($p_0 = 30$ bar), and this was supposed to be lower enough to not care about pressure drops. For our pipeline, it has been computed $4fL/D = 20.23$, which correspond in the Fanno table to a maximum Mach number $M \approx 0.172$, and thus the situation is perfectly explained.

7.3. Ensure supersonic capability for dual flow

To solve the problem, only two different approach were possible: decreasing the value of $4fL/D$ or reducing the Mach number at the pipe inlet. The first one requires a change in the pipeline, consisting in enlarging the test section or reducing the length. This approach has been evaluated too expensive for the present situation, and thus the chosen solution has been to reducing the inlet Mach number by decreasing the mass flow rate, by changing the nozzles geometry.
In order to impact as less as possible the project, and in particular the partners involved in CFD simulations, the nozzle would be simply scaled by a factor of 0.8. This would guarantee the matching of all the non-dimensional parameters taken into account in the simulations with the exception of the Reynolds number, which effect has been considered negligible. The new geometry would ensure a reduction of the mass flow rate by the 36%, decreasing the initial Mach number to

$M = 0.10$ at $p_(0) = 30$ bar. This mass flow rate has been tested with the present nozzles, reaching an endurance of 30 minutes running continuously At the time of the article the nozzles are under manufacturing.

8. Experiments with single stream supersonic jet

Meanwhile the new nozzles are manufacturing, in February 2016 it has been performed an extensive test campaign with the single jet only using microphones and PIV system. The aim of this campaign is to test the methodologies that will be used for the dual stream. In particular, two PIV cameras have been used to increase the field of view (FOV) and the laser pulse has been recorded together with the microphones. The idea at the base is to use the screech tone recorded by the microphones to select specific frames from the PIV sequence and then to perform a phase locked average. This could lead to identify the different phases of the jet oscillation that generate the screech, and eventually also to the shock-leakage experimental evidence.

8.1. Test matrix

The targeted test matrix has been decided in order to compare results with the work of Savarese [20] and André *et al* [21].

CNPR	M	CNPR	M
2.13	1.10	2.60	1.25
2.30	1.16	2.70	1.28
2.40	1.19	2.96	1.35
2.50	1.22	3.67	1.50

Table 2: Test matrix for single stream jet experiments.

8.2. Experimental setup

The PIV system is managed by LaVision Davis8 software and it is composed by two identical cameras Imager SX-4M, with a full resolution of 2360x1776 pixel^2, while the laser is a Nd:YAG 536 nm. The acoustic measurements are performed using 12 B&K microphones type 2670 mounted on a polar array at a distance of 960 mm (40 $Ø_p$) from the central nozzle outlet. Microphones are coupled with a Nexus amplifier and analogical filter. A sketch of the experimental setup is shown in Fig. 17.

Two different sets of FOV have been taken into account for this investigation. The first one is composed by the two cameras on top of each

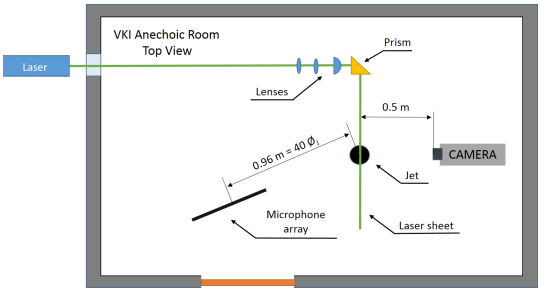

Figure 17: Sketch of the experimental setup inside the anechoic room.

other looking at the jet entirely, with a small FOV overlap. Two 50 mm objective are used to have an overall FOV includes a region of 250x130 mm^2 with a resolution of $r = 18$ pixel/mm. The second set is aimed to have a closer look at the shear layer region and at the nozzle lip, to investigate the areas involved in the screech feedback loop. The first FOV includes an areas of 80x55 mm^2 with a spatial resolution of $r = 30$ pixel/mm, while the second FOV capture a region of 21x13 mm^2 with a resolution of $r = 113$ pixel/mm. For each point of the test matrix 1800 images are collected at 15 Hz in three tranches of 600 pairs. Each tranche has a duration of 40 s and a dead time (to save images) of 4 minutes. An overview of the two sets of FOV is depicted in Fig. 18. The microphone polar array consists in eight thin

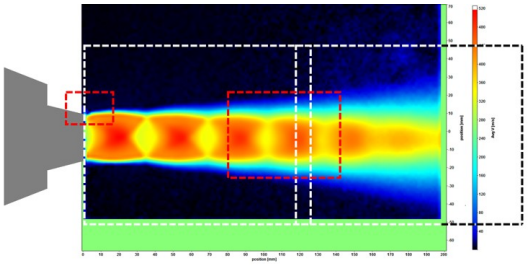

Figure 18: Sketch of the two sets of FOV used for the test campaign.

aluminum arms hold by an aluminum pole. Microphones are placed every 10 deg in the interval [50 deg −120 deg] starting from the jet axis, forward direction. Four microphones are redundantly placed at 90 deg only to test the acquisition system. The overall experimental setup is exposed in Fig.19.

Two different acquisition systems are used to record the microphones. The main one is a National Instrument (NI) PXI equipped with an FPGA card to ensure a very high acquisition rate. This is the only available acquisition system with a sampling frequency $f_s \geq 200$ KHz, in order to use the Nexus analogical filter set at 100 KHz.

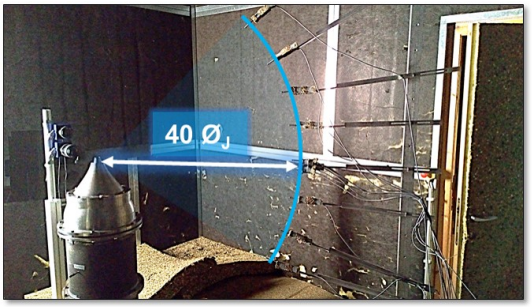

Figure 19: Picture of the experimental setup showing the microphone polar antenna and the PIV cameras.

The minimum acquisition frequency of this system is, however, equal to $f_{s_{min}}$ = 800 KHz, creating an issue for the file size due to the sampling duration. This system is then used as source for the acoustic data only, without PIV synchronization, due to the large time duration of a PIV acquisition. In order to have the microphones synchronized with the laser pulses, a NI cDAQ is used instead. This can record four microphones and the laser Q-switch at a f_s = 51.2 KHz for a long duration without creating big recording files.

8.3. Preliminary results

Here we present only the preliminary results of this investigation. At present time, the majority of PIV images are still post-processing, so a detailed analysis is postponed to a future paper. WIDIM is used as main PIV software, while TUCSOK and RABON are used for pre-processing ans statistical operations. Figs 20 and 21 show an example of instantaneous velocity field and signal-to-noise ratio (SNR) at CNPR = 2.5. Final window size is 12x12 pixel^2 (0.64x0.64 mm^2) with 75% overlapping, for a resolution of 140 vectors/$Ø_p$. Figs 22 and 23 show, instead, the second set of FOV at CNPR = 2.7. Final window size is 12x12 pixel^2 (0.39x0.39 and 106x106 mm^2) with 75% overlapping, for a resolution of 240 and 900 vectors/$Ø_p$

Acoustic spectra at four characteristic conditions are presented hereafter. Also for the acoustic part, a detailed analysis of the results will follow in future papers. We could however observe from the spectra the presence of screech tones and their harmonics, as well as the directionality of the shock-cell noise. Furthermore, from the variation of the screech frequency, we could infer the change between the screech modes, from symmetrical(CNPR = 2.30), to mixed (CNPR = 2.36), to anti-symmetrical (CNPR = 2.4 and 3.6). This is in accord with the studies carried out by Massey *et al* [22].

9. Conclusions and future works

A new aeroacoustic facility to study supersonic jet noise has been designed and built at VKI. The maximum capabilities in terms of total pressure and mass flow are p_0 = 11 bar and $\dot{m}$ = 0.9kg/s. A coaxial silencer has been designed to damp the noise produced by the air supply system and standing waves in the pipes. Simulations made with COMSOL Multiphisics® shown a consistent damping level in a range between 200 and 5000 Hz, giving a wide safety margin for the uncertainties in the computations. Preliminary commissioning tests at low Mach number have been performed in order to validate the jet rig, showing good agreement with the literature. Tests at high Mach number have shown a limitation in the maximum mass flow rate that can be supplied by the pressurization system, thus leading to the design of a new scaled coaxial nozzle in order to copy with the pressure conditions originally determined. Two PIV test campaigns with synchronized microphones on a single underexpanded jet have been conducted with the aim to test the experimental methodology that will be used for the coaxial jet. In the first test campaign the overall jet has been recorded within two contemporary FOV. Analysis show the jet symmetric and anti-symmetric modes associated with screech in high resolution. A phased locked average based on the microphone signal will be conducted with the aim to retrieve the periodicity of events related to the sound emissions that could be associated with the shock-leakage theory. The second test campaign was focused on a more detailed investigation at the regions directly involved in the sound emission, such as the jet shear layer and the nozzle lip.

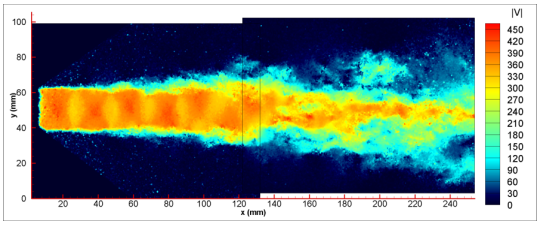

Figure 20: Instantaneous velocity field at CNPR = 2.5.

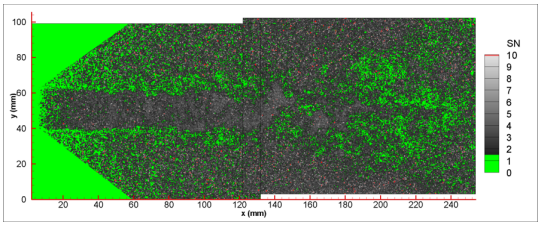

Figure 21: Instantaneour SNR at CNPR = 2.5.

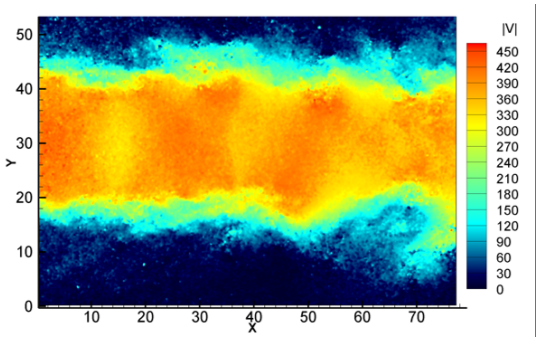

Figure 22: Instantaneous velocity field at CNPR = 2.7.

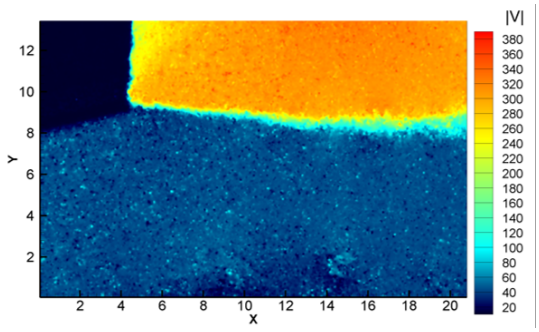

Figure 23: Instantaneour velocity field at CNPR = 2.7 near the nozzle lip.

Future works will consist in a detailed analysis of the acoustic and PIV database collected up to now. Furthermore, a new test campaign with the scaled coaxial nozzles will be performed at the targeted conditions chosen at the beginning of the project.

Acknowledgments

I wish to acknowledge the European Commission for funding this project through the Marie Curie Grant Agreement ITN AeroTraNet2 as part of FP7 program, the VKI Technical Drawing Office and Technical Staff for the high level of accuracy and cooperation.

References

[1] S. Miller, P. Morris, The Prediction of Broadband Shock-Associated Noise from Dualstream and Rectangular Jets Using RANS CFD, in: Aeroacoustics Conferences, American Institute of Aeronautics and Astronautics, 2010.

[2] A. Powell, On the mechanism of choked jet noise, Proceedings of the Physical Society. Section B 66 (12) 1953 1039.

[3] H. Tanna, An experimental study of jet noise part ii: Shock associated noise, Journal of Sound and Vibration 50 (3) 1977 429 – 444.

[4] M. Harper-Bourne, M. Fisher, The noise from shock waves in supersonic jets, in: AGARD Conference on Noise Mechanisms, 1973.

[5] C. Tam, H. Tanna, Shock associated noise of supersonic jets from convergent-divergent nozzles, Journal of Sound and Vibration 81 (3) 1982 337 – 358.

[6] T. D. Norum, J. M. Seiner, Broadband shock noise from supersonic jets, AIAA Journal 20 (1) 1982 68–73.

[7] T. D. Norum, J. M. Seiner, Measurements of Mean Static Pressure and Far Field Acoustics of Shock-Containing Supersonic Jets, NASA TM84521d (1982).

[8] C. Tam, J. Seiner, J. Yu, Proposed relationship between broadband shock associated noise and screech tones, Journal of Sound and Vibration 110 (2) 1986 309 – 321.

[9] C. Tam, Broadband shock-associated noise of moderately imperfectly expanded supersonic jets, Journal of Sound and Vibration 140 (1) 1990 55 – 71.

[10] C. W. Oseen, Neuere Methoden und Ergebnisse in der Hydrodynamik, Akademische Verlagsgesellschaft m. b. h., Leipzig, 1927.

[11] C.-M. Tchen, Mean value and correlation problems connected with the motion of small particles suspended in a turbulent fluid, Nijhoff, The Hague, 1947.

[12] A. Jeronimo, Application of PIV to a Supersonic Jet, Project Report 2001-28, von Karman Institute (June 2001).

[13] ISO/TR 15377:2007, Measurement of fluid flow by means of pressure-differential devices guidelines for the specification of orifice plates, nozzles and venturi tubes beyond the scope of iso 5167, Tech. rep.

[14] EMERSON, Conditioning orifice plate technology; taking the standard to a new level of capability, Tech. rep., 1595_2_01_*AA* (2004).

[15] D. Guariglia, C. Schram, Design of a facility for shock-cell noise investigation on a subsonic/supersonic coaxial jet, in: Symposium of VKI PhD Research 2015, von Karman Institute for Fluid Dynamics, 2015.

[16] N. Coudou, J.-B. Mandon, Özge Sinem Özçakmak, Measurement techniques acoustic laboratory, Tech. rep., von Karman Institute (2015).

[17] N. Bouanati, A. R. Carpio, L. Zavalan, Measurement techniques acoustic laboratory, Tech. rep., von Karman Institute (2015).

[18] V. M. Kuznetsov, A. G. Munin, Coaxial jet noise and isothermal jets, Akusticheskij Zhurnal 24 1978 878–886.

[19] G. M. Carlomagno, T. Astarita, Slides from course of Gasdynamics, Università degli Studi di Napoli "Federico II" (2009).

[20] A. Savarese, Experimental study and modelling of shock-cell noise, Ph.D. thesis, Ecole Nationale Suprieure D Ingenieurs De Poitiers (2014).

[21] B. André, T. Castelain, C. Bailly, Investigation of the mixing layer of underexpanded supersonic jets by particle image velocimetry, International Journal of Heat and Fluid Flow 50 2014 188 – 200.

[22] K. Massey, K. Ahuja, K. Massey, K. Ahuja, Screech frequency prediction in light of mode detection and convection speed measurements for heated jets, in: Aeroacoustics Conferences, American Institute of Aeronautics and Astronautics, 1997.

[23] A. Savarese, P. Jordan, S. Girard, E. Collin, M. Porta, Y. Gervais, Experimental study of shock-cell noise in underexpanded supersonic jets, in: Aeroacoustics Conferences, American Institute of Aeronautics and Astronautics, 2013, pp. –.

[24] A. Kiran, Jet Noise: Aeroacoustic Distribution of a Subsonic Co-Axial Jet, Ph.D. thesis, University of Warwick (2008).

[25] K. Viswanathan, Instrumentation Considerations for Accurate Jet Noise Measurements, AIAA Journal 44 (6) 2006 1137–1149.

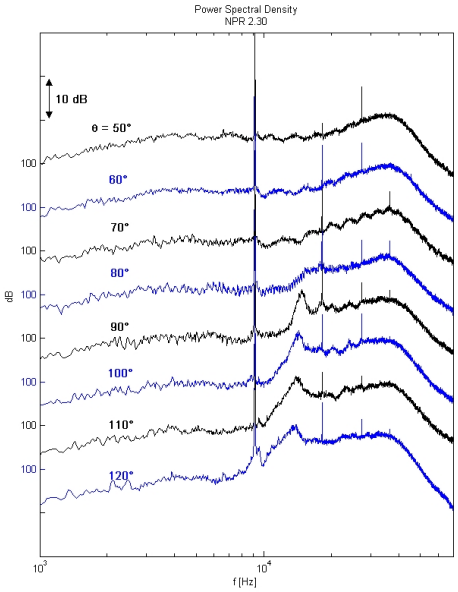

Figure 24: Sound power level at CNPR = 2.30.

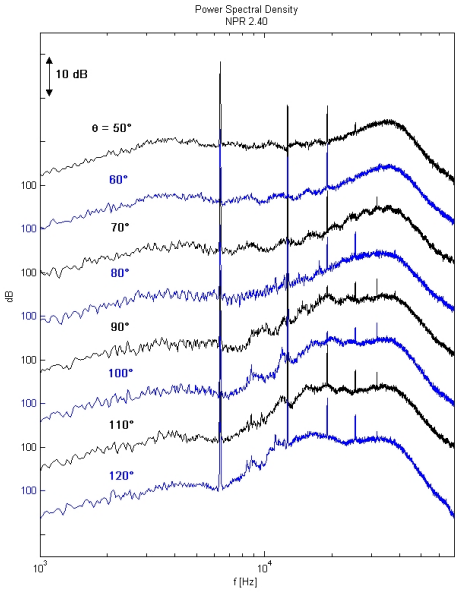

Figure 26: Sound power level at CNPR = 2.40.

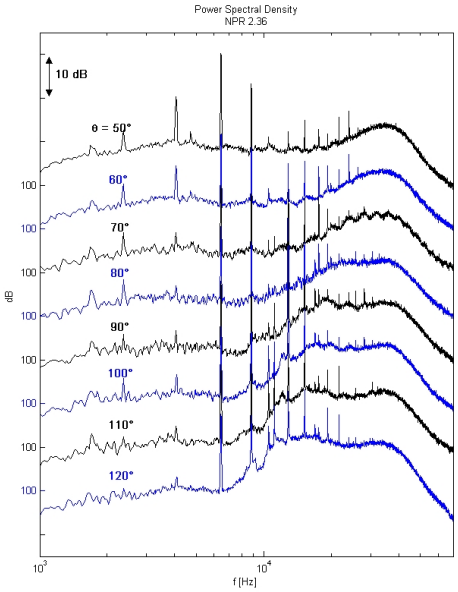

Figure 25: Sound power level at CNPR = 2.36.

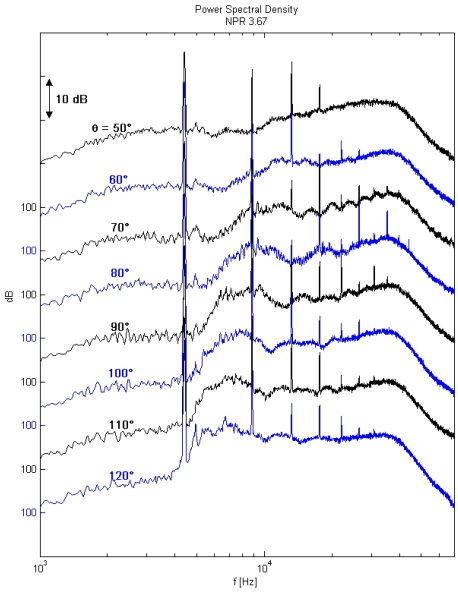

Figure 27: Sound power level at CNPR = 3.667.

SRM aeroacoustics

Lionel Hirschberg

Environmental and Applied Fluid Dynamics Department, von Karman Institute for Fluid Dynamics, Belgium, lionel.hirschberg@vki.ac.be

Supervisor: Christophe Schram

Associate Professor, Environmental and Applied Fluid Dynamics Department, von Karman Institute for Fluid Dynamics, Belgium, christophe.schram@vki.ac.be

Abstract

In large scale Solid Rocket Motors flow pulsations can be driven by coupling between vortex shedding and acoustic standing waves in the engine. Cold gas scale model experiments have shown that this process can produce pressure oscillations of the same level as observed in actual full scale engines. Published experiments indicate that when inhibitor rings are used the pulsation level is proportional to the volume of the cavity around the integrated nozzle as used in the Ariane 5 boosters. The air flow in the cold gas scale model is supplied through a porous wall. Using an energy balance approach, an analytical model is proposed in which the system is described as a purely harmonic linearly damped single mode acoustic resonator at a fixed resonance frequency. Losses of acoustic energy due to vortex shedding, acoustic radiation at the nozzle and dissipation in a porous wall are modeled using quasi steady models. Vortex sound theory combined with a simple flow model is used to model acoustic energy production. The model predicts the observed order of magnitude of the pulsation amplitude.

Keywords: SRMs, Aeroacoustics.

1. Introduction

Solid Rocket Motors (SRMs) as used for Ariane 5 can display strong acoustic pulsations. In the case of these large SRMs the acoustic oscillations can be driven by a coupling between vortex shedding and acoustic standing waves. Anthoine[1] used cold gas scale models to study acoustic oscillations in Solid Rocket Motors. In cold gas experiments combustion of the propellant grain is replaced by injection of air through a porous wall. Most notably Anthoine carried out axial injection experiments in which he found ratios of acoustic pulsation p' to static pressure p of the range $10^{-3} \leq p'/p \leq 10^{-2}$ for flow Mach number $0.05 \leq M \leq 0.15$.

In this communication[1] we will use an energy balance approach in conjunction with the Vortex Sound Theory for an acoustic source model and quasi-steady hydrodynamic models for the acoustic losses to calculate p'/p.

[1]An earlier version of this text co-authored with Prof. A. Hirschberg was used as a proceeding for the 2016 CFA in Le Mans.

2. Experimental setup

A sketch of the axial injection (1/30) scale model of the Ariane 5 booster as used by Anthoine [1] is shown in Figure 1. Air is injected from a reservoir at a pressure $p_r \simeq 5$ bar, through a porous wall in the head end. The air flows trough a cylindrical pipe, of inner radius r_p and length L_p, which is terminated down stream by an integrated nozzle. The static pressure in the pipe is around $p = 3$ bar. The integrated nozzle has a cavity volume V_c equivalent to the largest cavity volume that occurs during full scale test firing. There are several nozzles which can be mounted corresponding to different cavity volumes. The distance from the bottom of the cavity to the inlet of nozzle measured parallel to the axis is $\delta L_p \simeq 22$mm. The Mach number in the pipe can be varied by reducing the nozzle throat area by the introduction of a needle. The range of the Mach numbers at the nozzle inlet typically considered is $0.05 < M < 0.15$. To simulate an inhibitor, a solid sharp edged orifice of radius r_o is fixed at a distance L_o from the nozzle inlet. This orifice is the vortex generator in the experiments.

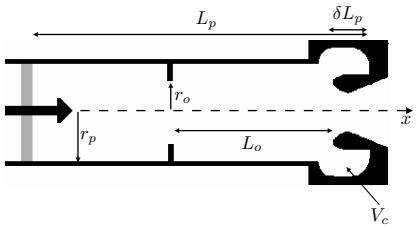

Figure 1: Scale model with axial injection through the upstream porous wall and an integrated nozzle at the downstream side.

A typical result of experiments by Anthoine [1] is shown in Figure 2, for this case $L_p = 0.393$ m, $L_0 = 0.071$ m, $V_c = 2.18 \times 10^{-4}$ m^3 (nozzle 9), $r_p = 0.038$ m and $r_0 = 0.029$ m. In this figure the measured root-mean-square amplitude p_{rms} of the pressure pulsations measured at the head-end normalized with static pressure p_{rms}/p, is shown as a function of the nozzle inlet Mach number M.

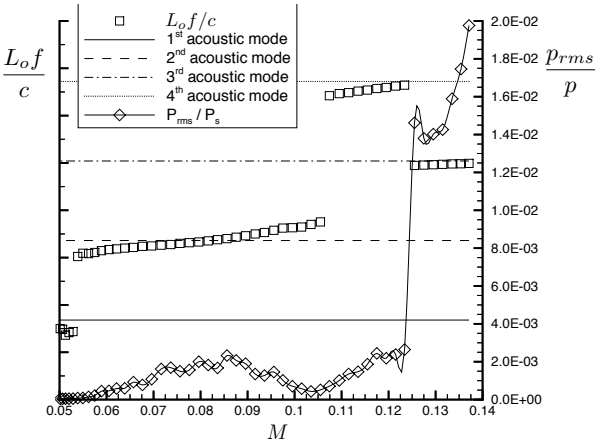

Figure 2: Anthoine's experimental results for $L_p = 0.393$ m, $r_0 = 0.029$ m, $L_o = 0.071$ m and $V_c = 2.18 \times 10^{-4}$ m^3 (nozzle 9). The pulsation amplitude is indicated using a diamond and the corresponding frequency by a square. On the righthand vertical axis we have pulsation levels p_{rms}/p and on the lefthand vertical axis the oscillation frequency $L_o f/c$ both as a function of the Mach number M. The horizontal lines indicate the resonance frequencies which Anthoine [1] calculates as follows: $f_n = nc/(2L_p)$ with $n = 1, 2, 3 \ldots$. Typical pulsation levels reach $O(10^{-2})$ and the oscillation frequency increases monotonously for each acoustic mode, passing the resonance frequency around the maximum pulsation level.

3. Theory

An energy balance is proposed to predict the amplitude of the pulsations. Using the fluctuation in total enthalpy $B' = p'/\rho + u'U$ as aeroacoustic variable for $M^2 << 1$ allows to take convective effects in the boundary conditions while neglecting these in the bulk of the acoustic field [7]. The total enthalpy is related to the velocity fluctuation u' by the linearized Euler equation $\partial u'/\partial t = -\partial B'/\partial x$. Assuming a stable limit cycle, the acoustic field is approximated by a single mode n of a close-close pipe of effective length $L_{eff} = L_p - \delta L_p + V_c/(\pi r_p^2)$:

$$B' = |b| \cos(\frac{\omega_n}{c} x) \cos(\omega t) \tag{1}$$

with $|b|$ the amplitude of B' at an anti-node, $\omega_n = n\pi c/L_{eff}$, c the speed of sound, x the distance from the upstream end of the pipe and ω the oscillation frequency. As proposed by Culick [2] the system is described as a damped oscillator:

$$M_{eff} \frac{d^2 b}{dt^2} + \gamma_{eff} \frac{db}{dt} + M_{eff} \omega_n^2 b = F_{vortex} \tag{2}$$

where $M_{eff} = \rho \pi r_p^2 L_{eff}/(\omega_n c)^2$. The linear damping γ_{eff} is de sum of nozzle radiation, vortex shedding at the orifice and viscous damping in the porous end-wall. Using quasi-steady models one obtains [5]:

$$\begin{aligned} \gamma_{eff} &= \frac{\rho \pi r_p^2}{\omega^2 c} [1 - R_{nozzle}^2 \left(\frac{1-M}{1+M}\right)^2 \\ &+ \frac{\omega_n}{\omega} M \left(\left(\frac{r_p}{r_{jet}}\right)^4 - 1 \right) \sin^2(\frac{\omega_n}{c} x_o) \\ &+ 1 - R_{porous}^2 \left(\frac{1+M}{1-M}\right)^2] \end{aligned} \tag{3}$$

The pressure reflection coefficient at the nozzle R_{nozzle} is given by the theory of Marble and Candel [6] $R_{nozzle} = (1 - \frac{\gamma-1}{2} M)/(1 + \frac{\gamma-1}{2} M)$ where γ is the Poisson ratio of specific heats. The pressure reflection coefficient R_{porous} end-wall is given by [5]: $R_{porous} = (1 + (p_r/p)^2(\gamma M - 1))/(1 - (p_r/p)^2(\gamma M - 1))$ where p_r is the reservoir pressure upstream of the porous wall and p the time averaged pressure in the pipe. The power generated by the vortex sound source term F_{vortex} is calculated using the energy corollary of Howe [4]:

$$< F_{vortex} \frac{db}{dt} >= -\rho < \int_V (\vec{\omega} \times \vec{v}) \cdot \vec{u}_{ac} dV > \tag{4}$$

where $\vec{v}$ is the local velocity field and $\vec{u}_{ac}$ is the unsteady potential flow component of the velocity identified by Howe [4] as the acoustic field. The brackets $< ... >$ indicate time averaging over a period of oscillation and the integral is carried out over the volume

in which the vorticity $\vec{\omega} = \nabla \times \vec{v}$ is non vanishing. The vorticity field is described in terms of line vortex rings of circulation Γ convected at constant speed $u_\Gamma = 0.4U(r_p/r_{jet})^2$:

$$\vec{\omega} = \Gamma\delta(r - r_{jet})\delta(x - x_o - u_\Gamma(t - \tau_0)). \quad (5)$$

Assuming quasi-steady shedding of vorticity followed by the concentration of this vorticity each period into a single vortex, the circulation is given by: $\Gamma = (\pi/\omega)[U(r_p/r_{jet})^2]^2$ where the vena contracta ratio r_{jet}/r_o of the jet cross-sectional radius r_{jet} and orifice radius r_o is determined from the experimental data of Gilbrag [3]. The acoustic field $\vec{u}_{ac}$ is assumed to have a uniform component v_{ac} normal to $\vec{\omega}$ and $\vec{v}$ over a distance L_c upstream from the nozzle inlet $x = L_p - \delta L_p$:

$$\begin{aligned} v_{ac} &= \frac{r_p|b|\omega_n}{2cL_c\omega}\sin(\frac{\omega_n}{c}(L_p - \delta L_p))\sin(\omega t) \\ &\times [H(x - (L_p - \delta L_p - L_c)) \\ &- H(x - (L_p - \delta L_p))] \end{aligned} \quad (6)$$

The distance L_c was estimated as $L_c = 2\sqrt{2}(r_p - r_n)$ where $r_n = 1.85$ cm is the nozzle radius at the minimum of the cavity inlet. Substitution in the energy corollary (4) yields:

$$\begin{aligned} < F_{vortex}\frac{db}{dt} > &= \\ \frac{\pi\rho\Gamma r_{jet}u_\Gamma r_p\omega_n}{cL_c\omega} &|b| \quad \sin(\frac{\omega_n}{c}L_p) \\ \times < \sin(\omega t)[H(t - \tau_0 - \frac{L_o - L_c}{u_\Gamma}) &- \\ H(t - \tau_0 &- \frac{L_0}{u_\Gamma})] > \end{aligned} \quad (7)$$

where $L_o = L_p - \delta L_p - x_o$ is the distance between the orifice and the nozzle inlet and $\tau_0 = 0$ or π/ω depending on the position x_o of the orifice relative to pressure nodes. The parameter τ_0 is chosen such that a new vortex is shed each time the acoustic velocity vanishes at the orifice turning into the direction of the main flow U. The amplitude $|b|$ is obtained from the energy balance:

$$< F_{vortex}\frac{db}{dt} >=< \gamma_{eff}\left(\frac{db}{dt}\right)^2 > \quad (8)$$

in which we use the approximation $\omega = \omega_n$.

4. Results

In Figure 3 results of the energy balance are compared to axial cold flow experiments for nozzle 9 with $V_c = 2.18\times10^{-4}$ m^3. The results of the energy balance prediction are shown in the plot on the lefthand side of Figure 3. The ratio of root mean square value of the pressure fluctuation over the static pressure p_{rms}/p is plotted as a function of the Mach number M. This is done for three cases viz. where the frequencies equal the resonance frequencies ω_1, ω_2 and ω_3 corresponding to the first $n = 1$ (dotted line) second $n = 2$ (solid line) and third $n = 3$ (dashed line) acoustic mode respectively.

For comparison the results of the experiments as published by Anthoine[1] are displayed on the righthand side in Figure 3. On the lefthand vertical axis the dimensionless frequency $L_o f/c$ is shown and on the righthand vertical axis the p_{rms}/p, both as a function of the Mach number M. From the Figure 3 we see that local maxima in relative pulsation amplitude p_{rms}/p are detected around $M = 0.085$ and $M = 0.14$. As we can see from Figure 3, these correspond to the second $n = 2$ and third $n = 3$ acoustic mode respectively.

The local maxima measured at around $M = 0.085$ and $M = 0.14$ respectively correspond to a hydrodynamic number $m = L_o f/u_\Gamma = 2.0$. The hydrodynamic number is the ratio of the convection time of the vortex from the orifice to the nozzle inlet and the oscillation period. I.e. it is a estimate of the number of equidistant vortices traveling from the orifice to the nozzle. Moreover, for $m = 1, 2, 3$ we speak of the first second and third hydrodynamic mode. For $M = 0.085$ the first, second and third hydrodynamic modes correspond to the first $n = 1$, second $n = 2$ and third $n = 3$ acoustic modes respectively. While for $M = 0.14$ the second and third hydrodynamic modes correspond to the first $n = 1$ and second $n = 2$ acoustic modes respectively. It is noteworthy that in simulations with $M = 0.09$ Anthoine[1] finds two vortices traveling down steam viz. the second hydrodynamic mode. This would explain the selection of the second acoustic mode $(m, n) = (2, 2)$ at $M = 0.085$ and the selection of $(m, n) = (2, 3)$ for $M = 0.14$.

We now concentrate on the second acoustic mode $n = 2$. However the procedure described can equally be applied to third mode $n = 3$. To compare the experimental data to the energy balance we do the following: locate the local maximum for $n = 2$ in the experiments. This yields a measured relative pressure pulsation $(p_{rms}/p)_{exp} = 2.3\times10^{-3}$ with an associated Mach

number $M_{exp} = 8.6 \times 10^{-2}$. We now turn to the plot of the energy balance on the lefthand side of Figure 3. As we are concerned with the second acoustic mode $n = 2$, we focus on the solid line. We find the local maximum closest to the one detected by Anthoine[1], which is $(p_{rms}/p)_{th} = 7.5 \times 10^{-3}$ with a corresponding Mach number $M_{th} = 8.5 \times 10^{-2}$. Thus in this case we accurately reproduce the corresponding Mach number within 1%. And the pulsation amplitude p_{rms}/p is calculated using the energy balance method is a factor 3 higher than what was measured.

The results depicted in Table 1 correspond to experiments for nozzle 7 with $V_c = 1.84 \times 10^{-4}$ m^3 in which the length of the test section L_p was varied. The local maxima in p_{rms}/p for the experiments (column 4) and the energy balance prediction (column 6) are compared (column 7). We have scaled the maxima in p_{rms}/p in Table 1 using the associated dynamic pressure i.e. $\rho u^2/2 = \gamma p M^2$. From the this table we see that using the energy balance approach, we can reproduce the measured pressure pulsations within and order of magnitude. Furthermore, we see that pulsations are of the order magnitude of the dynamical pressure i.e. $\frac{1}{2}\rho U^2 = \gamma p M^2$ can be used as an order of magnitude estimate for pressure amplitude of the pulsations.

In a companion paper we discuss a more detailed model which predicts the evolution of the frequency ω as a function of the Mach number M [5]. The present simpler energy balance approach appears to be more robust and does provide similar results for the pulsation amplitude.

5. Conclusion

In this communication we analyzed results of axial injection cold flow experiments, carried out using a (1/30) scale model for Ariane 5. We have shown that the energy balance method can reproduce measured maxima in pressure pulsation p_{rms}/p within a factor 6 and its associated Mach number M within 10%, when the oscillating mode number observed in the experiments is used as an input parameter. Its is thusly useful as a tool for interpreting measurements viz. the physical models for the source and the losses provide qualitative insight into the occurrence of dominant physical processes. What is more, we have shown that the dynamical pressure $\frac{1}{2}\rho U^2$ is a good order of magnitude estimate for typical maxima of pressure pulsations.

Acknowledgements

Support by Airbus Defense and Space and in particular Jean Collinet and Serge Radulovic is acknowledged.

References

[1] J. Anthoine, *Experimental and numerical study of aeroacoustic phenomena in large solid propellant boosters with application to Ariane 5 solid rocket motor*, von Karman Institute for Fluid Dynamics, Sint-Genesius-Rode, Belgium (2000)

[2] F. E. C. Culick, *Unsteady Motions in Combustion Chambers for Propulsion Systems*, RTO/NATO, RTO-AG-AVT-039 (2006)

[3] D. Gilbrag, *Handbuch der Physik: Strömungsmechanik III*, Springer-Verlag, (1960).

[4] M. S. Howe, The dissipation of sound at an edge, *Journal of Sound and Vibration* **3**, 407-411 (1980).

[5] L. Hirschberg, C. Schram , A. Hirschberg, Prediction of pulsations in a cold-gas scale-model of a solid rocket motor, *proceeding for 22nd AIAA/CEAS*, Lyon (2016).

[6] F. E. Marble, S. M. Candel, Acoustic disturbance from gas non-uniformities convected through a nozzle, *Journal of Sound and Vibration* **2**, 225-243 (1977).

[7] F. Nicoud, K. Wieczorek, About the zero Mach number assumption in the calculation of thermoacoustic instabilities, *International Journal of Spray and Combustion Dynamics* **1**, 67-111 (2009).

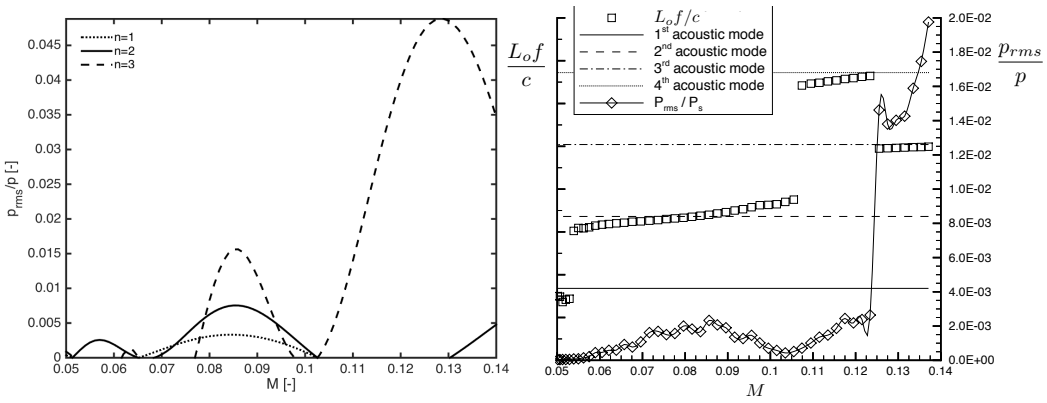

Figure 3: On the lefthand side the relative pulsations, for the first $n = 1$ (dotted line), second $n = 2$ (solid line) and third $n = 3$ (dashed line) acoustic modes, predicted by the energy balance are plotted as a function of the Mach number at the nozzle inlet. Anthoine's experimental results are shown on the righthand side for comparison ($L_p = 0.393$ m, $r_0 = 0.029$ m, $L_o = 0.071$ m). The pulsation amplitude is indicated using a diamond and the corresponding frequency by a square. On the righthand vertical axis we have pulsation levels p_{rms}/p and on the lefthand vertical axis the oscillation frequency $L_o f/c$ both as a function of the Mach number M. The horizontal lines indicate the resonance frequencies which Anthoine [1] calculates as follows: $f_n = nc/(2L_p)$ with $n = 1, 2, 3 \ldots$. Typical pulsation levels reach $O(10^{-2})$ and the oscillation frequency increases monotonously for each acoustic mode, passing the resonance frequency around the maximum pulsation level.

Table 1: Results for variable tube length L_p. The first five columns contain data taken from Anthoine's cold flow experiments [1]. The last two columns list the theoretical predictions, obtain with the energy balance ($L_o = 7.1 \times 10^{-2}\, m$, $r_o = 2.9 \times 10^{-2}\, m$, $\left(\frac{r_{jet}}{r_p}\right)^2 = 0.68$). In columns 4 and 6 the maxima in p_{rms} for the experiments and the energy balance prediction are scaled using the associated dynamic pressure i.e. $\rho u^2/2 = \gamma p M^2$

m	n	L_p	M_{exp}	$\left(\frac{2p_{rms}}{\gamma p M^2}\right)_{exp}$	M_{th}	$\left(\frac{2p_{rms}}{\gamma p M^2}\right)_{th}$	$\frac{p'_{th}}{p'_{exp}}$
$[-]$	$[-]$	$[m] \times 10^{-1}$	$[-] \times 10^{-2}$	$[-]$	$[-] \times 10^{-2}$	$[-]$	[-]
2	2	3.93	8.0	0.44	8.7	1.4	3.2
2	3	3.93	14	0.68	13.1	3.3	4.8
4	2	3.05	6.0	0.08	5.5	0.19	2.5
2	2	3.05	11	0.44	11.1	1.1	2.6
4	1	1.88	7.8	0.31	8.7	1.5	4.8
3	2	1.88	12	0.44	12.6	0.85	2.0
4	1	1.63	9.8	0.24	9.9	15	6.3

Rotor noise extraction by in-duct modal decomposition technique

Yakut Cansev Kucukosman

Environmental and Applied Fluid Dynamics Department, von Karman Institute for Fluid Dynamics, Belgium, y.c.kucukosman@vki.ac.be

Supervisor: Christophe Schram

Associate Professor, Aeronautics and Aerospace Department & Environmental and Applied Fluid Dynamics Department, von Karman Institute for Fluid Dynamics, Belgium, christophe.schram@vki.ac.be

Supervisor: Jeroen van Beeck

Professor, Environmental and Applied Fluid Dynamics Department, von Karman Institute for Fluid Dynamics, Belgium, jeroen.vanbeeck@vki.ac.be

Abstract

An experimental method is presented to measure the sound emitted from the Contra Rotating Open Rotor (CROR). The experimental method, called two-port analysis, is suited to ducted systems, making use of several microphone/loudspeaker circular array sections downstream and upstream the rotor. A remote microphone technique which connects the microphone to the surroundings through a pipe-cavity system is adopted to carry out the measurements where the microphones cannot be flushed-mounted to the surface due to the particular constrains. A model-based calibration method is discussed to account for the phase lag and dissipation within the microphone line.

Keywords: Aeroacoustics, contra-rotating rotors, remote microphone technique, two-port analysis

1. Introduction

The Contra Rotating Open Rotor (CROR) systems redraw great attention over the recent years for future transport aircrafts due to their light weight and high fuel efficiency configurations. However, the main drawback is that the noise levels emitted by these configurations are remarkably high making them unsuitable for utilization. Thus, accurate and robust noise measurement techniques are required to determine noise levels of CRORs which ensure passengers and community noise limits. The CROR systems produce great amount of tone noise that requires an effective experimental method to distinguish the CROR noise out of the other noise sources. In order to achieve this, in-duct aeroacoustic modal decomposition technique will be used in subsonic wind tunnel L1 in VKI which hosts a ducted contra-rotating rotor system. In this paper, the two port analysis is briefly explained where circular arrays of wall-mounted microphone and loudspeaker are to be installed upstream and downstream the contra-rotating propellers. Since the experimental setup of the L1 wind tunnel prevents such an extensive modifications to wall-mount the microphones, a dedicated design for mounting the microphones is proposed. In this design, the microphones are conserved horizontally inside of a mounting device to induce flow perturbations and they are connected to the surrounding through a pipe-cavity system. A remote microphone technique is presented in order to eliminate the response of the pipe-cavity system. Aerodynamic and aeroacoustics analysis of the mounting device are investigated in the presence of the different incoming flow velocities and the turbulence generators.

2. The two port microphone method- Two port analysis

The sound emitted from the ducted rotating machine will be analyzed by using the two-port analysis method, as a one port analysis is not sufficient for identification of the rotor noise, which requires simul-

taneous measurements of the reflected and the transmitted waves. In the two-port analysis, a set of wall-flush microphones and loudspeakers are installed in circular arrays as shown in Fig. 1. (See [1; 2; 3] for detail).



Figure 1: Sketch of the two-port system identification mock-up

A linear time-invariant system with a source term can be described in the frequency domain as follows [4] :

$$\underbrace{\begin{bmatrix} p_{A+} \\ p_{B+} \end{bmatrix}}_{p_+} = \underbrace{\begin{bmatrix} \rho_A & \tau_B \\ \tau_A & \rho_B \end{bmatrix}}_{S} \underbrace{\begin{bmatrix} p_{A-} \\ p_{B-} \end{bmatrix}}_{p_-} + \underbrace{\begin{bmatrix} p_A^S \\ p_B^S \end{bmatrix}}_{p_+^S} \tag{1}$$

where A and B refer to the both sides of the port, + and − signs denote the outwards and inwards waves, respectively, p_+^S represents the source term. The scattering matrix , S, is the coefficients of the reflection, ρ, and the transmission, τ, of the incoming waves. Since the microphones measure the summation of all these source, reflected and transmitted waves, the method is divided into two campaigns: passive and active parts to identify the each component.

Within the passive part, the source term is dominated by activating uncorrelated external sources (loudspeakers) at the each side of the ports. This way, the source term in Eq.1 becomes negligible ($p_+^S = 0$), and can be dropped which reduces the matrix to a simple weighted combination of the state variables. The incoming and outgoing waves can be determined from a matrix mentioned in [5]. Thus, the scattering matrix is found by the inversion of the simplified matrix. If the matrix is not square, a Moore-Penrose pseudo-inversion should be performed. Once the scattering matrix is determined, the source term can be computed by deactivating the external sources which is called the active part.

3. Remote Microphone Technique

As mentioned in two-port analysis method, wall-flushed microphones installed in circular arrays upstream and downstream the scattering object are required to perform the method. Particular constraints in set up of L1 wind tunnel diffuser which prevents such a flush mounted installation, the microphones are placed within the duct surface. To avoid direct exposure of the microphones to the flow field, a dedicated mounting device is designed and manufactured. The design conserves the microphone in a horizontal position and connects it to the field through a pipe cavity system which damps the pressure fluctuations. Therefore, a remote microphone technique is applied to obtain a better estimation of the signal perceived by the mounting device. When designing a remote microphone system, it is important to have the acoustic resonance frequency of the pipe-cavity outside of the interest frequency range. The resonance frequency of the pipe cavity system corresponds to the typical range of Strouhal number related to the instability of the shear flow where flow-acoustic feedback has been observed should be avoided. The typical range is $0.2 < St = fD/U < 0.8$ where D is the diameter of the pipe and U is the flow velocity. In order to determine the dimensions of the pipe cavity system, the analysis of Bergh and Tijdeman [6] is followed, giving the transfer function between the pressure at the port opening and the pressure sensed by the pressure sensor:

$$\frac{\hat{p_1}}{\hat{p_0}} = \left[cosh(\phi L) + \frac{V_\upsilon}{V_t} \left(\sigma + \frac{1}{k} n\phi L \, sinh(\phi L) \right) \right]^{-1} \tag{2}$$

where $\phi = \frac{\nu}{a_0} \sqrt{\frac{J_0<\alpha>}{J_2<\alpha>}} \sqrt{\frac{\gamma}{n}}$ with $\alpha = i^{3/2} R \sqrt{\frac{\rho_s \nu}{\mu}}$ is the shear wave number where the viscosity is taken into account, $n = \left[1 + \frac{(\gamma-1)}{\gamma} \sqrt{\frac{J_2<\alpha\sqrt{Pr}>}{J_0<\alpha\sqrt{Pr}>}} \right]^{-1}$ is a polytropic constant, $Pr = \frac{\mu C_p}{\lambda}$ is Prandlt number, $\gamma = C_p/C_v$ is specific heat ratio, L is the length of the pipe, V and V_t are the pressure transducer and tube volume, R is the tube radius [6].

The three parameters that affect the resonance frequency, which are length and radius of the pipe, and cavity volume, are investigated using this theory, implemented in the VKI in-house code PreMeSys [7]. A large radius guarantees that the viscous effects are negligible which signifies higher resonance frequency. For smaller radii, more damping is observed at the resonance frequency. Further decrease in the radius prevents resonance (Fig. 2).

When the length of the tube is increased, the time scale for pressure to propagate through the tube rises. Therefore, both resonance amplitude and frequency decrease. In the same manner, increasing the volume acts as if it introduces viscous effects which means that increasing cavity volume both decreases the resonance amplitude and frequency (Fig. 3 & Fig. 4).

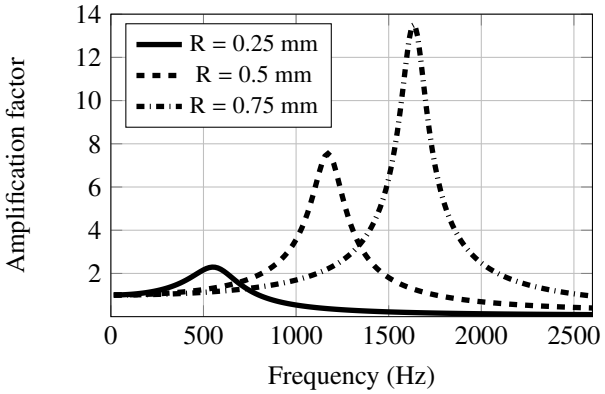

Figure 2: Effect of Radius Change

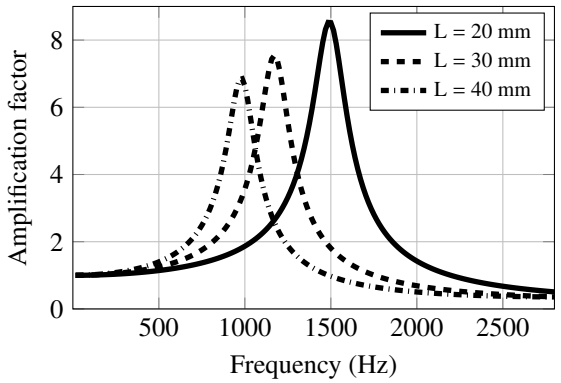

Figure 3: Effect of length change

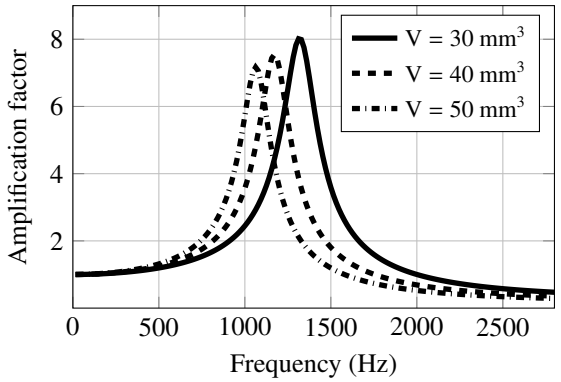

Figure 4: Effect of volume change

It is observed that changing the pipe length and the cavity volume in the limits of practicality do not affect the resonance frequency, while, changing the pipe diameter dramatically affects it. In order to obtain a high resonance frequency, the pipe length and the volume cavity should be as small as possible and the pipe diameter should be as large as possible. However, larger diameter increases the probing area leading the turbulence enter through the cavity which is an undesirable phenomenon. As a result, a smaller pipe diameter with a high resonance frequency needs to be optimized.

Another restriction emerges due to the calibration of the microphones since the effect of the pipe cavity system on the frequency response of the microphones are to be eliminated through a calibration procedure. Consequently, the pipe length of the pipe-cavity systems are designed according to a calibration tube that has been already utilized at the VKI. By considering the dimension of the microphone, the volume cavity size is minimized. For the diameter, the first attempt is to obtain the smallest diameter to avoid the acoustic pressure perturbations. 1 mm diameter pipe is selected since it is the smallest diameter that could be manufactured. Therefore, three pipe-cavity system with a diameter size of 1, 2 and 3 mm are designed and tested in PreMeSys to observe the resonance frequency. As it is specified before that PreMeSys simulates a straight pipe with a circular cavity, however, in the current case, there is a L shape pipe which is connected to a cone shape cavity. The other parameter that needs to be taken into consideration is the additional volume between the protection grid and membrane. Therefore, this configuration is simplified as shown in Fig. 5.

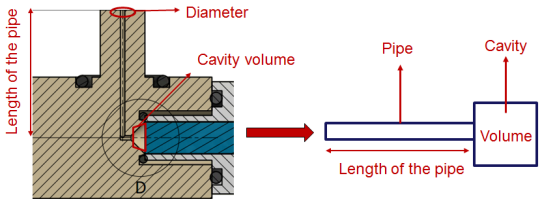

Figure 5: Simplification of the pipe-cavity system

The pipe-cavity system with three different diameters are manufactured in VKI and are tested with calibration tube to obtain the resonance frequency. In this process, three pipe-cavity systems with microphones and one reference microphone are placed to the calibration tube and are exposed to a chirp signal emitted from the loudspeaker (see Fig. 6). The chirp signal frequency range is determined by the lowest frequency emitted from the loudspeaker ($f_{min} \approx 100$ Hz) and the cut-off frequency of the pipe ($f_{max} \approx 5$ kHz).

A reference microphone is flushed-mounted to acquire the transfer function, the response of the pipe cavity system, for three different configuration. The

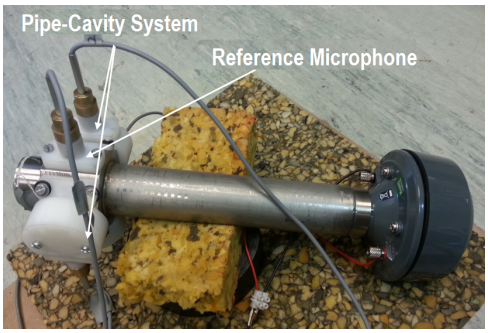

Figure 6: Test setup of the pipe-cavity systems

measured transfer function is defined as [8; 4]:

$$H(f) = S_{21}/S_{11} \tag{3}$$

Where 1 denotes the reference microphone and 2 is the pipe-cavity system, S_{21} is the cross power spectral density of the reference microphone and the pipe-cavity system and $S_{11}$is the power spectral density of the reference microphone. The comparison between PreMeSys and experiment is shown in Fig. 7. It has been observed that the larger diameter, increases the resonance frequency and amplitude as well. However, the value of the resonance frequency and the amplitude are not matching perfectly since the dimensions are not exactly the same as in the CAD drawings.

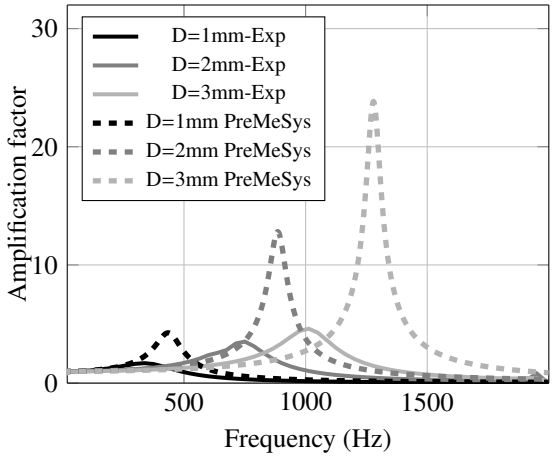

Figure 7: Comparison of the experimental results with PreMeSys

The coherence of the microphones is determined with respect to the reference microphone. It has observed that the smallest diameter shows poor coherence. The sound pressure level shows that at low frequencies, the 2mm and 3 mm show good match. In order to obtain point-wise measurements, 2 mm diameter one has selected.

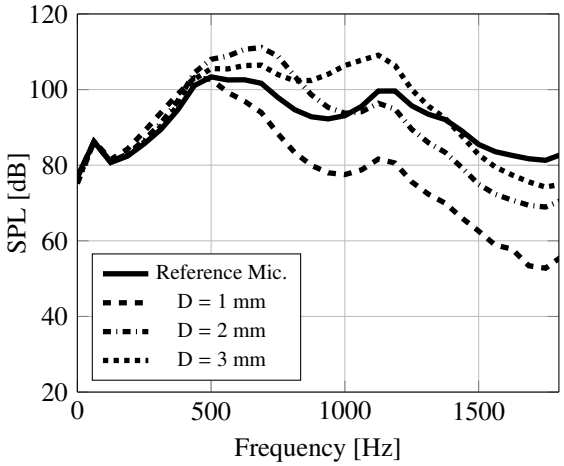

Figure 8: Comparison of the Sound Pressure Level of the pipe-cavity system with reference microphone

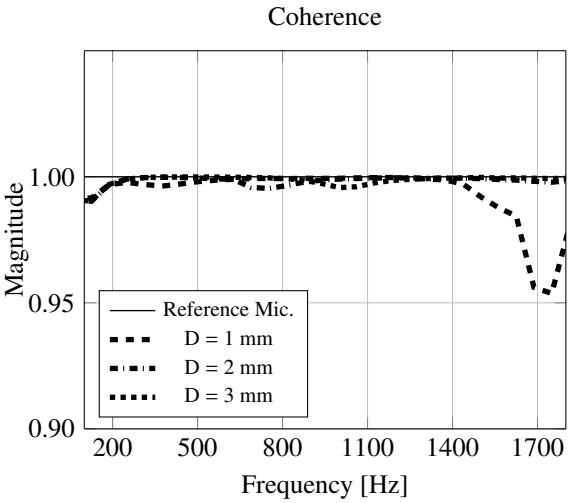

Figure 9: Comparison of the Coherence of the pipe-cavity system with reference microphone

4. Investigating the effect of the mounting device: Aerodynamics

The mounting device encapsulating the microphones are designed to have a streamlined profile to induce flow perturbations as less as possible as shown in Fig. 10.

In order to verify the effect of the mounting device in the presence of the flow, a set of hot-wire

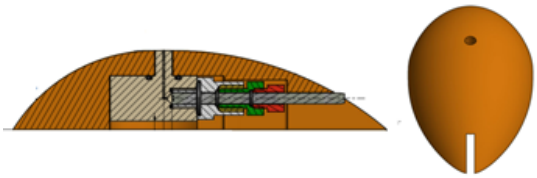

Figure 10: CAD drawing of the mounting device

measurements have been performed with and without the mounting device in L2B wind tunnel of VKI. The wind tunnel has a open circuit, suction type with a 4.4 kW variable-speed DC motor which provides a maximum velocity of 35 m/s. The rectangular test section is 0.35 m high 0.35 m wide and 2 m long. The boundary layer measurements are obtained at a single axial position in the transverse direction where the hole of the pipe-cavity system is located. The mean velocity profile and the turbulence intensity are shown in Fig. 11 and Fig. 12 with three different velocities: 5, 10 and 15 m/s, respectively where y is the distance from the wall and H is the height of the wind tunnel. In the presence of the mounting device, it has been observed that the velocity accelerates and causes a global reduction in the turbulence intensity. However, in the vicinity of the surface the turbulence intensity increases.

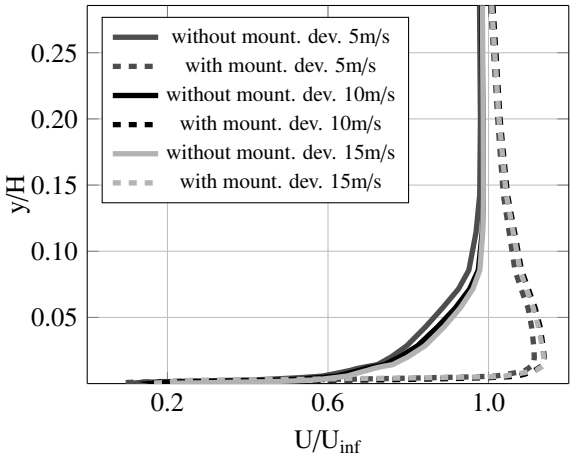

Figure 11: Mean velocity profile

The next step is to expose the mounting device to an intense turbulence intensity to observe the behavior of the flow in the presence of the mounting device. The same setup has been used by placing two wooden bars which are 1 cm shorter than the mounting device. They are located on the bottom and the top section of the wind tunnel to obtain higher turbulent intensity.

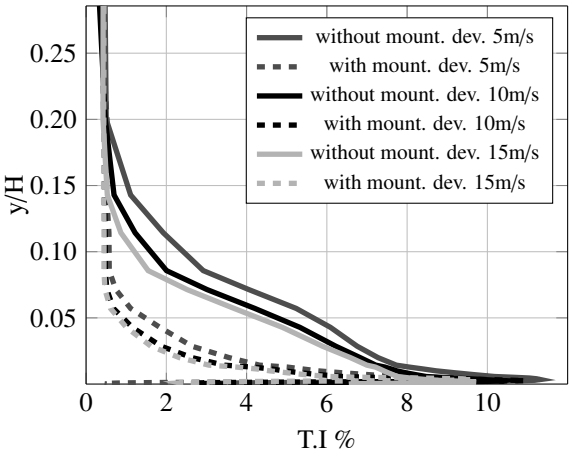

Figure 12: Turbulence intensity profile

It has been observed from Fig. 13 that the mounting device accelerated the flow in both cases as presumed. In the same manner, the turbulence intensity decreases at the outer part but increases in the vicinity as shown in Fig. 14.

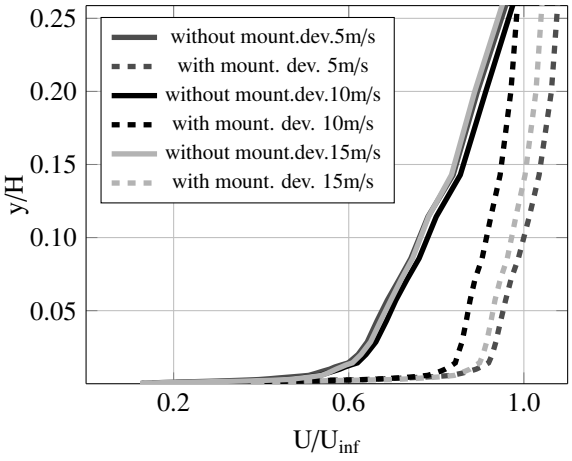

Figure 13: Mean velocity profile

It is observed in both cases that the existence of the mounting device increase the turbulent intensity close to its surface, where the pipe opening hole is located.

5. Investigating the effect of the mounting device: Aeroacoustics

As mentioned before that a dedicated device is needed in order to perform aeroacoustics measurements where it is not suitable to flushed-mount the microphones due to several constraints. Thus, it is pos-

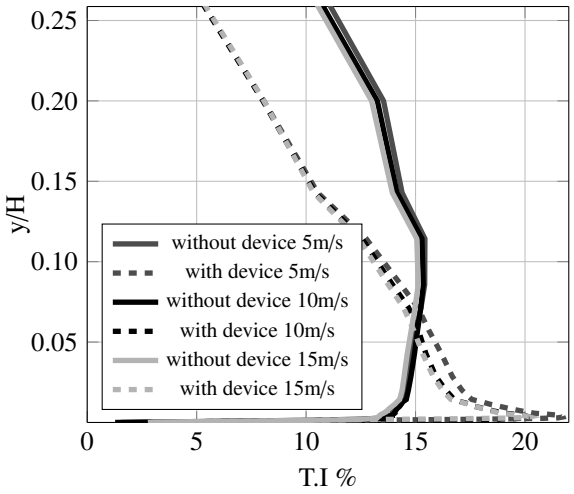

Figure 14: Turbulence intensity profile

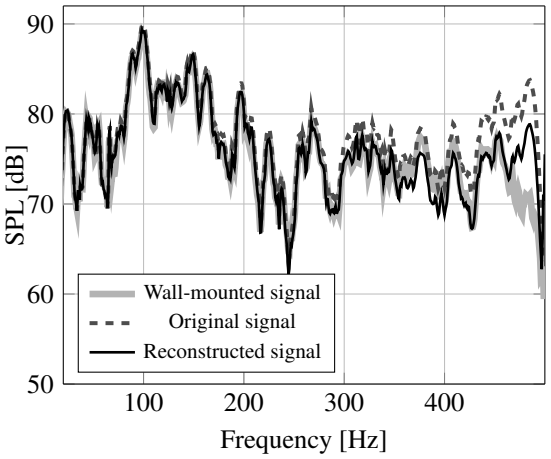

Figure 15: The comparison of the wall-mounted signal with the original signal and the reconstructed signal received by the mounting device at 5 m/s

sible to use a remote microphone technique to eliminate the resonance frequency of the pipe-cavity system to retrieve a better estimated signal. In order to perform this case, the same setup has been used by placing a flushed-mounted microphone at the top and at the same axial position as the mounting device so that both microphone receive the same plane wave. Since the purpose is to reconstruct the signal to the flushed-mounted one by using the remote microphone technique, it is essential to suppress the background noise. Therefore, a loudspeaker which covers a large range of frequency is located upstream of the tunnel. The experiment is performed by a chirp signal emitted by the loudspeaker with three different velocities 5, 10 and 15 m/s. The maximum frequency emitted is determined by the first cut-off frequency of the wind tunnel is around 495 Hz. The transfer function which is deducted from the calibration tube is applied to the signal received from the mounting device to reconstruct the reference signal through the following equation:

$$Reconstructed\ Signal = \frac{Mounting\ Device\ Signal}{H} \tag{4}$$

Even though the resonance frequency of the pipe-cavity system is selected to be higher than the interest frequency, a remote microphone technique is needed to be applied to eliminate the frequency response. Fig. 15 demonstrates the comparison of the wall-mounted signal with the original signal and the reconstructed signal received by the mounting device at 5 m/s. Although, the response is almost flat, with the reconstruction, a better estimation is obtained.

Figure 16 shows the comparison between the flushed-mounted microphone signal and the reconstructed signal of the pipe-cavity system with two different velocities. A good matching is observed all the cases except around the cut-off frequency of the wind tunnel. Moreover, the loudspeaker could not suppress the background noise at 15 m/s but the match is still good which also verifies that the mounting device does not cause additional noise.

The same experiment is performed by placing two wooden bars after the loudspeaker to have the same development in the flow for the top flushed mounted microphone and the bottom mounting device. Figure 17 shows the reference signal and the reconstructed signal received from the mounting device for two different velocities. It is observed that increasing the turbulence and eddy size affects the reconstruction process. For 10 m/s case, the reference signal still matches, however, a deviation is observed for the high velocity. The reconstructed signal detects the main behavior of the signal but there is a less than 2 dB difference with the reference signal. It could be the fact that the mounting device produces extra noise when it is exposed to a higher turbulence intensity.

In conclusion, when the turbulence intensity is low, the general behavior of the mounting device is to reduce the turbulence intensity which also results in a good reconstruction of the signal. Besides, in the first case the mounting device is not placed inside the boundary layer, the top of the mounting device where the signal enters is outside of the boundary layer. Therefore, it is observed that no significant noise is

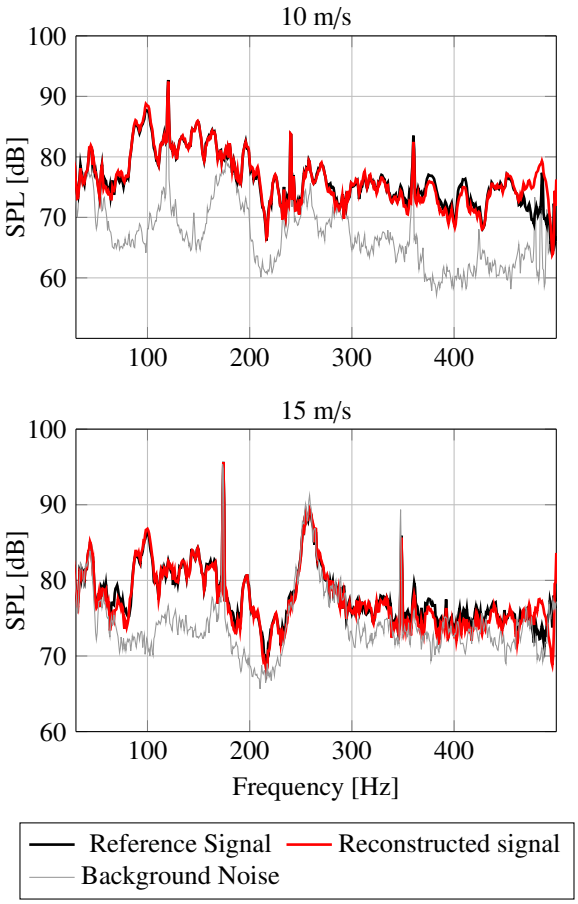

Figure 16: The comparison of the wall-mounted signal with the the reconstructed signal received by the mounting device at 10, 15 m/s

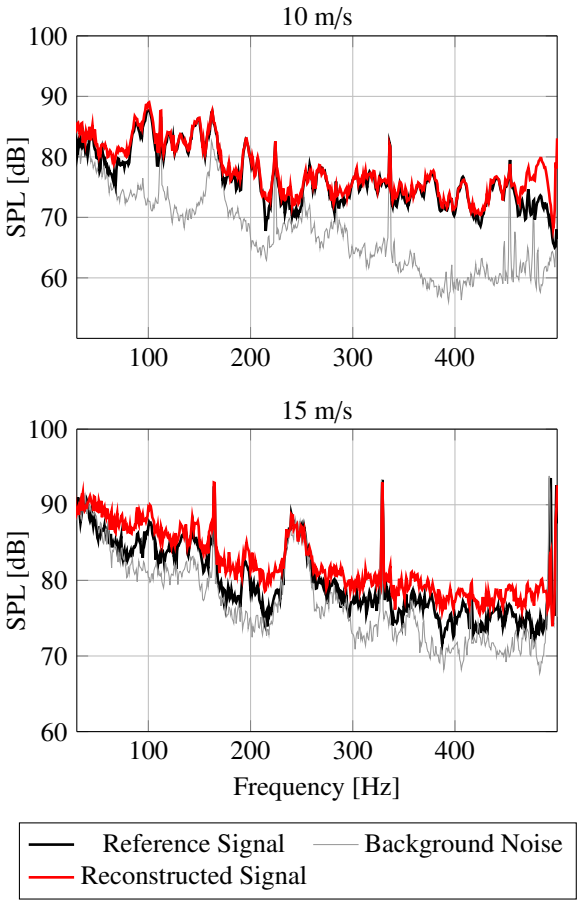

Figure 17: The comparison of the wall-mounted signal with the the reconstructed signal received by the mounting device at 10, 15 m/s

produced by the mounting device. However, in the second case where two wooden blocks are located, the mounting device expose to higher turbulence intensity and also large scale eddies which introduces disturbance that are more obvious at higher velocities. Moreover, the wake of the blocks grow larger when the velocity increases, thus, the mounting shape might be exposed to the wake rather than the developed boundary layer.

6. Conclusion and future work

CROR has a great potential to fulfill the need for less weight with a higher fuel efficiency configurations. In order to reduce the noise level of the CROR, an experimental method needs to be addressed. A brief explanation of the experimental method is explained. Later, an experimental technique where the microphones are attached to the surface with a pipe-cavity system is followed by a comparison with an analytical model. It has observed that the simplified model performs the same behavior with the analytical model. However, it is observed that the resonance frequency and amplitude are not matching perfectly. It is deduced that the dimensions of the mockups and the CAD drawings are not exactly the same. It is also concluded that decreasing the diameter of the pipe-cavity system results in decreasing the coherence. To have the point-wise measurements, the 2 mm diameter pipe-cavity system is selected. After, the mounting device which hosts the pipe-cavity system is explained. The aerodynamic effects of the mounting device in the presence of the flow is investigated with a moderate and higher turbulence intensities for two different velocities; 10 and 15 m/s in L2B wind tunnel of VKI. It is verified that that the mounting device accelerates the flow and results in decreasing the turbulence intensity further from the wall, on the other

hand, increasing the turbulence intensity in the vicinity of the surface. Later, the reconstruction of the signal from pipe-cavity system is performed by placing a loudspeaker in the same setup. A better estimation is achieved where the turbulent boundary layer is small compare to the mounting device and the turbulence intensity is moderate. For the higher turbulence intensity, it is observed that there is 2 dB deviation of the reconstructed signal.

It is verified that the mounting device can be used by applying remote microphone technique. For the future step the experimental setup will be assembled in the diffuser of the L1 wind tunnel to perform two-port analysis method.

Acknowledgments

The authors acknowledge with thanks the support of the European Commission's Framework Program "Horizon 2020", through the Marie SkÅodowska-Curie Innovative Training Networks (ITN) "AEOLUS4FUTURE - Efficient harvesting of the wind energy" (H2020-MSCA-ITN-2014: Grant agreement no. 643167) to the present research project.

References

[1] M. Åbom, Measurement of the scattering-matrix of acoustical two-ports, Mechanical Systems and Signal Processing 5 (2) (1991) 89 – 104.

[2] M. Åbom, J. Lavrentjev, A measurement method for determining the source data of acoustic two-port sources, Journal of Sound and Vibration 183 (3) (1995) 517 – 531.

[3] S. Sack, M. Åbom, C. F. Schram, K. Kucukcoskun, AIAA Aviation, American Institute of Aeronautics and Astronautics, 2014, Ch. Generation and scattering of acoustic modes in ducts with flow.

[4] A. Holmberg, M. Åbom, H. Bodén, Accurate experimental two-port analysis of flow generated sound, Journal of Sound and Vibration 330 (26) (2011) 6336 – 6354.

[5] J. Lavrentjev, M. Åbom, Characterization of fluid machines as acoustic multi-port sources, Journal of Sound and Vibration 197 (1) (1996) 1 – 16.

[6] H. Bergh, H. Tijdeman, Theoretical and experimental results for the dynamic response of pressure measuring systems, F: Nationaal Lucht- en Ruimtevaartlaboratorium, Nationaal lucht- en ruimtevaartlaboratorium, 1965.

[7] J. CaetanoAlves, PreMeSys V2.0: a software tool to characterize the dynamic response of apressure measurement system, 2005.

[8] H.-E. de Bree, F. van der Eerden, J. van Honschoten, A novel technique for measuring the reflection coefficient of sound absorbing materials, in: International Conference on Noise and Vibration, ISMA 25, 2000.

WHO’S WHO

WHO'S WHO



Mohamed Hassanine
Aissa



Alessi
Giacomo



Alejandro
Alvarez Laguna



Gilles
Bailet



Federico
Bariselli



Georgios
Bellas Chatzigeorgios



Aurélie
Bellemans



Elissavet
Boufidi



Sofia
Buckingham



Bogdan Cezar
Cernat



Christopher
Chahine



Julien
Clinckemaille



Andrea
Cortesi



Nicolas
De Cock



Cis
De Maesschalck



Ana Isabel
Del Val Benitez



Giulia
Dell'Era



Bruno Ricardo
Dias Barros



Claudia
Esposito



Jorge
Fernandes Lopes de Sousa
(PhD completed in 2015-2016)



Charline
Fouchier



Clara
García Sánchez



Sara
González Ruiz



Gian Luca
Gori



Gabriele
Grasso



Koen
Groot



Daniel
Guariglia



Lionel
Hirschberg



Zdeněk
Ilich



Yakut Cansev
Kucukosman



Aude
Lahalle



Ignacio
Mayo Yague



Miguel Alonso
Mendez



Fernando
Miró Miró



Lasse
Müller



Ismael
Sànchez Torreguitart



Marc
Schwalbach



Alessia
Simonini



Nikolaos
Stergiannis



Orkun
Temel



Roberto
Tomasssini



Alan
Viladegut



Augustin
Villa Ortiz



Marco
Virgilio

PhD candidates who have not presented a paper at the symposium



Tamas
Banyai
(PhD completed in 2015-2016)



Guéric
De Crombrugghe



Bernd
Helber
(PhD completed in 2015-2016)



Imre
Horváth
(PhD completed in 2015-2016)



Silvânia
Lopes
(PhD completed in 2015-2016)



Işil
Şakraker
(PhD completed in 2015-2016)



Sebastian
Scholl



Pierre-Louis
Schrooyen
(PhD completed in 2015-2016)



James B.
Scoggins



Chiara
Spaccapaniccia
(PhD completed in 2015-2016)



Erik
Torres



Stefano
Vagnoli
(PhD completed in 2015-2016)



Bart
Van Hove



Martin
Vymazal